Declaration of Authorship

I, Geoffroy Christian Paul CLAISSE , declare that the thesis entitled *Optimal Control Applied to Plane Couette Flow: (Towards the) Full-Information State-Feedback Stabilization of the Nagata Lower-Branch* and the work presented in the thesis are both my own, and have been generated by me as the result of my own original research. I confirm that:

- this work was done wholly or mainly while in candidature for a research degree at this University;
- where any part of this thesis has previously been submitted for a degree or any other qualification at this University or any other institution, this has been clearly stated;
- where I have consulted the published work of others, this is always clearly attributed;
- where I have quoted from the work of others, the source is always given. With the exception of such quotations, this thesis is entirely my own work;
- I have acknowledged all main sources of help;
- where the thesis is based on work done by myself jointly with others, I have made clear exactly what was done by others and what I have contributed myself;
- none of this work has been published before submission.

Signed:.....

Date:.....

UNIVERSITY OF SOUTHAMPTON

Optimal Control Applied to Plane Couette Flow: (Towards the) Full-Information State-Feedback Stabilization of the Nagata Lower-Branch

by

Geoffroy Christian Paul CLAISSE

Thesis for the degree of Doctor of Philosophy

in the

Faculty of Engineering and Physical Sciences
Department of Aeronautical and Astronautical Engineering
Aerodynamics and Flight Mechanics Group

Supervisors: Ati S. SHARMA and Davide LASAGNA
Examiners: Neil D. SANDHAM and Onofrio SEMERARO

September 2020

UNIVERSITY OF SOUTHAMPTON

ABSTRACT

FACULTY OF ENGINEERING AND PHYSICAL SCIENCES
DEPARTMENT OF AERONAUTICAL AND ASTRONAUTICAL ENGINEERING
AERODYNAMICS AND FLIGHT MECHANICS GROUP

Doctor of Philosophy

OPTIMAL CONTROL APPLIED TO PLANE COUETTE FLOW: (TOWARDS THE) FULL-INFORMATION STATE-FEEDBACK STABILIZATION OF THE NAGATA LOWER-BRANCH

by Geoffroy Christian Paul CLAISSE

Turbulence can be seen as deterministic chaos evolving within a finite dimensional dynamical state-space, where each invariant solution (IS) of the Navier-Stokes Equations (NSE) acts as an unstable attractor of the turbulent state. The mechanism by which the turbulent state remains/leaves the neighborhood of an IS is still not completely known. Supposedly, the turbulent dynamical state escapes the neighborhood of an IS along its unstable eigen-space, although recent work suggests that the non-normality of its stable eigen-space may help the turbulent trajectory to leave along stable directions.

To elucidate this process, we present a procedure to stabilize via linear optimal control the least-unstable IS of the NSE within a Plane Couette Flow (PCF) configuration, the Nagata lower-branch (EQ1).

Linear optimal control requires a linearized state-space model. Around an IS, this model is very high-dimensional, which prevents the solution of the associated Riccati equation and the finding of the optimal control law. Therefore, a new divergence-free model is derived and validated: the Orr-Sommerfeld Squire model Extended for an IS as baseflow. It resulted in a boundary actuated full-matrix state-space model. This model depicts faithfully the dynamical evolution of the flow in the neighborhood of an IS, reduces the dimension of the state and enables access to linear control theory.

It is now possible to build a full-information optimal control actuating via wall-transpiration and targeting the unstable eigenmodes of EQ1. Analytically, it was demonstrated that these modes are controllable with this actuation type, and that consequently, EQ1 is stabilizable. Within linear simulations, EQ1 was successfully stabilized. Yet, the stabilization was not achieved for the non-linear case. Further research would be needed to conclude on this limitation.

Contents

List of Figures

List of Tables

Acknowledgements

This mountaintop is beyond even eyesight.
How to reach it ? Not a single hint in my mind.
Only rocks, cliffs, wind and mist.
Tough is the ascension... is it only a mountain ?

I would like to thank my first supervisor, Ati Sharma, for his support and guidance through this research at the University of Southampton, and my second supervisor, Davide Lasagna, who was always attentive and helpful.

The researchers of the Aerodynamics and Fluid Mechanics (AFM) group collobarated remarkably and I would like to thank particurlarly Arslan Ahmed and Sabarish Vadarevu for their assistance, as well as my colleagues Rammah Shami, Adriano Cerminara, ThankGod Boye and Francis De Voogt for their support. I also won't forget researchers from other groups or universities, with whom we became friends, Yushan Gao and Georges Wagner. Your future is full of promise, Lebo Molefe. Keep going.

I would like to thank the University of Southampton and the Engineering and Physical Sciences Research Council (EPSRC), who not only believed in me and accepted to finance my Ph.D., but also created a favorable environment for my research.

Tobias Schneider and the entire ECPS group at the École Polytechnique Fédérale de Lausanne made my academic visit memorable. Thanks to Tobias, Florian Reetz, Sajjad Azimi, Omid Ashtari, Alessia Ferraro, Ayse Yesil, Emilio Vazquez, Simon Schütz and Mirko Farano. Moreover, thanks to Brigitte Larrieu and Arlette Lugeon, who made my sojourn realisable by according me to stay at their Swiss appartment for free.

In addition, I can not thank enough my two friends, the forward-floating fixed-point Kutalmis Bercin and Daryus Chandra, who taught me so much without even knowing it. I hope that English people will understand their universities build their reputation and prestige from people like you, and then ease the process for you to live and work in this country.

This thesis is the result of many life experiences. Many people will not have their names written on this pages, and some of them are even forgotten. However, without this multitude of interactions, I would not be where I am today. Thanks to the unnamed ones.

Finally, I can not forget my parents, Agnès and Philippe, and my girlfriend, Gaëlle. I am lucky to be born within a family where the parents did not count their hours to raise, educate and teach their child. They gave their best for me, and I aim to give the best of my lifetime to make them proud in return. It seems that my girlfriend is pursuing their work.

In this world, my life is fortunate. I will work hard to make yours and the ones of our children serene.

List of Acronyms

ADA Adjoint of the Direct-Adjoint 141–143, 149, 198, 208

AFM Aerodynamics and Fluid Mechanics xxi

CFBC ChannelFlow Boundary Condition package x, 88, 132, 161, 199, 200, 204, 206, 208, 211

CFD Computational Fluid Dynamics 12, 14, 87

DNS Direct Numerical Simulation 4, 14, 204

EQ1 PCF Nagata (1990) and Waleffe (2003) lower-branch solution 4, 5, 81, 105, 203, 204

FFT Fast Fourier Transform 48, 50, 51, 65

HPC High Performance Cluster 78, 149, 152, 172

IS Invariant Solution 61, 78, 80, 81, 85, 86, 89

LES Large-Eddy Simulations 14

LHS Left-Hand side 53

LNSE Linearised Navier-Stokes equations 88, 102

LQE Linear Quadratic Estimation 35, 36

LQG Linear Quadratic Gaussian 25, 27, 29, 32, 38–41, 44, 178, 200

LQR Linear Quadratic Regulation 5, 6, 29, 33, 38, 39, 44, 89, 103, 135, 143, 171, 204, 205, 207

LTI Linear time-invariant 45, 46, 56, 57, 61, 85, 88

MCE Minimum Control Energy Stabilization 141, 142, 149

NSE Navier-Stokes equations 2, 4, 11–14, 22–24, 43, 45, 46, 56, 57, 61, 75, 80, 81, 85, 86, 161, 198, 201, 203, 204, 209, 216

ODE Ordinary-differential equation 48, 272

OSS Orr-Sommerfeld Squire model 4, 45, 57, 61, 62, 66, 69, 75, 85, 88, 204, 216, 235

OSSE Orr-Sommerfeld Squire model Extended for a non-laminar solution xxvii, 5, 6, 45, 61, 65, 75, 77–81, 85–90, 96–100, 104–108, 132, 133, 148, 168, 204, 206, 208, 216–218, 245, 248, 250, 252

OSSI Oppositely-shifted Subspace Iteration 141, 142, 149

PCF Plane Couette Flow x, xii–xiv, xxiii, xxvi, xxvii, 4, 6, 10, 11, 16, 19, 21, 24, 45, 46, 48, 54, 57, 58, 61, 85–90, 113, 132, 151, 152, 156, 160–163, 165–169, 171, 172, 185–187, 190, 192, 193, 195, 197–199, 203–205, 207

PDAE Partial-differential algebraic equation 12, 46, 90, 91

POD Proper Orthogonal Decomposition 144

RANS Reynolds Averaged Navier-Stokes equations 14

RFFT Real Fast Fourier Transform 65, 73

RHS Righ-Hand side 53

ROSSE Real Orr-Sommerfeld Squire model Extended for a non-laminar solution xxvii, 6, 45, 65, 75, 77–81, 86–88, 105, 107, 108, 132, 133, 148, 168, 204–206, 208

SVD singular value decompositon 103, 105, 145, 258, 260

TPBVP Two-Point Boundary Value Problem 27

List of Symbols

Mathematics

$\mathbb{R}$	set of real numbers
$\mathbb{Z}$	set of natural numbers
$\mathbb{C}$	set of complex numbers
$\boldsymbol{\imath} = \sqrt{-1}$	imaginary unit
$\Re$	Real part
$\Im$	Imaginary part
t	time
I_n	identity matrix of dimension n
0	zero matrix
$\langle \, . \, , \, . \, \rangle$	dot product, scalar product
$\dot{x} \rightarrow \frac{\partial x}{\partial t}$	partial time differentiation of function x
∇	gradient operator
$\nabla \cdot$	divergence operator
∇^2	Laplacian operator
$.^T$	matrix transpose
$.^{-1}$	matrix inverse
$.^*$	Hermitian adjoint operator, conjugate transpose matrix
$\hat{.}$	Fourier coefficient
$\tilde{.}$	Chebyshev coefficient
T_{n_y}	Chebyshev polynomial of degree n_y
$\mathcal{D}^i$	Chebyshev differentiation matrix of degree i
k_x, k_z	streamwise and spanwise wavenumber indices
α, β	streamwise and spanwise wavenumbers
$k^2 := \alpha^2 + \beta^2$	
$\mathcal{W}$	Chebyshev grid weighting matrix (Weideman and Reddy, 2000, Clenshaw Curtis quadrature)
λ_i	ith eigenvalue
v_i,w_i	ith right and left eigenvectors
Λ	diagonal matrix of eigenvalues
$V = \begin{bmatrix} v_1 & \dots & v_n \end{bmatrix}$	matrix of right eigenvectors

$W = \begin{bmatrix} w_1 & \dots & w_n \end{bmatrix}^T$	matrix of left eigenvectors
φ_k	spatial-discretisation trial function (eq.4.11)
$\mathfrak{R}_N$	spatial-discretisation residual for approximation of order N (eq.4.12)
ψ_i	spatial-discretisation test function (eq.4.14)
$\mathcal{K}_m$	Standard Krylov subspace of reduced dimension m (§6.2.3)

Norms

For signals:

$\|\cdot\|_{2,[0,T]}$	finite-horizon Lebesgue 2-norm
$\mathcal{L}_2[0,T]$	finite-horizon Lebesgue 2-space
$\|\cdot\|_2$	infinite-horizon Lebesgue 2-norm
$\mathcal{L}_2(-\infty,\infty)$	infinite-horizon Lebesgue 2-space

For systems:

$\mathcal{L}_\infty$	space of systems mapping $\mathcal{L}_2(-\infty,\infty) \to \mathcal{L}_2(-\infty,\infty)$
$\|\cdot\|_\infty$	$\mathcal{L}_\infty$-norm
$\|\cdot\|$	norm induced by $\mathcal{L}_\infty$
$\bar{\sigma}$	maximal singular value of a system
$\|\cdot\|_{[0,T]}$	norm induced by $\mathcal{L}_2[0,T]$
$\|\cdot\|_{2,[0,T]}$	finite-horizon 2-norm
$\|\cdot\|_2$	infinite-horizon 2-norm

Fluid Dynamics

Θ	channel domain
L_x, L_z	streamwise and spanwise domain dimension
h	channel half-height, wall-normal dimension is $2h$
N_x, N_y, N_z	number of streamwise, wall-normal and spanwise discretisation points
ρ	fluid density
μ	fluid dynamic viscosity
ν	kinematic velocity
$Re = U_w\, h/\nu$	Reynolds number
$\mathfrak{M}$	momentum of a body
$\mathfrak{F}$	force applied to a body
U_w	absolute value of the streamwise velocity at the wall of a PCF configuration
$\vec{\boldsymbol{x}}$, $\vec{\boldsymbol{y}}$, $\vec{\boldsymbol{z}}$	unit-vectors for stream-wise, wall-normal and span-wise direction

$\mathcal{X} = (x, y, z)$	position in the domain Θ and coordinates
$\boldsymbol{U} = (U, V, W)$	velocity vector-field
$\boldsymbol{u} = (u, v, w)$	perturbation velocity vector-field
$\boldsymbol{U}_{lam}(y) = U_w\, y/h$	PCF laminar solution vector-field
$\bar{\boldsymbol{U}} = (\bar{U}, \bar{V}, \bar{W})$	Non-laminar baseflow velocity vector-field
$\hat{\boldsymbol{U}} = (\hat{U}, \hat{V}, \hat{W})$	Fourier coefficients of the non-laminar baseflow $\bar{\boldsymbol{U}}$
$\tilde{\boldsymbol{U}} = (\tilde{U}, \tilde{V}, \tilde{W})$	Chebyshev coefficients of non-laminar baseflow $\bar{\boldsymbol{U}}$
P	total pressure scalar-field
$\bar{P}$	base pressure scalar-field
p	perturbation pressure scalar-field
η_y, η	wall-normal vorticity vector-field
$\boldsymbol{\varrho} = (\varrho_x, \varrho_y, \varrho_z)$	non-linear terms
$A_{OSS}, E_{OSS}, B_{OSS}, \mathcal{L}_{OSS}$	Orr-Sommerfeld Squire operators
$\mathcal{L}_{OS}, \mathcal{L}_C, \mathcal{L}_{Sq}$	Orr-Sommerfeld, Coupling and Squire block matrices of $\mathcal{L}_{OSS}$
$\mathcal{L}$	OSSE and ROSSE operator eq.4.77 and eq.4.86
$A, B, C \ldots R, \Upsilon$	Block matrices used to define $\mathcal{L}$
$\mathbb{A}, \mathbb{B}, \mathbb{C} \ldots \mathbb{R}$	Block matrices used to define $\mathcal{L}$ actuated with wall-transpiration
$\mathcal{E}_T$	kinetic energy density eq.5.31
$\mathcal{C}$	transformation matrix between $[u, v, w]$ and $[v, \eta, u_{00}, w_{00}]$, app.C

Boundary condition notations for the non-actuated OSS, OSSE and ROSSE models:

∇_0^2, $\mathcal{D}_0$, ∇_0^4	differential operators non-imposed with boundary condition dedicated to the non-laminar baseflow $\bar{\boldsymbol{U}} = (\bar{U}, \bar{V}, \bar{W})$.
∇^2, $\mathcal{D}$, ∇^4	differential operators, imposed if necessary with boundary condition, e.g. Dirichlet and Neumann.

Boundary condition notations for the OSS, OSSE and ROSSE models actuated by wall-transpiration:

∇_0^2, $\mathcal{D}_0$, ∇_0^4	differential operators non-imposed with boundary condition dedicated to the non-laminar baseflow $\bar{\boldsymbol{U}} = (\bar{U}, \bar{V}, \bar{W})$.
$\mathring{\nabla}^2$, $\mathring{\mathcal{D}}$, $\mathring{\nabla}^4$	differential operators imperatively imposed with homogeneous boundary condition (Dirichlet, Neumann)
∇^2, $\mathcal{D}$, ∇^4	differential operators non-imposed with boundary condition

Flow Control

E_X	Expectation
τ	Actuation-time constant of the wall-transpiration low-pass filter
τ_c, f_c	Cutting-time and cutting frequency of τ
$\mathcal{A}, \mathcal{B}_{\{1,2\}}, \mathcal{C}_{\{1,2\}}, \mathcal{D}_{\{11,12,21,22\}}$	general controller matrices
$\boldsymbol{x} \in \mathbb{R}^n$	state-vector
$\boldsymbol{q} \in \mathbb{R}^m$	control signal, vector
$\boldsymbol{y} \in \mathbb{R}^q$	measurement signal, vector
$\boldsymbol{z} \in \mathbb{R}^p$	objective function, vector
$\boldsymbol{w}_{\{1,2\}} \in \mathbb{R}^l$	state and measurement disturbances
$.^0, .^+, .^-$	inner-field, upper-wall and lower-wall of a variable, eq.5.13
f^+, f^-	lifting functions for wall-transpiration associated with u, v, w
g^+, g^-	lifting functions for wall-transpiration associated with η_y
$\mathcal{T}$	transformation matrix between $[v^+, v, v^-]$ and $[v^+, v^0, v^-]$, eq.5.38
K	control feedback gain matrix
K^{opt}	optimal control feedback gain matrix
κ	weighting parameter associated with the actuation for the cost function

Chapter 1

Introduction

Throughout human history, populations moved and met other nations to love, battle, trade or learn. Within the last centuries, humans reached a dominant place on Earth, even becoming significant to its geology, ecosystems and climate (Oreskes, 2004; Rosenzweig et al., 2008). The International Commission on Stratigraphy is actually evaluating the definition of a new geological epoch, the "anthropocene" (Lewis and Maslin, 2015). In this day and age, it becomes apparent that resources and energy are limited and precious, concept in opposition with our current consumption (IPCC (2014): AR5 Synthesis Report on Climate Change; IPCC (2018): Special Report: Global Warming of 1.5 °C). Improvement in our scientific comprehension of physical phenomena and surrounding world is necessary, yet not sufficient, for a balanced and durable future. This Ph.D. aims to join this global movement by improving our fundamental understanding of fluid mechanics, and particularly fluid dynamics, namely how does a fluid —liquids or gases— behave in motion? Many disciplines are indeed directly impacted by our mastery of fluid dynamics: mechanical, civil, chemical and biomedical engineering, geophysics, oceanography, meteorology, astrophysics, biology, etc. Progress in fluid mechanics will cascade over these fields, and help us face the challenges of tomorrow.

Fluid Mechanics

Fluid mechanics is the physical science attempting to understand fluid behavior. One of the main focus of the discipline is the characterization of a phenomenon called "turbulence". Turbulence is the state of most commonly observed fluid flows. It usually appears as a disordered combination of unsteady vortices of different dimensions, in opposition to smooth and regular "laminar" flows, and exhibits a highly chaotic, multi-scale, three dimensional and non-linear evolution. These properties can be desired for mixing or heat transfer applications (Dimotakis, 2005; Hanjalić et al., 2019). However turbulence, as source of drag (Gatti and Quadrio, 2016), noise (Szoke and Azarpeyvand, 2017) or brief and localized energetic perturbations (Reddy and Henningson, 1993), is often regarded

as unfavorable. Hence researchers often try to delay, avoid or lessen turbulence (Gad-el Hak, 2000; Joslin and Miller, 2009).

Discovery of invariant solution, Dynamical State-Space, Naming convention

Turbulent flows are particularly complex to analyze due to a wide range of length scale interacting non-linearly and simultaneously. Nonetheless, experimental and numerical studies discovered coherent motions embedded in the turbulent flow (Robinson, 1991; Smits and Delo, 2001). These can be defined as regions where a fundamental flow variable, like velocity or pressure, exhibits a significant correlation with itself or another variable. In addition, improvement in computational power led to the recent findings of invariant solutions of the Navier-Stokes equations (the fundamental equations of fluid motion) by Nagata (1990, 1997); Gibson et al. (2008); Kawahara et al. (2012). Invariant solutions exist without any of the complex spatio-temporal intermittency characteristic of coherent structures observed in turbulent flows, hence they can be considered as "exact" (Waleffe, 2001). Invariant solutions are also referenced as "exact coherent structures" or "exact coherent state" to mark their connection to coherent motions, but this relation is still under active research (Waleffe, 2001, 2003).

How does the turbulent state leave an invariant solution & Research Problem

The discoveries of invariant solution set a new light on turbulence structure, and strengthened Hopf's (1948) concept of turbulence as a finite dimensional dynamical system. Each solution of the Navier-Stokes equations (NSE) is associated with a point motion in a state-space, where its phase motion can be followed — e.g. equilibria are fixed-point. The turbulent inertial manifold is depicted as a network of invariant solutions acting as unstable attractors of the turbulent dynamical state and interlinked via heteroclinic connections. Hamilton et al. (1995); Kawahara and Kida (2001) described the turbulent state dynamics as a chaotic walk around many of these attractors. Nonetheless, the mechanism by which the turbulent dynamical state remains and leaves the neighbourhood of an invariant solution is still unknown. By definition, the turbulent state cannot leave the neighbourhood of an invariant solution via its nonlinear unstable manifold. It is supposed that the turbulent dynamical state is pulled towards an invariant solution by its locally stable-attractive eigenmodes, but over some time, escapes its neighbourhood along its locally unstable-repulsive eigenmodes (Gibson et al., 2008), although recent work suggests that the non-normality of its locally stable eigenspace may help the turbulent trajectory to leave along locally stable directions (Farano et al., 2019). In the light of this, we will interfere via state-space control with the mechanism by which the turbulent dynamical state is leaving an invariant solution, in the hope to either explicate the process or stabilize the unstable invariant solution.

Introduction to state-space control

Originating from control engineering, "state-space" or "modern" control theory is a type of model-based control which exists alongside "classical" and "robust" control theory (Ogata, 2009). Model-based control denotes the attempt to mathematically design a given system with a set of differential equations to increase control efficiency, without appeal to trial and error or efforts based solely on physical intuition. While classical methods are established for frequency-domain analysis and rely on Laplace and Fourier transformations, modern state-space methods simplify the control design by analyzing the model in the time domain via simple matrix algebra and state-vector variables (Arrowsmith and Place, 1992). Therefore, state space control benefits from a broader range of applications compared to transfer function methods. Robust methods stand as an extension of modern control, where penalties are prescribed to mitigate potential errors in the model or perturbations (Green and Limebeer, 1995). The control approach in this thesis consists of active "closed-loop control", or "feedback control", i.e. it requires an external source of energy and the actuation is a real-time response to the measured state of the system. Such control has been applied to fluid dynamics problems and termed "flow control", notably with linear models by Joshi et al. (1997), Bewley and Liu (1998) and Kim and Bewley (2007).

Past studies on state-space flow control

Relaminarization of a channel flow has been accomplished by Sharma et al. (2011), using a passivity-based controller and actuation on the entire domain. In this approach, the non-linearity is considered as a passive feedback on the linear terms of the governing equation. The role of the controller is to enforce the linear system to be passive, such that the turbulent perturbation energy reduces and the flow becomes less turbulent. However, Martinelli et al. (2011) showed that a linear state-feedback control acting only on the domain border, even with full-state knowledge, is unable to ensure a strictly dissipative closed-loop system. Therefore, we do not expect the relaminarization of a channel flow to happen with linear state-feedback control whose actuation is limited to the wall. Despite this result, the turbulent energy production is still bounded and can be limited by a feedback control. For this reason, Heins (2015) developed a wall-transpiration controller to reduce the skin-friction drag with sensing of streamwise and spanwise wall shear stresses and wall pressure, which produces significant drag reduction when applied on the least passive streamwise constant modes. In this thesis, we will employ the benchmark developed by Heins (2015) in order to target a PCF invariant solution. However, the effect of non-normality between the stable-attractive modes might worsen when applying a controller and lead to quick energy growth and transition to turbulence.

Objective

A detailed representation of the turbulent state space, through the discoveries of new invariant solutions, and a deep understanding of its evolution mechanism are essential for technological applications that deal with fluid motion, i.e. the aeronautical, automotive or naval industries fighting for drag reduction, the chemical industry looking for better mixing properties or the energy sector troubled by unexpected heat-transfer. In this sense, certain coherent structures are better than others depending on the domain of application. Successfully describing the turbulent state-space is a crucial step to understand the non-linear, chaotic and high-dimensional properties of turbulence. Controlling and mastering its evolution mechanism is another, and this is where this project falls in.

The objective of this thesis is the stabilization via state-space control of the unstable eigenspace of a Plane Couette Flow (PCF) invariant solution, namely the Nagata (1990) lower-branch (referred to as EQ1). This requires to investigate the mechanism by which the turbulent state escapes an equilibrium, and particularly the role of the unstable manifold in the close neighborhood of the solution. The Nagata (1990) lower-branch solution was studied in detail by Clever and Busse (1997), as well as derived independently and extended to other boundary conditions by Waleffe (2003). This solution is the least unstable known invariant solution of the PCF configuration, and therefore constitutes the most accessible invariant solution to stabilize. To do so, direct numerical simulations (DNS) of a PCF channel flow initiated at EQ1 and regulated via optimal control are carried. Precisely, the controller is a state-feedback Linear Quadratic Regulator with full-information sensing — entire velocity and pressure fields are known — and enforced via wall-transpiration — blowing and suction at the upper and lower walls. This thesis is the initial step before trying to manipulate the turbulent state and target different invariant solution. Once the stabilization of the Nagata (1990) solution is successful, future works can focus on guiding the turbulent state towards the solution and stabilize it there, or enforcing the transition from one invariant solution to an other with a succession of specific control methods (see figure 1.1).

Procedure

The application of state-space control theory to invariant solutions requires a linearised state-space model. With this aim in mind, EQ1 is inserted as base-flow of the Navier-Stokes equations, instead of commonly used Couette laminar-state, in order to derive a simplified model the same fashion as the Orr-Sommerfeld Squire model (OSS) (Orr, 1907a,b; Sommerfeld, 1908). However, the derivation no longer diagonalises with Fourier wave-numbers due to the breaking of translational symmetry of the non-laminar base-flow. Henceforth, it requires taking account of crossed interactions between modes, which results in a divergence-free model, referenced in this thesis as the Orr-Sommerfeld Squire

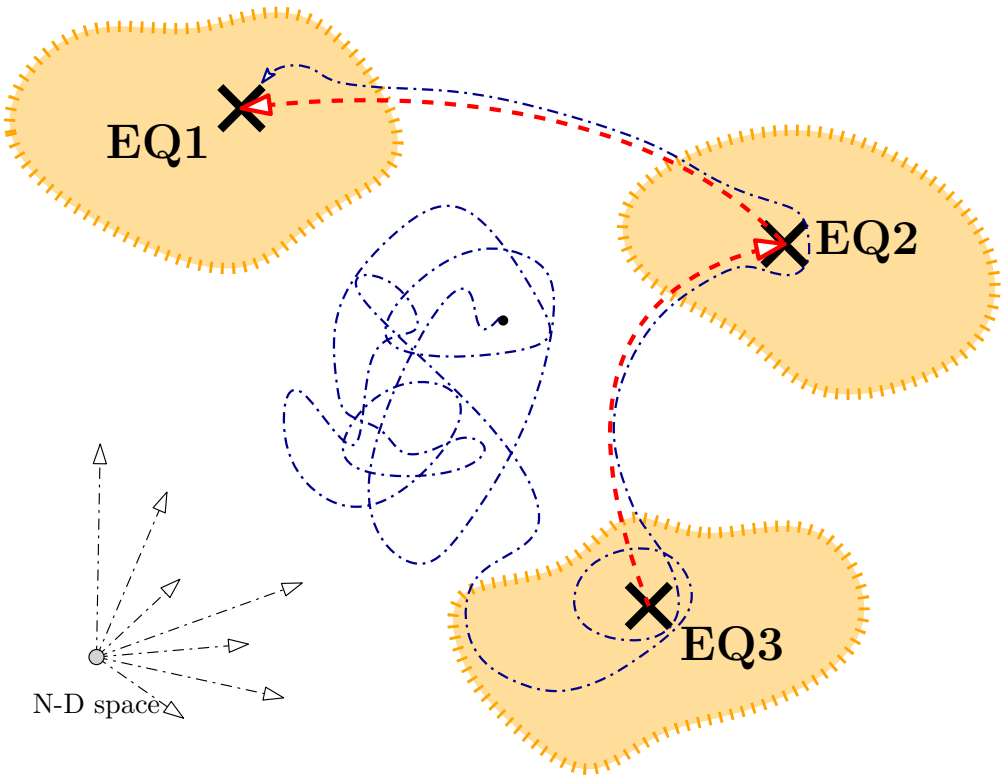

FIGURE 1.1: Idealized representation of the control of the turbulent state. Starting from a random initial condition (black dot), the turbulent state evolves in time along a chaotic trajectory (blue dotted-dashed line) within a high-dimensional manifold. One within the basin of attraction of a controlled equilibrium (orange-coloured area), e.g. EQ3, the turbulent state is attracted and stabilized on this specific solution. Through a different control method, the state is then repelled toward a different equilibrium, e.g. EQ2, along the connection between EQ3 and EQ3 (red dashed arrow), and stabilized once again. This "bridging" process is repeated in order to reach a desired equilibrium, e.g. EQ1, of lower energy level or more favorable for engineering applications.

model Extended for a non-laminar solution (OSSE). The OSSE model depicts faithfully the dynamical evolution of the flow in the neighbourhood of an invariant solution for small perturbations. It establishes a full-matrix state-space model that enables access to linear algebra and linear control theory for any non-laminar solution — not only invariant solutions, but any three-dimensional steady state — while reducing the dimension of the dynamical state by half. The model was then actuated to suit wall-forcing and validated against published literature by calculating the leading eigenmodes of different equilibria (Bewley and Liu, 1998; Gibson et al., 2008). Linear analysis of EQ1 identified its most unstable modes, i.e. the expected directions followed by the turbulent state to escape the solution (similarly to Cossu and Brandt (2004) on Tollmien-Schlichting waves which evaluates the energy production and dissipation of the most unstable waves and the stability of subharmonic modes). We showed that these modes are controllable by wall-transpiration, suggesting that EQ1 is stabilizable, and determined the most-effective actuation modes to target them. To stabilize the unstable mode of EQ1, an optimal control law is calculated via Linear Quadratic Regulation (LQR) (Green and Limebeer,

1995). This law stems from the solution of an high-dimensional algebraic Riccati equation, which consists in a full-order matrix characterized by the same high dimension n of the state and implies computational costs of order $\mathcal{O}(n^3)$ and storage requirements at least of order $\mathcal{O}(n^2)$ (Benner, 2004). Hence, a direct method is computationally intractable for systems of dimensions $n \approx 10^3 - 10^4$ (Benner et al. (2008), at the date of publication). Nonetheless, the reduction of state dimension in the OSSE model enables the direct solution of the Riccati equations for small yet meaningful dimensions. Therefore, the optimal control law is calculated once offline for different controller strengths. Linear analyses of the closed loop system are conducted to evaluate their stability and normality. We then initiate controlled simulations of the Nagata (1990) lower-branch solution monitored by these optimal control laws, firstly with the linear OSSE model and then the non-linear Channelflow software. To improve repeatability and the normality of the initial condition, simulations are initially perturbed in the direction of the leading eigenmode of EQ1 at a very small magnitude. Finally, the results and limitations of these simulations are presented and discussed alongside future directions of research.

Plan

After this introduction in chapter 1, chapter 2 introduces the definition and the representation of turbulence as deterministic chaos within a state-space representation. It particularly focuses on the role of invariant solutions in this description and establishes this thesis within the literature. Chapter 3 introduces the field of feedback control, and particularly LQR optimal control, the tool used in this thesis to stabilize an invariant solution. Chapter 4 constitutes the core of the model development. In this chapter, the numerical models representing the fluid flow in a channel configuration are derived. It includes notably the derivation of the Orr-Sommerfeld Squire model Extended for a non-laminar solution (OSSE) along its real-version, the Real Orr-Sommerfeld Squire model Extended for a non-laminar solution (ROSSE). Chapter 5 describes the controller synthesis. It implements the wall-transpiration actuation within the OSSE and ROSSE models, and defines the matrices composing the cost function of the controller. In this chapter, different linear analyses are conducted to determine the leading unstable eigenmodes, their controllability and the most effective actuation modes. It also demonstrates that the Nagata (1990) lower-branch is indeed the easiest non-laminar solution to stabilize. Chapter 6 delivers the mathematical derivation of the Riccati equation and a brief literature review on its resolution. It also includes a validation of our control design and its calculation, made by applying the process on the laminar Plane Couette Flow profile. Chapter 7 consists in the core result of this thesis, as the optimal control law is now employed on the Nagata (1990) lower-branch solution. The optimal control law is calculated along the procedure presented in chapter 6. After a linear analysis of the closed-loop system, the optimal control law is administered to both linear ROSSE and non-linear Channelflow simulations and the results of these simulations are presented.

Chapter 8 finally offers a discussion about these results and a conclusion. It specifies as well the future tasks necessary to pursue the project and new rising opportunities.

Literature Review

The literature review related to this project is inserted throughout the thesis in order to introduce some fundamental concepts beforehand. We hereby indicate their precise location to the reader.

The progress in the understanding of turbulence as a deterministic chaos is reviewed in section 2.4, notably the dynamical representation of turbulence, the finding of invariant solutions and the hypotheses about the behavior of the turbulent state in the neighborhood of invariant solutions. This research is introduced within this context in section 2.5.

Previous researches conducted on flow control are reviewed in sections 3.1 and 3.2. In particular, this project emerged from the previous publications of the main supervisor of this thesis, Ati Sharma, presented in section 3.6. They are focusing on robust control and passivity-based control with the purpose to stabilize a turbulent channelflow.

The main obstacle of this thesis consists in finding the solution of the optimal control problem associated with our system. It requires to solve a high-dimensional Riccati equation, which has been the focus of mathematicians for decades. Before attempting its solution, we reviewed the literature in section 6.2.

Finally, we performed a general review of linear algebra and of its fundamental concepts used in this thesis in appendix H.

Novel Contribution

The novel contribution contained within this thesis are as follows:

1. Update of the ChannelFlow Boundary Condition package of Heins (2015) and implementation of optimal control forcing within Channelflow version 1.5.1 (revison 452).
2. Derivation of the linear Orr-Sommerfeld Squire model Extended for a non-laminar solution (OSSE), and its real equivalent ROSSE model. Validation of these models against Channelflow by calculating the eigen-decomposition of different equilibria.
3. Full-information Linear Quadratic Regulation control design based on the OSSE and ROSSE models actuated via wall-transpiration. Validation against the actuation Channelflow for different actuation modes, for the laminar Plane Couette Flow profile and Nagata (1990) lower-branch solution.

4. Controllability and stabilizibility analysis of the Nagata (1990) lower-branch solution actuated by wall-transpiration: EQ1 is stabilizable via this type of actuation.

5. Procedure to determine to optimal control law based on the OSSE and ROSSE models. Validation on a laminar PCF profile with linear OSSE time-integrations and non-linear Channelflow simulations.

6. Linear stability achieved for the Nagata (1990) lower-branch solution actuated by wall-transpiration.

7. Attempt to stabilize the Nagata (1990) within a non-linear Channelflow configuration. Though this point failed, information was ascertained that will benefit future attempts.

Publications

At the time of the thesis defense on Friday the 10th of July 2020, no paper was yet sent to scientific journals for publication. Nonetheless, part of this work was presented during national and international conferences:

- 28 Aug. 2018 - Second Special Interest Group (SIG) Meeting in the UK Fluids Network: Flow instability, modelling and control, Imperial College London, UK.
- 27-29 Aug. 2019 - UK Fluid Network (UKFN) 2019 Conference, DAMPT University of Cambridge, UK.
- 3-6 Sept. 2019 - European Mechanics Society (Euromech), 17th European Turbulence Conference (ETC), Politecnico di Torino, Italy.
- 23-25 Mar. 2020 - 55th 3AF International Conference AERO2020, Poitiers, France (delayed to 2021 due to Covid-19 pandemic).

Chapter 2

Turbulence

2.1 Definition

Fluid motion —for liquid or gas— occurs in three different kinds: "laminar", "transitional" or "turbulent". Laminar flows are highly ordered in space and time and undisrupted. Such clean flows are mainly governed by diffusion and often evolve at a relatively low velocity, within small domains and/or for very viscous fluids. On the contrary, turbulent flows are highly disordered in both space and time, and often observed at high flow rate and/or in large domains. Turbulence is an unpredictable phenomenon, described by a chaotic, multi-scale, three-dimensional, highly disordered and non-linear evolution. It is the regime of convection and mixing, characterized by numerous swirls and wakes.

A "transition" from the laminar to the turbulent state appears when inertial forces strengthen in the fluid, e.g. at higher velocities. The ratio between diffusive and convective forces is altered: the diffusion is not sufficient to dissipate the inertial energy of the fluid and disturbances no longer decay. Due to the non-linearity —at least in part— of the governing equations of fluid motion, local patches of turbulence emerge and stay embedded within the laminar flows (Kline et al., 1967; Wygnanski and Champagne, 1973; Wygnanski et al., 1975). These patches expand with increasing inertial forces, up to a tipping point where the flow becomes fully turbulent.

The vast majority of flows generated in our surroundings are turbulent, e.g. wind, moving car, water in a sink, etc. The turbulent state is advantageous for mixing (Dimotakis, 2005), heat transfer (Hanjalić et al., 2019), or to reduce the drag of bluff bodies (Bearman and Morel, 1983). Nonetheless, turbulent flows also observe higher skin friction and produce more noise. Moreover, such flows are challenging to predict and simulate precisely. Their velocity and pressure fields can indeed fluctuate quickly and involve a wide range a length scale interacting non-linearly and simultaneously, whereas laminar flows can be described in simple equations.

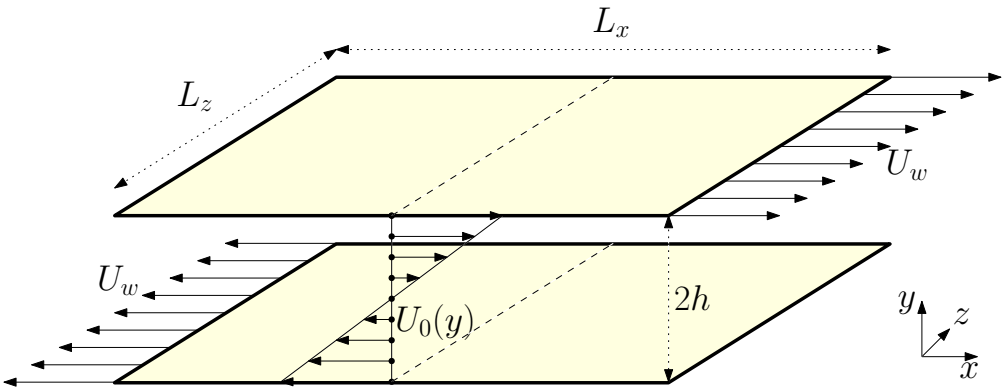

FIGURE 2.1: Diagram of a plane Couette Flow configuration.

2.2 Plane Couette Flow

The flow configuration considered in this thesis is a Plane Couette Flow (PCF): an incompressible viscous fluid is confined between two infinite parallel planes at height $+h$ and $-h$, moving at constant velocity U_w in opposite directions, see fig. 2.1. The streamwise, wall-normal and spanwise direction are respectively the x-axis, y-axis and z-axis, associated with the unit vectors $\vec{\boldsymbol{x}}$, $\vec{\boldsymbol{y}}$ and $\vec{\boldsymbol{z}}$. Bold characters will be used for three-dimensional vectors. As a notation example, the function associating a position $\mathcal{X}(x, y, z)$ of the PCF domain $\Theta \subset \mathbb{R}^3$ and a time $t \in \mathbb{R}_+$ to a velocity vector $\boldsymbol{U}(u, v, w) \in \mathbb{R}^3$, is defined as

$$\boldsymbol{U} : \quad \Theta \times \mathbb{R}_+ \to \mathbb{R}^3; \quad (\mathcal{X}(x, y, z), t) \mapsto \boldsymbol{U}(\mathcal{X}, t) = [u, v, w](x, y, z, t). \tag{2.1}$$

A periodic cell of size $L_x \times L_z$ is used to numerically approximate the infinite domain. Hence the domain Θ of this study is a periodic cell $[0, L_x] \times [-h, +h] \times [0, L_z]$. This configuration is advantageous for later discretisation into $Fourier \times Chebyshev \times Fourier$ modes.

Dirichlet and Neumann boundary conditions are applied to the channel upper and lower walls. An adherent (no-slip) and impermeable wall is specified by the Dirichlet condition

$$\boldsymbol{U}(x, y = \pm 1, z, t) = (\pm U_w \vec{\boldsymbol{x}}, 0, \pm U_w \vec{\boldsymbol{z}}) \tag{2.2}$$

as at the wall, wall-tangential fluid velocities are equal to the wall velocity $\pm U_w$ — adherence— and wall-normal velocities are set to zero —impermeability. Other applications of Dirichlet boundary conditions are pressure outlet, mass flow inlet, pressure far field, etc. The Neumann boundary condition

$$\frac{\partial \boldsymbol{U}}{\partial y}(x, y = \pm 1, z, t) = 0 \tag{2.3}$$

imposes a constraint on the derivative of a field at its borders. It is used to express a zero wall shear stress due to the wall roughness.

The pressure gradient is set to zero, hence no pressure drop occurs in streamwise or spanwise direction. The laminar Couette solution

$$\boldsymbol{U}_{lam}(y) = \frac{U_w y}{h} \tag{2.4}$$

can be deduced from the Navier-Stokes equations 2.16 using this assumption as well as flow symmetries.

A dimensionless quantity called "Reynolds number" is commonly used in fluid mechanics to express the degree of turbulence within a flow. The Reynolds number is the ratio of inertial forces to viscous forces within a fluid which is subjected to relative internal movement due to different fluid velocities, and defined as

$$Re = \frac{U_w h}{\nu} = \frac{\rho U_w h}{\mu}, \tag{2.5}$$

where ρ is the fluid density, μ the fluid dynamic viscosity and ν is the kinematic velocity. This study will focus on low-Reynolds number "transitional flow" (order less than $O(10^3)$).

PCF is the simplest of all shear flows and where roll-streak structures take their simplest form (Waleffe, 1997). It benefits of many symmetries which enable a reduction in the fluid degree of freedom, therefore reducing the complexity and cost of analytical or numerical analyses. Moreover, linear stability analyses demonstrated that PCF, along with Pipe Poiseuille flow, is linearly stable for all Reynolds numbers (Romanov, 1973; Schmiegel, 1999). The viscous instability does not occur for PCF (Drazin and Reid, 2004). For these reasons, PCF stands as a canonical configuration for new approaches and experiments, for instances: analyze shear-flow instabilities (Drazin and Reid, 2004); understand the self-sustaining regeneration mechanism of near-wall turbulence structures (Hamilton et al., 1995; Waleffe, 1997); describe the bursting phenomenon and hairpin structures in shear flows (Jiménez et al., 2005; Generalis and Itano, 2010; Itano and Generalis, 2009); discover invariant solutions of the Navier-Stokes equations (Nagata, 1990; Waleffe, 2001, 2003; Gibson et al., 2009); and explore dynamical state-space (Gibson et al., 2008; Halcrow, 2008). However, performing experimental PCF is difficult and the number of experimental studies is limited (Tillmark and Alfredsson, 1992).

The domain used here is the "W03 cell" from `channelflow.org` (Gibson et al., 2008; Gibson, 2014; Gibson et al., 2019) and first studied by Waleffe (2003), at $Re = 400$. It

corresponds to a channel of dimension given by $\alpha = 1.14$ and $\beta = 2.5$, where

$$\begin{aligned} L_x &= \frac{2\pi}{\alpha} \approx 5.511, \\ L_z &= \frac{2\pi}{\beta} \approx 2.513. \end{aligned} \tag{2.6}$$

2.3 Governing equations

The leading governing equations of fluid dynamics are the Navier-Stokes equations (NSE). They are composed of a set of Partial-differential algebraic equation (PDAE), essential to describe physical phenomena ranging from flows within blood vessels (Belardinelli and Cavalcanti, 1991) to interstellar gas motion (Boldyrev et al., 2002). Despite their major significance, their evolution is highly non-linear and chaotic, hence they stand as one of the most important problems in mathematics, namely the "Navier-Stokes existence and smoothness" problem. It has indeed not been proven that for arbitrary initial condition, smooth solutions always exist, or if they exists, that they have bounded energy. Computational Fluid Dynamics (CFD) aims to circumvent this problem by solving these equations with the help of numerical approximations, discretization and high performance computers.

Precisely, the NSE describes the condition of equilibrium between forces in a moving fluid, linking velocity, pressure, temperature and density. They are named after Claude-Louis Navier (1822) and George Gabriel Stokes (1842, 1843) and originates from the Newton (1687)'s second law of fluid motion:

> "In an inertial frame of reference, the vector sum of the forces $\mathfrak{F}$ on an object is equal to the rate of change of momentum $\mathfrak{M}$, namely the mass m of that object multiplied by its acceleration a", or in other terms,

$$\frac{\partial \mathfrak{M}}{\partial t} = \mathfrak{F} = ma. \tag{2.7}$$

The derivation of equation 2.7 towards the NSE is presented in Halcrow (2008) and Wikipedia contributors (2011d) and reproduced below. In a Eularian description, the change in momentum density over a period of time δt is given as

$$\delta \mathfrak{M} = \mathfrak{M}(\mathcal{X} + \boldsymbol{U}\delta t, t + \delta t) - \mathfrak{M}(\mathcal{X}, t) \tag{2.8}$$

for a small parcel of fluid at position $\mathcal{X}(x, y, z)$ within a domain $\Theta \subset \mathbb{R}^3$ and at velocity $\boldsymbol{U}(u, v, w) : \Theta \times \mathbb{R}_+ \to \mathbb{R}^3$. Expanding to the first order in δt gives

$$\delta \mathfrak{M} = \delta t \frac{\partial \mathfrak{M}}{\partial t} + u\delta t \frac{\partial \mathfrak{M}}{\partial x} + v\delta t \frac{\partial \mathfrak{M}}{\partial y} + w\delta t \frac{\partial \mathfrak{M}}{\partial z}, \tag{2.9}$$

implying that in a Lagrangian description, the rate of change in momentum density from the reference frame moving with the fluid is

$$\frac{D\mathfrak{M}}{Dt} = \frac{\partial \mathfrak{M}}{\partial t} + (\boldsymbol{U} \cdot \nabla)\mathfrak{M}. \tag{2.10}$$

Considering the fluid density $\rho(\mathcal{X}, t)$, implying a momentum density $\mathfrak{M} = \rho \boldsymbol{U}$, it follows

$$\boldsymbol{U}\frac{\partial \rho}{\partial t} + \rho \frac{\partial \boldsymbol{U}}{\partial t} + (\boldsymbol{U} \cdot \nabla)(\rho \boldsymbol{U}) = f, \tag{2.11}$$

where f is the force density. Considering the equation of the mass conservation

$$\frac{\partial \rho}{\partial t} + \nabla \cdot (\rho \boldsymbol{U}) = 0, \tag{2.12}$$

and restricting the derivation to incompressible fluid, for which the density ρ is constant, we obtain a divergence-free velocity field

$$\nabla \cdot \boldsymbol{U} = 0. \tag{2.13}$$

For a Newtonian fluid, the force density f derives from the Cauchy-stress tensor and is given by

$$f = -\nabla P + \mu \nabla^2 \boldsymbol{U}, \tag{2.14}$$

where $P : \Theta \times \mathbb{R}_+ \to \mathbb{R}$ is the pressure scalar field. Simplifying with the divergence-free condition 2.13 and inserting the forcing f from 2.14 into 2.11, leads to the final expression of the rate of change in momentum

$$\rho \frac{\partial \boldsymbol{U}}{\partial t} = -\rho\,(\boldsymbol{U} \cdot \nabla)\boldsymbol{U} - \nabla P + \mu \nabla^2 \boldsymbol{U}. \tag{2.15}$$

The NSE combined both rate of change in momentum and continuity equations. For incompressible Newtonian fluids, the NSE non-dimensionalised for a channel of half-height h and maximum laminar velocity U_w are expressed as

$$Momentum: \underbrace{\frac{\partial \boldsymbol{U}}{\partial t}}_{\text{Variation}} = -\underbrace{\boldsymbol{U} \cdot \nabla \boldsymbol{U}}_{\text{Convection}} - \underbrace{\frac{1}{\rho}\nabla P}_{\text{Pressure}} + \underbrace{\frac{1}{Re}\nabla^2 \boldsymbol{U}}_{\text{Diffusion}} + \underbrace{\boldsymbol{f}}_{\text{Forcing}}, \tag{2.16a}$$

$$Continuity: \nabla \cdot \boldsymbol{U} = 0, \tag{2.16b}$$

where $\boldsymbol{f} : \Theta \times \mathbb{R}_+ \to \mathbb{R}^3$ is a vector of body forces (gravity, inertial acceleration, electromagnetic forces).

The NSE are classified as convection-diffusion equations, i.e. is included the influence of both fluid motion via convective-advective terms and viscous stresses via diffusive terms (Brownian motion, particles collision...). Enforcing adiabatic and inviscid conditions, the NSE for incompressible and Newtonian flows simplify to the conservative (absence

of diffusive term) Euler equations

$$Momentum: \underbrace{\rho\frac{\partial \boldsymbol{U}}{\partial t}}_{\text{Variation}} = -\underbrace{\nabla P}_{\text{Pressure}} - \underbrace{\rho(\boldsymbol{U}\cdot\nabla)\boldsymbol{U}}_{\text{Convection}} + \underbrace{\boldsymbol{f}}_{\text{Forcing}}, \tag{2.17a}$$

$$Continuity: \nabla\cdot\boldsymbol{U} = 0. \tag{2.17b}$$

Finally, neglecting the convection term leads to vector diffusion equation, namely the Stokes equations, for incompressible Newtonian flows:

$$Momentum: \underbrace{\rho\frac{\partial \boldsymbol{U}}{\partial t}}_{\text{Variation}} = \underbrace{\mu\nabla^2\boldsymbol{U}}_{\text{Diffusion}} - \underbrace{\nabla P}_{\text{Pressure}} + \underbrace{\boldsymbol{f}}_{\text{Forcing}}, \tag{2.18a}$$

$$Continuity: \nabla\cdot\boldsymbol{U} = 0. \tag{2.18b}$$

2.4 Dynamical Representation of turbulence as deterministic chaos

2.4.1 Discovery of coherent motions/coherent structures

Broadly speaking, numerical simulations in Computational Fluid Dynamics are categorized according to their level of accuracy and speed in the computation of turbulence. The simplest and least accurate are simulations based on the Reynolds Averaged Navier-Stokes equations (RANS), as they capture the mean flow via a large number of the same experiment without any consideration for smaller scales. Then come the Large-Eddy Simulations (LES), which model the smaller scale by using a turbulence model and hence improve the modeling of turbulence. Finally, direct numerical simulations (DNS) directly solve the Navier-Stokes equations, even on the smaller scales, without resorting to turbulence models. The whole range of spatial and temporal scales of the turbulence are resolved, which is particularly costly, but also leads to more detailed flows results. With the huge improvement in computational power during the 2000s, DNS are now affordable for small domains. However, the non-linear and high-dimensional interactions within the NSE still evade our reach today and can not yet be fully explained. For that reason, observations from fluids dynamicists of large coherent motions in turbulence (e.g. in figure 2.2), through experimental (Liu, 1988; Liepmann, 1952; Lighthill, 1956; Kline et al., 1967; Reguera et al., 2000) and numerical studies (Kim et al., 1987; Gibson et al., 2008; Hamilton et al., 1995), are of particular interest.

Coherent motions have been described in the annual review of Robinson (1991), among other definitions, as a "three-dimensional region of the flow over which at least one fundamental flow variable (velocity component, density, temperature, etc.) exhibits significant correlation with itself or another variable over a range of space and/or time

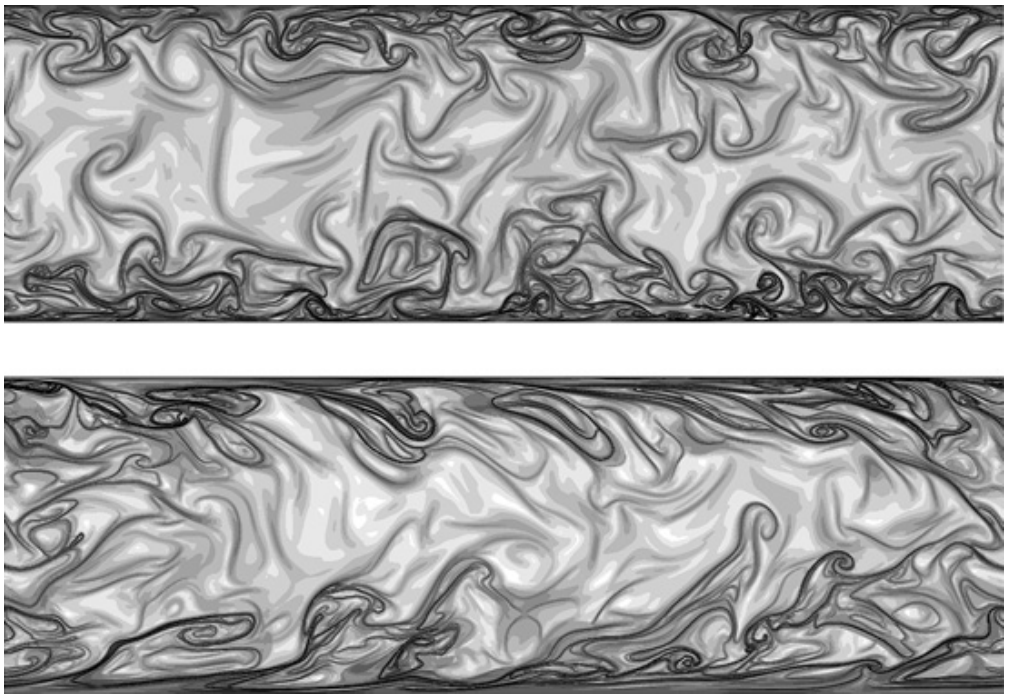

FIGURE 2.2: [Figure from Green et al. (2007)] Two-dimensional plots of structures identified using a method called Direct Lyapunov Exponent in a turbulent channel flow. Structures are three-dimensional and outlined in black. They are more dominant near the walls, as expected. (top - top view, bottom - side view)

that is significantly larger than the smallest local scales of the flow". Robinson (1991) and Smits and Delo (2001) reviewed the historical evolution of finding coherent structures and presented many of the conceptual models intended to explain these motions.

2.4.2 Chaotic State

Dynamical system theory aims to describe the characteristics of a system, like velocity profiles, pressure, etc., over time. If the dynamics of a given system are known, it may be possible to predict its evolution in time from initial conditions.

This section derives from the worthwhile book of Cvitanović et al. (2013), to which the reader is referred to deeply understand the notion of "chaos". A system is said to be deterministic when, given its evolution equations, its evolution is uniquely determined by its initial conditions and known exogenous inputs. In such condition, many trials of the same system within the same conditions will lead to the same results. Likewise, its evolution can be predicted forward or backward in time. On the contrary, stochastic systems evolve randomly and predicting their evolution is complex. The initial conditions determine their futures only partially. Many systems can be represented by a determined mathematical law and be qualified as deterministic. However, deterministic systems appear as stochastic if their dynamics are too complex. "Chaos" characterizes systems following deterministic laws of evolution, but their evolution is highly sensitive

to small changes in initial conditions. A chaotic system possesses hence two properties: high sensitivity to small uncertainties in initial conditions and dynamical laws confined in a finite dimensional state space, which makes the different trajectories mixing together.

Dynamical equations in fluid dynamics are well known, but also highly non-linear and complex. Small uncertainties in the state characteristics (approximation of the NSE, boundary conditions, initial conditions, calculation precision...) will result in different numerical or empirical evolutions. For that reason, turbulence is considered as a chaotic state. A dynamical representation based on the coherent structures can support a description of this chaos.

2.4.3 Dynamical representation of turbulence

Hopf (1948) was the first to introduce the idea of turbulence as a finite dimensional dynamical system (for a nice introduction to dynamical system, see Arrowsmith and Place (1992) and Strogatz (2018)). Hopf considered the velocity fields satisfying the NSE and associated boundary conditions as a phase or state included in a phase space Ω of "infinitely many dimensions". Each solution of the problem is associated with a point motion in Ω, and its phase motion can be followed in this space. Hopf wondered what would happen to the phase flow after an infinite time, and how the viscosity influences its behaviour. The steady laminar solution is embodied as a single point in Ω, an equilibrium, and after infinite time, every phase motion tends to this point for a sufficiently high viscosity. On the contrary, for low enough viscosity, the laminar solution is never reached and the flow is turbulent, forming chaotic trajectories in Ω. Hopf observed that the dimension of the manifold of solutions contracts with increasing viscosity, which let him conclude that after infinite time, the manifold of solutions has a finite dimension and is included within the infinite-dimensional space Ω. Nowadays, Ω is referenced as the "inertial manifold". Successfully describing this finite-dimensional manifold can help us understand the non-linear and high-dimensional structure of turbulence.

This new vision was investigated within a simple Plane Couette Flow configuration. Stability analysis of the PCF configuration demonstrated its stability to any infinitesimal perturbation for all finite Reynolds number (Romanov, 1973; Drazin and Reid, 2004; Nagata, 1990). The transition from a laminar flow with a linear velocity profile to a steady finite-amplitude solution is sudden and hard to track. For that reason, Nagata (1990) used a homotopy method applied on a Taylor Vortex Flow between two co-rotating cylinders, and found the first 3D steady solutions for a plane Couette flow. The same solutions were found by Busse and Clever (1992), who also used a homotopy method from a Rayleigh-Bénard flow, and by Waleffe (1998, 2003). Nagata (1997) discovered other solutions, in the form of travelling waves, and notably the upper branch of the Nagata (1990) solution.

These solutions look very similar to the coherent structures discovered in numerical and experimental turbulent flows of paragraph 2.4.1. Nonetheless, they exist without any of the complex spatio-temporal intermittency characteristic of coherent structures observed in turbulent flows, hence they can be considered as "pure" or "exact" coherent structures (Waleffe, 2001). In the literature, they are addressed as "exact coherent structures", "exact coherent states" or "invariant solutions" (Waleffe, 2003). In this thesis, we will employ the terminology "invariant solution" for solutions in continuous-time systems and "laminar-state" for the Couette and Poiseuille laminar profiles.

The significant progress in finding invariant solutions changed the way turbulence is considered. A promising idea emerging from dynamical theory and based on the vision of Hopf (1948) is to use these unstable invariant solutions to describe temporally and spatially complicated flows (Cvitanović, 1988; Artuso et al., 1990a,b). The newly found invariant solutions can serve as the basis of a new description in order to describe this chaotic evolution (Kerswell, 2005) and their connections and bifurcations could explain complex spatio-temporal intermittent process. In this perspective, the transition to turbulence could be explained as the succession of bifurcations from one solution to an other. The previously discovered coherent structures of §2.4.1 correspond to the least unstable invariant solutions; the dynamics of turbulence can be represented as a walk looping around these solutions (see figure 2.3); and the low-dimensionality explained by Hopf (1948) results from the low number of unstable modes for each state at a given Reynolds number, which attracts the turbulent state into a given direction. These solutions do not allow an effective prediction of turbulence, particularly at higher Reynolds number, but significant flow characteristics and theoretical understandings can be extracted from them (e.g. in section 2.4.5).

However, two points are important to note. Firstly, invariant solutions are full-scale unstable attractors of the turbulent phase, and do not constitute a modal decomposition of turbulence. It is not possible to employ the perspective used for spectral decomposition (see section 4.2), wherein the smallest length scale could be neglected to create a low order model. Secondly, invariant solutions and coherent structures are two distinct phenomena. To the best of the author's knowledge, no invariant solution has be found to correspond exactly to a coherent structure. Coherent structures are intermittent phenomena, while invariant solution are invariant/periodic under time evolution. Nonetheless, coherent structures may correspond to connections or bifurcations between different invariant solutions, or approach closely one or many periodic orbits.

2.4.4 Progress on finding Invariant Solutions

Invariant solutions emerge in different forms. Considering as Gibson et al. (2009) the velocity field $\boldsymbol{U}(\mathcal{X}, t)$, a representation $F_{NS}(\boldsymbol{U})$ of the Navier-Stoke equations for a given

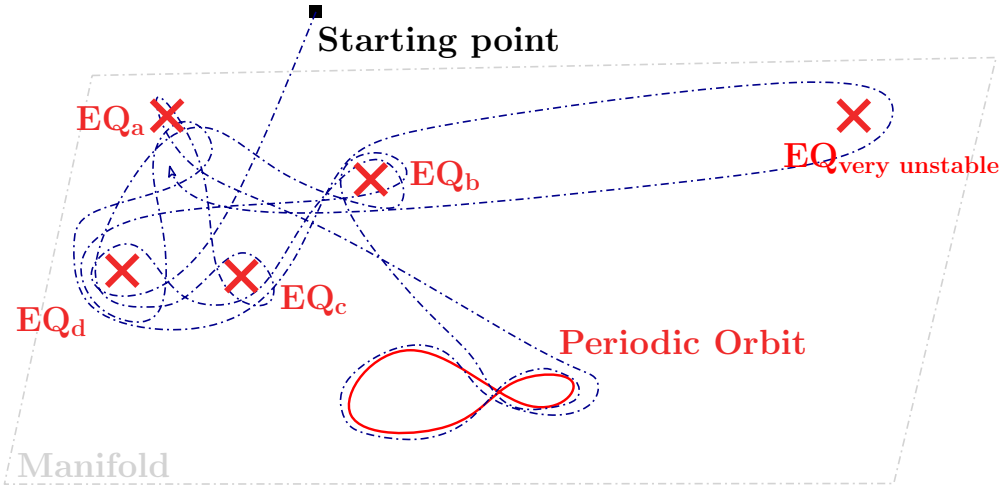

FIGURE 2.3: Dynamical evolution of a turbulent state: An initial condition (black square) decays rapidly to the inertial manifold (gray parallelogram) where the dynamics is governed by the invariant solutions (red crosses) or periodic orbits (red loop), acting as attractor of the dynamics. As the invariant solutions are unstable, the turbulent state is constantly repelled from the solution, never settles down and evolves in a chaotic manner (blue dotted-dashed line). Highly unstable invariant solution are rarely visited by the turbulent trajectory.

problem (§2.3), and its time-forward map f_{NS}^t, we can write

$$\frac{\partial \boldsymbol{U}}{\partial t} = F_{NS}(\boldsymbol{U}), \qquad f_{NS}^t(\boldsymbol{U}) = \boldsymbol{U} + \int_0^t F_{NS}(\boldsymbol{U}(\mathcal{X},\tau))d\tau. \tag{2.19}$$

For any period T, solutions are usually found in the form of:

- Equilibrium, $\boldsymbol{U}(\mathcal{X},t) = \boldsymbol{U}(\mathcal{X})$, satisfying $f_{NS}^T(\boldsymbol{U}) = \boldsymbol{U}$.
- Travelling wave, $\boldsymbol{U}(\mathcal{X},t) = \boldsymbol{U}(\mathcal{X} - ct)$, satisfying $f_{NS}^T(\boldsymbol{U}) = \mathcal{T}\boldsymbol{U}$ with $\mathcal{T} = \mathcal{T}(c_xT, c_zT)$, where c_x and c_z are wave velocities in streamwise and spanwise direction respectively and T is the time-period.
- Periodic orbit, $\boldsymbol{U}(\mathcal{X},t) = \boldsymbol{U}(\mathcal{X},t+T)$, satisfying $f_{NS}^T(\boldsymbol{U}) = \boldsymbol{U}$ with T the time-period.
- Relative periodic orbit, $\boldsymbol{U}(\mathcal{X},t) = \boldsymbol{U}(\mathcal{X} - ct, t+T)$, satisfying $f_{NS}^T(\boldsymbol{U}) = \mathcal{T}\boldsymbol{U}$.

Jiménez et al. (2005) compared equilibria and periodic solutions found previously and distinguished them with respect to their streamwise and wall-normal maximal velocities. They established two families of solutions: the "vortex dominated" solutions and the "streak dominated" ones. The vortex-dominated group gathers solutions similar to near-wall turbulence, with strong wall-normal velocities and slow streamwise component. It corresponds to the upper-branch solution of Nagata (1997), characterized by complex vortical structures. On the other side, streak-dominated solutions correspond to the lower branch of Nagata (1990) with weak vortical structures but strong

streamwise streaks. Fully developed turbulent simulations have closer statistics to the vortex-dominated group. Jiménez et al. (2005) saw these solutions as the main actor of the self-regeneration cycle of turbulence in viscous and buffer layers. Lower branch solutions and laminar ones only occasionally attract the state, even more rarely for perturbed flows, e.g. at higher Reynolds numbers or with a larger domain.

Gibson et al. (2008) produced a new method of visualization of the solutions of PCF, which projects the high dimensional state-space to one of much smaller dimension (e.g. 3D). This visualization is helpful to understand the dynamic of turbulent state and the attraction of unstable invariant solutions, and was notably used by Ahmed (2018) in his thesis. Gibson et al. (2009) continued this project by adding ten new equilibria and two travelling-wave solutions, finding again the one of the previous works of Nagata (1990, 1997). Details on the search process and geometries of PCF state space are presented in the thesis of Halcrow (2008), where the computation of equilibria, relative equilibria and heteroclinic connections is to link with the Ph.D. thesis of Schmiegel (1999), which was completed at a lower resolution. In his thesis, Halcrow (2008) speculates that the state space of a PCF configuration is composed of a multitude of invariant solutions, intertwined via different heteroclinic connections. These latter track the dynamical state of the flow between these solutions.

Itano and Generalis (2009) and Generalis and Itano (2010) found what they claim to be a new "hairpin" vortex solution in PCF, useful to describe the near-wall region of turbulent flows. They used the homotopy method, finding branches and bifurcations for a Lateral Heating Flow and then transforming them back to a PCF configuration. Their equilibria were also retrieved by Gibson et al. (2009).

The annual review of Kawahara et al. (2012) gathered many recently found solutions for different geometries and described how these invariant solutions embody statistical properties of turbulence. Velocity fields are qualitatively similar between solutions of different geometries (PCF, Poiseuille, Hagen-Poiseuille in circular pipe) as they often reproduce the same phenomena, for example the near-wall regeneration cycle of fully developed turbulent flows.

Many kinds of invariant solutions have been discovered in other configurations and improve our knowledge about coherent structures and turbulence intermittency (Jiménez and Kawahara, 2013). For example, in pipes flow, travelling waves have been discovered by Faisst and Eckhardt (2003); Wedin and Kerswell (2004); Pringle and Kerswell (2007), and relative periodic orbits by Duguet et al. (2008). In 2D Kolmogorov flows, invariant solutions were discovered by Chandler and Kerswell (2013) and, recently, Farazmand (2016) discovered 24 new steady states and periodic solutions using a method combining adjoint equations of Navier-Stokes equations and Newton-GMRES-hook-step iterations, which reproduced turbulence intermittency (see figure 2.4). In Plane Poiseuille Flow,

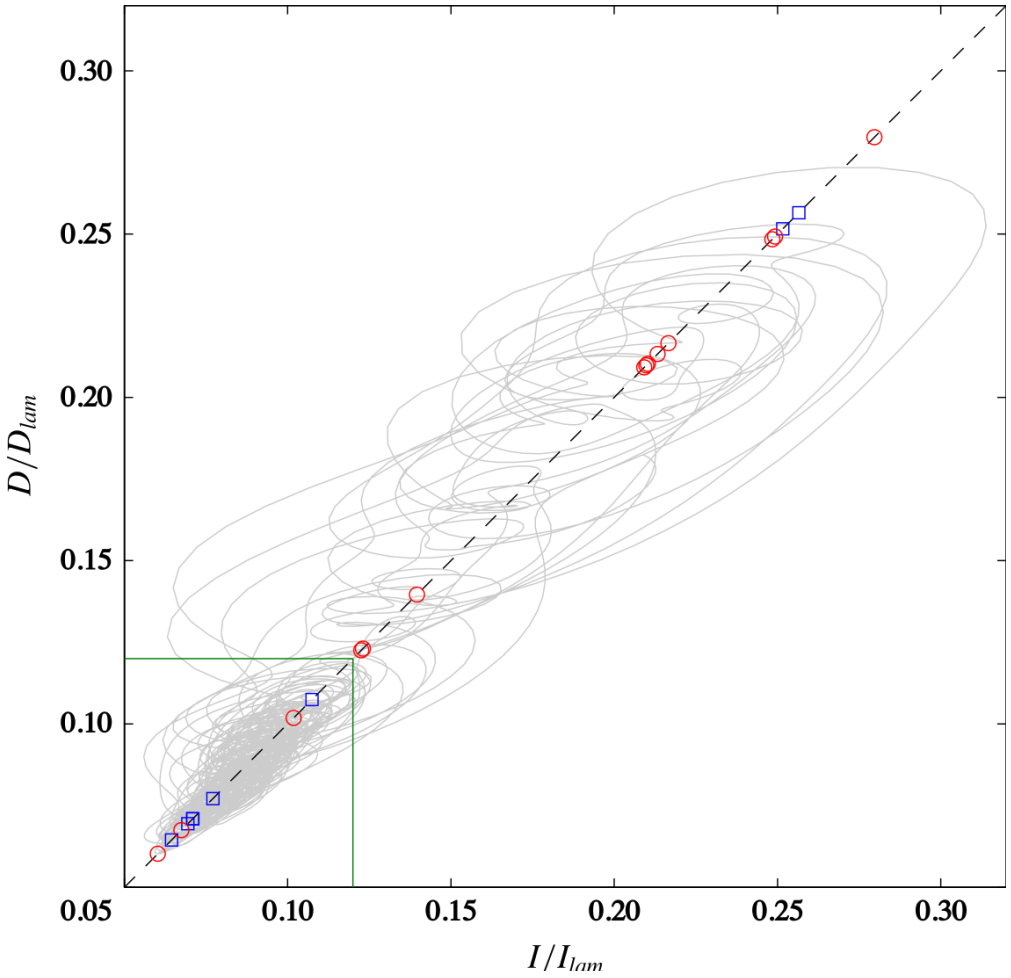

FIGURE 2.4: [Figure and label from Farazmand (2016), studying the generic turbulent trajectory in a Kolmogorov flow and representing the turbulent intermittency as well the importance of invariant solutions during high-energy phases.] (Colour outline) Results for Re = 40. Grey curve: turbulent trajectory spanning 10^3 time units. Red circles: equilibria. Blue squares: travelling waves. The green square marks the region where $I/I_{lam} < 0.12$ and $D/D_{lam} < 0.12$. The turbulent trajectory spends 86.62 % of the total 10^3 time units inside this region. The diagonal $I = D$ is marked by the dashed black line. Equilibria and travelling waves with $I/I_{lam} = D/D_{lam} > 0.32$ are not shown.

equilibria were found by Waleffe (2001) and travelling waves by Itano and Toh (2001) and Waleffe (2003) (also in PCF, both flows with free-slip and no-slip boundary conditions).

2.4.5 Examples of application of this new theory

Mean statistic

Mean statistic of a chaotic system can be retrieved from a limited number of unstable invariant solutions. For example, within a simple chaotic dynamical system with a large number of degrees of freedom, Kawasaki and Sasa (2005) managed to calculate the expected value of some macroscopic quantities as the energy dissipation rate from

a single periodic orbit. To do so, they used spatial averaging which possesses different properties than time averaging. It is therefore expected that statistical properties of turbulence can be obtained from a limited number of invariant solutions (Saiki and Yamada, 2008).

Self-sustaining cycle

A remarkable feature of near-wall structures observed in turbulent shear flow is that these structures are self-regenerative. The turbulence is sustained via the successive destruction and generation of coherent structures, which can be though as a "self-sustaining cycle". Hamilton et al. (1995) decomposed the regeneration process of a fully-developed turbulent flow into three phases: the formation of streaks by streamwise vortices, the breakdown of these streaks, and the generation of the streamwise vortices. Each phase is both the consequence and the cause of the other stages. On one hand, the streaks, defined as "elongated region of spanwise alternating low- and high-speed fluid", originates from the breakdown of the streamwise vortices, as they can transfer high-speed fluid from the mean flow closer to the wall and low-speed fluid from the near-wall region into the centerline. On the other hand, the vortices are generated via a non-linear interaction (Hall and Smith, 1991; Waleffe, 1995) after the rupture of the unstable streaks. This regeneration cycle was also described in Waleffe (1995, 1997). Nonetheless, the complete theoretical understanding and description of the self-sustaining cycle in a fully turbulent flow has not been exposed yet.

Invariant solutions offer the theoretical foundation to describe this phenomenon. Kawahara and Kida (2001) indeed reproduced the regeneration cycle within a PCF configuration. They found two time-periodic solutions connected with each other by a periodic orbit. These solutions are two unstable attractors, attracting the turbulent state occasionally before repelling it. The periodic orbit connecting these solutions approximates very well the turbulence self-sustaining cycle described by Hamilton et al. (1995); Waleffe (1995, 1997), and includes an energy burst similar to the rupture of the streaks. Viswanath (2007) also described the bursting phenomenon in a PCF after discovering five new solutions via a Newton-Krylov iteration and a locally constrained optimal hook step. Each of these five solutions demonstrates the breakup and re-formation of near-wall coherent structures.

Kawahara et al. (2012) reviewed the recent progresses in the discovery of invariant solutions and the advances in understanding the self-regeneration cycle of turbulence in low Reynolds number turbulent flows. They also noticed the similarity between the statistic of these solutions and different turbulent laws. The range of new non-linear solutions composes the simplest way to describe the coherent structures discovered in §2.4.1 and the near-wall self-sustaining cycle. Kerswell (2005) constitutes a useful review to understand these phenomena in pipe flow configuration.

Origin of self-organized oblique turbulent-laminar stripes observed in transitional flows

Invariant solutions can provide an explanation for the spatial structure of oblique stripe patterns observed in the laminar-turbulent transition to turbulence. This section relies on the recent publication in Nature Communication of Reetz et al. (2019), who discovered an invariant solution of the fully nonlinear NSE in PCF that captures the details of these structures. Within a PCF configuration, the laminar-turbulent transition appears as the breaking of the translational symmetries in both the streamwise and the spanwise directions. It causes regions of turbulent and laminar flow to coexist in space and even a regular pattern of alternating turbulent and laminar stripes to emerge. The wavelength of these stripes is much larger than the gap of the PCF configuration and they are obliquely oriented relatively to the streamwise direction. Both the large-scale wavelength and the oblique orientation of turbulent-laminar stripes must directly follow from the flow dynamics captured by the governing Navier-Stokes equations. However, even if experiments and numerical flow simulations reliably generate stripe patterns, a theory explaining the origin of the pattern characteristics is still missing. Experimental and numerical observations of self-organized oblique turbulent-laminar stripes in wall-bounded extended shear flows suggest the existence of exact invariant solutions underlying these patterns. Reetz et al. (2019) presented the first invariant solution that captures the detailed spatial structure of oblique stripe patterns, and provides a route towards explaining why turbulent-laminar stripes are oblique.

2.5 This research

The objective of this research is to evaluate the feasibility of the stabilization of the simplest form of invariant solution, an equilibrium, within an actuated PCF configuration those forcing is restricted to the wall of the domain. It requires to investigate the mechanism by which the turbulent dynamical state is leaving an invariant solution. The discoveries of coherent structures and invariant solutions set indeed a new light on turbulence structure, and strengthened Hopf's (1948) concept of turbulence as a finite dimensional dynamical system. Nonetheless, the mechanism by which the turbulent dynamical state remains and leaves the neighborhood of an invariant solution is still unknown. By definition, the turbulent state cannot leave the neighbourhood of an invariant solution via its nonlinear unstable manifold. In the context of dynamical representation, it is supposed that the turbulent state is attracted along the locally stable-attractive manifold of an invariant solution and then escapes the neighborhood of the solution along its locally unstable-repulsive manifold (Gibson et al., 2008), as sketched in figure 2.5a. In the light of this, we will interfere via state-space control with the mechanism by which the turbulent dynamical state is leaving an invariant solution, in the hope

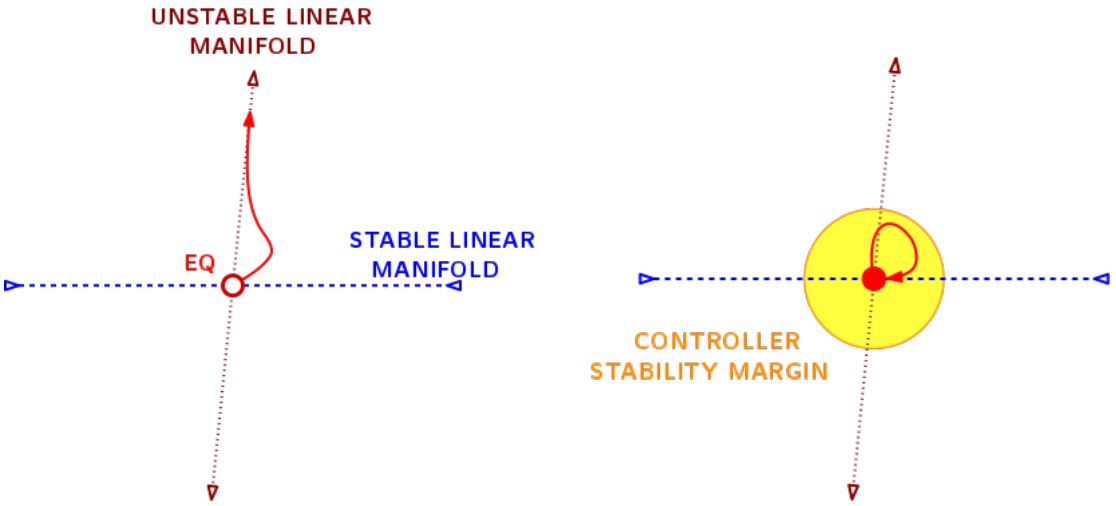

A) Dynamical state escaping an unstable invariant solution along its unstable linear manifold

B) Dynamical state maintained in the neighborhood of an invariant solution, now stable thanks to a stabilizing forcing.

FIGURE 2.5: Hypotheses on the mechanism by which the turbulent dynamical state is escaping the neighborbood of an invariant solution.

to either explicate the process or stabilize the unstable solution. Particularly, we will design an optimal control law in order to stabilize the locally unstable manifold of the Nagata (1990) lower-branch solution and consequently, maintain the dynamical state in the neighborhood of this solution. To make things clear, we do not plan to attract an arbitrary turbulent dynamical state towards Nagata (1990) solution and maintain it there as such an approach may not work given the lack of global stability guarantees. Rather, the idea is to locally stabilize EQ1 (introduce a radius of stability) and prevent the state to escape from the equilibrium (figure 2.5b).

This control law was capable of locally stabilizing linear simulations initiated at the Nagata (1990) solution, but our attempts with non-linear simulations were unsuccessful. This may arise due to the non-normality (see app. H.3.1) of the stable manifold of the Navier-Stokes equations linearized around an invariant solution. Some studies recently suggested indeed that non-normality may help the turbulent trajectory to leave along locally stable directions (Farano et al., 2019). This non-normality is associated with the curvature of the nonlinear unstable manifold and is responsible for a transient energy growth, characterized by a short time-scale and which may lead to non-linear instabilities. In opposition, the leading unstable eigen-directions are characterized by a long time-scale, expressing a long-term exponential growth. Therefore, the simple stabilization of the unstable manifold may not be sufficient to non-linearly stabilize the Nagata (1990) lower-branch solution.

Chapter summary

- The governing equations of fluid motion for a Plane Couette Flow configuration are the Navier-Stokes equations (NSE) 2.16. Despite being known for almost two centuries, they contain some of the most important problems in mathematics due to their non-linear and chaotic evolution.
- Turbulence is a multi-scale, three-dimensional, highly disordered, non-linear and chaotic phenomenon. Nonetheless, some patterns appear intermittently in the flow and are called "coherent motions". They can serve as fondation in the description of turbulence.
- "Exact" invariant solutions of the NSE were discovered numerically. They strengthened the dynamical representation of turbulence as deterministic chaos introduced by Hopf (1948). The dynamics of turbulence can be represented as a walk looping around these solutions within a high-dimensional state-space populated by many invariant solutions.
- There has been major progresses in the finding of invariant solutions. Collections of solutions under various form (equilibria, periodics orbits, torus, etc.) are now available for canonical flows like Plane Couette Flow, Plane Poiseuille Flow, Pipe Flows, etc.

Chapter 3

Feedback Control

Flow control designs a controller in order to alter a fluid flow into a desired outcome. This chapter introduces advances in flow control (§3.1, 3.2 & 3.3), before focusing on feedback control. Feedback control models a real system into a dynamical equivalent. Based on this model as well as the state of the system at a given time, it then derives a real-time control law. Particularly, we will employ a Linear Quadratic Gaussian feedback control, which is the reason why its mathematical foundations are presented in section 3.4. This chapter concludes on the robustness limitation of optimal control, and gives alternatives as robust control (§3.5) or passivity-based control (§3.6).

3.1 Introduction

Flow control refers to the research in fluid dynamics that aims at manipulating the dynamical state of fluid flows towards a desired result. Flow control is employed among other in order to reduce skin friction drag (Gatti and Quadrio, 2016), delay turbulence transition (Liepmann and Nosenchuck, 1982; Nouar et al., 2007), alter fluid mixing or combustion (Schuster et al., 2008; Luo and Schuster, 2009), reduce noise (Szoke and Azarpeyvand, 2017), prevent separation of the boundary layer to reduces structural loads (Gautier et al., 2015). In applications, it is applied to increase operability (lift increase), safety (stall prevention) and performance (fuel consumption, noise emission) in the aeronautical area, and similarly in the aerospace, naval and automotive sector, as well as in the chemical industry to mix agents or in agriculture to spread aerosols.

Feedback control is an engineering area investigated for many years already. We particularly recommend the books and reviews of Gad-el Hak (2000), Gunzburger (2002), Collis et al. (2004), Joslin and Miller (2009), Ogata (2009) and Wang and Feng (2018) for an overview of the theory, performances, limitations and promising possibilities of modern flow control. In brief, flow control can divided into different categories. The

first one is "passive" versus "active" control. Passive control is self-sufficient in energy and influence the flow by exploiting or altering properties of the boundary conditions, as for instances riblets (Bannier et al., 2016), Gourney flap (Wang and Feng, 2018, chapter 2), roughness (Wang and Feng, 2018, chapter 4), etc. On the other side, active control requires an external source of energy in order to actuate via wall-transpiration —blowing/suction at the wall— (Heins, 2015), wall oscillation (Jung et al., 1992), synthetic jets (Amitay and Glezer, 2006), etc. The second one is "open" versus "closed" loop systems. Open-loop systems do not consider the current state of the system to operate, and as a consequence, do not track any fluid characteristic. Parameters are set originally or independently of the current characteristics of the flow. Doing so reduces computational cost but also infringes performances as the "blind" controller will pursue the actuation even at inappropriate times. Closed-loop systems follow the state of the system in real-time via sensing devices (wall pressure, wall temperature, wall velocity, wall shear stress) and operate in response to a condition on the sensing quantities.

Early investigations of flow control were simple: The approach focused on the control of a specific phenomenon in order to prevent the appearance or enhancement of structures associated with turbulence. Nonetheless, no proper modeling of the flow was performed and the control design was based on intuition. Consequently, unexpected secondary events may emerge and lead to instabilities if the actuation ignites non-linear effects. An example of intuitive control is "opposition control", for which the interested reader can find references in Heins (2015) thesis.

In the 1990s, a new approach of flow control emerged, entitled model-based control. Based on this technique, described next section, we will build an active closed-loop control from a dynamical model of the flow, actuating via wall transpiration and supplied with entire knowledge of the velocity and pressure field, referred as "full-information".

3.2 Model based control

Model based control aims to model the dynamic of the fluid flow in order to alter precisely the state of the system. The desired outcome is translated into a mathematical cost function to minimize. This function targets characteristic of the flow as kinetic energy, wall-shear stress, temperature, etc., depending on the physical problem.

To our knowledge, the first attempt to control a laminar plane Poiseuille flow by combining both sensing and actuation was performed by Joshi et al. (1997) in a 2D configuration using a "classical" control design (proportional-integral control). Their objective was to stabilize the flow against the perturbations at the origin of the transition to turbulence. Unlike previous researches focusing solely on the actuation, their closed-loop system integrated sensing and estimation process. The locations of sensors and actuators dramatically changed the result of the control. Once the optimal locations were found, a

simple proportional integral controller stabilized the laminar Poiseuille system, and even remained robust at different Reynolds number.

A key publication of model based control and influential to this project is the paper of Bewley and Liu (1998). It introduces a new approach, often referred as "modern" control due to the application of optimal or robust control design. They created an active close-loop flow control of a linear system by breaking the system down into three "boxes": a "plant", an "estimator" and a "controller". The estimator estimates the state of the plant from limited measurement, while the controller determines the appropriate control signal according to the estimated state. They used the Orr-Sommerfeld-Squire equation to apply two different control methods: optimal $\mathcal{H}_2$ and robust $\mathcal{H}_\infty$ control. They aimed to stabilize the unstable eigenvalues of the model by minimizing the energy of the flow perturbations. This energy was estimated via streamwise and spanwise skin friction measurement and targeted with actuation by wall-transpiration. State disturbances and measurement disturbances were taken into account respectively in the "plant" and "estimator" and represented as uncorrelated white Gaussian noise for optimal $\mathcal{H}_2$ control, or worst-case disturbances for robust $\mathcal{H}_\infty$ control. A complete analysis of the controlled system was produced, including observability and controllability measure, eigenmodes decomposition, transfer function norms, and was compared with previous results from different type of control. For these reasons, Bewley and Liu (1998) stands as a benchmark in the realm of flow control. Bewley (2001) pushed further by reviewing the $\mathcal{H}_\infty$ control in plane Couette flow and giving insights for future promising research direction.

Kim and Bewley (2007) reviewed the recent advances in flow control. They divided the theory of model-based control design into two different approaches, differing in the procedure to derive the optimal control low. Firstly, the iterative Adjoint-based approach, applicable to nonlinear models or non-quadratic cost functions, consists, once the linear model associated with the system and the desired cost function defined, in extracting and solving the adjoint model. The optimal control and estimation laws then derives from the adjoint solutions and the cost function. Secondly, the direct-solution of the Riccati solution requires to derive a Two-Point Boundary Value Problem (TPBVP) from the Euler-Lagrange decomposition of the direct and adjoint system. Assuming a relation between direct and adjoint states, a differential or algebraic Riccati equation is formed, from which the optimal control and estimation law directly follows. Further details are given in chapter 6.

Many advances were made in the domain of model based control applied to fluid flow. Starting by Cortelezzi and Speyer (1998), a framework to derive optimal and robust reduced-order controllers of transitional boundary layers using Linear Quadratic Gaussian (LQG) design was presented and applied to 2D Poiseuille flow. Lee et al. (2001) followed with the design of a reduced-order LQG feedback control and its application to turbulent channel flow for drag reduction. Their system derived from the 2D Navier-Stokes equations and produced a wall-transpiration actuation from the measurement

of the turbulent streamwise wall-shear stress. Kim and Lim (2000) investigated the coupling between linear and non-linear processes in turbulent wall-bounded flows, and demonstrated that interior body forcing —forcing applied on the entire domain— was capable to relaminarize the turbulent flow. Hogberg et al. (2003) estimated the effectiveness of feedback control to significantly expand the basin of attraction of the laminar state in a subcritical nonlinear channel flow system, while Högberg et al. (2003) successfully applied linear full-state feedback optimal control to consistently relaminarize turbulent channel flow with particular mean-flow profiles, at $\Re_\tau = 100$, with full-state information and gain scheduling.

3.3 Linear Model

Linear models are employed to represent the dynamic of a system before designing an associated control. In the case of fluid dynamics, it is based on the linearised equations governing fluid motion for small perturbations, as for example the linearised Navier-Stokes equations presented in chapter 4. A linear model for flow control is represented in its state-space form as

$$\begin{aligned} E\dot{\boldsymbol{x}}(t) &= A\boldsymbol{x}(t) + B\boldsymbol{q}(t), \\ \boldsymbol{y}(t) &= C\boldsymbol{x}(t) + D\boldsymbol{q}(t), \end{aligned} \tag{3.1}$$

where $\boldsymbol{x} \in \mathbb{R}^n$ is a state vector, $\boldsymbol{q} \in \mathbb{R}^m$ is a control input vector, $\boldsymbol{y} \in \mathbb{R}^q$ is a measurement output vector, and matrices are all time-invariant matrices such as $A \in \mathbb{R}^{l\times l}$, $B \in \mathbb{R}^{l\times m}$, $C \in \mathbb{R}^{n\times l}$, $D \in \mathbb{R}^{n\times m}$ and $E \in \mathbb{R}^{l\times l}$.

Linearised models do not depict the non-linear interactions of fluid dynamics and fail to reproduce the energy transfer between large scale motions and small near-wall structures, responsible for the multi-scale property and the self-regeneration cycle of turbulence. Transition to turbulence driven by non-linearity is not be represented with such model Bewley and Liu (1998).

Nonetheless, linear models do not intend to represent precisely the dynamical evolution (bifurcations, equilibria, edge of chaos) or the statistic of the fluid system studied. A linear model only needs to approximate well enough a real fluid system in order to design a decent flow control. For that reason, the main characteristic required for this models is to faithfully embody the correlation between actuation inputs and physical outputs, and to include their influences on the energy cost function.

Special attention is required when dealing with matrix E, as its (nearly)-singularity may produce spurious modes. These latter are poorly resolved eigen-modes, present in the eigen-decomposition of the system but physically meaningless. For fluid dynamic

problem, projecting the state equations 2.16a on a divergence-free basis, where the continuity equation 2.16b is implicitly enforced, solves this limitation. This transformation is detailed in chapter 4 to derive the Orr-Sommerfeld Squire model and its equivalent model extended for an invariant solution.

3.4 Optimal Linear Quadratic Gaussian Control

Linear Quadratic Gaussian (LQG) control designs an optimal measurement-feedback control for linear systems where state and measurement disturbances are considered as uncorrelated zero-mean Gaussian white noise with known statistical properties. LQG control is actually composed of two separated entities: a Linear Quadratic Regulation (LQR) control, i.e. a full-information state-feedback control; and a Kalman filter, i.e. an optimal state estimation problem. Both are optimization problems in which an objective cost function subject to an equality constraint needs to be minimized. Hence, the process to form a LQG control consists in solving independently two optimization problems. The existence and uniqueness of an optimal solution to both problems has been demonstrated (Green and Limebeer, 1995). Moreover, the optimal solution is independent of the disturbances fed into the system. LQG control can be considered as a $\mathcal{H}_2$ control system. Details about each control design and this relations is given in Grimble and Kucera (1996).

Basic mathematical prerequisites are here introduced. They are established from the book of Green and Limebeer (1995), where the interested reader can find detailed demonstrations of the theorems presented below and lessons on robust control.

3.4.1 Robustness

Eigenvalues of the closed-loop model can be use to assert the stability of the model, or its observability and/or controllability (Green and Limebeer, 1995, Nyquist stability criterion, p.27). Despite this, these measures do not give any information about the robust stability or performance of the closed-loop. LQG does not automatically ensure good robustness properties (Green and Limebeer, 1995, p.27). Doyle (1978) indeed demonstrated that LQG optimal control have no guaranteed margins:

> "LQG solution provides no global system-independent guaranteed robustness properties."

As a consequence, optimal control is hardly applicable to real system, when minor modeling error can infringe the performance of the entire design. The robust stability of a LQG optimal closed loop must be checked a posteriori via the calculation of the sensitivities to different model error: additive (Green and Limebeer, 1995, theorem 2.4.3),

multiplicative (Green and Limebeer, 1995, theorem 2.4.4), inverse multiplicative (Green and Limebeer, 1995, theorem 2.4.5), etc. Yet, these error models do not constitute an exhaustive set of possible error. This fundamental drawback initiated the research into robust control, introduced in section 3.5.

3.4.2 Mathematical prerequisites

Size of signals

A signal f is considered as a measurable function

$$f: \quad \mathbb{R} \to \mathbb{R}^n; \quad t \mapsto f(t). \tag{3.2}$$

The size of a signal f is measured in the finite-horizon case thanks to its Lebesgue 2-norm $\|\cdot\|_{2,[0,T]}$, defined by

$$\|f\|_{2,[0,T]} = \left\{ \int_0^T \|f\|^2 dt \right\}^{\frac{1}{2}}. \tag{3.3}$$

Complementary, the finite-horizon Lebesgue 2-space $\mathcal{L}_2[0,T]$ is defined as the set of signals of finite 2-norm,

$$\mathcal{L}_2[0,T] = \left\{ f : \mathbb{R} \to \mathbb{R}^n \;\middle|\; \forall t < 0,\ f(t) = 0 \text{ and } \|f\|_{2,[0,T]} < \infty \right\}. \tag{3.4}$$

Similarly for the infinite-horizon case, the Lebesgue 2-norm $\|\cdot\|_2$ is defined as

$$\|f\|_2 = \left\{ \int_{-\infty}^{\infty} \|f\|^2 dt \right\}^{\frac{1}{2}}, \tag{3.5}$$

and the infinite-horizon Lebesgue 2-space $\mathcal{L}_2(-\infty,\infty)$ follows as

$$\mathcal{L}_2(-\infty,\infty) = \left\{ f : \mathbb{R} \mapsto \mathbb{R}^n \;\middle|\; \|f\|_2 < \infty \right\}. \tag{3.6}$$

Size of systems

A system G is a mapping from one signal space, the input space $\mathcal{S}_{in}$, to another signal space, the output space $\mathcal{S}_{out}$,

$$G: \quad \mathcal{S}_{in} \to \mathcal{S}_{out}. \tag{3.7}$$

The $\mathcal{L}_\infty$ space is defined as the set of systems mapping $\mathcal{L}_2(-\infty,\infty) \to \mathcal{L}_2(-\infty,\infty)$, or in others words, the set fo system G such that,

$$G: \quad \mathcal{L}_2(-\infty,\infty) \to \mathcal{L}_2(-\infty,\infty); \quad \boldsymbol{w} \mapsto \boldsymbol{z} = G\boldsymbol{w}, \tag{3.8}$$

which corresponds to the condition

$$\mathcal{L}_\infty = \Big\{ G : \|G\|_\infty < \infty \Big\}, \tag{3.9}$$

where the $\mathcal{L}_\infty$-norm is defined as

$$\|G\|_\infty = \sup_w \bar{\sigma}(G), \tag{3.10}$$

with $\bar{\sigma}$ is the maximal singular value of G.

The size of a system $G : \mathcal{S}_{in} \to \mathcal{S}_{out}$ with $\mathcal{S}_{in}$, $\mathcal{S}_{out}$ two normed spaces is measured with the induced norm $\|\cdot\|$ defined as

$$\|G\| = \sup_{w-\tilde{w}\neq 0} \frac{\|Gw - G\tilde{w}\|_{\mathcal{S}_{out}}}{\|w - \tilde{w}\|_{\mathcal{S}_{in}}}. \tag{3.11}$$

The norm of a system G induced by the finite 2-norm $\mathcal{L}_2[0,T]$ is denoted as $\|G\|_{[0,T]}$.

The 2-norm of a system $G : \boldsymbol{w} \mapsto \boldsymbol{z}$ can also be used in case the input is a unit variance white noise process, defined in the finite-horizon case by

$$\|G\|_{2,[0,T]} = E_X \left\{ \frac{1}{T} \int_0^T \boldsymbol{z}^*(t)\boldsymbol{z}(t)\, dt \right\}^{\frac{1}{2}}, \tag{3.12}$$

wher E_X is the expectation and in the infinite-horizon case by

$$\begin{aligned} \|G\|_2 &= \lim_{T\to\infty} \left(E_X \left\{ \frac{1}{T} \int_0^T \boldsymbol{z}^*(t)\boldsymbol{z}(t)\, dt \right\}^{\frac{1}{2}} \right) \\ &= \int_{-\infty}^{\infty} trace(G(t)G^*(t))dt. \end{aligned} \tag{3.13}$$

3.4.3 LQG problem - System and introductory statements

We introduce a general time-varying plant-system to present different notions of control theory,

$$\dot{\boldsymbol{x}}(t) = A(t)\,\boldsymbol{x}(t) + B_1(t)\,\boldsymbol{w}(t) + B_2(t)\,\boldsymbol{q}(t), \qquad \boldsymbol{x}(0) = 0, \tag{3.14a}$$

$$\boldsymbol{z}(t) = C_1(t)\,\boldsymbol{x}(t) + D_{12}(t)\,\boldsymbol{q}(t), \tag{3.14b}$$

$$\boldsymbol{y}(t) = C_2(t)\,\boldsymbol{x}(t) + D_{21}(t)\,\boldsymbol{w}(t), \tag{3.14c}$$

in which $\boldsymbol{q}$ is a m-vector control inputs (actuation), $\boldsymbol{w}$ is a l-vector of external disturbance inputs (state and measurement), $\boldsymbol{z}$ is a p-vector of objectives, $\boldsymbol{y}$ is a q-vector of controller

inputs (measurements) and $\boldsymbol{x}$ is a n-dimensional state-vector. It is assumed that

$$\begin{aligned} p &\geq m, \\ l &\geq q. \end{aligned} \tag{3.15}$$

We also considered the loop-shifting $D_{11} = D_{22} = 0$ and a scalings $D_{12}^* D_{12} = I_m$, $D_{21} D_{21}^* = I_q$ in our controller synthesis problem. These transformations are developed in Green and Limebeer (1995) [§4.6] using linear fractional transformations. They do not lead to any loss of generality but decrease the complexity of the following notions.

Finite horizon

The purpose of LQG is to seek a causal, linear controller $\boldsymbol{q} = K\boldsymbol{y}$ such that the finite-horizon 2-norm of the closed-loop system $R_{\boldsymbol{w}\mapsto\boldsymbol{z}}$ mapping the external disturbance inputs $\boldsymbol{w}$ to the objective $\boldsymbol{z}$ is minimized, given

$$\|R_{\boldsymbol{w}\mapsto\boldsymbol{z}}\|_{2,[0,T]} = E_X\left\{\frac{1}{T}\int_0^T \boldsymbol{z}^*\boldsymbol{z}\,dt\right\}^{\frac{1}{2}}. \tag{3.16}$$

Infinite horizon

The infinite horizon case, $T \to \infty$, is equivalent to consider considering the model 3.14 as time-invariant. In this scenario, the purpose of LQG is to seek a causal, linear controller $\boldsymbol{q} = K\boldsymbol{y}$ such that the infinite-horizon 2-norm of the closed-loop system $R_{\boldsymbol{w}\mapsto\boldsymbol{z}}$ mapping $\boldsymbol{w}$ to $\boldsymbol{z}$ is minimized, given

$$\|R_{\boldsymbol{w}\mapsto\boldsymbol{z}}\|_2 = \lim_{T\to\infty}\left(E_X\left\{\frac{1}{T}\int_0^T \boldsymbol{z}^*\boldsymbol{z}\,dt\right\}^{\frac{1}{2}}\right). \tag{3.17}$$

For the infinite horizon case, some "standard assumptions" are required, whose usefulness becomes apparent in sections 3.4.4 and 3.4.5:

Standard assumptions:

1. (A, B_2) *is stabilizable.*
2. $rank\begin{bmatrix} A - \boldsymbol{\imath} wI & B_2 \\ C_1 & D_{12} \end{bmatrix} = n + m$ *for all real* w.
3. (A, C_2) *is detectable.*
4. $rank\begin{bmatrix} A - \boldsymbol{\imath} wI & B_1 \\ C_2 & D_{21} \end{bmatrix} = n + q$ *for all real* w.

3.4.4 Full information controller - Linear Quadratic Regulator (LQR)

A Linear Quadratic Regulation (LQR) follows from the time-varying plant-system 3.14, with no consideration for the measurement $\boldsymbol{y}$,

$$\dot{\boldsymbol{x}}(t) = A(t)\,\boldsymbol{x}(t) + B_1(t)\,\boldsymbol{w}(t) + B_2(t)\,\boldsymbol{q}(t), \qquad \boldsymbol{x}(0) = 0, \tag{3.18a}$$

$$\boldsymbol{z}(t) = C_1(t)\,\boldsymbol{x}(t) + D_{12}(t)\,\boldsymbol{q}(t). \tag{3.18b}$$

Crossed-terms removal

A change of variable is operated to remove the crossed-terms in the expression the 2-norms $\|R_{\boldsymbol{w}\mapsto\boldsymbol{z}}\|_{2,[0,T]}$ and $\|R_{\boldsymbol{w}\mapsto\boldsymbol{z}}\|_2$, arising from the product $\boldsymbol{z}^*\boldsymbol{z}$. In system 3.18, the variable $\boldsymbol{q}$ is replaced by $\tilde{\boldsymbol{q}} = \boldsymbol{q} + D_{12}^* C_1 \boldsymbol{x}$. It leads to a new state and objective functions substituted of system 3.18,

$$\dot{\boldsymbol{x}}(t) = \tilde{A}(t)\,\boldsymbol{x}(t) + B_1(t)\,\boldsymbol{w}(t) + B_2(t)\,\tilde{\boldsymbol{q}}(t), \qquad \boldsymbol{x}(0) = 0, \tag{3.19a}$$

$$\tilde{\boldsymbol{z}}(t) = \begin{bmatrix} \tilde{C}\boldsymbol{x}(t) \\ \tilde{\boldsymbol{q}}(t) \end{bmatrix}, \tag{3.19b}$$

where

$$\tilde{A} = A - B_2 D_{12}^* C_1, \tag{3.20a}$$

$$\tilde{C}^*\tilde{C} = C_1'(I - D_{12}D_{12}^*)C_1. \tag{3.20b}$$

System 3.19 simplifies future derivation and theorems without any loss of generality, as $\tilde{\boldsymbol{z}}^*\tilde{\boldsymbol{z}} = \boldsymbol{z}^*\boldsymbol{z}$ and $\|R_{\boldsymbol{w}\mapsto\tilde{\boldsymbol{z}}}\|_2 = \|R_{\boldsymbol{w}\mapsto\boldsymbol{z}}\|_2$ hold. The transformation is fully detailed in Green and Limebeer (1995) [§5.2.3] and final results with the original expression 3.14 are given at the end of the section.

The purpose of LQR is to seek a causal, linear, full-information controller of the form

$$\tilde{\boldsymbol{q}} = \begin{bmatrix} K_1 & K_2 \end{bmatrix} \begin{bmatrix} \boldsymbol{x} \\ \boldsymbol{w} \end{bmatrix}. \tag{3.21}$$

Finite-horizon case

The 2-norm objective function $\|R_{\boldsymbol{w}\mapsto\boldsymbol{z}}\|_{2,[0,T]}$ of the closed-loop system,

$$\begin{aligned} \|R_{\boldsymbol{w}\mapsto\boldsymbol{z}}\|_{2,[0,T]} = \|R_{\boldsymbol{w}\mapsto\tilde{\boldsymbol{z}}}\|_{2,[0,T]} &= E_X\left\{\frac{1}{T}\int_0^T \tilde{\boldsymbol{z}}^*\tilde{\boldsymbol{z}}dt\right\}^{\frac{1}{2}}, \\ &= E_X\left\{\frac{1}{T}\int_0^T \boldsymbol{x}^*\tilde{C}^*\tilde{C}\boldsymbol{x} + \tilde{\boldsymbol{q}}^*\tilde{\boldsymbol{q}}dt\right\}^{\frac{1}{2}}, \end{aligned} \tag{3.22}$$

is minimized by the state-feedback optimal control law

$$\tilde{\boldsymbol{q}}^{opt} = -B_2^* P \boldsymbol{x}, \tag{3.23}$$

in which P is the solution of the differential Riccati equation

$$-\dot{P} = P\tilde{A} + \tilde{A}^* P - PB_2 B_2^* P + \tilde{C}^* \tilde{C}, \qquad P(T) = 0. \tag{3.24}$$

An unique non-negative solution of the differential Riccati equation 3.24 always exists. The optimal cost $\|R_{\boldsymbol{w}\mapsto\boldsymbol{z}}\|_{2,[0,T]}^{opt}$ derives from the state-feedback control law 3.23 (Green and Limebeer, 1995, theorem 3.3.1, p.94), as

$$\|R_{\boldsymbol{w}\mapsto\boldsymbol{z}}\|_{2,[0,T]}^{opt} = \min \|R_{\boldsymbol{w}\mapsto\boldsymbol{z}}\|_{2,[0,T]} = \left\{ \frac{1}{T} \int_0^T tr(B_1^* P B_1)\, dt \right\}^{\frac{1}{2}}. \tag{3.25}$$

It is possible to generate all controllers satisfying $\|R_{\boldsymbol{w}\mapsto\boldsymbol{z}}\|_{2,[0,T]} \leq \gamma$ using a set composed of two mapping systems, as long as $\gamma \geq \|R_{\boldsymbol{w}\mapsto\boldsymbol{z}}\|_{2,[0,T]}^{opt}$ (Green and Limebeer, 1995, §5.2.1).

Infinite-horizon case

In the infinite-horizon case, the system is assumed time-invariant. In this scenario, in order for a stabilizing controller to exist, it is necessary that the pair $(\tilde{A}, B_2)$ is stabilizable, which is true if the pair (A, B_2) is also stabilizable —Standard Assumption 1, (Green and Limebeer, 1995, App. A). Moreover, the existence of a solution to the algebraic Riccati equation 3.28 presented below will requires that the pair $(\tilde{A}, \tilde{C})$ has no unobserbable mode on the imaginary axis, i.e. the closed-loop dynamic of the controller be asymptotically stable —Standard Assumption 2, (Green and Limebeer, 1995, §5.2.2, p.189).

The 2-norm objective function $\|R_{\boldsymbol{w}\mapsto\boldsymbol{z}}\|_2$ of the closed-loop system,

$$\begin{aligned} \|R_{\boldsymbol{w}\mapsto\boldsymbol{z}}\|_2 = \|R_{\boldsymbol{w}\mapsto\tilde{\boldsymbol{z}}}\|_2 &= \lim_{T\to\infty} \left(E_X \left\{ \frac{1}{T} \int_0^T \tilde{\boldsymbol{z}}^* \tilde{\boldsymbol{z}}\, dt \right\}^{\frac{1}{2}} \right), \\ &= \lim_{T\to\infty} \left(E_X \left\{ \frac{1}{T} \int_0^T \boldsymbol{x}^* \tilde{C}^* \tilde{C} \boldsymbol{x} + \tilde{\boldsymbol{q}}^* \tilde{\boldsymbol{q}} dt \right\}^{\frac{1}{2}} \right), \end{aligned} \tag{3.26}$$

is minimized over the class of controllers that are internally stable —respect the standard assumptions— by the state-feedback optimal control law

$$\tilde{\boldsymbol{q}}^{opt} = -B_2^* P \boldsymbol{x}, \tag{3.27}$$

in which P is the solution of the algebraic Riccati equation

$$P\tilde{A} + \tilde{A}^*P - PB_2B_2^*P + \tilde{C}^*\tilde{C} = 0. \tag{3.28}$$

A unique non-negative stabilizing solution of the algebraic Riccati equation 3.28 always exists as long as the standard assumptions are satisfied. The optimal cost $\|R_{\boldsymbol{w}\mapsto\boldsymbol{z}}\|_2^{opt}$ derives from the state-feedback control law 3.27 (Green and Limebeer, 1995, theorem 3.3.1, p.94), as

$$\|R_{\boldsymbol{w}\mapsto\boldsymbol{z}}\|_2^{opt} = \min\|R_{\boldsymbol{w}\mapsto\boldsymbol{z}}\|_2 = \left\{tr(B_1^*PB_1)\right\}^{\frac{1}{2}}. \tag{3.29}$$

It is possible to generate all controllers satisfying $\|R_{\boldsymbol{w}\mapsto\boldsymbol{z}}\|_2 \leq \gamma$ using a set composed of two mapping systems, as long as $\gamma \geq \|R_{\boldsymbol{w}\mapsto\boldsymbol{z}}\|_2^{opt}$ (Green and Limebeer, 1995, §5.2.2).

Inclusion of crossed-terms

The full-information optimal control associated with the system 3.14 —including crossed-terms— is thus given by

$$\begin{aligned} \boldsymbol{q}^{opt} &= \tilde{\boldsymbol{q}} - D_{12}^*C_1\boldsymbol{x}, \\ &= -(B_2P + D_{12}^*C_1)\,\boldsymbol{x}, \\ &= -F\,\boldsymbol{x}, \end{aligned} \tag{3.30}$$

where P is the solution to the differential Riccati equation 3.24 in the finite-horizon case, or algebraic Riccati equation 3.28 in the infinite-horizon case.

3.4.5 Kalman Filter - optimal Linear Quadratic Estimation

Previous section focused on full-information control, hence complete knowledge of the state $\boldsymbol{x}$ and of the disturbance input $\boldsymbol{w}$ are assumed. However, the system 3.14c gathers information solely about the measurement $\boldsymbol{y}$. How shall we estimate the state and the input disturbance from this measurement? The Kalman filter, or Linear Quadratic Estimation (LQE), is the optimal solution to this problem. In other words, the Kalman filter seeks the optimal solution $\boldsymbol{x}_{est}^{opt}$ to estimate the state $\boldsymbol{x}$ and the Gaussian disturbance $\boldsymbol{w}$ from the measurement $\boldsymbol{y}$.

We consider the following general system

$$\dot{\boldsymbol{x}}(t) = A(t)\,\boldsymbol{x}(t) + B_1(t)\,\boldsymbol{w}(t) + B_2(t)\,\boldsymbol{q}(t), \qquad \boldsymbol{x}(0) = 0, \tag{3.31a}$$

$$\boldsymbol{y}(t) = C_2(t)\,\boldsymbol{x}(t) + D_{21}(t)\,\boldsymbol{w}(t), \tag{3.31b}$$

with the scaling $D_{21}D_{21}' = I$.

The purpose of LQE is to seek a causal, linear filter F such that $\boldsymbol{z}_{est}^{opt} = F\boldsymbol{y}$ is an optimal estimate of $\boldsymbol{z} = L\boldsymbol{x}$ with L a continuous matrix. We try to minimize the 2-norm $\|R_{\boldsymbol{w}\mapsto\boldsymbol{z}_{est}^{opt}-\boldsymbol{z}}\|_{2,[0,T]}$ or $\|R_{\boldsymbol{w}\mapsto\boldsymbol{z}_{est}^{opt}-\boldsymbol{z}}\|_2$ where $R_{\boldsymbol{w}\mapsto\boldsymbol{z}_{est}^{opt}-\boldsymbol{z}}$ is the system mapping the external disturbance input $\boldsymbol{w}$ to the difference $\boldsymbol{z}_{est}^{opt} - \boldsymbol{z}$ between optimal estimated and actual objective.

The filtering problem, without the interaction of the control $\boldsymbol{q}$, is represented as the linear fractional transformation

$$\begin{bmatrix} \dot{\boldsymbol{x}}(t) \\ (\boldsymbol{z}_{est}^{opt} - \boldsymbol{z})(t) \\ \boldsymbol{y}(t) \end{bmatrix} = \begin{bmatrix} A & B_1 & 0 \\ -L & 0 & I \\ C_2 & D_{21} & 0 \end{bmatrix} \begin{bmatrix} \boldsymbol{x}(t) \\ \boldsymbol{w}(t) \\ \boldsymbol{z}_{est}^{opt}(t) \end{bmatrix}, \qquad \boldsymbol{x}(0) = 0, \tag{3.32a}$$

$$\boldsymbol{z}_{est}^{opt}(t) = F\boldsymbol{y}(t). \tag{3.32b}$$

Minimizing the 2-norm objective $\|R_{\boldsymbol{w}\mapsto\boldsymbol{z}_{est}^{opt}-\boldsymbol{z}}\|_{2,[0,T]}$ or $\|R_{\boldsymbol{w}\mapsto\boldsymbol{z}_{est}^{opt}-\boldsymbol{z}}\|_2$ of the direct problem 3.32 is equivalent to minimize the 2-norm objective $\|\bar{R}_{\boldsymbol{w}\mapsto\boldsymbol{z}_{est}^{opt}-\boldsymbol{z}}\|_{2,[0,T]}$ or $\|\bar{R}_{\boldsymbol{w}\mapsto\boldsymbol{z}_{est}^{opt}-\boldsymbol{z}}\|_2$ of the adjoint associated problem,

$$\begin{bmatrix} \dot{\boldsymbol{p}}(\tau) \\ \bar{\boldsymbol{z}}(\tau) \\ \bar{\boldsymbol{w}}(\tau) \end{bmatrix} = \begin{bmatrix} A^* & -L^* & C_2^* \\ B_1^* & 0 & D_{21}^* \\ 0 & I & 0 \end{bmatrix} \begin{bmatrix} \boldsymbol{p}(\tau) \\ \bar{\boldsymbol{w}}(\tau) \\ \boldsymbol{q}(\tau) \end{bmatrix}, \qquad \boldsymbol{p}(\tau = 0) = 0, \tag{3.33a}$$

$$\boldsymbol{q}(\tau) = F^*\bar{\boldsymbol{w}}(\tau), \tag{3.33b}$$

where $\boldsymbol{p}$ is the adjoint state of $\boldsymbol{x}$, $\tau = T - t$ is the time-to-go variable of the adjoint system and $\bar{\cdot}$ stands for adjoint. Consequently, we try to minimize the 2-norm of the adjoint system $\|\bar{R}_{\boldsymbol{w}\mapsto\boldsymbol{z}_{est}^{opt}-\boldsymbol{z}}\|_{2,[0,T]}$ or $\|\bar{R}_{\boldsymbol{w}\mapsto\boldsymbol{z}_{est}^{opt}-\boldsymbol{z}}\|_2$.

It is noteworthy here to notice that the adjoint system 3.33 is a full-information control problem, in which the control signal $\boldsymbol{q}$ is function of the disturbance $\bar{\boldsymbol{w}}$ only, and independent of the adjoint-state $\bar{\boldsymbol{p}}$. However, for a full-information controller, knowledge of $\bar{\boldsymbol{w}}$ only is equivalent to knowledge of $\bar{\boldsymbol{w}}$ and $\bar{\boldsymbol{p}}$ (Green and Limebeer, 1995, §5.3.1, p.198). The optimal solution of the Kalman filter therefore proceeds from the full-information optimal control problem.

Crossed-terms removal

A change of variable is operated to remove the crossed-terms in expression the 2-norms $\|\bar{R}_{\boldsymbol{w}\mapsto\boldsymbol{z}_{est}^{opt}-\boldsymbol{z}}\|_{2,[0,T]}$ or $\|\bar{R}_{\boldsymbol{w}\mapsto\boldsymbol{z}_{est}^{opt}-\boldsymbol{z}}\|_2$, arising from the product $\bar{\boldsymbol{z}}^*\bar{\boldsymbol{z}}$. In system 3.33, the variable $\boldsymbol{q}$ is replaced by $\bar{\boldsymbol{q}} = \boldsymbol{q} + D_{21}B_1^*\boldsymbol{p}$. It leads to a new state and objective functions

$$\dot{\boldsymbol{p}}(\tau) = \bar{A}^* \, \boldsymbol{p}(\tau) - L^* \, \bar{\boldsymbol{w}}(\tau) + C_2^* \, \bar{\boldsymbol{q}}(\tau), \qquad \boldsymbol{p}(0) = 0, \tag{3.34a}$$

$$\bar{\boldsymbol{z}}(\tau) = \begin{bmatrix} \bar{B}^* \boldsymbol{p}(\tau) \\ D_{21}^* \bar{\boldsymbol{q}}(\tau) \end{bmatrix}, \tag{3.34b}$$

where

$$\bar{A} = A - B_1 D_{21}^* C_2, \tag{3.35a}$$

$$\bar{B}\bar{B}^* = B_1 (I - D_{21}^* D_{21}) B_1^*. \tag{3.35b}$$

The optimal solution of the full-information control adjoint-problem 3.34 follows from section 3.4.4, and will be transposed in the finite-horizon and infinite-horizon case for the original problem 3.31.

Finite-horizon case

In the finite-horizon case, the 2-norm objective

$$\begin{aligned} \|\bar{R}_{\boldsymbol{w} \mapsto \boldsymbol{z}_{est}^{opt} - \boldsymbol{z}}\|_{2,[0,T]} &= E_X \left\{ \frac{1}{T} \int_0^T (\boldsymbol{z}_{est}^{opt} - \boldsymbol{z})^* (\boldsymbol{z}_{est}^{opt} - \boldsymbol{z}) dt \right\}^{\frac{1}{2}}, \\ &= E_X \left\{ \frac{1}{T} \int_0^T (\boldsymbol{z}_{est}^{opt} - L\boldsymbol{x})^* (\boldsymbol{z}_{est}^{opt} - L\boldsymbol{x}) dt \right\}^{\frac{1}{2}}. \end{aligned} \tag{3.36}$$

is minimized by the optimal filter

$$\dot{\boldsymbol{x}}_{est}^{opt}(t) = (\bar{A} - QC_2^* C_2)(t) \, \boldsymbol{x}_{est}^{opt}(t) + Q(t) C_2^*(t) \boldsymbol{y}(t) + B_2(t) \, \boldsymbol{q}(t), \quad \boldsymbol{x}_{est}^{opt}(0) = 0, \tag{3.37a}$$

$$= \bar{A}(t) \, \boldsymbol{x}_{est}^{opt}(t) + Q(t) C_2^*(t) \; (\boldsymbol{y}(t) - C_2(t) \, \boldsymbol{x}_{est}^{opt}(t)) + B_2(t) \, \boldsymbol{q}(t), \tag{3.37b}$$

$$\boldsymbol{z}_{est}^{opt}(t) = L(t) \, \boldsymbol{x}_{est}^{opt}(t), \tag{3.37c}$$

in which $\boldsymbol{x}_{est}^{opt}$ is the optimal estimate of $\boldsymbol{x}$ and $Q(t)$ is the solution of the differential Riccati equation

$$\dot{Q} = Q\bar{A}^* + \bar{A}Q - QC_2^* C_2 Q + \bar{B}\bar{B}^*, \qquad Q(0) = 0. \tag{3.38}$$

This optimal estimation solution of 3.32 derives from the optimal state-feedback control law of the associated adjoint problem 3.34,

$$\bar{\boldsymbol{q}}^*(\tau) = -C_2(\tau) Q(\tau) \, \hat{\boldsymbol{p}}(\tau), \tag{3.39}$$

leading to the expression of the optimal adjoint state

$$\dot{\hat{\boldsymbol{p}}}(\tau) = \bar{A}^*(\tau)\,\hat{\boldsymbol{p}}(\tau) - L^*(\tau)\bar{\boldsymbol{w}}(\tau) - C_2^* C_2(\tau) Q(\tau)\hat{\boldsymbol{p}}(\tau), \qquad \hat{\boldsymbol{p}}(\tau = 0) = 0, \tag{3.40a}$$

$$= (\bar{A}^* - C_2^* C_2 Q)(\tau)\,\hat{\boldsymbol{p}}(\tau) - L^*(\tau)\bar{\boldsymbol{w}}(t). \tag{3.40b}$$

The optimal estimate of $\boldsymbol{z} = L\boldsymbol{x}$ is $\boldsymbol{z}_{est}^{opt} = F\boldsymbol{y} = L\boldsymbol{x}_{est}^{opt}$. The matrix QC_2^* is called the Kalman filter gain and the term $(\boldsymbol{y} - C_2(t)\,\boldsymbol{x}_{est}^{opt})$ is the innovations process. Finally, the optimal cost is

$$\|\bar{R}_{\boldsymbol{w}\mapsto \boldsymbol{z}_{est}^{opt}-\boldsymbol{z}}\|_{2,[0,T]}^{opt} = \min\|\bar{R}_{\boldsymbol{w}\mapsto \boldsymbol{z}_{est}^{opt}-\boldsymbol{z}}\|_{2,[0,T]} = E_X\left\{\frac{1}{T}\int_0^T trace(LQL^*)dt\right\}^{\frac{1}{2}}. \tag{3.41}$$

Infinite-horizon case

In the infinite-horizon case, the system 3.31 is assumed time-invariant. We want to minimize the cost $\|\bar{R}_{\boldsymbol{w}\mapsto \boldsymbol{z}_{est}^{opt}-\boldsymbol{z}}\|_2$ given as

$$\|\bar{R}_{\boldsymbol{w}\mapsto \boldsymbol{z}_{est}^{opt}-\boldsymbol{z}}\|_2 = \lim_{T\to\infty}\left(E_X\left\{\frac{1}{T}\int_0^T (\boldsymbol{z}_{est}^{opt} - \boldsymbol{z})^*(\boldsymbol{z}_{est}^{opt} - \boldsymbol{z})dt\right\}^{\frac{1}{2}}\right). \tag{3.42}$$

The optimal filter follows as

$$\dot{\boldsymbol{x}}_{est}^{opt}(t) = \bar{A}\,\boldsymbol{x}_{est}^{opt}(t) + QC_2^*\,(\boldsymbol{y}(t) - C_2\,\boldsymbol{x}_{est}^{opt}(t)) + B_2(t)\,\boldsymbol{q}(t), \qquad \boldsymbol{x}_{est}^{opt}(0) = 0, \tag{3.43a}$$

$$\boldsymbol{z}_{est}^{opt}(t) = L\,\boldsymbol{x}_{est}^{opt}(t), \tag{3.43b}$$

in which Q is the solution of the algebraic Riccati equation

$$Q\bar{A}^* + \bar{A}Q - QC_2^*C_2Q + \bar{B}\bar{B}^* = 0. \tag{3.44}$$

The solution Q exists if and only if the pair $(\bar{A}, C_2)$ is detectable, which is true is the pair (A, C_2) is also detectable —Standard Assumption 3— and the pair $(\bar{A}, \bar{B})$ has no unobservable mode on the imaginary axis — Standard Assumption 4.

Finally, the optimal cost is

$$\|\bar{R}_{\boldsymbol{w}\mapsto \boldsymbol{z}_{est}^{opt}-\boldsymbol{z}}\|_2^{opt} = \min\|\bar{R}_{\boldsymbol{w}\mapsto \boldsymbol{z}_{est}^{opt}-\boldsymbol{z}}\|_2 = \left\{trace(LQL^*)\right\}^{\frac{1}{2}}. \tag{3.45}$$

3.4.6 Measurement Feedback - Linear Quadratic Gaussian control

Measurement feedback control, or Linear Quadratic Gaussian (LQG) control, combines both LQR control and Kalman filter estimation. This sections assembles the results of previous sections 3.4.4 and 3.4.5. Firstly, the Kalman filter estimation allows for

the optimal estimation of the state $\boldsymbol{x}_{est}^{opt}$ from the measurement $\boldsymbol{y}$. Secondly, the LQR determines the optimal control law $\boldsymbol{q}^{opt}$ in order to stabilize the system. The separation principle guarantees that the solution of each problem can be designed independently.

Finite-horizon case

Considering the time-varying system 3.14, the purpose of LQG is to seek a causal, linear controller $\boldsymbol{q} = K\boldsymbol{y}$ such that the finite-horizon 2-norm $\|R_{\boldsymbol{w}\mapsto\boldsymbol{z}}\|_{2,[0,T]}$ in eq. 3.16 of the closed-loop system $R_{\boldsymbol{w}\mapsto\boldsymbol{z}}$ mapping the external disturbance inputs $\boldsymbol{w}$ to the objective $\boldsymbol{z}$ is minimized.

The solution comes from the fact that any measurement feedback controller is also a full-information controller, since

$$\begin{aligned}
\boldsymbol{q}(t) &= K(t)\boldsymbol{y}(t), && \text{(3.46a)}\\
&= K(t)C_2(t)\,\boldsymbol{x}(t) + K(t)D_{21}(t)\,\boldsymbol{w}(t), && \text{(3.46b)}\\
&= K(t)\begin{bmatrix} C_2(t) & D_{21}(t)\end{bmatrix}\begin{bmatrix}\boldsymbol{x}(t)\\ \boldsymbol{w}(t)\end{bmatrix}. && \text{(3.46c)}
\end{aligned}$$

The cost of any measurement feedback controller (Green and Limebeer, 1995, Remark 5.2.2, p.187) is

$$\begin{aligned}
\|R_{\boldsymbol{w}\mapsto\boldsymbol{z}}\|_{2,[0,T]}^2 &= \left(\|R_{\boldsymbol{w}\mapsto\boldsymbol{z}}\|_{2,[0,T]}^{opt}\right)^2 + \|U_{\boldsymbol{w}\mapsto\boldsymbol{q}-\boldsymbol{q}^{opt}}\|_{2,[0,T]}^2, && \text{(3.47a)}\\
&= \frac{1}{T}\int_0^T trace(B_1^* P B_1)\,dt + \|U_{\boldsymbol{w}\mapsto\boldsymbol{q}-\boldsymbol{q}^{opt}}\|_{2,[0,T]}^2. && \text{(3.47b)}
\end{aligned}$$

where $U_{\boldsymbol{w}\mapsto\boldsymbol{q}-\boldsymbol{q}^{opt}}$ is the system mapping the input disturbance $\boldsymbol{w}$ into the difference between the control signal $\boldsymbol{q} = K\,\boldsymbol{y}$ and the optimal control signal $\boldsymbol{q}^{opt} = -F\,\boldsymbol{x}$ (eq. 3.30). This signifies that the minimum cost of a measurement feedback control is the addition of the optimal cost of a full-information control giving $\boldsymbol{q}^{opt}$, given in eq. 3.25, and of the op;timal cost to estimate the state $\boldsymbol{x}$ from the measurement (y).

Therefore, the measurement feedback controller that minimizes $\|R_{\boldsymbol{w}\mapsto\boldsymbol{z}}\|_{2,[0,T]}$ is the optimal estimator given the measurement $\boldsymbol{y}$ (eq. 3.37, §3.4.5) of the optimal control law $\boldsymbol{q}^{opt}(t) = -F(t)\,\boldsymbol{x}(t)$ (eq. 3.23 & 3.30, §3.4.4).

Now combining these two optimal solutions, the optimal state-feedback system is

$$\begin{aligned}
\dot{\boldsymbol{x}}^{opt}(t) &= A\,\boldsymbol{x}^{opt}(t) + H\,(\boldsymbol{y}(t) - C_2\,\boldsymbol{x}^{opt}(t)\,) + B_2\boldsymbol{q}(t), \qquad \boldsymbol{x}^{opt}(0) = 0, && \text{(3.48a)}\\
\boldsymbol{q}(t) &= -F\,\boldsymbol{x}^{opt}(t), && \text{(3.48b)}
\end{aligned}$$

in which $F(t) = D_{12}^* C_1 + B_2^* P$ and $H(t) = B_1 D_{21}^* + Q C_2^*$. The matrices $P(t)$ and $Q(t)$ are solutions of the differential Riccati equations

$$-\dot{P} = P\tilde{A} + \tilde{A}^* P - P B_2 B_2^* P + \tilde{C}^* \tilde{C}, \qquad P(T) = 0, \tag{3.49a}$$

$$\dot{Q} = Q\bar{A}^* + \bar{A} Q - Q C_2^* C_2 Q + \bar{B}\bar{B}^*, \qquad Q(0) = 0, \tag{3.49b}$$

in which

$$\tilde{A} = A - B_2 D_{12}^* C_1, \qquad \tilde{C}^*\tilde{C} = C_1^*(I - D_{12} D_{12}^*) C_1, \tag{3.50a}$$

$$\bar{A} = A - B_1 D_{21}^* C_2, \qquad \bar{B}\bar{B}^* = B_1 (I - D_{21}^* D_{21}) B_1^*. \tag{3.50b}$$

Finally, the optimal cost is

$$\|R_{\boldsymbol{w}\mapsto\boldsymbol{z}}\|_{2,[0,T]}^{opt} = \min \|R_{\boldsymbol{w}\mapsto\boldsymbol{z}}\|_{2,[0,T]} = \left\{ \frac{1}{T} \int_0^T trace(B_1^* P B_1) + trace(F Q F^*) dt \right\}^{\frac{1}{2}}, \tag{3.51}$$

which is the square root of the sum of the square of the optimal, full-information cost (eq. 3.25) and the square of the cost of optimally estimating the optimal, full-information controller $F\boldsymbol{x}$ (eq. 3.41).

Infinite-horizon case

We now consider the system 3.14 as time-invariant. The Standard Assumptions 1, 2, 3 and 4 are required to solve the following algebraic Riccati equations and allow the existence of a stabilizing controller. In the infinite-horizon case, the purpose of LQG is to seek a controller $\boldsymbol{q} = K\boldsymbol{y}$ that minimizes $\|R_{\boldsymbol{w}\mapsto\boldsymbol{z}}\|_2$. Following from the previous results,

The measurement feedback controller that minimizes $\|R_{\boldsymbol{w}\mapsto\boldsymbol{z}}\|_2$ is the optimal estimator given the measurement $\boldsymbol{y}$ (eq. 3.43, §3.4.5) of the optimal control law $\boldsymbol{q}^{opt}(t) = -F\,\boldsymbol{x}(t)$ (eq. 3.27 & 3.30, §3.4.4).

Now combining these two optimal solutions, the optimal state-feedback system is

$$\dot{\boldsymbol{x}}^{opt}(t) = A\,\boldsymbol{x}^{opt}(t) + H\,(\boldsymbol{y}(t) - C_2\,\boldsymbol{x}^{opt}(t)\,) + B_2 \boldsymbol{q}(t), \qquad \boldsymbol{x}^{opt}(0) = 0, \tag{3.52a}$$

$$\boldsymbol{q}(t) = -F\,\boldsymbol{x}^{opt}(t), \tag{3.52b}$$

in which $F = D_{12}^* C_1 + B_2^* P$ and $H = B_1 D_{21}^* + Q C_2^*$. The matrices P and Q are solutions to the algebraic Riccati equations

$$P\tilde{A} + \tilde{A}^* P - P B_2 B_2^* P + \tilde{C}^*\tilde{C} = 0, \tag{3.53a}$$

$$Q\bar{A}^* + \bar{A} Q - Q C_2^* C_2 Q + \bar{B}\bar{B}^* = 0, \tag{3.53b}$$

in which

$$\tilde{A} = A - B_2 D_{12}^* C_1, \qquad \tilde{C}^* \tilde{C} = C_1^* (I - D_{12} D_{12}^*) C_1, \tag{3.54a}$$

$$\bar{A} = A - B_1 D_{21}^* C_2, \qquad \bar{B} \bar{B}^* = B_1 (I - D_{21}^* D_{21}) B_1^*. \tag{3.54b}$$

Finally, the optimal cost is

$$\|R_{\boldsymbol{w} \mapsto \boldsymbol{z}}\|_2^{opt} = \min \|R_{\boldsymbol{w} \mapsto \boldsymbol{z}}\|_2 = \left\{ trace(B_1^* P B_1) + trace(F Q F^*) \right\}^{\frac{1}{2}}, \tag{3.55}$$

which is the square root of the sum of the square of the optimal, full-information cost (eq. 3.29) and the square of the cost of optimally estimating the optimal, full-information controller $F\boldsymbol{x}$ (eq. 3.45).

3.5 $\mathcal{H}_\infty$ Robust Control

$\mathcal{H}_\infty$ robust control designs a controller with guaranteed performance against perturbations of given maximal amplitude. The final closed-loop system is stable up to a finite-amplitude disturbance, the worst bearable perturbation. The $\mathcal{H}_\infty$ generalized regulator problem consists in solving a $\mathcal{H}_\infty$ filter which estimates the $\mathcal{H}_\infty$ full-information control law. A cost functions is associated with each of these problems, which leads to two Riccati equations. The regulator expression follows from their solutions. Unlike LQG, state and measurement disturbances are unknown deterministic disturbances of finite energy gain relatively to the state; the manner these disturbances feed the system influences the expression of the full-information control; and the optimal state estimate of the $\mathcal{H}_\infty$ filter depends on the matrix F (see eq. 3.48a). The performances are guaranteed for a given model and a given cost function. $\mathcal{H}_\infty$ robust control requires the model to well-represent the real system, and computational power to solve the Riccati equations, which restrict its application in real cases. The following section is based on the book Green and Limebeer (1995) and focus solely on the full-information controller synthesis, as the estimation problem is not employed in this thesis.

Full-information $\mathcal{H}_\infty$ controller synthesis

We consider the same system 3.19, where loop-shifting, scaling and change of variable were applied,

$$\dot{\boldsymbol{x}}(t) = \tilde{A}(t)\, \boldsymbol{x}(t) + B_1(t)\, \boldsymbol{w}(t) + B_2(t)\, \tilde{\boldsymbol{q}}(t), \qquad \boldsymbol{x}(0) = 0, \tag{3.56a}$$

$$\tilde{\boldsymbol{z}}(t) = \begin{bmatrix} \tilde{C}(t) \boldsymbol{x}(t) \\ \tilde{\boldsymbol{q}}(t) \end{bmatrix}. \tag{3.56b}$$

Finite horizon

The purpose of robust control is to seek a causal, linear, full-information controller associated with the time-varying system 3.56 such that the closed-loop system $R_{\boldsymbol{zw}} : \boldsymbol{z} \mapsto \boldsymbol{w}$ satisfies

$$\int_0^T \big(\boldsymbol{z}^*\boldsymbol{z} - \gamma^2 \boldsymbol{w}^*\boldsymbol{w}\big)dt + \boldsymbol{x}^*(T)\Delta\boldsymbol{x}(T) \;\leq\; -\epsilon\|\boldsymbol{w}\|^2_{2,[0,T]} \tag{3.57}$$

for all $\boldsymbol{w} \in \mathcal{L}_2[0,T]$, some $\epsilon > 0$, and a nonnegative matrix Δ. It ensures that the $\mathcal{L}_2[0,T]$ induced norm of $R_{\boldsymbol{zw}}$ satisfies

$$\|R_{\boldsymbol{zw}}\|_{[0,T]} < \gamma. \tag{3.58}$$

There is full-information controller satisfying the objective 3.57 if and only if the Riccati differential equation

$$-\dot{P} = \tilde{A}^*P + P\tilde{A} - P\big(B_2B_2^* - \gamma^{-2}B_1B_1^*\big)P + \tilde{C}^*\tilde{C}, \qquad P(T) = \Delta, \tag{3.59}$$

has a solution $P(t)$ for all $t \in [0,T]$. The controller that achieves the objective is the linear, memoryless, state-feedback control signal $\boldsymbol{u}^{opt} = -B_2^*P\boldsymbol{x}$. The worst exogenous input is $\boldsymbol{w}^{worst} = \gamma^{-2}B_1^*P\boldsymbol{x}$. The solution P is non-negative-definite definite for all times $t \leq T$ and exists if the parameter γ is big enough. In the case $\gamma \to \infty$, the disturbance is not regarded and the Riccati differential equation 3.59 reduces into its optimal counterpart 3.24.

Infinite horizon

The system 3.56 is now considered as time-invariant. The purpose of robust control is to seek a causal, linear and stabilizing controller such that the $\mathcal{L}_\infty$-norm of the closed-loop system $R_{\boldsymbol{zw}} : \boldsymbol{z} \mapsto \boldsymbol{w}$ satisfies

$$\|R_{\boldsymbol{zw}}\|_\infty < \gamma, \tag{3.60}$$

or equivalently written

$$\|\boldsymbol{z}\|_2^2 - \gamma^2\|\boldsymbol{w}\|_2^2 \leq -\epsilon\|\boldsymbol{w}\|_2^2, \tag{3.61}$$

for all $\boldsymbol{w} \in \mathcal{L}_2[0,T]$ and some $\epsilon > 0$. As for optimal control, in order for a stabilizing controller to exist, it is also necessary that the pair $(\tilde{A}, B_2)$ is stabilizable —Standard Assumption 1— and that the closed-loop dynamic of the controller is asymptotically stable —Standard Assumption 2.

There exists a full-information control law such that $R_{\boldsymbol{zw}}$ is internally stable and satisfies the objective 3.60 if and only if the algebraic Riccati equation

$$P\tilde{A} + \tilde{A}^*P - P\big(B_2B_2^* - \gamma^{-2}B_1B_1^*\big)P + \tilde{C}^*\tilde{C} = 0, \tag{3.62}$$

has a stabilizing non-negative-definite solution P, i.e $P \geq 0$ and the closed-loop system $\tilde{A}-(B_2B_2^*-\gamma^{-2}B_1B_1^*)P$ is asymptotically stable. The stabilizing controller that achieves the objective is the linear, memoryless, state-feedback control signal $\boldsymbol{u}^{opt} = -B_2^*P\boldsymbol{x}$. The worst exogenous input is $\boldsymbol{w}^{worst} = \gamma^{-2}B_1^*P\boldsymbol{x}$. In the case $\gamma \to \infty$, the disturbance is not regarded and the algebraic Riccati equation 3.62 reduces into its optimal counterpart 3.28.

3.6 Nonlinearity and Passivity

Flow control synthesis is affected by two major drawbacks: the limitation of the dimension of the controlled system and the non-linearity of the Navier-Stokes equations. The former problem is addressed in section 6.2, when dealing with procedures to solve the Riccati equation. We are here devoted to the latter problem.

The NSE non-linearity is indeed neither stochastic nor bounded, as some transient external disturbances or model errors may generate large disorders in the dynamical state. This implies that $\mathcal{H}_2$ controllers are inappropriate, as they model disturbances as Gaussian, and neither are $\mathcal{H}_\infty$ controllers, as they are limited to bounded worst-case perturbations. Nonetheless, the non-linearity of the NSE in a closed or periodic domain is a conservative quantity in respect to the perturbation energy. This property is exploited to undertake a particular variety of control, known as "passivity-based control". An element is labeled as "passive" if only a finite amount of energy can be extracted out of it. A passive system only stores or dissipates energy and is unable to generate energy by itself.

Sharma et al. (2011) separated the passive non-linear terms from the linear terms of the NSE. As the feedback connection of two passive elements remains passive, they intended to enforce passivity of the linear part such that the whole system becomes passive. Their controller was thus dedicated to the stabilization of the linear terms and to the destruction of its non-normality, source of transient energy growth. They managed to stabilize a channel flow at friction Reynolds number $Re_\tau = 100$ with full-domain information and volume actuation on the wall-normal velocity component. The objective cost-function to minimize embodied the supply of turbulent energy of any perturbation arising from the interaction of the wall-normal velocities and the shear flow. The control law was calculated once off-line for each wave-number, which is computationally advantageous in comparison to adjoint-based methods described in Bewley (2001) (details in section 6.2).

Nevertheless, Martinelli et al. (2011) demonstrated (in an ideal case without any disturbance) that a linear state-feedback controller for Plane Poiseuille flow with actuation restricted to a part of the domain and full-information sensing can not be strictly dissipative. In order to obtain a strictly dissipative feedback loop, either the open-loop system

should already be monotonically stable, or the number of actuators should be equal to the dimension of the dynamical state. Either situation is unlikely to be fulfilled in shear flows with wall-transpiration actuation. This observation directly narrows the domain of application of passivity-based control. Martinelli et al. (2011) suggested instead to apply non-linear control or adjoint-based methods.

Despite this result, Heins et al. (2014, 2016) employed passivity-based control similarly to Sharma et al. (2011). The actuation was applied via wall-transpiration and the sensing was limited to the streamwise and spanwise wall shear-flow. They aimed to force the linear part of the NSE to become as passive as possible. By targeting the main source of turbulent perturbation energy, found to be the streamwise-constant modes ($\alpha = 0, \beta = 1, 2, 3, ...$), they managed to reduce the upper-bound of the turbulent perturbation energy production and reduce skin-friction drag.

Chapter summary

- Flow control is a mature field of research employed to reduce skin-friction drag, delay turbulence transition, alter fluid mixing in many sectors as aeronautics, aerospace, naval, automotive, etc.
- Control can either be passive —not requiring any external power input— (geometries or surface modification) or on the contrary, active.
- Control design either considers the current characteristics of the flow, hence "closed-loop control", or evolves independently, "open-loop control".
- Major advances were achieved with model based control, that defines a dynamical model, often linear, to describe the evolution of the flow.
- Optimal Linear Quadratic Gaussian (LQG) control designs an optimal measurement-feedback control for linear systems where state and measurement disturbances are considered as uncorrelated zero-mean Gaussian white noise with known statistical properties. The measurement-feedback loop is composed of a Kalman filter for the estimation associated with a Linear Quadratic Regulation (LQR) for the control. The optimal estimation and control laws derive from the solution of Riccati equations and always exist. Nonetheless, no global system-independent robustness properties are guaranteed.
- Robust control extends from optimal control and designs a controller with guaranteed performance against perturbations of given maximal amplitude. On the other side, solution of the associated Riccati equations are not guaranteed.

- Non-linear systems can be addressed with passivity-based control. However, for channel flows, the whole system can not be made fully passive.

Chapter 4

Modeling - The Linear Orr-Sommerfeld Squire model extended for a non-laminar solution

The theory behind turbulence and feedback control was presented in previous chapters 2 and 3. The application of state-space feedback control theory to invariant solutions requires a linearized state-space model. In this thesis, this model derives from the linearization (§4.1) and discretization with spectral method (§4.2) of the Navier-Stokes equations 2.16. For a PCF baseflow in a channel geometry (§4.4), the derivation is straightforward and leads to the Orr-Sommerfeld Squire model (4.5). However, the linearization around an invariant solution is very high-dimensional and the model no longer diagonalises with Fourier wave-numbers due to the breaking of translational symmetry of the baseflow. Therefore, we develop a new divergence-free full-matrix state-space model, called the Orr-Sommerfeld Squire model Extended for a non-laminar solution (OSSE) (§4.6). To reduce state dimension and memory requirement, we establish a purely-real equivalent, the Real Orr-Sommerfeld Squire model Extended for a non-laminar solution (ROSSE) (§4.7). Thanks to the validation in section 4.8, we demonstrate that the OSSE and ROSSE models depict faithfully the dynamical evolution of the flow in the neighbourhood of an ECS for small perturbations and enable access to linear control theory. The plant of future control system will be modeled with the ROSSE model.

4.1 Governing equations

Controller synthesis of Linear time-invariant (LTI) systems first and foremost requires the definition of a spatially discretised LTI system of the form presented in equations 3.1.

However, the non-dimensionalized NSE for a channel presented in equations 2.16 are continuous non-linear infinite-dimensional Partial-differential algebraic equations (PDAE). Hence, the Navier-Stokes equations are not a Linear time-invariant system. In order to be of practical use for the numerical methods, we intend to employ some transformations on of the NSE 2.16:

1. linearisation around a time-invariant parallel baseflow, §4.1.1.
2. transformation into a non-singular system, §4.5.1.
3. discretisation of the new system and simplication in §4.5 after presenting spectral methods in §4.2 and geometries in §4.4.

All calculations established in this section and section 4.5 will be given for a Plane Couette Flow (PCF) laminar baseflow, corresponding to a solution of the form $\bar{\boldsymbol{U}} = (U_{lam}(y), 0, 0)$. Such a baseflow enables many simplifications in the expression of the final OSS system 4.52.

However, from section 4.6 onwards, the baseflow will be considered as a steady non-laminar solution of the form $\bar{\boldsymbol{U}} = (\bar{U}(x,y,z), \bar{V}(x,y,z), \bar{W}(x,y,z))$. Consequently, the simplifications possible for the OSS model no longer apply as this solution is three-dimensional and dependent on x, y and z.

4.1.1 Linearised Navier-Stokes equations

The velocity field $\boldsymbol{U}$ of the Navier-Stokes equations 2.16 can be decomposed into a time-invariant base flow $\bar{\boldsymbol{U}}(x,y,z)$ and a time-dependent disturbance $\boldsymbol{u}(x,y,z,t)$ as

$$\boldsymbol{U}(x,y,z,t) = \bar{\boldsymbol{U}}(x,y,z) + \boldsymbol{u}(x,y,z,t), \tag{4.1}$$

with

$$u \ll \bar{U}, \quad v \ll \bar{V}, \quad w \ll \bar{W}, \tag{4.2}$$

where $\bar{\boldsymbol{U}} = [\bar{U}, \bar{V}, \bar{W}]$ and $\boldsymbol{u} = [u, v, w]$ denote streamwise, wall-normal and spanwise components in Cartesian coordinates. Similarly, we introduce $\bar{P}(x,y,z)$ and $p(x,y,z,t)$ as

$$P(x,y,z,t) = \bar{P}(x,y,z) + p(x,y,z,t) \quad \text{with} \quad p \ll \bar{P}. \tag{4.3}$$

The disturbance $\boldsymbol{u}$ from the laminar base flow physically represents the initial stage in transition to turbulence, as non-linear interaction will enhance or lessen its amplitude and impact the stability of the fluid. We hereby consider the unidirectional laminar baseflow of the form $\bar{\boldsymbol{U}} = (U_{lam}(y), 0, 0)$, As the base flow obeys the Navier-Stokes equations, substituting equations 4.1 and 4.3 in 2.16 and subtracting the base flow

equation give for an unidirectional mean flow as

$$\frac{\partial u}{\partial t} = \frac{1}{Re}\nabla^2 u - U_{lam}\frac{\partial u}{\partial x} - v\frac{\partial U_{lam}}{\partial y} - \varrho_x - \frac{\partial p}{\partial x} + f_x, \tag{4.4a}$$

$$\frac{\partial v}{\partial t} = \frac{1}{Re}\nabla^2 v - U_{lam}\frac{\partial v}{\partial x} - \varrho_y - \frac{\partial p}{\partial y} + f_y, \tag{4.4b}$$

$$\frac{\partial w}{\partial t} = \frac{1}{Re}\nabla^2 w - U_{lam}\frac{\partial w}{\partial x} - \varrho_z - \frac{\partial p}{\partial z} + f_z, \tag{4.4c}$$

$$\frac{\partial u}{\partial x} + \frac{\partial v}{\partial y} + \frac{\partial w}{\partial z} = 0, \tag{4.4d}$$

where $(f_x, f_y, f_z) = \boldsymbol{f}$ and $(\varrho_x, \varrho_y, \varrho_z) = \boldsymbol{\varrho}$ denote respectively streamwise, wall-normal and spanwise components of the vectors of body forces and of the non-linear term. The non-linear term $\boldsymbol{\varrho}$ is defined as

$$\begin{aligned}\boldsymbol{\varrho} &= \boldsymbol{u}\cdot\nabla\boldsymbol{u} \\ &= (u,v,w)\cdot\nabla(u,v,w) \\ &= (\underbrace{u\frac{\partial u}{\partial x} + v\frac{\partial u}{\partial y} + w\frac{\partial u}{\partial z}}_{\varrho_x}, \underbrace{u\frac{\partial v}{\partial x} + v\frac{\partial v}{\partial y} + w\frac{\partial v}{\partial z}}_{\varrho_y}, \underbrace{u\frac{\partial w}{\partial x} + v\frac{\partial w}{\partial y} + w\frac{\partial w}{\partial z}}_{\varrho_z}).\end{aligned} \tag{4.5}$$

By neglecting the non-linear terms $\boldsymbol{\varrho}$ and body forces $\boldsymbol{f}$ in equations 4.4, we obtain the non-dimensional linearised Navier-Stokes equations for a channel:

$$\frac{\partial u}{\partial t} = \frac{1}{Re}\nabla^2 u - U_{lam}\frac{\partial u}{\partial x} - v\frac{\partial U_{lam}}{\partial y} - \frac{\partial p}{\partial x}, \tag{4.6a}$$

$$\frac{\partial v}{\partial t} = \frac{1}{Re}\nabla^2 v - U_{lam}\frac{\partial v}{\partial x} - \frac{\partial p}{\partial y}, \tag{4.6b}$$

$$\frac{\partial w}{\partial t} = \frac{1}{Re}\nabla^2 w - U_{lam}\frac{\partial w}{\partial x} - \frac{\partial p}{\partial z}, \tag{4.6c}$$

$$\frac{\partial u}{\partial x} + \frac{\partial v}{\partial y} + \frac{\partial w}{\partial z} = 0. \tag{4.6d}$$

4.1.2 Poisson equation

The Poisson equation is used to retrieve the pressure field once the velocity field has been computed. By taking the divergence of momentum equations 2.16a and using the divergence free condition 2.16b, we obtain the Poisson equation

$$\nabla^2 P = -\nabla\cdot(\boldsymbol{U}\cdot\nabla\boldsymbol{U}). \tag{4.7}$$

In Cartesian coordinates and using assumption 4.1-4.3, equation 4.7 reduces to the linearised Poisson equation:

$$\begin{aligned}\nabla^2 p = \frac{\partial^2 p}{\partial x^2} + \frac{\partial^2 p}{\partial y^2} + \frac{\partial^2 p}{\partial y^2} = &-2\frac{\partial \bar{U}}{\partial x}\frac{\partial u}{\partial x} - 2\frac{\partial \bar{V}}{\partial x}\frac{\partial u}{\partial y} - 2\frac{\partial \bar{W}}{\partial x}\frac{\partial u}{\partial z} \\ &- 2\frac{\partial \bar{U}}{\partial y}\frac{\partial v}{\partial x} - 2\frac{\partial \bar{V}}{\partial y}\frac{\partial v}{\partial y} - 2\frac{\partial \bar{W}}{\partial y}\frac{\partial v}{\partial z} \\ &- 2\frac{\partial \bar{U}}{\partial z}\frac{\partial w}{\partial x} - 2\frac{\partial \bar{V}}{\partial z}\frac{\partial w}{\partial y} - 2\frac{\partial \bar{W}}{\partial z}\frac{\partial w}{\partial z}.\end{aligned} \tag{4.8}$$

Considering a unidirectional PCF laminar baseflow $\bar{\boldsymbol{U}} = (U_{lam}(y), 0, 0)$, the Poisson equation 4.8 simplifies to

$$\nabla^2 p = \frac{\partial^2 p}{\partial x^2} + \frac{\partial^2 p}{\partial y^2} + \frac{\partial^2 p}{\partial y^2} = -2\frac{\partial U_{lam}}{\partial y}\frac{\partial v}{\partial x}. \tag{4.9}$$

4.2 Spatial discretisation - Spectral Methods

Spatial discretisation is a necessary step to implement the mathematical system as a numerical model. The process transforms a continuous function or signal (velocity, pressure, vorticity, etc.) into its discrete counterpart. Different discretisation methods have been developed in applied mathematics and then applied to fluids mechanics. The predominant ones are spectral, finite-volume, finite-element or finite-difference methods. Due to the simplicity and periodicity of the spatial domain studied here (detailed in section 4.4), spectral methods are the prime choice. These methods are commonly used to solve Ordinary-differential equations (ODE), partial-differential equations or eigenvalue problems involving differential equations. Spectral methods take a "global approach", in the sense that the basis function of the discretization spans the entire domain. On the contrary, the basis functions of finite element methods are valid only on small and limited subdomains. Many bases needs to be interconnected to each-other in order to span the entire domain. This global approach enables spectral methods to converge at an exponential rate for smooth functions, which is called "spectral or infinite accuracy". Spectral methods decompose continuous signals into their associated spectral coefficients within a dedicated basis. Commonly used as basis functions are Fourier, Chebyshev or Legendre series, which became especially practical with the development of the Fast Fourier Transform (FFT) algorithm (Cooley and Tukey, 1965; Press et al., 2007). Nonetheless, spectral methods are limited to handle complex geometries, discontinuous or non-smooth phenomena, which can cause oscillations on the boundaries spreading to the entire domain. However, for simple smooth periodic domains, they are precise and computationally inexpensive.

Among the books devoted to spectral methods, we focused our attention on Peyret (2002). Interested readers may find useful the pioneering book of Gottlieb and Orszag

(1977), the comprehensive work including important theoretical results of Canuto et al. (1988) or Canuto et al. (2006) and the numerical recipes of Press et al. (2007).

4.2.1 Mathematical introduction

Peyret (2002) gathers the fundamental theory of Fourier and Chebyshev methods for the computation of incompressible flows, which is the basis of this section. To approximate functions via Fourier or Chebyshev series, the scalar product

$$\langle \mathfrak{u}, \mathfrak{v} \rangle_{\mathfrak{w}} = \int_{\mathfrak{a}}^{\mathfrak{b}} \mathfrak{u}\, \mathfrak{v}\, \mathfrak{w}\, \mathrm{d}x, \tag{4.10}$$

is required, where $\mathfrak{u}(x)$ and $\mathfrak{v}(x)$ are two functions defined on $[\mathfrak{a}, \mathfrak{b}]$ and $\mathfrak{w}(x)$ is a weight function.

The truncated series of a function $\mathfrak{f}(x)$ will be defined as

$$\mathfrak{f}_N(x) = \sum_{k=0}^{N} \hat{\mathfrak{f}}_k \varphi_k(x), \quad x \in [\mathfrak{a}, \mathfrak{b}], \tag{4.11}$$

where $\varphi_k(x)$ are given orthogonal "trial" functions depending on the employed spectral method (exponential, Chebyshev polynomials,...), such that $(\varphi_k, \varphi_l)_{\mathfrak{w}} = c_k \delta_{k,l}$ whih c_k a constant and δ the Kronecker function.

The residual $\mathfrak{R}_N$ is defined, if the function $\mathfrak{f}$ is given, as

$$\mathfrak{R}_N = \mathfrak{f} - \mathfrak{f}_N. \tag{4.12}$$

In the case where $\mathfrak{f}_N$ approximates the solution of a differential equation of the form $L\mathfrak{f} - l = 0$, the residual is defined as

$$\mathfrak{R}_N = L\mathfrak{f}_N - l. \tag{4.13}$$

Spectral methods aim to make the residual $\mathfrak{R}_N$ nought by enforcing the following equality,

$$(\mathfrak{R}_N, \psi_i)_{\mathfrak{w}_\star} = \int_{\mathfrak{a}}^{\mathfrak{b}} \mathfrak{R}_N\, \psi_i\, \mathfrak{w}_\star \mathrm{d}x = 0, \tag{4.14}$$

where ψ_i are test functions and $\mathfrak{w}_\star$ are weight functions.

The two most-common spectral methods are the Galerkin and the Collocation methods:

- Galerkin method uses the trial functions φ_i as test functions ψ_i, and the weight function $\mathfrak{w}$ as weight $\mathfrak{w}_\star$ as

$$\psi_i = \varphi_i, \quad \mathfrak{w}_\star = \mathfrak{w}. \tag{4.15}$$

- Collocation method uses different functions

$$\psi_i = \delta_0(x - x_i), \quad \mathfrak{w}_\star = 1, \tag{4.16}$$

with δ_0 the Dirac delta-function. The set $\{x_i\}$ is a set of collocation points and implies that the residual $\mathfrak{R}_N$ is zero only on these points. This method is simple to implement as linear operation can be performed directly on the collocations points. Nonetheless, an insufficient number of collocation points can lead to inaccurate result.

In this thesis, we are using the collocation method (section 4.5.2).

4.2.2 Fourier Method

The Fourier method is the most familiar spectral method. In this approach, the basis of trial functions is composed of trigonometric functions, such as sinusoids. The main benefits of Fourier series are their fast rate of convergence and the existence of the Fast Fourier Transform (FFT), an efficient algorithms to compute their discrete transformation (Cooley and Tukey, 1965; Press et al., 2007). Fourier series fit particularly well 2π-periodic smooth functions. Periodic and smooth functions will indeed result in an uniform set of Fourier coefficients and allow for "spectral or infinite accuracy", i.e. the convergence is exponential and the approximation error is smaller than $\frac{1}{K}$, where K is the number of coefficients (Peyret, 2002; Canuto et al., 2006). Periodicity and smoothness are important, otherwise the convergence of the associated Fourier series will not be uniform at the boundaries and lead to oscillations in the whole domain, called the "Gibbs phenomenon".

Truncated Fourier series

The assumed 2π-periodic function $\mathfrak{f}$ can be approximated by a truncated series expansion with trial functions $\{\mathrm{e}^{\imath kx}\}$ (noting that coefficients corresponding to indices k and $-k$ are complex conjugates if $\mathfrak{f}$ is real) as

$$\mathfrak{f}_K(x) = \sum_{k=-K}^{K} \hat{\mathfrak{f}}_k \, \mathrm{e}^{\imath kx}. \tag{4.17}$$

By calculating the residual $\mathfrak{R}_K = \mathfrak{f} - \mathfrak{f}_K$ and setting it to zero in the mean, we obtain the expression of the Galerkin Fourier coefficients as

$$\hat{\mathfrak{f}}_k = \frac{1}{2\pi} \int_0^{2\pi} \mathfrak{f} \, \mathrm{e}^{\imath kx} \mathrm{d}x. \tag{4.18}$$

Discrete Fourier series

The discrete Fourier coefficients are determined on a set of $N+1$ collocation points $\{x_i = 2\pi i/N\}$ with $i = 0, ..., N$, where $x_0 = 0$, $x_N = 2\pi$ and $\mathfrak{f}(x_0) = \mathfrak{f}(x_N)$. The value of N is imposed to $2K+1$ as the residual $\mathfrak{R}_K$ is set to zero at each x_i.

$$\forall i \in [0, N], \quad \mathfrak{R}_K(x_i) = \mathfrak{f}(x_i) - \mathfrak{f}_K(x_i) = 0. \tag{4.19}$$

We can then determine the expression of each discrete Fourier coefficients of the collocation method as

$$\hat{\mathfrak{f}}_k = \frac{1}{N} \sum_{i=1}^{N} \mathfrak{f}(x_i) \mathrm{e}^{\iota k x_i}, \quad k = -K, ..., K. \tag{4.20}$$

p-th differentiation in x is obtained directly, with $I_K = -K, ..., K$ for odd collocation and $I_K = -K+1, ..., K$ for even collocation, as

$$\mathfrak{f}_K^{(p)}(x) = \sum_{k \in I_K} \underbrace{(\iota k)^p \hat{\mathfrak{f}}_k}_{\hat{\mathfrak{f}}_k^{(p)}} \mathrm{e}^{\iota k x}. \tag{4.21}$$

4.2.3 Chebyshev Method

The Fourier method is well adapted to periodic domain, but less so to non-periodic domains due to the Gibbs phenomenon at the boundaries —large oscillations or overshoots of the Fourier series at simple discontinuities. Orthogonal polynomials, like the Chebyshev method, are a good alternative to Fourier series. Chebyshev series can be seen as cosine Fourier series. Therefore, they share the benefits of the Fourier series of a fast exponential rate of convergence and of the existence of the FFT, yet they do not suffer from the Gibbs phenomenon at the boundaries. Legendre polynomials stands also as a valuable alternative to Fourier series. However, no fast transformation algorithms akin to the FFT exists for this method.

Chebyshev Polynomials of the first kind

Chebyshev polynomials of the first kind are defined as

$$T_k(x) = \cos(k \cos^{-1}(x)), \quad \forall k > 0, \tag{4.22}$$

or with $x = \cos(z)$,

$$T_k(z) = \cos(kz), \quad \forall k > 0, \tag{4.23}$$

which gives

$$\begin{aligned} T_0 &= 1, \\ T_1 &= \cos(z) = x, \\ T_2 &= \cos(2z) = 2x^2 - 1. \end{aligned} \tag{4.24}$$

Truncated Chebyshev series

The function $\mathfrak{f}(x)$ is approximated for $x \in [-1, 1]$ with a Chebyshev series as

$$\mathfrak{f}_N(x) = \sum_{k=0}^{N} \tilde{\mathfrak{f}}_k \, T_k(x). \tag{4.25}$$

Similarly as for the Fourier coefficients, we use a Galerkin method to find the Chebyshev coefficients

$$\begin{aligned} \tilde{\mathfrak{f}}_k &= \frac{2}{\pi} \int_{-1}^{1} \mathfrak{f} \, T_k \, \mathfrak{w} \, \mathrm{d}x, \quad \text{for } 1 \leq k \leq N-1, \\ \tilde{\mathfrak{f}}_k &= \frac{1}{\pi} \int_{-1}^{1} \mathfrak{f} \, T_k \, \mathfrak{w} \, \mathrm{d}x, \quad \text{for } k = 0 \text{ or } N. \end{aligned} \tag{4.26}$$

Discrete Chebyshev series

As for the discrete Fourier series, the discrete Chebyshev coefficients are determined on a set of $N+1$ collocation points $\{x_i\}$, which are for best results the Gauss-Chebyshev-Lobatto collocation points

$$x_i = \cos(\frac{\pi i}{N}) \text{ with } i = 0, ..., N. \tag{4.27}$$

The expression of the Chebyshev coefficients on this set is as follow

$$\begin{aligned} \tilde{\mathfrak{f}}_k &= \frac{1}{N} \left(\mathfrak{f}_0 T_k(x_0) + 2 \sum_{i=1}^{N-1} \mathfrak{f}_i T_k(x_i) + \mathfrak{f}_N T_k(x_N) \right), \quad \text{for } 1 \leq k \leq N-1, \\ \tilde{\mathfrak{f}}_k &= \frac{1}{2N} \left(\mathfrak{f}_0 T_k(x_0) + 2 \sum_{i=1}^{N-1} \mathfrak{f}_i T_k(x_i) + \mathfrak{f}_N T_k(x_N) \right), \quad \text{for } k = 0 \text{ or } N. \end{aligned} \tag{4.28}$$

Matrix differentiation

Differentiation of Chebyshev polynomials is more intricate than the one of Fourier series. Chebyshev differentiation involves all the polynomials of opposite parity and lower

degree. The differentiation can be state into a matrix form as

$$\hat{\mathfrak{F}}^{(1)} = \begin{bmatrix} \hat{\mathfrak{f}}_0^{(1)} \\ .. \\ \hat{\mathfrak{f}}_N^{(1)} \end{bmatrix} = \hat{\mathcal{D}} \begin{bmatrix} \hat{\mathfrak{f}}_0 \\ .. \\ \hat{\mathfrak{f}}_N \end{bmatrix} = \hat{\mathcal{D}}\,\hat{\mathfrak{F}}, \tag{4.29}$$

where $\hat{\mathfrak{F}}^{(i)}$ denotes the i-th differentiation of $\hat{\mathfrak{F}}$, and for higher order:

$$\hat{\mathfrak{F}}^{(p)} = \hat{\mathcal{D}}^p\,\hat{\mathfrak{F}}. \tag{4.30}$$

Matrix $\hat{\mathcal{D}}$ coefficients are formed by recurrence. Many packages exist to build efficiently the differentiation matrices $[\hat{\mathcal{D}}, \hat{\mathcal{D}}^1, ..., \hat{\mathcal{D}}^p]$. This thesis employs the computation code of the package of Weideman and Reddy (2000), incorporating clamped boundary conditions ($\mathfrak{F}(\pm 1) = \mathfrak{F}^{(1)}(\pm 1) = 0$) and translated into `Python` by Arslan Muhammad Ahmed in his thesis (Ahmed, 2018). This differentiation method is working properly only if the extrema at the wall are zero (McKernan, 2006). In the case of non-zero values at the wall, inaccurate derivatives will occur through the entire domain.

Note on the implementation of boundary condition within the Chebyshev differentiation matrices

Dirichlet and/or Neumann boundary conditions are implemented though the set of differentiation matrix $\{\mathcal{D}^d\}$. The set of matrices $\{\mathcal{D}^d\}$ is formed from interpolation polynomials satisfying a given boundary condition. Different types of boundary condition imply a different polynomials and different sets $\{\mathcal{D}^d\}$. Computationally, it is necessary to impose different boundary conditions on $\mathcal{D}$, $\mathcal{D}^2$, $\mathcal{D}^3$ than the ones on $\mathcal{D}^4$. A 4^{th} order partial-differential equation can indeed be formulated under the following form

$$\frac{\partial^4 \dot{v}}{\partial y^4}(y,t) = \frac{\partial^2 v}{\partial y^2}(y,t), \tag{4.31}$$

which leads to the following expressions with a Chebyshev discretisation in y, imposing differents boundary conditions on the RHS and LHS,

$$\mathcal{D}_a^4 \dot{\tilde{v}}(t) = \mathcal{D}_b^2 \tilde{v}(t). \tag{4.32}$$

If $\mathcal{D}_a^4$ is non-singular, the time-evolution of $\tilde{v}(t)$ can be expressed as

$$\dot{\tilde{v}}(t) = (\mathcal{D}_a^4)^{-1} \mathcal{D}_b^2 \tilde{v}(t). \tag{4.33}$$

If both RHS and LHS were imposed the same boundary condition, $\mathcal{D}_a = \mathcal{D}_b$, the expression of $\tilde{v}(t)$ would simplify into $\dot{\tilde{v}}(t) = (\mathcal{D}^2)^{-1}\tilde{v}(t)$. The issue is that the matrix $\mathcal{D}^2$ is nearly singular, and therefore produces spurious modes in the eigen-problem 4.33. Using two different boundary conditions prevents the matrix $(\mathcal{D}_a^4)^{-1}\mathcal{D}_b^2$ in eq. 4.33 to be

nearly singular and makes it definite, a necessary yet not sufficient condition to eliminate spurious modes (Huang and Sloan, 1994; Weideman and Reddy, 2000). Taking the OSS model as an example, it is either possible to define $\mathcal{D}_a^4$ with clamped boundary conditions and $\mathcal{D}_b^2$ with Dirichlet ones, or $\mathcal{D}_a^4$ with Dirichlet and $\mathcal{D}_b^2$ clamped. However, if the same boundary conditions were applied to both matrices, the solution of this eigen-problem would contain spurious modes.

In this study, $\mathcal{D}$, $\mathcal{D}^2$, $\mathcal{D}^3$ are imposed with Dirichlet conditions and $\mathcal{D}^4$ with clamped conditions.

4.3 Time discretisation

Time discretisation will not be developed in this thesis, as it is not the main subject of the research. However, the interested reader may find useful section 4.2 of the thesis Halcrow (2008). Therein is described the algorithm for the time-integration in `Channelflow`, as well as the search for symmetries and equilibria for PCF.

4.4 Geometries

This numerical investigation is based on the implementation of a "FlowField" class-object, representing a fluid flow incorporating a set of fields (velocity, pressure, etc.) and properties (Reynolds number, dimensions, etc.). This "FlowField" is the core element of the implementation and allows for easy loading and storage of datasets (in HDF5 format, `www.hdfgroup.org`), or transformation back and forth between physical and spectral form. Each FlowField is included within a given domain, e.g. box, channel, pipe, boundary layer, etc. The most generic domain is a 3D-box, namely a three-dimensional parallelepipoid domain with periodic boundary conditions enabling a $Fourier \times Fourier \times Fourier$ discretisation. Channel geometries derives from the 3D-box, but breaking the symmetry by imposing a wall at the boundary on the domain in the vertical direction, and consequently discretized as $Fourier \times Chebyshev \times Fourier$. Boundary layer and pipe geometries involve specific discretisation (e.g. solenoidal Fourier-Chebyshev spectral method for pipe (Meseguer and Mellibovsky, 2007), boundary layer theory (Schlichting and Gersten, 1979)), which are not developed here. This thesis is focusing of Plane Couette Flow, hence on Channel geometries only.

4.4.1 3D-box

A 3D-box is a domain of dimension $[L_x \times L_y \times L_z]$, periodic in the streamwise, wall-normal and spanwise direction. Therefore, any dataset $\mathfrak{D}(x, y, z, t)$ of the flowfield $\mathcal{F}$ in

that 3D-box will respect

$$\begin{aligned}\mathfrak{D}(x,y,z,t) &= \mathfrak{D}(x+L_x,y,z,t),\\ \mathfrak{D}(x,y,z,t) &= \mathfrak{D}(x,y+L_y,z,t),\\ \mathfrak{D}(x,y,z,t) &= \mathfrak{D}(x,y,z+L_z,t).\end{aligned} \tag{4.34}$$

The prime choice of discretisation is $Fourier \times Fourier \times Fourier$, allowing the decompositon into a spectral form of the dataset $\mathfrak{D}(x,y,z,t)$ of $\mathcal{F}$ as

$$\mathfrak{D}(x,y,z,t) = \sum_{k_x=-\frac{N_x}{2}+1}^{N_x/2} \sum_{k_y=-\frac{N_y}{2}+1}^{N_y/2} \sum_{k_z=-\frac{N_z}{2}+1}^{N_z/2} \hat{\mathfrak{D}}_{k_x,k_y,k_z}(t) \mathrm{e}^{2\pi\iota(\frac{k_x x}{L_x}+\frac{k_y y}{L_y}+\frac{k_z z}{L_z})}, \tag{4.35}$$

where (N_x, N_y, N_z) are the number of equispaced discretisation points in streamwise, wall-normal and spanwise direction respectively, (k_x, k_y, k_z) are the streamwise, wall-normal and spanwise wavenumber indices. The streamwise and spanwise wavenumber are respectively defined as

$$\alpha := \frac{2\pi k_x}{L_x} \quad \text{and} \quad \beta := \frac{2\pi k_z}{L_z}. \tag{4.36}$$

4.4.2 Channel

A Channel object extends from a 3D-box. Nonetheless, the wall-normal domain is not periodic, but limited by two walls at abscissa $y = \pm 1$. Chebyshev discretisation for the wall-normal direction is well-fitted. Chebyshev polynomials are indeed defined on the same interval and offer flexibility to impose complex boundary condition. The choice of spectral discretisation is thus $Fourier \times Chebyshev \times Fourier$. In this configuraiton, any dataset $\mathfrak{D}(x,y,z,t)$ of the flowfield $\mathcal{F}$ included in the channel $\mathcal{C}$ takes the spectral form

$$\mathfrak{D}(x,y,z,t) = \sum_{k_x=-\frac{N_x}{2}+1}^{N_x/2} \sum_{n_y=0}^{N_y} \sum_{k_z=-\frac{N_z}{2}+1}^{N_z/2} \tilde{\hat{\mathfrak{D}}}_{k_x,n_y,k_z}(t)\, \gamma(y)\, T_{n_y}(y) \mathrm{e}^{2\pi\iota(\frac{k_x x}{L_x}+\frac{k_z z}{L_z})}, \tag{4.37}$$

where $T(y)$ are Chebyshev polynomials of the first kind and $\gamma(y)$ a weighting factor to fit the boundary conditions. This discretisation increases intervals between nodes around the channel centerline and reduces intervals between nodes close to the wall. This shift will improve accuracy of simulation close to the wall, which is particularly useful when actuation by wall-transpiration occurs.

Boundary conditions at the walls

Dirichlet and Neumann boundary conditions are applied on the velocity and vorticity fields at the walls ($y = \pm 1$),

$$\hat{v}(y = \pm 1, t) = 0, \tag{4.38a}$$

$$\frac{\partial \hat{v}}{\partial y}(y = \pm 1, t) = 0, \tag{4.38b}$$

$$\hat{\eta}(y = \pm 1, t) = 0. \tag{4.38c}$$

The velocity component v is imposed a Dirichlet boundary condition 4.38a to consider the wall impermeability and a Neumann condition 4.38b in result of the divergence free condition 4.4d. The association of both Dirichlet and Neumann conditions is called a "clamped" boundary condition. The wall-normal vorticity η is imposed by a Dirichlet boundary condition 4.38c in order to take into account the no-slip condition on the wall.

These boundary conditions are applied during the mathematical derivation of the respective models (§4.5 & 4.6). For the case of the OSS and later models, they are implicit and included within the expression of the Laplacian operator. One way to implement these conditions is to build a new basis of weighted Chebyshev polynomials incorporating the appropriate boundary condition, and then determine the Chebyshev coefficients for the wall-normal velocity and wall-normal vorticity. A more straightforward way is to use a package of spectral differentiation matrices incorporating the specific boundary condition. This thesis will make use of the Weideman and Reddy (2000) package, that uses the collocation method and translated into `Python` by Arslan Muhammad Ahmed in his thesis (Ahmed, 2018).

Domain size

The domain used here is the "W03 cell" on `channelflow.org` (Gibson et al., 2008; Gibson, 2014; Gibson et al., 2019) and first studied by Waleffe (2003), at $Re = 400$. It corresponds to a channel of dimension given by $\alpha = 1.14$ and $\beta = 2.5$, where

$$\begin{aligned} L_x &= \frac{2\pi}{\alpha} \approx 5.511, \\ L_z &= \frac{2\pi}{\beta} \approx 2.513. \end{aligned} \tag{4.39}$$

4.5 Orr-Sommerfeld Squire model

The procedure below describes the projection of the state vector $\boldsymbol{x}$ of the NSE 4.6a-4.6d on a divergence-free fasis, in which the continuity equation is implicitly satisfied. This

allows for the formation of a new LTI model of lower dimension than the NSE, yet with the same physical properties. This model is called the Orr-Sommerfeld Squire model (OSS) after its main contributors, William McFadden Orr (Orr, 1907a,b) and Arnold Sommerfeld (Sommerfeld, 1908). The OSS model is an eigenvalue problem helpful to establish the hydrodynamic stability of the NSE.

4.5.1 Derivation of the Orr-Sommerfeld Squire model

The linearised Navier-Stokes equations 4.6a-4.6d around the PCF laminar solution can be described as a LTI system (see 3.1) of the form

$$E_{OSS}\,\frac{d\boldsymbol{x}(t)}{dt} = A_{OSS}\,\boldsymbol{x}(t), \tag{4.40}$$

where

$$\boldsymbol{x} = \begin{bmatrix} u \\ v \\ w \\ p \end{bmatrix}, \qquad E_{OSS} = \begin{bmatrix} I & 0 & 0 & 0 \\ 0 & I & 0 & 0 \\ 0 & 0 & I & 0 \\ 0 & 0 & 0 & 0 \end{bmatrix}, \tag{4.41a}$$

$$A_{OSS} = \begin{bmatrix} \left(\frac{1}{Re}\nabla^2 - U_{lam}\frac{\partial}{\partial x}\right) & -\frac{\partial U_{lam}}{\partial y} & 0 & -\frac{\partial}{\partial x} \\ 0 & \left(\frac{1}{Re}\nabla^2 - U_{lam}\frac{\partial}{\partial x}\right) & 0 & -\frac{\partial}{\partial y} \\ 0 & 0 & \left(\frac{1}{Re}\nabla^2 - U_{lam}\frac{\partial}{\partial x}\right) & -\frac{\partial}{\partial z} \\ \frac{\partial}{\partial x} & \frac{\partial}{\partial y} & \frac{\partial}{\partial z} & 0 \end{bmatrix}. \tag{4.41b}$$

Unfortunately, the matrix E_{OSS} in eq. 4.41a is non-invertible. The system 4.40 is thus singular and does not represent a standard state-space system. For this reason, the state-vector $\boldsymbol{x}$ is projected on a divergence-free fasis, where the continuity equation is implicitly satisfied. The Laplacian of equation 4.6b is firstly calculated as

$$\frac{\partial}{\partial t}\nabla^2 v = \frac{1}{Re}\nabla^2(\nabla^2 v) + \frac{\partial^2 U_{lam}}{\partial y^2}\frac{\partial v}{\partial x} - U_{lam}\frac{\partial}{\partial x}\nabla^2 v. \tag{4.42}$$

The pressure has been eliminated from this equation with the relation 4.9. To describe the complete 3D problem, a second equation is needed. For that purpose, the wall-normal vorticity η_y is defined as

$$\eta_y := \frac{\partial u}{\partial z} - \frac{\partial w}{\partial x}. \tag{4.43}$$

Subtracting the streamwise-derivative of equation 4.6c to the spanwise-derivative of 4.6a leads to

$$\begin{aligned}\frac{\partial \eta_y}{\partial t} &= \frac{\partial}{\partial z}\frac{\partial u}{\partial t} - \frac{\partial}{\partial x}\frac{\partial w}{\partial t}, \\ &= \frac{1}{Re}\nabla^2\eta_y - U_{lam}\frac{\partial \eta_y}{\partial x} - \frac{\partial U_{lam}}{\partial y}\frac{\partial v}{\partial z}.\end{aligned} \tag{4.44}$$

Equations 4.42 and 4.44 are named the velocity-vorticity formulation, and can be represented under matrix form as

$$E_{OSS}\,\frac{d\boldsymbol{x}(t)}{dt} = A_{OSS}\,\boldsymbol{x}(t), \tag{4.45a}$$

$$\boldsymbol{x} = \begin{bmatrix} v \\ \eta_y \end{bmatrix}, \tag{4.45b}$$

$$E_{OSS} = \begin{bmatrix} \nabla^2 & 0 \\ 0 & I \end{bmatrix}, \tag{4.45c}$$

$$A_{OSS} = \begin{bmatrix} \left(\frac{1}{Re}\nabla^4 + \frac{\partial^2 U_{lam}}{\partial y^2}\frac{\partial}{\partial x} - U_{lam}\frac{\partial}{\partial x}\nabla^2\right) & 0 \\ -\frac{\partial U_{lam}}{\partial y}\frac{\partial}{\partial z} & \left(\frac{1}{Re}\nabla^2 - U_{lam}\frac{\partial}{\partial x}\right) \end{bmatrix}. \tag{4.45d}$$

The former singularity of E_{OSS} has been replaced by an implicit boundary condition expressed in the Laplacian operator. Once the right boundary conditions are imposed, the matrix E_{OSS} is invertible, and the system can be solved. However, despite the fact E_{OSS} is non-singular, it can still be ill-conditioned if the wrong boundary conditions are applied. The Orr-Sommerfeld Squire model is finally

$$\frac{\partial \boldsymbol{x}(t)}{\partial t} = \mathcal{L}_{OSS}\,\boldsymbol{x}(t) = \begin{bmatrix} \mathcal{L}_{OS} & 0 \\ \mathcal{L}_C & \mathcal{L}_{Sq} \end{bmatrix}\begin{bmatrix} v \\ \eta_y \end{bmatrix}, \tag{4.46}$$

where $\mathcal{L}_{OS} = (\nabla^2)^{-1}\left(\frac{1}{Re}\nabla^4 + \frac{\partial^2 U_{lam}}{\partial y^2}\frac{\partial}{\partial x} - U_{lam}\frac{\partial}{\partial x}\nabla^2\right)$ is the Orr-Sommerfeld Operator, $\mathcal{L}_C = -\frac{\partial U_{lam}}{\partial y}\frac{\partial}{\partial z}$ is the Coupling operator and $\mathcal{L}_{Sq} = \left(\frac{1}{Re}\nabla^2 - U_{lam}\frac{\partial}{\partial x}\right)$ is the Squire operator.

4.5.2 Discretisation of the Orr-Sommerfeld Squire model

In this section, the OSS system 4.46 will be discretized for the PCF configuration presented in §2.2. PCF corresponds to a Channel geometry (see §4.4.2) and will thus be discretized in the form $Fourier \times Chebyshev \times Fourier$ as equation 4.37.

Streamwise and Spanwise Discretisation

Discretisation in streamwise and spanwise direction with Fourier modes splits the entire OSS system into many sets of pairs modes (α, β). Wall-normal velocity and vorticity

are approximated with a Fourier decomposition as in equation 4.17,

$$v(x,y,z,t) \approx \sum_{k_x=-\frac{N_x}{2}+1}^{N_x/2} \sum_{k_z=-\frac{N_z}{2}+1}^{N_z/2} \hat{v}_{\alpha,\beta}(y,t)\, \mathrm{e}^{\iota(\alpha x+\beta z)}, \tag{4.47a}$$

$$\eta_y(x,y,z,t) \approx \sum_{k_x=-\frac{N_x}{2}+1}^{N_x/2} \sum_{k_z=-\frac{N_z}{2}+1}^{N_z/2} \hat{\eta}_{\alpha,\beta}(y,t)\, \mathrm{e}^{\iota(\alpha x+\beta z)}, \tag{4.47b}$$

where $\hat{v}_{\alpha,\beta}$ and $\hat{\eta}_{\alpha,\beta}$ are the Fourier coefficients of v and η_y for a pair (α,β).

For each wavenumber pair (α,β), the system 4.46 can be discretised as

$$E_{OSS}\dot{\boldsymbol{x}} = A_{OSS}\boldsymbol{x}, \tag{4.48a}$$

$$\boldsymbol{x} = \begin{bmatrix} \hat{v}_{\alpha,\beta}(y,t) \\ \hat{\eta}_{\alpha,\beta}(y,t) \end{bmatrix}, \tag{4.48b}$$

$$E_{OSS} = \begin{bmatrix} \hat{\nabla}^2 & 0 \\ 0 & I \end{bmatrix}, \tag{4.48c}$$

$$A_{OSS} = \begin{bmatrix} A_{11} & 0 \\ A_{21} & A_{22} \end{bmatrix}, \tag{4.48d}$$

where

$$A_{11} = \frac{1}{Re}\hat{\nabla}^4 + \iota\alpha\frac{\partial^2 U_{lam}}{\partial y^2} - \iota\alpha U_{lam}\hat{\nabla}^2, \tag{4.49a}$$

$$A_{21} = -\iota\beta\frac{\partial U_{lam}}{\partial y}, \tag{4.49b}$$

$$A_{22} = \frac{1}{Re}\hat{\nabla}^2 - \iota\alpha U_{lam}, \tag{4.49c}$$

and

$$\hat{\nabla}^2 = \frac{\partial^2}{\partial y^2} - k^2 I, \tag{4.50a}$$

$$\hat{\nabla}^4 = \frac{\partial^4}{\partial y^4} - 2k^2\frac{\partial^2}{\partial y^2} + k^4 I, \tag{4.50b}$$

$$k^2 = \alpha^2 + \beta^2. \tag{4.50c}$$

Wall-normal Discretisation

As presented in section 4.4.2, clamped boundary conditions are imposed on the upper and lower walls of the channel geometry, beaking the periodicity in the wall-normal direction. Therefore, Chebyshev method is adopted for the discretisation in this direction.

Nevertheless, once the Dirichlet condition is imposed by setting to zero the first and last columns rows of the Laplacian operator, the matrix E_{OSS} becomes rank-deficient and

singular. To remedy this problem, only the internal block matrix of the Laplacian is considered, i.e. the block-matrix of size $(N_y - 2) \times (N_y - 2)$ excluding the column and rows of zero. The whole system will thus be reduced the same way.

The Fourier coefficients $\hat{v}_{\alpha,\beta}$ and $\hat{\eta}_{\alpha,\beta}$ in equation 4.47 can be approximated for each wavenumber pair (α, β) as

$$\hat{v}_{\alpha,\beta}(y,t) \approx \sum_{n_y=0}^{N_y} \tilde{v}_{\alpha,\beta}(t)\, T_{n_y}(y), \tag{4.51a}$$

$$\hat{\eta}_{\alpha,\beta}(y,t) \approx \sum_{n_y=0}^{N_y} \tilde{\eta}_{\alpha,\beta}(t)\, T_{n_y}(y), \tag{4.51b}$$

where $\tilde{v}_{\alpha,\beta}$ and $\tilde{\eta}_{\alpha,\beta}$ are the associated Chebyshev coefficients.

Coefficients $\tilde{v}_{\alpha,\beta}$ and $\tilde{\eta}_{\alpha,\beta}$ will be determined with a collocation method on a set of Gauss-Chebyshev-Lobatto points $\{y_i\}$ (see §4.2.3). The following system, reduced to size $(N_y - 2) \times (N_y - 2)$, derives from 4.48,

$$E_{OSS}\dot{\boldsymbol{x}} = A_{OSS}\boldsymbol{x}, \tag{4.52a}$$

$$\boldsymbol{x} = \begin{bmatrix} \tilde{v}_{\alpha,\beta}(t) \\ \tilde{\eta}_{\alpha,\beta}(t) \end{bmatrix}, \tag{4.52b}$$

$$E_{OSS} = \begin{bmatrix} \tilde{\nabla}^2 & 0 \\ 0 & I \end{bmatrix}, \tag{4.52c}$$

$$A_{OSS} = \begin{bmatrix} \tilde{A}_{11} & 0 \\ \tilde{A}_{21} & \tilde{A}_{22} \end{bmatrix}, \tag{4.52d}$$

where

$$\tilde{A}_{11} = \frac{1}{Re}\tilde{\nabla}^4 + \iota\alpha\mathcal{D}_0^2 U_{lam} I - \iota\alpha U_{lam}\tilde{\nabla}^2, \tag{4.53a}$$

$$\tilde{A}_{21} = -\iota\beta\mathcal{D}_0 U_{lam} I, \tag{4.53b}$$

$$\tilde{A}_{22} = \frac{1}{Re}\tilde{\nabla}^2 - \iota\alpha U_{lam} I, \tag{4.53c}$$

and

$$\tilde{\nabla}^2 = \mathcal{D}^2 - k^2 I, \tag{4.54a}$$

$$\tilde{\nabla}^4 = \mathcal{D}^4 - 2k^2\mathcal{D}^2 + k^4 I. \tag{4.54b}$$

4.6 Orr-Sommerfeld Squire Model extended for a steady non-laminar solution as base-flow (OSSE)

The application of LTI state-space control theory to an Invariant Solution (IS) requires a state-space model linearised around a three-dimensional base-flow. From this perspective, the OSS derived in §4.5 is not useful as it consists of a linearisation around the PCF laminar-state. For this reason, an alternative model is created by inserting a three-dimensional steady state as base-flow of the NSE instead of the Couette laminar-state and undertaking the derivation on the same fashion as the OSS model. However, due to the breaking of translational symmetry of the non-laminar baseflow, the derivation no longer diagonalises with Fourier wave-numbers. Henceforth, it requires taking account of crossed interactions between modes, which results in a new divergence-free model, called in this thesis as the Orr-Sommerfeld Squire model Extended for a non-laminar solution (OSSE). The derivation of the OSSE model is given below, while a detailed derivation is available in Appendix F. The derivation was not performed via automatic differentiation tools as symbolic `Python`, but manually. It requires indeed at many occasions to combine terms in order to simplify the mathematical expressions, notably with the continuity equation. This operation was not feasible automatically when the formulation is slightly different (e.g. order of the partial differentiation or dot products) and the automatically-derived equations lacked structure to interfere manually.

This section establishes a full-matrix state-space model that enables access to linear algebra and linear control theory for any non-laminar solution — not only invariant solutions, but any three-dimensional steady state — while reducing the dimension of the dynamical state by half. This latter point is particularly important for the later chapter 6 on the determination of the optimal control law. This law indeed derives from the solution of high-dimensional quadratic equation, called the "Riccati equation", which requires a large amount of memory and computational time when targeting an Invariant Solution (IS). The reduction in dimension is a game-changer to access this solution and determine the optimal control law.

4.6.1 Derivation of the OSSE model

A steady non-laminar state of the form

$$\bar{\boldsymbol{U}} = (\bar{U}(x,y,z), \bar{V}(x,y,z), \bar{W}(x,y,z)). \tag{4.55}$$

is inserted into the NSE 4.4. The linearisation around this steady non-laminar state, after neglecting body forces and non-linear terms, follows as

$$\frac{\partial u}{\partial t} = \frac{1}{Re}\nabla^2 u - \frac{\partial p}{\partial x} - u\frac{\partial \bar{U}}{\partial x} - \bar{U}\frac{\partial u}{\partial x} - v\frac{\partial \bar{U}}{\partial y} - \bar{V}\frac{\partial u}{\partial y} - w\frac{\partial \bar{U}}{\partial z} - \bar{W}\frac{\partial u}{\partial z}, \tag{4.56a}$$

$$\frac{\partial v}{\partial t} = \frac{1}{Re}\nabla^2 v - \frac{\partial p}{\partial y} - u\frac{\partial \bar{V}}{\partial x} - \bar{U}\frac{\partial v}{\partial x} - v\frac{\partial \bar{V}}{\partial y} - \bar{V}\frac{\partial v}{\partial y} - w\frac{\partial \bar{V}}{\partial z} - \bar{W}\frac{\partial v}{\partial z}, \tag{4.56b}$$

$$\frac{\partial w}{\partial t} = \frac{1}{Re}\nabla^2 w - \frac{\partial p}{\partial z} - u\frac{\partial \bar{W}}{\partial x} - \bar{U}\frac{\partial w}{\partial x} - v\frac{\partial \bar{W}}{\partial y} - \bar{V}\frac{\partial w}{\partial y} - w\frac{\partial \bar{W}}{\partial z} - \bar{W}\frac{\partial w}{\partial z}, \tag{4.56c}$$

$$\frac{\partial u}{\partial x} + \frac{\partial v}{\partial y} + \frac{\partial w}{\partial z} = 0. \tag{4.56d}$$

Equations 4.56 are then transformed in the same manner as the derivation of the OSS model presented in section 4.5.

Time-variation of the wall-normal velocity v

Firstly, the Laplacian of equation 4.56b is taken and the pressure scalar-field p is eliminated via the Poisson equation 4.8. Rearranging the terms, the time-variation of the velocity v can be expressed in function of the velocities u, v and w as

$$\begin{aligned}
\frac{\partial}{\partial t}\nabla^2 v = &\left[+ 2\frac{\partial^2 \bar{U}}{\partial xy}\frac{\partial}{\partial x} + 2\frac{\partial \bar{U}}{\partial x}\frac{\partial^2}{\partial xy} + 2\frac{\partial \bar{V}}{\partial x}\frac{\partial^2}{\partial y^2} + 2\frac{\partial^2 \bar{W}}{\partial xy}\frac{\partial}{\partial z} + 2\frac{\partial \bar{W}}{\partial x}\frac{\partial^2}{\partial yz} \right. \\
&\left. - \frac{\partial \bar{V}}{\partial x}\nabla^2 - 2\frac{\partial^2 \bar{V}}{\partial x^2}\frac{\partial}{\partial x} - 2\frac{\partial^2 \bar{V}}{\partial xz}\frac{\partial}{\partial z} - \frac{\partial \nabla^2 \bar{V}}{\partial x} \right] u \\
&+ \left[\frac{1}{Re}\nabla^4 + 2\frac{\partial^2 \bar{U}}{\partial y^2}\frac{\partial}{\partial x} + 2\frac{\partial^2 \bar{V}}{\partial y^2}\frac{\partial}{\partial y} + 2\frac{\partial^2 \bar{W}}{\partial y^2}\frac{\partial}{\partial z} \right. \\
&- \nabla^2 \bar{U}\frac{\partial}{\partial x} - 2\frac{\partial \bar{U}}{\partial x}\frac{\partial^2}{\partial x^2} - 2\frac{\partial \bar{U}}{\partial z}\frac{\partial^2}{\partial xz} - \bar{U}\frac{\partial \nabla^2}{\partial x} \\
&- \frac{\partial \bar{V}}{\partial y}\nabla^2 - 2\frac{\partial^2 \bar{V}}{\partial xy}\frac{\partial}{\partial x} - 2\frac{\partial^2 \bar{V}}{\partial y^2}\frac{\partial}{\partial y} - 2\frac{\partial^2 \bar{V}}{\partial yz}\frac{\partial}{\partial z} - \frac{\partial \nabla^2 \bar{V}}{\partial y} \\
&- \nabla^2 \bar{V}\frac{\partial}{\partial y} - 2\frac{\partial \bar{V}}{\partial x}\frac{\partial^2}{\partial xy} - 2\frac{\partial \bar{V}}{\partial z}\frac{\partial^2 v}{\partial yz} - \bar{V}\frac{\partial \nabla^2}{\partial y} \\
&\left. - \nabla^2 \bar{W}\frac{\partial}{\partial z} - 2\frac{\partial \bar{W}}{\partial x}\frac{\partial^2}{\partial xz} - 2\frac{\partial \bar{W}}{\partial z}\frac{\partial^2}{\partial z^2} - \bar{W}\frac{\partial \nabla^2}{\partial z} \right] v \\
&+ \left[2\frac{\partial^2 \bar{U}}{\partial yz}\frac{\partial}{\partial x} + 2\frac{\partial \bar{U}}{\partial z}\frac{\partial^2}{\partial xy} + 2\frac{\partial \bar{V}}{\partial z}\frac{\partial^2}{\partial y^2} + 2\frac{\partial^2 \bar{W}}{\partial yz}\frac{\partial}{\partial z} + 2\frac{\partial \bar{W}}{\partial z}\frac{\partial^2}{\partial yz} \right. \\
&\left. - \frac{\partial \bar{V}}{\partial z}\nabla^2 - 2\frac{\partial^2 \bar{V}}{\partial xz}\frac{\partial}{\partial x} - 2\frac{\partial^2 \bar{V}}{\partial z^2}\frac{\partial}{\partial z} - \frac{\partial \nabla^2 \bar{V}}{\partial z} \right] w.
\end{aligned} \tag{4.57}$$

Time-variation of the wall-normal vorticity η_y

To describe the complete 3D problem, the wall-normal vorticity $\eta(y)$ 4.43 is introduced and differentiated in time,

$$\frac{\partial \eta_y}{\partial t} = \frac{\partial}{\partial z}\frac{\partial u}{\partial t} - \frac{\partial}{\partial x}\frac{\partial w}{\partial t}. \tag{4.58}$$

The time-differentiation of stream-wise u and span-wise w components are eliminated with expressions 4.56a and 4.56c. After some rearranging, the time-evolution of wall-normal vorticity η_y follows as

$$\begin{aligned}
\frac{\partial \eta_y}{\partial t} = &\left[\frac{1}{Re}\nabla^2 - \bar{U}\frac{\partial}{\partial x} - \bar{V}\frac{\partial}{\partial y} - \bar{W}\frac{\partial}{\partial z} - \frac{\partial \bar{U}}{\partial x} - \frac{\partial \bar{W}}{\partial z}\right]\eta_y \\
&+\left[-\frac{\partial^2 \bar{U}}{\partial x z} - \frac{\partial \bar{U}}{\partial z}\frac{\partial}{\partial x} - \frac{\partial \bar{V}}{\partial z}\frac{\partial}{\partial y} + \frac{\partial \bar{W}}{\partial x}\frac{\partial}{\partial x} + \frac{\partial^2 \bar{W}}{\partial x^2}\right]u \\
&+\left[-\frac{\partial \bar{U}}{\partial y}\frac{\partial}{\partial z} - \frac{\partial^2 \bar{U}}{\partial y z} + \frac{\partial \bar{W}}{\partial y}\frac{\partial}{\partial x} + \frac{\partial^2 \bar{W}}{\partial x y}\right]v \\
&+\left[-\frac{\partial \bar{U}}{\partial z}\frac{\partial}{\partial z} - \frac{\partial^2 \bar{U}}{\partial z^2} + \frac{\partial \bar{V}}{\partial x}\frac{\partial}{\partial y} + \frac{\partial \bar{W}}{\partial x}\frac{\partial}{\partial z} + \frac{\partial^2 \bar{W}}{\partial x z}\right]w.
\end{aligned} \tag{4.59}$$

Equations 4.57 and 4.59 form the velocity-vorticity formulation for the OSSE.

4.6.2 Streamwise and spanwise discretisation of the OSSE model

Fourier series

The system formed by equations 4.57 and 4.59 is discretised with Fourier methods in the steam-wise and span-wise direction, as it corresponds to a Channel geometry (see §4.4.2). For this reason, Fourier discretisation of each variable in the stream- and

spanwise directions are introduced as

$$u(x,y,z,t) \approx \sum_{k_x=-\frac{N_x}{2}+1}^{N_x/2} \sum_{k_z=-\frac{N_z}{2}+1}^{N_z/2} \hat{u}_{\alpha,\beta}(y,t)\, \mathrm{e}^{\iota(\alpha x+\beta z)}, \tag{4.60a}$$

$$v(x,y,z,t) \approx \sum_{k_x=-\frac{N_x}{2}+1}^{N_x/2} \sum_{k_z=-\frac{N_z}{2}+1}^{N_z/2} \hat{v}_{\alpha,\beta}(y,t)\, \mathrm{e}^{\iota(\alpha x+\beta z)}, \tag{4.60b}$$

$$w(x,y,z,t) \approx \sum_{k_x=-\frac{N_x}{2}+1}^{N_x/2} \sum_{k_z=-\frac{N_z}{2}+1}^{N_z/2} \hat{w}_{\alpha,\beta}(y,t)\, \mathrm{e}^{\iota(\alpha x+\beta z)}, \tag{4.60c}$$

$$\eta_y(x,y,z,t) \approx \sum_{k_x=-\frac{N_x}{2}+1}^{N_x/2} \sum_{k_z=-\frac{N_z}{2}+1}^{N_z/2} \hat{\eta}_{\alpha,\beta}(y,t)\, \mathrm{e}^{\iota(\alpha x+\beta z)}, \tag{4.60d}$$

$$\bar{U}(x,y,z) \approx \sum_{k'_x=-\frac{N'_x}{2}+1}^{N'_x/2} \sum_{k'_z=-\frac{N'_z}{2}+1}^{N'_z/2} \hat{U}_{\alpha',\beta'}(y)\, \mathrm{e}^{\iota(\alpha' x+\beta' z)}, \tag{4.60e}$$

$$\bar{V}(x,y,z) \approx \sum_{k'_x=-\frac{N'_x}{2}+1}^{N'_x/2} \sum_{k'_z=-\frac{N'_z}{2}+1}^{N'_z/2} \hat{V}_{\alpha',\beta'}(y)\, \mathrm{e}^{\iota(\alpha' x+\beta' z)}, \tag{4.60f}$$

$$\bar{W}(x,y,z) \approx \sum_{k'_x=-\frac{N'_x}{2}+1}^{N'_x/2} \sum_{k'_z=-\frac{N'_z}{2}+1}^{N'_z/2} \hat{W}_{\alpha',\beta'}(y)\, \mathrm{e}^{\iota(\alpha' x+\beta' z)}. \tag{4.60g}$$

Correlation property of Fourier series

The correlation property of Fourier series is necessary for the following steps,

$$\sum_{k'} c'_{k'} e^{\iota k' t} \sum_{k} c_k e^{\iota k t} = \sum_{k} \Big(\sum_{k'} c'_{k'} c_{k-k'} \Big) e^{\iota k t}, \tag{4.61}$$

which applies in this case as

$$\begin{aligned} &\sum_{k'_x=-\frac{N'_x}{2}+1}^{N'_x/2} \sum_{k'_z=-\frac{N'_z}{2}+1}^{N'_z/2} \hat{A}_{\alpha',\beta'}(y) e^{\iota(\alpha' x+\beta' z)} \sum_{k_x=-\frac{N_x}{2}+1}^{N_x/2} \sum_{k_z=-\frac{N_z}{2}+1}^{N_z/2} \hat{B}_{\alpha,\beta}(y,t) e^{\iota(\alpha x+\beta z)} = \\ &\sum_{k_x=-\frac{N_x}{2}+1}^{N_x/2} \sum_{k_z=-\frac{N_z}{2}+1}^{N_z/2} \Big(\sum_{k'_x=-\frac{N'_x}{2}+1}^{N'_x/2} \sum_{k'_z=-\frac{N'_z}{2}+1}^{N'_z/2} \hat{A}_{\alpha',\beta'}(y) \hat{B}_{\alpha-\alpha',\beta-\beta'}(y,t) \Big) e^{\iota(\alpha x+\beta z)}. \end{aligned} \tag{4.62}$$

Note on correlation of Fourier series and Real Fast Fourier Transform

The Fourier discretisation in the stream- and span-wise directions of a function $u(x, y, z, t)$,

$$u(x, y, z, t) = \sum_{k_x=-\frac{N_x}{2}+1}^{N_x/2} \sum_{k_z=-\frac{N_z}{2}+1}^{N_z/2} \hat{u}_{k_x,k_z}(y, t) \mathrm{e}^{\iota(k_x x + k_z z)}, \tag{4.63}$$

is in practice operated by two successive Fast Fourier Transforms. The first FFT performs the span-wise discretisation: the real-type dataset of physical variables is transformed into a complex-type dataset of Fourier coefficients in the span-wise direction, but still physical in the stream-wise direction. The second FFT performs the stream-wise discretisation: the latter dataset is transformed into a complex-type dataset of Fourier coefficients for both stream- and span-wise directions. The final spectral dataset is of dimension $N_x \times N_z$.

$$\underset{\text{Real, } N_x \times N_z}{\overset{x}{\text{Physical}} \times \overset{z}{\text{Physical}}} \xRightarrow[\text{FFT}]{} \underset{\text{Complex, } N_x \times N_z}{\overset{x}{\text{Physical}} \times \overset{z}{\text{Fourier}}} \xRightarrow[\text{FFT}]{} \underset{\text{Complex, } N_x \times N_z}{\overset{x}{\text{Fourier}} \times \overset{z}{\text{Fourier}}}$$

In the case of a purely real dataset, the positive and negative Fourier coefficients are complex conjugate,

$$\hat{u}_{k_z}(x, y, t) = \hat{u}_{-k_z}(x, y, t)^*. \tag{4.64}$$

Therefore, calculating only the positive Fourier coefficients lead to the same accuracy, for a final spectrum of dimension $N_x \times \left(\frac{N_z}{2} + 1\right)$. This method is called Real Fast Fourier Transform (RFFT), and can be applied instead of the first FFT —before the coefficients become complex.

$$\underset{\text{Real, } N_x \times N_z}{\overset{x}{\text{Physical}} \times \overset{z}{\text{Physical}}} \xRightarrow[\textbf{RFFT}]{} \underset{\text{Complex, } N_x \times (\frac{N_z}{2}+1)}{\overset{x}{\text{Physical}} \times \overset{z}{\text{Fourier}}} \xRightarrow[\text{FFT}]{} \underset{\text{Complex, } N_x \times (\frac{N_z}{2}+1)}{\overset{x}{\text{Fourier}} \times \overset{z}{\text{Fourier}}}$$

`Channelflow` takes advantage of this property. Nonetheless, the implementation of the RFFT into the OSSE model is not straightforward, even if the method `numpy.fft.rfft` is available in `Python`. The convolution of Fourier series wraps indeed "around the edges" of the domain, thus requiring both positive and negative Fourier modes. Furthermore, the complex-conjugation operation is not a linear process, and thereby can not be translated into a linear algebraic operation. For these reasons, the RFFT can not be employed directly within the OSSE model, and the entire Fourier spectrum is stored.

Even so, a modification in the structure of the system can avoid this limitation. It consists in separating the real and imaginary part of the state-vector $\boldsymbol{x}$ and reshaping the entire model. This is actually the purpose of the Real Orr-Sommerfeld Squire model Extended for a non-laminar solution (ROSSE) detailed in section 4.7.

Stream-wise and span-wise discretisation of the wall-normal vorticity η_y

Correlation of Fourier series applied to 4.59 leads to the expression of the wall-normal vorticity time-variation as a function of the different modes of η_y, u, v and w as

$$\begin{aligned}
\frac{\partial \eta_y}{\partial t} = & \sum_{k_x=-\frac{N_x}{2}+1}^{N_x/2} \sum_{k_z=-\frac{N_z}{2}+1}^{N_z/2} \frac{1}{Re}\nabla^2 \hat{\eta}_{\alpha,\beta}(y,t)\, \mathrm{e}^{\iota(\alpha x+\beta z)} \\
& + \sum_{k_x=-\frac{N_x}{2}+1}^{N_x/2} \sum_{k_z=-\frac{N_z}{2}+1}^{N_z/2} \sum_{k'_x=-\frac{N'_x}{2}+1}^{N'_x/2} \sum_{k'_z=-\frac{N'_z}{2}+1}^{N'_z/2} \mathrm{e}^{\iota(\alpha x+\beta z)} \\
& \Bigg[- \Big(\iota(\alpha-\alpha')\hat{U}_{\alpha',\beta'}(y,t) + \hat{V}_{\alpha',\beta'}(y,t)\frac{\partial}{\partial y} + \iota(\beta-\beta')\hat{W}_{\alpha',\beta'}(y,t) \\
& \quad + \iota\alpha'\hat{U}_{\alpha',\beta'}(y,t) + \iota\beta'\hat{W}_{\alpha',\beta'}(y,t) \Big) \hat{\eta}_{\alpha-\alpha',\beta-\beta'}(y,t) \\
& + \Big(\alpha'\beta'\hat{U}_{\alpha',\beta'}(y,t) + \beta'(\alpha-\alpha')\hat{U}_{\alpha',\beta'}(y,t) - \iota\beta'\hat{V}_{\alpha',\beta'}(y,t)\frac{\partial}{\partial y} \\
& \quad - \alpha'(\alpha-\alpha')\hat{W}_{\alpha',\beta'}(y,t) - \alpha'^2\hat{W}_{\alpha',\beta'}(y,t) \Big) \hat{u}_{\alpha-\alpha',\beta-\beta'}(y,t) \\
& + \Big(- \iota(\beta-\beta')\frac{\partial \hat{U}_{\alpha',\beta'}(y,t)}{\partial y} - \iota\beta'\frac{\partial \hat{U}_{\alpha',\beta'}(y,t)}{\partial y} \\
& \quad + \iota(\alpha-\alpha')\frac{\partial \hat{W}_{\alpha',\beta'}(y,t)}{\partial y} + \iota\alpha'\frac{\partial \hat{W}_{\alpha',\beta'}(y,t)}{\partial y} \Big) \hat{v}_{\alpha-\alpha',\beta-\beta'}(y,t) \\
& + \Big(\beta'(\beta-\beta')\hat{U}_{\alpha',\beta'}(y,t) + \beta'^2\hat{U}_{\alpha',\beta'}(y,t) + \iota\alpha'\hat{V}_{\alpha',\beta'}(y,t)\frac{\partial}{\partial y} \\
& \quad - \alpha'(\beta-\beta')\hat{W}_{\alpha',\beta'}(y,t) - \alpha'\beta'\hat{W}_{\alpha',\beta'}(y,t) \Big) \hat{w}_{\alpha-\alpha',\beta-\beta'}(y,t) \Bigg].
\end{aligned} \tag{4.65}$$

The Fourier bases $\{\mathrm{e}^{\iota\alpha x}\}$ and $\{\mathrm{e}^{\iota\beta z}\}$ are orthogonal. Consequently, each Fourier coefficient $\hat{\eta}_{\alpha,\beta}$ of the LHS of eq. 4.65 can be expressed individually. Nonetheless, and in contrast to the OSS derivation, due to the correlation of Fourier series on the RHS of eq. 4.65, the coefficient $\hat{\eta}_{\alpha_i,\beta_j}$ is function of the entire set of coefficients $\hat{u}_{\alpha_k\neq\alpha_i,\beta_l\neq\beta_j}$, $\hat{v}_{\alpha_k\neq\alpha_i,\beta_l\neq\beta_j}$, $\hat{w}_{\alpha_k\neq\alpha_i,\beta_l\neq\beta_j}$ and $\hat{\eta}_{\alpha_k\neq\alpha_i,\beta_l\neq\beta_j}$. In other words, the derivation no longer diagonalizes with Fourier wavenumber.

For each wavenumber pair (α,β), the Fourier coefficients $\{\hat{u}_{\alpha,\beta}\}$ and $\{\hat{w}_{\alpha,\beta}\}$ of the steam- and span-wise velocity components are replaced by their respective expressions given in C.5 and C.4. The wavenumber pair $(\alpha=0,\beta=0)$ is a particular case, as $\hat{\eta}_{0,0}$ is not defined. Therefore, the Fourier coefficients $\{\hat{u}_{0,0}\}$ and $\{\hat{w}_{0,0}\}$ can not be retrieved with expressions C.5 and C.4. For this reason, the state will be composed of all the modes of the wall-normal velocity $\{\hat{v}_{\alpha,\beta}\}$, all the modes excepted the pair $(0,0)$ of the wall-normal vorticity $\{\hat{\eta}_{\alpha,\beta}\}$, and the Fourier coefficients $\hat{u}_{0,0}$ and $\hat{w}_{0,0}$.

By applying these remarks to eq. 4.65 and rearranging, the Fourier coefficients $\hat{\eta}_{\alpha,\beta}$ can be expressed as

$$\begin{aligned}\frac{\partial \hat{\eta}_{\alpha,\beta}}{\partial t} = &\sum_{k'_x=-\frac{N'_x}{2}+1}^{N'_x/2}\sum_{k'_z=-\frac{N'_z}{2}+1}^{N'_z/2} F_{\substack{\alpha,\beta,\\ \alpha',\beta'}}\ \hat{v}_{\alpha-\alpha',\beta-\beta'}(y,t)\\ &+\sum_{\substack{k'_x=-\frac{N'_x}{2}+1\\(k_x-k'_x,k_z-k'_z)\neq(0,0)}}^{N'_x/2}\sum_{k'_z=-\frac{N'_z}{2}+1}^{N'_z/2} G_{\substack{\alpha,\beta,\\ \alpha',\beta'}}\ \hat{v}_{\alpha-\alpha',\beta-\beta'}(y,t)\\ &+\sum_{\substack{k'_x=-\frac{N'_x}{2}+1\\(k_x-k'_x,k_z-k'_z)\neq(0,0)}}^{N'_x/2}\sum_{k'_z=-\frac{N'_z}{2}+1}^{N'_z/2}\left[H_{\substack{\alpha,\beta,\\ \alpha',\beta'}} + J_{\substack{\alpha,\beta,\\ \alpha',\beta'}}\right]\hat{\eta}_{\alpha-\alpha',\beta-\beta'}(y,t)\\ &+\frac{1}{Re}\nabla^2\hat{\eta}_{\alpha,\beta}(y,t) + K_{\substack{\alpha,\beta,\\ 0,0}}\ \hat{u}_{0,0}(y,t) + L_{\substack{\alpha,\beta,\\ 0,0}}\ \hat{w}_{0,0}(y,t),\end{aligned} \tag{4.66}$$

where the coefficients F, G, H, JK, L are given in the appendix D.1.

Streamwise and spanwise discretisation of the wall-normal velocity v

Equation 4.57 receives the same treatment in order to obtain an expression for all the Fourier coefficients $\hat{v}_{\alpha,\beta}$ as a function of all the modes of the wall-normal velocity $\{\hat{v}_{\alpha,\beta}\}$, all the modes excepted the pair $(0,0)$ of the wall-normal vorticity $\{\hat{\eta}_{\alpha,\beta}\}$, and the Fourier coefficients $\hat{u}_{0,0}$ and $\hat{w}_{0,0}$. After rearranging, it leads to the expression

$$\begin{aligned}\frac{\partial}{\partial t}\hat{\nabla}^2\hat{v}_{\alpha,\beta}(y,t) = &\frac{1}{Re}\hat{\nabla}^4_{\alpha,\beta}\hat{v}_{\alpha,\beta}(y,t) + \sum_{k'_x=-\frac{N'_x}{2}+1}^{N'_x/2}\sum_{k'_z=-\frac{N'_z}{2}+1}^{N'_z/2} A_{\substack{\alpha,\beta,\\ \alpha',\beta'}}\ \hat{v}_{\alpha-\alpha',\beta-\beta'}(y,t)\\ &+\sum_{\substack{k'_x=-\frac{N'_x}{2}+1\\(k_x-k'_x,k_z-k'_z)\neq(0,0)}}^{N'_x/2}\sum_{k'_z=-\frac{N'_z}{2}+1}^{N'_z/2} B_{\substack{\alpha,\beta,\\ \alpha',\beta'}}\ \hat{v}_{\alpha-\alpha',\beta-\beta'}(y,t)\\ &+\sum_{\substack{k'_x=-\frac{N'_x}{2}+1\\(k_x-k'_x,k_z-k'_z)\neq(0,0)}}^{N'_x/2}\sum_{k'_z=-\frac{N'_z}{2}+1}^{N'_z/2} C_{\substack{\alpha,\beta,\\ \alpha',\beta'}}\ \hat{\eta}_{\alpha-\alpha',\beta-\beta'}(y,t)\\ &+D_{\substack{\alpha,\beta,\\ 0,0}}\ \hat{u}_{0,0}(y,t) + E_{\substack{\alpha,\beta,\\ 0,0}}\ \hat{w}_{0,0}(y,t),\end{aligned} \tag{4.67}$$

where the coefficients A, B, C, D, E are given in the appendix D.1.

Streamwise and spanwise discretisation of the streamwise velocity to determine $\hat{u}_{0,0}(y,t)$

The OSSE still requires the expression of $\hat{u}_{0,0}(y,t)$, which is obtained from equation 4.56a, considering only the pair $(\alpha = 0, \beta = 0)$

$$\begin{aligned}\frac{\partial \hat{u}_{\alpha=0,\beta=0}}{\partial t} &= \frac{1}{Re}\hat{\nabla}^2_{0,0}\hat{u}_{0,0} + \sum_{k'_x=-\frac{N'_x}{2}+1}^{N'_x/2}\sum_{k'_z=-\frac{N'_z}{2}+1}^{N'_z/2}\Big[-\iota\alpha'\hat{U}_{\alpha',\beta'}\hat{u}_{\alpha-\alpha',\beta-\beta'} - \iota(\alpha-\alpha')\hat{U}_{\alpha',\beta'}\hat{u}_{\alpha-\alpha',\beta-\beta'} \\ &\qquad - \frac{\partial \hat{U}_{\alpha',\beta'}}{\partial y}\hat{v}_{\alpha-\alpha',\beta-\beta'} - \hat{V}_{\alpha',\beta'}\frac{\partial \hat{u}_{\alpha-\alpha',\beta-\beta'}}{\partial y} \\ &\qquad - \iota\beta'\hat{U}_{\alpha',\beta'}\hat{w}_{\alpha-\alpha',\beta-\beta'} - \iota(\beta-\beta')\hat{W}_{\alpha',\beta'}\hat{u}_{\alpha-\alpha',\beta-\beta'}\Big], \\ &= \frac{1}{Re}\hat{\nabla}^2_{0,0}\hat{u}_{0,0} + \sum_{k'_x=-\frac{N'_x}{2}+1}^{N'_x/2}\sum_{k'_z=-\frac{N'_z}{2}+1}^{N'_z/2}\Big[-\frac{\partial \hat{U}_{\alpha',\beta'}}{\partial y}\hat{v}_{-\alpha',-\beta'} - \hat{V}_{\alpha',\beta'}\frac{\partial \hat{u}_{-\alpha',-\beta'}}{\partial y} \\ &\qquad - \iota\beta'\hat{U}_{\alpha',\beta'}\hat{w}_{-\alpha',-\beta'} + \iota\beta'\hat{W}_{\alpha',\beta'}\hat{u}_{-\alpha',-\beta'}\Big].\end{aligned} \tag{4.68}$$

Replacing $\hat{u}_{\alpha,\beta}$ and $\hat{w}_{\alpha,\beta}$ by their expressions C.5 and C.4 leads to the final expression

$$\begin{aligned}\frac{\partial \hat{u}_{0,0}}{\partial t} &= \left[\frac{1}{Re}\hat{\nabla}^2_{0,0} - \hat{V}_{0,0}\frac{\partial}{\partial y}\right]\hat{u}_{0,0} + \sum_{k'_x=-\frac{N'_x}{2}+1}^{N'_x/2}\sum_{k'_z=-\frac{N'_z}{2}+1}^{N'_z/2} M_{\alpha',\beta'}\hat{v}_{-\alpha',-\beta'} \\ &\quad + \sum_{\substack{k'_x=-\frac{N'_x}{2}+1 \\ (k_x-k'_x,k_z-k'_z)\neq(0,0)}}^{N'_x/2}\sum_{k'_z=-\frac{N'_z}{2}+1}^{N'_z/2} N_{\alpha',\beta'}\ \hat{v}_{-\alpha',-\beta'} + \sum_{\substack{k'_x=-\frac{N'_x}{2}+1 \\ (k_x-k'_x,k_z-k'_z)\neq(0,0)}}^{N'_x/2}\sum_{k'_z=-\frac{N'_z}{2}+1}^{N'_z/2} O_{\alpha',\beta'}\ \hat{\eta}_{-\alpha',-\beta'},\end{aligned} \tag{4.69}$$

where the coefficients M, N, O are given in the appendix D.1.

Streamwise and spanwise discretisation of the spanwise velocity to determine $\hat{w}_{0,0}(y,t)$

Finally, the expression of $\hat{w}_{0,0}(y,t)$ is obtained from equation 4.56c, considering only the pair $(\alpha = 0, \beta = 0)$ and rearranging,

$$\begin{aligned}\frac{\partial \hat{w}_{0,0}}{\partial t} = \left[\frac{1}{Re}\hat{\nabla}^2_{0,0} - \hat{V}_{0,0}\frac{\partial}{\partial y}\right]\hat{w}_{0,0} + \sum_{k'_x=-\frac{N'_x}{2}+1}^{N'_x/2}\sum_{k'_z=-\frac{N'_z}{2}+1}^{N'_z/2} P_{\alpha',\beta'}\hat{v}_{-\alpha',-\beta'} \\ + \sum_{\substack{k'_x=-\frac{N'_x}{2}+1 \\ (k_x-k'_x,k_z-k'_z)\neq(0,0)}}^{N'_x/2}\sum_{k'_z=-\frac{N'_z}{2}+1}^{N'_z/2} Q_{\alpha',\beta'}\hat{v}_{-\alpha',-\beta'} + \sum_{\substack{k'_x=-\frac{N'_x}{2}+1 \\ (k_x-k'_x,k_z-k'_z)\neq(0,0)}}^{N'_x/2}\sum_{k'_z=-\frac{N'_z}{2}+1}^{N'_z/2} R_{\alpha',\beta'}\hat{\eta}_{-\alpha',-\beta'},\end{aligned} \tag{4.70}$$

where the coefficients P, Q, R are given in the appendix D.1.

4.6.3 Wall-normal discretisation of the Orr-Sommerfeld Squire Model extended for a non-laminar solution

Chebyshev series

For a channel geometry (§4.4.2), clamped boudary conditions are imposed at the upper and lower borders of the domain, breaking the wall-normal periodicity. Chebyshev method is adopted for the discretisation in this direction. We remind the reader that due to the Dirichlet boundary condition, only the internal block matrices are considered, i.e. the block-matrix of size $(N_y - 2) \times (N_y - 2)$ excluding the column and rows of zero.

Just as the derivation of the OSS model (§4.5.2), the Fourier coefficients for each

wavenumber pair (α, β) introduced in equations 4.60 can be approximated in the wall-normal direction with their associated Chebyshev series as

$$\hat{u}_{\alpha,\beta}(y,t) \approx \sum_{n_y=0}^{N_y} \tilde{u}_{\alpha,\beta}(t)\, T_{n_y}(y), \tag{4.71a}$$

$$\hat{v}_{\alpha,\beta}(y,t) \approx \sum_{n_y=0}^{N_y} \tilde{v}_{\alpha,\beta}(t)\, T_{n_y}(y), \tag{4.71b}$$

$$\hat{w}_{\alpha,\beta}(y,t) \approx \sum_{n_y=0}^{N_y} \tilde{w}_{\alpha,\beta}(t)\, T_{n_y}(y), \tag{4.71c}$$

$$\hat{\eta}_{\alpha,\beta}(y,t) \approx \sum_{n_y=0}^{N_y} \tilde{\eta}_{\alpha,\beta}(t)\, T_{n_y}(y), \tag{4.71d}$$

$$\hat{U}_{\alpha',\beta'}(y) \approx \sum_{n_y=0}^{N_y} \tilde{U}_{\alpha',\beta'}\, T_{n_y}(y), \tag{4.71e}$$

$$\hat{V}_{\alpha',\beta'}(y) \approx \sum_{n_y=0}^{N_y} \tilde{V}_{\alpha',\beta'}\, T_{n_y}(y), \tag{4.71f}$$

$$\hat{W}_{\alpha',\beta'}(y) \approx \sum_{n_y=0}^{N_y} \tilde{W}_{\alpha',\beta'}\, T_{n_y}(y). \tag{4.71g}$$

Remark on notations: In the following development, we distinguish the differentiation operators dedicated to the baseflow $\bar{\boldsymbol{U}}$ from the ones dedicated to the perturbation $\boldsymbol{u}$. The differentiation matrices of the baseflow are noted with with $\cdot_0$, e.g. $\mathcal{D}_0$ and ∇_0^2. They are never imposed with any boundary condition. On the contrary, the differentiation matrices of the perturbations are not marked with any notation, e.g. $\mathcal{D}$, ∇^2 and ∇^4. They can be imposed with Dirichlet or Neumann boundary condition if necessary.

As a reminder, the expressions of $\tilde{\nabla}^2$, $\tilde{\nabla}^4$ and $\tilde{\nabla}_0^2$ are

$$\tilde{\nabla}_0^2 = \mathcal{D}_0^2 - k^2 I, \tag{4.72a}$$

$$\tilde{\nabla}^2 = \mathcal{D}^2 - k^2 I, \tag{4.72b}$$

$$\tilde{\nabla}^4 = \mathcal{D}^4 - 2k^2\mathcal{D}^2 + k^4 I. \tag{4.72c}$$

Wall-normal discretisation of the wall-normal velocity v

Applying the Chebyshev method to equation 4.67 leads to

$$\begin{aligned}\frac{\partial}{\partial t}\tilde{\nabla}^2\tilde{v}_{\alpha,\beta}(y,t) \;=\; \frac{1}{Re}\tilde{\nabla}^4_{\alpha,\beta}\tilde{v}_{\alpha,\beta}(y,t) &+ \sum_{k'_x=-\frac{N'_x}{2}+1}^{N'_x/2}\sum_{k'_z=-\frac{N'_z}{2}+1}^{N'_z/2} \tilde{A}_{\substack{\alpha,\beta,\\ \alpha',\beta'}}\;\tilde{v}_{\alpha-\alpha',\beta-\beta'}(y,t)\\ &+ \sum_{\substack{k'_x=-\frac{N'_x}{2}+1\\ (k_x-k'_x,k_z-k'_z)\neq(0,0)}}^{N'_x/2}\sum_{k'_z=-\frac{N'_z}{2}+1}^{N'_z/2} \tilde{B}_{\substack{\alpha,\beta,\\ \alpha',\beta'}}\;\tilde{v}_{\alpha-\alpha',\beta-\beta'}(y,t)\\ &+ \sum_{\substack{k'_x=-\frac{N'_x}{2}+1\\ (k_x-k'_x,k_z-k'_z)\neq(0,0)}}^{N'_x/2}\sum_{k'_z=-\frac{N'_z}{2}+1}^{N'_z/2} \tilde{C}_{\substack{\alpha,\beta,\\ \alpha',\beta'}}\;\tilde{\eta}_{\alpha-\alpha',\beta-\beta'}(y,t)\\ &+ \tilde{D}_{\substack{\alpha,\beta,\\ 0,0}}\;\tilde{u}_{0,0}(y,t) + \tilde{E}_{\substack{\alpha,\beta,\\ 0,0}}\;\tilde{w}_{0,0}(y,t),\end{aligned} \tag{4.73}$$

where the coefficients $\tilde{A}, \tilde{B}, \tilde{C}, \tilde{D}, \tilde{E}$ are given in the appendix D.2.

Wall-normal discretisation of the wall-normal vorticity η_y

Applying the Chebyshev method to equation 4.66 leads to

$$\begin{aligned}\frac{\partial\tilde{\eta}_{\alpha,\beta}}{\partial t} = &\sum_{k'_x=-\frac{N'_x}{2}+1}^{N'_x/2}\sum_{k'_z=-\frac{N'_z}{2}+1}^{N'_z/2} \tilde{F}_{\substack{\alpha,\beta,\\ \alpha',\beta'}}\;\tilde{v}_{\alpha-\alpha',\beta-\beta'}(y,t)\\ &+ \sum_{\substack{k'_x=-\frac{N'_x}{2}+1\\ (k_x-k'_x,k_z-k'_z)\neq(0,0)}}^{N'_x/2}\sum_{k'_z=-\frac{N'_z}{2}+1}^{N'_z/2} \tilde{G}_{\substack{\alpha,\beta,\\ \alpha',\beta'}}\;\tilde{v}_{\alpha-\alpha',\beta-\beta'}(y,t)\\ &+ \sum_{\substack{k'_x=-\frac{N'_x}{2}+1\\ (k_x-k'_x,k_z-k'_z)\neq(0,0)}}^{N'_x/2}\sum_{k'_z=-\frac{N'_z}{2}+1}^{N'_z/2} \left[\tilde{H}_{\substack{\alpha,\beta,\\ \alpha',\beta'}} + \tilde{J}_{\substack{\alpha,\beta,\\ \alpha',\beta'}}\right]\tilde{\eta}_{\alpha-\alpha',\beta-\beta'}(y,t)\\ &+ \frac{1}{Re}\tilde{\nabla}^2\tilde{\eta}_{\alpha,\beta}(y,t) + \tilde{K}_{\substack{\alpha,\beta,\\ 0,0}}\;\tilde{u}_{0,0}(y,t) + \tilde{L}_{\substack{\alpha,\beta,\\ 0,0}}\;\tilde{w}_{0,0}(y,t),\end{aligned} \tag{4.74}$$

where the coefficients $\tilde{F}, \tilde{G}, \tilde{H}, \tilde{J}, \tilde{K}, \tilde{L}$ are given in the appendix D.2.

Wall-normal discretisation of the streamwise velocity to determine $\tilde{u}_{0,0}(y,t)$

Applying the Chebyshev method to equation 4.69 leads to

$$\begin{aligned}\frac{\partial \tilde{u}_{0,0}}{\partial t} = &\left[\frac{1}{Re}\tilde{\nabla}^2_{0,0} - \tilde{V}_{0,0}\frac{\partial}{\partial y}\right]\tilde{u}_{0,0} + \sum_{k'_x=-\frac{N'_x}{2}+1}^{N'_x/2}\sum_{k'_z=-\frac{N'_z}{2}+1}^{N'_z/2} \tilde{M}_{\alpha',\beta'}\ \tilde{v}_{-\alpha',-\beta'} \\ &+ \sum_{\substack{k'_x=-\frac{N'_x}{2}+1 \\ (k_x-k'_x,k_z-k'_z)\neq(0,0)}}^{N'_x/2}\sum_{k'_z=-\frac{N'_z}{2}+1}^{N'_z/2} \tilde{N}_{\alpha',\beta'}\ \tilde{v}_{-\alpha',-\beta'} + \sum_{\substack{k'_x=-\frac{N'_x}{2}+1 \\ (k_x-k'_x,k_z-k'_z)\neq(0,0)}}^{N'_x/2}\sum_{k'_z=-\frac{N'_z}{2}+1}^{N'_z/2} \tilde{O}_{\alpha',\beta'}\ \tilde{\eta}_{-\alpha',-\beta'},\end{aligned} \tag{4.75}$$

where the coefficients $\tilde{M}, \tilde{N}, \tilde{O}$ are given in the appendix D.2.

Wall-normal discretisation of the spanwise velocity to determine $\tilde{w}_{0,0}(y,t)$

Applying the Chebyshev method to equation 4.70 leads to

$$\begin{aligned}\frac{\partial \tilde{w}_{0,0}}{\partial t} = &\left[\frac{1}{Re}\tilde{\nabla}^2_{0,0} - \tilde{V}_{0,0}\frac{\partial}{\partial y}\right]\tilde{w}_{0,0} + \sum_{k'_x=-\frac{N'_x}{2}+1}^{N'_x/2}\sum_{k'_z=-\frac{N'_z}{2}+1}^{N'_z/2} \tilde{P}_{\alpha',\beta'}\tilde{v}_{-\alpha',-\beta'} \\ &+ \sum_{\substack{k'_x=-\frac{N'_x}{2}+1 \\ (k_x-k'_x,k_z-k'_z)\neq(0,0)}}^{N'_x/2}\sum_{k'_z=-\frac{N'_z}{2}+1}^{N'_z/2} \tilde{Q}_{\alpha',\beta'}\ \tilde{v}_{-\alpha',-\beta'} + \sum_{\substack{k'_x=-\frac{N'_x}{2}+1 \\ (k_x-k'_x,k_z-k'_z)\neq(0,0)}}^{N'_x/2}\sum_{k'_z=-\frac{N'_z}{2}+1}^{N'_z/2} \tilde{R}_{\alpha',\beta'}\ \tilde{\eta}_{-\alpha',-\beta'},\end{aligned} \tag{4.76}$$

where the coefficients $\tilde{P}, \tilde{Q}, \tilde{R}$ are given in the appendix D.2.

4.6.4 On the need for odd resolution for streamwise, wall-normal and spanwise directions

Stream- and spanwise direction

The correlation of Fourier coefficients necessitates an odd number N of Fourier coefficients in the stream- and spanwise directions: one fundamental mode, $\frac{N-1}{2}$ coefficients for the positive modes, and $\frac{N-1}{2}$ for the negative ones, where positive and negative modes are complex conjugate. Otherwise, the complex conjugation property of the model is broken, leading to non-physical results. A treatment of the even case could be implemented by adding a row of zero, but it would increase the dimension on the system without any benefit for the calculation.

The correlation of Fourier coefficients indeed wraps around the edges of the domain. For an even number of Fourier coefficients, the Fourier mode $v_{\frac{-N}{2}}$ will not be associated with its missing complex-conjugate counterpart $v_{\frac{+N}{2}}$. This mode is here referred to as "solitary". Within the correlation process, the Fourier coefficients $\{v_\alpha\}$ of the state-vector are correlated with the solitary mode $v_{\frac{-N}{2}}$ at the edge of the domain (the red boxes in fig. 4.1(a)), but not with its missing complex-conjugate counterpart. As a result, the imaginary parts of an integrated state-vector or the eigen-decomposition of the model is not distributed evenly, leading to flowfields with an non-physical imaginary part once transformed into their physical state. This demonstration is supported by fig. 4.1(a), where the coefficients of the correlated operator $A_{\alpha,\alpha'}$ are made explicit for the stream-wise direction, and by fig.4.1(b) for an odd number of coefficients, where the correlation operates properly.

Note: the Fourier modes with indices outside the spectrum are not defined, and therefore replaced by zeros (the black crosses in fig. 4.1(a) and 4.1(b)).

Wall-normal direction

To the author's knowledge, the requirement for an odd resolution in the Chebyshev discretisation of the wall-normal direction has not been fully explained in the literature. Most studies (Gibson et al., 2008, 2009, 2019; Ahmed, 2018) actually use an odd resolution, but do not give details or argument. The conclusion of discussions with Florian Reetz (Gibson et al., 2019) was that the odd-resolution is necessary to enforce complex-conjugation of the spectrum. Chebyshev series can indeed be considered as cosine Fourier series, and an even number of Fourier modes breaks the complex-conjugation if the input data is not purely real and RFFT used.

4.6.5 Block expression of the Orr-Sommerfeld Squire Model extended for a non-laminar solution

The expressions of the wall-normal velocity modes 4.73, wall-normal vorticity modes 4.74, streamwise velocity fundamental mode 4.75 and spanwise velocity fundamental

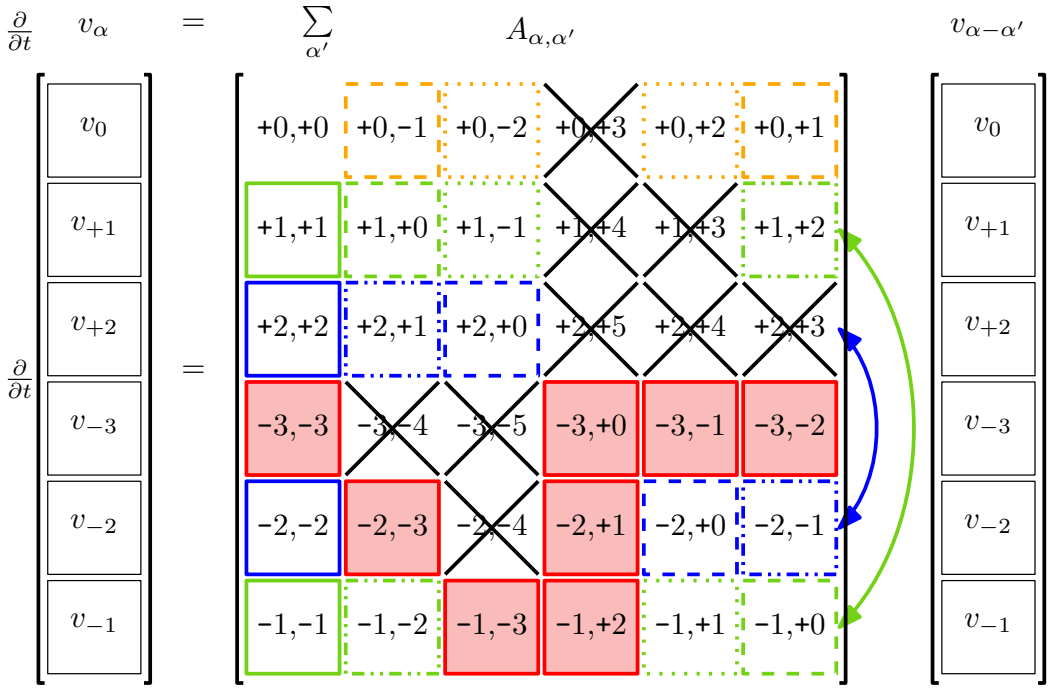

A) Even number of Fourier coefficients.

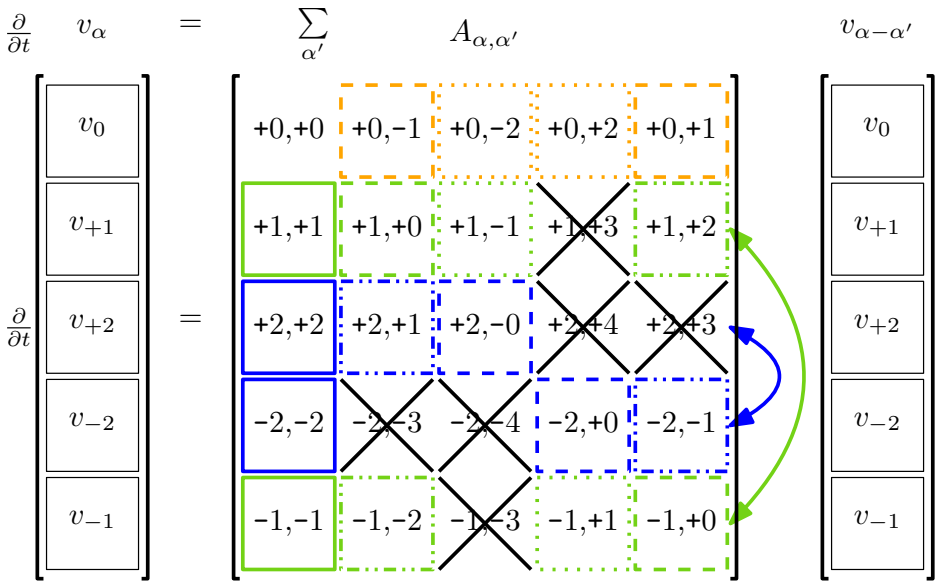

B) Odd number of Fourier coefficients.

FIGURE 4.1: Correlation for an even or odd number of Fourier coefficients. The complex-conjugate pairs are indicated by the identical dash-style and colour. The fundamental mode $(0, 0)$ is always purely real. The modes outside of the Fourier spectrum are eliminated and replaced with zeros, as not defined (black crosses). For even numbers, due to the presence of the state-vector coefficient v_{-3},the solitary coefficients (red boxes) does not possess their complex-conjugate counterpart. For odd number, each mode can be associated with its complex-conjugate counterpart and the correlation is evenly distributed and the correlated model is perfectly defined.

mode 4.76 can be assembled into a unique matrix as

$$\frac{\partial \tilde{\boldsymbol{x}}(t)}{\partial t} = \mathcal{L}\,\tilde{\boldsymbol{x}}(t)$$

$$= \Upsilon \begin{bmatrix} \frac{1}{Re}\tilde{\nabla}^4 + \tilde{A} + \tilde{B} & \tilde{C} & \tilde{D} & \tilde{E} \\ \tilde{F} + \tilde{G} & \frac{1}{Re}\tilde{\nabla}^2 + \tilde{H} + \tilde{J} & \tilde{K} & \tilde{L} \\ \tilde{M} + \tilde{N} & \tilde{O} & \frac{1}{Re}\tilde{\nabla}^2_{0,0} - \tilde{V}_{0,0}\frac{\partial}{\partial y} & 0 \\ \tilde{P} + \tilde{Q} & \tilde{R} & 0 & \frac{1}{Re}\tilde{\nabla}^2_{0,0} - \tilde{V}_{0,0}\frac{\partial}{\partial y} \end{bmatrix} \begin{bmatrix} \tilde{v}_{\substack{0\leq i<N_\alpha,\\ 0\leq j<N_\beta}} \\ \tilde{\eta}_{\substack{0\leq i<N_\alpha,\\ 0\leq j<N_\beta\\ (i,j)\neq(0,0)}} \\ \tilde{u}_{0,0} \\ \tilde{w}_{0,0} \end{bmatrix}, \tag{4.77}$$

where

$$\Upsilon = \begin{bmatrix} \tilde{\nabla}^{-2} & 0 & 0 & 0 \\ 0 & I & 0 & 0 \\ 0 & 0 & I & 0 \\ 0 & 0 & 0 & I \end{bmatrix}. \tag{4.78}$$

We remind the reader, that unlike the OSS model derived in section 4.5, all wavenumbers pairs (α, β) of the wall-normal velocity v and wall-normal vorticity η_y (except the pair $(0, 0)$) are considered. Moreover, due to the wall-normal discretisation and the imposition of the Dirichlet boundary conditions, each block is of dimension $(N_y - 2) \times (N_y - 2)$. Therefore, the total dimension of the model is

$$dim(\mathcal{L}) = \left[N_\alpha \times N_\beta + (N_\alpha \times N_\beta - 1) + 2\right]^2 \times (N_y - 2)^2 \tag{4.79}$$

instead of $\left[4 \times N_\alpha \times N_\beta\right]^2 \times (N_y - 2)^2$ for the original linearized NSE (§4.1.1).

4.7 Real Orr-Sommerfeld Squire Model extended for a non-laminar solution as base-flow (ROSSE), using complex conjugation property

The state-vector of the OSSE model possess a complex-conjugation symmetry: the wavenumber pair (α, β) is the complex conjugate of the pair $(-\alpha, -\beta)$. This implies that only half of the Fourier coefficients could be required to determine the entire spectrum. The OSSE model does not benefit from this property, as the correlation of Fourier series wraps around the edges of the domain and the complex-conjugation is not a linear operation (see §4.6). It is impossible to directly profit from this symmetry when the state-vector of the model is a vector of complex Fourier coefficients.

Nonetheless, apprehending the issue in a different manner can solve it. A new definition of the state-vector and data management is indeed advantageous: a real-valued state-vector can be formed by separating and stacking the real and imaginary part of the

former complex-valued state-vector. This results in an equivalent purey-real model, the Real Orr-Sommerfeld Squire model Extended for a non-laminar solution (ROSSE), in which the complex-conjugation symmetry can be exploited.

4.7.1 Textbook case

Let's consider a simple linear system

$$\frac{\partial x}{\partial t} = Ax, \tag{4.80}$$

where the Fourier spectrum of x is composed of three coefficients, such that $x = [x_{-1}, x_0, x_{+1}]^T$. The complex-conjugation symmetry translates as

$$\dot{x}_{+1} = \dot{x}^*_{-1} \qquad \text{and} \qquad x_{+1} = x^*_{-1}. \tag{4.81}$$

In matrix form, considering only the evolution of x_{+1} for this demonstration, this simple linear system can be expressed as

$$\frac{\partial}{\partial t}\begin{bmatrix} x_{+1} \\ x_0 \\ x_{-1} \end{bmatrix} = \begin{bmatrix} A_{+1} & A_0 & A_{-1} \\ \cdot & \cdot & \cdot \\ \cdot & \cdot & \cdot \end{bmatrix}\begin{bmatrix} x_{+1} \\ x_0 \\ x_{-1} \end{bmatrix} = \begin{bmatrix} A_{-1} & A_0 & A_{+1} \\ \cdot & \cdot & \cdot \\ \cdot & \cdot & \cdot \end{bmatrix}\begin{bmatrix} x^*_{-1} \\ x_0 \\ x^*_{+1} \end{bmatrix}. \tag{4.82}$$

The Fourier coefficient $\dot{x}_{+1}$ can be expressed as a function of x_0 and x_{+1} without any complex-conjugation operation, with $\Re$ and $\Im$ standing for real and imaginary part

respectively,

$$
\begin{aligned}
\frac{\partial x_{+1}}{\partial t} &= A_{+1}x_{+1} + A_0 x_0 + A_{-1}x_{-1} \\
&= \big(\Re(A_{+1}) + \imath\Im(A_{+1})\big)\ \big(\Re(x_{+1}) + \imath\Im(x_{+1})\big) \\
&\quad + \big(\Re(A_0) + \imath\Im(A_0)\big)\ \big(\Re(x_0) + \imath\Im(x_0)\big) \\
&\quad + \big(\Re(A_{-1}) + \imath\Im(A_{-1})\big)\ \big(\Re(x_{-1}) + \imath\Im(x_{-1})\big) \\
&= \big(\Re(A_{+1}) + \imath\Im(A_{+1})\big)\ \big(\Re(x_{+1}) + \imath\Im(x_{+1})\big) \\
&\quad + \big(\Re(A_0) + \imath\Im(A_0)\big)\ \big(\Re(x_0) + \imath\Im(x_0)\big) \\
&\quad + \big(\Re(A_{-1}) + \imath\Im(A_{-1})\big)\ \big(\Re(x_{\mathbf{+1}}) - \imath\Im(x_{\mathbf{+1}})\big) \\
&= +\Re(A_{+1})\ \Re(x_{+1}) - \Im(A_{+1})\ \Im(x_{+1}) \\
&\quad\ + \Re(A_0)\ \Re(x_0) - \Im(A_0)\ \Im(x_0) \\
&\quad\ + \Re(A_{-1})\ \Re(x_{+1}) + \Im(A_{-1})\ \Im(x_{+1}) \\
&\quad + \imath\Big(+ \Im(A)\ \Re(x_{+1}) + \Re(A)\ \Im(x_{+1}) \\
&\quad\quad + \Im(A_0)\ \Re(x_0) + \Re(A_0)\ \Im(x_0) \\
&\quad\quad + \Im(A_{-1})\ \Re(x_{+1}) - \Re(A_{-1})\ \Im(x_{+1})\Big) \\
&= +\Re(A_0)\ \Re(x_0) - \Im(A_0)\ \Im(x_0) \\
&\quad\ + \big(+ \Re(A_{+1}) + \Re(A_{-1})\big)\ \Re(x_{+1}) + \big(- \Im(A_{+1}) + \Im(A_{-1})\big)\ \Im(x_{+1}) \\
&\quad + \imath\Big(+ \Im(A_0)\ \Re(x_0) + \Re(B)\ \Im(x_0) \\
&\quad\quad + \big(+ \Im(A_{+1}) + \Im(A_{-1})\big)\ \Re(x_{+1}) + \big(+ \Re(A_{+1}) - \Re(A_{-1})\big)\ \Im(x_{+1})\Big) \\
&= \Re(\frac{\partial x}{\partial t}) + \imath\Im(\frac{\partial x}{\partial t}).
\end{aligned}
\tag{4.83}
$$

By separating and stacking the real and imaginary part of the former complex-valued state-vector, it is possible to define a new purely-real state-vector,

$$
x_{OSSE} = \begin{bmatrix} x_{+1} \\ x_0 \\ x^*_{+1} \end{bmatrix} \qquad \Longrightarrow \qquad x_{ROSSE} = \begin{bmatrix} \Re(x_{+1}) \\ \Re(x_0) \\ \Im(x_{+1}) \\ \Im(x_0) \end{bmatrix}, \tag{4.84}
$$

and exploit the result of eq.4.83 in matrix form,

$$
\begin{aligned}
\frac{\partial x_{+1}}{\partial t} &= \begin{bmatrix} \Re(\frac{\partial x}{\partial t}) \\ \Im(\frac{\partial x}{\partial t}) \end{bmatrix} \\
&= \begin{bmatrix} +\Re(A_{+1}) + \Re(A_{-1}) & +\Re(A_0) & -\Im(A_{+1}) + \Im(A_{-1}) & -\Im(A_0) \\ +\Im(A_{+1}) + \Im(A_{-1}) & +\Im(A_0) & +\Re(A_{+1}) - \Re(A_{-1}) & +\Re(A_0) \end{bmatrix} \begin{bmatrix} \Re(x_{+1}) \\ \Re(x_0) \\ \Im(x_{+1}) \\ \Im(x_0) \end{bmatrix}.
\end{aligned}
\tag{4.85}
$$

The coefficient v_{-1} was eliminated without any loss of accuracy. The matrix A_{-1} is required, but immediately summed to their associated complex-conjugate counterpart, therefore not requiring any extra memory.

4.7.2 Block expression of the Real Orr-Sommerfeld Squire Model extended for a non-laminar solution

The substitution into a purely-real state-vector is applied to the final expression 4.77 of the OSSE model by separating the positive span-wise modes ($\beta \geq 0$) from the strictly negative span-wise modes ($\beta < 0$). It leads to the final block expression of the Real Orr-Sommerfeld Squire model Extended for a non-laminar solution (ROSSE),

$$\begin{aligned}\frac{\partial \tilde{\boldsymbol{x}}(t)}{\partial t} &= \mathcal{L}_{ROSSE}\, \tilde{\boldsymbol{x}}(t) \\ &= \begin{bmatrix} +\Re(\mathcal{L}_{OSSE,\beta\geq 0}) + \Re(\mathcal{L}_{OSSE,\beta<0}) & -\Im(\mathcal{L}_{OSSE,\beta\geq 0}) + \Im(\mathcal{L}_{OSSE,\beta<0}) \\ +\Im(\mathcal{L}_{OSSE,\beta\geq 0}) + \Im(\mathcal{L}_{OSSE,\beta<0}) & +\Re(\mathcal{L}_{OSSE,\beta\geq 0}) - \Re(\mathcal{L}_{OSSE,\beta<0}) \end{bmatrix} \tilde{\boldsymbol{x}}(t),\end{aligned} \tag{4.86}$$

where the state-vector $\boldsymbol{x}$ is expressed as

$$\boldsymbol{x}(t) = \begin{bmatrix} \Re(x_{OSSE,\beta\geq 0}) \\ \Im(x_{OSSE,\beta\geq 0}) \end{bmatrix} = \begin{bmatrix} \Re\begin{bmatrix} \tilde{v}_{\beta\geq 0} \\ \tilde{\eta}_{\beta\geq 0} \\ \tilde{u}_{0,0} \\ \tilde{w}_{0,0} \end{bmatrix} \\ \Im\begin{bmatrix} ... \end{bmatrix} \end{bmatrix}. \tag{4.87}$$

4.8 Validation of OSSE and ROSSE models against Channelflow

The OSSE and ROSSE models are validated by comparing the leading eigenvalues of different equilibria against the ones obtained with Channelflow (Gibson et al., 2008; Gibson, 2014; Gibson et al., 2019). Exactly, table 4.1 gathers the largest real-part eigenvalues of matrices $\mathcal{L}$ in eq.4.77 for the OSSE model and eq.4.86 for the ROSSE model. The chosen equilibria are EQ1 (Nagata, 1990; Waleffe, 2003), EQ2 (Nagata, 1997), EQ5, EQ9, EQ11 (Gibson et al., 2009; Halcrow, 2008) and EQ19, EQ24 (Ahmed and Sharma, 2017). They are available in the database on `channelflow.org` and in the files uploaded alongside this thesis (app. A).

The original resolution of these equilibria is $32 \times 35 \times 32$ and is used to calculate the eigenmodes with Channelflow. To build the OSSE and ROSSE matrix operators within memory limitation, this resolution is reduced to $21 \times 35 \times 21$ with the method `changegrid` of Channelflow. A Newton-Krylov-hookstep search is necessary as the reduction — a truncation of high order Fourier modes— only results in an approximated solution,

which may not be an actual Invariant Solution at this resolution. The low-dimensional equilibria are thus obtained by calling the following methods from `channelflow`:

```
changegrid --Nx 32 --Nz 32 eqX_32x35x32.h5 eqX_21x35x21.h5
findsoln -eqb -R 400 eqX_21x35x21.h5
```

For `Channelflow`, the leading eigenvalues are calculated via the `arnoldi` command with default parameters. This method uses an Arnoldi iteration, which estimates the eigenvalues of a matrix A by iteratively constructing a QR decomposition of a matrix whose columns are $[Ab, A^2b, ...]$ where b is an arbitrary starting vector (Viswanath, 2007; Bau and Trefethen, 1997).

For the OSSE and ROSSE linear models, calculations are operated with the method `eigs` of the `Python` scientific package `scipy.sparse.linalg`. This method is a wrapper to ARPACK functions using the Implicitly Restarted Arnoldi Method to find the eigenvalues and eigenvectors (scipy documentation). `eigs` is called in `osse_eigen.py` and `rosse_eigen.py` in the OSSE package (app. A) with parameters:

```
k = 20
sigma = 0.2
which = 'SR'
tolerance = 0
```

This method is the most straightforward within `Python` to compute a limited number k of eigenvalues, as alternatives like `numpy.linalg.eig` or `scipy.linalg.eig` target the entire eigen-decomposition, which is out-of-reach in this case. For a resolution of $21 \times 35 \times 21$, the calculations takes a couple minute on High Performance Cluster (HPC) Iridis5 and requires around 73Gb of memory for the OSSE model and 53Gb for the ROSSE model.

Eigenvalues are gathered in table 4.1. They are considered valid when matching at the $3rd$ rounded decimal. The OSSE and ROSSE models are validated for solutions EQ1, EQ2, EQ9 and EQ19. All the leading eigenvalues of EQ1 and EQ19 are found, up to the $15th$ for EQ1 —which may actually be hidden by the spurious modes— and up to the $10th$ for EQ19. Two eigenvalues are missing for EQ2 (incl. one positive), and three for EQ9, within the ten leading values. Nonetheless, the algorithm likely misses them as they are adjacent to others values. The assessment is more problematic for EQ5, EQ11 and EQ24. Within the ten leading eigenvalues, four are missing for EQ5 (incl. two positive) and five for EQ11 (incl. 4 positive). Out of the ten leading positive eigenvalues of EQ24, only the four with biggest real-part are found. The model can not be considered as validated for EQ5, EQ11 and EQ24.

Two spurious eigenmodes -0.02467401 and -0.05047682 are always present in the eigen-decomposition. These modes are not related to any physical properties of the solution, but to the linear models themselves. They are indeed likely due to the rows/columns

associated with the imaginary part of the fundamental mode v_{00}. These rows/columns do not interfere in the time-integration of the model, as the imaginary part of v_{00} is always null, but brings non-physical eigenmodes. Others spurious modes were actually appearing for the ROSSE model, and the removal of the rows/columns associated with the imaginary parts of u_{00} and w_{00}, which are always null as both modes are fundamental and therefore purely real, solved the problem. The same operation can be done here for the OSSE model, but the issue appeared too late in the development.

The discrepancies between Channelflow and the linear models can be caused by different factors:

- Eigenvalues with higher positive real-part are usually the easiest ones to find numerically. Therefore, we expect the find these with greater accuracy than eigenvalues with smaller absolute real-part (slow dynamical evolution) or with a high negative real-part (highly stable, impact on longer time span).
- The reduction into a resolution $21 \times 35 \times 21$ seems sufficient for stable and highly symmetric solutions (EQ1, EQ2, EQ9), but may be problematic for more unstable ones (EQ5, EQ11, EQ24). First, the truncation of higher Fourier modes operated by `changegrid` is straightforward, but the truncated modes may be necessary to represent the dynamics of the solutions. Others model-reduction methods might improve these results (see §6.2.3). Second, the new resolution may be too low. Higher resolutions will presumably increase precision, at the cost of memory requirement. However, it appeared through trials that a resolution of $13 \times 35 \times 13$ already delivers good approximations of the 5 leading eigenmodes. Further research are needed on the grid sensitivity of the eigenvalues calculated for both Channelflow and linear models. A first comparison can be made with the eigenvalues of EQ1 calculated at resolution $17 \times 27 \times 17$ in table 6.1. They did not show any major discrepancy.
- The eigen-decomposition in Channelflow and `scipy` are implemented with different algorithms, which may result in different performance and precision even if the models are equivalent. Particularly, `scipy` method seems to struggle to separate different yet very close eigenvalues. For instance, the spurious modes -0.02467401 of EQ2 seems to conceal four different eigenvalues, and for EQ5, only $+0.00979860$ was found against $+0.00993106$, $+0.00965382$ and $+0.00960047$ in Channelflow. Besides that, Channelflow is matrix-free while OSSE is matrix-based.
- The method `scipy.sparse.linalg.eigs` is designed for sparse matrices. Yet, the sparsity of matrices $\mathcal{L}$ in eq.4.77 and eq.4.86 is decreasing with more sophisticated equilibrium. Therefore, the `sparse` package may not be appropriate for some solutions. Nonetheless, this point should rather affect performance than accuracy.

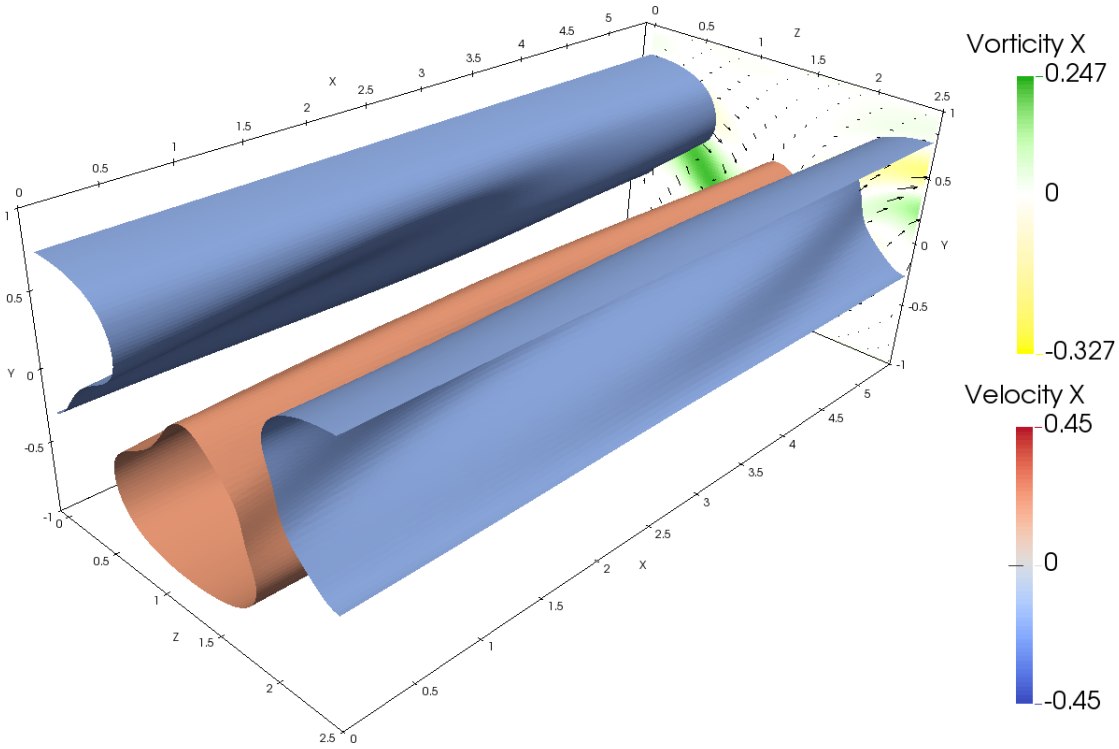

FIGURE 4.2: Nagata (1990) and Waleffe (2003) equilibrium EQ1: Surfaces of constant streamwise velocity u at ± 0.2. The vertical plane in the background is coloured with the streamwise vorticity η_x. (EQ1, $21 \times 35 \times 21$, $Re = 400$)

- The missing eigen-modes in the OSSE and ROSSE models may be found by changing the parameters, notably `sigma`, and targeting specifically their neighborhood.
- As a side note, the dissipation rate is not a decisive parameter in the accuracy of the problem, as EQ2 is among the most dissipative solutions and EQ9 among the least dissipative ones (Halcrow (2008)[App.2], Ahmed (2018)).

In conclusion, the OSSE and ROSSE reproduces faithfully the eigen-decomposition and can be used as a linearised approximation of the full NSE around a given Invariant Solution, for weakly unstable (EQ1, EQ2, EQ9) and/or highly symmetric (EQ19) solutions. For more unstable solutions (EQ5, EQ11, EQ24), the linear models does not perform as well and the author does not expect them to describe faithfully the dynamical state-space around these solutions. Improvements (e.g. increase in resolution) are required before further application.

The lower-branch Nagata (1990) and Waleffe (2003) equilibrium EQ1, shown in figure 4.2, is the least unstable known Invariant Solution of the NSE. This characteristic is retrieved in table 4.1, where EQ1 possesses a signle real-part eigenvalue alongside a pair of eigenvalues on the imaginary axis. Therefore, there exists only a single unstable direction repelling the turbulent dynamical state. Furthermore, the OSSE and ROSSE demonstrated their ability to reproduce its dynamical evolution. For these reasons, EQ1 is expected to be the most accessible IS to stabilize and will be used as target solution

for the following chapters. Another accessible target could be the upper-branch Nagata (1997) solution EQ2, as within the S-invariant subspace, it only possess one complex unstable eigenvalue pair (Halcrow, 2008; Gibson et al., 2008).

TABLE 4.1: Eigenvalues ranked in order of decreasing real-part and computed with the OSSE model, the ROSSE model and Channelflow for 7 different invariant solutions, $Re = 400$. When values rounded at 3 decimals matched, they are marked with ✓ and spurious modes with 'SP'. Symbols ⌜ and ⌞ means that these values are masked in the linear model by the one below/above.

EQ1 - Nagata (1990) Lower branch

	OSSE	$21 \times 35 \times 21$	ROSSE	$21 \times 35 \times 21$	Channelflow	$32 \times 35 \times 32$
✓	$+0.05012054$		$+0.05012054$		$+0.05012078$	
✓	$+0.00000138$		$+0.00000138$		10^{-7}	$\pm 10^{-7}\iota$
✓	$+0.00000001$		$+0.00000001$		10^{-7}	$\pm 10^{-7}\iota$
✓	-0.00200534		-0.00200534		-0.00200445	
✓	-0.00659910		-0.00659910		-0.00659911	
✓	-0.00692664		-0.00692664		-0.00692292	
✓	-0.00972618		-0.00972618		-0.00972762	
✓	-0.01359296		-0.01359296		-0.01359316	
✓	-0.02393202		-0.02393202		-0.02393151	
SP	-0.02467401		-0.02467401			
✓	-0.03346018		-0.03346018		-0.03346004	
✓	-0.03702671		-0.03702671		-0.03702731	
✓	-0.04260477		-0.04260477		-0.04260414	
✓	-0.04535169	$\pm 0.01888110\iota$	-0.04535169	$\pm 0.01888110\iota$	-0.04535161	$\pm 0.01888120\iota$
					-0.04846660	$\pm 0.10251464\iota$
SP	-0.05047682		-0.05047682			
✓	-0.05181904	$\pm 0.02604207\iota$	-0.05181904	$\pm 0.02604207\iota$	-0.05181919	$\pm 0.02604184\iota$
✓	-0.06239186	$\pm 0.03118407\iota$	-0.06239186	$\pm 0.03118407\iota$	-0.06239202	$\pm 0.03118377\iota$

EQ2 - Nagata (1990) Upper branch

	OSSE	$21 \times 35 \times 21$	ROSSE	$21 \times 35 \times 21$	Channelflow	$32 \times 35 \times 32$
✓	$+0.05555202$		$+0.05555202$		$+0.05558373$	
✓	$+0.03255877$	$\pm 0.10711583\iota$	$+0.03255877$	$\pm 0.10711583\iota$	$+0.03252937$	$\pm 0.10704298\iota$
✓	$+0.01601887$	$\pm 0.03913811\iota$	$+0.01601887$	$\pm 0.03913811\iota$	$+0.01605911$	$\pm 0.03923833\iota$
					$+0.01529245$	$\pm 0.02998246\iota$
✓	$+0.01103831$		$+0.01103831$		$+0.01060373$	
✓	$+0.00000713$		$+0.00000713$		$+0.00000132$	
✓	-0.00065954		-0.00065954		-0.00000014	
✓	-0.01409445	$\pm 0.05780379\iota$	-0.01409445	$\pm 0.05780379\iota$	-0.01412155	$\pm 0.05774740\iota$
✓	-0.01811532		-0.01811532		-0.01818263	
			-0.02285790		-0.02091925	$\pm 0.14056723\iota$

↰					−0.02429576	±0.14794725ι
SP	−0.02467401		−0.02467401			
↱					−0.02646828	±0.00196768ι
↱					−0.02741358	±0.14714704ι
					−0.02936282	±0.13875483ι
✓	−0.03013278		−0.03013278		−0.03030128	±0.06246476ι

EQ5

	OSSE	$21 \times 35 \times 21$	ROSSE	$21 \times 35 \times 21$	Channelflow	$32 \times 35 \times 32$
✓	+0.07210159	±0.04064693ι	+0.07210159	±0.04064693ι	+0.07212103	±0.04075036ι
✓	+0.06259841		+0.06259841		+0.06209489	
✓	+0.06168816		+0.06168816		+0.06162058	
✓	+0.02061638	±0.07305312ι	+0.02061638	±0.07305312ι	+0.02073339	±0.07355100ι
↰					+0.00993106	
✓	+0.00979860	±0.04548006ι	+0.00979860	±0.04548006ι	+0.00965382	±0.04551335ι
↱					+0.00960047	±0.08394279ι
	+0.00574598	±0.00800997ι	+0.00574598	±0.00800997ι		
					−0.00000267	
					−0.00000696	
	−0.00132926		−0.00132926		−0.00013456	±0.08303027ι
	−0.00406003		−0.00406003			
					−0.00617177	
					−0.00778639	±0.13720939ι
					−0.01064599	
✓	−0.01285079		−0.01285079		−0.01220323	±0.03672581ι
					−0.01539742	±0.03662021ι
SP	−0.02467401		−0.02467401			
					−0.03451090	±0.08674001ι
↰					−0.03719165	±0.09884040ι
✓	−0.03756857		−0.03756857		−0.03748275	
✓	−0.04008928		−0.04008928		−0.04016649	

EQ9

	OSSE	$21 \times 35 \times 21$	ROSSE	$21 \times 35 \times 21$	Channelflow	$32 \times 35 \times 32$
✓	+0.02629998	±0.04209693ι	+0.02629998	±0.04209693ι	+0.02629552	±0.04209125ι
✓	+0.02530910		+0.02530910		+0.02529671	
✓	+0.01933696		+0.01933696		+0.01933566	
✓	+0.01028392		+0.01028392		+0.01031501	
✓	+0.00001539	±0.00003944ι	+0.00001539	±0.00003944ι	−0.00000036	
↱					−0.00000162	
✓	−0.00501738	±0.00059604ι	−0.00501738	±0.00059604ι	−0.00501190	±0.00062749ι

✓	-0.02346857	$\pm 0.00530498\iota$	-0.02346857	$\pm 0.00530498\iota$	-0.02346866	$\pm 0.00530618\iota$
SP	-0.02467401		-0.02467401			
↹					-0.02501237	$\pm 0.05424261\iota$
					-0.02873648	$\pm 0.02233396\iota$
✓	-0.03718196		-0.03718196		-0.03719305	
✓	-0.04516535	$\pm 0.03238501\iota$	-0.04516535	$\pm 0.03238501\iota$	-0.04516177	$\pm 0.03240437\iota$
↹					-0.04538517	$\pm 0.14231959\iota$
↰					-0.05011678	$\pm 0.08033021\iota$
SP	-0.05047682		-0.05047682			
					-0.05615180	$\pm 0.07082476\iota$
✓	-0.06120994		-0.06120994		-0.06120824	
					-0.07014509	$\pm 0.13116546\iota$
✓	-0.07044091	$\pm 0.06334584\iota$	-0.07044091	$\pm 0.06334584\iota$	-0.07044820	$\pm 0.06335238\iota$

EQ11

	OSSE	$21 \times 35 \times 21$	ROSSE	$21 \times 35 \times 21$	Channelflow	$32 \times 35 \times 32$
✓	$+0.14091050$	$\pm 0.10532217\iota$	$+0.14091050$	$\pm 0.10532217\iota$	$+0.14083617$	$\pm 0.10427852\iota$
✓	$+0.13495067$	$\pm 0.09708295\iota$	$+0.13495067$	$\pm 0.09708295\iota$	$+0.13443208$	$\pm 0.09650974\iota$
✓	$+0.09700629$	$\pm 0.12295428\iota$			$+0.09663490$	$\pm 0.12338217\iota$
					$+0.03449817$	$\pm 0.03905176\iota$
	$+0.02621630$		$+0.02621630$		$+0.02401259$	
✓	$+0.01757360$	$\pm 0.07280808\iota$	$+0.01757360$	$\pm 0.07280808\iota$	$+0.01714800$	$\pm 0.07257894\iota$
					$+0.01690493$	$\pm 0.06862555\iota$
✓	$+0.00025081$		$+0.00025081$		$+0.00006550$	$\pm 0.14479453\iota$
↹					$+0.00000151$	$\pm 0.00003784\iota$
	-0.00297442	$\pm 0.00230137\iota$	-0.00297442	$\pm 0.00230137\iota$		
					-0.00743487	
					-0.00880385	$\pm 0.13129410\iota$
					-0.01034586	$\pm 0.13129410\iota$
↰					-0.01368603	$\pm 0.05015424\iota$
✓	-0.01438079	$\pm 0.04215840\iota$	-0.01438079	$\pm 0.04215840\iota$	-0.01438754	$\pm 0.04224533\iota$
✓	-0.01574640	$\pm 0.04820812\iota$	-0.01574640	$\pm 0.04820812\iota$	-0.01588289	$\pm 0.13817927\iota$
					-0.01808066	$\pm 0.01780519\iota$
					-0.01828959	$\pm 0.04545832\iota$
					-0.01962418	$\pm 0.13656874\iota$
SP	-0.02467401		-0.02467401			
			-0.02617119			
			-0.02635417			
✓	-0.03513514		-0.03513514		-0.03465455	$\pm 0.04689063\iota$
↹					-0.03475625	
					-0.04193686	$\pm 0.08342170\iota$

	−0.04589086		−0.04589086		−0.04699639	
					−0.04791049	$\pm 0.14621116\iota$
SP	−0.05047682		−0.05047682			

EQ19 - Projection of EQ8

	OSSE	$21 \times 35 \times 21$	ROSSE	$21 \times 35 \times 21$	Channelflow	$32 \times 35 \times 32$
✓	+0.02537583	$\pm 0.00857920\iota$	+0.02537583	$\pm 0.00857920\iota$	+0.02537546	$\pm 0.00858003\iota$
✓	+0.00847810		+0.00847810		+0.00847590	
✓	−0.00000080	$\pm 0.00000081\iota$	−0.00000080	$\pm 0.00000081\iota$	−0.00000061	
✓	−0.00757815		−0.00757815		−0.00757575	
✓	−0.00847916		−0.00847916		−0.00848010	
✓	−0.01040149		−0.01040149		−0.01040251	
✓	−0.02444955		−0.02444955		−0.02445030	
SP	−0.02467401		−0.02467401			
✓	−0.03027252		−0.03027252		−0.03027183	
✓	−0.03292603		−0.03292603		−0.03292489	
					−0.03442651	$\pm 0.11920975\iota$
✓	−0.04673041	$\pm 0.05437204\iota$	−0.04673041	$\pm 0.05437204\iota$	−0.04673127	$\pm 0.05437211\iota$
SP	−0.05047682		−0.05047682			
✓	−0.05163835		−0.05163835		−0.05163896	
✓	−0.05394340	$\pm 0.03713194\iota$	−0.05394340	$\pm 0.03713194\iota$	−0.05394367	$\pm 0.03713251\iota$
✓	−0.06013870	$\pm 0.02903442\iota$	−0.06013870	$\pm 0.02903442\iota$	−0.06013751	$\pm 0.02903358\iota$

EQ24

	OSSE	$21 \times 35 \times 21$	ROSSE	$21 \times 35 \times 21$	Channelflow	$32 \times 35 \times 32$
✓	+0.14806833		+0.14806833		+0.14776917	
✓	+0.09447673	$\pm 0.03522622\iota$	+0.09447673	$\pm 0.03522622\iota$	+0.09541285	$\pm 0.03438392\iota$
✓	+0.09288452	$\pm 0.08991673\iota$	+0.09288452	$\pm 0.08991673\iota$	+0.09265970	$\pm 0.09009525\iota$
✓	+0.02779187	$\pm 0.06697849\iota$	+0.02779187	$\pm 0.06697849\iota$	+0.02799530	$\pm 0.06710772\iota$
	+0.00227874		+0.00227874		+0.02165429	$\pm 0.02519515\iota$
					+0.01747257	$\pm 0.03941158\iota$
					+0.00406371	$\pm 0.14025831\iota$
					+0.00356350	$\pm 0.13727776\iota$
					+0.00000843	
					+0.00000045	
			−0.00006982		−0.00158435	$\pm 0.03374232\iota$
	−0.00929059		−0.00929059		−0.00762270	
✓	−0.01117349	$\pm 0.04562195\iota$	−0.01117349	$\pm 0.04562195\iota$	−0.01112176	$\pm 0.04553695\iota$
					−0.01188410	$\pm 0.02284327\iota$
					−0.01287108	
					−0.01352032	$\pm 0.15338662\iota$

	-0.01455833		-0.01455833		-0.01580320	$\pm 0.15437111\iota$
			-0.02311609		-0.02169399	$\pm 0.04627077\iota$
					-0.02444743	$\pm 0.13057070\iota$
SP	-0.02467401		-0.02467401			
			-0.02649698		-0.02763111	$\pm 0.07822968\iota$
	-0.02842553	$\pm 0.06602866\iota$	-0.02842553	$\pm 0.06602866\iota$	-0.02937453	$\pm 0.06513648\iota$
					-0.03600361	$\pm 0.11609411\iota$
					-0.03732098	$\pm 0.08548847\iota$
					-0.04568060	$\pm 0.12317903\iota$
					-0.04574999	$\pm 0.06801671\iota$
SP	-0.05047682		-0.05047682			

Chapter summary

- Controller synthesis of Linear time-invariant (LTI) systems first and foremost requires the definition of a spatially discretised LTI system.
- For flow control, the governing equations are the non-linear Navier-Stokes equations (NSE). To be of practical use for the numerical methods and LTI, they are linearized around a time-invariant baseflow, then transformed into a non-singular system and finally discretised with spectral methods.
- In the case of the laminar Plane Couette Flow (PCF) profile, the final transformed system is the Orr-Sommerfeld Squire model.
- To employ an Invariant Solution (IS) as baseflow, a new model is derived: the Orr-Sommerfeld Squire model Extended for a non-laminar solution (OSSE). Odd resolution is required for the streamwise, wall-normal and spanwise directions.
- By separating real and imaginary parts, the Real Orr-Sommerfeld Squire model Extended for a non-laminar solution (ROSSE) reduces the memory requirement of the OSSE model for the same performance.
- The OSSE and ROSSE reproduces faithfully the eigen-decomposition and can be used as a linearised approximation of the full NSE around a given Invariant Solution, for weakly unstable and/or highly symmetric solutions. For more unstable solutions, the linear models do not perform as well and the author does not expect them to describe faithfully the dynamical state-space around these solutions. Improvements (e.g. increase in resolution) are required before further application.

- The Nagata (1990) lower branch is the least unstable IS known for the PCF configuration. It is expected to be the most accessible IS to stabilize and will be used as target solution for the following chapters.

Chapter 5

Controller Design

This chapter focuses on the implementation and design of the control based on the linear OSSE and ROSSE models derived in the previous chapter. The numerical implementation is described in section 5.1, where the software, packages and libraries employed in this thesis are detailed. Section 5.2 and 5.3 describes the control design respectively for the OSSE and ROSSE models, i.e. the mathematical derivation of the matrices defining the controller and the implementation of wall-transpiration actuation. Following this definition, linear analyses are conducted in section 5.4 in order to evaluate the controllability and modal controllability of the system. Finally, the implementation of the wall-transpiration actuation is validated in section 5.5, firstly with the Couette laminar-state as baseflow and then with a invariant solution.

5.1 Simulation

The configuration of the simulation, including the state-feedback control, is represented in figure 5.1. The simulation of turbulent flows within a channel will be realized with the spectral CFD software Channelflow. This software has been written in `C++` for numerical analysis of the incompressible Navier-Stokes equations. Channelflow supplies different algorithms to compute invariant solutions in channel, and is highly accessible and flexible. This software is particularly appropriate in this case as it offers all the tools to simulate PCF with a spectral discretisation $Fourier \times Chebyshev \times Fourier$. Channelflow-1.5 is developped by John F. Gibson at the University of New Hampshire and is available on `channelflow.org` (Gibson et al., 2008, 2009). A parallelized version, Channelflow-2.0, is developed by the research group on "Emergent Complexity in Physical Systems Laboratory" (ECPS) at the Swiss Federal Institute of Technology Lausanne (EPFL), and is available on `channelflow.ch` (Gibson et al., 2019). The release of Channelflow-2.0 happened too late in the development for the project to benefit from it. Therefore, all methods introduced here concern Channelflow-1.5.1 - revision 451.

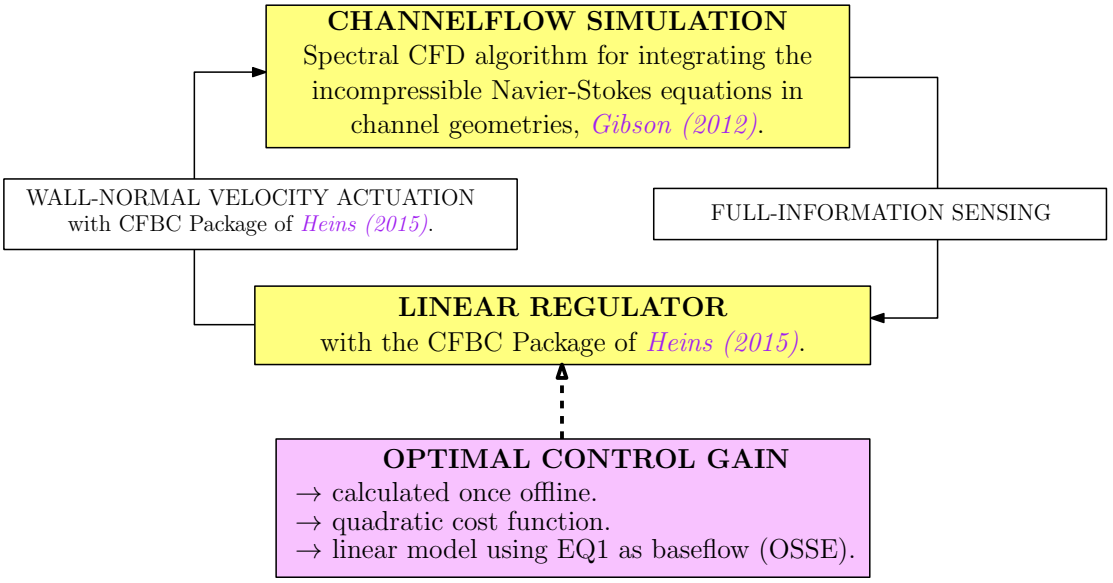

FIGURE 5.1: Configuration of the simulation operated with Channelflow, CFBC and a Python program to determine the optimal control gain.

Wall actuation is implemented in Channelflow with the ChannelFlow Boundary Condition package (CFBC) v1.0 of Peter Heins. This package was originally developed for Channelflow-1.4.2, and has been updated by the author for Channelflow-1.5.1. The package is not included within the official Channelflow release, but is available on online repositories (see A). This extension allows the user to implement inhomogeneous wall boundary conditions into a PCF simulation of *ChannelFlow*. The package also includes a controller class to create LTI feedback controllers applied to turbulent flows. Peter Heins validated and used the package to publish research papers as Jones et al. (2015); Heins et al. (2016) and his Ph.D. thesis Heins (2015).

The CFBC needs to be fed with sensor and actuation matrices. A few approaches were attempted. The first used a matrix-free program written in `Python`, implementing different differentiation methods. The program aimed to use `LinearOperator` objects, instead of directly operating the spectral differentiation matrices. By doing so, the user needed only to define a function associated with the `LinearOperator`, not necessarily depending on high-dimensional matrices. This would allow for flexibility and memory saving. However, the implementation of `LinearOperator` objects was tedious and impractical, and as a consequence, this method was pursued.

The different models representing the system (LNSE, OSS, OSSE, ROSSE), the controller wall-actuation, the objective function and the Riccati solutions of the optimal control problem are all implemented in `Python`, using extensively scientific library `Numpy` and `Sympy`. The post-processing is also using `Python`, as well as the `Paraview` software (Henderson, 2004).

This configuration as well as the implementation of wall-actuation and control can serve as a general benchmark to be applied for the development of other numerical software.

5.2 Full-Information LQR control design based on the OSSE model

This section introduces the essential matrices to build an infinite-horizon full-information feedback control controller, or LQR control, actuated by wall-transpiration from the OSSE model §4.6. Actuation by wall-transpiration is described in §5.2.1, precisely the lifting procedure and the evolution for each actuated component. The objective function is derived from the kinetic energy density in §5.2.2.2.

An infinite-horizon full-information LQR controller actuated by wall-transpiration as the model 3.19, without perturbation $\boldsymbol{w}$, is considered,

$$\begin{bmatrix} \dot{\boldsymbol{x}} \\ \boldsymbol{z} \end{bmatrix} = \left[\begin{array}{c|c} \mathcal{A} & \mathcal{B}_2 \\ \hline \begin{bmatrix} \mathcal{C}_1 \\ 0 \end{bmatrix} & \begin{bmatrix} 0 \\ \mathcal{D}_{12} \end{bmatrix} \end{array}\right] \begin{bmatrix} \boldsymbol{x} \\ \boldsymbol{q} \end{bmatrix}, \quad \boldsymbol{x}(0) = 0. \tag{5.1}$$

The objective is to stabilize an Invariant Solution of PCF while spending the least-possible energy in the control process. Therefore, an objective cost-function is defined to minimize both the kinetic energy of the state-vector $\boldsymbol{x}$, representing the distance $\boldsymbol{u}$ between the target base-flow solution $\bar{\boldsymbol{U}}$ and the current flow-field $\boldsymbol{U}$ (eq.4.1), and the energy spent in the control process, function of the control signal $\boldsymbol{q}$,

$$||\boldsymbol{z}||_2^2 = \boldsymbol{z}^*\boldsymbol{z} = \boldsymbol{x}^*\mathcal{C}_1^*\mathcal{C}_1\boldsymbol{x} + \kappa^2\, \boldsymbol{q}^*\mathcal{D}_{12}^*\mathcal{D}_{12}\boldsymbol{q}. \tag{5.2}$$

This minimization problem is a convex optimization problem as the model is linear, the cost function function is quadratic and both matrices $\mathcal{C}_1^*\mathcal{C}_1$ and $\mathcal{D}_{12}^*\mathcal{D}_{12}$ are semi-positive-definite (and strictly convex if the matrices are strictly positive). As a consequence, this problem possess a unique optimal solution.

Matrices $\mathcal{A}$ and $\mathcal{B}_2$ are derived in §5.2.1, and matrices $\mathcal{C}_1$ and $\mathcal{D}_{12}$ in §5.2.2.2 and 5.2.2.3. The parameter $\kappa \geq 0$ is adjusted empirically and fix the importance of each norm in the cost function. Increasing κ gives more priority on minimizing the controller effort, and decreasing κ to the minimization of the state perturbations. In the limit $\kappa \to 0$, the cost of the control is no more considered and its amplitude is unbounded.

Note: in the case where the perturbations $\boldsymbol{w}$ is preserved in eq. 5.1, its associated matrix $\mathcal{B}_1$ (eq. 3.19) is required to be energy-weighted appropriately, for example with $\mathcal{B}_1 = \mathcal{C}_1^{-1}$ (Heins, 2015).

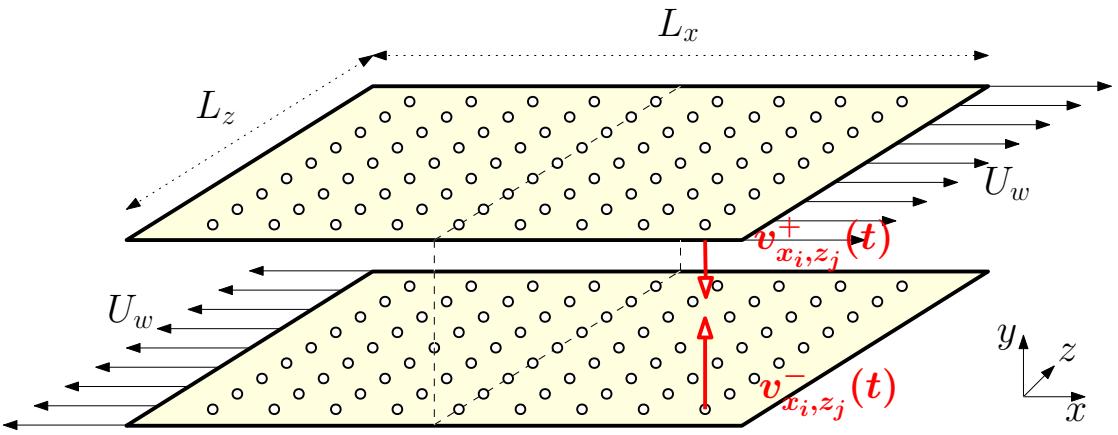

FIGURE 5.2: Diagram of wall-transpiration actuation in a Plane Couette Flow configuration, i.e. imposing the wall-normal velocity at the upper and lower walls at given discrete physical position (x_i, z_j).

5.2.1 OSSE model actuated by wall-transpiration

Actuation is here enforced by wall-transpiration, i.e. applying at the wall a forcing on the wall-normal component $v(t)$ of the velocity field $\boldsymbol{u}(u, v, w, t)$ (fig. 5.2). The main drawback of actuation and/or sensing on the wall consists in the near un-controllability and/or un-observability of "center-modes". The predominant oscillations of such modes reside far away from the wall, and therefore sensing or actuating them is nearly impossible. Nonetheless, controllability and stabilizility analysis in section 5.4 will demonstrate that wall-transpiration is in theory sufficient for our objective.

It is not possible to implement directly this type of actuation on the OSSE model 4.77, due to the requirement for homogeneous boundary conditions. The OSSE model 4.77 is indeed an homogeneous PDAE, meaning it can be expressed as $\mathfrak{F}(\boldsymbol{x}) = 0$, imposed by a set of inhomogeneous boundary conditions when wall-transpiration is applied. This inhomogeneity would make the matrix ∇^2 contained in Υ (eq. 4.77) singular, and prevent access to solutions of the model. To bypass this limitation, McKernan et al. (2006) and Heins (2015) used a "lifting-procedure". It transforms the homogeneous PDAE 4.77 imposed with inhomogeneous boundary conditions into a inhomogeneous PDAE imposed with homogeneous boundary conditions. Herein below are given the milestones of the derivation of the OSSE model, while a detailed derivation is available in appendix G.

Lifting procedure theory

Let's consider the homogeneous PDAE,

$$E\dot{x} = Lx, \tag{5.3}$$

imposed by homogeneous Dirichlet boundary conditions at the walls, $x(+1) = x(-1) = 0$, and where E contains the Laplacian operator ∇^2. Actuation by wall-transpiration of the wall-normal velocity component $v^{\pm}$ at the upper- and lower-wall is applied with the forcing $q^{\pm}$ via a low-pass filter of actuation-time τ,

$$\dot{x}^{+}(t) = -\frac{1}{\tau}x^{+}(t) + \frac{1}{\tau}q^{+}, \tag{5.4a}$$

$$\dot{x}^{-}(t) = -\frac{1}{\tau}x^{-}(t) + \frac{1}{\tau}q^{-}. \tag{5.4b}$$

The system is now a set of homogeneous PDAE 5.3 imposed by inhomogeneous boundary conditions 5.4, and the matrix E becomes singular or nearly singular. To solve this issue, the system is transformed into a set of inhomogeneous PDAE imposed by homogeneous boundary conditions.

To do so, the state-vector x is separated between the homogeneous inner-field x^0, respecting the homogeneous Dirichlet boundary condition, and the value $x^{\pm}$ at the upper- and lower-wall, imposed with inhomogeneous boundary condition $q^{\pm}$, by introducing a continuous "lifting function" $f^{\pm}$ such that

$$x(t) = x^0(y,t) + f^{+}(y)x^{+}(t) + f^{-}(y)x^{-}(t), \tag{5.5a}$$

$$x^0(+1,t) = 0, \quad x^0(-1,t) = 0, \tag{5.5b}$$

$$f^{+}(+1) = 1, \quad f^{+}(-1) = 0, \tag{5.5c}$$

$$f^{-}(+1) = 0, \quad f^{-}(-1) = 1, \tag{5.5d}$$

or considering a wall-normal discretisation with N_y coefficient,

$$x(t) = \begin{bmatrix} 0 \\ x_1^0(t) \\ x_2^0(t) \\ \cdots \\ 0 \end{bmatrix} + \begin{bmatrix} 1 \\ f_1^{+} \\ f_2^{+} \\ \cdots \\ 0 \end{bmatrix} x^{+}(t) + \begin{bmatrix} 0 \\ f_1^{-} \\ f_2^{-} \\ \cdots \\ 1 \end{bmatrix} x^{-}(t), \tag{5.6a}$$

$$x_0^0(t) = 0, \quad x_{N_y}^0(t) = 0, \tag{5.6b}$$

$$f_0^{+} = 1, \quad f_{N_y}^{+} = 0 \tag{5.6c}$$

$$f_0^{-} = 0, \quad f_{N_y}^{-} = 1. \tag{5.6d}$$

Introduced this formulation into the model 5.3, it leads to

$$E\dot{x}^0(y,t) + Ef^{+}(y)\dot{x}^{+}(t) + Ef^{-}(y)\dot{x}^{-}(t) = Lx^0(y,t) + Lf^{+}(y)x^{+}(t) + Lf^{-}(y)x^{-}(t). \tag{5.7}$$

Since the homogeneous state-vector x^0 always respects the Dirichlet boundary condition, the following equality holds,

$$\mathring{E}x^0 = Ex^0, \quad \mathring{L}x^0 = Lx^0, \tag{5.8}$$

where $\mathring{\cdot}$ corresponds to the matrix imposed with homogeneous boundary conditions, i.e. the first/last row/column are replaced with zeros for the Dirichlet boundary condition. As a consequence, the evaluation of the homogeneous state-vector x^0 is limited on the inner-field —excluding the value at the upper-wall. Once the first/last row/column of zeros removed, the matrix $\mathring{E}$ is invertible, unlike E. As a consequence, the inner-field x^0 can be expressed as

$$\mathring{E}\dot{x}^0(y,t)+Ef^+(y)\dot{x}^+(t)+Ef^-(y)\dot{x}^-(t) = \mathring{L}x^0(y,t)+Lf^+(y)x^+(t)+Lf^-(y)x^-(t), \quad (5.9)$$

and inverting $\mathring{E}$,

$$\begin{aligned}\dot{x}^0(y,t) = &-\mathring{E}^{-1}Ef^+(y)\dot{x}^+(t) - \mathring{E}^{-1}Ef^-(y)\dot{x}^-(t)\\ &+\mathring{E}^{-1}\mathring{L}x^0(y,t) + \mathring{E}^{-1}Lf^+(y)x^+(t) + \mathring{E}^{-1}Lf^-(y)x^-(t).\end{aligned} \quad (5.10)$$

Introducing the expression of $\dot{x}^{\pm}(t)$ from eq. 5.4, it leads to the final expression

$$\begin{aligned}\dot{x}^0(y,t) = \mathring{E}^{-1}\mathring{L}x^0(y,t) &+ \left[\mathring{E}^{-1}Lf^+(y) + \frac{1}{\tau}\mathring{E}^{-1}Ef^+(y)\right]x^+(t) - \frac{1}{\tau}\mathring{E}^{-1}Ef^+(y)q^+\\ &+ \left[\mathring{E}^{-1}Lf^-(y) + \frac{1}{\tau}\mathring{E}^{-1}Ef^-(y)\right]x^-(t) - \frac{1}{\tau}\mathring{E}^{-1}Ef^-(y)q^-\end{aligned} \quad (5.11)$$

which can be described in matrix form as

$$\begin{aligned}\frac{\partial}{\partial t}\begin{bmatrix}x^+\\x^0\\x^-\end{bmatrix} &= \begin{bmatrix}1&0&0\\0&\mathring{E}^{-1}&0\\0&0&1\end{bmatrix}\begin{bmatrix}-\frac{1}{\tau}&0&0\\\left[Lf^+(y)+\frac{1}{\tau}Ef^+(y)\right]&\mathring{L}&\left[Lf^-(y)+\frac{1}{\tau}Ef^-(y)\right]\\0&0&-\frac{1}{\tau}\end{bmatrix}\begin{bmatrix}x^+\\x^0\\x^-\end{bmatrix}\\ &+\begin{bmatrix}1&0&0\\0&\mathring{E}^{-1}&0\\0&0&1\end{bmatrix}\begin{bmatrix}\frac{1}{\tau}&0\\-\frac{1}{\tau}Ef^+(y)&-\frac{1}{\tau}Ef^-(y)\\0&\frac{1}{\tau}\end{bmatrix}\begin{bmatrix}q^+\\q^-\end{bmatrix},\\ &= \mathring{E}^{-1}Lx + \mathring{E}^{-1}Bq.\end{aligned} \quad (5.12)$$

Lifting procedure applied to the OSSE model

The lifting procedure is applied the variable expressions for all modes of v, all modes of η excluded the pair $(0,0)$, $u_{0,0}$ and $w_{0,0}$,

$$\hat{v}_{\alpha,\beta}(y,t) = \hat{v}^0_{\alpha,\beta}(y,t) + f^+(y)\ v^+_{\alpha,\beta}(t) + f^-(y)\ v^-_{\alpha,\beta}(t), \quad (5.13a)$$

$$\hat{\eta}_{\alpha,\beta}(y,t) = \hat{\eta}^0_{\alpha,\beta}(y,t) + g^+(y)\ \eta^+_{\alpha,\beta}(t) + g^-(y)\ \eta^-_{\alpha,\beta}(t), \quad (5.13b)$$

$$\hat{u}_{0,0}(y,t) = \hat{u}^0_{0,0}(y,t) + f^+(y)\ u^+_{0,0}(t) + f^-(y)\ u^-_{0,0}(t), \quad (5.13c)$$

$$\hat{w}_{0,0}(y,t) = \hat{w}^0_{0,0}(y,t) + f^+(y)\ w^+_{0,0}(t) + f^-(y)\ w^-_{0,0}(t), \quad (5.13d)$$

where $\cdot^0$ denotes the coefficients imposed with homogeneous boundary condition, clamped for u, v, w and Dirichlet for η, and leads for each mode to

$$\hat{v}^0_{\alpha,\beta}(y=\pm1,t) = \frac{\partial \hat{v}^0_{\alpha,\beta}}{\partial y}(y=\pm1,t) = 0, \tag{5.14a}$$

$$\hat{\eta}^0_{\alpha,\beta}(y=\pm1,t) = 0, \tag{5.14b}$$

$$\hat{u}^0_{0,0}(y=\pm1,t) = \frac{\partial \hat{u}^0_{0,0}}{\partial y}(y=\pm1,t) = 0, \tag{5.14c}$$

$$\hat{w}^0_{0,0}(y=\pm1,t) = \frac{\partial \hat{w}^0_{0,0}}{\partial y}(y=\pm1,t) = 0. \tag{5.14d}$$

The notations $\cdot^+$ and $\cdot^-$ correspond to the inhomogeneous values imposed on the upper and lower wall respectively, notated as

$$\hat{v}_{\alpha,\beta}(y=\pm1,t) = \hat{v}^\pm_{\alpha,\beta}(t), \tag{5.15a}$$

$$\hat{\eta}_{\alpha,\beta}(y=\pm1,t) = \hat{\eta}^\pm_{\alpha,\beta}(t), \tag{5.15b}$$

$$\hat{u}_{0,0}(y=\pm1,t) = \hat{u}^\pm_{0,0}(t), \tag{5.15c}$$

$$\hat{w}_{0,0}(y=\pm1,t) = \hat{w}^\pm_{0,0}(t). \tag{5.15d}$$

Functions f^+ and f^- are the lifting functions associated with u, v, w, for the upper and lower walls respectively, and similarly g^+ and g^- to η. These functions are used to ensure that the set of equations 5.13 respects the conditions 5.15. Thereby, $f^\pm$ and $g^\pm$ need to comply with the conditions

$$f^+(y=+1) = g^+(y=+1) = 1, \tag{5.16a}$$

$$f^+(y=-1) = g^+(y=-1) = 0, \tag{5.16b}$$

$$f^-(y=+1) = g^-(y=+1) = 0, \tag{5.16c}$$

$$f^-(y=-1) = g^-(y=-1) = 1, \tag{5.16d}$$

$$\frac{\partial f^+(y=\pm1)}{\partial y} = \frac{\partial f^-(y=\pm1)}{\partial y} = 0. \tag{5.16e}$$

Fitting functions are given by Heins (2015) (McKernan et al. (2006)[p.198] used different expressions) as

$$f^+(y) = \frac{1}{4}(2y^4 - y^3 - 4y^2 + 3y + 4), \tag{5.17a}$$

$$f^-(y) = \frac{1}{4}(2y^4 + y^3 - 4y^2 - 3y + 4), \tag{5.17b}$$

$$g^+(y) = \frac{1}{2}(x + 1), \tag{5.17c}$$

$$g^-(y) = \frac{1}{2}(-x + 1). \tag{5.17d}$$

The introduction of the lifting equations 5.13 into the Fourier discretisation 4.60 leads to the expression of each Fourier coefficient as

$$\hat{v}_{\alpha,\beta}(y,t) \approx \sum_{n_y=1}^{N_y-1} \tilde{v}^0_{\alpha,\beta}(t)\, T_{n_y}(y) + f^+(y)\; v^+_{\alpha,\beta}(t) + f^-(y)\; v^-_{\alpha,\beta}(t), \tag{5.18a}$$

$$\hat{\eta}_{\alpha,\beta}(y,t) \approx \sum_{n_y=1}^{N_y-1} \tilde{\eta}^0_{\alpha,\beta}(t)\, T_{n_y}(y) + g^+(y)\; \eta^+_{\alpha,\beta}(t) + g^-(y)\; \eta^-_{\alpha,\beta}(t), \tag{5.18b}$$

$$\hat{u}_{0,0}(y,t) \approx \sum_{n_y=1}^{N_y-1} \tilde{u}^0_{0,0}(t)\, T_{n_y}(y) + f^+(y)\; u^+_{0,0}(t) + f^-(y)\; u^-_{0,0}(t), \tag{5.18c}$$

$$\hat{w}_{0,0}(y,t) \approx \sum_{n_y=1}^{N_y-1} \tilde{w}^0_{0,0}(t)\, T_{n_y}(y) + f^+(y)\; w^+_{0,0}(t) + f^-(y)\; w^-_{0,0}(t). \tag{5.18d}$$

The actuation vector $\boldsymbol{q}$ is composed of the actuation components as

$$\boldsymbol{q}(t) = \begin{bmatrix} \begin{bmatrix} q^+_{v_{\alpha,\beta}}(t) \\ q^-_{v_{\alpha,\beta}}(t) \end{bmatrix}_{\substack{0\le\alpha<N_\alpha,\\ 0\le\beta<N_\beta}} \\ \begin{bmatrix} q^+_{\eta_{\alpha,\beta}}(t) \\ q^-_{\eta_{\alpha,\beta}}(t) \end{bmatrix}_{\substack{0\le\alpha<N_\alpha,\\ 0\le\beta<N_\beta\\ (\alpha,\beta)\neq(0,0)}} \\ q^+_{u_{0,0}}(t) \\ q^-_{u_{0,0}}(t) \\ q^+_{w_{0,0}}(t) \\ q^-_{w_{0,0}}(t) \end{bmatrix}, \tag{5.19}$$

where $q^{\pm}_{X_{\alpha,\beta}}$ is the actuation imposed at the upper $(+)$/lower$(-)$ wall in order to set the variable $X^{\pm}$ for the wave-number pair (α,β). These terms feed the model using a low-pass filter to simulate the time-dynamic of the actuator, leading to following expressions

$$\dot{\hat{v}}^{+}_{\alpha,\beta}(t) = -\frac{1}{\tau_{v_{\alpha,\beta}}}\hat{v}^{+}_{\alpha,\beta}(t) + \frac{1}{\tau_{v_{\alpha,\beta}}}q^{+}_{v_{\alpha,\beta}}(t), \tag{5.20a}$$

$$\dot{\hat{v}}^{-}_{\alpha,\beta}(t) = -\frac{1}{\tau_{v_{\alpha,\beta}}}\hat{v}^{-}_{\alpha,\beta}(t) + \frac{1}{\tau_{v_{\alpha,\beta}}}q^{-}_{v_{\alpha,\beta}}(t), \tag{5.20b}$$

$$\dot{\hat{\eta}}^{+}_{\alpha,\beta}(t) = -\frac{1}{\tau_{\eta_{\alpha,\beta}}}\hat{\eta}^{+}_{\alpha,\beta}(t) + \frac{1}{\tau_{\eta_{\alpha,\beta}}}q^{+}_{\eta_{\alpha,\beta}}(t), \tag{5.20c}$$

$$\dot{\hat{\eta}}^{-}_{\alpha,\beta}(t) = -\frac{1}{\tau_{\eta_{\alpha,\beta}}}\hat{\eta}^{-}_{\alpha,\beta}(t) + \frac{1}{\tau_{\eta_{\alpha,\beta}}}q^{-}_{\eta_{\alpha,\beta}}(t), \tag{5.20d}$$

$$\dot{\hat{u}}^{+}_{0,0}(t) = -\frac{1}{\tau_{u_{0,0}}}\hat{u}^{+}_{0,0}(t) + \frac{1}{\tau_{u_{0,0}}}q^{+}_{u_{0,0}}(t), \tag{5.20e}$$

$$\dot{\hat{u}}^{-}_{0,0}(t) = -\frac{1}{\tau_{u_{0,0}}}\hat{u}^{-}_{0,0}(t) + \frac{1}{\tau_{u_{0,0}}}q^{-}_{u_{0,0}}(t), \tag{5.20f}$$

$$\dot{\hat{w}}^{+}_{0,0}(t) = -\frac{1}{\tau_{w_{0,0}}}\hat{w}^{+}_{0,0}(t) + \frac{1}{\tau_{w_{0,0}}}q^{+}_{w_{0,0}}(t), \tag{5.20g}$$

$$\dot{\hat{w}}^{-}_{0,0}(t) = -\frac{1}{\tau_{w_{0,0}}}\hat{w}^{-}_{0,0}(t) + \frac{1}{\tau_{w_{0,0}}}q^{-}_{w_{0,0}}(t), \tag{5.20h}$$

where $\tau_{X_{\alpha,\beta}}$ represents the actuation-time for component X at mode (α, β). The low-pass filter requires an initial condition, fixed as

$$v^{\pm}_{\alpha,\beta}(t=0) = \eta^{\pm}_{\alpha,\beta}(t=0) = u^{\pm}_{0,0}(t=0) = w^{\pm}_{0,0}(t=0) = 0. \tag{5.21}$$

Therefore, the introduction of wall-transpiration transforms the OSSE model into an inhomogeneous system of the form $\mathfrak{F}(\boldsymbol{x}^0, \boldsymbol{x}^+, \boldsymbol{x}^-) = -\mathfrak{F}(\boldsymbol{q}^+, \boldsymbol{q}^-)$, with homogeneous boundary conditions 5.14.

Remark on notations: In the following development, matrices imposed with homogeneous boundary conditions are always noted with the symbol $\mathring{\cdot}$. For example, wall-normal differentiation matrix $\mathring{\mathcal{D}}$, Laplacian operator $\mathring{\nabla}^2$ and square Laplacian $\mathring{\nabla}^4$ are all imposed with homogeneous boundary conditions (Dirichlet and Neumann), while $\mathcal{D}$, ∇^2 and ∇^4 are not. In this way, the matrix Υ in equation 4.77 will contain the operator $\mathring{\nabla}^2$ and be invertible. As a reminder, matrices noted with $\cdot_0$, like $\mathcal{D}_0$ or ∇^2_0, are differentiation operators dedicated to the base-flow $\boldsymbol{U}_0$ only, without any boundary condition applied.

Actuated wall-normal velocity evolution $v_{\alpha,\beta}$

The lifted coefficients 5.18 are introduced into the OSSE system 4.73,

$$
\begin{aligned}
&\frac{\partial}{\partial t}\mathring{\nabla}^2\Big(\hat{v}^0_{\alpha,\beta}(y,t)+f^+(y)v^+_{\alpha,\beta}(t)+f^-(y)v^-_{\alpha,\beta}(t)\Big) = \\
&\quad\frac{1}{Re}\mathring{\nabla}^4_{\alpha,\beta}\Big(\hat{v}^0_{\alpha,\beta}(y,t)+f^+(y)v^+_{\alpha,\beta}(t)+f^-(y)v^-_{\alpha,\beta}(t)\Big) \\
&\quad+\sum_{k'_x=-\frac{N'_x}{2}+1}^{N'_x/2}\sum_{k'_z=-\frac{N'_z}{2}+1}^{N'_z/2} A_{\substack{\alpha,\beta,\\ \alpha-\alpha',\beta-\beta'}}\Big(\hat{v}^0_{\substack{\alpha-\alpha'\\ \beta-\beta'}}(y,t)+f^+(y)\,v^+_{\substack{\alpha-\alpha'\\ \beta-\beta'}}(t)+f^-(y)\,v^-_{\substack{\alpha-\alpha'\\ \beta-\beta'}}(t)\Big) \\
&\quad+\sum_{\substack{k'_x=-\frac{N'_x}{2}+1\\ (k_x-k'_x,k_z-k'_z)\neq(0,0)}}^{N'_x/2}\sum_{k'_z=-\frac{N'_z}{2}+1}^{N'_z/2} B_{\substack{\alpha,\beta,\\ \alpha-\alpha',\beta-\beta'}}\Big(\hat{v}^0_{\substack{\alpha-\alpha'\\ \beta-\beta'}}(y,t)+f^+(y)\,v^+_{\substack{\alpha-\alpha'\\ \beta-\beta'}}(t)+f^-(y)\,v^-_{\substack{\alpha-\alpha'\\ \beta-\beta'}}(t)\Big) \\
&\quad+\sum_{\substack{k'_x=-\frac{N'_x}{2}+1\\ (k_x-k'_x,k_z-k'_z)\neq(0,0)}}^{N'_x/2}\sum_{k'_z=-\frac{N'_z}{2}+1}^{N'_z/2} C_{\substack{\alpha,\beta,\\ \alpha-\alpha',\beta-\beta'}}\Big(\hat{\eta}^0_{\substack{\alpha-\alpha'\\ \beta-\beta'}}(y,t)+g^+(y)\,\eta^+_{\substack{\alpha-\alpha'\\ \beta-\beta'}}(t)+g^-(y)\,\eta^-_{\substack{\alpha-\alpha'\\ \beta-\beta'}}(t)\Big) \\
&\quad+D_{\substack{\alpha,\beta,\\ 0,0}}\Big(\hat{u}^0_{0,0}(y,t)+f^+(y)\;u^+_{0,0}(t)+f^-(y)\;u^-_{0,0}(t)\Big) \\
&\quad+E_{\substack{\alpha,\beta,\\ 0,0}}\Big(\hat{w}^0_{0,0}(y,t)+f^+(y)\;w^+_{0,0}(t)+f^-(y)\;w^-_{0,0}(t)\Big).
\end{aligned}
\tag{5.22}
$$

The fully-discretized system for all coefficients of the wall-normal velocity can be expressed after a) replacing the time-differentiation of $v^{\pm}_{\alpha,\beta}$ with equations 5.20; b) considering the equality 5.8 applied $\mathring{\nabla}$ and c) using Chebyshev series and differentiation matrices, as

$$
\begin{aligned}
&\frac{\partial}{\partial t}\begin{bmatrix}1&0&0\\0&\mathring{\tilde{\nabla}}^2&0\\0&0&1\end{bmatrix}\begin{bmatrix}v^+_{\alpha,\beta}(t)\\ \tilde{v}^0_{\alpha,\beta}(y,t)\\ v^-_{\alpha,\beta}(t)\end{bmatrix} = \mathbb{E}_1\begin{bmatrix}v^+_{\alpha,\beta}(t)\\ \tilde{v}^0_{\alpha,\beta}(y,t)\\ v^-_{\alpha,\beta}(t)\end{bmatrix}+\sum_{k'_x=-\frac{N'_x}{2}+1}^{N'_x/2}\sum_{k'_z=-\frac{N'_z}{2}+1}^{N'_z/2}\mathbb{A}\begin{bmatrix}v^+_{\alpha-\alpha',\beta-\beta'}(t)\\ \tilde{v}^0_{\alpha-\alpha',\beta-\beta'}(y,t)\\ v^-_{\alpha-\alpha',\beta-\beta'}(t)\end{bmatrix} \\
&\quad+\sum_{\substack{k'_x=-\frac{N'_x}{2}+1\\ (k_x-k'_x,k_z-k'_z)\neq(0,0)}}^{N'_x/2}\sum_{k'_z=-\frac{N'_z}{2}+1}^{N'_z/2}\mathbb{B}\begin{bmatrix}v^+_{\alpha-\alpha',\beta-\beta'}(t)\\ \tilde{v}^0_{\alpha-\alpha',\beta-\beta'}(y,t)\\ v^-_{\alpha-\alpha',\beta-\beta'}(t)\end{bmatrix}+\sum_{\substack{k'_x=-\frac{N'_x}{2}+1\\ (k_x-k'_x,k_z-k'_z)\neq(0,0)}}^{N'_x/2}\sum_{k'_z=-\frac{N'_z}{2}+1}^{N'_z/2}\mathbb{C}\begin{bmatrix}\eta^+_{\alpha-\alpha',\beta-\beta'}(t)\\ \tilde{\eta}^0_{\alpha-\alpha',\beta-\beta'}(y,t)\\ \eta^-_{\alpha-\alpha',\beta-\beta'}(t)\end{bmatrix} \\
&\quad+\mathbb{D}\begin{bmatrix}u^+_{0,0}(t)\\ \tilde{u}^0_{0,0}(y,t)\\ u^-_{0,0}(t)\end{bmatrix}+\mathbb{E}\begin{bmatrix}w^+_{0,0}(t)\\ \tilde{w}^0_{0,0}(y,t)\\ w^-_{0,0}(t)\end{bmatrix}+\mathbb{B}_1\begin{bmatrix}q^+_{v_{\alpha,\beta}}(t)\\ q^-_{v_{\alpha,\beta}}(t)\end{bmatrix},
\end{aligned}
\tag{5.23}
$$

where matrices $\mathbb{E}_1, \mathbb{A}, \mathbb{B}, \mathbb{C}, \mathbb{D}, \mathbb{E}, \mathbb{B}_1$ are given in the appendix E.

Actuated wall-normal vorticity evolution $\eta_{\alpha,\beta}$

The lifted coefficients 5.18 are introduced into the OSSE system 4.74,

$$
\begin{aligned}
&\frac{\partial}{\partial t}\Big(\eta^0_{\alpha,\beta}(y,t) + g^+(y)\ \eta^+_{\alpha,\beta}(t) + g^-(y)\ \eta^-_{\alpha,\beta}(t)\Big) = \\
&\sum_{k'_x=-\frac{N'_x}{2}+1}^{N'_x/2}\ \sum_{k'_z=-\frac{N'_z}{2}+1}^{N'_z/2} F_{\substack{\alpha,\beta,\\ \alpha-\alpha',\beta-\beta'}}\ \Big(v^0_{\alpha,\beta}(y,t) + f^+(y)\ v^+_{\alpha,\beta}(t) + f^-(y)\ v^-_{\alpha,\beta}(t)\Big) \\
&+ \sum_{\substack{k'_x=-\frac{N'_x}{2}+1\\ (k_x-k'_x,k_z-k'_z)\neq(0,0)}}^{N'_x/2}\ \sum_{k'_z=-\frac{N'_z}{2}+1}^{N'_z/2} G_{\substack{\alpha,\beta,\\ \alpha-\alpha',\beta-\beta'}}\ \Big(v^0_{\alpha,\beta}(y,t) + f^+(y)\ v^+_{\alpha,\beta}(t) + f^-(y)\ v^-_{\alpha,\beta}(t)\Big) \\
&+ \frac{1}{Re}\nabla^2\Big(\eta^0_{\alpha,\beta}(y,t) + g^+(y)\ \eta^+_{\alpha,\beta}(t) + g^-(y)\ \eta^-_{\alpha,\beta}(t)\Big) \\
&+ \sum_{\substack{k'_x=-\frac{N'_x}{2}+1\\ (k_x-k'_x,k_z-k'_z)\neq(0,0)}}^{N'_x/2}\ \sum_{k'_z=-\frac{N'_z}{2}+1}^{N'_z/2} \left[H_{\substack{\alpha,\beta,\\ \alpha-\alpha',\beta-\beta'}} + J_{\substack{\alpha,\beta,\\ \alpha-\alpha',\beta-\beta'}}\right]\Big(\eta^0_{\alpha,\beta}(y,t) + g^+(y)\ \eta^+_{\alpha,\beta}(t) + g^-(y)\ \eta^-_{\alpha,\beta}(t)\Big) \\
&+ K_{\substack{\alpha,\beta,\\ 0,0}}\ \Big(\hat{u}^0_{0,0}(y,t) + f^+(y)\ u^+_{0,0}(t) + f^-(y)\ u^-_{0,0}(t)\Big) \\
&+ L_{\substack{\alpha,\beta,\\ 0,0}}\ \Big(\hat{w}^0_{0,0}(y,t) + f^+(y)\ w^+_{0,0}(t) + f^-(y)\ w^-_{0,0}(t)\Big)
\end{aligned}
\tag{5.24}
$$

and similarly to the wall-normal velocity v, the fully-discretized system for all coefficients of the wall-normal vorticity can be expressed after

$$
\begin{aligned}
\frac{\partial}{\partial t}\begin{bmatrix} \eta^+_{\alpha,\beta}(t) \\ \tilde{\eta}^0_{\alpha,\beta}(y,t) \\ \eta^-_{\alpha,\beta}(t) \end{bmatrix} &= \mathbb{E}_2 \begin{bmatrix} \eta^+_{\alpha,\beta}(t) \\ \tilde{\eta}^0_{\alpha,\beta}(y,t) \\ \eta^-_{\alpha,\beta}(t) \end{bmatrix} \\
&+ \sum_{k'_x=-\frac{N'_x}{2}+1}^{N'_x/2}\ \sum_{k'_z=-\frac{N'_z}{2}+1}^{N'_z/2} \mathbb{F}\begin{bmatrix} v^+_{\alpha-\alpha',\beta-\beta'}(t) \\ \tilde{v}^0_{\alpha-\alpha',\beta-\beta'}(y,t) \\ v^-_{\alpha-\alpha',\beta-\beta'}(t) \end{bmatrix} + \sum_{\substack{k'_x=-\frac{N'_x}{2}+1\\ (k_x-k'_x,k_z-k'_z)\neq(0,0)}}^{N'_x/2}\ \sum_{k'_z=-\frac{N'_z}{2}+1}^{N'_z/2} \mathbb{G}\begin{bmatrix} v^+_{\alpha-\alpha',\beta-\beta'}(t) \\ \tilde{v}^0_{\alpha-\alpha',\beta-\beta'}(y,t) \\ v^-_{\alpha-\alpha',\beta-\beta'}(t) \end{bmatrix} \\
&+ \sum_{\substack{k'_x=-\frac{N'_x}{2}+1\\ (k_x-k'_x,k_z-k'_z)\neq(0,0)}}^{N'_x/2}\ \sum_{k'_z=-\frac{N'_z}{2}+1}^{N'_z/2} \Big[\mathbb{H}+\mathbb{J}\Big]\begin{bmatrix} \eta^+_{\alpha-\alpha',\beta-\beta'}(t) \\ \tilde{\eta}^0_{\alpha-\alpha',\beta-\beta'}(y,t) \\ \eta^-_{\alpha-\alpha',\beta-\beta'}(t) \end{bmatrix} \\
&+ \mathbb{K}\begin{bmatrix} u^+_{0,0}(t) \\ \tilde{u}^0_{0,0}(y,t) \\ u^-_{0,0}(t) \end{bmatrix} + \mathbb{L}\begin{bmatrix} w^+_{0,0}(t) \\ \tilde{w}^0_{0,0}(y,t) \\ w^-_{0,0}(t) \end{bmatrix} + \mathbb{B}_2\begin{bmatrix} q^+_{\eta_{\alpha,\beta}}(t) \\ q^-_{\eta_{\alpha,\beta}}(t) \end{bmatrix},
\end{aligned}
\tag{5.25}
$$

where the coefficients $\mathbb{E}_2, \mathbb{F}, \mathbb{G}, \mathbb{H}, \mathbb{J}, \mathbb{K}, \mathbb{L}, \mathbb{B}_2$ are given in the appendix E.

Actuated stream-wise velocity evolution $u_{0,0}$

The lifted coefficients 5.18 are introduced into the OSSE system 4.75

$$
\begin{aligned}
\frac{\partial}{\partial t}\hat{u}^0_{0,0}(y,t) = &\left[\frac{1}{Re}\mathring{\nabla}^2_{0,0} - \bar{V}_{0,0}\frac{\mathring{\partial}}{\partial y}\right]\hat{u}^0_{0,0}(y,t) \\
&+ \left[\frac{1}{Re}\nabla^2_{0,0} - \bar{V}_{0,0}\frac{\partial}{\partial y}\right] f^+(y)\; u^+_{0,0}(t) + \frac{1}{\tau_{u_{0,0}}} f^+(y)\; u^+_{0,0}(t) \\
&+ \left[\frac{1}{Re}\nabla^2_{0,0} - \bar{V}_{0,0}\frac{\partial}{\partial y}\right] f^-(y)\; u^-_{0,0}(t)) + \frac{1}{\tau_{u_{0,0}}} f^-(y)\; u^-_{0,0}(t) \\
&- \frac{1}{\tau_{u_{0,0}}} f^+(y)\; q^+_{u_{0,0}}(t) - \frac{1}{\tau_{u_{0,0}}} f^-(y)\; q^-_{u_{0,0}}(t) \\
&+ \sum_{k'_x=-\frac{N'_x}{2}+1}^{N'_x/2} \sum_{k'_z=-\frac{N'_z}{2}+1}^{N'_z/2} M_{\alpha',\beta'}\left(v^0_{-\alpha',-\beta'}(y,t) + f^+(y)\; v^+_{-\alpha',-\beta'}(t) + f^-(y)\; v^-_{-\alpha',-\beta'}(t)\right) \\
&+ \sum_{\substack{k'_x=-\frac{N'_x}{2}+1 \\ (k_x-k'_x,k_z-k'_z)\neq(0,0)}}^{N'_x/2} \sum_{k'_z=-\frac{N'_z}{2}+1}^{N'_z/2} N_{\alpha',\beta'}\left(v^0_{-\alpha',-\beta'}(y,t) + f^+(y)\; v^+_{-\alpha',-\beta'}(t) + f^-(y)\; v^-_{-\alpha',-\beta'}(t)\right) \\
&+ \sum_{\substack{k'_x=-\frac{N'_x}{2}+1 \\ (k_x-k'_x,k_z-k'_z)\neq(0,0)}}^{N'_x/2} \sum_{k'_z=-\frac{N'_z}{2}+1}^{N'_z/2} O_{\alpha',\beta'}\left(\eta^0_{-\alpha',-\beta'}(y,t) + g^+(y)\; \eta^+_{-\alpha',-\beta'}(t) + g^-(y)\; \eta^-_{-\alpha',-\beta'}(t)\right)
\end{aligned}
\tag{5.26}
$$

and similarly to the wall-normal velocity v, the fully-discretized system for the fundamental mode of the stream-wise velocity can be expressed as

$$
\begin{aligned}
\frac{\partial}{\partial t}\begin{bmatrix} u^+_{0,0}(t) \\ \tilde{u}^0_{0,0}(y,t) \\ u^-_{0,0}(t) \end{bmatrix} = \mathbb{E}_3 \begin{bmatrix} u^+_{0,0}(t) \\ \tilde{u}^0_{0,0}(y,t) \\ u^-_{0,0}(t) \end{bmatrix} &+ \sum_{k'_x=-\frac{N'_x}{2}+1}^{N'_x/2} \sum_{k'_z=-\frac{N'_z}{2}+1}^{N'_z/2} \mathbb{M} \begin{bmatrix} v^+_{-\alpha',-\beta'}(t) \\ \tilde{v}^0_{-\alpha',-\beta'}(y,t) \\ v^-_{-\alpha',-\beta'}(t) \end{bmatrix} \\
&+ \sum_{\substack{k'_x=-\frac{N'_x}{2}+1 \\ (k_x-k'_x,k_z-k'_z)\neq(0,0)}}^{N'_x/2} \sum_{k'_z=-\frac{N'_z}{2}+1}^{N'_z/2} \mathbb{N} \begin{bmatrix} v^+_{-\alpha',-\beta'}(t) \\ \tilde{v}^0_{-\alpha',-\beta'}(y,t) \\ v^-_{-\alpha',-\beta'}(t) \end{bmatrix} + \sum_{\substack{k'_x=-\frac{N'_x}{2}+1 \\ (k_x-k'_x,k_z-k'_z)\neq(0,0)}}^{N'_x/2} \sum_{k'_z=-\frac{N'_z}{2}+1}^{N'_z/2} \mathbb{O} \begin{bmatrix} \eta^+_{-\alpha',-\beta'}(t) \\ \tilde{\eta}^0_{-\alpha',-\beta'}(y,t) \\ \eta^-_{-\alpha',-\beta'}(t) \end{bmatrix} \\
&+ \mathbb{B}_3 \begin{bmatrix} q^+_{u_{0,0}}(t) \\ q^-_{u_{0,0}}(t) \end{bmatrix},
\end{aligned}
\tag{5.27}
$$

where the coefficients $\mathbb{E}_3, \mathbb{M}, \mathbb{N}, \mathbb{O}, \mathbb{B}_3$ are given in the appendix E.

Actuated spanwise velocity evolution $w_{0,0}$

The lifted coefficients 5.18 are introduced into the OSSE system 4.76

$$
\begin{aligned}
\frac{\partial}{\partial t}\hat{w}^0_{0,0}(y,t) = &\left[\frac{1}{Re}\mathring{\nabla}^2_{0,0} - \bar{V}_{0,0}\frac{\mathring{\partial}}{\partial y}\right]\hat{w}^0_{0,0}(y,t) \\
&+ \left[\frac{1}{Re}\nabla^2_{0,0} - \bar{V}_{0,0}\frac{\partial}{\partial y}\right] f^+(y)\ w^+_{0,0}(t) + \frac{1}{\tau_{w_{0,0}}} f^+(y)\ w^+_{0,0}(t) \\
&+ \left[\frac{1}{Re}\nabla^2_{0,0} - \bar{V}_{0,0}\frac{\partial}{\partial y}\right] f^-(y)\ w^-_{0,0}(t)) + \frac{1}{\tau_{w_{0,0}}} f^-(y)\ w^-_{0,0}(t) \\
&- \frac{1}{\tau_{w_{0,0}}} f^+(y)\ q^+_{w_{0,0}}(t) - \frac{1}{\tau_{w_{0,0}}} f^-(y)\ q^-_{w_{0,0}}(t) \\
&+ \sum_{k'_x=-\frac{N'_x}{2}+1}^{N'_x/2} \sum_{k'_z=-\frac{N'_z}{2}+1}^{N'_z/2} P_{\alpha',\beta'}\left(v^0_{-\alpha',-\beta'}(y,t) + f^+(y)\ v^+_{-\alpha',-\beta'}(t) + f^-(y)\ v^-_{-\alpha',-\beta'}(t)\right) \\
&+ \sum_{\substack{k'_x=-\frac{N'_x}{2}+1 \\ (k_x-k'_x,k_z-k'_z)\neq(0,0)}}^{N'_x/2} \sum_{k'_z=-\frac{N'_z}{2}+1}^{N'_z/2} Q_{\alpha',\beta'}\left(v^0_{-\alpha',-\beta'}(y,t) + f^+(y)\ v^+_{-\alpha',-\beta'}(t) + f^-(y)\ v^-_{-\alpha',-\beta'}(t)\right) \\
&+ \sum_{\substack{k'_x=-\frac{N'_x}{2}+1 \\ (k_x-k'_x,k_z-k'_z)\neq(0,0)}}^{N'_x/2} \sum_{k'_z=-\frac{N'_z}{2}+1}^{N'_z/2} R_{\alpha',\beta'}\left(\eta^0_{-\alpha',-\beta'}(y,t) + g^+(y)\ \eta^+_{-\alpha',-\beta'}(t) + g^-(y)\ \eta^-_{-\alpha',-\beta'}(t)\right)
\end{aligned}
\tag{5.28}
$$

and similarly to the wall-normal velocity v, the fully-discretized system for the fundamental mode of the span-wise velocity can be expressed as

$$
\begin{aligned}
\frac{\partial}{\partial t}\begin{bmatrix} w^+_{0,0}(t) \\ \tilde{w}^0_{0,0}(y,t) \\ w^-_{0,0}(t) \end{bmatrix} = &\mathbb{E}_4 \begin{bmatrix} w^+_{0,0}(t) \\ \tilde{w}^0_{0,0}(y,t) \\ w^-_{0,0}(t) \end{bmatrix} + \sum_{k'_x=-\frac{N'_x}{2}+1}^{N'_x/2} \sum_{k'_z=-\frac{N'_z}{2}+1}^{N'_z/2} \mathbb{P} \begin{bmatrix} v^+_{-\alpha',-\beta'}(t) \\ \tilde{v}^0_{-\alpha',-\beta'}(y,t) \\ v^-_{-\alpha',-\beta'}(t) \end{bmatrix} \\
&+ \sum_{\substack{k'_x=-\frac{N'_x}{2}+1 \\ (k_x-k'_x,k_z-k'_z)\neq(0,0)}}^{N'_x/2} \sum_{k'_z=-\frac{N'_z}{2}+1}^{N'_z/2} \mathbb{Q} \begin{bmatrix} v^+_{-\alpha',-\beta'}(t) \\ \tilde{v}^0_{-\alpha',-\beta'}(y,t) \\ v^-_{-\alpha',-\beta'}(t) \end{bmatrix} + \sum_{\substack{k'_x=-\frac{N'_x}{2}+1 \\ (k_x-k'_x,k_z-k'_z)\neq(0,0)}}^{N'_x/2} \sum_{k'_z=-\frac{N'_z}{2}+1}^{N'_z/2} \mathbb{R} \begin{bmatrix} \eta^+_{-\alpha',-\beta'}(t) \\ \tilde{\eta}^0_{-\alpha',-\beta'}(y,t) \\ \eta^-_{-\alpha',-\beta'}(t) \end{bmatrix} \\
&+ \mathbb{B}_4 \begin{bmatrix} q^+_{w_{0,0}}(t) \\ q^-_{w_{0,0}}(t) \end{bmatrix},
\end{aligned}
\tag{5.29}
$$

where the coefficients $\mathbb{E}_4, \mathbb{P}, \mathbb{Q}, \mathbb{R}, \mathbb{B}_4$are given in the appendix E.

Actuated final system

Finally, gathering equations 5.23 , 5.25 , 5.27 and 5.29 build the entire actuated plant system and define the matrices $\mathcal{A}$ and $\mathcal{B}_2$ as

$$\frac{\partial \boldsymbol{x}(t)}{\partial t} = \mathcal{A}\,\boldsymbol{x}(t) + \mathcal{B}_2\,\boldsymbol{q}(t)$$

$$= \begin{bmatrix} \mathring{\nabla}^{-2} & 0 & 0 & 0 \\ 0 & I & 0 & 0 \\ 0 & 0 & I & 0 \\ 0 & 0 & 0 & I \end{bmatrix} \begin{bmatrix} \mathbb{E}_1 + \mathbb{A} + \mathbb{B} & \mathbb{C} & \mathbb{D} & \mathbb{E} \\ \mathbb{F} + \mathbb{G} & \mathbb{E}_2 + \mathbb{H} + \mathbb{J} & \mathbb{K} & \mathbb{L} \\ \mathbb{M} + \mathbb{N} & \mathbb{O} & \mathbb{E}_3 & 0 \\ \mathbb{P} + \mathbb{Q} & \mathbb{R} & 0 & \mathbb{E}_4 \end{bmatrix} \begin{bmatrix} \begin{bmatrix} v^+_{\alpha,\beta}(t) \\ v^0_{\alpha,\beta}(y,t) \\ v^-_{\alpha,\beta}(t) \end{bmatrix}_{\substack{0\le\alpha<N_\alpha,\\ 0\le\beta<N_\beta}} \\ \begin{bmatrix} \eta^+_{\alpha,\beta}(t) \\ \eta^0_{\alpha,\beta}(y,t) \\ \eta^-_{\alpha,\beta}(t) \end{bmatrix}_{\substack{0\le\alpha<N_\alpha,\\ 0\le\beta<N_\beta\\ (\alpha,\beta)\neq(0,0)}} \\ \begin{bmatrix} u^+_{0,0}(t) \\ \hat{u}^0_{0,0}(y,t) \\ u^-_{0,0}(t) \end{bmatrix} \\ \begin{bmatrix} w^+_{0,0}(t) \\ \hat{w}^0_{0,0}(y,t) \\ w^-_{0,0}(t) \end{bmatrix} \end{bmatrix}$$

$$+ \begin{bmatrix} \mathring{\nabla}^{-2} & 0 & 0 & 0 \\ 0 & I & 0 & 0 \\ 0 & 0 & I & 0 \\ 0 & 0 & 0 & I \end{bmatrix} \begin{bmatrix} \mathbb{B}_1 & 0 & 0 & 0 \\ 0 & \mathbb{B}_2 & 0 & 0 \\ 0 & 0 & \mathbb{B}_3 & 0 \\ 0 & 0 & 0 & \mathbb{B}_4 \end{bmatrix} \begin{bmatrix} \begin{bmatrix} q^+_{v_{\alpha,\beta}}(t) \\ q^-_{v_{\alpha,\beta}}(t) \end{bmatrix}_{\substack{0\le\alpha<N_\alpha,\\ 0\le\beta<N_\beta}} \\ \begin{bmatrix} q^+_{\eta_{\alpha,\beta}}(t) \\ q^-_{\eta_{\alpha,\beta}}(t) \end{bmatrix}_{\substack{0\le\alpha<N_\alpha,\\ 0\le\beta<N_\beta\\ (\alpha,\beta)\neq(0,0)}} \\ \begin{bmatrix} q^+_{u_{0,0}}(t) \\ q^-_{u_{0,0}}(t) \end{bmatrix} \\ \begin{bmatrix} q^+_{w_{0,0}}(t) \\ q^-_{w_{0,0}}(t) \end{bmatrix} \end{bmatrix}. \tag{5.30}$$

The matrices $\mathcal{A}$ and $\mathcal{B}_2$ of the final actuated OSSE system preserves the complex-conjugation symmetry of the original OSSE model, at the condition that the actuation q respects the complex-conjugation as well. Nonetheless, this requirement is not an issue. The optimal actuation q^{opt} derives indeed from the actuated OSSE model (later section 6.1), thereby passing the complex-conjugation of the model onto the forcing signal.

5.2.2 Cost function

5.2.2.1 Introduction - What to target?

The determination of a cost function to minimize is decisive in the control design process. An adequate cost function entails both a straightforward physical interpretation as well as an accessible and universal definition, the ultimate goal being to compare different configurations.

Drag-reduction and turbulence dissipation usually adopt a statistical perspective: for a given configuration, the cost function evaluates a reduction of the turbulent energy against the energy spent in the control process. There are commonly two different types of forcing in this case, equivalent in laminar regimes: the constant pressure gradient (CPG, defined by constant friction-based Reynolds number Re_τ) or constant flow rate (CFR, defined by a constant bulk-velocity Reynolds number Re_b). These two categories are not equivalent, and results can not be compared together. Ricco et al. (2012) introduced a more universal approach, the constant power input concept (CPI), associated with a constant-power Reynolds number Re_π (Hasegawa et al., 2014; Gatti et al., 2018). Nonetheless, even if these advances improved the ability to compare numerous wall-actuation configurations, they are dedicated to drag-reduction.

Within a dynamical space representation, defining the cost function as the distance to the targeted state is in fact the most obvious choice. It corresponds to the norm of the state-vector $\boldsymbol{x}$ in eq.5.30. But which norm? Including weights specific to each discretisation is tedious and not practical. For that reason, the chosen norm needs to be grid-independent. Bewley and Liu (1998), McKernan (2006), Martinelli et al. (2011) and Gomes et al. (2015) used the kinetic energy density $\mathcal{E}_T$ to determine the expression of $\mathcal{C}_1$ —without actually giving a fundamental reason for this choice. It embodies the evolution of the perturbation for each velocity component, with an inherent physical meaning for the reader. Kinetic energy density is a "natural" choice, in the sense that the non-linearity does not change this quantity instantaneously. During this research, no alternative was found in the literature and in order to facilitate cross-comparison, the kinetic energy density is used as a norm in the following. As an extra bonus, the kinetic energy density is also at the basis of passivity-based control —otherwise leading to problems with non-linearity— which may be employed in the future to treat this problem.

However, other norms could be defined with a particular consideration of leading quantities, like the wall-normal velocity perturbation, and result in better performances for a specific control problem. Particularly, the present author became aware of the paper of Bewley et al. (2001) during his final PhD viva. Bewley et al. (2001) gives an an in-depth review of different forms of cost functional and compare their performance for the control problem. It included the minimization of drag, the terminal control of the

turbulent kinetic energy, the regulation of the turbulent kinetic energy, of the enstrophy or of large-scale and intermediate-scale structures. They also discussed the impact on performance of including a gradient-based sensitivity to small modifications within the cost function. The formulation of the cost function via the terminal control of the kinetic energy density appeared to be superior. We recommend the interested reader to take advantage of this paper in his or her research.

5.2.2.2 OSSE Energy matrix - Expression of $C_1^* C_1$

The derivation of the energy matrix $\mathcal{C}_1^*\mathbb{C}_1$ below targets homogeneous velocity-fields, respecting the Dirichlet boundary conditions at the walls, and is not directly applicable to inhomogeneous velocity fields. The expression of this matrix is indeed obtained from the Chebyshev differentiation package of Weideman and Reddy (2000), designed for homogeneous velocity fields and producing spurious oscillations —Gibbs phenomenon— when the velocity values at the wall are non-zero (McKernan, 2006, p.11,p.28). This same energy matrix would not converge with increasing resolution if applied to an inhomogeneous velocity field (Hogberg et al., 2003). Therefore, once the energy matrix $\mathcal{C}_1^*\mathbb{C}_1$ is fully-defined for the homogeneous fields, a transformation for the inhomogeneous case is introduced (§5.2.2.4).

The matrix $\mathcal{C}_1$ of the cost function 5.2 for a homogeneous velocitiy-field derives from the kinetic energy density $\mathcal{E}_T$,

$$\mathcal{E}_T = \boldsymbol{x}^* \mathcal{C}_1^* \mathcal{C}_1 \boldsymbol{x}. \tag{5.31}$$

The Hermitian positive-definite matrix $\mathcal{C}_1^*\mathbb{C}_1$ is referred as the "energy matrix". Bewley and Liu (1998); McKernan (2006) defined the kinetic energy density for a flow perturbation of the LNSE model 4.6, at a given volume $V = 2L_xL_z$ and with state components (u, v, w, p), as

$$\mathcal{E}_T = \frac{1}{V}\int_{-1}^{1}\int_{0}^{L_x}\int_{0}^{L_z} \frac{u^2(x,y,z,t) + v^2(x,y,z,t) + w^2(x,y,z,t)}{2} dzdxdy. \tag{5.32}$$

The application of stream- and span-wise Fourier discretisation ($dx = \frac{L_x di_x}{N_x}$ and $dz = \frac{L_z di_z}{N_z}$) follows as

$$\begin{aligned}
\mathcal{E}_T &= \frac{1}{2N_xN_z} \sum_{k_x=-\frac{N_x}{2}+1}^{N_x/2} \sum_{k_z=-\frac{N_z}{2}+1}^{N_z/2} \int_{-1}^{1} \frac{\hat{u}^2_{\alpha,\beta}(y,t) + \hat{v}^2_{\alpha,\beta}(y,t) + \hat{w}^2_{\alpha,\beta}(y,t)}{2} dy, \\
&= \frac{1}{2N_xN_z} \sum_{k_x=-\frac{N_x}{2}+1}^{N_x/2} \sum_{k_z=-\frac{N_z}{2}+1}^{N_z/2} \int_{-1}^{1} \frac{\hat{u}^*_{\alpha,\beta}\hat{u}_{\alpha,\beta} + \hat{v}^*_{\alpha,\beta}\hat{v}_{\alpha,\beta} + \hat{w}^*_{\alpha,\beta}\hat{w}_{\alpha,\beta}}{2} dy.
\end{aligned} \tag{5.33}$$

Considering the expression C.5 and C.4 of components u and w in sole function of v and η, the products u^*u and w^*w are replaced for the all wave-number pairs $(\alpha, \beta) \neq (0, 0)$

with the expression

$$\hat{u}^*_{\alpha,\beta}\hat{u}_{\alpha,\beta} + \hat{w}^*_{\alpha,\beta}\hat{w}_{\alpha,\beta} = \frac{1}{k^2}\left(\frac{\partial \hat{v}_{\alpha,\beta}}{\partial y}^* \frac{\partial \hat{v}_{\alpha,\beta}}{\partial y} + \hat{\eta}^*_{\alpha,\beta}\hat{\eta}_{\alpha,\beta}\right). \tag{5.34}$$

As a consequence, the kinetic energy density $\mathcal{E}_T$ discretised in stream- and span-wise directions follows as

$$\begin{aligned}\mathcal{E}_T = \frac{1}{4N_xN_z}\Bigg[&\int_{-1}^{1} \hat{u}^*_{0,0}\hat{u}_{0,0} + \hat{v}^*_{0,0}\hat{v}_{0,0} + \hat{w}^*_{0,0}\hat{w}_{0,0}\, dy \\ &+ \sum_{\substack{k_x=-\frac{N_x}{2}+1 \\ (k_x,k_z)\neq(0,0)}}^{N_x/2} \sum_{k_z=-\frac{N_z}{2}+1}^{N_z/2} \int_{-1}^{1} \hat{v}^*_{\alpha,\beta}\hat{v}_{\alpha,\beta} + \frac{1}{k^2}\left(\frac{\partial \hat{v}_{\alpha,\beta}}{\partial y}^* \frac{\partial \hat{v}_{\alpha,\beta}}{\partial y} + \hat{\eta}^*_{\alpha,\beta}\hat{\eta}_{\alpha,\beta}\right) dy\Bigg].\end{aligned} \tag{5.35}$$

Finally considering the Chebyshev discretisation in the wall-normal direction, the expression of the kinetic energy density is

$$\begin{aligned}\mathcal{E}_T = \frac{1}{4N_xN_z}\Bigg[&\tilde{u}^*_{0,0}W\tilde{u}_{0,0} + \tilde{v}^*_{0,0}W\tilde{v}_{0,0} + \tilde{w}^*_{0,0}W\tilde{w}_{0,0} \\ &+ \sum_{\substack{k_x=-\frac{N_x}{2}+1 \\ (k_x,k_z)\neq(0,0)}}^{N_x/2} \sum_{k_z=-\frac{N_z}{2}+1}^{N_z/2} \tilde{v}^*_{\alpha,\beta}W\tilde{v}_{\alpha,\beta} + \frac{1}{k^2}\left(\tilde{v}^*_{\alpha,\beta}\mathring{\mathcal{D}}^*W\mathring{\mathcal{D}}\tilde{v}_{\alpha,\beta} + \tilde{\eta}^*_{\alpha,\beta}W\tilde{\eta}_{\alpha,\beta}\right)\Bigg],\end{aligned} \tag{5.36}$$

from which the energy matrix $\mathcal{C}_1^*\mathcal{C}_1$ can be expressed under matrix form as defined in eq. 5.31 and required in the cost function 5.2,

$$\mathcal{C}_1^*\mathcal{C}_1 = \frac{1}{4N_xN_z}\left[\begin{array}{cccc|ccc|cc} \Phi_1 & 0 & \cdots & 0 & 0 & \cdots & 0 & 0 & 0 \\ 0 & \Phi_1+\frac{1}{k^2}\Phi_2 & \cdots & 0 & 0 & \cdots & 0 & 0 & 0 \\ \vdots & \vdots & \ddots & \vdots & \vdots & \ddots & \vdots & 0 & 0 \\ 0 & 0 & \cdots & \Phi_1+\frac{1}{k^2}\Phi_2 & 0 & \cdots & 0 & 0 & 0 \\ \hline 0 & 0 & \cdots & 0 & \frac{1}{k^2}\Phi_1 & \cdots & 0 & 0 & 0 \\ \vdots & \vdots & \ddots & \vdots & \vdots & \ddots & \vdots & 0 & 0 \\ 0 & 0 & \cdots & 0 & 0 & \cdots & \frac{1}{k^2}\Phi_1 & 0 & 0 \\ \hline 0 & 0 & \cdots & 0 & 0 & \cdots & 0 & \Phi_1 & 0 \\ 0 & 0 & \cdots & 0 & 0 & \cdots & 0 & 0 & \Phi_1 \end{array}\right], \tag{5.37}$$

where $\Phi_1 = W$, $\Phi_2 = \mathring{\mathcal{D}}^*W\mathring{\mathcal{D}}$ and the state $\boldsymbol{x}$ defined as in 5.30.

The expression of the matrix $\mathcal{C}_1$ can not be deduced directly with a Cholesky decomposition as operated in Heins (2015). From the LQR problem definition eq.5.1, the matrix $\mathcal{C}_1$ is of shape $p \times n$, and consequently $\mathcal{C}_1^*\mathcal{C}_1$ a rank-deficient matrix of shape $n \times n$. A full-rank energy-matrix would require the condition $p \geq n$, which is not applicable in our case-study. The same problem arises later with the definition of $\mathcal{D}_{12}$, of shape

$p \times m$, from $\mathcal{D}_{12}^{*}\mathcal{D}_{12}$, requiring that $p \geq m$ for a fully-resolved problem. Nonetheless, the expression of $\mathcal{C}_1$ and $\mathcal{D}_{12}$ on their own is not habitually needed. Otherwise, these matrices could be expressed from a pseudo-Cholesky factorization (§H.3) or singular value decompositon (§H.2).

5.2.2.3 OSSE Expression of $\mathcal{D}_{12}$

The loop-shifting and scaling operated on the system 3.14 to define the LQG controller implies that the matrix $\mathcal{D}_{12}$ of the cost function 5.2 is defined such that $\mathcal{D}_{12}'\mathcal{D}_{12} = I$.

5.2.2.4 Targeting the actuated velocity-field

The energy matrix defined in §5.2.2.2 is targeting a homogeneous velocity-field with homogeneous boundary conditions at the walls of the form $[0, v^0, 0]$. Yet, the OSSE model considers a discontinuous velocity-field composed of a homogeneous inner-field with inhomogeneous boundary condition of the form $[v^+, \hat{v}^0, v^-]$. The first/last rows/columns of the energy matrix $\mathcal{C}_1^{*}\mathcal{C}_1$ 5.37 are replaced with zeros to exclude the inhomogeneous value v^+ and v^- at the walls.

Channelflow considers a continuous velocity-field with an inhomogeneous inner-field and boundary conditions of the form $[v^+, \hat{v}, v^-]$. For this reason, a change of basis is operated with the transformation matrix $\mathcal{T}_{\alpha,\beta}$ for each Fourier wave-number pair, such that

$$\begin{bmatrix} v^+_{\alpha,\beta} \\ \hat{v}_{\alpha,\beta} \\ v^-_{\alpha,\beta} \end{bmatrix} = \begin{bmatrix} 1 & 0 & 0 \\ f^+ & I & f^- \\ 0 & 0 & 1 \end{bmatrix} \begin{bmatrix} v^+_{\alpha,\beta} \\ \hat{v}^0_{\alpha,\beta} \\ v^-_{\alpha,\beta} \end{bmatrix} = \mathcal{T}_{\alpha,\beta} \begin{bmatrix} v^+_{\alpha,\beta} \\ \hat{v}^0_{\alpha,\beta} \\ v^-_{\alpha,\beta} \end{bmatrix} \tag{5.38}$$

Moreover, the state-vector of Channelflow considers the stream-wise, wall-normal and span-wise velocity components $[\hat{u}, \hat{v}, \hat{w}]$ while the OSSE considers the wall-normal velocity and vorticity components. Therefore, the transformation matrix $\mathcal{T}_{\alpha,\beta}$ needs to be extended to its equivalent $\mathcal{T}$ for all Fourier modes and combined with the change-of-basis matrix $\mathcal{C}$ of §C.3, as

$$\boldsymbol{x}_{CHFL} = \begin{bmatrix} \hat{u} \\ v^+ \\ \hat{v} \\ v^- \\ \hat{w} \end{bmatrix} = \mathcal{C} \begin{bmatrix} v^+ \\ \hat{v} \\ v^- \\ \hat{\eta} \\ \hat{u}_{00} \\ \hat{w}_{00} \end{bmatrix} = \mathcal{C}\mathcal{T} \begin{bmatrix} v^+ \\ \hat{v}^0 \\ v^- \\ \hat{\eta} \\ \hat{u}_{00} \\ \hat{w}_{00} \end{bmatrix} = \mathcal{C}\mathcal{T}\boldsymbol{x}_{OSSE} \tag{5.39}$$

It is also possible to define analytically matrices $\mathcal{C}\mathcal{T}$ and $\mathcal{T}^{-1}\mathcal{C}^{-1}$, see §C.4.

5.2.3 Choice of actuation-time constant τ

In the literature, it is recognized that high gains accrue the benefits of feedback control, but also exacerbates the risk of loop instability, actuator saturation and/or sensor noise amplification (Green and Limebeer, 1995, p.52):

> A feedback system designer will try to *shape* the loop gain as a function of frequency so that the low-frequency, high gain requirements (benefits) are met without infringing on the high-frequency, low-gain limits (disadvantages) imposed by plant model, sensor errors and actuator limits.

For this reason, a low-pass filter eq.5.4 is introduced in the implementation of the wall-transpiration actuation: the disturbances, characterized by a high frequencies, are eliminated while the modes of the system and of the actuation, characterized by lower frequencies, are preserved. The proper setting of the frequency cut-off of this low-pass filter is decisive and is performed via the choice of the actuation-time constant τ (or equivalently in terms of frequencies). On one hand, a small actuation-time means a fast but expensive controller. On the other hand, a big actuation-time implies that some of important modes of the system and some of the response modes of the controller are filtered out and not transferred into the actuated field.

The estimation of the actuation-time τ is performed via its associated actuation-frequency $f_\tau = 1/\tau$. To determine its optimal value, we estimate the timescale (or frequencies) of the leading unstable —or least stable— modes of EQ1 by calculating the biggest singular value of the actuated system. The actuation time-constant is firstly set to an unrealistically small value of $\tau = 10^{-6}$, or $f_\tau = 10^{+6}$. Such a value implies that the low-pass filter does not filter any of the useful response modes of the system and preserve its timescale. The 20 biggest singular value (SVD, §H.2) of the actuated OSSE model based on EQ1 at resolution $17 \times 27 \times 17$ are plotted in figure 5.3 for a range of a hundred frequencies from 10^{-2} to 10^{+6}.

In fig. 5.3, the response modes are removed above the cutting frequency $f_c = 1/\tau_c = 10^{+6}$ due to the current setting. For frequencies above 10^{+2}, all singular values posses the same gain. Previous studies (Heins, 2015) used an actuation-time $\tau = 0.005$, i.e. $f_\tau = 2\times10^{+2}$. In order to remove high-frequencies without damaging the controller response mode and maintain some analogy with the literature, the low-pass filter actuation-frequency is fixed at $2 \times 10^{+2}$, As a remark, this estimation was performed and is valid for the invariant solution EQ1, but may require updates for other solutions.

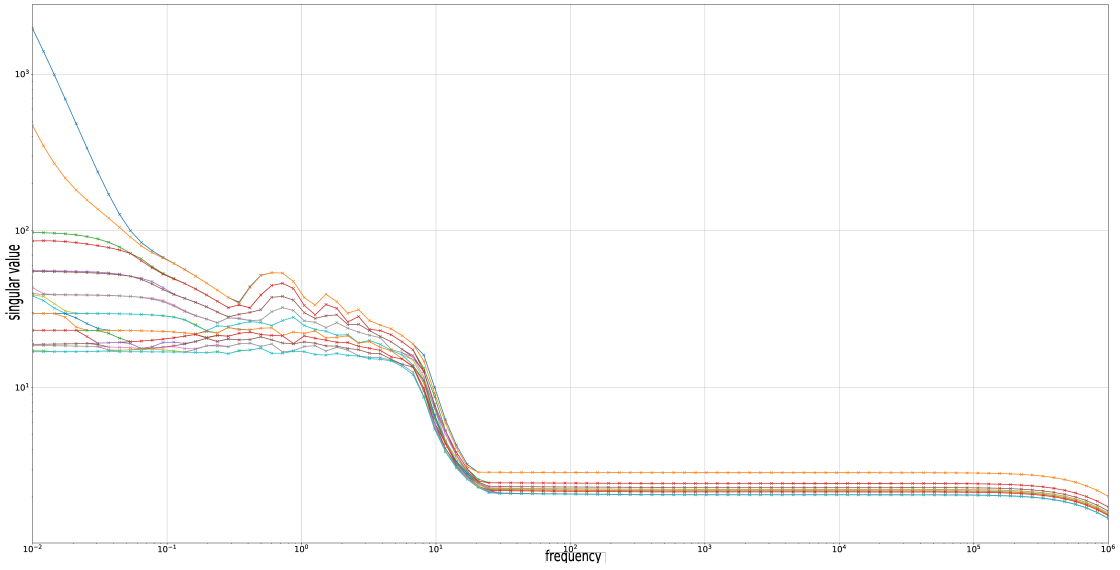

FIGURE 5.3: Singular values for EQ1, $17 \times 27 \times 17$, $Re = 400$, $\tau = 1E-6$ for 100 frequencies from $1E-2$ to $1E+6$. The cut-off at $f = 10^{+6}$ is due to the actuation time-constant τ being fixed at an unrealistically small value of 10^{-6} for now. The cut-off at $f = 10^{+2}$ correspond to the system timescale.

5.3 Full-Information LQR control design based on the ROSSE model

5.3.1 ROSSE model actuated by wall-transpiration

The ROSSE model actuated by wall-transpiration derives from the actuated OSSE system 5.30 in the exact same manner employed in §4.7 to derive the ROSSE system 4.86 from the OSSE system 4.77. It follows directly

$$\begin{aligned}
&\frac{\partial \boldsymbol{x}(t)}{\partial t} = \mathcal{A}\,\boldsymbol{x}(t) + \mathcal{B}_2\,\boldsymbol{q}(t) \\
&= \begin{bmatrix} +\Re(\mathcal{A}_{OSSE,\beta\geq 0}) + \Re(\mathcal{A}_{OSSE,\beta<0}) & -\Im(\mathcal{A}_{OSSE,\beta\geq 0}) + \Im(\mathcal{A}_{OSSE,\beta<0}) \\ +\Im(\mathcal{A}_{OSSE,\beta\geq 0}) + \Im(\mathcal{A}_{OSSE,\beta<0}) & +\Re(\mathcal{A}_{OSSE,\beta\geq 0}) - \Re(\mathcal{A}_{OSSE,\beta<0}) \end{bmatrix} x \\
&+ \begin{bmatrix} +\Re(\mathcal{B}_{2,OSSE,\beta\geq 0}) + \Re(\mathcal{B}_{2,OSSE,\beta<0}) & -\Im(\mathcal{B}_{2,OSSE,\beta\geq 0}) + \Im(\mathcal{B}_{2,OSSE,\beta<0}) \\ +\Im(\mathcal{B}_{2,OSSE,\beta\geq 0}) + \Im(\mathcal{B}_{2,OSSE,\beta<0}) & +\Re(\mathcal{B}_{2,OSSE,\beta\geq 0}) - \Re(\mathcal{B}_{2,OSSE,\beta<0}) \end{bmatrix} q,
\end{aligned} \tag{5.40}$$

where the ROSSE state-vector $\boldsymbol{x}$ and the ROSSE control signal $\boldsymbol{q}$ corresponds to their OSSE counterparts with real and imaginary parts separated, as

$$\boldsymbol{x} = \begin{bmatrix} \Re(\boldsymbol{x}_{OSSE,\beta\geq 0}) \\ \Im(\boldsymbol{x}_{OSSE,\beta\geq 0}) \end{bmatrix} = \begin{bmatrix} \Re\left[\begin{array}{c} \begin{bmatrix} v^+_{\alpha,\beta}(t) \\ v^0_{\alpha,\beta}(y,t) \\ v^-_{\alpha,\beta}(t) \end{bmatrix}_{\substack{0\leq\alpha<N_\alpha,\\ \beta\geq 0}} \\ \begin{bmatrix} \eta^+_{\alpha,\beta}(t) \\ \eta^0_{\alpha,\beta}(y,t) \\ \eta^-_{\alpha,\beta}(t) \end{bmatrix}_{\substack{0\leq\alpha<N_\alpha,\\ \beta\geq 0\\ (\alpha,\beta)\neq(0,0)}} \\ \begin{bmatrix} u^+_{0,0}(t) \\ \hat{u}^0_{0,0}(y,t) \\ u^-_{0,0}(t) \end{bmatrix} \\ \begin{bmatrix} w^+_{0,0}(t) \\ \hat{w}^0_{0,0}(y,t) \\ w^-_{0,0}(t) \end{bmatrix} \end{array}\right] \\ \Im[\boldsymbol{x}_{OSSE,\beta\geq 0}] \end{bmatrix}, \tag{5.41a}$$

$$\boldsymbol{q} = \begin{bmatrix} \Re(\boldsymbol{q}_{OSSE,\beta\geq 0}) \\ \Im(\boldsymbol{q}_{OSSE,\beta\geq 0}) \end{bmatrix} = \begin{bmatrix} \Re\left[\begin{array}{c} \begin{bmatrix} q^+_{v_{\alpha,\beta}}(t) \\ q^-_{v_{\alpha,\beta}}(t) \end{bmatrix}_{\substack{0\leq\alpha<N_\alpha,\\ \beta\geq 0}} \\ \begin{bmatrix} q^+_{\eta_{\alpha,\beta}}(t) \\ q^-_{\eta_{\alpha,\beta}}(t) \end{bmatrix}_{\substack{0\leq\alpha<N_\alpha,\\ \beta\geq 0\\ (\alpha,\beta)\neq(0,0)}} \\ \begin{bmatrix} q^+_{u_{0,0}}(t) \\ q^-_{u_{0,0}}(t) \end{bmatrix} \\ \begin{bmatrix} q^+_{w_{0,0}}(t) \\ q^-_{w_{0,0}}(t) \end{bmatrix} \end{array}\right] \\ \Im[\boldsymbol{q}_{OSSE,\beta\geq 0}] \end{bmatrix}. \tag{5.41b}$$

The actuation on the wall-normal vorticity η_y and fundamental mode of stream- and span-wise velocities u_{00} and w_{00} are removed from the control signal $\boldsymbol{q}$, as these actuation would not correspond to a realistic forcing and only q_v is decisive in the control. It leads to the smaller dimension forcing

$$\boldsymbol{q}(t) = \begin{bmatrix} \Re(q_{OSSE,\beta\geq 0,red}) \\ \Im(q_{OSSE,\beta\geq 0,red}) \end{bmatrix} = \begin{bmatrix} \Re\left[\begin{bmatrix} q^+_{v_{\alpha,\beta}}(t) \\ q^-_{v_{\alpha,\beta}}(t) \end{bmatrix}_{\substack{0\leq\alpha<N_\alpha,\\ \beta\geq 0}}\right] \\ \Im\left[\begin{bmatrix} q^+_{v_{\alpha,\beta}}(t) \\ q^-_{v_{\alpha,\beta}}(t) \end{bmatrix}_{\substack{0\leq\alpha<N_\alpha,\\ \beta\geq 0}}\right] \end{bmatrix}. \tag{5.42}$$

5.3.2 ROSSE Energy matrix - Expression of $C_1^* C_1$

The energy matrix $C_1^* C_1$ for the ROSSE model derives as well from its OSSE counterpart eq.5.37. In order for the energy matrix of both models to be equivalent to the same amount of energy, the positive modes of the ROSSE model are doubled, such that

$$\mathcal{C}_1^* \mathcal{C}_1 = \frac{1}{4N_x N_z} \left[\begin{array}{cccc|ccc|cc||c} \Phi_1 & 0 & \cdots & 0 & 0 & \cdots & 0 & 0 & 0 & 0 \\ 0 & 2\big(\Phi_1 + \frac{1}{k^2}\Phi_2\big) & \cdots & 0 & 0 & \cdots & 0 & 0 & 0 & 0 \\ \vdots & \vdots & \ddots & \vdots & \vdots & \ddots & \vdots & 0 & 0 & 0 \\ 0 & 0 & \cdots & 2\big(\Phi_1 + \frac{1}{k^2}\Phi_2\big) & 0 & \cdots & 0 & 0 & 0 & 0 \\ \hline 0 & 0 & \cdots & 0 & 2\big(\frac{1}{k^2}\Phi_1\big) & \cdots & 0 & 0 & 0 & 0 \\ \vdots & \vdots & \ddots & \vdots & \vdots & \ddots & \vdots & 0 & 0 & 0 \\ 0 & 0 & \cdots & 0 & 0 & \cdots & 2\big(\frac{1}{k^2}\Phi_1\big) & 0 & 0 & 0 \\ \hline 0 & 0 & \cdots & 0 & 0 & \cdots & 0 & \Phi_1 & 0 & 0 \\ 0 & 0 & \cdots & 0 & 0 & \cdots & 0 & 0 & \Phi_1 & 0 \\ \hline\hline 0 & 0 & \cdots & 0 & 0 & \cdots & 0 & 0 & 0 & \text{id.} \end{array}\right], \tag{5.43}$$

5.3.3 ROSSE Expression of $\mathcal{D}_{12}$

Similarly for matrix $\mathcal{D}_{12}$ with the reduced control signal $\boldsymbol{q}$ eq.5.42,

$$\mathcal{D}_{12}' \mathcal{D}_{12} = \left[\begin{array}{cc|cc} I & 0 & 0 & 0 \\ 0 & 2I & 0 & 0 \\ \hline 0 & 0 & I & 0 \\ 0 & 0 & 0 & 2I \end{array}\right], \tag{5.44}$$

where the first row/column of each block correspond to the mode $\boldsymbol{q}_{v_{0,0}}$.

5.4 Controllability & Stabilizibility

A system is stated as controllable if it is feasible to find a finite-energy controller sequence such that any final state can be reached from any initial state in finite time. Typically, accurate discretisation of partial-differential equations systems are uncontrollable as some highly damped modes (which, in the closed-loop system, ultimately have very little effect) nearly always have negligible support at the actuators (Kim and Bewley, 2007). As a consequence, controllability is not of practical interest. Stabilizibility is a weaker but more practical notion than controllability. A system is stated as stabilizable when all uncontrollable state variables can be made to have stable dynamics, i.e.

if all unstable eigenmodes can be made stable by control feedback. Thus, even though some of the state variables cannot be controlled, they will all remain bounded during the system's behavior. When linear stabilizibility is lost, for example with increasing Reynolds number, stabilization of the system is impossible. The objective of a controllability & stabilizibility evaluation is to determine if the unstable modes of a system are all controllable, and as consequence if the entire system is stabilizable, as well as which actuation-mode is preponderant for the control.

5.4.1 Full system Controllability - Controllability Gramian

For the following development, we will consider the general control system 3.14 with n states, m inputs and q outputs as

$$\begin{bmatrix} \dot{\boldsymbol{x}} \\ \boldsymbol{y} \end{bmatrix} = \left[\begin{array}{c|c} \mathcal{A} & \mathcal{B}_2 \\ \hline \mathcal{C}_2 & 0 \end{array}\right] \begin{bmatrix} \boldsymbol{x} \\ \boldsymbol{q} \end{bmatrix}, \qquad \boldsymbol{x}(0) = \boldsymbol{x}_0. \tag{5.45}$$

Bewley and Liu (1998) presented a standard practice to determine the controllability of the system 5.45. It consists in the calculation of the controllability Gramian $\mathcal{F}_c$ associated with the pair $(\mathcal{A}, \mathcal{B}_2)$, and solution of the Lyapunov equation

$$\mathcal{A}\mathcal{F}_c + \mathcal{F}_c\mathcal{A}^* + \mathcal{B}_2\mathcal{B}_2^* = 0. \tag{5.46}$$

The controllability of the system stems from the rank of the $\mathcal{F}_c$. A (nearly) singular solution means that at least one eigenvalue is (nearly) unaffected by the control signal $\boldsymbol{x}$. This method suffers from four drawbacks. Firstly, the Lyapunov equation is a very high dimensional problem of similar complexity to the Riccati solution (later section §6.1). Secondly, assuming a solution is found, the answer will assess the controllability of the entire problem —even if only a few eigen-modes are here useful— and will be binary —'yes' or 'no'. Thirdly, there is also the problem of approximate controllability – where any discretisation is controllable but the condition number of the Gramian gets worse as the order of the discretisation is increased. Finally, some of the stable eigen-modes may be uncontrollable, hence a singular Gramian masking the controllability of the unstable modes of concern. For these reasons, alternatives methods will be used to determine the controllability of the system 5.45.

5.4.2 Unstable eigenmodes modal Controllability

This section determines a scalar measure of the controllability of the system based on an normalized eigen-values decomposition (app. H.1). The ith eigen-mode of the system 5.45 is said controllable with the actuation embodied via the matrix $\mathcal{B}_2$ if and only if the scalar $\mathcal{B}_2^* w_i$ is non-zero, with w_i the ith left-eigenvectors of $\mathcal{A}$ (Bewley and Liu,

1998; McKernan, 2006). The entire system is controllable if and only if this proposition holds for all i. In addition, a scalar measure of the controllability of the ith eigenmode, without normalization, is defined from McKernan (2006)[p.60] and Bewley and Liu (1998) as

$$Controllability(\lambda_i) = \sqrt{w_i^* \mathcal{B}_2 \mathcal{B}_2^* w_i}. \tag{5.47}$$

The table 5.1 gathers the controllability measures with actuation by wall-transpiration for the most unstable eigenvalues of EQ1 listed previously in table 4.1. For the lower dimension $17 \times 27 \times 17$ (used in later chapters), values are given in table 5.2. As a side remark, eigenvalues 1 and 2 are two distinct yet very close modes (see tables 4.1 for comparison against published literature). Moreover, it is not clear to the author why the OSSE and ROSSE models possess different controllability measures. Tables 5.1 and 5.2 are close enough to demonstrate that the controllability measure is converging. Further discretisation would be necessary to evaluate precisely the convergence rate of this measure. Nonetheless, it is to be noted here that only an order of magnitude in the controllability measure is required. Therefore, table 5.2 is sufficient for this study and the lower dimension $17 \times 27 \times 17$ approximates well enough the measures found at $21 \times 35 \times 21$.

Table 5.1 shows that the unstable eigenmodes of EQ1 are all controllable, and in particular the most unstable: eigenmode 0. Actuation by wall-transpiration as implemented with the lifting-procedure in §5.2.1 is now proven to be an adequate actuation type for this project. All the unstable modes of EQ1 are controllable, and as a consequence, the Nagata (1990) lower branch EQ1 is stabilizable with an actuation by wall-transpiration. The dynamical state is indeed supposed to escape the neighborhood of EQ1 within the space defined by these three unstable directions. A controller effectively preventing any perturbation growth within this sub-space would stabilize the equilibrium.

The different eigenmodes of 5.4 lead to some observations. Firstly, each eigenmode respects the symmetries of a PCF, as equilibrium EQ1, namely a reflection in the spanwise direction, rotation by π about the spanwise direction, and a streamwise and/or spanwise periodic translation. From these symmetries, Halcrow (2008) defined a group of symmetric operations composed by a 'shift-reflect' and a 'shift-rotate' symmetries, also referred as the 'Nagata-Busse-Clever-symmetry' in the literature. The eigenmodes are all invariant under these operations. Secondly, all streamwise velocity components of the controllable modes are bidirectional. Each mode possess at a similar intensity, both a streamwise-positive and streamwise-negative flows. This property is to be expected. The controller actuates indeed only the wall-normal velocity, for each streamwise and spanwise Fourier modes. It implies that a controller mode, different from the fundamental mode, will necessarily possess a positive and negative actuation on the streamwise velocity. Thirdly, the most controllable modes appear to be the ones occurring near the walls. It is also to be expected considering the actuation operates on the upper and lower wall of the channel.

TABLE 5.1: Controllability measures of the leading eigenvalues of EQ1, at resolution $21 \times 35 \times 21$, $Re = 400$, $\tau = 0.005$.

Index	Eigenvalues	OSSE Controllability measure	ROSSE Controllability measure
0	+0.05012053	0.01655933	0.02032953
1	+0.00000137	0.03732345	0.03964573
2	+0.00000001	0.01349217	0.01734703
3	−0.00200533	0.01640100	0.02013419
4	−0.00659909	0.03144298	0.02026799
5	−0.00692663	0.02832299	0.03269400
6	−0.00972617	0.01758872	0.02259494
7	−0.01359296	0.01809390	0.01985532
8	−0.02393202	0.01875427	0.02088320
9	−0.03346017	0.03336322	0.03580877
10	−0.03702671	0.03007846	0.02929896
11	−0.04260476	0.02868559	0.02693365

Furthermore, the streamwise vortices apparent for each eigenmodes are a major factor of mixing and a source of turbulence. These vortices are indeed streamwise-oriented, it implies that they transfer high-fluid fluid from the center of the channel to the wall, and conversely, low-speed fluid from the near-wall area directly into the center of the channel. This observation is particularly true for eigenmode 0. It can be a reason why eigenmode 0 is the main direction to destabilize the equilibria, as its geometries is well-suited to increase the vortices at different scales in the channel and lead to further turbulence.

TABLE 5.2: Controllability measures of the leading eigenvalues of EQ1, at resolution $17 \times 27 \times 17$, $Re = 400$, $\tau = 0.005$.

Index	Eigenvalues	OSSE Controllability measure	ROSSE Controllability measure
0	+0.05012082	0.01547851	0.01875050
1	+0.00002215	0.01323467	0.01685453
2	−0.00001902	0.03562319	0.03787299
3	−0.00203379	0.01609176	0.01951696
4	−0.00659876	0.03032545	0.01934189
5	−0.00688399	0.02722562	0.03148305
6	−0.00974591	0.01669840	0.02152723
7	−0.01359193	0.01761533	0.01907834
8	−0.02392832	0.01691946	0.01889844
9	−0.03347443	0.03128420	0.03387720
10	−0.03704233	0.02908588	0.02811455
11	−0.04260227	0.02699718	0.02511516

5.4.3 Modal controllability and observability

A high-number of sensing probes or actuators modes, as in the case of a full-information control via wall-transpiration, can often be reduced to its most influential subset without

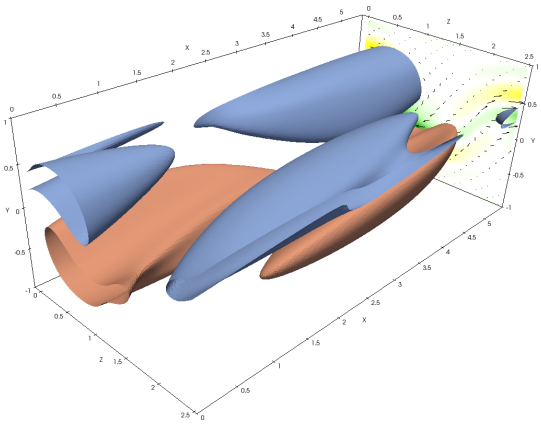

A) Eigenmode 0, contour u at ± 0.05.

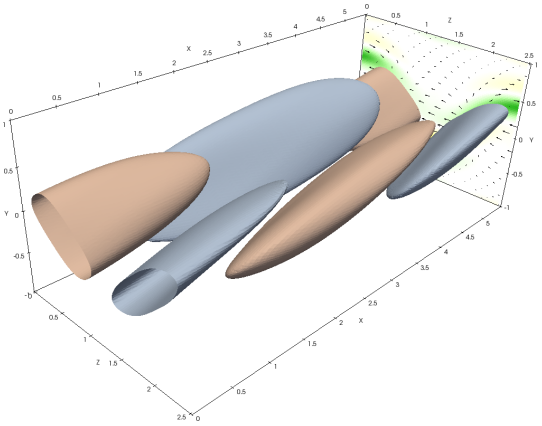

B) Eigenmode 1, contour u at ± 0.05.

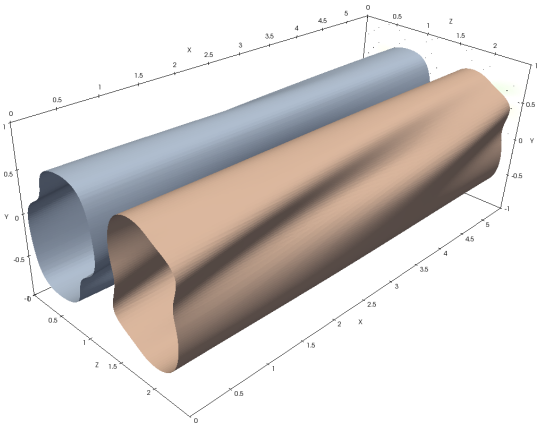

C) Eigenmode 2, contour u at ± 0.03.

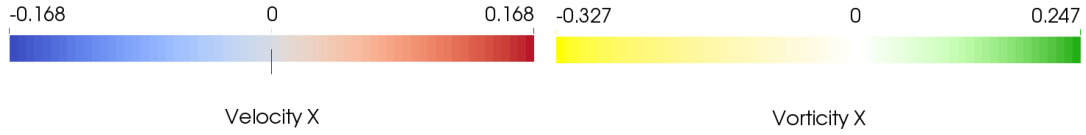

FIGURE 5.4: Most unstable eigenmodes of EQ1. Surfaces of constant streamwise velocity u for different amplitudes, with vector arrows representing the wall-normal and span-wise velocities, v and w, in direction and relative amplitude. The vertical plane in the background is coloured with the stream-wise vorticity η_x. (EQ1, $21 \times 35 \times 21$, $Re = 400$, $\tau = 0.005$)

infringing the observability/controllability of the system. Some of these modes do not indeed play any significant role while still requiring their associated optimal law being solved. In this thesis, only controllability measure is of interest. As a consequence, this section improves the controllability measure of table 5.1 by exploring its "modal" controllability, i.e. ranking the individual contribution of each actuation mode.

A measure a the modal observability and controllability of the system 5.45 derives from the expression of the output signal $\boldsymbol{y}$ (Chan, 1984)

$$\boldsymbol{y}(t) = \sum_{i=1}^{n} \left(\mathcal{C}_2 v_i \left[w_i^T \boldsymbol{x}_0 + w_i^T \mathcal{B}_2 \int_0^t e^{-\lambda_i \tau} \boldsymbol{q}(\tau) \right] e^{\lambda_i t} \right), \tag{5.48}$$

where it appears that the impact of the input $\boldsymbol{q}$ on the output $\boldsymbol{y}$ is determined by the matrix $w_i^T \mathcal{B}_2$, and the preponderance of each actuated mode in the output $\boldsymbol{y}$ is determined by $\mathcal{C}_2 v_i$. The modal observability and modal controllability matrices are constructed from the observations.

Modal observability

Considering the rows c_i^T of matrix $\mathcal{C}_2$ of dimension $q \times n$,

$$\mathcal{C}_2 = row \begin{bmatrix} c_1^T & \dots & c_p^T \end{bmatrix}, \tag{5.49}$$

the modal observability matrix is defined as

$$\mathcal{C}_2 V = \begin{bmatrix} c_1^T v_1 & \cdots & c_1^T v_n \\ \vdots & \ddots & \vdots \\ c_q^T v_1 & \cdots & c_q^T v_n \end{bmatrix}. \tag{5.50}$$

The coefficient $c_i^T v_j$ measures the observability of the j-th mode of the state $\boldsymbol{x}$ in the i-th output of $\boldsymbol{y}$.

Modal controllability

Considering the columns b_i of matrix $\mathcal{B}_2$ of dimension $n \times m$,

$$\mathcal{B}_2 = \begin{bmatrix} b_1 & \dots & b_m \end{bmatrix}, \tag{5.51}$$

the modal controllability matrix is defined as

$$W \mathcal{B}_2 = \begin{bmatrix} w_1^T b_1 & \cdots & w_1^T b_m \\ \vdots & \ddots & \vdots \\ w_n^T b_1 & \cdots & w_n^T b_m \end{bmatrix}. \tag{5.52}$$

The coefficient $w_i^T b_j$ measures the excitation of the j-th input modes of $\boldsymbol{q}$ on the i-th mode of the state-vector $\boldsymbol{x}$.

Modal controllability of the actuated system

The absolute value of each coefficient of the modal controllability matrix $W\mathcal{B}_2$ is calculated for the final OSSE model actuated via wall-transpiration eq.5.30. They are gathered in figures 5.5, 5.6 and 5.7, corresponding respectively to the three leading eigen-modes of the PCF Nagata (1990) lower-branch solution EQ1, at Reynolds 400, resolution $17 \times 27 \times 17$ and actuation-time $\tau = 0.005$.

The most predominant actuation-modes to stabilize eigen-mode 0 of EQ1 are the 6 upper- and lower-wall actuation modes $v^{\pm}_{(\pm 2,0)}$ and $v^{\pm}_{(\pm 1,\pm 1)}$. $v^{\pm}_{(0,0)}$ is excluded as it corresponds to a vertical translation of the wall. Eigen-modes 1 and 2 are highly affected by the upper- and lower-wall actuation at the 2 modes $v^{\pm}_{(\pm 1,0)}$, and almost insensitive to any other mode.

Figures 5.8 and 5.9 outline the respective effects of a wall-actuation q_v on the wall-normal velocity and q_η on the wall-normal vorticity, transposed into a (u, v, w) basis (app.C) for three of the most influential actuation-modes. It appears that the actuation q_v impacts all three velocity components, on the contrary to q_η only affecting the stream- and span-wise components. This phenomenon is due to the divergence free-condition eq.4.6d, and therefore to the change of basis matrix $\mathcal{C}$ (app.C), and not to the actuation matrix $\mathcal{B}_2$ nor to the time-integration. Moreover, the actuation q_v is more potent in the mid-field and observes an anti-symmetric property in the wall-normal direction, and is consequently characterized by a strong stream-wise vorticity η_x. On the other side, q_η only stimulates the area near the actuated wall, without any streamwise vorticity component. The justification why the actuation q_v is more adequate than q_η to stabilize the eigenmode 0 (see fig.5.4) is not straightforward. However, the fact that this eigen-mode is entirely contained within the mid-field of the channel, and null at the wall may be a source of explanation.

5.5 Validation of implemented actuation

The implementation of the inhomogeneous wall-normal velocity boundary conditions in the OSSE model and the upgrade of the package for Channelflow v442 (post 1.5.1) are validated by the present author in two stages in the same fashion as originally operated by Heins (2015): a linear stage and a nonlinear stage. Moreover, only wall-normal velocity actuation is validated, as the actuation is limited to this component only. The actuation of the other velocity components (equivalent to the wall-normal vorticity for the OSSE and ROSSE models) were indeed implemented by Heins (2015) but not validated. The present author integrated the actuation on these components but did not validated them neither. In the linear stage, simulations are run with a Couette baseflow and actuated with an identical boundary condition for the two already validated systems (OSS model and Channelflow 1.4.2) as well as for the two new systems (OSSE model and Channelflow v452). The actuated Fourier modes are then compared qualitatively and quantitatively.

In the nonlinear case, OSSE linear simulations are compared against non-linear Channelflow simulations implementing the skew symmetric formulation of the non-linear term. They both use Nagata (1990) lower-branch EQ1 as baseflow and are actuated with identical wall-actuation forcing: either converging-to-constant or sinusoidal.

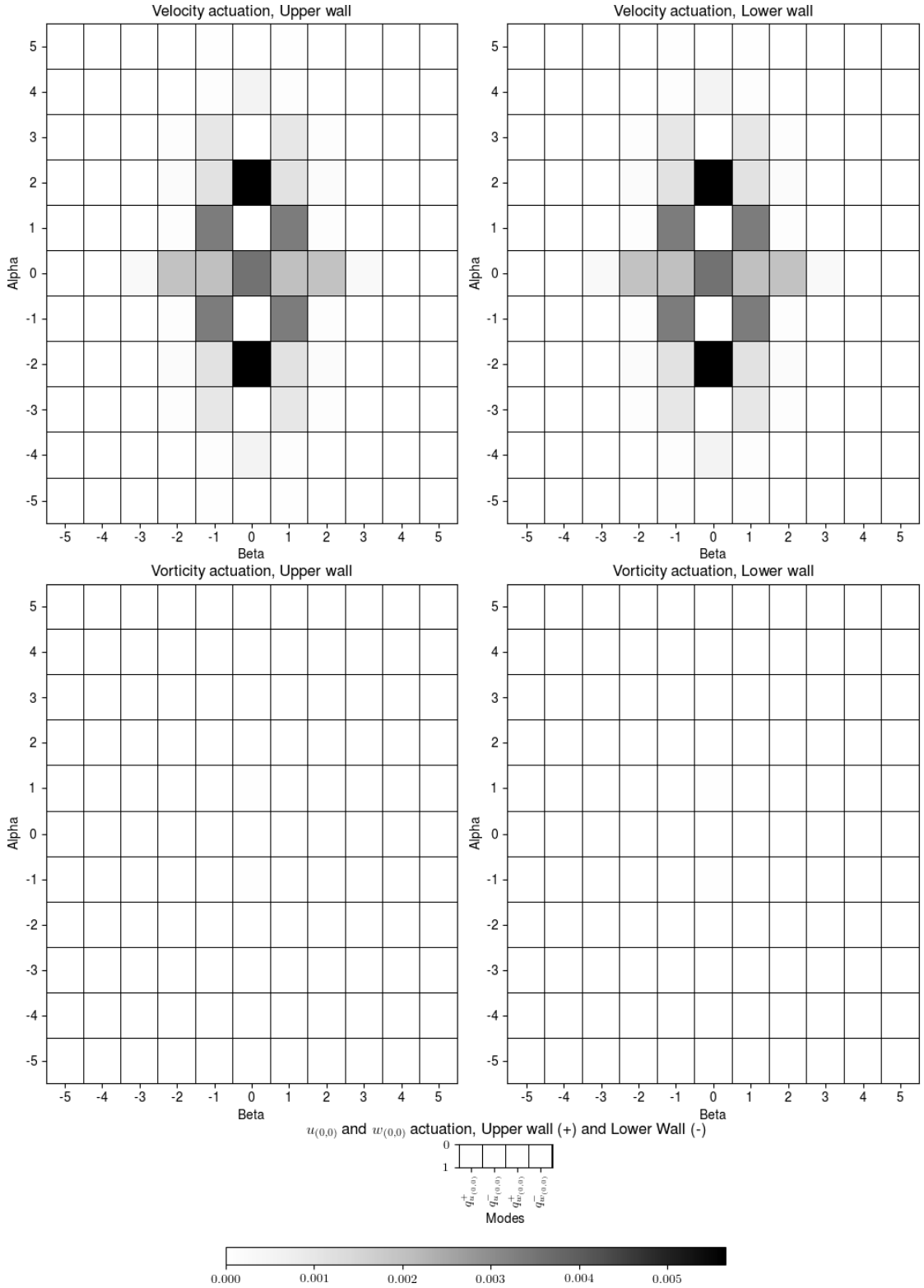

FIGURE 5.5: Absolute value of the first row the modal controllability matrix $W\mathcal{B}_2$ of the OSSE model, corresponding to the impact (black - strong, white - weak) on the 0st leading eigen-mode of EQ1, +0.05012082, of the wall-transpiration actuation by the different modes (α, β) of the wall-normal velocity, wall-normal vorticity, and fundamental of stream- and span-wise velocities, at the upper (right-side) and lower (left-side) walls.
(EQ1, $17 \times 27 \times 17$, $Re = 400$, $\tau = 0.005$)

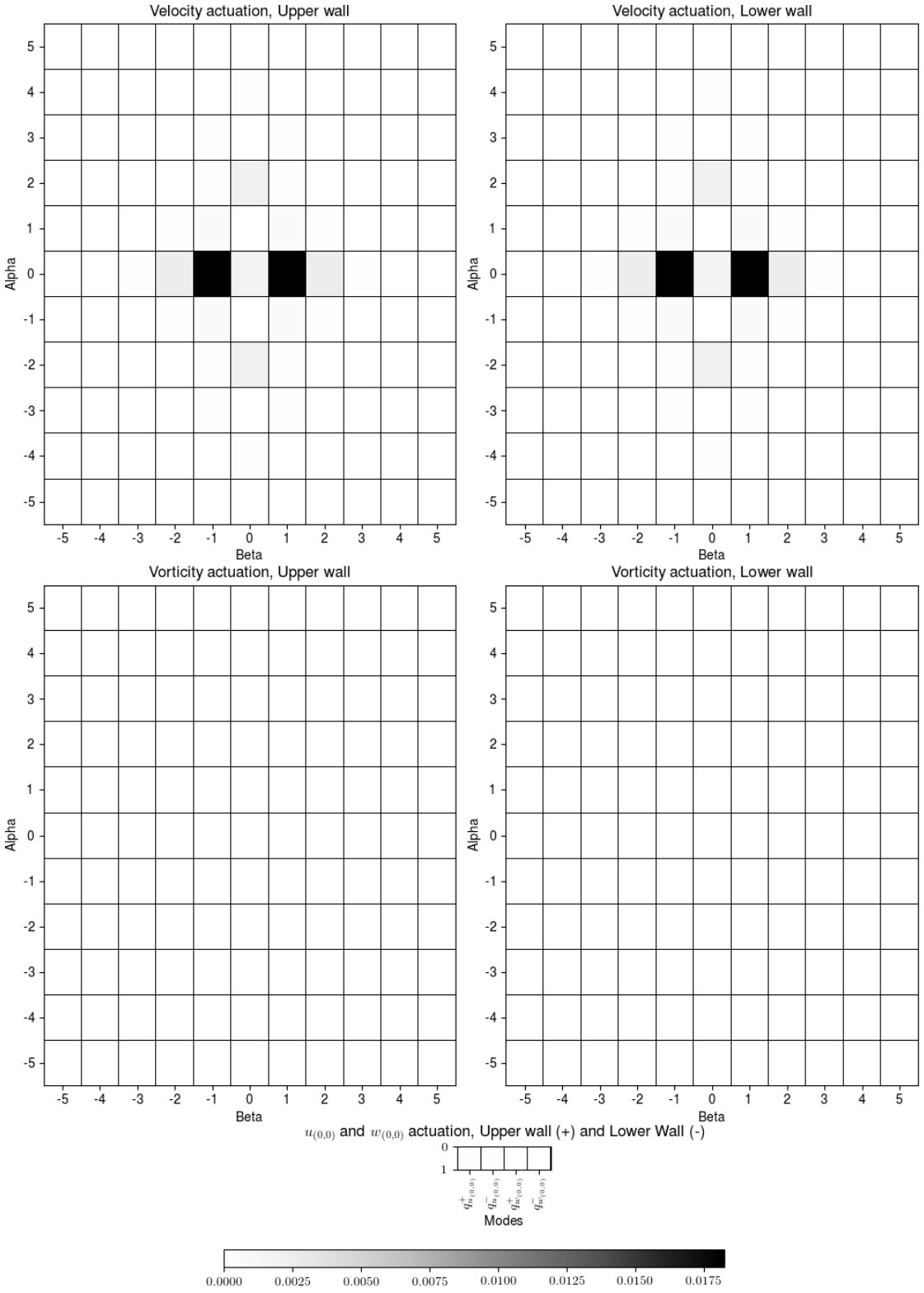

FIGURE 5.6: Absolute value of the second row the modal controllability matrix $W\mathcal{B}_2$ of the OSSE model, corresponding to the impact (black - strong, white - weak) on the 1st leading eigen-mode of EQ1, +0.00000137, of the wall-transpiration actuation by the different modes (α, β) of the wall-normal velocity, wall-normal vorticity, and fundamental of stream- and span-wise velocities, at the upper (right-side) and lower (left-side) walls.
(EQ1, $17 \times 27 \times 17$, $Re = 400$, $\tau = 0.005$)

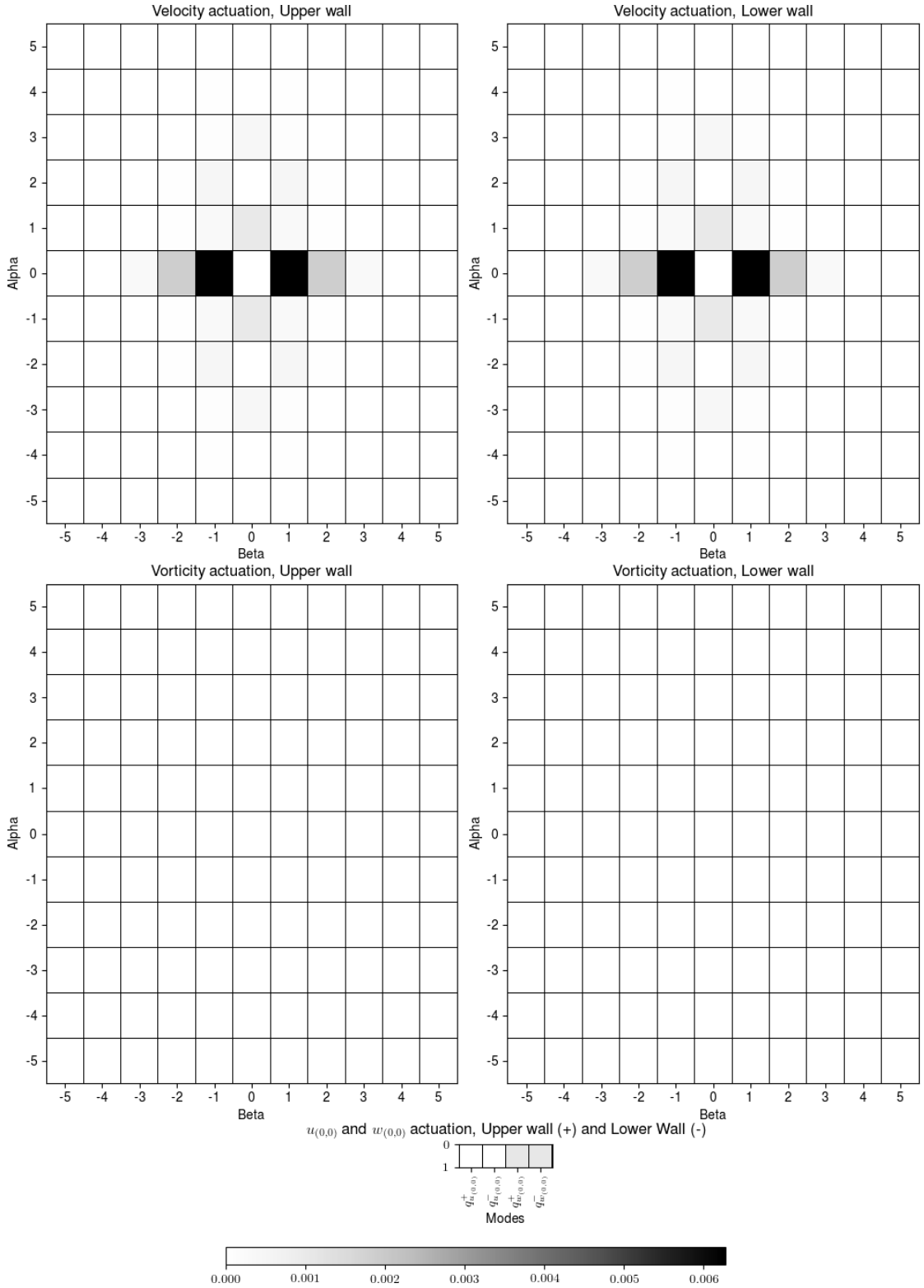

FIGURE 5.7: Absolute value of the third row the modal controllability matrix $W\mathcal{B}_2$ of the OSSE model, corresponding to the impact (black - strong, white - weak) on the 2nd leading eigen-mode of EQ1, -0.00001902, of the wall-transpiration actuation by the different modes (α, β) of the wall-normal velocity, wall-normal vorticity, and fundamental of stream- and span-wise velocities, at the upper (right-side) and lower (left-side) walls.
(EQ1, $17 \times 27 \times 17$, $Re = 400$, $\tau = 0.005$)

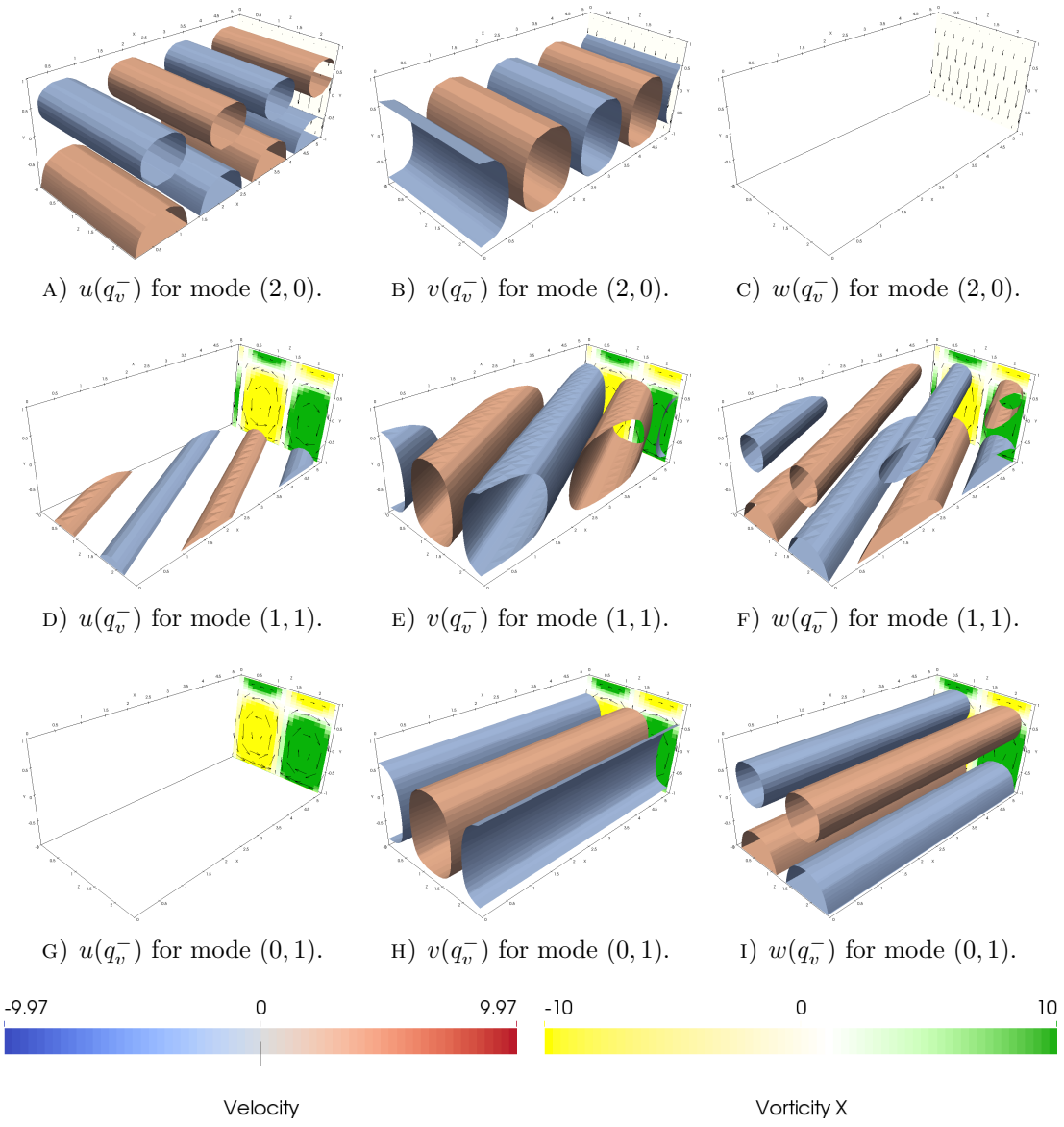

A) $u(q_v^-)$ for mode $(2,0)$. B) $v(q_v^-)$ for mode $(2,0)$. C) $w(q_v^-)$ for mode $(2,0)$.

D) $u(q_v^-)$ for mode $(1,1)$. E) $v(q_v^-)$ for mode $(1,1)$. F) $w(q_v^-)$ for mode $(1,1)$.

G) $u(q_v^-)$ for mode $(0,1)$. H) $v(q_v^-)$ for mode $(0,1)$. I) $w(q_v^-)$ for mode $(0,1)$.

FIGURE 5.8: Actuation q_v^-, i.e. actuation on the lower-wall wall-normal velocity v, for modes $(2,0)$, $(1,1)$ and $(0,1)$. The actuation is transformed into its equivalent (u,v,w) field components (see app. C). The surfaces are contours of constant velocity component at amplitude ± 1. The vertical plane in the background are coloured with the streamwise vorticity η_x. $(17 \times 27 \times 17,\ \tau = 0.005)$

Validation data are stored online, see appendix A.

5.5.1 Validation with the laminar Couette baseflow

The implementation of the wall-normal velocity component actuation is already validated for the OSS model and Channelflow 1.4.2 (Heins, 2015). For this reason, the new actuated simulations, run with the OSSE model and Channelflow v452, are compared against the OSS model and Channelflow 1.4.2, in the same way that Heins (2015) validated the previous version.

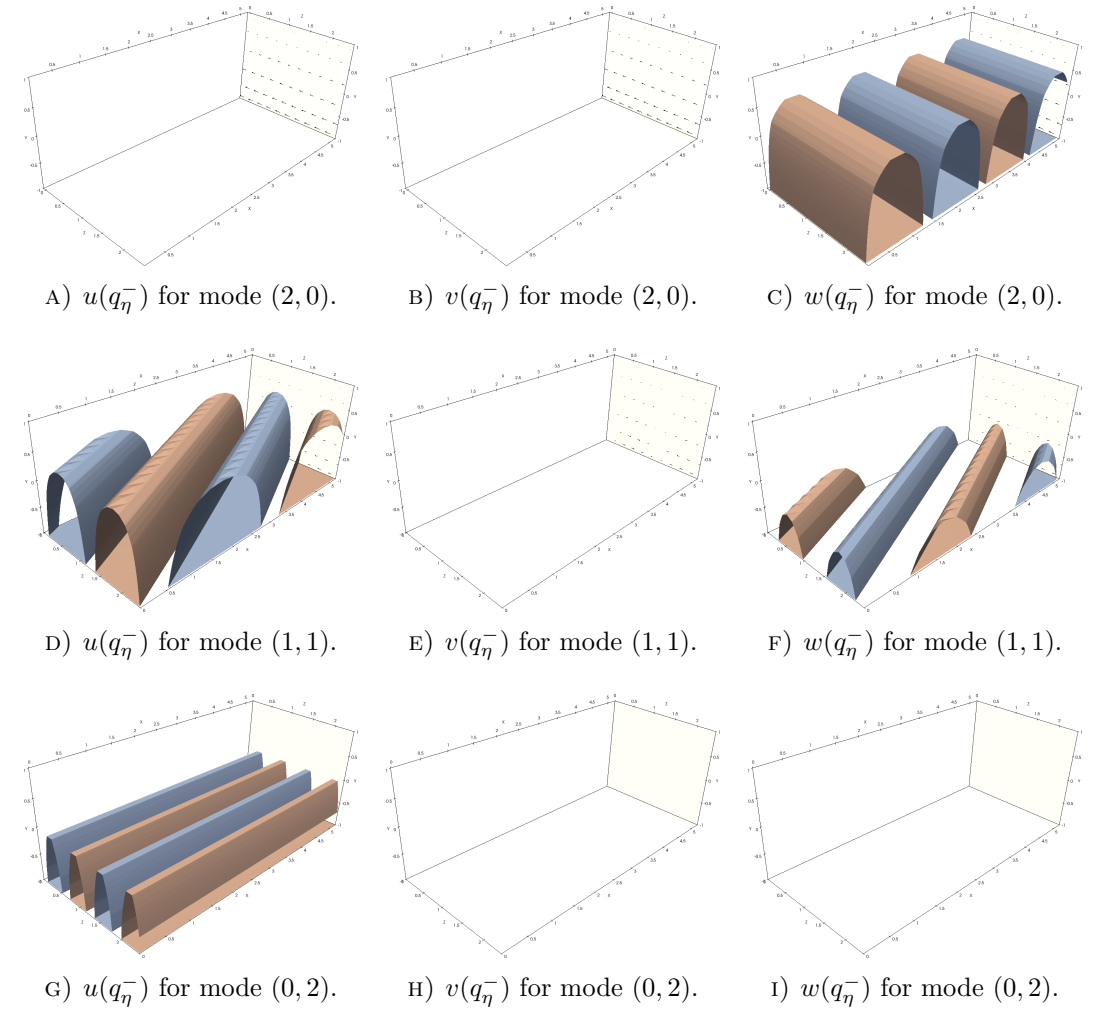

A) $u(q_\eta^-)$ for mode $(2,0)$. B) $v(q_\eta^-)$ for mode $(2,0)$. C) $w(q_\eta^-)$ for mode $(2,0)$.

D) $u(q_\eta^-)$ for mode $(1,1)$. E) $v(q_\eta^-)$ for mode $(1,1)$. F) $w(q_\eta^-)$ for mode $(1,1)$.

G) $u(q_\eta^-)$ for mode $(0,2)$. H) $v(q_\eta^-)$ for mode $(0,2)$. I) $w(q_\eta^-)$ for mode $(0,2)$.

FIGURE 5.9: Actuation q_η^-, i.e. actuation on the lower-wall wall-normal vorticity η, for modes $(2,0)$, $(1,1)$ and $(0,2)$. The actuation is transformed into its equivalent (u,v,w) field components (see app. C). The surfaces are contours of constant velocity component at amplitude ± 1. The vertical plane in the background are coloured with the streamwise vorticity η_x. $(17 \times 27 \times 17,\ \tau = 0.005)$

All simulations used a dynamical model linearised around the Couette laminar solution. Particularly, both Channelflow simulations are run with the nonlinear term computed in the linearised form (Gibson, 2014),

$$N(v) = \bar{U}\frac{\partial v}{\partial x} + \frac{\partial \bar{U}}{\partial y}\vec{\boldsymbol{x}}. \tag{5.53}$$

The following inhomogeneous boundary conditions are imposed for each simulation at the upper and lower walls,

$$q^+_{v_{\alpha,\beta}} = q^-_{v_{\alpha,\beta}} = cos(0.05t + \frac{\pi}{2})\,(0.05 - 0.01j), \tag{5.54}$$

with zero initial condition. Three different actuation modes are chosen for the linear validation:

- $k_x = 0, k_z = 1$,
- $k_x = 1, k_z = 0$,
- $k_x = 1, k_z = 1$.

These are chosen as they correspond to stream-wise constant, span-wise constant and oblique modes. Simulations are run at Reynolds number of 10^4, with dimension $L_x = 2\pi/1.14$ and $L_z = f2\pi/2.5$, spatial resolution $11 \times 65 \times 11$, for 100 time-units and with an actuator time-constant $\tau = 0.05$. Both Channelflow 1.4.2 and v452 use the SBDF4 time-stepping algorithm and CNRK2 initial-stepping, with a variable time-step bounded within $[10^{-2}, 10^{-5}]$. The OSS and OSSE models are integrated in time via the BDF algorithm of the method `scipy.integrate.solve_ivp`, with absolute and relative tolerances of 10^{-8}.

Qualitatively, figures 5.10, 5.11, 5.12 show profiles of the three velocity components for each simulation at time $t = 0$, 50, 100, for the three actuation modes. Only the actuated mode is displayed. The other un-actuated modes are all zero, as expected in a linearised simulation without crossed interaction between modes and zero initial condition. These figures demonstrate that the profiles from the actuated OSS model, the actuated OSSE model, Channelflow 1.4.2 and Channelflow v452 match well qualitatively for all velocity components and modes at these given time.

A quantitative comparison of each velocity component was also performed via calculations of the "point-by-point" error-norms (Heins, 2015) and of the Lebesgue 2-error-norms, introduced in section 3.4.2. The "point-by-point" error-norms for each velocity component are defined as

$$\|\delta(u)_{\text{model / OSS}}\|_{1,[0,N_t]} = \frac{1}{N_t}\sum_{n_t=0}^{N_t}\left(\frac{1}{N_y}\|u_{model} - u_{OSS}\|\right), \tag{5.55}$$

$$\|\delta(v)_{\text{model / OSS}}\|_{1,[0,N_t]} = \frac{1}{N_t}\sum_{n_t=0}^{N_t}\left(\frac{1}{N_y}\|v_{model} - v_{OSS}\|\right), \tag{5.56}$$

$$\|\delta(w)_{\text{model / OSS}}\|_{1,[0,N_t]} = \frac{1}{N_t}\sum_{n_t=0}^{N_t}\left(\frac{1}{N_y}\|w_{model} - w_{OSS}\|\right), \tag{5.57}$$

where the subscript *model* stands either for OSSE or Channelflow, and $\|\cdot\|$ refers to the "point-by-point" Euclidean norm. The discrete-time Lebesgue 2-error-norms are

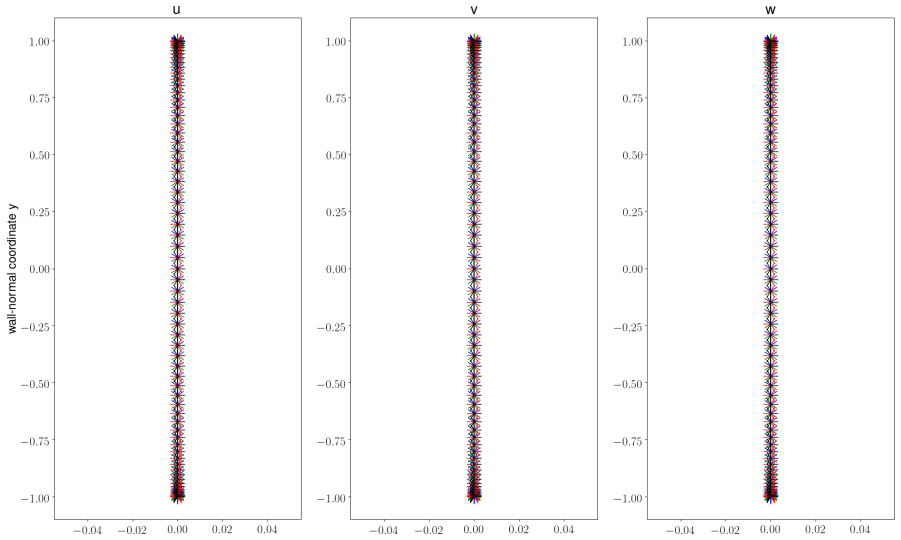

A) $t = 0$

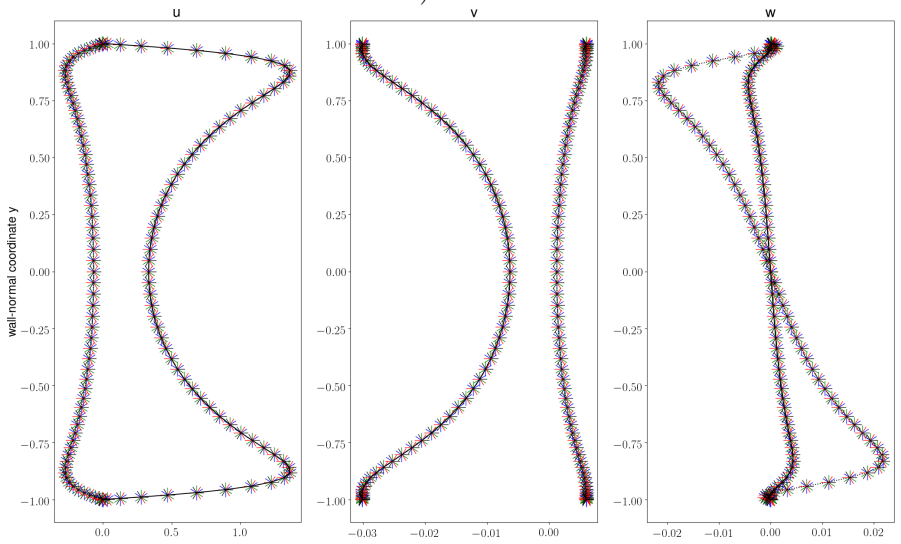

B) $t = 50$

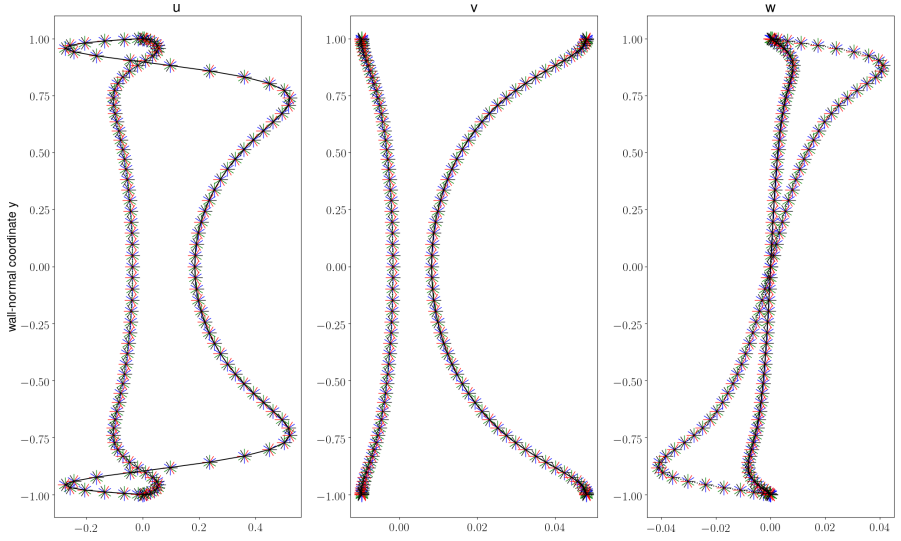

C) $t = 100$

FIGURE 5.10: Linear validation: Velocity components profiles (thick line - real part, dotted-line - imaginary part) of Fourier mode $(0, 1)$ actuated under the boundary constraints 5.54, for different simulations: OSS model (black $\succ$), OSSE model (green $\prec$), Channelflow v452 (red $\curlyvee$) and Channelflow 1.4.2 (blue $\curlywedge$) (times $t = 0$, 50, 100, Couette baseflow, resolution $11 \times 65 \times 11$, $Re = 10^4$, $\tau = 0.05$).

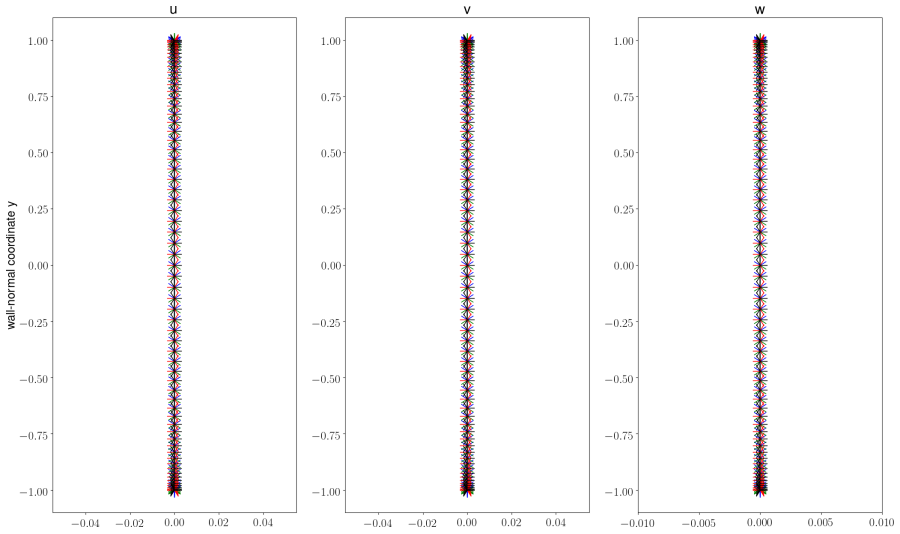

A) $t = 0$

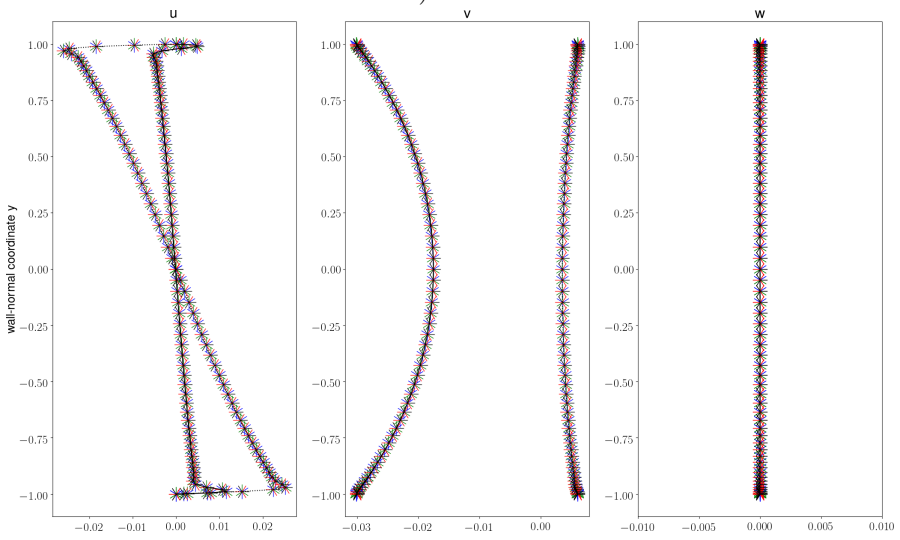

B) $t = 50$

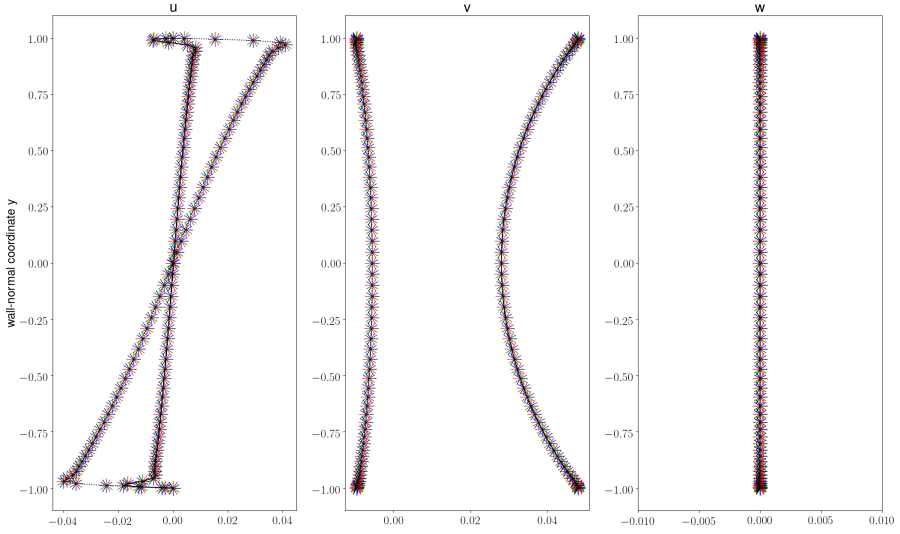

C) $t = 100$

FIGURE 5.11: Linear validation: Velocity components profiles (thick line - real part, dotted-line - imaginary part) of Fourier mode $(1, 0)$ actuated under the boundary constraints 5.54, for different simulations: OSS model (black $\succ$), OSSE model (green $\prec$), Channelflow v452 (red γ) and Channelflow 1.4.2 (blue $\curlywedge$) (times $t = 0$, 50, 100, Couette baseflow, resolution $11 \times 65 \times 11$, $Re = 10^4$, $\tau = 0.05$).

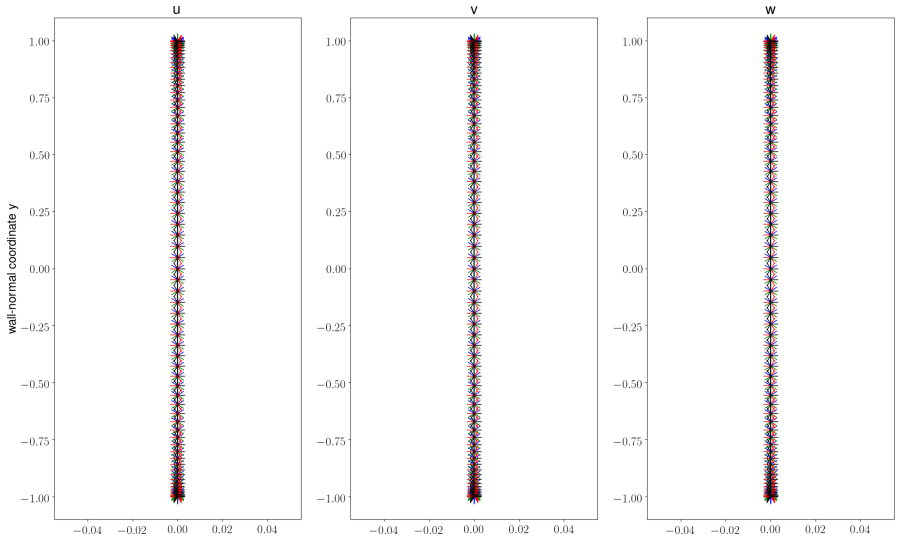

A) $t = 0$

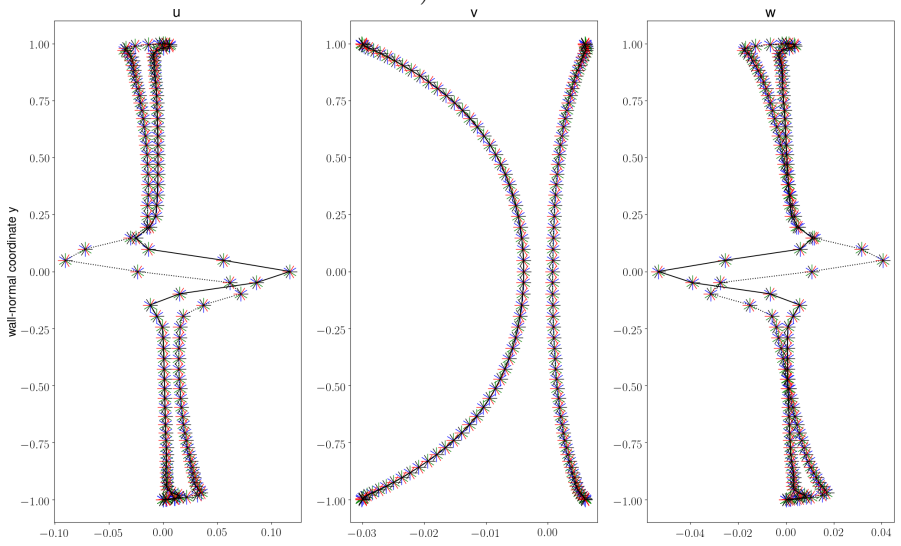

B) $t = 50$

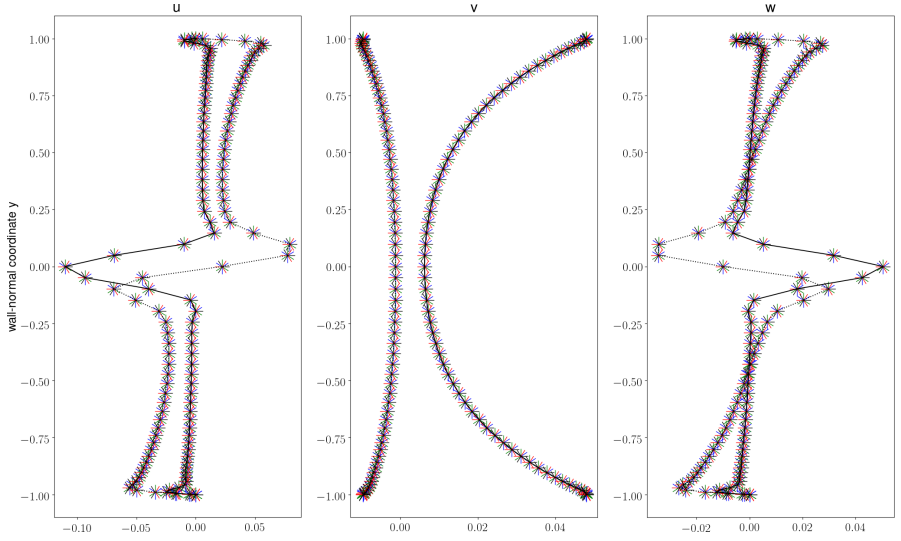

C) $t = 100$

FIGURE 5.12: Linear validation: Velocity components profiles (thick line - real part, dotted-line - imaginary part) of Fourier mode $(1, 1)$ actuated under the boundary constraints 5.54, for different simulations: OSS model (black $\succ$), OSSE model (green $\prec$), Channelflow v452 (red $\curlyvee$) and Channelflow 1.4.2 (blue $\curlywedge$) (times $t = 0$, 50, 100, Couette baseflow, resolution $11 \times 65 \times 11$, $Re = 10^4$, $\tau = 0.05$).

expressed for one Fourier mode and a Chebyshev wall-normal discretisation as,

$$\begin{aligned}\|\delta(u)_{\text{model / OSS}}\|_{2,[0,N_t]} &= \left\{\frac{1}{N_t}\sum_{n_t=0}^{N_t}\|u_{model}-u_{OSS}\|^2\right\}^{\frac{1}{2}} \\ &= \left\{\frac{1}{N_t}\sum_{n_t=0}^{N_t}(u_{model}-u_{OSS})^* W^* W (u_{model}-u_{OSS})\right\}^{\frac{1}{2}}\end{aligned} \tag{5.58}$$

$$\begin{aligned}\|\delta(v)_{\text{model / OSS}}\|_{2,[0,N_t]} &= \left\{\frac{1}{N_t}\sum_{n_t=0}^{N_t}\|v_{model}-v_{OSS}\|^2\right\}^{\frac{1}{2}} \\ &= \left\{\frac{1}{N_t}\sum_{n_t=0}^{N_t}(v_{model}-v_{OSS})^* W^* W (v_{model}-v_{OSS})\right\}^{\frac{1}{2}}\end{aligned} \tag{5.59}$$

$$\begin{aligned}\|\delta(w)_{\text{model / OSS}}\|_{2,[0,N_t]} &= \left\{\frac{1}{N_t}\sum_{n_t=0}^{N_t}\|w_{model}-w_{OSS}\|^2\right\}^{\frac{1}{2}} \\ &= \left\{\frac{1}{N_t}\sum_{n_t=0}^{N_t}(w_{model}-w_{OSS})^* W^* W (w_{model}-w_{OSS})\right\}^{\frac{1}{2}}\end{aligned} \tag{5.60}$$

Table 5.3 presents the error-norms between the different simulations for each actuation configuration over a period $N_t = 100$, and leads to the conclusion that all the error-norms are shown to be satisfactory small. This validation analysis demonstrated, both qualitatively and quantitatively, that the inhomogeneous boundary condition is successfully implemented, in the OSSE model as well as in Channelflow v452, for the linear case.

5.5.2 Validation with the non-laminar Nagata (1990) lower-branch as baseflow

The linearization of Channelflow is only available around an unidirectional laminar baseflow, namely Poiseuille or Couette laminar solution. The linearization around a three dimensional non-laminar equilibrium is not implemented: it is impossible to perform a linear Channelflow simulation with a non-laminar baseflow. For this reason, in the case of a non-laminar baseflow, the OSSE model is validated against Channelflow simulations implementing the skew symmetric formulation of the nonlinear term.

Channelflow and OSSE results are obtained with different resolutions. A wall-normal resolution of $N_y = 65$ is required for Channelflow to converge with the CFBC package. However, for the OSSE model, a wall-normal resolution of $N_y = 35$ is sufficient to obtain similar results within computational power and memory limitations. For streamwise and spanwise direction, a dimension of 21×21 is used in order to obtain the same leading eigenvalues of EQ1. For this reason, the resolution chosen for the OSSE model

TABLE 5.3: Linear validation: Table of error-norms $\|\delta\|$ for the three velocity components of the three simulation cases (OSSE model, Channelfow 1.4.2 and v452) in reference to the OSS model. Each actuation mode is regarded separately. $Re = 10000$ and resolution $11 \times 65 \times 11$.

OSSE

Modes	$(0,1)$	$(1,0)$	$(1,1)$
$\|\delta(u)_{\text{OSSE / OSS}}\|_{1,[0,N_t]}$	3.013×10^{-5}	2.751×10^{-6}	3.220×10^{-5}
$\|\delta(v)_{\text{OSSE / OSS}}\|_{1,[0,N_t]}$	1.317×10^{-7}	5.083×10^{-7}	1.550×10^{-7}
$\|\delta(w)_{\text{OSSE / OSS}}\|_{1,[0,N_t]}$	3.723×10^{-7}	0	1.478×10^{-5}
$\|\delta(u)_{\text{OSSE / OSS}}\|_{2,[0,N_t]}$	6.953×10^{-5}	3.543×10^{-6}	4.662×10^{-5}
$\|\delta(v)_{\text{OSSE / OSS}}\|_{2,[0,N_t]}$	2.701×10^{-7}	1.329×10^{-6}	3.623×10^{-7}
$\|\delta(w)_{\text{OSSE / OSS}}\|_{2,[0,N_t]}$	5.591×10^{-7}	0	2.147×10^{-5}

Channelflow v452

Modes	$(0,1)$	$(1,0)$	$(1,1)$
$\|\delta(u)_{\text{cf v452 / OSS}}\|_{1,[0,N_t]}$	3.012×10^{-5}	5.907×10^{-6}	3.234×10^{-5}
$\|\delta(v)_{\text{cf v452 / OSS}}\|_{1,[0,N_t]}$	5.896×10^{-6}	7.594×10^{-6}	5.743×10^{-6}
$\|\delta(w)_{\text{CF v452 / OSS}}\|_{1,[0,N_t]}$	5.365×10^{-6}	0	1.613×10^{-5}
$\|\delta(u)_{\text{CF v452 / OSS}}\|_{2,[0,N_t]}$	6.967×10^{-5}	9.436×10^{-6}	4.664×10^{-5}
$\|\delta(v)_{\text{CF v452 / OSS}}\|_{2,[0,N_t]}$	9.045×10^{-6}	1.659×10^{-5}	8.463×10^{-6}
$\|\delta(w)_{\text{CF v452 / OSS}}\|_{2,[0,N_t]}$	8.343×10^{-6}	0	2.259×10^{-5}

Channelflow 1.4.2

Modes	$(0,1)$	$(1,0)$	$(1,1)$
$\|\delta(u)_{\text{CF 1.4.2 / OSS}}\|_{1,[0,N_t]}$	2.896×10^{-5}	5.905×10^{-6}	3.247×10^{-5}
$\|\delta(v)_{\text{CF 1.4.2 / OSS}}\|_{1,[0,N_t]}$	5.896×10^{-6}	7.594×10^{-6}	5.743×10^{-6}
$\|\delta(w)_{\text{CF 1.4.2 / OSS}}\|_{1,[0,N_t]}$	5.366×10^{-6}	0	1.614×10^{-5}
$\|\delta(u)_{\text{CF 1.4.2 / OSS}}\|_{2,[0,N_t]}$	6.790×10^{-5}	9.428×10^{-6}	4.674×10^{-5}
$\|\delta(v)_{\text{CF 1.4.2 / OSS}}\|_{2,[0,N_t]}$	9.045×10^{-6}	1.659×10^{-5}	8.465×10^{-6}
$\|\delta(w)_{\text{CF 1.4.2 / OSS}}\|_{2,[0,N_t]}$	8.343×10^{-6}	0	2.259×10^{-5}

is $21 \times 35 \times 21$, and for Channelflow $21 \times 65 \times 21$. This difference impacts certainly the comparison process, but as it will appear later, in a limited fashion.

All simulations are performed with the Nagata (1990) lower-branch solution, EQ1, as baseflow. Channelflow simulations compute the nonlinear term in the skew-symmetric form (Gibson (2014)),

$$N(v) = \frac{1}{2}\boldsymbol{U} \cdot \nabla \boldsymbol{U} + \frac{1}{2}\nabla \cdot (\boldsymbol{U}\boldsymbol{U}). \tag{5.61}$$

The following inhomogeneous boundary conditions, referred in the following as "converging-to-constant", are imposed for each simulation at the upper and lower walls,

$$q^{+}_{v_{\alpha,\beta}} = q^{-}_{v_{\alpha,\beta}} = 0.0005\ (1 - \exp(-t/10)), \tag{5.62}$$

and the initial velocity components are all set to zero. The same actuation modes as the linear validation §5.5.1 are selected (i.e. $(k_x, k_z) = (0,1)$, $(1,0)$ and $(1,1)$). The channel flow is configured with a Reynolds number of 400, dimensions $L_x =$

$2\pi/1.14$, $[a, b] = [-1, +1]$, and $L_z = 2\pi/2.5$, running over a period $T = 150$ and with an actuator time-constant $\tau = 0.05$. The time-stepping algorithm used in Channelflow is SBDF4, initialized with CNRK2, with a variable time-step bounded within $[10^{-2}, 10^{-5}]$. The OSSE model is integrated in time via the BDF algorithm of the method `scipy.integrate.solve_ivp`, with absolute and relative tolerances of 10^{-8}. Figures 5.13, 5.14 and 5.15 show the norm over time for Channelflow and OSSE simulations for the three actuation cases and the converging-to-constant forcing. Each figure shows the norm of the respective actuated mode with a diamond-marked dot-lined, as well as the norm of the two other non-actuated harmonics with a simple dot-lined, such that the modes $(0, 1)$, $(1, 0)$ and $(1, 1)$ are always displayed.

Despite the same initial conditions, Channelflow and OSSE simulations observe a slight difference in their initial behaviour (for $t \leq 10$), similar to a time delay. Is this initial difference detrimental to the validation process ?

As the OSSE model is linear, a different initial perturbation or actuation will linearly affect the long-term behaviour of the simulation. The relatively small amplitude of the perturbation implies a limited effect and no major modification of the long term behaviour of the simulation.

To estimate the impact of the initial condition on the long-term behavior of Channelflow, a second simulation is started from the already-initialized state of the OSSE simulation at time $t = 10$ for each actuation case. They are represented in red in figures 5.13, 5.14 and 5.15. Due to the interpolation from a grid resolution $N_y = 35$ to $N_y = 65$, the initial states of these new simulations actually differ from the state at time $t = 10$ of the corresponding OSSE simulations. Moreover, anomalies in the initial behavior ($t = [10, 15]$) are observed. This is within expectation as a different time-stepping is used for the initialization, and the interpolated initial state is an approximation from a lower resolution. However, despite these differences, the second Channelflow simulations observe the same long-term time-evolution as the original ones, with only a time-shift depending on the actuation case. To quantify the differences between the two sets of Channelflow simulations, the same error-norms as in §5.5.1 are calculated and gathered in the table 5.4 for each actuation case and velocity component (the time-domain were reduced and synchronized beforehand in order to remove the initial anomalies). The error-norms are all of small order of magnitude. Only the error norm of the streamwise velocity component for the actuation mode $(0, 1)$ arises slightly, which is mainly the consequence of the time-domain being too narrow to allow proper synchronization. The two sets of Channelflow simulations observe the same long-term time-evolution for close but different starting points, respectively to the actuation case. Therefore, the Channelflow simulations are not sensitive to the initial perturbation within this range of actuation amplitude (see eq. 5.62), time-scale and precision. The divergence between Channelflow and OSSE simulations is not due to a discrepancy in their starting points and/or initial behaviors. The causative factor for their distinctive behaviors is the introduction

TABLE 5.4: Non-linear validation: Table of error-norms $\|\delta\|$ for the three velocity components and three different actuations, between two simulations of Channelflow (CF: zero initial condition - CF2: initial condition being the already-initialized state of the OSSE simulation at time $t = 10$), for $Re = 400$ and resolution $21 \times 65 \times 21$. The comparisons for each actuation case (respectively $(0, 1)$, $(1, 0)$ and $(1, 1)$) are performed on the time intervals $[35, 150]$, $[40, 150]$ and $[30, 150]$ after time-shifting CF2 by -30, -9 and -6 units 'so that the initial anomalies are removed (non-integer time-shift would require an interpolation method).

Modes	$(0, 1)$	$(1, 0)$	$(1, 1)$
$\|\delta(u)_{\text{CF2 / CF}}\|_{1,[0,N_t]}$	2.048×10^{-4}	2.085×10^{-7}	4.393×10^{-5}
$\|\delta(v)_{\text{CF2 / CF}}\|_{1,[0,N_t]}$	5.749×10^{-6}	6.008×10^{-8}	1.586×10^{-7}
$\|\delta(w)_{\text{CF2 / CF}}\|_{1,[0,N_t]}$	7.323×10^{-6}	4.230×10^{-8}	2.827×10^{-5}
$\|\delta(u)_{\text{CF2 / CF}}\|_{2,[0,N_t]}$	1.778×10^{-2}	1.454×10^{-5}	5.576×10^{-3}
$\|\delta(v)_{\text{CF2 / CF}}\|_{2,[0,N_t]}$	5.311×10^{-4}	4.156×10^{-6}	2.000×10^{-3}
$\|\delta(w)_{\text{CF2 / CF}}\|_{2,[0,N_t]}$	6.509×10^{-4}	4.223×10^{-6}	3.565×10^{-3}

of a nonlinear term. Moreover, as Channelflow simulations experience the same time-evolution for cases with different time-dependent disturbances $\boldsymbol{u}$ but the same invariant non-laminar baseflow $\bar{\boldsymbol{U}}$ (here EQ1, cf. equation 4.1), we conjecture that for this range of amplitude, time-scale and precision, the nonlinear effects are mainly the result of the interaction between velocity components of the baseflow, and not of the disturbances. Therefore, the initial variance is here not detrimental to the validation process.

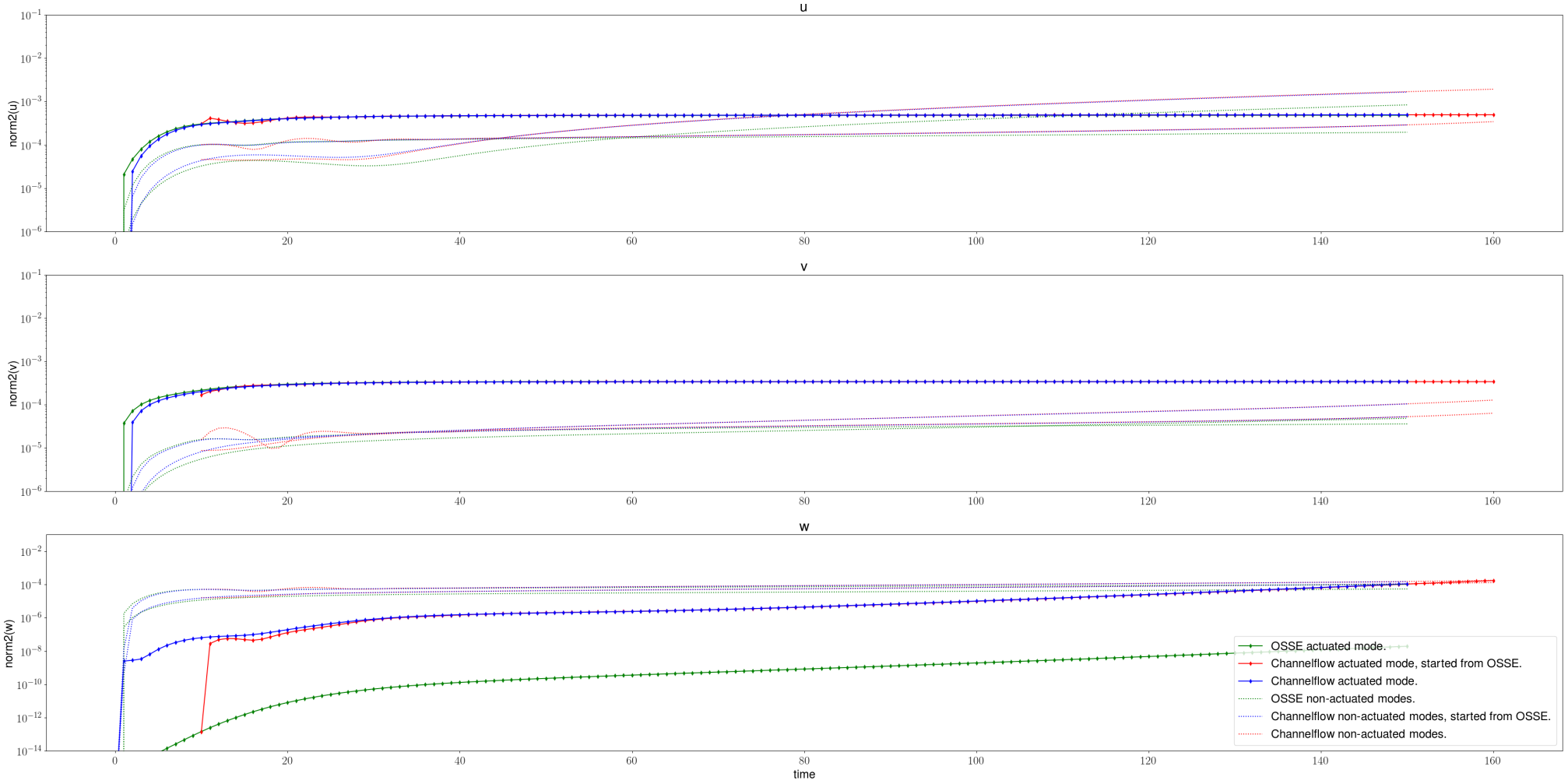

FIGURE 5.13: Non-linear validation: Time-evolution of the norm of the three velocity components of the Fourier mode $(1,0)$ actuated under the converging-to-constant boundary constraints 5.62 (diamond-thick line) and of the other non-actuated modes $(0,1)$ and $(1,1)$ (dotted lines) for three different simulations: OSSE model (green), Channelflow (blue) and Channelflow started from the state of the OSSE simulation at $t = 10$ (red). (times $t = [0, 150]$, EQ1 baseflow, resolution $21 \times 65 \times 21$ for Channelflow and $21 \times 35 \times 21$ for the OSSE model, $Re = 400$, $\tau = 0.05$).

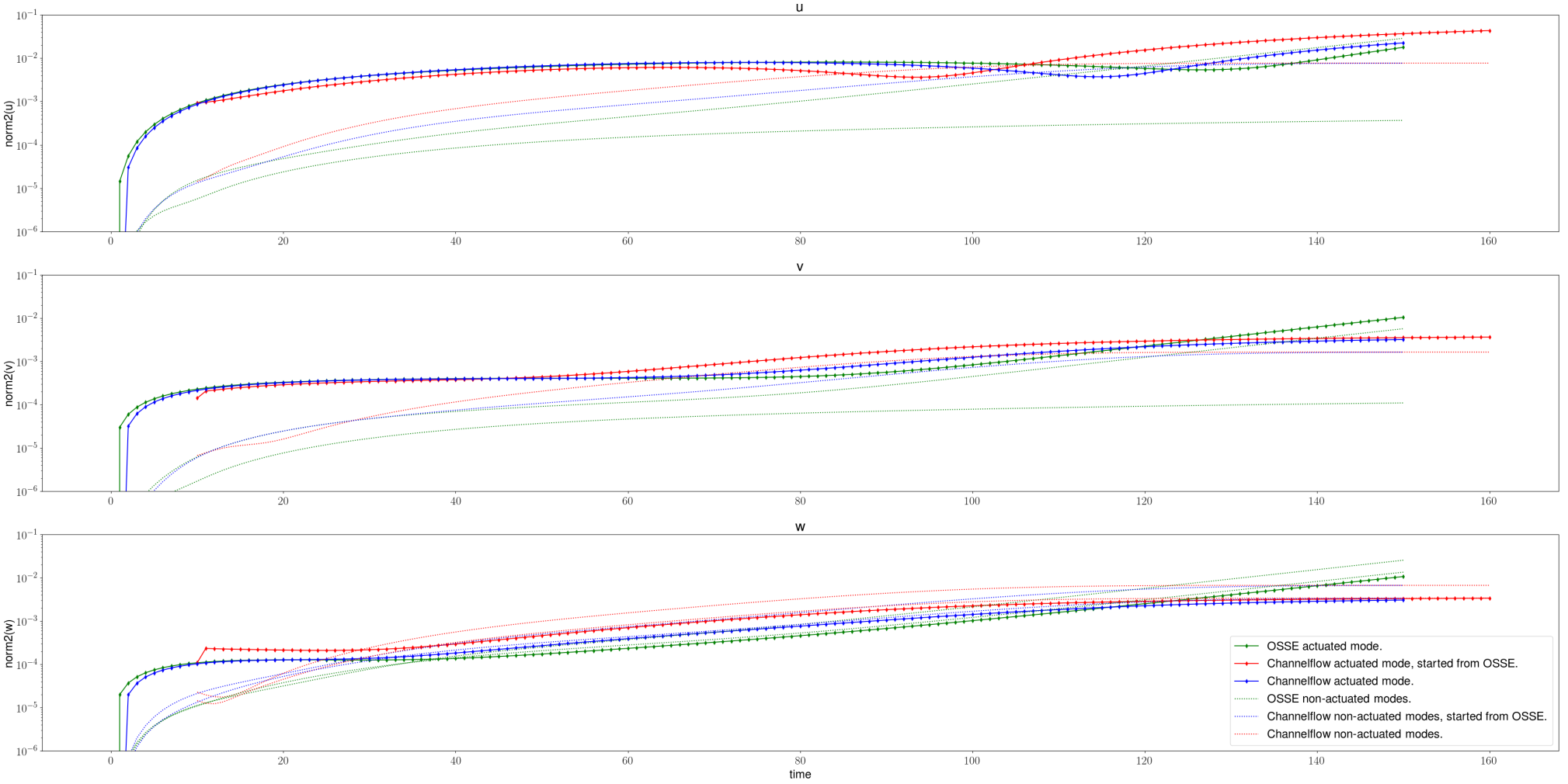

FIGURE 5.14: Non-linear validation: Time-evolution of the norm of the three velocity components of the Fourier mode $(0, 1)$ actuated under the converging-to-constant boundary constraints 5.62 (diamond-thick line) and of the other non-actuated modes $(1, 0)$ and $(1, 1)$ (dotted lines) for three different simulations: OSSE model (green), Channelflow (blue) and Channelflow started from the state of the OSSE simulation at $t = 10$ (red). (times $t = [0, 150]$, EQ1 baseflow, resolution $21 \times 65 \times 21$ for Channelflow and $21 \times 35 \times 21$ for the OSSE model, $Re = 400$, $\tau = 0.05$).

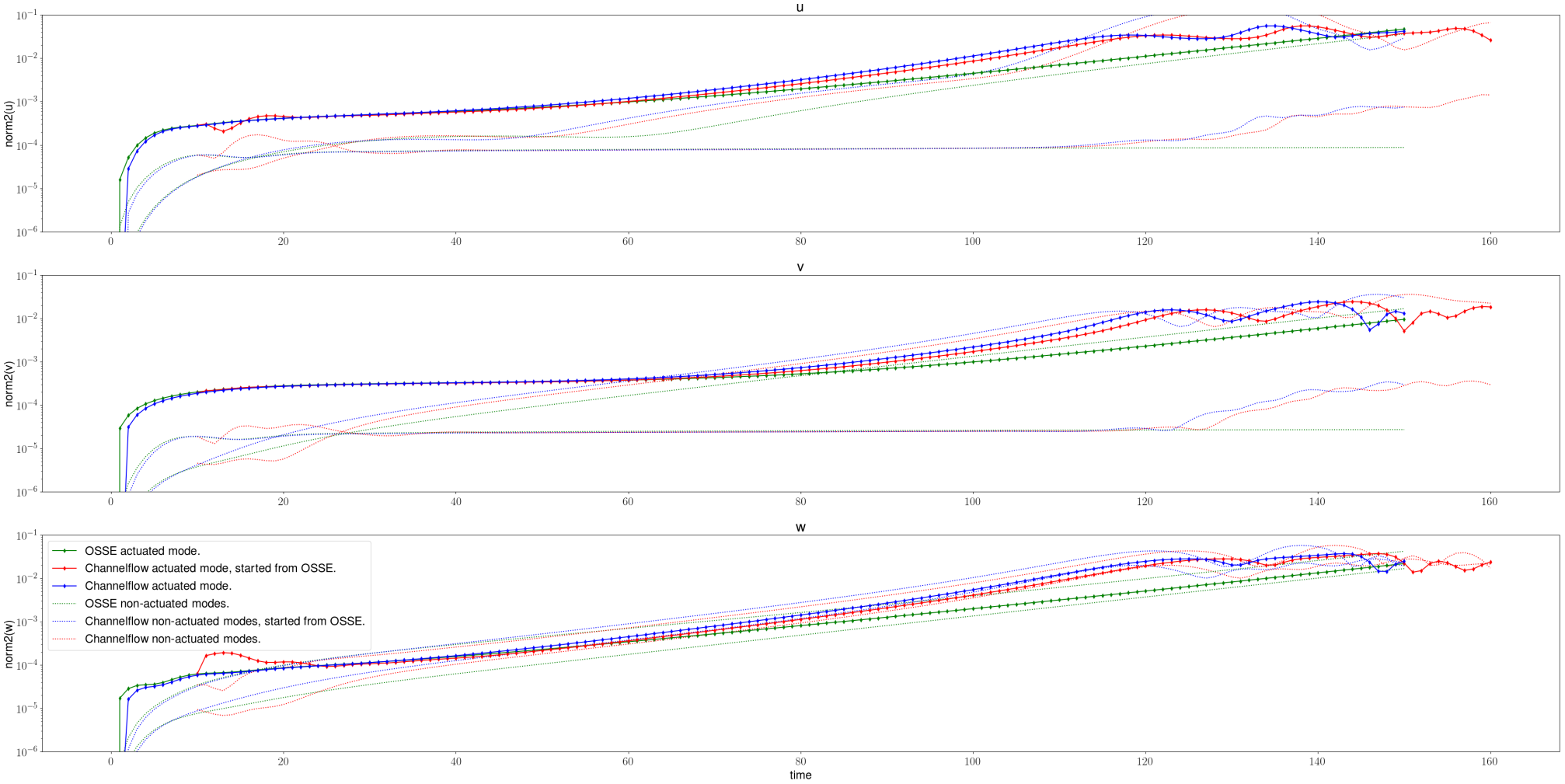

FIGURE 5.15: Non-linear validation: Time-evolution of the norm of the three velocity components of the Fourier mode $(1,1)$ actuated under the converging-to-constant boundary constraints 5.62 (diamond-thick line) and of the other non-actuated modes $(0,1)$ and $(1,0)$ (dotted lines) for three different simulations: OSSE model (green), Channelflow (blue) and Channelflow started from the state of the OSSE simulation at $t = 10$ (red). (times $t = [0, 150]$, EQ1 baseflow, resolution $21 \times 65 \times 21$ for Channelflow and $21 \times 35 \times 21$ for the OSSE model, $Re = 400$, $\tau = 0.05$).

Ignoring the initial variance, we can now focus on the main question of this section: is the linearised OSSE model sufficient to apply a feedback controller on a non-linear turbulent Channelflow simulation ?

For this purpose, the previous results for the converging-to-constant forcing 5.62 (figures 5.13, 5.14 and 5.15) will be exploited, as well as new simulations presented in figures I.1, I.2 and I.3, corresponding to the sinusoidal forcing

$$q^{+}_{v_{\alpha,\beta}} = q^{-}_{v_{\alpha,\beta}} = 0.0005 \ \sin(\frac{2\pi t}{10}). \tag{5.63}$$

From these figures, the evolution of the actuated flow can be separated into three phases, depicting periods when either wall-actuation, unstable eigenmodes, or non-linearity prevails. The appearance and/or timing of each phase vary with the setup of the simulation.

1. an actuation-dominated phase, where the state dynamics is governed by the wall-actuation. This phase is recognizable by a strictly periodic evolution of the norm for the sinusoidal forcing cases (e.g. $v(t)$ for $t = [0, 80]$ in figure I.3), and a constant norm for the converging-to-constant forcing (e.g. $v(t)$ for $t = [0, 60]$ in figure 5.15). The actuation of the wall-normal velocity at a given wave-number affects the other velocity components at the same wave-number mode in accordance to the continuity equation 2.16b. For some cases, and to a lesser extent, the actuation is influencing the non-actuated modes as well. This modal interaction is active both in the linear (OSSE) and non-linear (Channelflow) models. However, non-linear interaction is already at play for some non-actuated modes, explaining the slight variance between the two models. Despite this fact, the velocity profiles observed for both linear and non-linear simulations are matching in shape and amplitude concomitantly (cf. figure I.4 at time $t = 40$).

2. an eigenmodes-dominated phase, where the unstable eigenmodes of the baseflow become dominant in the evolution of the actuated modes. This phase is identifiable in the sinusoidal forcing by the periodic oscillations slowly being surpassed (e.g. $v(t)$ for $t = [80, 150]$ in figure I.3) and in the converging-to-constant forcing by an increasing norm (e.g. $v(t)$ for $t = [60, 120]$ in figure 5.15). The growth-rate of the norm of the linear simulations converges towards the unstable eigenvalues of the baseflow, thus approaching a linear behaviour. Nevertheless, non-linear simulations are not only affected by linear growth, but as well by non-linearity, leading to a faster non-linear growing rate. Velocity profiles of the linear and non-linear simulations still maintain analogous shapes, though at different amplitudes (cf. figure I.4 at time $t = 100$).

3. a turbulent phase (only for non-linear simulations), where non-linearity overcomes actuation and unstable eigenmodes altogether. This phase is not apparent for the

sinusoidal forcing case over this time-frame, but remarkable for the converging-to-constant case, when the flow dynamics becomes unstable and unsettles the other non-actuated modes (e.g. $v(t)$ for $t = [120, 150]$ in figure 5.15). Non-linearity induces an unstable interplay between modes, leading to a chaotic behavior characteristic of turbulence. Henceforth, velocity profiles of the non-linear simulations pursued their own evolution, differing in shape and amplitude from the linear ones (cf. figure I.4 at time = 150).

This analysis evaluated qualitatively the introduction of inhomogeneous boundary conditions, either constant or varying in time, in the OSSE model against equally constrained Channelflow simulations. The OSSE simulations agree with the Channelflow results, provided the non-linearity does not prevail. Precisely, OSSE and Channelflow dynamics coincide during the actuation-dominated phase, which is linearly-driven, and observe analogous shapes but distinctive amplitudes during the eigenmode-dominated phase. Consequently this analysis demonstrates that the non-laminar baseflow EQ1 and inhomogeneous boundary conditions are well-implemented mathematically in the OSSE model and numerically in its source-code. Furthermore, the OSSE model depicts the behavior of a Channelflow simulation sufficiently well to be used as control model, surely during the actuation-dominated phase and conceivably during the eigenmode-dominated one.

Chapter summary

- Direct numerical simulation of a controlled PCF are operated with the CFD software Channelflow, actuated by wall-transpiration via an update of the ChannelFlow Boundary Condition package. The optimal control laws are calculated beforehand with the linear OSSE and ROSSE models, which are implemented separately in `Python` and actuated by wall-transpiration via a lifting procedure.
- The full-information LQR control is designed based on the actuated OSSE and ROSSE models. It targets the kinetic density energy of a perturbation away from the targeted state.
- A controllability analysis demonstrated that all the unstable eigenmodes of EQ1 are controllable with an actuation via wall-transpiration. As a consequence, the Nagata (1990) lower-branch solution is stabilizable with this type of actuation. Moreover, a modal controllability analysis determined that the most predominant actuation-modes to stabilize eigenmode 0 of EQ1 are the 6 upper- and lower-wall actuation modes $v^{\pm}_{(\pm 2,0)}$ and $v^{\pm}_{(\pm 1,\pm 1)}$.

- The actuated OSSE and ROSSE models are validated in two stages (linear and non-linear) by comparing their time-integration with simulations run in Channelflow. It demonstrated that the non-laminar baseflow EQ1 and inhomogeneous boundary conditions are well-implemented mathematically in the OSSE model and numerically in its source-code. The OSSE and ROSSE models depict the behavior of a Channelflow simulation sufficiently well to be used as control model, surely during the actuation-dominated phase and conceivably during the eigenmode-dominated one.

Chapter 6

Optimal Control Law and Riccati Solution

This chapter describes the procedure to determine the Riccati solution associated with an optimal control problem. This solution is required in the control design to define the optimal control gain K^{opt} (see chapter 3). The detailed derivations of the Riccati equations and the optimal control law for each model are given in section 6.1. Solving the Riccati equation is the main obstacle of this thesis due to its computational cost for high and meaningful dimensions. Therefore, we perform a literature review of the different method to obtain its solution in section 6.2. The practical procedure employed in this thesis is given in section 6.3. The implementation of the optimal control law within the OSSE and ROSSE linear models and within the Channelflow software are validated in section 6.4.

6.1 Derivation of the Riccati solution and optimal control law

6.1.1 Mathematical Derivation

Lets consider the linear time-invariant LQR system 3.18

$$\dot{\boldsymbol{x}}(t) = A\,\boldsymbol{x}(t) + B_1\,\boldsymbol{w}(t) + B_2\,\boldsymbol{q}(t), \qquad \boldsymbol{x}(0) = 0, \tag{6.1a}$$

$$\boldsymbol{z}(t) = C_1\,\boldsymbol{x}(t) + \kappa D_{12}\,\boldsymbol{q}(t). \tag{6.1b}$$

The parameter κ denotes the predominance of the state against the actuation signal in the cost function. A small value of κ implies a smaller cost of the actuation, and therefore a stronger and "cheaper" control. The range of κ is limited empirically as a too intense actuation will actually create a discontinuity at the wall between the field

and the actuator. Even with finer grid resolution or small integration time-step, the numerical simulation will eventually crash. The objective is to minimize the 2-norm of the transfer function $R_{\boldsymbol{w}\mapsto\boldsymbol{z}}$ (§3.4.3), defined in the infinite horizon case as

$$\|R_{\boldsymbol{w}\mapsto\boldsymbol{z}}\|_2 = \lim_{T\to\infty}\left(E_X\left\{\frac{1}{T}\int_0^T \boldsymbol{z}^*\boldsymbol{z}\,dt\right\}^{\frac{1}{2}}\right), \tag{6.2}$$

or equivalently, to minimize the cost-function $\mathcal{J}$,

$$\mathcal{J} = \int_0^T \boldsymbol{z}^*\boldsymbol{z}\,dt. \tag{6.3}$$

A possible derivation of the Riccati equation is described by Green et al. (2007). It requires to remove/add beforehand/afterwards the cross-terms of the objective function 6.2, and derive the Riccati equation separately. This method was already employed in section 3.4.4, and is relatively convoluted due to the change of variables. Instead, a more straightforward procedure consists in imposing the orthogonality of matrices C_1 and D_{12} by padding them with zeros, such that $C_1^* D_{12} = 0$, and

$$\boldsymbol{z}(t) = \frac{1}{\sqrt{2}}\begin{bmatrix} C_1 \\ 0 \end{bmatrix}\boldsymbol{x}(t) + \frac{1}{\sqrt{2}}\kappa\begin{bmatrix} 0 \\ D_{12} \end{bmatrix}\boldsymbol{q}(t). \tag{6.4}$$

The cost function $\mathcal{J}$ follows directly as

$$\begin{aligned}\mathcal{J} = \int_0^T \boldsymbol{z}^*\boldsymbol{z}\,dt &= \frac{1}{2}\int_0^T \boldsymbol{x}^* C_1^* C_1 \boldsymbol{x} + \kappa^2 \boldsymbol{q}^* D_{21}^* D_{12}\boldsymbol{q}\,dt, \\ &= \frac{1}{2}\int_0^T \boldsymbol{x}^* Q_x \boldsymbol{x} + \boldsymbol{q}^* Q_q \boldsymbol{q}\,dt,\end{aligned} \tag{6.5}$$

where $Q_x = C_1^* C_1$ and $Q_q = \kappa^2 D_{21}^* D_{12}$.

Following Pralits and Luchini (2010), the cost function is augmented with the adjoint-state $\boldsymbol{p}$,

$$\tilde{J} = \frac{1}{2}\int_0^T \boldsymbol{x}^* Q_x \boldsymbol{x} + \boldsymbol{q}^* Q_q \boldsymbol{q}\,dt + \int_0^T \boldsymbol{p}^*(A\boldsymbol{x} + B_2\boldsymbol{q} - \frac{\partial \boldsymbol{x}}{\partial t})\,dt. \tag{6.6}$$

The calculus of the variation is given from the Euler-Lagrange equations for $\tilde{J}$,

$$\frac{\partial \tilde{J}}{\partial \boldsymbol{x}} - \frac{\partial}{\partial t}\left(\frac{\partial \tilde{J}}{\partial \dot{\boldsymbol{x}}}\right) = 0, \tag{6.7a}$$

$$\frac{\partial \tilde{J}}{\partial \boldsymbol{p}} - \frac{\partial}{\partial t}\left(\frac{\partial \tilde{J}}{\partial \dot{\boldsymbol{p}}}\right) = 0, \tag{6.7b}$$

$$\frac{\partial \tilde{J}}{\partial \boldsymbol{q}} - \frac{\partial}{\partial t}\left(\frac{\partial \tilde{J}}{\partial \dot{\boldsymbol{q}}}\right) = 0, \tag{6.7c}$$

which leads, once integrated by part, to the direct-adjoint system

$$-\frac{\partial \boldsymbol{p}}{\partial t} = A^*\boldsymbol{p} + \boldsymbol{x}^* Q_x, \tag{6.8a}$$

$$\frac{\partial \boldsymbol{x}}{\partial t} = A\boldsymbol{x} + B_2\boldsymbol{q}, \tag{6.8b}$$

$$\boldsymbol{q} = -Q_q^{-1} B_2^* \boldsymbol{p}, \tag{6.8c}$$

and consequently,

$$\frac{\partial \boldsymbol{x}}{\partial t} = A\boldsymbol{x} - B_2 Q_q^{-1} B_2^* \boldsymbol{p}. \tag{6.9}$$

The direct-ajoint problem forms the Hamiltonian Z (Luchini and Bottaro (2014) and Bewley et al. (2016) used opposite sign for $\boldsymbol{p}$) as

$$Z = \begin{bmatrix} A & -B_2 Q_q^{-1} B_2^* \\ -Q_x & -A^* \end{bmatrix}. \tag{6.10}$$

There exists a matrix P such that $\boldsymbol{p} = P\boldsymbol{x}$ (Green et al., 2007). Inserting P into the previous system leads to the algebraic Riccati equation

$$0 = PA + A^*P - PB_2 Q_q^{-1} B_2^* P + Q_x, \tag{6.11}$$

and the optimal control law

$$\boldsymbol{q}_{opt} = -Q_q^{-1} B_2^* P\boldsymbol{x} = -\frac{1}{\kappa^2} B_2^* P\boldsymbol{x}, \tag{6.12}$$

and consequently $K^{opt} = -Q_q^{-1} B_2^* P$. Application to the optimal estimation problem follows the same procedure. Final results were given in the Kalman filter section 3.4.5 of the feedback control chapter, and are outlined in Semeraro et al. (2013)(§3.2). Thanks to the separation principle, the calculation of the estimation and control problems can be made separately (§3.4.6).

6.1.2 OSSE optimal control implementation within Channelflow

The definition of the matrices A, B_2, C_1, D_{12} of the system 6.1 are defined for the OSSE model actuated by wall-transpiration in sections 5.2.1 and 5.2.2. The optimal control gain K^{opt}_{OSSE} can be inserted as such into linear simulation of the OSSE model. On the other hand, a transformation into the (u, v, w) basis is necessary when using this gain for non-linear simulations in Channelflow. As a consequence, the control gain for

Channelflow is defined as $K_{CHFL} = K_{OSSE}\mathcal{T}^{-1}\mathcal{C}^{-1}$ (app.C.4), such that

$$q = K \begin{bmatrix} v^+ \\ v^0 \\ v^- \\ \eta \\ u_{00} \\ w_{00} \end{bmatrix} = K\mathcal{T}^{-1} \begin{bmatrix} v^+ \\ v \\ v^- \\ \eta \\ u_{00} \\ w_{00} \end{bmatrix} = K\mathcal{T}^{-1}\mathcal{C}^{-1} \begin{bmatrix} u^+ \\ u \\ u^- \\ v^+ \\ v \\ v^- \\ w^+ \\ w \\ w^- \end{bmatrix}. \tag{6.13}$$

6.1.3 ROSSE optimal control implementation within Channelflow

As for the OSSE model, the definition of the matrices A, B_2, C_1, D_{12} of the system 6.1 are defined for the ROSSE model actuated by wall-transpiration in sections 5.3.1, 5.3.2 and 5.3.3. The optimal control gain K^{opt}_{ROSSE} can be inserted as such into linear simulation of the ROSSE model. On the other hand, a transformation into the (u, v, w) basis is necessary when using the ROSSE gain for non-linear simulations in Channelflow, as well as a separation of the real and imaginary parts. Depending when this separation happens, two different methods were implemented.

First method - via OSSE formulation

The transformation of the ROSSE optimal control gain K_{ROSSE} via the OSSE model into its Channelflow equivalent $K_{\substack{\text{CHFL} \\ \text{ROSSE via OSSE}}}$ requires to

1. Transform the continuous Channelflow state-vector $[u, v, w]^T$ into its equivalent discontinuous OSSE formulation $[v^+, v^0, v^-, \eta]^T$ using matrices $\mathcal{T}^{-1}\mathcal{C}^{-1}$ (app.C.4).
2. Separate the state-vector $[v^+, v^0, v^-, \eta]^T$ into real and imaginary parts via a non-linear separation function $\mathcal{F}_{sep}$.
3. Multiply the state by the gain K_{ROSSE} and reconstruct q_{CHFL} from its separated real and imaginary parts.

$$
\begin{aligned}
\boldsymbol{q}_{\substack{\text{CHFL}\\\text{ROSSE via OSSE}}} &= \Big[\Re(\boldsymbol{q}_{CHFL}) + \iota\Im(\boldsymbol{q}_{CHFL})\Big] \\
&= \begin{bmatrix} I & \iota I \end{bmatrix} \begin{bmatrix} \Re(\boldsymbol{q}_{CHFL}) \\ \Im(\boldsymbol{q}_{CHFL}) \end{bmatrix}, \\
&= \begin{bmatrix} I & \iota I \end{bmatrix} \boldsymbol{q}_{ROSSE}, \\
&= \begin{bmatrix} I & \iota I \end{bmatrix} K_{ROSSE}\, \boldsymbol{x}_{ROSSE}, \\
&= \begin{bmatrix} I & \iota I \end{bmatrix} K_{ROSSE} \begin{bmatrix} \Re(\boldsymbol{x}_{OSSE}) \\ \Im(\boldsymbol{x}_{OSSE}) \end{bmatrix}, \\
&= \begin{bmatrix} I & \iota I \end{bmatrix} K_{ROSSE}\, \mathfrak{F}_{sep}\, \boldsymbol{x}_{OSSE}, \\
&= \begin{bmatrix} I & \iota I \end{bmatrix} K_{ROSSE}\, \mathfrak{F}_{sep}\, \mathcal{T}^{-1}\, \mathcal{C}^{-1} \begin{bmatrix} u^+ \\ u \\ u^- \\ v^+ \\ v \\ v^- \\ w^+ \\ w \\ w^- \end{bmatrix}, \\
&= K_{\substack{\text{CHFL}\\\text{ROSSE via OSSE}}}\, \boldsymbol{x}_{CHFL},
\end{aligned}
$$

with

$$
K_{\substack{\text{CHFL}\\\text{ROSSE via OSSE}}} = \begin{bmatrix} I & \iota I \end{bmatrix} K_{ROSSE}\, \mathfrak{F}_{sep}\, \mathcal{T}^{-1}\, \mathcal{C}^{-1}\,. \tag{6.14}
$$

As the separation function $\mathfrak{F}_{sep}$ is a non-linear operation, the linear process in Channelflow needs to be broken into two stages, each requiring a high-dimensional matrix multiplication. For this reason, a more efficient and direct method was implemented.

Second method - direct

This method requires the definition of the ROSSE transformation matrices $\mathcal{T}^{-1}_{ROSSE}$ and $\mathcal{C}^{-1}_{ROSSE}$, which follow easily from their OSSE equivalent. They enable the derivation of $K_{\substack{\text{CHFL}\\\text{ROSSE direct}}}$ without employing any OSSE formulation and requiring high-dimensional

matrix multiplication only once,

$$\begin{aligned}
\boldsymbol{q}_{\substack{\text{CHFL}\\\text{ROSSE direct}}} &= \Big[\Re(\boldsymbol{q}_{CHFL}) + \imath\Im(\boldsymbol{q}_{CHFL})\Big], \\
&= \begin{bmatrix} I & \imath I \end{bmatrix} \begin{bmatrix} \Re(\boldsymbol{q}_{CHFL}) \\ \Im(\boldsymbol{q}_{CHFL}) \end{bmatrix}, \\
&= \begin{bmatrix} I & \imath I \end{bmatrix} \boldsymbol{q}_{ROSSE}, \\
&= \begin{bmatrix} I & \imath I \end{bmatrix} K_{ROSSE}\, \boldsymbol{x}_{ROSSE}, \\
&= \begin{bmatrix} I & \imath I \end{bmatrix} K_{ROSSE}\, \mathcal{T}_{ROSSE}^{-1}\, \mathcal{C}_{ROSSE}^{-1}\, \mathfrak{F}_{sep}\, \boldsymbol{x}_{CHFL}, \\
&= K_{\substack{\text{CHFL}\\\text{ROSSE direct}}}\, \boldsymbol{x}_{CHFL},
\end{aligned} \tag{6.15}$$

with

$$K_{\substack{\text{CHFL}\\\text{ROSSE direct}}} = \begin{bmatrix} I & \imath I \end{bmatrix} K_{ROSSE}\, \mathcal{T}_{ROSSE}^{-1}\, \mathcal{C}_{ROSSE}^{-1}\, \mathfrak{F}_{sep}. \tag{6.16}$$

We remind the reader that this calculation is computed at each time-step of the Channelflow simulation, and therefore needs to be as straightforward as possible.

6.2 Literature review: Solving the Riccati equation

Solving the high-dimensional Riccati equation is the main obstacle of this thesis and constitutes the focus of many researchers since the early 1970's. The scientific literature offers different methods that can be classified into three types: direct methods, solving directly the Riccati equation via gradient-based descents; Riccati-less methods, avoiding the Riccati equation via mathematical tricks; and model reduction, producing an equivalent system of lower-dimension to allow a direct solution.

6.2.1 Direct Solution of the Riccati equation

Gradient-descent

The Riccati problem is an optimization problem, and therefore can be solved with the numerous gradient-based iteration algorithm dedicated to that purpose. In other words, for n given initial conditions $\{\boldsymbol{x}_0^i\}_{i=1..n}$, it is possible to find the n optimal input $\{\boldsymbol{q}^i\}_{i=1..n}$ and the optimal control gain K, such that

$$[\boldsymbol{q}^1 \quad \boldsymbol{q}^2 \quad \dots \quad \boldsymbol{q}^n] = K\,[\boldsymbol{x}_0^1 \quad \boldsymbol{x}_0^2 \quad \dots \quad \boldsymbol{x}_0^n], \tag{6.17}$$

by solving the direct and the adjoint equations in the system 6.8 in an iterative manner with a gradient descent, such that the cost function $\mathcal{J}$ in 6.3 is minimized (Kim and Bewley, 2007, §3.1 & §4.1).

For this purpose, efficient gradient-based classical methods exist: steepest-descent & conjugate-gradient descent (see Shewchuk (1994) for a painless introduction), Broyden-Fletcher-Goldfarb-Shanno algorithm (BFGS), Nelder-Mead method, Newton search, etc. Good references for further research are the numerical implementation of these method in (Press et al., 2007, Chapter 10), and the application of gradient methods for large and distributed linear quadratic control in the Ph.D. thesis of Mårtensson (2012). Nonetheless, the computation cost of these methods is prohibitive when n is large.

Chandrasekhar Method

The Chandrasekhar method (Kailath, 1973) is an effective method to find the solution of a high-dimensional differential Riccati equation (eq.3.24). It was exploited for time-varying models by Lainiotis (1976) and optimal control of delay-differential systems by Powers (1983). In the case of high-dimensional system, it was tested numerically by Kenney and Leipnik (1985) against two Bernoulli substitution methods, the direct integration of the Riccati equation and the Davison-Make method for large sets of data, and demonstrated high-efficiency when the dimension of the actuation and/or estimation are relatively small compared to the one of the state. This method was applied for the continuous control design of a heat equation system (Borggaard and Burns, 2002), the feedback control of a two-dimensional Burgers' equation system (Camphouse and Myatt, 2004), or to estimate the Navier-Stokes equations in a wall-bounded flow system (Hoepffner et al., 2005). Nonetheless, this method still requires the solution of the high-dimensional differential Riccati equation at time $t = 0$, before accessing low-dimensional solutions at other times (Bewley et al., 2016).

6.2.2 Bypassing the Riccati equation

A first remedy to the intractable solution of the Riccati equation for large system is to bypass the Riccati equation and determine the optimal control law by alternative ways. With this aim in mind, Bewley et al. (2016) enumerates three different methods from the literature: the Minimum Control Energy Stabilization (MCE), the Oppositely-shifted Subspace Iteration (OSSI) (the main new result of their paper) and the Adjoint of the Direct-Adjoint (ADA).

Minimum Control Energy Stabilization (MCE)

The Minimum Control Energy Stabilization is a mathematically rigorous procedure to determine the optimal control law by pole-assignment. First introduced by Lauga and Bewley (2003), it was then exploited in the process to characterize the gradual decay

of stabilizability when increasing the Reynolds number in a linear complex Ginzburg-Landau model of spatially developing flow systems (Bewley et al., 2016). This procedure was also employed to study the wake behind a steady cylinder (Pralits et al., 2008, conference). However, the MCE technique requires the assumption $\kappa \to \infty$ ($Q_x = 0$) — the solution of the optimization problem is only minimizing the cost of the control signal without any consideration for the state— hence the denomination "minimal control". This limits the application of MCE to theoretical investigations.

Oppositely-shifted Subspace Iteration (OSSI)

The Oppositely-shifted Subspace Iteration is a prototype method published in Bewley et al. (2016). It brings a small modification to the algorithms of *subspace iteration*, which is a mature topic of algorithmic (references given in Bewley et al. (2016)). *Subspace iteration* refers to a group of iterative eigenvalue solvers, which efficiently converge towards the m leading eigenvalues and eigenvectors of a high-dimensional $n \times n$ matrix, when $m \ll n$. This method is commonly employed on sparse matrices of dimensions up to order 10^6 and offers different algorithms to accelerate the convergence of the solvers.

Bewley et al. (2016) "oppositely shifted" the time-forward march in the iteration process, or "propagation formula". It allows the algorithm to converge towards the central eigenvalues, located around the imaginary axis, instead of the usual extreme ones. These central eigenvalues can lead to the relation between the state and its adjoint, therefore determine the solution P of the Riccati equation 6.11 and the optimal control gain K^{opt}. The OSSI method is a promising technique as it enables access to a wide variety of efficient algorithms. However, due to its limited application to very small dimension ($n = 10$), it remains for the time-being a prototype. The implementation of other algorithms is required to access high-dimensional system and fast computation.

Worth noting, as the OSSI method is not matrix-based, i.e. does not require the matrices $\mathcal{A}$ (eq.5.30)or its inverse, future implementation with matrix-free `Python` object `LinearOperator` may be of interest.

Adjoint of the Direct-Adjoint (ADA)

No mathematically rigorous method exists to determine the optimal control gain K for large and complex systems, except for the case $\kappa \to \infty$ ($Q_x \to 0$) where some solutions as the MCE stabilization exist. In addition, the classical gradient-based iteration algorithms are not efficient solutions. They rely on the heavy computation at each iteration of a large input system, in order to output an improvement measure of much lower dimension. For this type of application, a clever and elegant alternative exists, as it is indeed the *raison d'être* of adjoint methods (Luchini and Bottaro, 2014).

The Adjoint of the Direct-Adjoint (ADA) method was firstly introduced in Pralits et al. (2008) and Pralits and Luchini (2010). The authors considered the direct-adjoint problem 6.8 as an input-output system. In this high-dimensional system, the optimization problem outputs the optimal control signal $\boldsymbol{q}$ corresponding to an initial state input $\boldsymbol{x}_0$. In most problems, the dimension of the output control signal $\boldsymbol{q}$ is much smaller than the dimension of the state $\boldsymbol{x}$. Therefore, Pralits et al. (2008) decided to take a reverse approach by investigating the adjoint of the direct-adjoint system. Instead of evaluating the behavior of an improvement measure (sensitivity or cost function) upon modification of the flow parameters or geometries, they focused on why and how this measure varies via the adjoint problem. By taking as input an adjoint-initial condition of small dimension, $\boldsymbol{q}_0^+$ and as output the high-dimensional adjoint-state, they established the optimal the optimal control gain K^{opt} of bluff-body wakes (Pralits and Luchini, 2010) and managed to suppress the von Kármán vortex shedding past a circular cylinder at $Re = 55$ (Pralits et al., 2008).

The Adjoint of the Direct-Adjoint (ADA) was used extensively and promisingly. Luchini and Bottaro (2014) reviewed the use of adjoints in the domain of hydrodynamic stability theory, and gave two application examples (the noise-amplifying instability of a flat-plate boundary layer and the global mode occurring in the wake of a cylinder) as well as a very informative supplement (Luchini and Bottaro, 2014). Semeraro et al. (2013) applied the same method to the estimation problem, entitled the Adjoint of the Adjoint-Direct method (AAD), for a single-input-single-output system. They stabilized a full-dimension linear quadratic Gaussian controller on a Tollmien-Schlichting wave developing in a two-dimensional boundary layer flow. Semeraro and Pralits (2017) extended that progress on the multiple-input-multiple-output case and to robust $\mathcal{H}_\infty$ control. Their decentralized (i.e. restricting the interaction between pairs of sensor and actuator at the same streamwise location) controller computed with ADA and AAD was applied on a modified version of two-dimensional Kuramoto-Sivashinsky equation to mimic a 3D configuration.

The ADA method outperforms analogous techniques in terms of convergence performances for many configurations. In the infinite-horizon case, the control gain K becomes constant and equal to $K(t = 0)$, which recovers the original infinite-horizon LQR design (§3.4.4) (Semeraro et al., 2013). The ADA algorithm is also useful as its solution is independent of the initial condition fed to the system, and thus on the external disturbances (Semeraro and Pralits, 2017, §6).

The downside of the ADA method is its requirement for a cycle of forward integration of the direct-adjoint, together with a backward integration of adjoint-of-the-direct-adjoint systems, both over a period T. In the infinite-horizon case, the period T needs to tend to the infinity to obtain the optimal gain. Finding the adequate initial condition and integration parameters for unstable and high-dimensional systems to allow an iterative increase of T is feasible, but not always evident.

6.2.3 Model reduction

A second possibility to avoid the intractable solution of the original high-dimensional optimal control problem is to produce its equivalent low-dimension counterpart, for which the Riccati solution is accessible.

Low order models

Low order models, or reduced models, aim to reproduce the same characteristic of a given system yet at lower dimension. Reduced models require less storage and computational time. Hence they can replace the original system for real time simulation or be aggregated with other models at lower cost. Low order models are helpful in the modeling of invariant solutions and were studied by many researchers for this purpose. In this context, the OSSE system is characterized by a high dimension and a size reduction could be an advantage.

The first idea of a truncated system comes from Moore (1981), who applied the minimal realization theory to reduce a linear system. Firstly transforming the full system into a balanced one, he then truncated it to build an internal dominant subsystem, which contributes mainly to the full-model impulse response matrix. Balanced truncation has an advantageous error bound, close to the lowest error possible from any reduced-order model, and was also extended to non-linear systems (details in Rowley, 2005). Still, it can only fit states of low dimension (less than 10 000). Starting with the definition of the controllability and observability Gramians, the balanced truncation method then "balances" these two matrices. A system is said to be "balanced" if its associated Gramians are equal and diagonal, i.e. each of its modes is equally observable and controllable. Truncating the least observable and controllable modes produces a lower order model. The method of balanced truncation is also detailed in the book of Green and Limebeer(1995, chapter 9) and has been used for boundary-layer control (details in Kim and Bewley, 2007).

Proper Orthogonal Decomposition (POD), also called Karhunen-Loève expansion, is a model reduction technique often used in fluid dynamics. It projects the data of dimension n into a subspace of smaller dimension r. To define the projection basis, a matrix associated with the state of the system, of size $n \times n$, is formed, and its eigenvectors are computed. These eigenvectors are called the "POD modes" of the optimal projection. A Galerkin projection is then used to reduce the size of the subspace formed by the POD modes. Different methods exist to define the optimal projection span of reduced size, like the snapshots method (Rowley, 2005). The drawback is that POD is sensitive to empirical data from which the projection basis is formed and that it can ignore low-energy modes which nonetheless influence greatly the flow dynamics (e.g. acoustic

waves). Berkooz et al. (1993) wrote an annual review about this decomposition, explaining the fundamental mathematical development, as well as experimental and numerical results strengthening the concept. The same group published a book (Holmes et al., 2012), wherein theoretical and practical aspects of coherent structures, POD, dynamical systems and low dimensional models with some applications are gathered. The second edition (Rowley, 2005) added the work of Rowley on balanced POD and compared POD, balanced truncation and balanced POD with a linearised flow in a plane channel.

Balanced POD makes the balanced truncation method feasible for large systems, by applying beforehand a balanced transformation on the controllability and observability Gramians. Firstly, a balancing transformation as in a balanced truncation is computed from snapshots of empirical Gramians, hence skipping the calculation of two high-dimensional Gramians. Secondly, an output projection similar to the POD is applied to reduce the size of the system. Rowley (2005) exploited this method on large systems by computing the balancing transformation via an orthogonal projection, avoiding the Gramians.

We refer the interested reader to the many other methods available to reduce both linear and nonlinear systems, based either on the SVD or on moment matching (Antoulas, 2006), or forming analytic basis functions explicitly designed to represent physical phenomena observed in turbulent flows (details given in (Gibson et al., 2008)). Nonetheless, model reduction dedicated to the purpose of control design (Semeraro et al., 2013; Bewley et al., 2016) are more appropriate for this thesis and are reviewed in the following paragraphs.

Reduce-then-Design vs. Design-then-Reduce

When considering model-reduction methods for the purpose of control design, two different approaches are conceivable. The first "reduce-then-design" possibility consists in approximating the system with a low-order model, and only then designing the controller. The second "design-then-reduce" one performs a full-dimensional controller design first, and then reduces the controller to a lower dimension as a high-dimensional control is not of practical interest for engineering applications. These strategies are not equivalent and their usage depends on the user's objectives and on the problem (Semeraro et al., 2013). The focus of this project is obviously on the reduce-then-design strategies, as solving the high-dimensional Riccati equation is impossible for high-dimensions.

Both approaches suffer from known drawbacks, sometimes severe (Bewley et al., 2016). Firstly, the model-reductions techniques as presented above are open-loop truncations. Only the controllability and observability of the system are taken into account through matrices $\mathcal{B}_2$ and $\mathcal{C}_1$. No consideration for the control objective is embodied in these matrices, and therefore in the reduction protocol. Some important components of the

cost function may not be included in the reduced model. Secondly, if the eigenmodes of the reduced matrix are non-orthogonal or not acknowledged in the approximation, a substantial transient energy growth may arise initially and ignite non-linear mechanisms. The delay for their destructive interference to disappear is indeed not synchronized as distinct modes decay at distinct paces. A simple study of the eigenmodes of the system is not sufficient to describe this phenomenon. Model reduction based on retaining solely the major eigenmodes won't reproduce the turbulent evolution faithfully. Thirdly, performing a model-reduction requires the solution of a problem of complexity similar to an eigenvalue problem, which is computationally inefficient.

Reduce-while-solve strategy: Extended and Rational Krylov subspaces

A different strategy to determine the solution of the high-dimensional Riccati equation consists in determining the reduction base while solving the reduced Riccati equation via a traditional method. The reduction base is generated iteratively via an Arnoldi process of Galerkin type, while the reduced Riccati equation is solved at each iteration. The quality of the approximate solution is evaluated via the residual of the reduced Riccati equation. Further increase in the dimension of the reduction base minimizes the residual and extracts an approximation of the stabilizing solution of the high-dimensional Riccati equation.

One of the first idea to use projection of lower-dimensional orthogonal subspaces appeared in Saad (1990), where Krylov projection process of Galerkin type are presented among other methods to solve high-dimensional Lyapunov equations for single-input system (i.e. matrix $\mathcal{B}_2$ has one column). Jaimoukha and Kasenally (1994, 1995) extended the previous work of Saad (1990) to problems where $\mathcal{B}_2$ has more than one column by using a block Krylov schemes. The standard Krylov subspace of reduced dimension m for the couple $(\mathcal{A}, \mathcal{B}_2)$ is defined as

$$\mathcal{K}_m(\mathcal{A}, \mathcal{B}_2) = span\Big\{\mathcal{B}_2, \mathcal{A}\mathcal{B}_2, \mathcal{A}^2\mathcal{B}_2, ..., \mathcal{A}^{m-1}\mathcal{B}_2\Big\}. \tag{6.18}$$

They also derived an expression of the residual error and considered the low rank solutions of discrete-time Lyapunov equations and continuous time algebraic Riccati equations. Krylov subspaces were getting attention at this time for large eigenvalues problems but also applications in control theory, computational chemistry and physics (Jaimoukha and Kasenally, 1994). Further mathematical and algorithmic improvement of the Krylov projection methods followed shortly. Jbilou (2003) introduced a deflation technique to delete the linearly and almost-linearly dependent vectors in the block Krylov subspaces sequences and Jbilou (2006) brought further theoretical results as well as large-scale numerical experiments. An "extended" block Krylov method was proposed by Simoncini (2007) to solve large-scale Lyapunov equations, and later applied to large-scale Riccati equation by Heyouni and Jbilou (2008). This "extended" method combined two block

Krylov subspaces associated with matrices $\mathcal{A}$ and $\mathcal{A}^{-1}$. It is referred as "Extended block Arnoldi algorithm" and defined for an extended block Krylov subspace of reduced dimension m as

$$\mathcal{K}_m(\mathcal{A}, \mathcal{B}_2) = span\Big\{\mathcal{B}_2, \mathcal{A}^{-1}\mathcal{B}_2, \mathcal{A}\mathcal{B}_2, \mathcal{A}^{-2}\mathcal{B}_2, \mathcal{A}^{2}\mathcal{B}_2, ..., \mathcal{A}^{-(m-1)}\mathcal{B}_2, \mathcal{A}^{m-1}\mathcal{B}_2\Big\}. \quad (6.19)$$

This method is more efficient than the later block Arnoldi Process, but requires at each iteration the construction of a Krylov subspaces based on the inverse matrix A^{-1}. For high-dimensional system, the direct computation of the inverse is tricky, and the use of iterative solver and preconditonner is recommanded instead.

An other variant of the Krylov subspaces is the "Rational Krylov method", originally proposed to approximate large eigenvalues problems (Ruhe, 1984). This method introduces a series of shifts $s = [s_1, s_1, ..., s_m]^T$ in the standard Krylov subspaces to improve their convergence rate. The rational Krylov subspace of reduced dimension m is defined as

$$\mathcal{K}_m(\mathcal{A}, \mathcal{B}, s) = span\Big\{(\mathcal{A} - s_1 I)^{-1}\mathcal{B}, ..., \prod_{j=1}^{m}(\mathcal{A} - s_j I)^{-1}\mathcal{B}\Big\}. \quad (6.20)$$

However, the choice of shift s was limited to either trial & error or costly methods in terms computational time and memory. An adaptive computation of the shifts was proposed by Druskin and Simoncini (2011). This method, referred as Adaptive Rational Krylov, is almost parameter-free and time-efficient. Druskin and Simoncini (2011) applied this method to large Lyapunov problems, while Simoncini (2016) provided new theoretical ground and applied it to algebraic Riccati equations. Simoncini et al. (2014) compared this approach against iterative inexact Newton-Kleinman method for high-dimensional algebraic Riccati equations. The Galerkin Adaptive Rational Krylov seemed to be superior for realistic problems and the best solution to approximate large scale Riccati solutions. More recently, Alla and Simoncini (2017) introduced the Petrov-Galerkin Adaptive Rational Krylov with promising results.

Despite these promising mathematical and algorithmic advances, the Krylov subspaces method are until now limited to cases where the rank of the matrix C_1 is very low. The dimension of the reduction base is indeed linked with the rank of $\mathcal{C}_1$, and the dimension of the reduced Riccati equation which needs to be solved at each iteration is equal to the rank of C_1. In this thesis, C_1 derives from the definition of $Q_x = \mathcal{C}_1^*\mathcal{C}_1$, a matrix of dimension $n \times n$ and almost full-rank. C_1 is here a rank-deficient rectangular matrix of dimension $p \times n$ (§5.2.2.2). Yet, p is of the same order as n. After discussions with Valeria Simoncini (personal communication via email, March 2019), it was confirmed that Krylov subspaces can not fit to our need, unless an other expression of $\mathcal{C}_1$ where $p \ll n$ is found.

In parallel to Krylov based methods, other promising methods emerged and notably the Alternating Direction Implicit (ADI) iteration (Benner et al., 2008). Benner and

Saak (2013) summarized both Krylov and ADI methods applied to continuous time problems, as well as sketching their respective advantages and drawbacks. However, Valeria Simoncini advised us that ADI would not bring any major advantages for our problem.

Quasi-separability

An alternative method was proposed by Valeria Simoncini (Dipartimento di Matematica, Università di Bologna, Simoncini (2007); Druskin and Simoncini (2011); Simoncini et al. (2014); Simoncini (2016); Alla and Simoncini (2017)) after some online exchanges. Her collaborator Davide Palitta indeed studied an innovative method based on hierarchical matrices (i.e. a sparse approximation of a non-sparse matrices), that intends to circumvent the limitation of the Krylov-subspaces iteration to low-rank matrices $\mathcal{C}_1$ by taking advantage of its particular structure (e.g. band or block matrices).

The discrete operator coming from partial-differential equations can be well approximated by a quasi-separable matrix (Massei et al., 2019). Informally, a matrix is said to be quasi-separable if its off-diagonal blocks are low-rank matrices (Massei et al., 2018). This approximation helps to design solvers for problems where the spatial domain can be reformulated as matrix equations (Massei et al., 2019, on 2D cases). It was employed to solve Sylvester and Lyapunov equations as the quasi-separable structure is guaranteed to be numerically present in the solution (Massei et al., 2018). Their experiments showed that the approach based on the use of rank-structured arithmetic is particularly effective and outperforms current state of the art techniques. Massei et al. (2018) and Massei et al. (2019) developed a MATLAB toolbox that allows easy replication of their experiments and a ready-to-use interface for the solvers. This toolbox can directly be applied to the OSSE and ROSSE Riccati equaiton to determine an optimal solution.

However, the methods based on quasi-separability requires the computation of a stabilizing initial guess. Palitta (2019) combined the very appealing computational features of projection methods with the convergence properties of the inexact Newton-Kleinman procedure equipped with a line search in order to find the solution of the algebraic Riccati equation. The initial guess was computed with the method described in Bänsch et al. (2015).

Due to the time-limitation of this project, this method was unfortunately not exploited. Nonetheless, the author highly recommends research on similar problems to examine the work of Valeria Simoncini and Davide Palitta for the solution of high-dimensional Lyapunov and Riccati solutions.

6.2.4 Final choice

Despite the considerable literature available to determine the solution of a high-dimensional Riccati equation, many of these approach are impractical: gradient-based descents are ineffective; the MCE is limited to $Q_x = 0$; the OSSI is still a prototype and the Krylov-subspace requires a low-rank objective. Only the ADA and quasi-separability methods seem to hold a real potential. Solving the Riccati equation is the bottleneck of this endeavor, and developing a robust and efficient Riccati solver is key for future research. For this purpose, the authors highly recommend dedicated mathematicians as Valeria Simoncini, Davide Palitta, Peter Benner or Daniel Kressner.

As a consequence, a reduce-then-design approach is here employed. The full-dimension problem is reduced by spectral truncation, i.e. only the leading Fourier and Chebyshev modes are conserved, which may not reproduce the transition to turbulence faithfully. The control design is then performed with the `Python` method

```
scipy.linalg.solve_continuous_are
```

based on a Schur algorithm using a QZ decomposition. The dimension of the reduced model is chosen such that the memory requirement of the `Scipy` method is conformed to the maximum memory available. This procedure is far from optimal: as not dedicated to such high-dimensional problem, the Schur algorithm is slow and the QZ decomposition requires an excessive amount of memory. It can be regarded as brute force, but in simple words, it works well enough.

6.3 Brute force direct solution of the Riccati equation

The computation of the optimal control law is operated via a reduce-then-design approach. The direct solution of the Riccati equation via the Schur method can not be performed at the original dimension of $32 \times 35 \times 32$ used in Channelflow to compute the Nagata (1990) lower-branch EQ1. As a consequence, the high-order modes of this equilibrium are truncated and a Newton-Krylov-hookstep search is operated to find the corresponding equilibrium at this lower resolution, as in section 4.8:

```
changegrid --Nx 26 --Ny 27 --Nz 26 eqX_32x35x32.h5 eqX_17x27x17.h5
findsoln -eqb -R 400 eqX_17x27x17.h5
```

As the `Scipy` implementation of the Schur method is serial, the memory can not be shared on the HPC Iridis5 between computational nodes. Therefore, the physical amount of memory available on one computational node is the limiting factor. Each node of Iridis5 gathers Intel(R) Xeon(R) Gold 6138 CPUs at 2.00GHz and posses 192Gb of RAM, of which approximately 170Gb is available. All calculations are here serial. We remind the reader that an odd resolution is necessary for the stream-wise, wall-normal

and span-wise directions (see section 4.6.4). Moreover, due to the actuation via wall-normal transpiration, prevalence is given to the wall-normal direction.

Within these specifications, the maximal resolution reachable with the OSSE model is $17 \times 21 \times 17$, for which the direct solution of the Riccati equation approximately requires 169.8 MB and 28.3 hours. Nonetheless, such a low resolution does not allow Channelflow to converge into an equilibrium. At that resolution, it is unclear for the authors if either Channelflow is unable to achieve a decent precision or the Nagata (1990) lower-branch does not exist. A hint can be found in the work of Keefe et al. (1992) and Kawahara et al. (2012), where turbulence was sustained at $Re_\tau = 80$ and resolution $16 \times 33 \times 16$. Regardless, the OSSE model is here inoperative due to its memory demand.

The ROSSE is conceived to minimize the memory limitation. For comparison, the direct solution of the Riccati equation at resolution $17 \times 21 \times 17$ with the ROSSE model approximately requires 94.9 MB and 47.1 hours at this resolution. The memory saving of the ROSSE model suffices to reach the maximal resolution of $17 \times 27 \times 17$. Unfortunately, the computational time required to solve the Riccati equation at that resolution lays beyond 60-hours wall-time of Iridis5. Thanks to the support of the ECPS group of Tobias Schneider at the École Polytechnique Fédérale de Lausanne (EPFL, Switzerland), we are able to compute the Riccati solution on their server. We decided to keep a resolution of $17 \times 27 \times 17$, which seems to be the lowest one for which Channelflow can find EQ1, as it already requires 300 hours (12.4 days) of computational time on their ECPS-C01 server.

Table 6.1 gathers the eigenvalues of EQ1 at resolution $17 \times 27 \times 17$ for the OSSE model —even if the Riccati solution is inaccessible, eigen-decomposition is feasible—, ROSSE model, as well as Channelflow. These values are close, but different, from the ones presented at resolution $21 \times 35 \times 21$ (OSSE, ROSSE) and $32 \times 35 \times 32$ (Channelflow) in section 4.8 (table 4.1, eigenvalues of EQ1). It indicates that the EQ1 is different between resolution $17 \times 27 \times 17$ and resolution $32 \times 35 \times 32$. In other words, EQ1 at resolution $17 \times 27 \times 17$ is not equivalent to EQ1 at resolution $32 \times 35 \times 32$. These are two distinctive states. In practice, it implies that stabilizing EQ1 at resolution $32 \times 35 \times 32$ with a controller designed to target EQ1 at resolution $17 \times 27 \times 17$ is impossible: the control forcing would guide the dynamical state away from EQ1 at $32 \times 35 \times 32$ and towards the position of EQ1 at $17 \times 27 \times 17$, which is meaningless in this case. As a consequence, in order to target the relevant state, Channelflow is required to adopt the same resolution as the controller designed with the ROSSE model, hence $17 \times 27 \times 17$.

This observation is problematic, as the wall-actuation is validated for Channelflow with a wall-normal resolution $N_y = 65$. It is obscure if the implementation of the wall-transpiration is effective at lower resolution, particularly for the control of unstable

invariant solutions. Increasing the controller resolution appears as a key factor to improve in this project. Nonetheless, the `Scipy` Schur method (§6.2.4) stands as the only solution employable within our time constraint.

TABLE 6.1: Eigenvalues ranked in order of decreasing real-part and computed with the OSSE model, the ROSSE model and Channelflow for EQ1, $Re = 400$. When values rounded at 3 decimals matched, they are marked with ✓ and spurious modes with 'SP'. Same protocol as §4.8 and table 4.1.

EQ1 - Low-Dimension - Nagata (1990) Lower branch

	OSSE	$17 \times 27 \times 17$	ROSSE	$17 \times 27 \times 17$	Channelflow	$17 \times 27 \times 17$
✓	$+0.05012082$		$+0.05012082$		$+0.05012170$	
✓	$+0.00002215$		$+0.00002215$		$+0.00000025$	
✓	-0.00001902		-0.00001902		-0.00000133	
✓	-0.00203379		-0.00203379		-0.00200393	
✓	-0.00659876		-0.00659876		-0.00660315	
✓	-0.00688399		-0.00688399		-0.00692660	
✓	-0.00974591		-0.00974591		-0.00972886	
✓	-0.01359193		-0.01359193		-0.01359344	
✓	-0.02392832		-0.02392832		-0.02393420	
SP	-0.02467401		-0.02467401			
✓	-0.03347443		-0.03347443		-0.033485138	
✓	-0.03704233		-0.03704233		-0.037024950	
✓	-0.04260227		-0.04260227		-0.042615339	
✓	-0.04535135	$\pm 0.01888320\iota$	-0.04535135	$\pm 0.01888320\iota$	-0.045351524	$\pm 0.01887272\iota$
					-0.048491699	$\pm 0.10250483\iota$
SP	-0.05047682		-0.05047682			
✓	-0.05181479	$\pm 0.02605732\iota$	-0.05181479	$\pm 0.02605732\iota$	-0.051820653	$\pm 0.02604382\iota$
✓	-0.06237648	$\pm 0.03117230\iota$	-0.06237648	$\pm 0.03117230\iota$	-0.062366408	$\pm 0.03115481\iota$

6.4 Validation of optimal control implementation: control of Couette laminar baseflow

The procedure to determine the optimal control law and its implementation in Channelflow is validated with a laminar Plane Couette Flow (PCF) profile, at a Reynolds number of 400. We will perform a linear analysis (§6.4.1) and simulations of the closed-loop system, either with the linear OSSE model (§6.4.2) or the Channelflow software (linear simulations are not feasible, see §6.4.3, but non-linear ones are in §6.4.4). The laminar Plane Couette Flow profile is already a stable solution. As a consequence, the validation does not intend to stabilize the solution, but to increase its degree of stability.

We expect the controller to improve the rate of convergence towards the laminar profile when the state is perturbed and pushed away from the solution.

Due to memory limitations and to evaluate the behavior of the method for low resolutions, the Riccati solution is calculated at resolution $11 \times 21 \times 11$, which is sufficient for the convergence of the eigenvalues of the PCF profile but may not be adequate for wall-transpiration actuation. Details on the influence of the wall-normal resolution are given in section 6.4.5. Moreover, the actuation is limited solely to the wall-normal velocity at the wall, as the Channelflow Boundary Condition Package of Heins (2015) is only validated for this component u_{00} and w_{00}. It implies that the matrix B_2 is reduced to remove the modes of the wall-normal vorticity η_y, as well as fundamental modes of the stream- and spanwise velocity components. This reduction leads to a small saving in memory and time requirement of approximately 2%. Finally, for every simulation, the actuation-time constant is set at $\tau = 0.005$.

The Riccati solutions are calculated along the procedure given in section 6.2.4 for different values of κ,

$$\kappa = [1.0,\ 0.75,\ 0.5,\ 0.25,\ 0.1,\ 0.05,\ 0.01]. \tag{6.21}$$

In each case, the calculation approximately requires 2 hours and 30Gb of RAM memory on the HPC Iridis5, with a slight increase in time requirement (~ 10 min) with decreasing value of κ.

6.4.1 Linear analysis

Data location	`osse/database/THESIS/06_couette_controlled_OSSE`
Script for Riccati...	`python3 osse/osse_riccati_couette.py`
solutions and analysis	`11 21 11 $1000kappa`

Eigen-decomposition

The eigenvalues of the open- and closed-loop systems are calculated as in §4.8 with `Python` packages. The leading values are gathered in table 6.1 for each value of κ and compared against the open-loop system.

A first observation from table 6.1 is the presence of modes unaffected by the feedback control. Some of them are uncontrollable spurious modes of the OSSE model, here coloured in gray and found previously in table 4.1, while the others, for example the first and seventh leading eigenvalues of the PCF profile, are likely uncontrollable via actuation by wall-transpiration. We dismiss these modes as they are unaffected by the control law.

For decreasing values of κ —higher control "strength"—, the real part of each eigenvalue is moved further onto the left hand side (their negative real part decreases). For instance, all the eigenvalues for $\kappa = 0.01$ are shifted to the left in comparison to the open-loop system. As a consequence, the linear stability of the PCF profile improves with decreasing value of κ. In brief, a stronger control improves the linear stability of the OSSE model.

Normality

When the eigenmodes of linear system are non-normal or non-orthogonal under the energy norm, a transient energy growth can occur in the initial phase of a simulation. This transient growth can trigger non-linear effects and ignite the transition to turbulence, despite the presence of an optimal control. Therefore, an attentive evaluation of the normality of the system is necessary. Further explanations, references and mathematical details on normality are given in appendix section H.3.1. Normality is here evaluated to estimate the impact of the feedback control on potential transient energy growth. Measures of the normality are gathered in table 6.2 for the open- and closed-loop OSSE systems.

It appears that weak controller —large values of $\kappa = \{1.0, 0.75\}$, marginally affect the normality of the OSSE model. However, for smaller values of κ, the normality measure drastically escalates: the system becomes non-normal. For instance, the leading eigenvalue for $\kappa = 0.01$ is twenty-five times higher than the one for $\kappa = 1.0$. As a consequence, we expect the optimal control to disrupt the initial phase of the simulations by prompting an energy burst. This energy growth is benign for linear simulations: as the OSSE model is linearly stable, this perturbation will remain transient for the linear case. Nonetheless, its repercussions on the non-linear simulations are less predictable. A slight perturbation can indeed initiate the transition turbulence. Therefore, we expect powerful optimal control law (small values of κ) to disturb the initial phase of non-linear simulations and likely push the state away from the laminar profile, hence breaking the hypothesis of small-perturbation fundamental to the linearization procedure of §4.1.1.

Conclusion

To conclude, an increase in optimal control strength (lower values of κ) improves the linear stability of the OSSE model but enhances the risk of transient energy growth as the normality of the system deteriorates. For very powerful control ($\kappa = \{0.05, 0.01\}$), it might even push the state away from the neighborhood of the laminar solution and render the linearization around this solution invalid.

FIGURE 6.1: Measure of the stability of the linear OSSE model for different κ: leading eigenvalues of A (open-loop) and $A + B_2K$ (closed-loop). Couette, $Re = 400$, resolution $11 \times 21 \times 11$, $\tau = 0.005$. Rows in gray colour are spurious modes of the OSSE model.

Open-loop	Closed-loop						
N/A	$\kappa = 1$	$\kappa = 0.75$	$\kappa = 0.5$	$\kappa = 0.25$	$\kappa = 0.1$	$\kappa = 0.05$	$\kappa = 0.01$
-0.00616850	-0.00616850	-0.00616850	-0.00616850	-0.00616850	-0.00616850	-0.00616850	-0.00616850
-0.02179350							
-0.02467401	-0.02467401	-0.02467401	-0.02467401	-0.02467401	-0.02467401	-0.02467401	-0.02467401
-0.02916371	$-0.02978409 \pm 0.01038326\iota$		$-0.03610096 \pm 0.01517840\iota$	$-0.04326076 \pm 0.01582502\iota$	$-0.04644707 \pm 0.01416857\iota$	$-0.04687619 \pm 0.01379233\iota$	$-0.04700984 \pm 0.01366497\iota$
-0.04029901		$-0.03197992 \pm 0.01261613\iota$					
-0.05047682	-0.05047682	-0.05047682	-0.05047682	-0.05047682	-0.05047682	-0.05047682	-0.05047682
	$-0.05199851 \pm 0.00507496\iota$	$-0.05358207 \pm 0.009.86820\iota$					
-0.05551652	-0.05551652	-0.05551652	-0.05551652	-0.05551652	-0.05551652	-0.05551652	-0.05551652
-0.05901236	$-0.07053345 \pm 0.00391896\iota$	$-0.07071389 \pm 0.005.33353\iota$	$-0.05735143 \pm 0.01582169\iota$	$-0.06912810 \pm 0.02320258\iota$	$-0.07769243 \pm 0.01811447\iota$	$-0.07934635 \pm 0.01886384\iota$	$-0.07998151 \pm 0.01904488\iota$
-0.06866850	-0.07411077	-0.07673632	$-0.07120304 \pm 0.00787277\iota$	$-0.07326254 \pm 0.01334365\iota$	$-0.08194622 \pm 0.01996398\iota$	$-0.08372417 \pm 0.01786389\iota$	$-0.08421364 \pm 0.01711437\iota$
-0.07114152	$-0.09317853 \pm 0.00200176\iota$	$-0.09347193 \pm 0.00554212\iota$	$-0.08976814 \pm 0.00369312\iota$	$-0.09808445 \pm 0.02006354\iota$			
-0.07192011			$-0.09428345 \pm 0.01013237\iota$				
-0.08717401							
-0.09841352							
-0.09869604	-0.09869604	-0.09869604	-0.09869604	-0.09869604	-0.09869604	-0.09869604	-0.09869604
-0.10224890	-0.10072903	-0.09927279	-0.11902676	$-0.09971596 \pm 0.02421341\iota$	$-0.11081107 \pm 0.03107793\iota$	$-0.11763357 \pm 0.03113639\iota$	$-0.11999820 \pm 0.03021476\iota$
-0.11432104	-0.11541478	-0.11630037	$-0.12980223 \pm 0.00400872\iota$	$-0.13250573 \pm 0.01852294\iota$	$-0.12574878 \pm 0.02809039\iota$	$-0.13207913 \pm 0.02185926\iota$	$-0.13352325 \pm 0.01916191\iota$
-0.11801652	-0.12001821	-0.12180225	$-0.14786280 \pm 0.00370250\iota$	$-0.14100002 \pm 0.01131878\iota$	$-0.14367599 \pm 0.03671235\iota$		
-0.13950375	-0.13804263	-0.13666929		$-0.14808844 \pm 0.00703254\iota$			
-0.14679350	$-0.14780919 \pm 0.00168446\iota$	$-0.14782284 \pm 0.00239698\iota$					
-0.14879044							
-0.14919879	-0.14919879	-0.14919879	-0.14919879	-0.14919879	-0.14919879	-0.14919879	-0.14919879
					$-0.14923247 \pm 0.01250264\iota$	$-0.15034323 \pm 0.01486941\iota$	$-0.15104529 \pm 0.01588740\iota$
						$-0.15366955 \pm 0.04240710\iota$	
-0.15421257	-0.15421257	-0.15421257	-0.15421257	-0.15421257	-0.15421257	-0.15421257	-0.15421257
-0.15735274	-0.15678471	-0.15631817	-0.15484001	$-0.17003865 \pm 0.01199405\iota$	$-0.17285279 \pm 0.03873418\iota$	$-0.18167713 \pm 0.03230722\iota$	$-0.15936312 \pm 0.04319127\iota$
-0.16119604	-0.16217892	-0.16296987	-0.16539535	-0.17839700	$-0.17450459 \pm 0.02520954\iota$	$-0.19303438 \pm 0.02571140\iota$	$-0.18749492 \pm 0.03372762\iota$
-0.16529901	-0.16730760	$-0.16916197 \pm 0.00224870\iota$	$-0.16929930 \pm 0.00532826\iota$	$-0.17986566 \pm 0.01164185\iota$	$-0.19143711 \pm 0.04148866\iota$	$-0.21240553 \pm 0.03625705\iota$	$-0.19615101 \pm 0.01678437\iota$
-0.16983757	-0.17030175	-0.17066828	-0.17174286	$-0.20494564 \pm 0.01220681\iota$	$-0.20830883 \pm 0.02737797\iota$	$-0.21634406 \pm 0.05458492\iota$	$-0.21595864 \pm 0.04108894\iota$
-0.17280556	-0.17092035	-0.19267449	-0.19090706	-0.22038325	$-0.21313838 \pm 0.03327261\iota$		
-0.19391361	-0.19323249	-0.19819186	-0.20258515				
-0.19614152	-0.19723524	-0.20986362	-0.20578389				
-0.21165422	-0.21070762	-0.21762640	-0.21878293				
-0.21671257	-0.21722548						
-0.22206611	-0.22206611	-0.22206611	-0.22206611	-0.22206611	-0.22206611	-0.22206611	-0.22206611

FIGURE 6.2: Measure of the normality of the linear OSSE model for different κ: leading eigenvalues of the $A^*Q_x + Q_xA$ (open-loop) and $(A + B_2K)^*Q_x + Q_x(A + B_2K)$ (closed-loop). Couette, $Re = 400$, resolution $11 \times 21 \times 11$, $\tau = 0.005$.

Open-loop	Closed-loop						
N/A	$\kappa = 1$	$\kappa = 0.75$	$\kappa = 0.5$	$\kappa = 0.25$	$\kappa = 0.1$	$\kappa = 0.05$	$\kappa = 0.01$
0.25534294	0.25391966	0.26309881	0.33314871	0.49245581	0.84054753	1.41054276	6.41837695
0.14686111	0.22453096	0.25282097	0.24972123	0.23393151	0.35979122	0.64371785	3.00203619
0.14177512	0.14630307	0.14587161	0.14465117	0.18889113	0.18367987	0.29417572	1.42196373
0.13760128	0.13791829	0.13817513	0.14351150	0.14392400	0.15556558	0.17892250	1.42196373
0.13111264	0.13079359	0.13342113	0.13895328	0.13835903	0.13885029	0.17084295	0.66537071
0.13085706	0.13038674	0.13054775	0.12985629	0.12638381	0.12744047	0.14780200	0.61372269
0.12685361	0.12972318	0.13002310	0.12899437	0.12502270	0.12505027	0.12765787	0.61372269
0.12628036	0.12644331	0.12612623	0.12578499	0.12432311	0.12017012	0.12317206	0.53363341
0.12586618	0.12615614	0.12605970	0.12522994	0.12377386	0.12016776	0.12017012	0.43876991
0.12483006	0.12541831	0.12507203	0.12432174	0.12368848	0.11505044	0.09841040	0.35722550
0.12458061	0.12451184	0.12446026	0.12409254	0.12062424	0.11051349	0.09303791	0.35722550
0.12445257	0.12402479	0.12369411	0.12282067	0.12017012	0.10480284	0.09258779	0.34690518
0.12396531	0.12364502	0.12339785	0.12275894	0.12016776	0.10476387	0.08977320	0.34690518
0.12367954	0.12323974	0.12289973	0.12275894	0.11915927	0.10180798	0.08126615	0.26678608
0.12323760	0.12285122	0.12255267	0.12270088	0.11904247	0.09987475	0.07638985	0.26678608
0.12306410	0.12263242	0.12240266	0.12193803	0.11824711	0.09651028	0.07623769	0.26570409
0.12257114	0.12225552	0.12229871	0.12170898	0.11794278	0.09587545	0.07420585	0.26570409
0.12206567	0.12215985	0.12184196	0.12135494	0.11737859	0.09527823	0.07104638	0.25747665
0.12202530	0.12176474	0.12157067	0.12102358	0.11698163	0.09516528	0.06506599	0.25747665
0.12201625	0.12160327	0.12127703	0.12094318	0.11657746	0.09483797	0.06349623	0.23895700
0.12188033	0.12152375	0.12124828	0.12047003	0.11649323	0.09253048	0.06154045	0.13769140
0.12168771	0.12129438	0.12099041	0.12035455	0.11648125	0.09235355	0.06086662	0.13591696
0.12147086	0.12106031	0.12074299	0.12017012	0.11631933	0.09219725	0.06050795	0.13369529
0.12125431	0.12083457	0.12055055	0.12016776	0.11571568	0.09203659	0.05949183	0.12544405
0.12108039	0.12078139	0.12051013	0.12013120	0.11570614	0.09189381	0.05686314	0.12452551
0.12106359	0.12070993	0.12043670	0.11989915	0.11560567	0.09189381	0.05583428	0.12163784
0.12101544	0.12062676	0.12032639	0.11984582	0.11523055	0.09149016	0.05572832	0.12017012
0.12094183	0.12053580	0.12022198	0.11966472	0.11511439	0.09084023	0.05554087	0.11555748
0.12085040	0.12043456	0.12017012	0.11959276	0.11487156	0.09077736	0.05520952	0.10071506
0.12074863	0.12032677	0.12011315	0.11947734	0.11477191	0.09068315	0.05417818	0.08657887

6.4.2 OSSE Linear Simulations

Data location	`osse/database/THESIS/06_couette_controlled_OSSE`
Script for simulations	`python3 osse/osse_riccati_couette.py 11 21 11 $1000kappa`
Script for comparison	`python3 osse/run_comparison_couette_thesis_642.py 11 21 11 1`
Script for cost	`python3 osse/osse_cost.py 11 21 11`

The OSSE model is simulated starting from the laminar PCF profile perturbed with a real unitary state-vector multiplied by a factor of 0.05 (the amplitude of the perturbation is not meaningful as the model is linear), and the optimal control law is enforced from time $t = 5$. The OSSE model is integrated in time via the BDF algorithm of the method `scipy.integrate.solve_ivp`, with absolute and relative tolerances of 10^{-8} over a period $T = 500$. The energy time-evolution for the open-loop and closed-loop systems for different values of κ are presented in figure 6.4.

When introducing the optimal forcing at $t = 5$, the energy of the system rises and becomes almost discontinuous. As expected, this rise is proportional to the intensity of the controller and likely due to the BDF algorithm requiring some time to adapt to the forcing, which can be considered as an external perturbation. After a couple of steps, this "discontinuity" disappears.

Following the perturbation, the un-actuated simulation faces an energy growth, peaking at $t = 40$. The optimal control diminishes the amplitude of this surge for each value of κ. The intensity of the energy growth decreases with higher controller strength and even disappears for $\kappa \leq 0.25$. The most powerful controllers (small κ) are even able maintain the energy norm at a lower level. Overall, after 150 time-units, all simulations are converging along the same stable eigenmode towards the laminar PCF profile. Even if the most powerful optimal control managed to avoid the energy growth following the initial perturbations, they do not lead to any long term benefit.

This can be interpreted thanks to the linear analysis: the leading eigenvalue -0.00616850 of the PCF profile in table 6.1 remains unaffected by the optimal control, whichever value of κ, while the other eigenvalues of smaller real-part magnitude are all shifted further in the left hand side by the optimal control law. The leading eigenmode -0.00616850 is predominant on the long term evolution of the system, hence leading to the same behavior beyond $t = 150$ for each simulation. The other eigenvalues are responsible for the rapid energy growth after the perturbation. As their amplitude is diminished with the optimal forcing, they are not influential in controlled simulations and the energy growth is weakened or does not develop. Beyond $t = 150$, all the other eigenmodes faded and the state is literally parallel to the stable eigenmode -0.00616850, with decreasing amplitude.

The costs associated with the state and optimal forcing are gathered in table 6.2 and in figure 6.3. They give insight on the predominance of the state versus the control in the optimization process, as their sum corresponds to the cost function to minimize in the Riccati problem (see section 5.2.2). The cost of the state actually corresponds to the kinetic energy density. As a consequence, the previous observations made on figure 6.4 are also valid here. The cost associated with the state follows the same evolution for each value of κ, except during the transient energy growth. The cost associated with the control also observes the same behavior for each kappa, at different order of magnitude. The parameter κ is directly responsible for the different order of magnitude as it is included in the matrix Q_q. It is interesting to note here that while the cost of the state decreases by up to 3 orders of magnitude over the period $T = 500$, the cost of the forcing is reduced by 13 orders of magnitude for $\kappa = 1.0$ and even 22 for $\kappa = 0.01$. This implies that at this stage of the simulation, the forcing is minimal and the state is almost at its optimal position.

TABLE 6.2: OSSE linear simulations: cost associated with the state and to the control forcing for different values of κ at different time steps corresponding to the simulations presented in fig. 6.4, as well as the time required on one core of Iridis5 to compute the time-integration.

κ	Time-step	cost($\boldsymbol{x}$) = $\boldsymbol{x}Q_x\boldsymbol{x}$	cost($\boldsymbol{q}$) = $\boldsymbol{q}Q_q\boldsymbol{q}$	Calculation time
1.0	1	1.77×10^{-3}	1.09×10^{-3}	0
	25	2.71×10^{-3}	9.00×10^{-4}	6
	100	7.19×10^{-4}	3.70×10^{-5}	9
	500	5.01×10^{-6}	9.80×10^{-16}	29
0.75	1	3.54×10^{-3}	2.66×10^{-3}	0
	25	4.82×10^{-3}	1.96×10^{-3}	5
	100	1.20×10^{-3}	4.38×10^{-5}	9
	500	1.00×10^{-5}	3.89×10^{-17}	29
0.5	1	1.77×10^{-3}	1.49×10^{-3}	0
	25	2.00×10^{-3}	8.63×10^{-4}	5
	100	5.21×10^{-4}	6.21×10^{-6}	9
	500	1.01×10^{-6}	2.00×10^{-18}	29
0.25	1	3.55×10^{-3}	2.68×10^{-3}	0
	25	3.05×10^{-3}	7.50×10^{-4}	6
	100	9.85×10^{-4}	9.21×10^{-47}	9
	500	1.00×10^{-5}	8.19×10^{-22}	28
0.1	1	1.77×10^{-3}	1.01×10^{-3}	1
	25	1.28×10^{-3}	6.01×10^{-5}	6
	100	4.89×10^{-4}	4.74×10^{-8}	10
	500	1.15×10^{-6}	5.34×10^{-24}	29
0.05	1	1.77×10^{-3}	9.33×10^{-4}	1
	25	1.22×10^{-3}	1.41×10^{-5}	8
	100	4.89×10^{-4}	1.14×10^{-8}	11
	500	5.01×10^{-6}	6.86×10^{-25}	31
0.01	1	1.77×10^{-3}	9.64×10^{-4}	7
	25	1.19×10^{-3}	5.53×10^{-7}	35
	100	4.89×10^{-5}	4.50×10^{-10}	38
	500	5.01×10^{-6}	2.02×10^{-26}	58

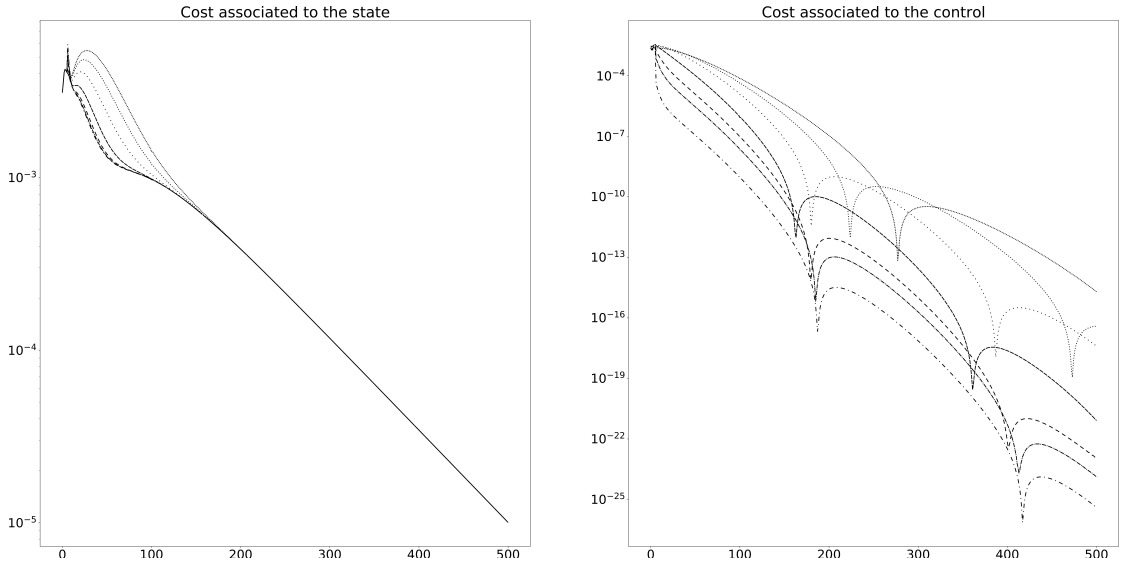

A) Time-evolution over $t = [0 : 500]$

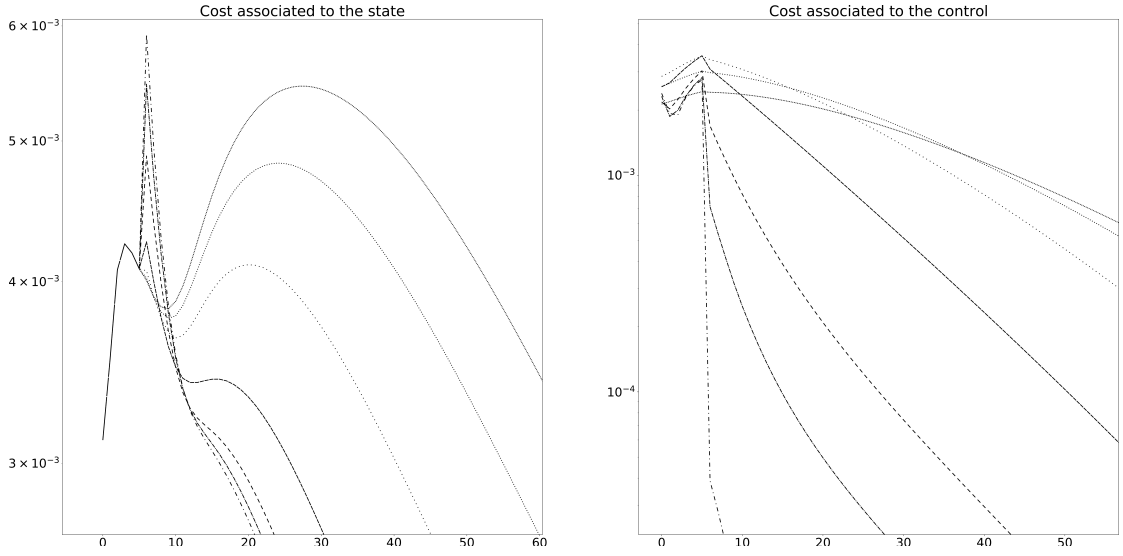

B) Time-evolution over $t = [0 : 60]$

FIGURE 6.3: OSSE linear simulations: Time-evolution of the cost associated with the state and to the control forcing for different values of κ corresponding to the simulations presented in fig. 6.4.

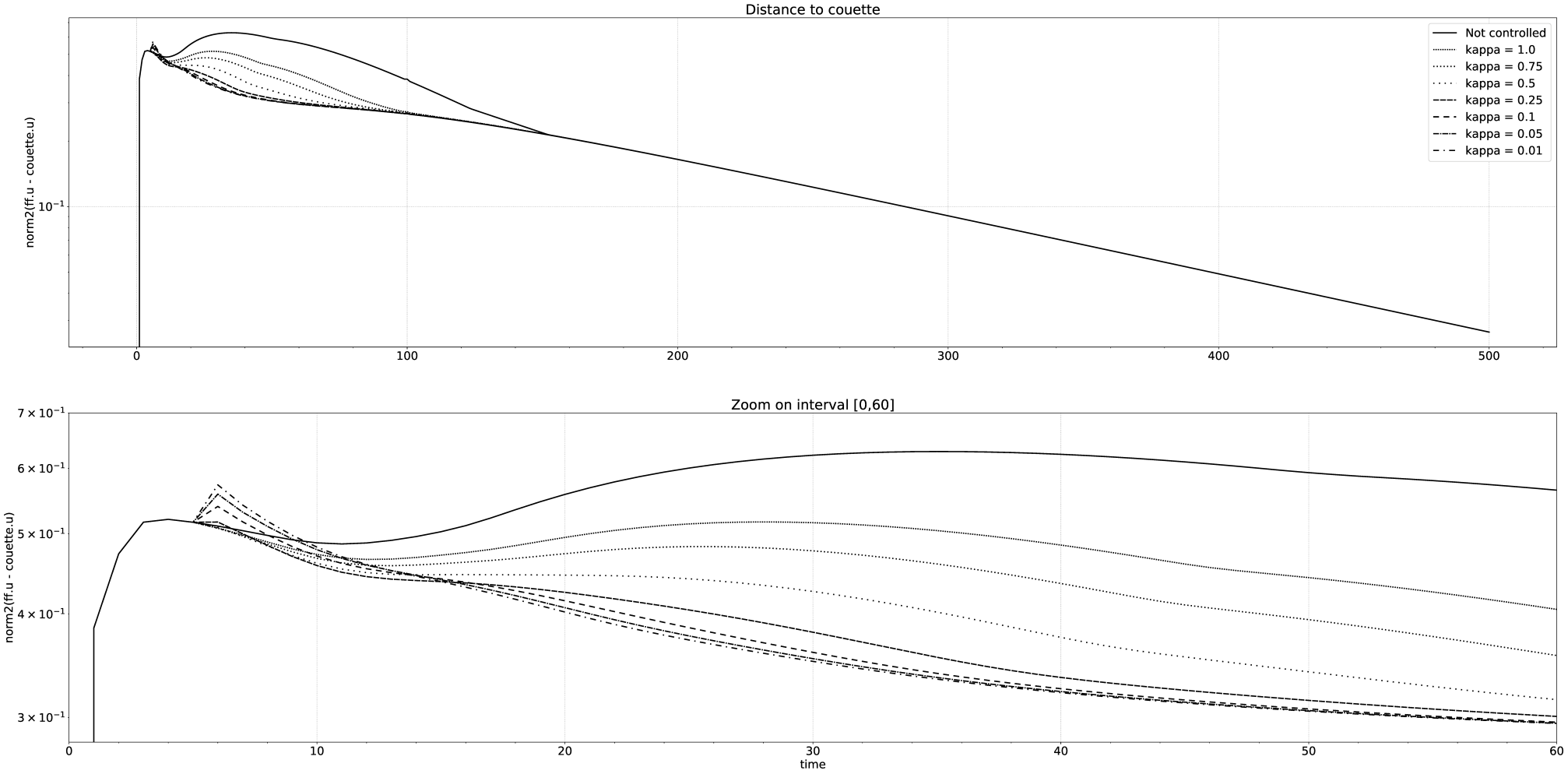

FIGURE 6.4: OSSE linear simulations: Time-evolution of the energy norm of the state-vector (i.e. distance to the laminar PCF profile) controlled by an optimal forcing for different value of κ. The continuous black line represents the un-actuated system. The system is initially perturbed with a real unitary vector multiplied by a factor 0.05. The control starts at $t = 5$. (time horizon $[0, 500]$ and zoom over $[0, 60]$, resolution $11 \times 21 \times 11$, $Re = 400$, $\tau = 0.005$).

6.4.3 Linearized Channelflow simulations

Data location	`osse/database/THESIS/`
	`06_couette_controlled_channelflow/`
	`controller_K_OSSE/couette/Re=400/LinearAboutProfile`

Channelflow Simulation	`channelflow/trunk/PHD/controller_k_couette.cpp`
Script for comparison	`python3 osse/run_comparison_couette_thesis_643.py` `11 21 11 1`

As explained in section 5.5, the linearization of the Navier-Stokes equations is only available around a laminar profile in Channelflow. As a consequence, the results previously obtained with the linear OSSE model shall be recovered within Channelflow. Parameters and DNS flags for the linearized Channelflow simulations are given in table 6.3. The non-linear terms are expressed in their linearized form given in eq. 5.53.

Linearized Channelflow simulations with optimal control are presented in figure 6.5. They are initialized with a impulse perturbation of magnitude 10^{-8} at time $t = 10$ and the control is prompted at $t = 5$. Unfortunately, the actuation is unsettling the simulations and leads to an excessive CFL number (> 1), therefore interrupting the simulation early. With higher perturbation amplitude and/or more powerful control, this phenomenon arises sooner. For value of κ below 0.25, the actuation is so disruptive that the simulations immediately interrupt.

Unfortunately, the optimal control law enforced via the ChannelFlow Boundary Condition package (CFBC) of Heins (2015) is failing when used within linearized Channelflow simulations. The implementation of the actuation via the CFBC was validated for a linearized Channelflow simulation and a laminar PCF profile for different wave-number pairs in section 5.5.1. However, this validation and the one presented in the Ph.D thesis of Heins (2015) were restricted to a limited collection of wave-number pairs. This complication may be related to the actuation of higher-order modes, or to the control itself. We believe that this problem is due to the association of the linearized Channelflow model, the optimal control and the ChannelFlow Boundary Condition package package. Despite this issue, simulations performed with a non-linear Channelflow in the next section are actually satisfying (except for very powerful controller).

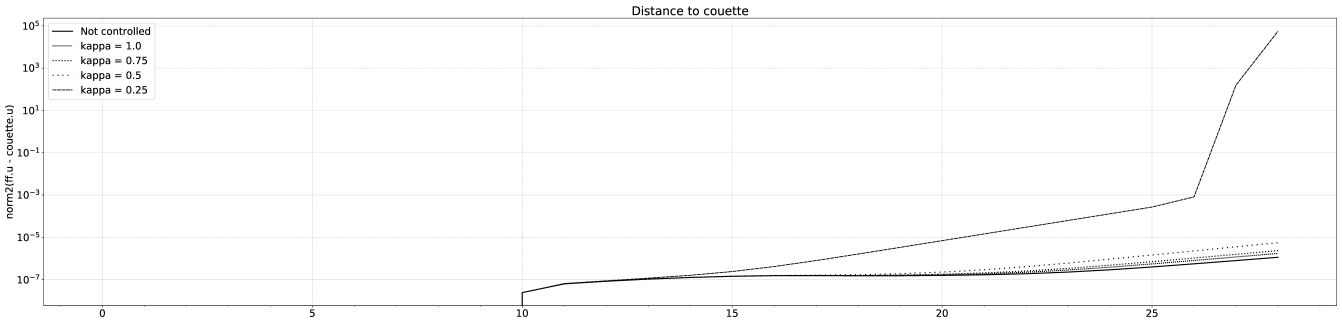

FIGURE 6.5: Channelflow simulations with non-linear terms under a linearized form (eq. 5.53): Time-evolution of the energy norm of the state-vector (i.e. distance to the laminar PCF profile) controlled by an optimal forcing for different value of κ. The continuous black line represents the un-actuated system. The system is perturbed at $t = 10$ with a Dirac of magnitude $1E - 8$ The control is applied at $t = 5$ for different value of κ. The time-horizon is limited to $t = 28$ when the actuation perturbs the simulation up to an excessive CFL number (> 1). (time horizon $[0, 500]$ and zoom over $[0, 60]$, resolution $11 \times 21 \times 11$, $Re = 400$, $\tau = 0.005$).

6.4.4 Non-linear Channelflow simulations

Data location	`osse/database/THESIS/ 06_couette_controlled_channelflow/ controller_K_OSSE/couette/Re=400/skewsymmetric`
Channelflow Simulation	`channelflow/trunk/PHD/controller_k_couette.cpp`
Script for comparison	`python3 osse/run_comparison_couette_thesis_644.py 11 21 11 1`

Non-linear Channelflow simulations with optimal control are presented in figure 6.7. They are computed with the non-linear terms under the skew-symmetric form (eq. 5.61). They are initialized with a Dirac perturbation of magnitude 10^{-8} at time $t = 10$ and the control is prompted at $t = 5$. Due to the low amplitude of the perturbations, the non-linearity is marginal. The simulations are behaving as in the linear OSSE simulations, except for $\kappa = 0.25$. After a slight energy growth following the perturbation, all simulations (except $\kappa = 0.25$) are converging along the same stable eigenmode towards the laminar PCF profile. The most powerful optimal controls (except $\kappa = 0.25$) avoid the energy growth following the initial perturbations, but do not lead to any benefit on the long term, as in the linear OSSE simulations.

Nonetheless, the simulation for $\kappa = 0.25$ is different. Immediately after the energy burst due to the perturbation, the simulation is linearly diverging away from the PCF profile for this κ. This evolution does not correspond to any eigen-mode found during the linear analysis, as it would correspond to a positive real-part eigenvalue. It appears from figure 6.6 that the case $\kappa = 0.25$ is dominated by the actuation at the wall, and not by the eigen-spectrum, on the contrary to higher values of κ (e.g. $\kappa = 0.5$ in fig.6.6) where the actuation is not predominant against the perturbation around the baseflow. The

TABLE 6.3: Parameters and DNS flags for Channelflow simulations presented in sections 6.4.3, 6.4.4 and 6.4.5.

PARAMETER	VALUE
baseflow	Couette
Nx, Ny, Nz	§6.4.3 and 6.4.4: $11 \times 21 \times 11$
	§6.4.5: $11 \times \{21, 27, 35, 65\} \times 11$
Reynolds	`400.0`
nu	`1 / Re`
Lx	`eq1.Lx() = 2*pi/1.14`
a	`eq1.a() = -1.0`
b	`eq1.b() = +1.0`
Lz	`eq1.Lz() = 2*pi/2.5`
Baseflow	`LinearBase`
Nonlinearity	§6.4.3: `LinearAboutProfile`
	§6.4.4 and 6.4.5: `SkewSymmetric`
Initstepping	`CNRK2`
Timestepping	`SBDF4`
Dealiasing	`DealiasXZ`
taucorrection	`true`
constraint	`PressureGradient`
dPdx	`0.0`
uupperwall	`+1.0`
ulowerwall	`-1.0`
CFLmin	`0.10`
CFLmax	`0.80`
dtmax	`0.005 (= tau)`
dtmin	`0.0000001`
dt0	`dtmax`
variable_dt	`true`
T0	`0.0`
T1	`1000.0`
dt	`1`
controller starts at	`5`
perturbation initiated at	`10`
perturbation magnitude	`1E-8`
perturbation method	`addPerturbations(3,3,1E-8,0.5)`

fields at $t = 200$ for $\kappa = 0.25$ is indeed very similar to the actuation field presented in figures 5.8. Exactly, it is dominated by the actuation q_v on the wall-normal velocity for the particular Fourier mode $(0, 1)$. Interestingly, this mode was found to be the most effective actuation mode to target the 1st and 2nd eigenmodes of EQ1 during the modal controllability analysis operated in section 5.4.3.

The possibility that the optimal solution is not valid for $\kappa = 0.25$ is unlikely, as linear analysis and linear OSSE simulations demonstrated the relaminarization of the PCF profile for values of κ down to 0.01. A deficiency in the implementation of the control law in Channelflow is unlikely as well, as it would have affected the simulations for other

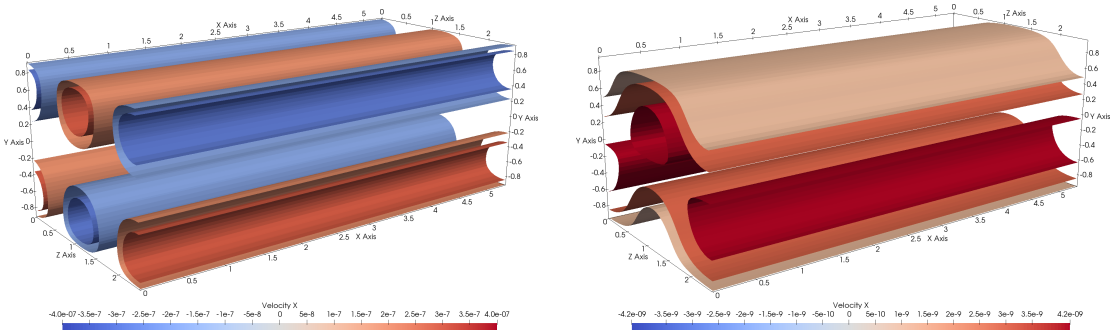

A) $\kappa = 0.25$, contour u at $\pm 2 \times 10^{-7}$ and $\pm 3 \times 10^{-7}$.

B) $\kappa = 0.5$, contour u at 1×10^{-9}, $\pm 3 \times 10^{-9}$ and 6×10^{-9}.

FIGURE 6.6: Velocity field at $t = 200$ for simulations at $\kappa = 0.25$ and $\kappa = 0.5$ of section 6.4.4 and associated with fig.6.7. Surfaces of constant streamwise velocity u for different amplitudes. (Couette, $11 \times 21 \times 11$, $Re = 400$, $\tau = 0.005$)

values of κ. Yet, the actuation at $\kappa = 0.25$ may be so intense that it requires particular numerical requirements, i.e. better precision, smaller actuation-time or integration time, higher resolution. Nonetheless, despite changes within these parameters, we did not manage to improve this result. The origin of the problem may lie deeper within the implementation of the CFBC package and is not clear to the author. Linearized simulations of Channelflow with the CFBC package would likely elucidate this problem but are impossible at the moment (§6.4.3).

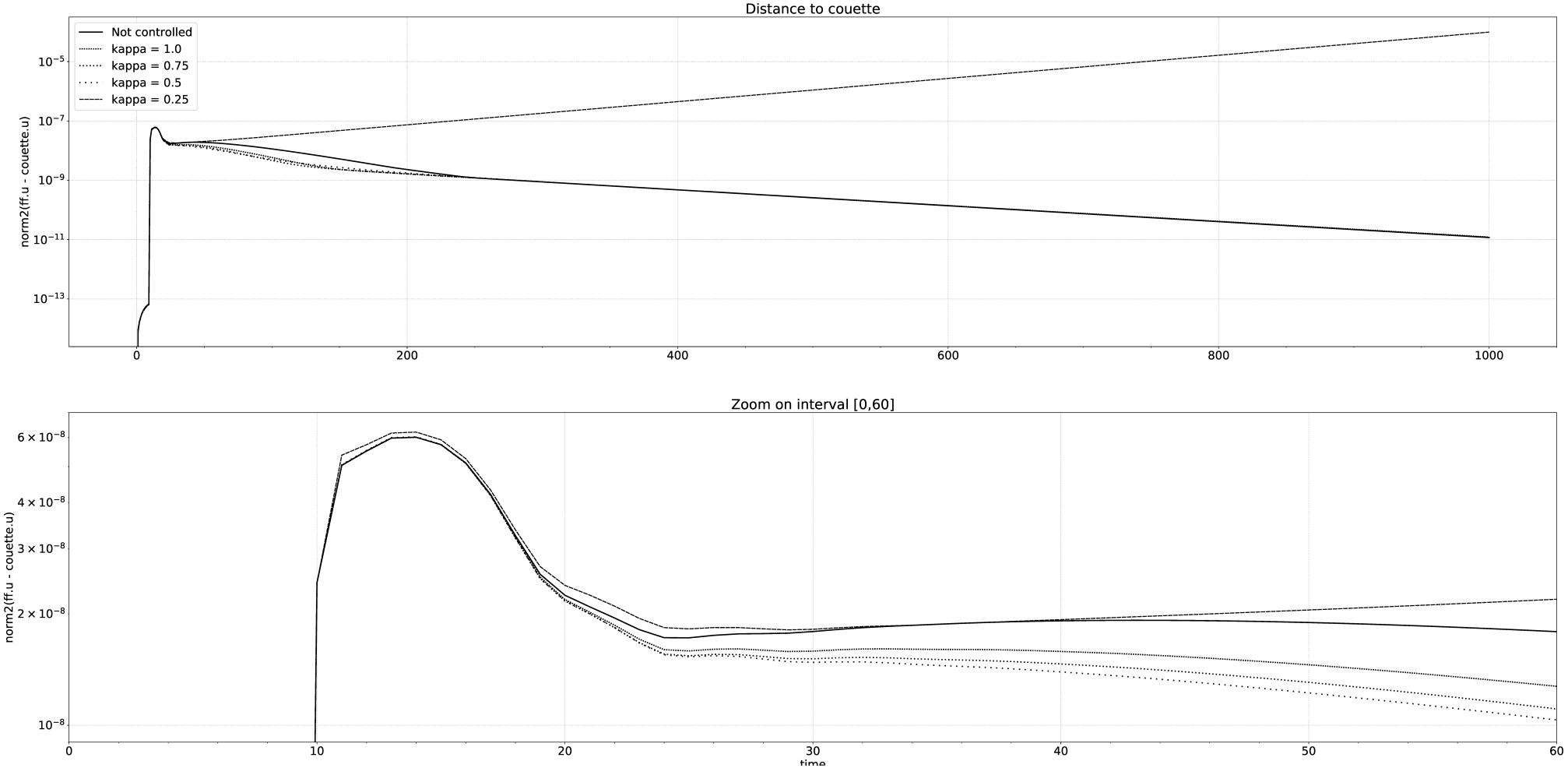

FIGURE 6.7: Channelflow simulations with non-linear terms under a skew-symmetric form (eq. 5.61): Time-evolution of the energy norm of the state-vector (i.e. distance to the laminar PCF profile) controlled by an optimal forcing for different value of κ. The continuous black line represents the un-actuated system. The system is perturbed at $t = 10$ with a Dirac of magnitude $1E - 8$. The control is applied at $t = 5$ for different value of κ. (time horizon $[0, 500]$ and zoom over $[0, 60]$, resolution $11 \times 21 \times 11$, $Re = 400$, $\tau = 0.005$).

6.4.5 Impact of the wall-normal resolution

Script for...	`python3 osse/osse_riccati_couette.py 11 $Ny 11 250`
Riccati solutions	`python3 osse/rosse_riccati_couette.py 11 $Ny 11 250`
	`python3 osse/osse_riccati_block_get_K.py 11 $Ny 11 250`
Location of the...	`osse/database/THESIS/`
Riccati solutions	`06_couette_CFBC_kappa=0.25_resolution/`
	`OSSE`
	`OSSE_block`
	`ROSSE`
Channelflow simulations	`channelflow/trunk/PHD/controller_k_couette.cpp`
	`channelflow/trunk/PHD/controller_k_couette_rosse.cpp`
Data location	`osse/database/THESIS/`
	`06_couette_CFBC_kappa=0.25_resolution/`
	`channelflow_simulations`
Script for comparison	`python3 osse/run_comparison_couette_thesis_645.py`

We investigate here the impact of the wall-normal resolution on Channelflow simulations controlled at $\kappa = 0.25$ with a PCF laminar baseflow. Non-linear Channelflow simulations with optimal control at $\kappa = 0.25$ are presented for different resolutions in figure 6.8. Stream- and spanwise resolutions are still here 11×11. Simulations are computed with the non-linear terms under the skew-symmetric form (eq. 5.61). They are initialized with a Dirac perturbation of magnitude 10^{-8} at time $t = 10$ and the control is prompted at $t = 5$. The optimal control laws are calculated for the OSSE and ROSSE model at wall-normal resolution $N_y = \{21, 27, 35\}$. Moreover, the optimal control law for $N_y = 65$ is calculated by "block" for each wave-number pair separately with the OSS model, i.e. the same approach followed by Heins (2015) or Bamieh et al. (2002), as this resolution is not accessible with the OSSE or ROSSE model within current time and memory limitations.

First of all, it is important to note here that the optimal control law calculated with the OSSE and ROSSE model are strictly identical. Equivalent simulations are exactly overlapping each-other in figure 6.8. Therefore, the Riccati solution and the Channelflow implementation is equivalent for both cases.

It then appears the wall-normal resolution does not influence the results of the simulation, even for resolution up to $N_y = 65$. In each case, the simulations at $\kappa = 0.25$ diverges linearly away from the linear PCF profile along the same unstable eigenmode. This hypothesis can consequently be excluded.

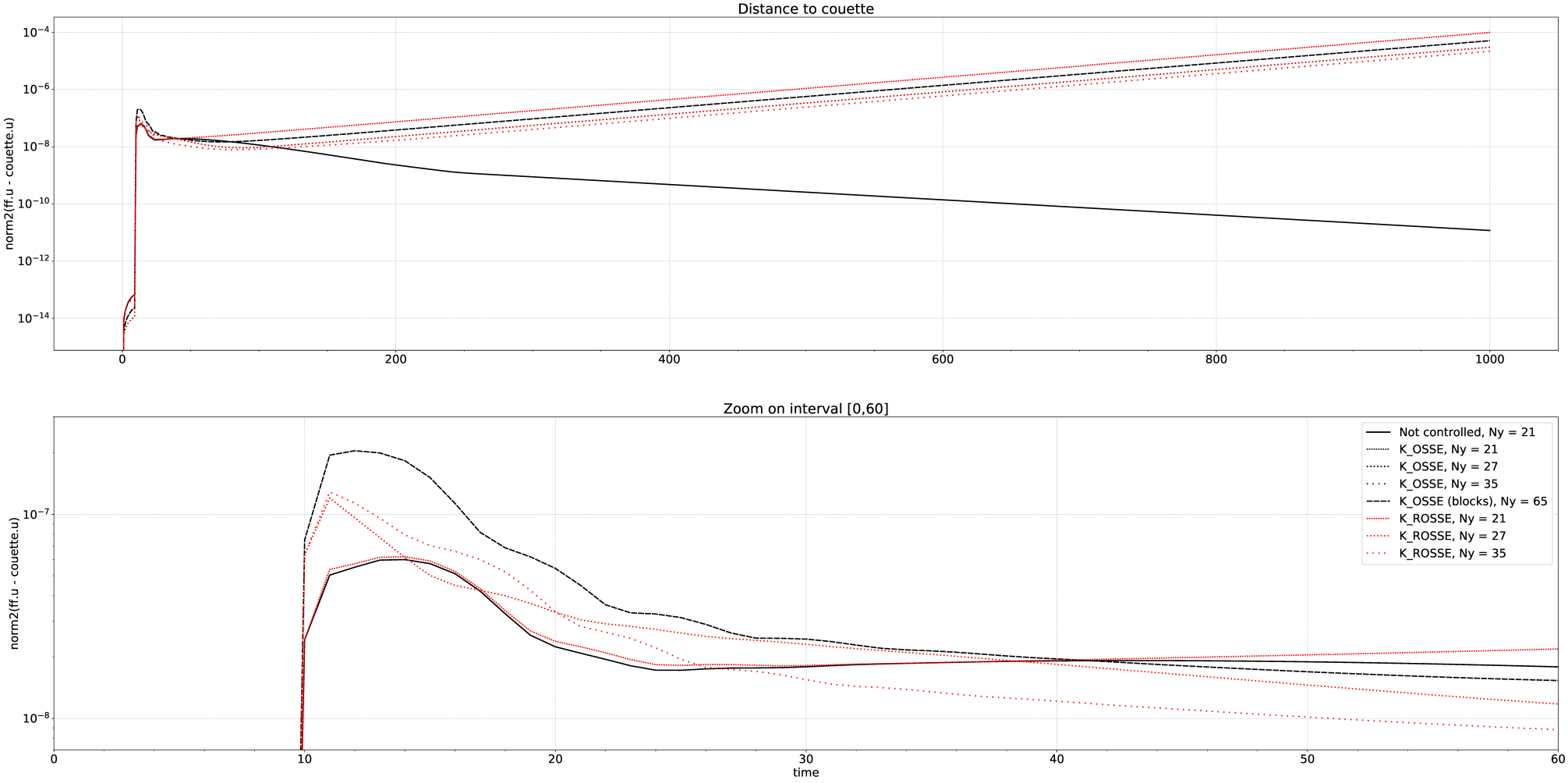

FIGURE 6.8: Channelflow simulations with non-linear terms under a skew-symmetric form (eq. 5.61) for different wall-normal resolutions: Time-evolution of the energy norm of the state-vector (i.e. distance to the laminar PCF profile) controlled by an optimal forcing at the same value of $\kappa = 0.25$. The continuous black line represents the un-actuated system. The wall-normal resolution corresponds to the one used to calculate the optimal control law with the OSSE model ($N_y = 21, 27, 35$), OSSE model by blocks ($N_y = 65$) and ROSSE model ($N_y = 21, 27, 35$). The system is perturbed at $t = 10$ with a Dirac of magnitude $1E-8$ The control is applied at $t = 5$ for different value of κ. (time horizon $[0, 500]$ and zoom over $[0, 60]$, resolution $11 \times N_y \times 11$, $\kappa = 0.25$, $Re = 400$, $\tau = 0.005$).

6.4.6 Conclusion

The optimal control law improves the linear stability of the laminar Plane Couette Flow profile and reduces the energy growth following a perturbation. As the controller intensifies, the linear stability is enhanced but on the other hand, the normality of the closed-loop system deteriorates. OSSE linear simulations are all converging appropriately along the leading stable eigenmode. Unfortunately, this result can not be reproduced with a linear Channelflow simulation as it would require an update of the CFBC package of Heins (2015) for Channeflow 2.0. The optimal control law and their Channelflow implementation is strictly equivalent with the OSSE and ROSSE model.

The implementation of the optimal control law in non-linear Channelflow simulations is valid but limited to values of κ above a certain threshold. For the Plane Couette Flow profile, this critical value is situated between $\kappa = 0.25$ and $\kappa = 0.5$. The source of this problem remains unclear, but is not related to the wall-normal resolution. We presume that Channelflow and the CFBC package of Heins (2015) can not handle intense forcing at the walls. The wall-actuation likely unsettle the integration algorithm and lead to nonphysical results. The critical value κ_c is hardly predictable: it might indeed be case-dependent and affect other system and/or set of parameters in different manner.

Chapter summary

- The derivation of the optimal control gain via the Riccati equation is demonstrated and developed with the OSSE and ROSSE models.
- Different methods exist to determine the optimal control gain, either by solving directly the Riccati equation or bypassing it. Model reduction can be applied beforehand to ease the computation, or during the process while solving the Riccati equation.
- It was not possible to derive or implement a specific procedure in this thesis, and we will use as a consequence the method implemented in `Python` based on the Schur algorithm using a QZ decomposition.
- The calculation of the optimal control law and its implementation via the OSSE or ROSSE models are strictly equivalent.
- The optimal control law and its implementation in Channelflow are validated with a laminar Plane Couette Flow profile. It is shown via a linear analysis that the optimal control law improves the stability but deteriorates the normality of the closed-loop system.

- The implementation of the optimal control law in non-linear Channelflow simulations is valid but limited to values of κ above a certain threshold. For the Plane Couette Flow profile, this critical value is situated between $\kappa = 0.25$ and $\kappa = 0.5$. We presume that Channelflow and the CFBC package of Heins (2015) can not handle intense forcing at the walls.

Chapter 7

Stabilization of the Nagata Lower-Branch solution

This chapter is dedicated to the stabilization via LQR optimal regulation of the Nagata (1990) lower-branch solution, or EQ1, at a Reynolds number of 400. This application necessitates both the controller design targeting an invariant solution in chapter 5 and the procedure to determine the optimal control law in chapter 6 to be functional and validated. It is now possible to reach the final stage of this thesis and apply the procedure developed in these chapters to the Nagata (1990) lower-branch solution. Precisely, we intend to initiate controlled simulations of the linear ROSSE model and non-linear Channelflow software with the Nagata (1990) lower-branch solution. We expect the optimal control law, designed specifically to stabilize EQ1 along the same procedure as for the laminar PCF in section 6.4, to maintain the dynamical state of the closed-loop system at this particular position. To make things clear, we do not plan to attract an arbitrary turbulent dynamical state towards EQ1 and stabilize it there. Such an approach may not work given the current lack of global stability guarantees, and may constitute a future direction of research. Rather, the idea is to locally stabilize EQ1 by introducing a radius of stability via the optimal control and prevent the state to escape the equilibrium.

7.1 Optimal control gain

Data location	`osse/database/THESIS/07_eq1_controlled_ROSSE`
Script for Riccati...	`python3 osse/rosse_riccati.py`
solutions and analysis	`1 17 27 17 $1000kappa`

As advocated in section 6.3, the resolution for the Nagata (1990) lower-branch is $17 \times 27 \times 17$. The actuation-time constant is set at $\tau = 0.005$. The optimal control gain is performed along the same procedure as for the laminar PCF profile in section 6.4. In particular, the actuation is limited solely to the wall-normal velocity at the wall, implying a reduction of the dimensions of matrix B_2.

All calculations are here performed with the ROSSE model: the OSSE model can not reach the sufficient resolution of $17 \times 27 \times 17$ in order for EQ1 to converge with the method `findsoln`. The ROSSE model indeed reduces the dimension of the state by approximately two, and in practice only requires approximately two thirds of the memory taken by the equivalent OSSE model to solve the Riccati equation. The Riccati solutions are calculated with the `Python` method given in section 6.2.4 for different values of κ,

$$\kappa = \big[8.0,\ 7.0,\ 6.0,\ 5.0,\ 4.0,\ 3.0,\ 2.0,\ 1.0,\ 0.9,\ 0.8,\ 0.7,\ 0.6,\ 0.5,\ 0.4,\ 0.3,\ 0.2\big], \tag{7.1}$$

on the ECPSC01 server of the ECPS group of Tobias Schneider at the École Polytechnique Fédérale de Lausanne (Switzerland). This server was exploited rather than the HPC Iridis5 as the calculation is single-thread and requires computational time well beyond the wall-time of Iridis5. On this clusters, each Riccati solution necessitates a calculation time of 10 to 12 days, as well as RAM memory requirement up to 140Gb.

Unfortunately, the `Python` method did not converge for the values $\kappa = \{1.0, 2.0\}$. The reason for this interruption is not clear and relates to the internal issue. It may be noted however that for $\kappa = \{1.0, 2.0\}$, the terms in the cost function associated with the state and with the forcing possess the order of magnitude. On the contrary, for lower or higher value of κ, one of these terms dominates the other. We presume that this configuration complicates the optimization problem, leading to either the system not fulfilling the mathematical prerequisite of the method, or the convergence rate deteriorating.

7.2 Linear Analysis

Eigenvalues

The eigenvalues of the open- and closed-loop systems are calculated as in §4.8 with `Python` packages. The leading values are gathered in table 7.1 and 7.2 for each value of κ and compared against the open-loop system. The spurious modes of the OSSE model are here coloured in gray and were found previously in table 4.1.

As a reminder, we here study the leading eigenvalues, i.e. with the highest real part, as a dynamical system is stable if all its eigenvalues are strictly negative. The imaginary part is not a major importance, as only associated to an oscillation frequency in the signal but not with stability. Therefore, we compare the original unstable open-loop

system (without any control applied) against the new closed-loop systems, enforced at the wall by an optimal forcing.

The closed-loop systems do not posses any positive real-part eigenvalue: the optimal control law manages to stabilize the linear ROSSE system and makes the Nagata (1990) lower-branch solution linearly stable. For decreasing values of κ —higher control "strength"—, the real part of each eigenvalue is moved further onto the left hand side (their negative real part decreases). For instance, all the eigenvalues for $\kappa = 0.2$ are shifted to the left in comparison to $\kappa = 0.3$. As a consequence, the linear stability of the closed-loop system improves with decreasing value of κ. In brief, the optimal control makes the Nagata (1990) lower-branch solution linearly stable and a stronger control improves its linear stability.

Normality

Explanations, references and mathematical details on normality are given in appendix section H.3.1. Normality is here evaluated to estimate the impact of the feedback control on potential transient energy growth. This risk aggravates with lower normality degree. Measures of the normality, i.e. leading eigenvalues of the "normality" operator $A^*Q_x + Q_xA$ or $(A+B_2K)^*Q_x + Q_x(A+B_2K)$, are gathered in table 7.3 and 7.4 for the open- and closed-loop ROSSE linear systems.

Any control strength is deeply affecting the normality of the ROSSE system. Particularly, as soon as an optimal control forcing is applied, the normality measure is multiplied by four. With increasing controller strength —decreasing κ—, this value slightly increases. It appears that the other eigenvalues of this normality operator are not drastically affected by the optimal control law, as long as κ is above or equal to 3.0. For values of κ below 0.9, new leading eigenvalues of the normality measure emerges and deteriorates the normality of the linear closed-loop system.

The non-normality of the linear ROSSE model and the risk of transient energy growth escalate with increasing controller strength. As a consequence, we expect the optimal control to disrupt the initial phase of the simulations by prompting an energy burst. This energy growth is benign for linear simulations: as the ROSSE model is now linearly stable, this perturbation will remain transient for the linear case. Nonetheless, its repercussions on the non-linear simulations are less predictable. A slight perturbation can indeed initiate the transition to turbulence. Therefore, we expect powerful optimal control law (small values of κ) to disturb the initial phase of non-linear simulations and likely push the state away from EQ1. This may bring the state outside the basin of attraction of the optimal control law or break the hypothesis of small-perturbation, which is fundamental in the linearization procedure of §4.1.1 and for the entire control design.

Conclusion

To conclude, the optimal control law makes the Nagata (1990) lower-branch solution linearly stable. An increase in the optimal control strength (lower values of κ) improves the linear stability of the OSSE model. Nonetheless, the optimal control enhances the risk of transient energy growth as the normality of the system deteriorates with increasing controller strength. For very powerful control, e.g. $\kappa = \{0.3, 0.2\}$, it might even push the state away from the neighborhood of the laminar solution, either outside the basin of attraction of the controller or beyond the area of validity of the linearization procedure.

FIGURE 7.1: Measure of the stability of the linear OSSE model for different κ: leading eigenvalues of A (open-loop) and $A + B_2K$ (closed-loop). EQ1, $Re = 400$, resolution $17 \times 27 \times 17$, $\tau = 0.005$. Rows in gray colour are spurious modes of the OSSE model.

Open-loop	Closed-loop					
N/A	$\kappa = 8.0$	$\kappa = 7.0$	$\kappa = 6.0$	$\kappa = 5.0$	$\kappa = 4.0$	$\kappa = 3.0$
$+0.05012030$	$-0.00388118 \pm 0.00358370\iota$	$-0.00413135 \pm 0.00384501\iota$	$-0.00444264 \pm 0.00416562\iota$	$-0.00484431 \pm 0.00457182\iota$	$-0.00538966 \pm 0.00510973\iota$	$-0.00619016 \pm 0.00586766\iota$
$+0.00000822$	-0.00667719	-0.00670080	-0.00673695	-0.00679631	-0.00690372	-0.00712792
-0.00001535	$-0.00833997 \pm 0.00773078\iota$	$-0.00880053 \pm 0.00831104\iota$	$-0.00938113 \pm 0.00901934\iota$	$-0.01014020 \pm 0.00991730\iota$	$-0.01118258 \pm 0.01111822\iota$	-0.01142518
-0.00201851	-0.01095112	-0.01104001	-0.01113438	-0.0112325	-0.01133125	$-0.01272189 \pm 0.01285811\iota$
-0.00659922	-0.01364789	-0.01366389	-0.0136882	-0.01372738	-0.01379621	-0.01393283
-0.00689421	-0.02396828	-0.02398039	-0.0239989	-0.02402906	-0.02408287	-0.02419234
-0.00974286						
-0.01359392						
-0.02392780						
-0.02467401	-0.02467401	-0.02467401	-0.02467401	-0.02467401	-0.02467401	-0.02467401
-0.03347429	-0.03360269	-0.03364197	-0.03370246	-0.03380293	-0.03398785	-0.0343878
-0.03704042	-0.03711474	-0.03713715	-0.03717148	-0.03722763	-0.03732882	-0.03753807
-0.04260237	-0.04265473	-0.04267073	-0.04269530	-0.04273608	-0.04281091	-0.04297146
$-0.04535368 \pm 0.01888011\iota$	$-0.04534383 \pm 0.01889635\iota$	$-0.04534084 \pm 0.01890136\iota$	$-0.04533623 \pm 0.01890901\iota$	$-0.04532865 \pm 0.01892175\iota$	$-0.04531476 \pm 0.01894531\iota$	$-0.04528537 \pm 0.01899638\iota$
$-0.04850491 \pm 0.10251949\iota$	$-0.04850667 \pm 0.10251664\iota$	$-0.04850719 \pm 0.10251576\iota$	$-0.04850801 \pm 0.10251443\iota$	$-0.04850933 \pm 0.10251219\iota$	$-0.04851179 \pm 0.10250810\iota$	$-0.04851707 \pm 0.10249926\iota$
	-0.05010931	-0.05010605	-0.05010115	-0.05009274	-0.05007726	-0.05004298
-0.05047682	-0.05047682	-0.05047682	-0.05047682	-0.05047682	-0.05047682	-0.05047682
$-0.05181504 \pm 0.02605578\iota$	$-0.05181274 \pm 0.02605499\iota$	$-0.05181203 \pm 0.02605471\iota$	$-0.05181096 \pm 0.02605434\iota$	$-0.05180918 \pm 0.02605366\iota$	$-0.05180588 \pm 0.02605256\iota$	$-0.05179877 \pm 0.02604994\iota$
$-0.06237659 \pm 0.03117288\iota$	$-0.06235730 \pm 0.03121732\iota$	$-0.06235144 \pm 0.03123090\iota$	$-0.06234236 \pm 0.03125197\iota$	$-0.06232743 \pm 0.03128680\iota$	$-0.06230028 \pm 0.03135104\iota$	$-0.06224260 \pm 0.03149035\iota$
$-0.06869189 \pm 0.00656215\iota$	$-0.06870562 \pm 0.00657556\iota$	$-0.06870985 \pm 0.00657967\iota$	$-0.06871633 \pm 0.00658597\iota$	$-0.06872712 \pm 0.00659644\iota$	$-0.06874696 \pm 0.00661570\iota$	$-0.06878985 \pm 0.00665716\iota$
-0.08774949	-0.08775525	-0.08775704	-0.08775977	-0.08776423	-0.08777259	-0.08779052
-0.09197342	-0.09199415	-0.09200049	-0.09201028	-0.09202648	-0.09205615	-0.09212006
-0.09869605	-0.09869605	-0.09869605	-0.09869605	-0.09869605	-0.09869605	-0.09869605
-0.10570541	-0.10569814	-0.10569594	-0.10569253	-0.10568681	-0.10567669	-0.10565487
-0.10686890	-0.10687750	-0.10688016	-0.10688421	-0.10689091	-0.10690335	-0.10693013
-0.11424447	-0.11425500	-0.11425828	-0.11426325	-0.11427148	-0.11428666	$-0.11428951 \pm 0.03268113\iota$
$-0.11432006 \pm 0.03263808\iota$	$-0.11431568 \pm 0.03264423\iota$	$-0.11431433 \pm 0.03264610\iota$	$-0.11431234 \pm 0.03264900\iota$	$-0.11430905 \pm 0.03265373\iota$	$-0.11430282 \pm 0.03266241\iota$	-0.11431933
$-0.11850773 \pm 0.07274100\iota$	$-0.11850722 \pm 0.07274741\iota$	$-0.11850709 \pm 0.07274940\iota$	$-0.11850685 \pm 0.07275243\iota$	$-0.11850643 \pm 0.07275741\iota$	$-0.11850572 \pm 0.07276669\iota$	$-0.11850415 \pm 0.07278658\iota$
$-0.11969786 \pm 0.07344955\iota$	$-0.11970198 \pm 0.07345787\iota$	$-0.11970330 \pm 0.07346038\iota$	$-0.11970531 \pm 0.07346428\iota$	$-0.11970861 \pm 0.07347074\iota$	$-0.11971472 \pm 0.07348267\iota$	$-0.11972794 \pm 0.07350837\iota$
-0.12793835	-0.12786721	-0.12784743	-0.12781803	-0.12777194	-0.12769400	-0.12755159
-0.12905582	-0.12913521	-0.12915743	-0.12919064	-0.12924303	-0.12933277	-0.12950049
-0.13375003	-0.13376819	-0.13377386	-0.13378241	-0.13379696	-0.13382304	-0.13387972
-0.13789927	-0.13790688	-0.13790925	-0.13791307	-0.13791921	-0.13793071	-0.13795534

FIGURE 7.2: Measure of the stability of the linear OSSE model for different κ: leading eigenvalues of A (open-loop) and $A + B_2K$ (closed-loop). EQ1, $Re = 400$, resolution $17 \times 27 \times 17$, $\tau = 0.005$. Rows in gray colour are spurious modes of the OSSE model.

Closed-loop							
$\kappa = 0.9$	$\kappa = 0.8$	$\kappa = 0.7$	$\kappa = 0.6$	$\kappa = 0.5$	$\kappa = 0.4$	$\kappa = 0.3$	$\kappa = 0.2$
-0.01059986	-0.01126587	-0.01161232	-0.01163124	-0.01165977	-0.01170762	-0.01179878	-0.01200047
$-0.01126611 \pm 0.009215\iota$	-0.01159858	-0.01208174	-0.01307884	-0.01428265	-0.01569508	-0.01727505	-0.01898329
-0.01158778	$-0.01197560 \pm 0.009432\iota$	$-0.01283625 \pm 0.009605\iota$	$-0.01390095 \pm 0.009679\iota$	$-0.01524106 \pm 0.009538\iota$	$-0.01692957 \pm 0.008916\iota$	$-0.01886275 \pm 0.007152\iota$	$-0.01930025 \pm 0.003856\iota$
-0.01557597	-0.01586672	-0.0162329	-0.01671005	-0.01736515	-0.01835063	-0.02021839	
$-0.02197981 \pm 0.022843\iota$	$-0.02320728 \pm 0.024039\iota$						
-0.02467401	-0.02467401	-0.02467401	-0.02467401	-0.02467401	-0.02467401	-0.02467401	-0.02467401
-0.02550295	-0.02571265	$-0.02469815 \pm 0.025433\iota$	-0.02631409	-0.02680032	-0.02758406	-0.02908933	-0.02658167
-0.04068449	-0.04131302	-0.02597296	$-0.02656669 \pm 0.027093\iota$	$-0.02900508 \pm 0.029133\iota$	$-0.03234293 \pm 0.031790\iota$	$-0.03701135 \pm 0.035631\iota$	-0.03287631
-0.04311592	$-0.04474527 \pm 0.020558\iota$	-0.0421176	-0.04317645	-0.04462364	$-0.04521190 \pm 0.024223\iota$	$-0.04627236 \pm 0.026210\iota$	$-0.04300619 \pm 0.041279\iota$
$-0.04481496 \pm 0.020211\iota$	$-0.04675077 \pm 0.000261\iota$	$-0.04468649 \pm 0.021047\iota$	$-0.04467390 \pm 0.021748\iota$	$-0.04478986 \pm 0.022764\iota$	-0.04671128	$-0.04933698 \pm 0.100848\iota$	$-0.04837372 \pm 0.028576\iota$
-0.04627872	-0.04710547	$-0.04779862 \pm 0.002782\iota$	$-0.04877990 \pm 0.102035\iota$	$-0.04888416 \pm 0.101835\iota$	$-0.04905310 \pm 0.101491\iota$	-0.04996837	-0.04955074
$-0.04863406 \pm 0.102298\iota$	$-0.04866646 \pm 0.102241\iota$	-0.04821629	$-0.04908608 \pm 0.003712\iota$				$-0.04985214 \pm 0.099675\iota$
-0.04871007		$-0.04871231 \pm 0.102159\iota$	-0.04974282				
-0.05047682	-0.05047682	-0.05047682	-0.05047682	-0.05047682	-0.05047682	-0.05047682	-0.05047682
$-0.05163516 \pm 0.025974\iota$	$-0.05158780 \pm 0.025946\iota$	$-0.05151935 \pm 0.025900\iota$	$-0.05141600 \pm 0.025819\iota$	$-0.05061810 \pm 0.003994\iota$	$-0.05100143 \pm 0.025260\iota$	$-0.05080882 \pm 0.024175\iota$	$-0.05186586 \pm 0.021819\iota$
$-0.06135748 \pm 0.034781\iota$	$-0.06125553 \pm 0.035725\iota$	$-0.06121224 \pm 0.037054\iota$	$-0.06133700 \pm 0.038963\iota$	$-0.05125316 \pm 0.025654\iota$	$-0.05236981 \pm 0.003350\iota$	-0.05205086	-0.0555928
$-0.06976738 \pm 0.007565\iota$	$-0.07004754 \pm 0.007814\iota$	$-0.07045132 \pm 0.008167\iota$	$-0.07106131 \pm 0.008686\iota$	-0.05190400	-0.05511443	-0.0566001	-0.0635234
-0.08820349	-0.08832370	-0.08849911	-0.08876982	$-0.06186870 \pm 0.041739\iota$	$-0.06330386 \pm 0.045792\iota$	-0.06031656	-0.06964077
-0.09349553	-0.09386498	-0.09438184	-0.09513241	$-0.07203671 \pm 0.009490\iota$	$-0.07369883 \pm 0.010813\iota$	$-0.06670832 \pm 0.051716\iota$	$-0.07475787 \pm 0.060171\iota$
				-0.0892223	-0.09007693	$-0.07665277 \pm 0.013100\iota$	$-0.08142385 \pm 0.016812\iota$
				-0.0962737	-0.09811355	-0.0921059	
-0.09869605	-0.09869605	-0.09869605	-0.09869605	-0.09869605	-0.09869605	-0.09869605	-0.09869605
-0.10523545	-0.10514174	-0.10502634	-0.10489626	-0.10479856	-0.1049586	-0.10132323	-0.10292358
-0.10754191	-0.10771777	-0.10797202	-0.10835823	-0.10898323	-0.11007845	-0.10645924	-0.10766411
$-0.11398966 \pm 0.033107\iota$	$-0.11390474 \pm 0.033229\iota$	$-0.11378306 \pm 0.033405\iota$	$-0.11359996 \pm 0.033672\iota$	$-0.11330773 \pm 0.034109\iota$	$-0.11280560 \pm 0.034896\iota$	$-0.11188331 \pm 0.036563\iota$	-0.10962555
-0.11505279	-0.11525857	-0.1155517	-0.11598623	-0.11665808	-0.11771062	-0.11215434	$-0.11056472 \pm 0.040999\iota$
$-0.11847406 \pm 0.073239\iota$	$-0.11846731 \pm 0.073368\iota$	$-0.11845889 \pm 0.073555\iota$	$-0.11844934 \pm 0.073837\iota$	$-0.11844205 \pm 0.074292\iota$	$-0.11845332 \pm 0.075087\iota$	$-0.11856414 \pm 0.076629\iota$	-0.11396134
$-0.12003532 \pm 0.074091\iota$	$-0.12012574 \pm 0.074257\iota$	$-0.12025829 \pm 0.074496\iota$	$-0.12046356 \pm 0.074857\iota$	$-0.12080667 \pm 0.075438\iota$	$-0.12144460 \pm 0.076448\iota$	-0.11884944	-0.11548808
-0.12612391	-0.12589457	-0.12561705	-0.12528016	-0.12487754	-0.12444357	$-0.12283441 \pm 0.078392\iota$	$-0.11922821 \pm 0.079942\iota$
-0.13150949	-0.13190781	-0.13243116	-0.13314577	-0.1341741	-0.13576376	-0.12428998	$-0.12669311 \pm 0.082510\iota$
-0.13511574	-0.13545348	-0.13592976	-0.1366291	-0.13770917	-0.13948892	-0.1337664	-0.1272933
-0.13852495	-0.1386911	-0.13893346	-0.13930673	-0.13992584	-0.14106613	-0.13849347	-0.13420103

FIGURE 7.3: Measure of the normality of the linear OSSE model for different κ: leading eigenvalues of the $A^*Q_x + Q_xA$ (open-loop) and $(A + B_2K)^*Q_x + Q_x(A + B_2K)$ (closed-loop). EQ1, $Re = 400$, resolution $11 \times 27 \times 11$, $\tau = 0.005$.

Open-loop	Closed-loop					
N/A	$\kappa = 8.0$	$\kappa = 7.0$	$\kappa = 6.0$	$\kappa = 5.0$	$\kappa = 4.0$	$\kappa = 3.0$
0.14304340	0.46982739	0.46987469	0.46994778	0.47006785	0.47028702	0.47075125
0.14304243	0.14304340	0.14304340	0.1430434	0.1430434	0.14304340	0.14773148
0.14299452	0.14304250	0.14304252	0.14304256	0.14304266	0.14304309	0.14304340
0.14299347	0.14299451	0.14299451	0.14299452	0.14299453	0.14299455	0.14304131
0.10412175	0.14298605	0.14298605	0.14298605	0.14298605	0.14298605	0.14299459
0.10412093	0.12213648	0.12436501	0.12731746	0.13142797	0.13756304	0.14298605
0.10105418	0.10106321	0.10110140	0.10119349	0.10149527	0.10250391	0.10464972
0.10105412	0.10105667	0.10105745	0.10105865	0.10106066	0.10106436	0.10107246
0.10105378	0.10061144	0.10059626	0.1005863	0.10058910	0.10062358	0.10074693
0.10105360	0.10035548	0.10035831	0.10036271	0.10037017	0.10058080	0.10073359
0.09629103	0.09820267	0.09875121	0.09941593	0.10013235	0.10038439	0.10041749
0.09629103	0.09639554	0.09639881	0.09640395	0.09641276	0.09642999	0.09647210
0.09628996	0.09633465	0.09633326	0.09633141	0.09632904	0.09632623	0.09632376
0.09628996	0.09629081	0.09629075	0.09629065	0.09629049	0.09629020	0.09628961
0.09379298	0.09625812	0.09626140	0.09626368	0.09626515	0.09626579	0.09626517
0.09379293	0.09385152	0.09386281	0.09388036	0.09390989	0.09396551	0.09409061
0.09379181	0.09378303	0.09378972	0.09380648	0.09383290	0.09387758	0.09396206
0.09379171	0.09377858	0.09378036	0.09377628	0.09376955	0.09375734	0.09373176
0.09316529	0.09316417	0.09316379	0.09316314	0.09316196	0.09315987	0.09315975
0.09316529	0.09316353	0.09316265	0.09316171	0.09316074	0.09315959	0.09315410
0.09316429	0.09316242	0.09316184	0.09316096	0.09315950	0.09315681	0.09315101
0.09316429	0.09181960	0.09182353	0.09182956	0.09183949	0.09188615	0.09204244
0.09168222	0.09173318	0.09174882	0.09177294	0.09181289	0.09185753	0.09189510
0.09168211	0.09150559	0.09150281	0.09150083	0.09149910	0.09149719	0.09149435
0.09149256	0.09149378	0.09149402	0.09149431	0.09149460	0.09149476	0.09149410
0.09149246	0.09148059	0.09148059	0.09148092	0.09148181	0.09148362	0.09148692
0.09149243	0.09140056	0.09139994	0.09139910	0.09139770	0.09139515	0.09138972
0.09149239	0.09140049	0.09139982	0.09139870	0.09139692	0.09139379	0.09138735
0.09139984	0.09139962	0.09139825	0.09139694	0.09139519	0.09139227	0.09138627

FIGURE 7.4: Measure of the normality of the linear OSSE model for different κ: leading eigenvalues of the $A^*Q_x + Q_xA$ (open-loop) and $(A + B_2K)^*Q_x + Q_x(A + B_2K)$ (closed-loop). EQ1, $Re = 400$, resolution $11 \times 27 \times 11$, $\tau = 0.005$.

Closed-loop							
$\kappa = 0.9$	$\kappa = 0.8$	$\kappa = 0.7$	$\kappa = 0.6$	$\kappa = 0.5$	$\kappa = 0.4$	$\kappa = 0.3$	$\kappa = 0.2$
0.47911520	0.48099619	0.48345903	0.48676667	0.49137047	0.49816260	0.50937887	0.53313208
0.23568610	0.24955980	0.26649953	0.28754364	0.31420485	0.34876827	0.39505928	0.46227444
0.14304340	0.14304340	0.14304341	0.14304342	0.14457748	0.15594654	0.17426993	0.20798098
0.14304233	0.14304240	0.14304251	0.14304273	0.14304345	0.14304508	0.15327213	0.19180328
0.14299641	0.14299737	0.14299949	0.14300705	0.14304321	0.14304352	0.15048624	0.18406224
0.14298612	0.14298614	0.14298618	0.14298625	0.14298640	0.14298710	0.14304376	0.14304495
0.12364566	0.12693676	0.13115198	0.13673796	0.14292573	0.14298217	0.14303472	0.14304179
0.10528597	0.10681536	0.10962826	0.11485771	0.12271551	0.13464936	0.14298644	0.14298786
0.10392986	0.10616463	0.10912567	0.11278846	0.11892507	0.12984231	0.14298517	0.14298626
0.10128831	0.10136088	0.10147418	0.10166703	0.10206502	0.10452063	0.11093064	0.12469639
0.10102411	0.10110289	0.10122670	0.10144089	0.10187502	0.10308760	0.10801163	0.12308935
0.09899487	0.09929496	0.09951960	0.09970877	0.10069807	0.10256883	0.10443747	0.11089051
0.09641874	0.09646515	0.09704896	0.09851250	0.09992209	0.10028556	0.10196803	0.10674597
0.09629989	0.09635665	0.09654639	0.09670382	0.09704557	0.09904897	0.10120823	0.10666683
0.09624322	0.09624532	0.09626148	0.09634298	0.09688266	0.09786199	0.09999852	0.10457905
0.09557104	0.09585630	0.09621232	0.09624226	0.09625603	0.09630203	0.09663317	0.09936146
0.09515103	0.09560417	0.09560822	0.09557610	0.09550289	0.09560877	0.09558570	0.09539432
0.09489949	0.09503712	0.09518968	0.09535131	0.09549083	0.09560172	0.09547976	0.09518819
0.09335632	0.09349907	0.09379773	0.09441423	0.09529871	0.09531277	0.09494176	0.09508283
0.09326785	0.09322232	0.09319955	0.09324102	0.09341987	0.09385809	0.09467748	0.09407538
0.09301800	0.09297838	0.09292088	0.09283296	0.09268859	0.09242615	0.09211620	0.09386484
0.09301489	0.09297568	0.09291857	0.09283071	0.09268533	0.09241913	0.09187613	0.09371162
0.09217702	0.09216767	0.09213667	0.09210072	0.09222268	0.09223098	0.09185967	0.09181042
0.09156781	0.09169284	0.09189450	0.09207057	0.09194502	0.09171607	0.09185114	0.09087990
0.09147402	0.09145786	0.09142784	0.09136970	0.09134930	0.09139142	0.09154720	0.09036726
0.09134711	0.09134657	0.09134559	0.09134483	0.09125356	0.09104647	0.09121626	0.09028357
0.09133624	0.09126099	0.09125918	0.09122908	0.09115953	0.09102155	0.09089504	0.09015995
0.09126419	0.09124467	0.09115106	0.09106156	0.09091367	0.09067578	0.09072211	0.08988929
0.09124912	0.09120912	0.09114632	0.09105378	0.09090008	0.09064573	0.09046189	0.08955684

7.3 Initial starting conditions

Data location	`osse/database/THESIS/controller_K_ROSSE_eigenmode1/eq1_findsoln/Re=400/rotational/controller=17x27x17/dealiasXZ/COMPARISON_amplitude_perturbation`
Script for simulations	`channelflow/trunk/PHD/controller_k_eq1_rosse_eigenmode.cpp`
Script for comparison	`python3 osse/run_comparison_eq1_thesis_73.py 17 27 17 1`

The initial condition of the simulations is the Nagata (1990) lower-branch solution. This state is calculated via the method `findsoln` of Channelflow at resolution $17 \times 27 \times 17$ and $Re = 400$, as detailed in section 6.3. The minimal residual for the calculation is of order $R = 10^{-14}$ for a period $T = 20$ in Channelflow, which corresponds to a precision of $R * T = 2 \times 10^{-13}$. As a consequence, the minimal distance to EQ1 reachable in Channelflow is of order 10^{-13}. Yet, at time $t = 0$ of Channelflow simulations, the distance will obviously be exactly zero, or $-\infty$ on a log-scale. LQG optimal control provides no global system-independent guaranteed robustness properties (see §3.4.1). In other words, we do not possess any estimation on the distance beyond which the optimal control law is overrun. Nonetheless, we expect the margin of our optimal control to reside above this threshold. It is valuable to note here that the Riccati solutions are calculated at the `Python float` type precision, i.e. 2.2×10^{-16}.

The initial time-steps are particularly important for the controlled Channelflow simulations. The margins of our optimal controllers may indeed reside in the close neighborhood of the initial condition. A transient energy growth or a numerical instability in these first iterations could immediately repel the dynamical state outside these boundaries. To avoid such situation, we will perturb —to a very small extent— the initial state in the direction of the leading unstable eigenmode of EQ1. The benefit of such an approach is twofold. Firstly, the non-normality of the initial state-vector, namely some noise of order 10^{-13}, diminishes. Secondly, the initial condition is now not only characterized by its state-space position, but also by its developing direction, hence increasing the repeatability of the simulations. A perturbation in the leading unstable eigenmode direction is less detrimental for the controller than one along the non-normal stable eigen-space (see later chapter 8), as the optimal control law is tailored to this particular direction.

The question now rising is how to define "to a very small extent" quantitatively? A large range of magnitude of the leading eigenmode of the Nagata (1990) lower-branch solution are evaluated, from order 10^{-10} down to order 10^{-15}. Below 2×10^{-12}, the perturbations are so weak that they do not impact the dynamical evolution. Above 8×10^{-12}, no further reduction of the transient energy growth are observed, while the distance to

EQ1 simply increases. Figure 7.5 gathers the Channelflow simulations initiated with a range of magnitude within $[2\times10^{-12}, 8\times10^{-12}]$. We consider the magnitude 6×10^{-12} as the optimal combination of least increase in energy norm and minimal transient energy growth. As a consequence, the following Channelflow and ROSSE simulations will be initiated with the Nagata (1990) lower-branch solution combined with a perturbation in its leading unstable eigenmode of magnitude factored by 6×10^{-12}.

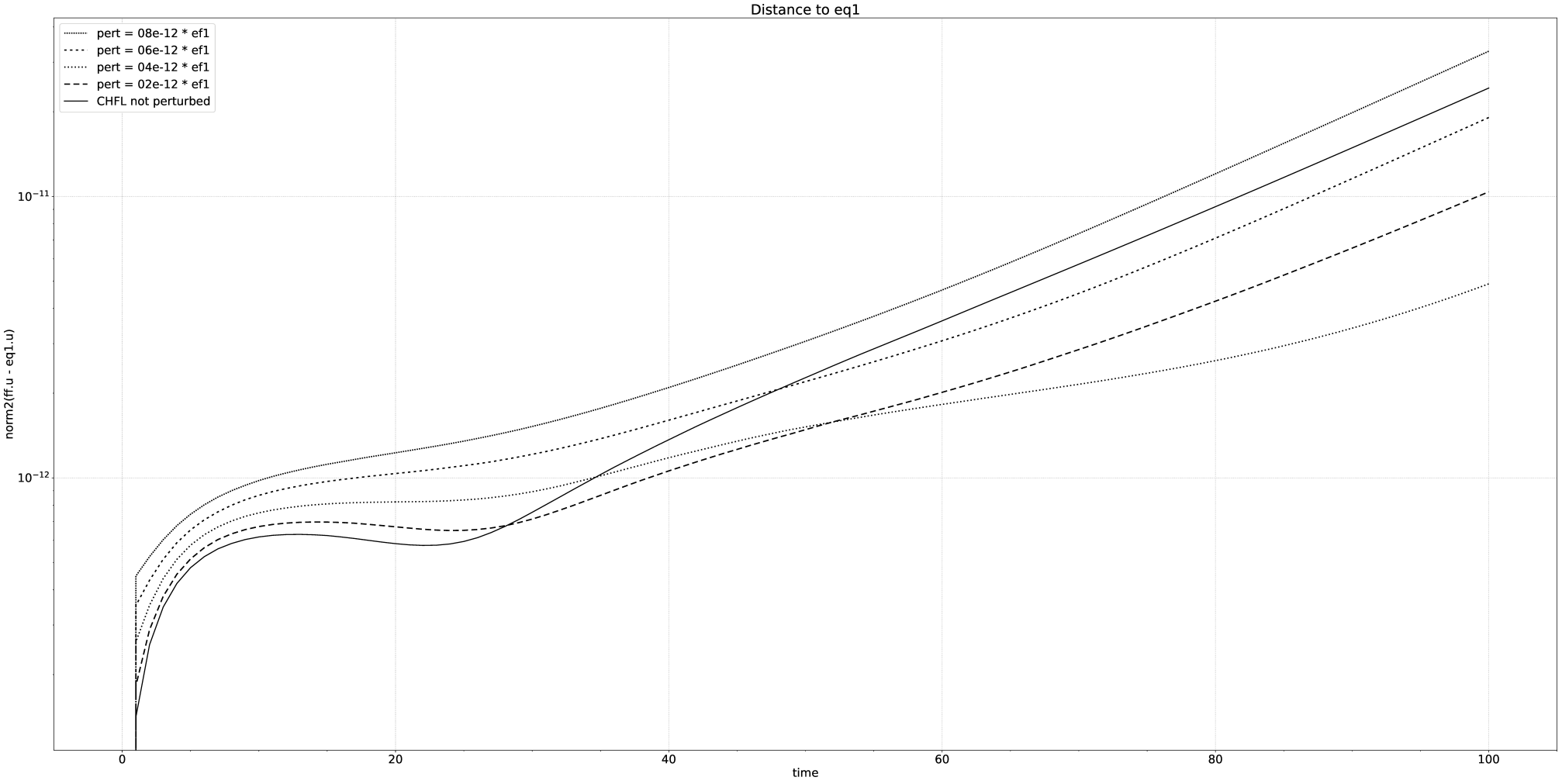

FIGURE 7.5: Channelflow simulations starting from EQ1 at resolution $17 \times 27 \times 17$ with an initial perturbation along the leading unstable eigenmode of EQ1 for different magnitudes. The continuous correspond to the un-perturbed system. (time horizon $[0, 100]$, resolution $17 \times 27 \times 17$, $Re = 400$).

7.4 Controlled Linear ROSSE simulations of the Nagata (1990) lower-branch solution

Data location	`osse/database/THESIS/07_eq1_controlled_ROSSE`
Script for simulations	`python3 osse/rosse_riccati.py 1 17 27 17 $1000kappa`
Script for comparison	`python3 osse/run_comparison_thesis_74.py 17 27 17 1`

The ROSSE linear model is simulated starting from the Nagata (1990) lower-branch solution with a perturbation in its leading eigenmode direction of magnitude 6×10^{-12} (§7.3). The ROSSE model is integrated in time via the BDF algorithm of the method `scipy.integrate.solve_ivp`, with absolute and relative tolerances of 10^{-16} over a period $T = 500$. The optimal control law is enforced from time $t = 0$. The energy time-evolution for the open-loop and closed-loop systems for the different values of κ are presented in figure 7.6 and 7.7. First and foremost, it is important to note that the tolerance for the linear integration is of order 10^{-16}, which is higher than the order 10^{-13} used for the Channelflow `findsoln` method. This is the reason why the initial distance to EQ1 is of order 10^{-13}, while the final converged state is of order 10^{-16}.

From figure 7.6, it appears that the open-loop system (continuous line) is following as expected a linear evolution along the unstable eigenmode of EQ1, +0.05012030. From figure 7.7, we observe that the energy of any closed-loop system is higher than the one of the open-loop system at the initial time-step and for all κ. This difference is likely due to the BDF integration algorithm having to handle the wall-actuation. However, thanks to the stabilizing control, this situations changes within a couple iterations. From time $t \backsimeq 3$ and for the rest of the integrated period, the energy level of each closed-loop system is lower than the one of the open-loop.

Nonetheless, after this transitional period, the closed-loop systems are all facing an energy growth peaking around $t = 40$. The predominance of this surge decreases with more powerful control, and actually, for $\kappa = 0.2$, this growth does not arise. We do not expect this energy growth to be related to the non-normality of the system, as the closed-loop system at $\kappa = 0.2$ is characterized by the lowest degree of normality.

Following this energy bump, every closed-loop system is linearly converging to the Nagata (1990) lower-branch solution. Their rate of convergence respectively corresponds to the maximal eigenvalues of each κ in tables 7.3 and 7.4. These values are very close, yet distinct. We retrieved in figure 7.7 the fact that the most powerful controllers possess more negative leading eigenvalues, as they are converging at higher rate. The undulation observable on the period $t < 100$ for values of $\kappa \leq 0.5$ may be related to the non-zero imaginary part of some of their leading eigenvalues.

Overall, and as predicted by the linear analysis, the Nagata (1990) lower-branch solution is now linearly stable. Our optimal control law for values of κ ranging from 8.0 down to 0.2 is positively fulfilling its objective. The chapter 5 on controller design and the chapter 6 on the Riccati solution therefore describe an effective linear procedure to determine a stabilizing optimal control law.

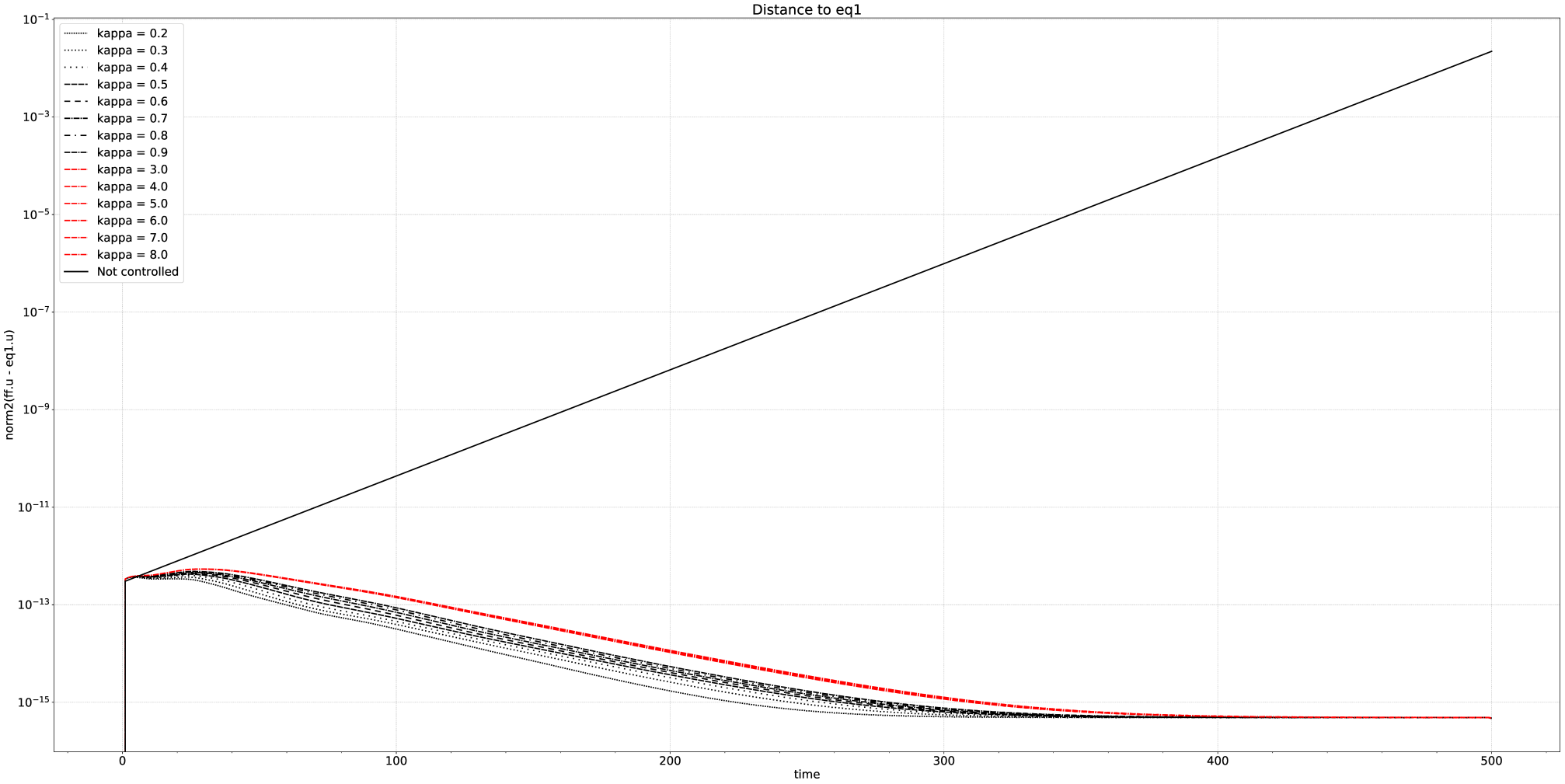

FIGURE 7.6: OSSE linear simulations: Time-evolution of the energy norm of the state-vector (i.e. distance to the Nagata (1990) lower-branch solution) controlled by an optimal forcing for different value of κ. The continuous black line represents the un-actuated system. The control starts at $t = 0$. (time horizon $[0, 500]$, resolution $17 \times 27 \times 17$, $Re = 400$, $\tau = 0.005$).

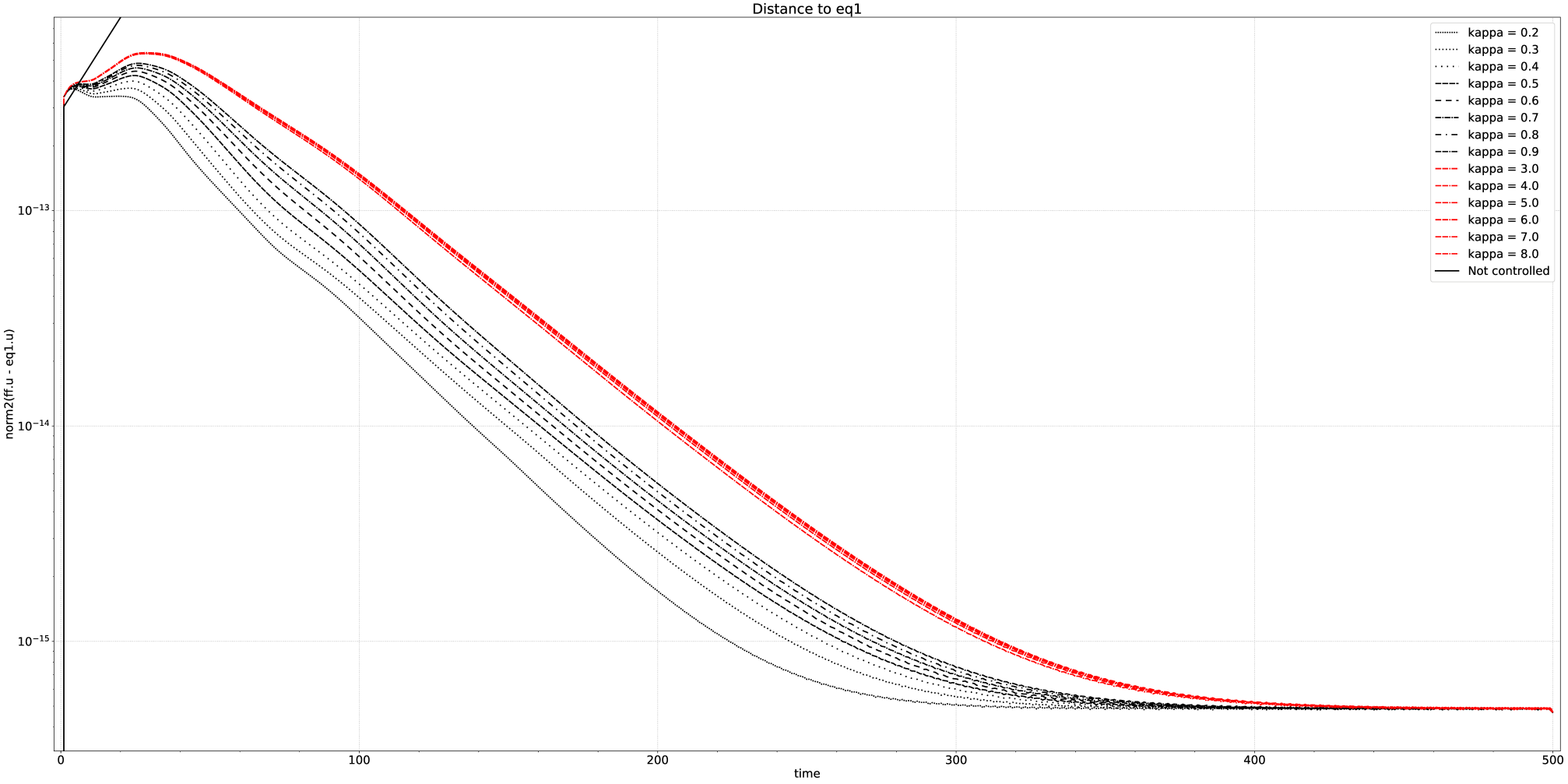

FIGURE 7.7: OSSE linear simulations: Time-evolution of the energy norm of the state-vector (i.e. distance to the Nagata (1990) lower-branch solution) controlled by an optimal forcing for different value of κ. The continuous black line represents the un-actuated system. The control starts at $t = 0$. (time horizon $[0, 500]$, resolution $17 \times 27 \times 17$, $Re = 400$, $\tau = 0.005$).

7.5 Controlled Non-linear Channelflow simulations of the Nagata (1990) lower-branch solution

Data location	`osse/database/THESIS/ controller_K_ROSSE_eigenmode1`
Channelflow Simulation	`channelflow/trunk/PHD/controller_k_eq1_rosse_eigenmode.cpp`
Script for comparison	`python3 run_comparison_eq1_thesis_75.py 17 27 17 1`

Non-linear Channelflow simulations with optimal control are run at resolution of $17\times27\times17$ and for a period $T = 1000$. As Channelflow and the Channelflow Boundary Condition package of Heins (2015) can not be employed with the non-linear terms linearized around an invariant solution, simulations are computed directly with the non-linear terms under the rotational form,

$$N(v) = (\nabla \times \boldsymbol{U}) \times \boldsymbol{U} + \frac{1}{2}\nabla(\boldsymbol{U} \cdot \boldsymbol{U}). \tag{7.2}$$

Simulations were also run with the non-linear terms under the skew-symmetric form (eq. 5.61) and lead to equivalent results. In the hypothesis of small amplitude perturbations, we expect the non-linearity to play a marginal role. We chose the rotational form of the nonlinear terms here. It allows for a fast computation in comparison to a Skewsymmetric form but it introduces errors in the high spatial frequencies unless dealiased transforms are used (Gibson, 2014). We favour this form as this is the default one, and therefore the one we expect to be the most robust against glitches or numerical anomalies as it has been widely used and tested. The simulations are initialized with the Nagata (1990) lower-branch solution and a perturbation in its leading eigenmode direction of magnitude 6×10^{-12} (§7.3). The optimal control law is enforced from time $t = 0$. The detailed list of the settings for the simulations are given in table 7.1. The energy time-evolution for the open-loop and closed-loop systems for the different values of κ are presented in figures 7.8 and 7.9.

In figure 7.8, the continuous black line represents the open-loop simulation. This time-evolution corresponds to the hetero-clinic connection from the Nagata (1990) lower-branch back to the laminar PCF profile. Following the perturbation in the leading eigenmode direction of EQ1, the open-loop system pursues a linear growth along this same direction. Around $t = 500$, the system experiences a transitional turbulence phase for approximately 200 times units. This phase disintegrates the energy of the system, which finally settles down on the stable laminar PCF profile.

For the closed-loop systems, it appears directly in figures 7.8 and 7.9 that none of the optimal control law manages to stabilize the Nagata (1990) lower-branch solution. The transition to turbulence is delayed by the optimal control law by up to 200 time units, but the distance to EQ1 is not bounded by the optimal control law. Despite many

different setup (time-steps, non-linear forms, initial conditions) and discussion with the EPFL group of Tobias Schneider (personnal communication, April to Jul 2019), no improvement were achieved: when the distance from EQ1 becomes too substantial, the actuation unsettles the Channelflow simulation and break the time-forward march. This is the reason, why none of the controlled simulations persists for distances to EQ1 greater than 10^{-3}.

Despite the perturbation in the leading eigenmode direction to avoid transient energy growth, each closed-loop system observes a transitory phase from the initial starting time and up to $t = 50$, visible in figure 7.9. This period is marked by oscillations of order 10^{-12}. The amplitude of these oscillations is larger for weaker controllers. They do not actualy arise for powerful controllers, e.g. $\kappa = 0.2$.

Nevertheless, beyond the time $t = 50$, the state of each simulation escapes the neighborhood of EQ1 definitively. Similarly to the validation case for the laminar PCF profile at $\kappa = 0.25$ (§6.4.4), each simulation is diverging linearly away from the Nagata (1990) lower-branch solution. This direction does not correspond to any eigenmode found during the linear analysis, as it would correspond to a positive real-part eigenvalue. For $\kappa \leq 0.9$, the divergence rate varies depending on the strength of the controller: for small κ, i.e. powerful control, the divergence rate is higher. For the most powerful controllers $\kappa < 0.5$, this divergence rate is actually higher than the open-loop system. We presume that beyond their basin of attraction, the optimal control law does not contribute to the stabilization of the dynamical state, but rather acts as a constant source of perturbation. Here, the most powerful controllers have the maximal disruption potential. For $\kappa \geq 3.0$, we do no notice any difference between the different forcings. For these values, the Channelflow simulations do not actually crash when the distance to EQ1 reaches order 10^{-3}, but experiences a succession of discontinuities/catch-ups. We do not expect this phase to be physically meaningful.

The causes behind the failure of the optimal control laws are not clear to the author. The same hypothesis as for the failure of the relaminarization of a laminar PCF profile with $\kappa = 0.25$ (§6.4.4) can be suggested:

- The ROSSE model may not describe the non-linear Channelflow model properly. However, we demonstrated in section 5.5 that the ROSSE model and Channelflow, both actuated, are equivalent during the phases dominated by the actuation and the linear eigenmodes.
- The possibility that the optimal solution is not valid is unlikely, as linear analysis and linear ROSSE simulations demonstrated the linear stability of the Nagata (1990) lower-branch solution when optimal control is enforced.
- A deficiency in the implementation of the control law in Channelflow is possible but unlikely, as the control procedure was validated in section 6.4. The stabilization

of EQ1 may require better precision, smaller actuation-time, integration time, etc. Yet, varying these parameters did not improve our results.

- An inadequate resolution can be problematic. Nonetheless, within the current limitations, this point can not be improved. It was also shown in section 6.4.5 that the wall-normal resolution did not impact drastically the results of the controlled simulations, at least when targeting the laminar PCF profile.
- The optimal forcing is too intense and might either ignite un-expected non-linear effects or break the Channelflow simulation. Yet, the energy norm is following a linear evolution away from EQ1, which would denote a linear unstable eigenmode rather than a non-linear phenomenon.

Linearized simulations of Channelflow with the CFBC package would likely elucidate this problem but are impossible at the moment (see §6.4.3). This failure may also be the consequence of deeper theoretical limitations. For now, a definitive conclusion can not be drawn. Details about these theoretical interpretations as well as directions for improvements and futures researches are discussed in chapter 8.

TABLE 7.1: Parameters and DNS flags for Channelflow simulations presented in sections 7.5.

PARAMETER	VALUE
baseflow	EQ1
Nx, Ny, Nz	$17 \times 27 \times 17$
Reynolds	`400.0`
nu	`1 / Re`
Lx	`eq1.Lx() = 2*pi/1.14`
a	`eq1.a() = -1.0`
b	`eq1.b() = +1.0`
Lz	`eq1.Lz() = 2*pi/2.5`
Baseflow	`LinearBase`
Nonlinearity	`Rotational`
Initstepping	`SMRK2`
Timestepping	`SBDF3`
Dealiasing	`DealiasXZ`
taucorrection	`true`
constraint	`PressureGradient`
dPdx	`0.0`
uupperwall	`+1.0`
ulowerwall	`-1.0`
CFLmin	`0.10`
CFLmax	`0.30`
dtmax	`0.005 (= tau)`
dtmin	`0.0000001`
dt0	`dtmax`
variable_dt	`true`
T0	`0.0`
T1	`1000.0`
dt	`1`
controller starts at	`0`
perturbation initiated at	`0`
perturbation magnitude	EQ1 leading eigenmode factor `0.6E-12`

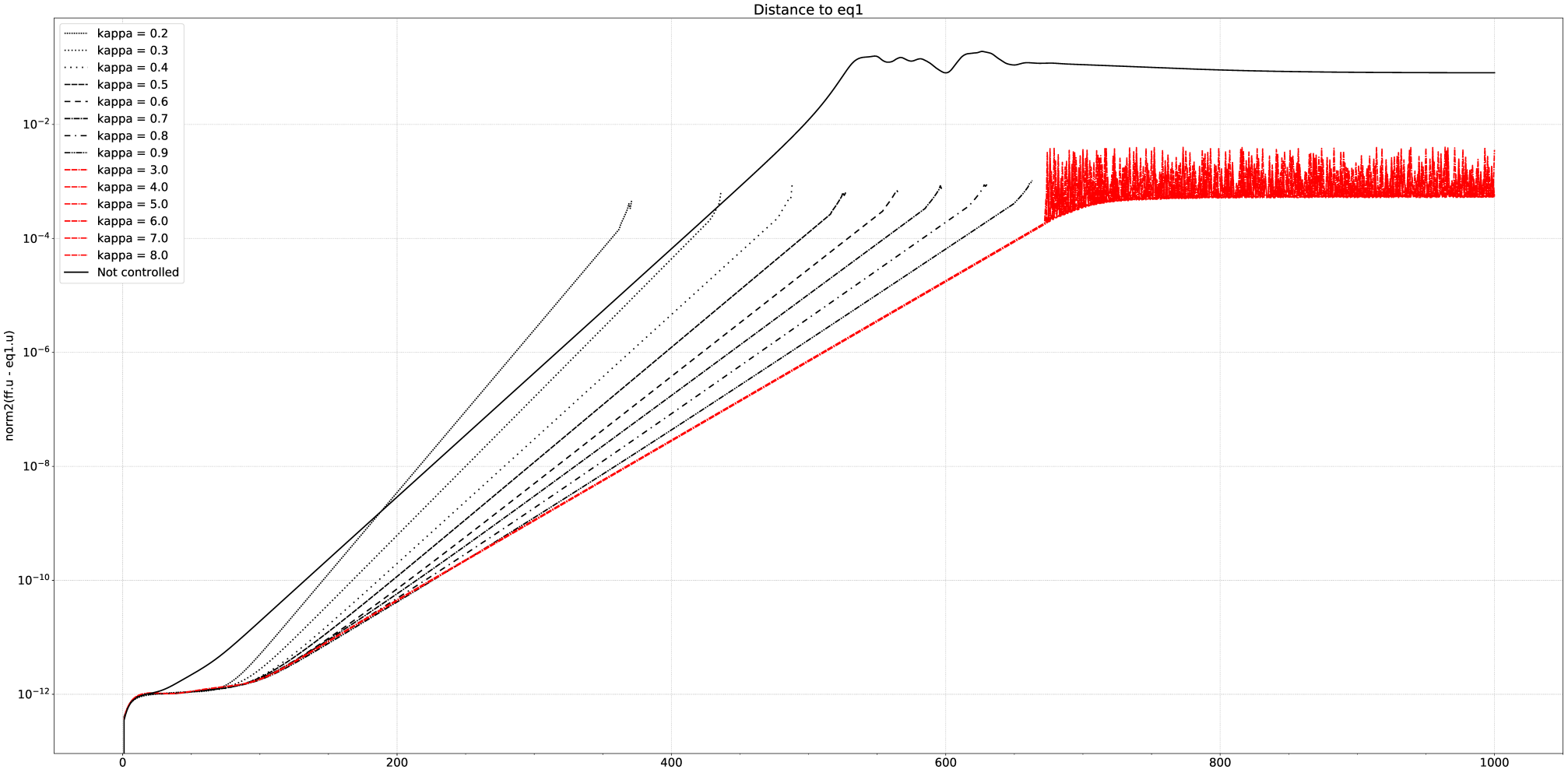

FIGURE 7.8: Channelflow simulations with non-linear terms under a rotational form (eq. 7.2): Time-evolution of the energy norm of the state-vector (i.e. distance to the Nagata (1990) lower-branch solution) controlled by an optimal forcing for different value of κ. The continuous black line represents the un-actuated system. The control is applied at $t = 0$ for different value of κ. (time horizon $[0, 1000]$, resolution $17 \times 27 \times 17$, $Re = 400$, $\tau = 0.005$).

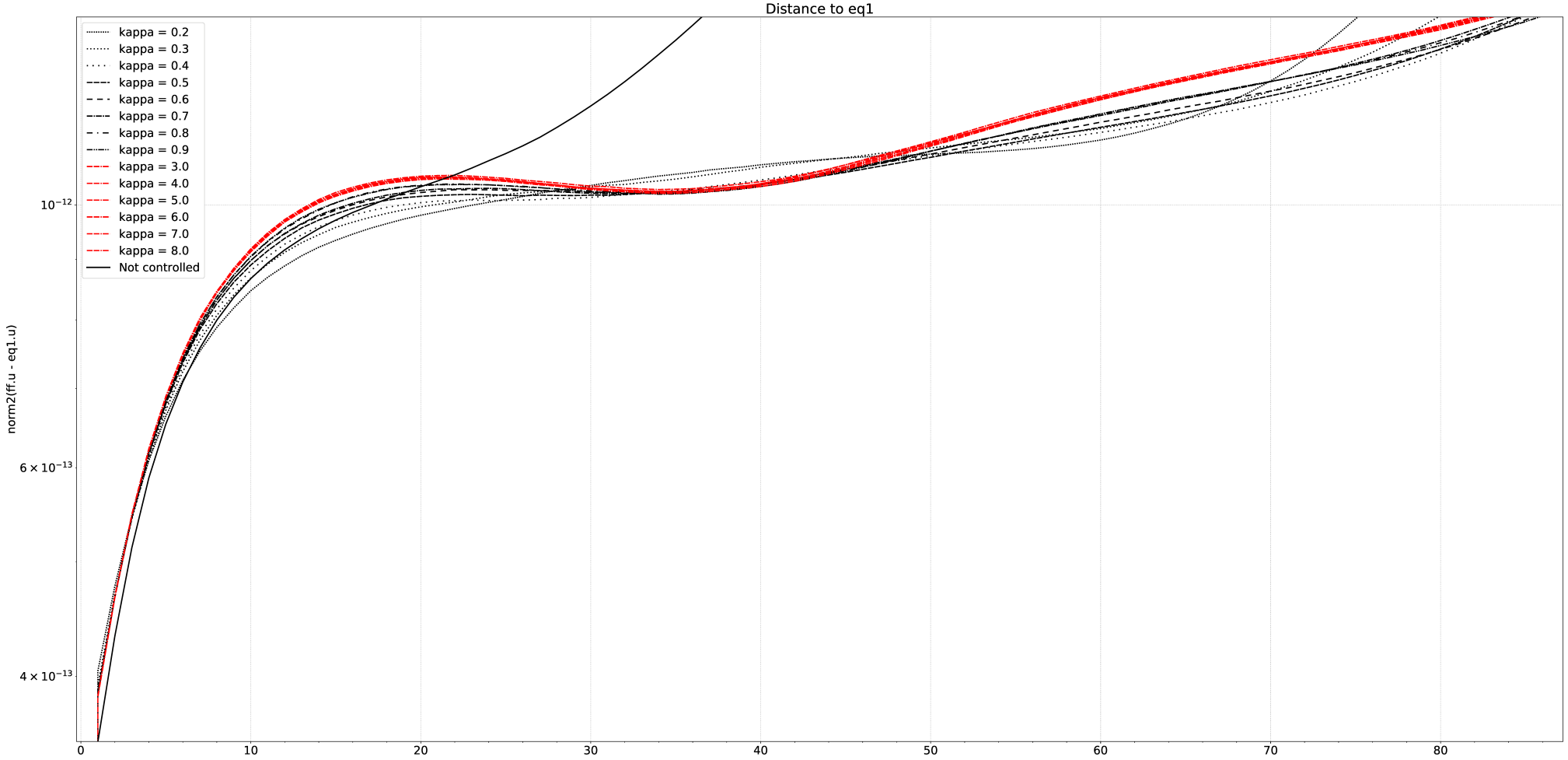

FIGURE 7.9: Channelflow simulations with non-linear terms under a rotational form (eq. 7.2): Time-evolution of the energy norm of the state-vector (i.e. distance to the Nagata (1990) lower-branch solution) controlled by an optimal forcing for different value of κ. The continuous black line represents the un-actuated system. The control is applied at $t = 0$ for different value of κ. (zoom over the time horizon $[0, 90]$, resolution $17 \times 27 \times 17$, $Re = 400$, $\tau = 0.005$).

Chapter summary

- The optimal control law to stabilize the Nagata (1990) lower-branch solution are calculated with the ROSSE model for different controller strengths, ranging from $\kappa = 8.0$ to $\kappa = 0.2$. However, for $\kappa = \{1.0, 2.0\}$, the solution did not converge.
- A linear analysis demonstrated that the Nagata (1990) lower-branch solution is linearly stable with the optimal control law enforced. Increasing the controller strength improves the linear stability of the system, but also deteriorates its normality.
- Simulations are initiated with the Nagata (1990) lower-branch solution. To improve repeatability and normality of the initial condition, simulations are initially perturbed in the direction of the leading eigenmode of EQ1 at a very small magnitude.
- Time-integration of the linear ROSSE closed-loop system demonstrated that the optimal control law for each value of κ is stabilizing EQ1. The most powerful controller leads to the fastest convergence rate.
- In the non-linear cases run in Channelflow, the Nagata (1990) lower-branch solution is not stabilized. In the best cases, the transition to turbulence is delayed, but not avoided, and the most powerful controllers are associated with higher divergence rates. The cause behind this failure are not clear to the author, but suggestions and interpretations are given next chapter 8.

Chapter 8

Discussion, Summary, Conclusion and Future Work

8.1 Discussion

Throughout this thesis, we achieved many of our objectives. We successfully established in chapter 4 a new divergence-free linear model to depict the dynamical evolution of the flow in the neighborhood of weakly unstable invariant solutions, the Orr-Sommerfeld Squire model Extended for a non-laminar solution (OSSE) . It establishes a full-matrix state-space representation that enables access to linear algebra and linear control theory for any non-laminar solution — not only invariant solutions, but any three-dimensional steady state — while reducing the dimension of the dynamical state by half. A purely-real and equivalent version, entitled Real Orr-Sommerfeld Squire model Extended for a non-laminar solution (ROSSE), was derived as well to save even more memory.

Based on the previous research of Heins (2015) and thanks to the new OSSE model, we developed and validated a procedure to target and linearly stabilize an invariant solution of the PCF configuration (chapter 5). Each stage of the development performed well and was validated, notably the actuation by wall-transpiration of the OSSE model and the analyses of the stability and controllability of EQ1. We demonstrated that all the unstable eigenmodes of EQ1 are controllable with this type of actuation, and as a consequence, that the Nagata (1990) lower-branch solution is linearly stabilizable.

The procedure to determine the optimal control presented in chapter 6 performed adequately as well. We managed to obtain the solution of the associated high-dimensional Riccati equation thanks to the reduction of state dimension enable by the ROSSE model. The resulting control law was validated by improving the stability of the PCF laminar state.

Finally, we enforced the linear stability via LQR optimal regulation of the Nagata (1990) lower-branch solution (EQ1) at Reynolds number 400 in chapter 7. This accomplishment was demonstrated via linear analysis and linear time-integration. The Nagata (1990) lower-branch solution is linearly stable for a wide set of optimal control "strength". We showed that increasing the controller strength improved the linear stability of the system, but also deteriorated its normality.

Nonetheless, the stability of EQ1 is not achieved within a non-linear context, as revealed in the Channelflow simulations of section 7.4. Instead, the state of the closed-loop systems linearly diverges from the targeted invariant solution along unexpected directions. Similar issues raised when targeting a laminar Plane Couette Flow profile with a powerful controller ($\kappa = 0.25$), which limited the validation of the optimal actuation in Channelflow (§6.4.4).

The origin, likely related, of these failures is not known. Yet, we estimate that they can potentially stem from three different —and maybe combined— sources: either the procedure to determine the Riccati solution, or the implementation of the actuation and control within the Channelflow software, or a limitation of the underlying theoretical hypotheses. Isolating these elements to determine their respective influence would require further effort.

8.1.1 Limitations associated with the Optimal Control Law and Riccati solution

Finer range of controller strength κ

The optimal control law for the Nagata (1990) lower-branch solution are calculated in chapter 7 for the range of controller strength κ,

$$\kappa = \big[8.0,\ 7.0,\ 6.0,\ 5.0,\ 4.0,\ 3.0,\ 2.0,\ 1.0,\ 0.9,\ 0.8,\ 0.7,\ 0.6,\ 0.5,\ 0.4,\ 0.3,\ 0.2\big]. \tag{8.1}$$

In the controlled non-linear Channelflow simulations initiated with the Nagata (1990) lower-branch solution (§7.5), it appeared that for increasing values of κ above 3.0 and up to 8.0, no improvement was taking place and each simulation followed the same dynamical evolution. On the other hand, for decreasing value of κ below 0.9 and down to 0.2, no further delay in the transition to turbulence was achieved. On the contrary, the most powerful controllers actually unsettle the simulations and trigger the transition to turbulence within a shorter period of time. As a consequence, we do not expect any amelioration when increasing the range of κ below 0.2 (actually, Chanellflow simulations will likely crash immediately) or above 8.0.

Nonetheless, the Riccati solutions for $\kappa = \{1.0,\ 2.0\}$ did not converge. We can not conjecture on the behavior of the closed-loop Channelflow system for κ in the range

$[0.9, 3.0]$. Either the dynamical evolution of the closed-loop simulations would fit in figure 7.8 in between the ones of $\kappa = 0.9$ and $\kappa = 3.0$ with the befitting divergence rate, or this range would include an ideal "sweet-spot" value of κ that enhanced the performance of the controller. This ideal value of κ would require a more sophisticated algorithm to determine the optimal control law, superior choice of parameters (initial condition) or less restrictive constraints (wall-time, memory, convergence rate), which would explain why the solutions did not converge within this range.

Controller and Channelflow Resolution

The validation of the implementation of the Channelflow Boundary Condition Package of Heins (2015) updated for Channelflow version 1.5.1 (revision 452) was performed in section 5.5.2. For this purpose, a $21 \times 65 \times 21$ resolution, respectively in stream-wise, wall-normal and span-wise direction, was adopted in Channelflow simulations when the invariant solution EQ1 was set as initial condition. A smaller $21 \times 35 \times 21$ resolution in the linear ROSSE model was then sufficient to replicate the behavior of non-linear Channelflow simulations during the actuation- and eigenmode-dominated phases.

Nonetheless, the validation and applications of the Channelflow Boundary Condition Package were performed at much higher resolutions in the thesis of Heins (2015). The validation was operated at resolution $110 \times 65 \times 110$, which is in part due to a the higher Reynolds number $Re = 10^3$, but also to the wall-actuation itself (Heins, 2015, p.55). Depending on the method used for the design, the controllers were built at a wall-normal resolution $N_y = 168$ or $N_y = 250$ (the control was designed for a single wavenumber pair, hence not requiring stream- and spanwise resolutions) and Channelflow used a $182 \times 151 \times 158$ resolution, also due to the larger domain $4\pi \times 2 \times 2\pi$ (Heins, 2015, p.96).

These resolution are all well above the $17 \times 27 \times 17$ which we are using for the control design and Channelflow simulations. This resolution is not only small for the Channelflow Boundary Condition package, but also for Channelflow itself, even at $Re = 400$. A wall-normal resolution $N_y = 27$ seemed sufficient in section 6.4.5 when targeting a laminar PCF profile, as no improvement was detected at higher resolution $N_y = 35$ or $N_y = 65$. Nonetheless, this conclusion may not extend to the stabilization of an unstable invariant solution embedded in transitioning turbulence.

The control design here constitutes the limiting factor. $17 \times 27 \times 17$ is the maximal resolution reachable within this configuration. The issue is that the Nagata (1990) lower-branch solution did not fully converge at $17 \times 27 \times 17$: its eigen-decomposition is different at higher resolutions (see tables 4.1 or 5.1 and 5.2). This implies that EQ1 at resolution $17 \times 27 \times 17$ does not correspond to the same state-space position than EQ1 at higher resolution. This solution is not pertinent for higher resolution. In other words, increasing the resolution in Channelflow is surely straightforward within the

current computational power, but would render the control law useless as the targeted equilibrium is not a meaningful state at this resolution. This point was actually retrieved when we tried to use the optimal control law at resolution $17 \times 27 \times 17$ for Channelflow simulations up to $33 \times 65 \times 33$.

As a consequence, we would recommend to calculate the optimal control law at a resolution for which the Nagata (1990) lower-branch solution actually fully converged, at least $33 \times 35 \times 33$, or even more in the wall-normal direction where the actuation is applied (reminder of §4.6.4: odd-resolution required). It would then allow to target the Nagata (1990) lower-branch solution within non-linear Channelflow simulations at even higher resolutions, e.g. $182 \times 151 \times 158$ as (Heins, 2015, p.96), consequently enhancing the precision of the time-integration while targeting the same state-space position.

Model reduction and Riccati solution method

To overcome the two preceding limitations, a different approach to determine the solution of the high-dimensional quadratic Riccati equation is required, precisely a different model reduction method and an advanced Riccati solver. For the time being, the system is reduced via the truncation of the highest-order Fourier modes (section 6.3), even if some of these high-order modes have an impact on the dynamics of the system. Regarding the Riccati solver, the currently-employed `Python` method is not optimized for high-dimensional problem (section 6.2.4) and is single-thread. These techniques were pushed to their limits by using the maximal computational resources available.

A key element for future research is to concentrate on the development of an effective model reduction and a fast, reliable, parallel Riccati solver. For this purpose, the literature review presented in section 6.2 can serve as a good starting point. Particularly, the methods using the Adjoint of the Direct-Adjoint (ADA) (Semeraro et al., 2013; Semeraro and Pralits, 2017), the quasi-separability (Simoncini, 2007; Palitta, 2019) or reinforced learning tools (Bucci et al., 2019) were the most promising.

8.1.2 Limitations associated with Channelflow and the Channelflow Boundary condition package

Non-linear terms linearized around an invariant solution in Channelflow

The validation of the linear OSSE model (§4.8) consisted in the comparison of the eigenmode decomposition of the linear OSSE and non-linear Channelflow, both configured with the Nagata (1990) lower-branch solution as baseflow. The OSSE does not take the non-linear terms of the NSE into account, and therefore this procedure is only valid during the initial state of the simulations when the non-linear effects remain marginal.

An ideal validation procedure would be to compare the linear OSSE model against a linearized Channelflow simulation. It would allow a comparison for the entire time-horizon and without any interference from the non-linear terms. This policy was actually adopted to validate the actuation by wall-transpiration of a laminar PCF profile (§5.5.1). The non-linearity flag was then set as "linearAboutProfile" in Channelflow.

Unfortunately, the non-linear terms can not be linearized around an non-laminar base-flow profile in Channelflow, but only around the laminar Plan Couette or Plane Poiseuille flows. An update in the implementation of Channelflow would be required to improve our validation procedure. Actually, this effort was already made by Mirko Farano during his time wihtin the ECPS group of Tobias Schneider at the École Polytechnique Fédérale de Lausanne, Switzerland. Sadly, this code was not released yet and will only be available for the Channelflow version 2.0 and above.

Non-linear terms linearized around a laminar profile in Channelflow, Channelflow Boundary Condition package and Optimal control law

The implementation within Channelflow of the optimal control law was validated in section 6.4 by using the laminar PCF profile. After verifying that the optimal control laws are stabilizing solutions through a linear analysis (§6.4.1) and linear simulations (§6.4.2), we operated different Channelflow simulations. All the simulations performed with the non-linear terms linearized around the laminar profile failed (§6.4.3), while the simulations employing the non-linear terms under the `SkewSymmetric` form did well, except for extreme control strength (§6.4.4).

The causes of this failure are not clear. The implementation of the actuation via the CFBC was validated for a linearized Channelflow simulation and a laminar PCF profile for different wave-number pairs (§5.5.1). However, this validation and the one presented in the Ph.D thesis of Heins (2015) were restricted to a limited collection of wave-number pairs: a streamwise, a spanwise and a diagonal modes. This complication may be related to the actuation of higher-order modes, or to implementation of the control itself.

The optimal control law enforced via the CFBC package is not performing as expected. An update and correction of the package to manage this situation would likely improve the validation process and perhaps clarify the failures observed when controlling a laminar flow with extreme control strenght ($\kappa = 0.25$ in §6.4.4) or when targeting an invariant solution (§7.4).

Non-linear terms linearized around an invariant solution in Channelflow, Channelflow Boundary Condition package and Optimal control law

The chapter 7 was dedicated to the stabilization of an invariant solution, namely the Nagata (1990) lower-branch solution. The optimal control laws for the different controller strengths (§7.1) were proven to be stabilizing solutions through a linear analysis (§7.2) and linear ROSSE time-integrations (§7.4). Nevertheless, this chapter raised two issues. Firstly, it was impossible to compare head-to-head simulations of an invariant solution made with the linear ROSSE model and the linearized Channelflow (see first point of this section). Secondly, all the non-linear simulations operated in Channelflow failed to stabilize EQ1, and in the best case, only managed to delay the transition to turbulence (§7.5).

The origins of this failure are not clear. Fixing the two preceding issues would likely clarify this present problem. In order to pursue this research, the interaction between the Channelflow algorithm, the CFBC package and the optimal control law needs to be carefully reviewed as well as completely validated, including the comparison of linearized Channelflow and linear ROSSE simulations of invariant solution enforced via the CFBC package. Only after this stage will the result for the non-linearity under a Rotational or Skew-symmetric form be significant. These tasks were unfortunately not achievable within this project.

Summary

In order to pursue the stabilization of the Nagata (1990) lower-branch solution within Channelflow, the following steps are necessary in order to produce conclusive results:

1. Upgrade the ChannelFlow Boundary Condition package package for Channelflow versions 2.0 and above in oder to take full benefits of the parallel computation implemented in these versions.

2. As stated in the first point, upgrade Channelflow such that the non-linear terms can be linearized around an invariant solution.

3. As stated in the second point, update and correct the ChannelFlow Boundary Condition package package and the implementation of the optimal control law in order to perform controlled Channelflow simulations linearized around a laminar profile and compare them head-to-head against the linear ROSSE model.

4. As stated in the third point, evaluate the interaction between the Channelflow algorithm, the CFBC package and the optimal control law. Only then, attempt the stabilization of an invariant solution within a non-linear Channelflow configuration.

8.1.3 Theoretical Limitation

No global system-independent guaranteed robustness properties for optimal control

As pointed out in section 3.4.1, LQG optimal control does not automatically ensure good robustness properties (Green and Limebeer, 1995, p.27). Actually, LQG solution provides no global system-independent guaranteed robustness properties (Doyle, 1978). This implies that the margins of the different optimal control laws may be very narrow. A poor precision, a numerical instability, a non-linear effect, etc., may push the state of the closed-system away from the basin of attraction of the controller a priori. It is sometimes possible to get robustness estimates a posteriori via the calculation of the sensitivity to different type of errors, but it does not constitute an exhaustive examination (Green and Limebeer, 1995).

A promising alternative to this limitation is $\mathcal{H}_\infty$ robust control (§3.5). Robust control designs a controller with guaranteed margins against perturbations of given maximal amplitude. Robustness from $\mathcal{H}_\infty$ robust control is under the assumption that the non-linear term is bounded in gain. Yet, in the NSE, the nonlinear term is not bounded since it involves a quadratic and a spatial derivative (Sharma et al., 2011). As such the $\mathcal{H}_\infty$ control would not result in absolute stability guarantees to a given size of perturbation. We attempted to design a robust controller by extending the cost function of the optimal control design with a weight to account for an external perturbation. We used the same method to determine the associated Riccati solution as for the optimal control problem (§6.2.4). However, the existence of the Riccati solution associated with the robust problem is not guaranteed. In fact, either the Riccati solution failed to converge (or when it did, it was for extremely low magnitude of perturbation), or the system did not comply any longer with its mathematical prerequisite.

As a consequence, we do not expect the current Riccati solution method (§6.2.4) to determine any practical robust control law. Yet, guaranteed margins are a major asset and we can only recommend future researchers to investigate on robust control or other methods that ensure robustness.

Leaving along the stable non-linear manifold

The idea of turbulence as a deterministic chaos evolving within a dynamical state-space is at the beginning of this research (chapter 2). In this context, it is supposed that the turbulent dynamical state escapes the neighborhood of an invariant solution along its unstable manifold (Gibson et al., 2008), as sketched in figure 8.1a. That is why we intended to design an optimal control law capable of locally stabilizing the unstable manifold of the Nagata (1990) lower-branch solution and consequently, maintaining the dynamical

state in the neighborhood of this solution (figure 8.1b). Nevertheless, the mechanism by which the turbulent dynamical state remains and leaves the neighbourdhood of an invariant solution is still unknown, and may not comply with this hypothesis.

Recent works suggest indeed that the non-normality of the stable eigenspace of the Navier-Stokes equations linearized around an invariant solution may help the turbulent trajectory to leave along stable directions. Notably, Farano et al. (2019) computed the optimal trajectory for the dynamical turbulent state to leave the neighborhood of an invariant solution and in this case, create hairpin vortices. The optimal perturbation is not an unstable eigenmode of the NSE linearized around an invariant solution, but a linear combination of stable eigenmodes that due to their non-normality generate a strong energetic growth over a finite time. As demonstrated in the publications reviewed in appendix H.3.1, a linear combination of non-normal stable directions can lead to a substantial energy growth over a finite amount of time and ignite the transition to turbulence.

This transient energy growth is not negligible in the description of the mechanism by which the state is escaping an invariant solution. As sketched in figure 8.1c, the state may in fact wander along the stable non-linear manifold and then escape along the unstable manifold of EQ1 once outside the controller stability margins. Actually, stable linear and non-linear manifolds may not be matched away from the exact solution and the controller may not be effective for these directions.

Nonetheless, to draw a conclusion on the state escaping along the stable non-normal manifold would firstly require to exclude the other potential limitations listed above. To do so, a volume forcing may turn out to be useful.

8.2 Summary and Conclusion

In the opening chapter 1, we firstly introduced the domain of research addressed in this thesis: fluid mechanics through the theoretical study of the laminar-turbulent transition and state-space control as we employed flow control. We also exposed where this research situates itself within the literature and its expected benefits. We hoped to better understand and control the non-linear and chaotic mechanisms involved within turbulent flows. Finally, we defined in details our objectives and the procedure to achieve them.

In chapter 2, we reviewed the literature on turbulence and the laminar-turbulent transition. Following a broad definition of turbulence, we defined the configuration here studied, a Plane Couette Flow, and derived the fundamental equations used to model fluid motion, i.e. the Navier-Stokes equations. The second part of the chapter is dedicated to the dynamical representation of turbulence. The recent finding of invariant

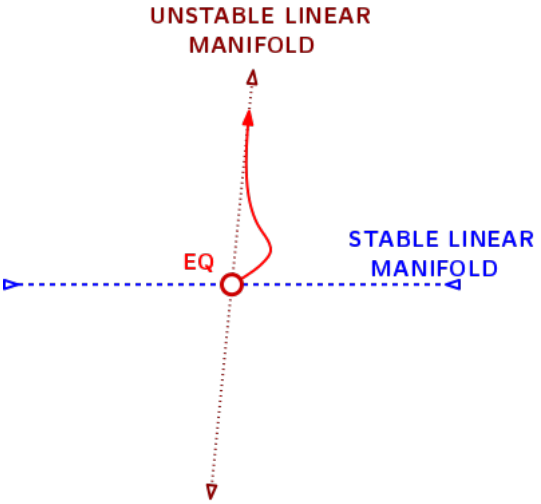

A) (Uncontrolled - Linearly Unstable) Dynamical state escaping an unstable invariant solution along its unstable linear manifold (Gibson et al., 2008).

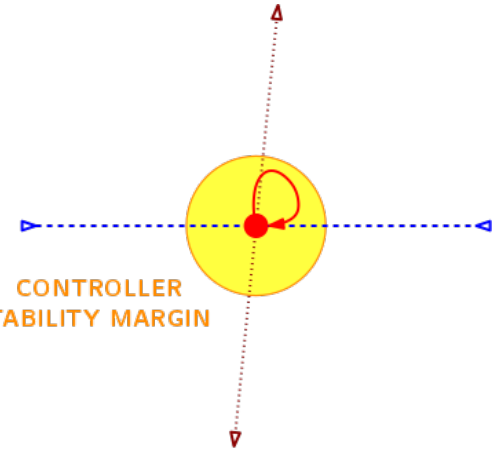

B) (Controlled - Linearly Stable) Dynamical state maintained in the neighborhood of an invariant solution, now linearly stable thanks to a controlled stability basin (§7.4).

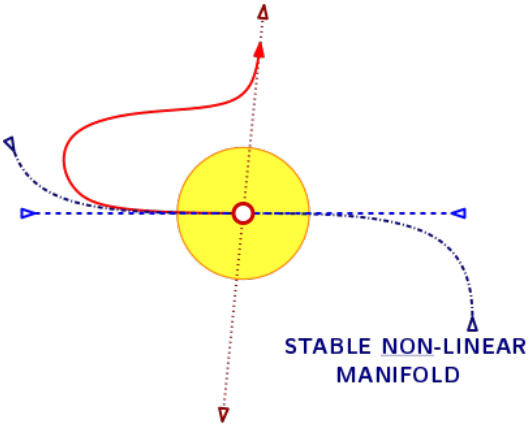

C) (Controlled - Linearly stable - Non-linear Unstable) Dynamical state linearly stable thanks to the controlled stability basin, but non-linearly unstable as escaping the invariant solution along the stable non-linear manifold due to a transient energy growth and then repelled along the unstable non-linear manifold once outside the controller stability margins (Farano et al., 2019).

FIGURE 8.1: Hypotheses on the mechanism by which the turbulent dynamical state is escaping the neighborhood of an invariant solution. The controller turns situation 8.1a into 8.1b, but may fail in the manner of 8.1c.

solutions of the Navier-Stokes equations, similar to the coherent structures found in some turbulent flows, reshaped the way turbulence is contemplated. These newly found invariant solutions can serve as the basis of a new description in order to describe its chaotic evolution, and their connections and bifurcations could explain its complex spatio-temporal intermittent process. The dynamics of turbulence can be represented as a walk within a finite-dimensional dynamical state-space, where these invariant solutions acts as unstable attractors of the turbulent state. Moreover, the previously discovered coherent structures correspond to the least unstable invariant solutions. Finally, we

developed the theoretical foundation of this research: the mechanism by which the turbulent dynamical state remains and leaves the neighborhood of an invariant solution is still unknown. By definition, the turbulent state cannot leave the neighbourhood of an invariant solution via its nonlinear unstable manifold. It is supposed that the turbulent state is attracted along the locally stable-attractive manifold of an invariant solution and then escapes its neighborhood along its locally unstable-repulsive manifold. We aimed to understand this phenomenon by attempting the stabilization via state-space control of the locally unstable eigenspace of the Plane Couette Flow Nagata (1990) lower-branch solution (referred to as EQ1). This solution is known as the least unstable solution of the Plane Couette Flow configuration. To do so, direct numerical simulations (DNS) of a PCF channel flow initiated at EQ1 and regulated via optimal control were carried.

Chapter 3 summarizes the theory related to optimal feedback control, the tool used in this thesis to operate flow control. An optimal feedback control is divided between a Kalman filter (optimal estimation) and an Linear Quadratic Regulation (optimal regulation). The estimation process assess the state of the system while the optimal regulator calculates the fitting control signal. This thesis considered a full-information controller, i.e. the entire velocity and pressure fields are known and only the regulator is designed. The actuation is enforced by blowing and suction at the upper and lower walls, also called "wall-transpiration". However, the optimal solution does not provide any global system-independent guaranteed robustness properties. Moreover, the non-linearity of the Navier-Stokes equations limits the application of linear control law. For this reason, robust control and passivity-based, the respective remedy to these issues, were presented briefly at the end of the chapter.

The application of state-space control theory to invariant solutions requires a linearised state-space model, which is the focus of chapter 4. The governing NSE were linearized and spatially discretized with spectral methods. The appropriate boundary conditions associated with a PCF configuration were applied. When linearized around a laminar baseflow profile, the NSE reduce into the simple Orr-Sommerfeld Squire model (OSS). However, when a non-laminar solution is inserted as baseflow of the NSE instead of the laminar-state, the derivation no longer diagonalises with Fourier wave-numbers due to the breaking of translational symmetry of the non-laminar baseflow. Henceforth, we derived a new model on the same fashion as the OSS model but taking into account the crossed interactions between modes. It resulted in a new divergence-free model, referenced in this thesis as the Orr-Sommerfeld Squire model Extended for a non-laminar solution (OSSE). The complex-conjugation symmetry of the OSSE state-vector can be exploited in order to derive an equivalent purely-real version of the OSSE model, the Real Orr-Sommerfeld Squire model Extended for a non-laminar solution (ROSSE). Both models were validated by calculating the eigen-spectrum of different equilibria and comparing them to the literature. They both depict faithfully the dynamical evolution of the flow in the neighborhood of a weakly unstable and/or highly periodic invariant solution

for small perturbations. Moreover, they establish a full-matrix state-space representation that enables access to linear algebra and linear control theory for any non-laminar solution — not only invariant solutions, but any three-dimensional steady state — while reducing the dimension of the dynamical state by half.

Chapter 5 describes the controller synthesis. It starts with the numerical configuration of the simulations: direct numerical simulations of turbulence were operated within the Channelflow software, actuated by wall-transpiration via the ChannelFlow Boundary Condition package. The LQR optimal control law was calculated with the OSSE or ROSSE model beforehand. This calculation first necessitated to actuate these models by wall-transpiration via a lifting-procedure, and then to define a meaningful and appropriate cost function. We chose here to target the kinetic energy density of the OSSE/ROSSE state-vector, i.e. the distance to a targeted solution. In this chapter, different linear analyses were conducted to evaluate the leading unstable eigenmodes of EQ1, their controllability and their most effective actuation modes. They demonstrated that all the unstable eigenmodes of EQ1 were controllable with this type of actuation, and as a consequence, the Nagata (1990) lower-branch solution became linearly stabilizable. It also showed that the Nagata (1990) lower-branch is indeed the easiest non-laminar solution to stabilize. Moreover, a modal controllability analysis determined that the most predominant actuation-modes to stabilize the leading eigenmode of EQ1 are the 6 upper- and lower-wall actuation modes $v^{\pm}_{(\pm 2,0)}$ and $v^{\pm}_{(\pm 1,\pm 1)}$. Finally, the implementation of the wall-transpiration in the OSSE and ROSSE models was validated. It demonstrated that the non-laminar baseflow EQ1 and inhomogeneous boundary conditions were well-implemented mathematically in the OSSE and ROSSE models, and numerically in their source-code. Furthermore, these models depict the behavior of an actuated Channelflow simulation sufficiently well to be used as control model.

The procedure to determine the optimal control law of the previously designed controller is described in chapter 6. This law governs the control signal in order to stabilize the Nagata (1990) lower-branch solution and stems from the solution of a high-dimensional algebraic Riccati equation, whose mathematical derivation is given in details at the beginning of the chapter. The Riccati solution is a full-order matrix characterized by the same high dimension of the state. Its finding implies substantial computational costs and storage requirements, and consequently, a direct method is computationally intractable for high-dimensional systems. For this reason, we performed a literature review of alternative methods to solve or bypass the Riccati solution. Unfortunately, we were not able to implement any of these in this project due to time-limitation. We used instead the method already available in `Python` based on the Schur algorithm and QZ decomposition. This method is not conceived for such high-dimensional systems, but the reduction of state dimension in the ROSSE models enabled the direct solution of the Riccati equation for small yet meaningful dimensions. The implementation of the optimal control law within the linear OSSE and ROSSE models as well as Channelflow

were validated with the laminar PCF profile. This solution is already stable, but the controller actually improved its stability. On the other side, it deteriorated the normality of the system, which increases the likelihood of transient energy growth. Finally, we noted that the implementation within a non-linear Channelflow configuration is valid but an overly intense forcing will break the simulation due to discontinuities at the walls.

Chapter 7 is dedicated to the stabilization via LQR optimal regulation of the Nagata (1990) lower-branch solution (EQ1) at Reynolds number 400. Different optimal control gains for controller strengths ranging from $\kappa = 8.0$ to $\kappa = 0.2$ were firstly calculated along the same procedure given in chapter 6. However, for $\kappa = 1.0$ and $\kappa = 2.0$, the solutions did not converge. Linear analyses of the closed-loop systems were then performed. They demonstrated that the Nagata (1990) lower-branch solution is linearly stable for each optimal control laws. Increasing the controller strength improved the linear stability of the system, but also deteriorated its normality. Thence, we initiated controlled simulations of the Nagata (1990) lower-branch solution, firstly with the linear ROSSE model and then with the non-linear Channelflow software. To make things clear, we did not plan to attract an arbitrary turbulent dynamical state towards EQ1 and stabilize it there, but instead we aimed to start from EQ1 itself and prevent the state to escape the equilibrium. To improve repeatability and the normality of the initial condition, simulations were initially perturbed in the direction of the leading eigenmode of EQ1 at a very small magnitude. Time-integration of the linear ROSSE closed-loop system demonstrated that the optimal control law for each value of κ is stabilizing EQ1. The most powerful controller led to the fastest convergence rate. Nonetheless, the stabilization of EQ1 with a non-linear algorithm of the Channelflow software was not successful. In the best cases, the transition to turbulence was delayed, but not avoided, and the most powerful controller were associated with higher divergence rates.

The origin of this failure were not clear to the author, but suggestions and interpretations were given at the beginning of this chapter 8. For now, it is not possible to conclude on the effect of the non-normality and/or non-linearity on the mechanism by which the turbulent state is escaping the close neighborhood of an invariant solution in the non-linear case. Potential numerical inaccuracies in our simulations were indeed hindering any theoretical discussion and need to be dismissed before concluding. However, their resolution is not straightforward due to theoretical and practical limitations, but the requisite tasks are listed carefully for future research in the following section. Once these limitations lifted, we hope to get a direct insight on the mechanism by which the turbulent state is leaving EQ1.

8.3 Novel contribution

The novel contributions contained within this thesis are as follows:

1. Update of the ChannelFlow Boundary Condition package of Heins (2015) and implementation of optimal control forcing within Channelflow version 1.5.1 (revison 452).

2. Derivation of the linear Orr-Sommerfeld Squire model Extended for a non-laminar solution (OSSE), and its real equivalent ROSSE model. Validation of these models against Channelflow by calculating the eigen-decomposition of different equilibria.

3. Full-information Linear Quadratic Regulation control design based on the OSSE and ROSSE models actuated via wall-transpiration. Validation against the actuation Channelflow for different actuation modes, for the laminar Plane Couette Flow profile and Nagata (1990) lower-branch solution.

4. Controllability and stabilizibility analysis of the Nagata (1990) lower-branch solution actuated by wall-transpiration: EQ1 is stabilizable via this type of actuation.

5. Procedure to determine to optimal control law based on the OSSE and ROSSE models. Validation on a laminar PCF profile with linear OSSE time-integrations and non-linear Channelflow simulations.

6. Linear stability achieved for the Nagata (1990) lower-branch solution actuated by wall-transpiration.

7. Attempt to stabilize the Nagata (1990) within a non-linear Channelflow configuration. Though this point failed, information was ascertained that will benefit future attempts.

8.4 Future Work

Remaining tasks in order to achieve the stabilization of an invariant solution and pursue this research are identified and listed below.

Choice of the control and its design

1. Conceive a volume forcing actuation to stabilize the unstable direction of an invariant solution. It would help to evaluate the behavior of the dynamical state in the neighborhood of an invariant solution or other physical phenomena without the uncertainties due to an actuation restricted to the wall. For instance, it is difficult for the moment to conclude if the failure of the stabilization of EQ1 within non-linear Channelflow (§7.5) is due to a control failure, the nature of turbulence, or any disregarded physical phenomenon. Moreover, volume forcing is a more robust actuation than wall-transpiration and is very likely to stabilize the Nagata (1990) lower-branch solution. It will then give insights on the physical mechanisms by

which the dynamical state is leaving an invariant solution, and hopefully give some guidance for a successful stabilization via wall-transpiration.

2. Design an $\mathcal{H}_\infty$ robust control law to guarantee robust margins (§3.5).
3. Investigate other cost functional formulations (see Bewley et al. (2001) and §5.2.2).
4. Investigate other control choice: passivity-based control, non-linear control, reinforced learning, non-linear control via machine learning, etc.

Resolution and range of Riccati solution and the optimal control law

4. Employ advanced model reduction methods to the linear OSSE and ROSSE models in order to capture the entire dynamics within the least amount of spatial modes. For the moment, only truncation of the high-order mode was applied (§6.3).
5. Investigate new methods to solve the Riccati equation and determine the optimal control law, notably the Adjoint of the Direct-Adjoint method or approaches based on matrix structures like the quasi-separability (§6.2.3).

Implementation of the actuation and control within the Channelflow software

6. Impose symmetries in the Channelflow simulations in order to reduce their degree of freedom and ease the stabilization of an invariant solutions.
7. Update of the CFBC package of Heins (2015) for parallel Channelflow (versions 2.0 or above, `www.channelflow.ch`), developed by the ECPS group of Tobias Schneider at the École Polytechnique Fédérale de Lausanne, Switzerland.
8. Linearize in Channelflow the non-linear terms around an invariant solution and not only around laminar profiles.
9. Review, validate and, if necessary, correct the implementation of the CFBC package and optimal control methods for Channelflow configurations linearized around a laminar profile.
10. Review, validate and, if necessary, correct the implementation of the CFBC package and optimal control methods for Channelflow configurations linearized around an invariant solution.
11. Only then, attempt the stabilization of an invariant solution within a non-linear Channelflow simulation.

Theoretical understanding of turbulence

12. Apply volume forcing (see above) to isolate the escape from an invariant solution and restrict the potential sources of discrepancies and perturbations.

13. Estimate the impact of non-normality by tracking the dynamical evolution of the state when leaving an invariant solution, and project the state onto the stable and unstable manifolds. Volume forcing can also be helpful here if targeting a particular direction.

8.5 Opening possibilities

The OSSE and ROSSE models generate a linearized operator from the Navier-Stokes equations for any time-invariant state-space position. This translates into a new high-dimensional matrix defined for a specific state. The fact that this operator constitutes an actual matrix opens many possibilities, as different mathematical tools and libraries from linear algebra are now directly applicable. For instance, linear analysis like eigenvalues-decomposition or singular-values decomposition ensues straight from numerical `Python` libraries executed on the matrix. Similarly, resolvent mode decomposition (McKeon and Sharma, 2010; Ahmed, 2018, p.39 & appendix A) can now be calculated easily for an invariant solution, instead of a laminar profile or mean flow, and compared against dynamical mode decomposition or Koopman mode decomposition (Rowley et al., 2009; Schmid, 2010; Tu et al., 2014; Sharma et al., 2016).

If achieved, the stabilization of the Nagata (1990) lower-branch can pave the way to new discoveries. Firstly, by targeting particular directions or dynamical states, it can help understand the chaotic nature of turbulence by restricting its degree of freedom. Secondly, the stabilization of other equilibria can then be achieved and the basin of attraction and robustness of different type of control for different equilibria can be evaluated. Other types of invariant solution may also be targeted. For example, unstable periodic orbits may be stabilized by discretizing the orbit into a succsion of invariant solution and exercising a specific control gain to each of them. Finally, we can imagine that the ability to direct the dynamical state in a particular direction can support the search for new invariant solution.

Appendix A

Online repositories

Validation data are stored online within
`https://doi.org/10.5258/SOTON/D1508`

For the thesis, Channelflow 1.5.1 was employed (Gibson, 2014), available on
`http://channelflow.org/`
The latest (but not compatible with the CFBC package) version 2.0 of Channelflow (Gibson et al., 2019) is now available on
`https://www.channelflow.ch/`

The ChannelFlow Boundary Condition package (CFBC) v1.0 of Peter Heins is available for Channelflow-1.4.2 on
`https://github.com/P-Heins/CFBC`

It update for Channelflow-1.5.1, as well as the implementation of optimal control forcing by the present author, are available on
`https://bitbucket.org/claisse/channelflow_controlled/`

The OSSE and ROSSE models implemented in Python by the present author are available on
`https://bitbucket.org/claisse/osse/`

Appendix B

References and aknowledgement for support

Throughout this research, we were able to access many platform for resources, data, tutorials or use software available online and often maintained by a small communities or groups of researchers. These software and platform were essential for our progress, and we would like here to acknowledge their contribution.

- The IRIDIS4 and IRIDIS5 High Performance Computing Facilities and associated support services at the University of Southampton (United-Kingdom).
- The ECPS group of Tobias Schneider at the École Polytechnique Fédérale de Lausanne (Switzerland).
- `Python3`, the dynamic, open source programming language (Foundation, 2015).
- The Python scientific libraries, `Numpy` (Oliphant, 2006) and `Scipy` (Jones et al., 2001).
- `C++`, the general-purpose programming language created by Bjarne Stroustrup as an extension of the C programming language (ISO, 2011).
- `Matplotlib`, the 2D graphics package used for `Python` for application development, interactive scripting, and publication-quality image generation across user interfaces and operating systems (Hunter, 2007).
- `Paraview`, the free post-production software (Henderson, 2004).
- The website of Mark Embree and Lloyd N. Trefethen, Pseudospectra Gateway, `http://www.comlab.ox.ac.uk/pseudospectra`.
- The book on Nonlinear Dynamics and Chaos of Strogatz (2018).

- The Youtube channel of Steven Brunton, https://www.youtube.com/channel/UCm5mt-A4w61lknZ9lCsZtBw/featured.
- The Free Encyclopedia, Wikipedia (Wikipedia contributors, 2011l).

Appendix C

Retrieving velocity components and expression of $\mathcal{C}$

This appendix details the necessary steps and matrix in order to retrieve the expression of stream- and span-wise velocity components from the expression of the wall-normal vorticity η_y

$$\eta_y := \frac{\partial u}{\partial z} - \frac{\partial w}{\partial x}. \tag{C.1}$$

REMARK: The discretisation into Fourier series of η_y is only defined for wave-numbers pairs $(\alpha, \beta) \neq (0, 0)$, i.e. $\eta_{0,0}$ is not defined.

C.1 Retrieving velocity components from the wall-normal vorticity

For a given wave-number pair $(\alpha, \beta) \neq (0, 0)$, the differentiation in x-direction of η_y is

$$\begin{aligned} \frac{\partial \eta_y}{\partial x} &= \frac{\partial}{\partial z}\frac{\partial u}{\partial x} - \frac{\partial^2 w}{\partial x^2} \\ &= \frac{\partial}{\partial z}(-\frac{\partial v}{\partial y} - \frac{\partial w}{\partial z}) - \frac{\partial^2 w}{\partial x^2} \\ &= -\frac{\partial^2 v}{\partial y z} - \frac{\partial^2 w}{\partial^2 z} - \frac{\partial^2 w}{\partial x^2}. \end{aligned} \tag{C.2}$$

which gives with a discretisation for the wavenumber pair (α, β),

$$i\alpha\,\hat{\eta}_y + i\beta\frac{\partial \hat{v}}{\partial y} = (\alpha^2 + \beta^2)\hat{w}, \tag{C.3}$$

where $k^2 = \alpha^2 + \beta^2$. The expression of the span-wise velocity component $\hat{w}$, for a given wave-number pair $(\alpha, \beta) \neq (0, 0)$, follows directly as

$$\hat{w} = \frac{1}{k^2}(i\beta\frac{\partial\hat{v}}{\partial y} + i\alpha\,\hat{\eta}_y). \tag{C.4}$$

Similarly, the expression of the steam-wise velocity component $\hat{u}$, for a given wave-number pair $(\alpha, \beta) \neq (0, 0)$, follows from the differentiation in the z-direction of η_y,

$$\hat{u} = \frac{1}{k^2}(i\alpha\frac{\partial\hat{v}}{\partial y} - i\beta\,\hat{\eta}_y). \tag{C.5}$$

C.2 Expression of $\mathcal{C}$ for the OSS model

For a given wave-number pair $(\alpha, \beta) \neq (0, 0)$, the matrix $\mathcal{C}$ depicts the change from the OSS basis $\{\hat{v}, \hat{\eta}_y\}$ into the NSE basis $\{\hat{u}, \hat{v}, \hat{w}\}$. It derives directly from equations C.5 and C.4 as

$$\begin{aligned}\begin{bmatrix}\hat{u}\\ \hat{v}\\ \hat{w}\end{bmatrix} &= \mathcal{C}\begin{bmatrix}\hat{v}\\ \hat{\eta}_y\end{bmatrix},\\ &= \frac{1}{k^2}\begin{bmatrix}i\alpha\partial_y & -i\beta\\ k^2 & 0\\ i\beta\partial_y & i\alpha\end{bmatrix}\begin{bmatrix}\hat{v}\\ \hat{\eta}_y\end{bmatrix}.\end{aligned} \tag{C.6}$$

C.3 Expression of $\mathcal{C}$ for the OSSE model

The change-of-base matrix $\mathcal{C}$ for the OSSE model follows as well from the expressions of $\hat{u}$ and $\hat{w}$ in equations C.5 and C.4. However, the OSSE model takes the entire span of stream- and span-wise wavenumbers pair,

$$\begin{bmatrix}\hat{u}_{0,0}\\ \hat{u}_{\substack{0\leq i<N_\alpha,\\ 0\leq j<N_\beta\\ (i,j)\neq(0,0)}}\\ \hat{v}_{\substack{0\leq i<N_\alpha,\\ 0\leq j<N_\beta}}\\ \hat{w}_{0,0}\\ \hat{w}_{\substack{0\leq i<N_\alpha,\\ 0\leq j<N_\beta\\ (i,j)\neq(0,0)}}\end{bmatrix} = \mathcal{C}\begin{bmatrix}\hat{v}_{\substack{0\leq i<N_\alpha,\\ 0\leq j<N_\beta}}\\ \hat{\eta}_{\substack{0\leq i<N_\alpha,\\ 0\leq j<N_\beta\\ (i,j)\neq(0,0)}}\\ \hat{u}_{0,0}\\ \hat{w}_{0,0}\end{bmatrix}. \tag{C.7}$$

Therefore, as the Fourier coefficients $\hat{u}_{0,0}$ and $\hat{w}_{0,0}$ can not be derived from $\hat{\eta}$, they are kept as such in the OSSE state-vector. The expression of $\mathcal{C}$ follows as

$$\begin{bmatrix} \hat{u}_{0,0} \\ \hat{u}_{1,1} \\ \vdots \\ \hat{u}_{N_\alpha,N_\beta} \\ \hline \hat{v}_{0,0} \\ \hat{v}_{1,1} \\ \vdots \\ \hat{v}_{N_\alpha,N_\beta} \\ \hline \hat{w}_{0,0} \\ \hat{w}_{1,1} \\ \vdots \\ \hat{w}_{N_\alpha,N_\beta} \end{bmatrix} = \mathcal{C} \begin{bmatrix} \hat{v}_{0,0} \\ \hat{v}_{1,1} \\ \vdots \\ \hat{v}_{N_\alpha,N_\beta} \\ \hline \hat{\eta}_{1,1} \\ \vdots \\ \hat{\eta}_{N_\alpha,N_\beta} \\ \hline \hat{u}_{0,0} \\ \hat{w}_{0,0} \end{bmatrix},$$

$$= \left[\begin{array}{cccc|ccc|cc} 0 & 0 & \cdots & 0 & 0 & \cdots & 0 & I & 0 \\ 0 & \frac{1}{k^2}i\alpha\partial_y & \cdots & 0 & -\frac{1}{k^2}i\beta & \cdots & 0 & 0 & 0 \\ \vdots & \vdots & \ddots & \vdots & \vdots & \ddots & \vdots & 0 & 0 \\ 0 & 0 & \cdots & \frac{1}{k^2}i\alpha\partial_y & 0 & \cdots & -\frac{1}{k^2}i\beta & 0 & 0 \\ \hline I & 0 & \cdots & 0 & 0 & \cdots & 0 & 0 & 0 \\ 0 & I & \cdots & 0 & 0 & \cdots & 0 & 0 & 0 \\ \vdots & \vdots & \ddots & \vdots & \vdots & \ddots & \vdots & 0 & 0 \\ 0 & 0 & \cdots & I & 0 & \cdots & 0 & 0 & 0 \\ \hline 0 & 0 & \cdots & 0 & 0 & \cdots & 0 & 0 & I \\ 0 & \frac{1}{k^2}i\beta\partial_y & \cdots & 0 & \frac{1}{k^2}i\alpha & \cdots & 0 & 0 & 0 \\ \vdots & \vdots & \ddots & \vdots & \vdots & \ddots & \vdots & 0 & 0 \\ 0 & 0 & \cdots & \frac{1}{k^2}i\beta\partial_y & 0 & \cdots & \frac{1}{k^2}i\alpha & 0 & 0 \end{array}\right] \left[\begin{array}{c} \hat{v}_{0,0} \\ \hat{v}_{1,1} \\ \vdots \\ \hat{v}_{N_\alpha,N_\beta} \\ \hline \hat{\eta}_{1,1} \\ \vdots \\ \hat{\eta}_{N_\alpha,N_\beta} \\ \hline \hat{u}_{0,0} \\ \hat{w}_{0,0} \end{array}\right] \tag{C.8}$$

The inverse transformation corresponds to the matrix $\mathcal{C}^{-1}$ as

$$\begin{bmatrix} \hat{v}_{0,0} \\ \hat{v}_{1,1} \\ \vdots \\ \hat{v}_{N_\alpha,N_\beta} \\ \hline \hat{\eta}_{1,1} \\ \vdots \\ \hat{\eta}_{N_\alpha,N_\beta} \\ \hline \hat{u}_{0,0} \\ \hat{w}_{0,0} \end{bmatrix} = \mathcal{C}^{-1} \begin{bmatrix} \hat{u}_{0,0} \\ \hat{u}_{1,1} \\ \vdots \\ \hat{u}_{N_\alpha,N_\beta} \\ \hline \hat{v}_{0,0} \\ \hat{v}_{1,1} \\ \vdots \\ \hat{v}_{N_\alpha,N_\beta} \\ \hline \hat{w}_{0,0} \\ \hat{w}_{1,1} \\ \vdots \\ \hat{w}_{N_\alpha,N_\beta} \end{bmatrix},$$

$$= \left[\begin{array}{cccc|cccc|cccc} 0 & 0 & \cdots & 0 & I & 0 & \cdots & 0 & 0 & 0 & \cdots & 0 \\ 0 & 0 & \cdots & 0 & 0 & I & \cdots & 0 & 0 & 0 & \cdots & 0 \\ \vdots & \vdots & \ddots & \vdots & \vdots & \vdots & \ddots & \vdots & 0 & 0 & \cdots & 0 \\ 0 & 0 & \cdots & 0 & 0 & 0 & \cdots & I & 0 & 0 & \cdots & 0 \\ \hline 0 & i\beta & \cdots & 0 & 0 & 0 & \cdots & 0 & 0 & -i\alpha & \cdots & 0 \\ \vdots & \vdots & \ddots & \vdots & \vdots & \vdots & \ddots & \vdots & 0 & 0 & \cdots & 0 \\ 0 & 0 & \cdots & i\beta & 0 & 0 & \cdots & 0 & 0 & 0 & \cdots & -i\alpha \\ \hline I & 0 & \cdots & 0 & 0 & 0 & \cdots & 0 & 0 & 0 & \cdots & 0 \\ 0 & 0 & \cdots & 0 & 0 & 0 & \cdots & 0 & I & 0 & \cdots & 0 \end{array}\right] \begin{bmatrix} \hat{u}_{0,0} \\ \hat{u}_{1,1} \\ \vdots \\ \hat{u}_{N_\alpha,N_\beta} \\ \hline \hat{v}_{0,0} \\ \hat{v}_{1,1} \\ \vdots \\ \hat{v}_{N_\alpha,N_\beta} \\ \hline \hat{w}_{0,0} \\ \hat{w}_{1,1} \\ \vdots \\ \hat{w}_{N_\alpha,N_\beta} \end{bmatrix} \tag{C.9}$$

C.4 Expression of $\mathcal{C}$ for the OSSE model with actuation not applied to the inner field

The introduction of wall-transpiration in the OSSE is presented in §5.2.1. It transforms the homogeneous PDAE 4.77 imposed with inhomogeneous boundary conditions into a inhomogeneous PDAE imposed with homogeneous boundary conditions, by changing the variable expressions for all modes of $\hat{v}$, all modes of $\hat{\eta}$ excluded the pair $(0,0)$, $\hat{u}_{0,0}$ and $\hat{w}_{0,0}$ as presented in equations 5.13. As a remainder,

$$\hat{v}_{\alpha,\beta}(y,t) = \hat{v}^0_{\alpha,\beta}(y,t) + f^+(y)\ v^+_{\alpha,\beta}(t) + f^-(y)\ v^-_{\alpha,\beta}(t), \tag{C.10}$$

where $\hat{v}$ is the inhomogeneous velocity field where $\hat{v}(\pm 1) = \hat{v}^{\pm}$ and $\hat{v}^0$ is the homogeneous velocity field $\hat{v}(\pm 1) = 0$.

Two different perspectives can be taken to develop the linear model: either the state-vector is continuous in the wall-normal direction and defined with the inhomogeneous velocity field $\hat{v}$ as $\boldsymbol{x} = [v^+, \hat{v}, v^-, \hat{\eta}, \hat{u}_{00}, \hat{w}_{00}]$; or the state-vector is discontinuous in the wall-normal direction and defined with the homogeneous velocity $\hat{v}^0$ as $\boldsymbol{x} = [v^+, \hat{v}^0, v^-, \hat{\eta}, \hat{u}_{00}, \hat{w}_{00}]$. The OSSE model actuated by wall-transpiration is formulated with the homogeneous velocity field v^0 and the discontinuous state-vector $\boldsymbol{x} = [v^+, \hat{v}^0, v^-, \hat{\eta}, \hat{u}_{00}, \hat{w}_{00}]$ (eq.**??**).

In order to retrieve a velocity field of the form $[\hat{u}, \hat{v}, \hat{w}]$ used in Channelflow, two transformations are applied to the OSSE state-vector **??**:

$$[v^+, \hat{v}^0, \overset{\boldsymbol{x}_{OSSE}}{v^-}, \hat{\eta}, \hat{u}_{00}, \hat{w}_{00}] \quad \underset{\mathcal{T}}{\Longrightarrow} \quad [v^+, \hat{v}, v^-, \hat{\eta}, \hat{u}_{00}, \hat{w}_{00}] \quad \underset{\mathcal{C}}{\Longrightarrow} \quad \overset{\boldsymbol{x}_{CHFL}}{[\hat{u}, \hat{v}, \hat{w}]}$$

1. The operator $\mathcal{T}$ (§5.2.2.4) transforms the discontinuous and homogeneous state-vector $[v^+, \hat{v}^0, v^-, \hat{\eta}, \hat{u}_{00}, \hat{w}_{00}]$ into the continuous and inhomogeneous state-vector $[v^+, \hat{v}, v^-, \hat{\eta}, \hat{u}_{00}, \hat{w}_{00}]$.
2. The operator $\mathcal{C}$ (§C.3) transforms the state-vector $[v^+, \hat{v}, v^-, \hat{\eta}, \hat{u}_{00}, \hat{w}_{00}]$ into a field $[\hat{u}, \hat{v}, \hat{w}]$.

$$\boldsymbol{x}_{CHFL} = \begin{bmatrix} \hat{u} \\ v^+ \\ \hat{v} \\ v^- \\ \hat{w} \end{bmatrix} = \mathcal{C} \begin{bmatrix} v^+ \\ \hat{v} \\ v^- \\ \hat{\eta} \\ \hat{u}_{00} \\ \hat{w}_{00} \end{bmatrix} = \mathcal{C}\mathcal{T} \begin{bmatrix} v^+ \\ \hat{v}^0 \\ v^- \\ \hat{\eta} \\ \hat{u}_{00} \\ \hat{w}_{00} \end{bmatrix} = \mathcal{C}\mathcal{T}\boldsymbol{x}_{OSSE}, \tag{C.11}$$

where $\mathcal{T}$ is composed of the block-matrices $\mathcal{T}_{\alpha,\beta}$ for each Fourier wave-number pair, such that

$$\begin{bmatrix} v^+_{\alpha,\beta} \\ \hat{v}_{\alpha,\beta} \\ v^-_{\alpha,\beta} \end{bmatrix} = \begin{bmatrix} 1 & 0 & 0 \\ f^+ & I & f^- \\ 0 & 0 & 1 \end{bmatrix} \begin{bmatrix} v^+_{\alpha,\beta} \\ \hat{v}^0_{\alpha,\beta} \\ v^-_{\alpha,\beta} \end{bmatrix} = \mathcal{T}_{\alpha,\beta} \begin{bmatrix} v^+_{\alpha,\beta} \\ \hat{v}^0_{\alpha,\beta} \\ v^-_{\alpha,\beta} \end{bmatrix}. \tag{C.12}$$

In the numerical implementation, the matrices $\mathcal{T}^{-1}\mathcal{C}^{-1}$ or $\mathcal{C}\mathcal{T}$ are calculated once and stored in order to obtain a single matrix transformation.

Howbeit, an equivalent possibility is to bypass the operator $\mathcal{T}$ analytically by defining a transformation from the state-vector $[v^+, \hat{v}^0, v^-, \hat{\eta}, \hat{u}_{00}, \hat{w}_{00}]$ directly into $[\hat{u}, \hat{v}, \hat{w}]$ as

follow

$$\begin{aligned}\hat{u} &= \frac{1}{k^2}(i\alpha\frac{\partial\hat{v}}{\partial y} - i\beta\,\hat{\eta}_y)\\ &= \frac{1}{k^2}(i\alpha\frac{\partial(\hat{v}^0 + f^+v^+ + f^-v^-)}{\partial y} - i\beta\,\hat{\eta}_y)\\ &= \frac{1}{k^2}(i\alpha\frac{\partial\hat{v}^0}{\partial y} - i\beta\,\hat{\eta}_y + i\alpha\frac{\partial f^+}{\partial y}v^+ + i\alpha\frac{\partial f^-}{\partial y}v^-).\end{aligned} \tag{C.13}$$

This imply to modify the matrix $\mathcal{C}$ by inserting the actuation as follows (and similarly for $\hat{w}$)

$$\hat{u}_{\alpha,\beta} = \frac{1}{k^2}\left[\begin{array}{ccc|c} \vdots & 0 & \vdots & \\ \iota\alpha\frac{\partial f^+}{\partial y} & \iota\alpha\partial_y & \iota\alpha\frac{\partial f^-}{\partial y} & -\iota\beta I \\ \vdots & 0 & \vdots & \end{array}\right]\left[\begin{array}{c} v^+ \\ \hat{v}^0 \\ v^- \\ \hline \hat{\eta} \end{array}\right]. \tag{C.14}$$

Appendix D

OSSE: blocks matrices

D.1 Matrices of the streamwise and spanwise discretisation for the OSSE

$$
\begin{aligned}
A_{\substack{\alpha,\beta,\\ \alpha',\beta'}} = +\imath(\alpha-\alpha')\Big[&+2\frac{\partial^2\hat{U}_{\alpha',\beta'}(y,t)}{\partial y^2} - \hat{\nabla}^2_{\alpha',\beta'}\hat{U}_{\alpha',\beta'}(y,t) - \hat{U}_{\alpha',\beta'}(y,t)\ \hat{\nabla}^2_{\alpha-\alpha',\beta-\beta'} \\
&+2\ \big(\alpha'(\alpha-\alpha')+\beta'(\beta-\beta')\big)\ \hat{U}_{\alpha',\beta'}(y,t)\Big] \\
&- \frac{\partial\hat{V}_{\alpha',\beta'}(y,t)}{\partial y}\ \hat{\nabla}^2_{\alpha-\alpha',\beta-\beta'} \quad - \hat{V}_{\alpha',\beta'}(y,t)\ \hat{\nabla}^2_{\alpha-\alpha',\beta-\beta'}\frac{\partial}{\partial y} \\
&+2\big(\alpha'(\alpha-\alpha')+\beta'(\beta-\beta')\big)\Big[\frac{\partial\hat{V}_{\alpha',\beta'}(y,t)}{\partial y} + \hat{V}_{\alpha',\beta'}(y,t)\frac{\partial}{\partial y}\Big] \\
&- \hat{\nabla}^2_{\alpha',\beta'}\frac{\partial\hat{V}_{\alpha',\beta'}(y,t)}{\partial y} - \hat{\nabla}^2_{\alpha',\beta'}\hat{V}_{\alpha',\beta'}(y,t)\frac{\partial}{\partial y} \\
&+\imath(\beta-\beta')\Big[+2\frac{\partial^2\hat{W}_{\alpha',\beta'}(y,t)}{\partial y^2} - \hat{\nabla}^2_{\alpha',\beta'}\hat{W}_{\alpha',\beta'}(y,t) - \hat{W}_{\alpha',\beta'}(y,t)\ \hat{\nabla}^2_{\alpha-\alpha',\beta-\beta'} \\
&+2\ \big(\alpha'(\alpha-\alpha')+\beta'(\beta-\beta')\big)\ \hat{W}_{\alpha',\beta'}(y,t)\Big], \qquad \text{(D.1a)}
\end{aligned}
$$

$$
\begin{aligned}
B_{\substack{\alpha,\beta,\\ \alpha',\beta'}} = \frac{\alpha'(\alpha-\alpha')+\beta'(\beta-\beta')}{(\alpha-\alpha')^2+(\beta-\beta')^2}\Big[&-2\imath(\alpha-\alpha')\Big[\frac{\partial\hat{U}_{\alpha',\beta'}(y,t)}{\partial y} + \hat{U}_{\alpha',\beta'}(y,t)\frac{\partial}{\partial y}\Big] \\
&-2\imath(\beta-\beta')\Big[\frac{\partial\hat{W}_{\alpha',\beta'}(y,t)}{\partial y} + \hat{W}_{\alpha',\beta'}(y,t)\frac{\partial}{\partial y}\Big] \\
&+\hat{V}_{\alpha',\beta'}(y,t)\ \hat{\nabla}^2_{\alpha-\alpha',\beta-\beta'} + \hat{\nabla}^2_{\alpha',\beta'}\hat{V}_{\alpha',\beta'}(y,t) \\
&-2\Big(\alpha'(\alpha-\alpha')+\beta'(\beta-\beta')\Big)\hat{V}_{\alpha',\beta'}(y,t) \\
&-2\hat{V}_{\alpha',\beta'}(y,t)\ \frac{\partial^2}{\partial y^2}\Big]\frac{\partial}{\partial y}, \qquad \text{(D.1b)}
\end{aligned}
$$

$$C_{\substack{\alpha,\beta,\\ \alpha',\beta'}} = \frac{\alpha'\beta - \beta'\alpha}{(\alpha-\alpha')^2+(\beta-\beta')^2}\Bigg[+ 2\iota(\alpha-\alpha')\Bigg[\frac{\partial \hat{U}_{\alpha',\beta'}(y,t)}{\partial y} + \hat{U}_{\alpha',\beta'}(y,t)\ \frac{\partial}{\partial y}\Bigg]$$
$$+ 2\iota(\beta-\beta')\Bigg[\frac{\partial \hat{W}_{\alpha',\beta'}(y,t)}{\partial y} + \hat{W}_{\alpha',\beta'}(y,t)\ \frac{\partial}{\partial y}\Bigg]$$
$$- \hat{V}_{\alpha',\beta'}(y,t)\ \hat{\nabla}^2_{\alpha-\alpha',\beta-\beta'} - \hat{\nabla}^2_{\alpha',\beta'}\hat{V}_{\alpha',\beta'}(y,t)$$
$$+ 2\Big(\alpha'(\alpha-\alpha') + \beta'(\beta-\beta')\Big)\hat{V}_{\alpha',\beta'}(y,t)$$
$$+ 2\hat{V}_{\alpha',\beta'}(y,t)\ \frac{\partial^2}{\partial y^2}\Bigg], \tag{D.1c}$$

$$D_{\substack{\alpha,\beta,\\ 0,0}} = \iota\alpha\hat{V}_{\alpha,\beta}\frac{\partial^2}{\partial y^2} - \iota\alpha\hat{\nabla}^2_{\alpha,\beta}\hat{V}_{\alpha,\beta}, \tag{D.1d}$$

$$E_{\substack{\alpha,\beta,\\ 0,0}} = \iota\beta\hat{V}_{\alpha,\beta}\frac{\partial^2}{\partial y^2} - \iota\beta\hat{\nabla}^2_{\alpha,\beta}\hat{V}_{\alpha,\beta}, \tag{D.1e}$$

$$F_{\substack{\alpha,\beta,\\ \alpha',\beta'}} = -\iota\beta\frac{\partial \hat{U}_{\alpha',\beta'}(y,t)}{\partial y} + \iota\alpha\frac{\partial \hat{W}_{\alpha',\beta'}(y,t)}{\partial y}, \tag{D.1f}$$

$$G_{\substack{\alpha,\beta,\\ \alpha',\beta'}} = \frac{1}{(\alpha-\alpha')^2+(\beta-\beta')^2}\ \Bigg[- \big(\alpha'\beta - \beta'\alpha\big)\hat{V}_{\alpha',\beta'}(y,t)\frac{\partial}{\partial y} \tag{D.1g}$$
$$+ \iota\big(\alpha(\alpha-\alpha') + \beta(\beta-\beta')\big)\big(\beta'\hat{U}_{\alpha',\beta'}(y,t) - \alpha'\hat{W}_{\alpha',\beta'}(y,t)\big)\Bigg]\frac{\partial}{\partial y}, \tag{D.1h}$$

$$H_{\substack{\alpha,\beta,\\ \alpha',\beta'}} = -\iota\alpha\hat{U}_{\alpha',\beta'}(y,t) - \hat{V}_{\alpha',\beta'}(y,t)\ \frac{\partial}{\partial y} - \iota\beta\hat{W}_{\alpha',\beta'}(y,t), \tag{D.1i}$$

$$J_{\substack{\alpha,\beta,\\ \alpha',\beta'}} = \frac{1}{(\alpha-\alpha')^2+(\beta-\beta')^2}\Bigg[- \big(\alpha'(\alpha-\alpha') + \beta'(\beta-\beta')\big)\hat{V}_{\alpha',\beta'}(y,t)\frac{\partial}{\partial y} \tag{D.1j}$$
$$- \iota\big(\alpha'\beta - \beta'\alpha\big)\big(\beta'\hat{U}_{\alpha',\beta'}(y,t) - \alpha'\hat{W}_{\alpha',\beta'}(y,t)\big)\Bigg], \tag{D.1k}$$

$$K_{\substack{\alpha,\beta,\\ 0,0}} = \alpha\beta\hat{U}_{\alpha,\beta} - \iota\beta\hat{V}_{\alpha,\beta}\frac{\partial}{\partial y} - \alpha^2\hat{W}_{\alpha,\beta}, \tag{D.1l}$$

$$L_{\substack{\alpha,\beta,\\ 0,0}} = \beta^2\hat{U}_{\alpha,\beta} + \iota\alpha\hat{V}_{\alpha,\beta}\frac{\partial}{\partial y} - \alpha\beta\hat{W}_{\alpha,\beta}, \tag{D.1m}$$

$$M_{\alpha',\beta'} = -\frac{\partial \hat{U}_{\alpha',\beta'}}{\partial y}, \tag{D.1n}$$

$$N_{\alpha',\beta'} = \frac{1}{\alpha'^2+\beta'^2}\ \Bigg[+ \iota\alpha'\hat{V}_{\alpha',\beta'}\frac{\partial^2}{\partial y^2} - \beta'^2\hat{U}_{\alpha',\beta'}\frac{\partial}{\partial y} + \alpha'\beta'\hat{W}_{\alpha',\beta'}\frac{\partial}{\partial y}\Bigg], \tag{D.1o}$$

$$O_{\alpha',\beta'} = \frac{1}{\alpha'^2+\beta'^2}\ \Bigg[- \iota\beta'\hat{V}_{\alpha',\beta'}\frac{\partial}{\partial y} - \alpha'\beta'\hat{U}_{\alpha',\beta'} - \beta'^2\hat{W}_{\alpha',\beta'}\Bigg], \tag{D.1p}$$

$$P_{\alpha',\beta'} = -\frac{\partial \hat{W}_{\alpha',\beta'}}{\partial y}, \tag{D.1q}$$

$$Q_{\alpha',\beta'} = \frac{1}{\alpha'^2+\beta'^2}\ \Bigg[- \alpha'^2\hat{W}_{\alpha',\beta'}\frac{\partial}{\partial y} + \alpha'\beta'\hat{U}_{\alpha',\beta'}\frac{\partial}{\partial y} + \iota\beta'\hat{V}_{\alpha',\beta'}\frac{\partial^2}{\partial y^2}\Bigg], \tag{D.1r}$$

$$R_{\alpha',\beta'} = \frac{1}{\alpha'^2+\beta'^2}\ \Bigg[+ \alpha'\beta'\hat{W}_{\alpha',\beta'} + \alpha'^2\hat{U}_{\alpha',\beta'} + \iota\alpha'\hat{V}_{\alpha',\beta'}\frac{\partial}{\partial y}\Bigg]. \tag{D.1s}$$

D.2 Matrices of the wall-normal discretisation for the OSSE

$$
\begin{aligned}
\tilde{A}_{\substack{\alpha,\beta,\\ \alpha',\beta'}} = +\iota(\alpha-\alpha')\Big[&+ 2\mathcal{D}_0^2\tilde{U}_{\alpha',\beta'}(y,t) - \tilde{\nabla}^2_{0\ \alpha',\beta'}\tilde{U}_{\alpha',\beta'}(y,t) - \tilde{U}_{\alpha',\beta'}(y,t)\ \tilde{\nabla}^2_{\alpha-\alpha',\beta-\beta'} \\
&\qquad + 2\ \big(\alpha'(\alpha-\alpha') + \beta'(\beta-\beta')\big)\ \tilde{U}_{\alpha',\beta'}(y,t)\Big] \\
&- \mathcal{D}_0\tilde{V}_{\alpha',\beta'}(y,t)\ \tilde{\nabla}^2_{\alpha-\alpha',\beta-\beta'} \quad - \tilde{V}_{\alpha',\beta'}(y,t)\ \tilde{\nabla}^2_{\alpha-\alpha',\beta-\beta'}\mathcal{D} \\
&+ 2\big(\alpha'(\alpha-\alpha') + \beta'(\beta-\beta')\big)\Big[\mathcal{D}_0\tilde{V}_{\alpha',\beta'}(y,t) + \tilde{V}_{\alpha',\beta'}(y,t)\mathcal{D}\Big] \\
&- \tilde{\nabla}^2_{0\ \alpha',\beta'}\mathcal{D}_0\tilde{V}_{\alpha',\beta'}(y,t) - \tilde{\nabla}^2_{0\ \alpha',\beta'}\tilde{V}_{\alpha',\beta'}(y,t)\mathcal{D} \\
&+ \iota(\beta-\beta')\Big[+ 2\mathcal{D}_0^2\tilde{W}_{\alpha',\beta'}(y,t) - \tilde{\nabla}^2_{0\ \alpha',\beta'}\tilde{W}_{\alpha',\beta'}(y,t) - \tilde{W}_{\alpha',\beta'}(y,t)\ \tilde{\nabla}^2_{\alpha-\alpha',\beta-\beta'} \\
&\qquad + 2\ \big(\alpha'(\alpha-\alpha') + \beta'(\beta-\beta')\big)\ \tilde{W}_{\alpha',\beta'}(y,t)\Big], \qquad \text{(D.2a)}
\end{aligned}
$$

$$
\begin{aligned}
\tilde{B}_{\substack{\alpha,\beta,\\ \alpha',\beta'}} = \frac{\alpha'(\alpha-\alpha') + \beta'(\beta-\beta')}{(\alpha-\alpha')^2 + (\beta-\beta')^2}\Big[&- 2\iota(\alpha-\alpha')\Big[\mathcal{D}_0\tilde{U}_{\alpha',\beta'}(y,t) + \tilde{U}_{\alpha',\beta'}(y,t)\mathcal{D}\Big] \\
&- 2\iota(\beta-\beta')\Big[\mathcal{D}_0\tilde{W}_{\alpha',\beta'}(y,t) + \tilde{W}_{\alpha',\beta'}(y,t)\mathcal{D}\Big] \\
&+ \tilde{V}_{\alpha',\beta'}(y,t)\ \tilde{\nabla}^2_{\alpha-\alpha',\beta-\beta'} + \tilde{\nabla}^2_{0\ \alpha',\beta'}\tilde{V}_{\alpha',\beta'}(y,t) \\
&- 2\Big(\alpha'(\alpha-\alpha') + \beta'(\beta-\beta')\Big)\tilde{V}_{\alpha',\beta'}(y,t) \\
&- 2\tilde{V}_{\alpha',\beta'}(y,t)\ \mathcal{D}^2\Big]\mathcal{D}, \qquad \text{(D.2b)}
\end{aligned}
$$

$$
\begin{aligned}
\tilde{C}_{\substack{\alpha,\beta,\\ \alpha',\beta'}} = \frac{\alpha'\beta - \beta'\alpha}{(\alpha-\alpha')^2 + (\beta-\beta')^2}\Big[&+ 2\iota(\alpha-\alpha')\Big[\mathcal{D}_0\tilde{U}_{\alpha',\beta'}(y,t) + \tilde{U}_{\alpha',\beta'}(y,t)\ \mathcal{D}\Big] \\
&+ 2\iota(\beta-\beta')\Big[\mathcal{D}_0\tilde{W}_{\alpha',\beta'}(y,t) + \tilde{W}_{\alpha',\beta'}(y,t)\ \mathcal{D}\Big] \\
&- \tilde{V}_{\alpha',\beta'}(y,t)\ \tilde{\nabla}^2_{\alpha-\alpha',\beta-\beta'} - \tilde{\nabla}^2_{0\ \alpha',\beta'}\tilde{V}_{\alpha',\beta'}(y,t) \\
&+ 2\Big(\alpha'(\alpha-\alpha') + \beta'(\beta-\beta')\Big)\tilde{V}_{\alpha',\beta'}(y,t) \\
&+ 2\tilde{V}_{\alpha',\beta'}(y,t)\ \mathcal{D}^2\Big], \qquad \text{(D.2c)}
\end{aligned}
$$

$$
\tilde{D}_{\substack{\alpha,\beta,\\ 0,0}} = \iota\alpha\tilde{V}_{\alpha,\beta}\mathcal{D}^2 - \iota\alpha\tilde{\nabla}^2_{0\ \alpha,\beta}\hat{V}_{\alpha,\beta}, \qquad \text{(D.2d)}
$$

$$
\tilde{E}_{\substack{\alpha,\beta,\\ 0,0}} = \iota\beta\tilde{V}_{\alpha,\beta}\mathcal{D}^2 - \iota\beta\tilde{\nabla}^2_{0\ \alpha,\beta}\hat{V}_{\alpha,\beta}, \qquad \text{(D.2e)}
$$

$$
\tilde{F}_{\substack{\alpha,\beta,\\ \alpha',\beta'}} = -\iota\beta\mathcal{D}_0\tilde{U}_{\alpha',\beta'}(y,t) + \iota\alpha\mathcal{D}_0\tilde{W}_{\alpha',\beta'}(y,t), \qquad \text{(D.2f)}
$$

$$
\begin{aligned}
\tilde{G}_{\substack{\alpha,\beta,\\ \alpha',\beta'}} = \frac{1}{(\alpha-\alpha')^2 + (\beta-\beta')^2}\ \Big[&- \big(\alpha'\beta - \beta'\alpha\big)\tilde{V}_{\alpha',\beta'}(y,t)\mathcal{D} \qquad \text{(D.2g)} \\
&+ \iota\big(\alpha(\alpha-\alpha') + \beta(\beta-\beta')\big)\big(\beta'\tilde{U}_{\alpha',\beta'}(y,t) - \alpha'\tilde{W}_{\alpha',\beta'}(y,t)\big)\Big]\mathcal{D}, \qquad \text{(D.2h)}
\end{aligned}
$$

$$\tilde{H}_{\substack{\alpha,\beta,\\ \alpha',\beta'}} = -\iota\alpha\tilde{U}_{\alpha',\beta'}(y,t) - \tilde{V}_{\alpha',\beta'}(y,t)\ \mathcal{D} - \iota\beta\tilde{W}_{\alpha',\beta'}(y,t), \tag{D.2i}$$

$$\tilde{J}_{\substack{\alpha,\beta,\\ \alpha',\beta'}} = \frac{1}{(\alpha-\alpha')^2+(\beta-\beta')^2}\Big[- \big(\alpha'(\alpha-\alpha') + \beta'(\beta-\beta')\big)\tilde{V}_{\alpha',\beta'}(y,t)\mathcal{D} \tag{D.2j}$$

$$- \iota\big(\alpha'\beta - \beta'\alpha\big)\big(\beta'\tilde{U}_{\alpha',\beta'}(y,t) - \alpha'\tilde{W}_{\alpha',\beta'}(y,t)\big)\Big], \tag{D.2k}$$

$$\tilde{K}_{\substack{\alpha,\beta,\\ 0,0}} = \alpha\beta\tilde{U}_{\alpha,\beta} - \iota\beta\tilde{V}_{\alpha,\beta}\mathcal{D} - \alpha^2\tilde{W}_{\alpha,\beta}, \tag{D.2l}$$

$$\tilde{L}_{\substack{\alpha,\beta,\\ 0,0}} = \beta^2\tilde{U}_{\alpha,\beta} + \iota\alpha\tilde{V}_{\alpha,\beta}\mathcal{D} - \alpha\beta\tilde{W}_{\alpha,\beta}, \tag{D.2m}$$

$$\tilde{M}_{\alpha',\beta'} = -\mathcal{D}_0\tilde{U}_{\alpha',\beta'}, \tag{D.2n}$$

$$\tilde{N}_{\alpha',\beta'} = \frac{1}{\alpha'^2+\beta'^2}\ \Big[+ \iota\alpha'\tilde{V}_{\alpha',\beta'}\mathcal{D}^2 - \beta'^2\tilde{U}_{\alpha',\beta'}\mathcal{D} + \alpha'\beta'\tilde{W}_{\alpha',\beta'}\mathcal{D}\Big], \tag{D.2o}$$

$$\tilde{O}_{\alpha',\beta'} = \frac{1}{\alpha'^2+\beta'^2}\ \Big[- \iota\beta'\tilde{V}_{\alpha',\beta'}\mathcal{D} - \alpha'\beta'\tilde{U}_{\alpha',\beta'} - \beta'^2\tilde{W}_{\alpha',\beta'}\Big], \tag{D.2p}$$

$$\tilde{P}_{\alpha',\beta'} = -\mathcal{D}_0\tilde{W}_{\alpha',\beta'}, \tag{D.2q}$$

$$\tilde{Q}_{\alpha',\beta'} = \frac{1}{\alpha'^2+\beta'^2}\ \Big[- \alpha'^2\tilde{W}_{\alpha',\beta'}\mathcal{D} + \alpha'\beta'\tilde{U}_{\alpha',\beta'}\mathcal{D} + \iota\beta'\tilde{V}_{\alpha',\beta'}\mathcal{D}^2\Big], \tag{D.2r}$$

$$\tilde{R}_{\alpha',\beta'} = \frac{1}{\alpha'^2+\beta'^2}\ \Big[+ \alpha'\beta'\tilde{W}_{\alpha',\beta'} + \alpha'^2\tilde{U}_{\alpha',\beta'} + \iota\alpha'\tilde{V}_{\alpha',\beta'}\mathcal{D}\Big]. \tag{D.2s}$$

Appendix E

OSSE actuated by wall-transpiration: blocks matrices

$$\mathbb{E}_1 = \begin{bmatrix} -\frac{1}{\tau_{v_{\alpha,\beta}}} & 0 & 0 \\ \left[\frac{1}{\tau_{v_{\alpha,\beta}}}\tilde{\nabla}^2 f^+(y) + \frac{1}{Re}\tilde{\nabla}^4_{\alpha,\beta} f^+(y)\right] & \frac{1}{Re}\mathring{\tilde{\nabla}}^4_{\alpha,\beta} & \left[\frac{1}{\tau_{v_{\alpha,\beta}}}\tilde{\nabla}^2 f^-(y) + \frac{1}{Re}\tilde{\nabla}^4_{\alpha,\beta} f^-(y)\right] \\ 0 & 0 & -\frac{1}{\tau_{v_{\alpha,\beta}}} \end{bmatrix}, \tag{E.1a}$$

$$\mathbb{E}_2 = \begin{bmatrix} -\frac{1}{\tau_{\eta_{\alpha,\beta}}} & 0 & 0 \\ \left[\frac{1}{Re}\tilde{\nabla}^2_{\alpha,\beta}\, g^+(y) + \frac{1}{\tau_{\eta_{\alpha,\beta}}}\, g^+(y)\right] & \frac{1}{Re}\mathring{\tilde{\nabla}}^2_{\alpha,\beta} & \left[\frac{1}{Re}\tilde{\nabla}^2_{\alpha,\beta}\, g^-(y) + \frac{1}{\tau_{\eta_{\alpha,\beta}}}\, g^-(y)\right] \\ 0 & 0 & -\frac{1}{\tau_{\eta_{\alpha,\beta}}} \end{bmatrix}, \tag{E.1b}$$

$$\mathbb{E}_3 = \begin{bmatrix} -\frac{1}{\tau_{u_{0,0}}} & 0 & 0 \\ \mathcal{M} f^+(y) + \frac{1}{\tau_{u_{0,0}}} f^+(y) & \mathring{\mathcal{M}} & \mathcal{M} f^-(y) + \frac{1}{\tau_{u_{0,0}}} f^-(y) \\ 0 & 0 & -\frac{1}{\tau_{u_{0,0}}} \end{bmatrix}, \tag{E.1c}$$

$$\mathbb{E}_4 = \begin{bmatrix} -\frac{1}{\tau_{w_{0,0}}} & 0 & 0 \\ \mathcal{M} f^+(y) + \frac{1}{\tau_{w_{0,0}}} f^+(y) & \mathring{\mathcal{M}} & \mathcal{M} f^-(y) + \frac{1}{\tau_{w_{0,0}}} f^-(y) \\ 0 & 0 & -\frac{1}{\tau_{w_{0,0}}} \end{bmatrix}, \tag{E.1d}$$

$$\mathbb{A} = \tilde{A}_{\substack{\alpha,\beta,\\ \alpha-\alpha',\beta-\beta'}} \begin{bmatrix} 0 & 0 & 0 \\ f^+(y) & I & f^-(y) \\ 0 & 0 & 0 \end{bmatrix}, \tag{E.1e}$$

$$\mathbb{B} = \tilde{B}_{\substack{\alpha,\beta,\\ \alpha-\alpha',\beta-\beta'}} \begin{bmatrix} 0 & 0 & 0 \\ f^+(y) & I & f^-(y) \\ 0 & 0 & 0 \end{bmatrix}, \tag{E.1f}$$

$$\mathbb{C} = \tilde{C}_{\substack{\alpha,\beta,\\ \alpha-\alpha',\beta-\beta'}} \begin{bmatrix} 0 & 0 & 0 \\ g^+(y) & I & g^-(y) \\ 0 & 0 & 0 \end{bmatrix}, \tag{E.1g}$$

$$\mathbb{D} = \tilde{D}_{\substack{\alpha,\beta,\\ 0,0}} \begin{bmatrix} 0 & 0 & 0 \\ f^+(y) & I & f^-(y) \\ 0 & 0 & 0 \end{bmatrix}, \tag{E.1h}$$

$$\mathbb{E} = \tilde{E}_{\substack{\alpha,\beta,\\ 0,0}} \begin{bmatrix} 0 & 0 & 0 \\ f^+(y) & I & f^-(y) \\ 0 & 0 & 0 \end{bmatrix}, \tag{E.1i}$$

$$\mathbb{F} = \tilde{F}_{\substack{\alpha,\beta,\\ \alpha-\alpha',\beta-\beta'}} \begin{bmatrix} 0 & 0 & 0 \\ f^+(y) & I & f^-(y) \\ 0 & 0 & 0 \end{bmatrix}, \tag{E.1j}$$

$$\mathbb{G} = \tilde{G}_{\substack{\alpha,\beta,\\ \alpha-\alpha',\beta-\beta'}} \begin{bmatrix} 0 & 0 & 0 \\ f^+(y) & I & f^-(y) \\ 0 & 0 & 0 \end{bmatrix}, \tag{E.1k}$$

$$\mathbb{H} = \tilde{H}_{\substack{\alpha,\beta,\\ \alpha-\alpha',\beta-\beta'}} \begin{bmatrix} 0 & 0 & 0 \\ g^+(y) & I & g^-(y) \\ 0 & 0 & 0 \end{bmatrix}, \tag{E.1l}$$

$$\mathbb{J} = \tilde{J}_{\substack{\alpha,\beta,\\ \alpha-\alpha',\beta-\beta'}} \begin{bmatrix} 0 & 0 & 0 \\ g^+(y) & I & g^-(y) \\ 0 & 0 & 0 \end{bmatrix}, \tag{E.1m}$$

$$\mathbb{K} = \tilde{K}_{\substack{\alpha,\beta,\\ 0,0}} \begin{bmatrix} 0 & 0 & 0 \\ f^+(y) & I & f^-(y) \\ 0 & 0 & 0 \end{bmatrix}, \tag{E.1n}$$

$$\mathbb{L} = \tilde{L}_{\substack{\alpha,\beta,\\ 0,0}} \begin{bmatrix} 0 & 0 & 0 \\ f^+(y) & I & f^-(y) \\ 0 & 0 & 0 \end{bmatrix}, \tag{E.1o}$$

$$\mathbb{M} = \tilde{M}_{\alpha',\beta'} \begin{bmatrix} 0 & 0 & 0 \\ f^+(y) & I & f^-(y) \\ 0 & 0 & 0 \end{bmatrix}, \tag{E.1p}$$

$$\mathbb{N} = \tilde{N}_{\alpha',\beta'} \begin{bmatrix} 0 & 0 & 0 \\ f^+(y) & I & f^-(y) \\ 0 & 0 & 0 \end{bmatrix}, \tag{E.1q}$$

$$\mathbb{O} = \tilde{O}_{\alpha',\beta'} \begin{bmatrix} 0 & 0 & 0 \\ g^+(y) & I & g^-(y) \\ 0 & 0 & 0 \end{bmatrix}, \tag{E.1r}$$

$$\mathbb{P} = \tilde{P}_{\alpha',\beta'} \begin{bmatrix} 0 & 0 & 0 \\ f^+(y) & I & f^-(y) \\ 0 & 0 & 0 \end{bmatrix}, \tag{E.1s}$$

$$\mathbb{Q} = \tilde{Q}_{\alpha',\beta'} \begin{bmatrix} 0 & 0 & 0 \\ f^+(y) & I & f^-(y) \\ 0 & 0 & 0 \end{bmatrix}, \tag{E.1t}$$

$$\mathbb{R} = \tilde{R}_{\alpha',\beta'} \begin{bmatrix} 0 & 0 & 0 \\ g^+(y) & I & g^-(y) \\ 0 & 0 & 0 \end{bmatrix}, \tag{E.1u}$$

$$\mathbb{B}_1 = \begin{bmatrix} \frac{1}{\tau_{v_{\alpha,\beta}}} & 0 \\ -\frac{1}{\tau_{v_{\alpha,\beta}}}\tilde{\nabla}^2 f^+(y) & -\frac{1}{\tau_{v_{\alpha,\beta}}}\tilde{\nabla}^2 f^-(y) \\ 0 & \frac{1}{\tau_{v_{\alpha,\beta}}} \end{bmatrix}, \tag{E.1v}$$

$$\mathbb{B}_2 = \begin{bmatrix} \frac{1}{\tau_{\eta_{\alpha,\beta}}} & 0 \\ -\frac{1}{\tau_{\eta_{\alpha,\beta}}} g^+(y) & -\frac{1}{\tau_{\eta_{\alpha,\beta}}} g^-(y) \\ 0 & \frac{1}{\tau_{\eta_{\alpha,\beta}}} \end{bmatrix}, \tag{E.1w}$$

$$\mathbb{B}_3 = \begin{bmatrix} \frac{1}{\tau_{u_{0,0}}} & 0 \\ -\frac{1}{\tau_{u_{0,0}}} f^+(y) & -\frac{1}{\tau_{u_{0,0}}} f^-(y) \\ 0 & \frac{1}{\tau_{u_{0,0}}} \end{bmatrix}, \tag{E.1x}$$

$$\mathbb{B}_4 = \begin{bmatrix} \frac{1}{\tau_{w_{0,0}}} & 0 \\ -\frac{1}{\tau_{w_{0,0}}} f^+(y) & -\frac{1}{\tau_{w_{0,0}}} f^-(y) \\ 0 & \frac{1}{\tau_{w_{0,0}}} \end{bmatrix}, \tag{E.1y}$$

with $\mathcal{M} = \left[\frac{1}{Re}\tilde{\nabla}^2_{0,0} - \bar{V}_{0,0}\mathcal{D}\right]$ and $\overset{\circ}{\mathcal{M}} = \left[\frac{1}{Re}\overset{\circ}{\tilde{\nabla}}{}^2_{0,0} - \bar{V}_{0,0}\overset{\circ}{\mathcal{D}}\right]$.

Appendix F

OSSE: Detailed derivation of the model

F.1 Derivation of the OSSE model

A steady non-laminar state of the form

$$\bar{\boldsymbol{U}} = (\bar{U}(x,y,z), \bar{V}(x,y,z), \bar{W}(x,y,z)). \tag{F.1}$$

is inserted into the NSE 4.4. The linearisation around this steady non-laminar state follows as

$$\begin{aligned}\frac{\partial u}{\partial t} = \frac{1}{Re}\nabla^2 u - \frac{\partial p}{\partial x} &- u\frac{\partial \bar{U}}{\partial x} - \bar{U}\frac{\partial u}{\partial x} - u\frac{\partial u}{\partial x} \\ &- v\frac{\partial \bar{U}}{\partial y} - \bar{V}\frac{\partial u}{\partial y} - v\frac{\partial u}{\partial y} \\ &- w\frac{\partial \bar{U}}{\partial z} - \bar{W}\frac{\partial u}{\partial z} - w\frac{\partial u}{\partial z},\end{aligned} \tag{F.2a}$$

$$\begin{aligned}\frac{\partial v}{\partial t} = \frac{1}{Re}\nabla^2 v - \frac{\partial p}{\partial y} &- u\frac{\partial \bar{V}}{\partial x} - \bar{U}\frac{\partial v}{\partial x} - u\frac{\partial v}{\partial x} \\ &- v\frac{\partial \bar{V}}{\partial y} - \bar{V}\frac{\partial v}{\partial y} - v\frac{\partial v}{\partial y} \\ &- w\frac{\partial \bar{V}}{\partial z} - \bar{W}\frac{\partial v}{\partial z} - w\frac{\partial v}{\partial z},\end{aligned} \tag{F.2b}$$

$$\begin{aligned}\frac{\partial w}{\partial t} = \frac{1}{Re}\nabla^2 w - \frac{\partial p}{\partial z} &- u\frac{\partial \bar{W}}{\partial x} - \bar{U}\frac{\partial w}{\partial x} - u\frac{\partial w}{\partial x} \\ &- v\frac{\partial \bar{W}}{\partial y} - \bar{V}\frac{\partial w}{\partial y} - v\frac{\partial w}{\partial y} \\ &- w\frac{\partial \bar{W}}{\partial z} - \bar{W}\frac{\partial w}{\partial z} - w\frac{\partial w}{\partial z},\end{aligned} \tag{F.2c}$$

$$\frac{\partial u}{\partial x} + \frac{\partial v}{\partial y} + \frac{\partial w}{\partial z} = 0. \tag{F.2d}$$

REMARK: Special care when dealing with the Laplacian:

$$\begin{aligned}\Delta(ab) =&\nabla^2(ab) = (\nabla\cdot\nabla)(ab)\\ =&\frac{\partial^2 a}{\partial x^2}b + 2\frac{\partial a}{\partial x}\frac{\partial b}{\partial x} + a\frac{\partial^2 b}{\partial x^2} + \frac{\partial^2 a}{\partial y^2}b + 2\frac{\partial a}{\partial y}\frac{\partial b}{\partial y} + a\frac{\partial^2 b}{\partial y^2} + \frac{\partial^2 a}{\partial z^2}b + 2\frac{\partial a}{\partial z}\frac{\partial b}{\partial z} + a\frac{\partial^2 b}{\partial z^2}\\ =&(\nabla^2 a)b + a(\nabla^2 b) + 2\frac{\partial a}{\partial x}\frac{\partial b}{\partial x} + 2\frac{\partial a}{\partial y}\frac{\partial b}{\partial y} + 2\frac{\partial a}{\partial z}\frac{\partial b}{\partial z}\end{aligned} \tag{F.3}$$

Neglecting the body forces and non-linear terms, it follows [eq. 4.56]

$$\frac{\partial u}{\partial t} = \frac{1}{Re}\nabla^2 u - \frac{\partial p}{\partial x} - u\frac{\partial \bar{U}}{\partial x} - \bar{U}\frac{\partial u}{\partial x} - v\frac{\partial \bar{U}}{\partial y} - \bar{V}\frac{\partial u}{\partial y} - w\frac{\partial \bar{U}}{\partial z} - \bar{W}\frac{\partial u}{\partial z}, \tag{F.4a}$$

$$\frac{\partial v}{\partial t} = \frac{1}{Re}\nabla^2 v - \frac{\partial p}{\partial y} - u\frac{\partial \bar{V}}{\partial x} - \bar{U}\frac{\partial v}{\partial x} - v\frac{\partial \bar{V}}{\partial y} - \bar{V}\frac{\partial v}{\partial y} - w\frac{\partial \bar{V}}{\partial z} - \bar{W}\frac{\partial v}{\partial z}, \tag{F.4b}$$

$$\frac{\partial w}{\partial t} = \frac{1}{Re}\nabla^2 w - \frac{\partial p}{\partial z} - u\frac{\partial \bar{W}}{\partial x} - \bar{U}\frac{\partial w}{\partial x} - v\frac{\partial \bar{W}}{\partial y} - \bar{V}\frac{\partial w}{\partial y} - w\frac{\partial \bar{W}}{\partial z} - \bar{W}\frac{\partial w}{\partial z}, \tag{F.4c}$$

$$\frac{\partial u}{\partial x} + \frac{\partial v}{\partial y} + \frac{\partial w}{\partial z} = 0. \tag{F.4d}$$

Time-variation of the wall-normal velocity v

Firstly, the Laplacian of equation 4.56b is taken and the pressure scalar-field p is eliminated via the Poisson equation 4.8.

$$\begin{aligned}\frac{\partial}{\partial t}\nabla^2 v =& \frac{1}{Re}\nabla^4 v + 2\frac{\partial^2 \bar{U}}{\partial xy}\frac{\partial u}{\partial x} + 2\frac{\partial \bar{U}}{\partial x}\frac{\partial^2 u}{\partial xy} + 2\frac{\partial^2 \bar{V}}{\partial xy}\frac{\partial u}{\partial y} + 2\frac{\partial \bar{V}}{\partial x}\frac{\partial^2 u}{\partial y^2} + 2\frac{\partial^2 \bar{W}}{\partial xy}\frac{\partial u}{\partial z} + 2\frac{\partial \bar{W}}{\partial x}\frac{\partial^2 u}{\partial yz}\\ &+ 2\frac{\partial^2 \bar{U}}{\partial y^2}\frac{\partial v}{\partial x} + 2\frac{\partial \bar{U}}{\partial y}\frac{\partial^2 v}{\partial xy} + 2\frac{\partial^2 \bar{V}}{\partial y^2}\frac{\partial v}{\partial y} + 2\frac{\partial \bar{V}}{\partial y}\frac{\partial^2 v}{\partial y^2} + 2\frac{\partial^2 \bar{W}}{\partial y^2}\frac{\partial v}{\partial z} + 2\frac{\partial \bar{W}}{\partial y}\frac{\partial^2 v}{\partial yz}\\ &+ 2\frac{\partial^2 \bar{U}}{\partial yz}\frac{\partial w}{\partial x} + 2\frac{\partial \bar{U}}{\partial z}\frac{\partial^2 w}{\partial xy} + 2\frac{\partial^2 \bar{V}}{\partial yz}\frac{\partial w}{\partial y} + 2\frac{\partial \bar{V}}{\partial z}\frac{\partial^2 w}{\partial y^2} + 2\frac{\partial^2 \bar{W}}{\partial yz}\frac{\partial w}{\partial z} + 2\frac{\partial \bar{W}}{\partial z}\frac{\partial^2 w}{\partial yz}\\ &- \nabla^2 u\frac{\partial \bar{V}}{\partial x} - 2\frac{\partial u}{\partial x}\frac{\partial^2 \bar{V}}{\partial x^2} - 2\frac{\partial u}{\partial y}\frac{\partial^2 \bar{V}}{\partial xy} - 2\frac{\partial u}{\partial z}\frac{\partial^2 \bar{V}}{\partial xz} - u\frac{\partial \nabla^2 \bar{V}}{\partial x}\\ &- \nabla^2 \bar{U}\frac{\partial v}{\partial x} - 2\frac{\partial \bar{U}}{\partial x}\frac{\partial^2 v}{\partial x^2} - 2\frac{\partial \bar{U}}{\partial y}\frac{\partial^2 v}{\partial xy} - 2\frac{\partial \bar{U}}{\partial z}\frac{\partial^2 v}{\partial xz} - \bar{U}\frac{\partial \nabla^2 v}{\partial x} - \nabla^2\left(u\frac{\partial v}{\partial x}\right)\\ &- \nabla^2 v\frac{\partial \bar{V}}{\partial y} - 2\frac{\partial v}{\partial x}\frac{\partial^2 \bar{V}}{\partial xy} - 2\frac{\partial v}{\partial y}\frac{\partial^2 \bar{V}}{\partial y^2} - 2\frac{\partial v}{\partial z}\frac{\partial^2 \bar{V}}{\partial yz} - v\frac{\partial \nabla^2 \bar{V}}{\partial y}\\ &- \nabla^2 \bar{V}\frac{\partial v}{\partial y} - 2\frac{\partial \bar{V}}{\partial x}\frac{\partial^2 v}{\partial xy} - 2\frac{\partial \bar{V}}{\partial y}\frac{\partial^2 v}{\partial y^2} - 2\frac{\partial \bar{V}}{\partial z}\frac{\partial^2 v}{\partial yz} - \bar{V}\frac{\partial \nabla^2 v}{\partial y} - \nabla^2\left(v\frac{\partial v}{\partial y}\right)\\ &- \nabla^2 w\frac{\partial \bar{V}}{\partial z} - 2\frac{\partial w}{\partial x}\frac{\partial^2 \bar{V}}{\partial xz} - 2\frac{\partial w}{\partial y}\frac{\partial^2 \bar{V}}{\partial yz} - 2\frac{\partial w}{\partial z}\frac{\partial^2 \bar{V}}{\partial z^2} - w\frac{\partial \nabla^2 \bar{V}}{\partial z}\\ &- \nabla^2 \bar{W}\frac{\partial v}{\partial z} - 2\frac{\partial \bar{W}}{\partial x}\frac{\partial^2 v}{\partial xz} - 2\frac{\partial \bar{W}}{\partial y}\frac{\partial^2 v}{\partial yz} - 2\frac{\partial \bar{W}}{\partial z}\frac{\partial^2 v}{\partial z^2} - \bar{W}\frac{\partial \nabla^2 v}{\partial z} - \nabla^2\left(w\frac{\partial v}{\partial z}\right)\end{aligned} \tag{F.5a}$$

Then rearranging and making explicit the simplicition,

$$
\begin{aligned}
\frac{\partial}{\partial t}\nabla^2 v \;=\; & +2\,\frac{\partial^2\bar{U}}{\partial xy}\frac{\partial u}{\partial x}+2\,\frac{\partial\bar{U}}{\partial x}\frac{\partial^2 u}{\partial xy}+2\,\frac{\partial^2\bar{V}}{\partial xy}\frac{\partial u}{\partial y}+2\,\frac{\partial\bar{V}}{\partial x}\frac{\partial^2 u}{\partial y^2}+2\,\frac{\partial^2\bar{W}}{\partial xy}\frac{\partial u}{\partial z}+2\,\frac{\partial\bar{W}}{\partial x}\frac{\partial^2 u}{\partial yz}\\
&-\nabla^2 u\frac{\partial\bar{V}}{\partial x}-2\frac{\partial u}{\partial x}\frac{\partial^2\bar{V}}{\partial x^2}-2\frac{\partial u}{\partial y}\frac{\partial^2\bar{V}}{\partial xy}-2\frac{\partial u}{\partial z}\frac{\partial^2\bar{V}}{\partial xz}-u\frac{\partial\nabla^2\bar{V}}{\partial x}\\
&+\frac{1}{Re}\nabla^4 v+2\,\frac{\partial^2\bar{U}}{\partial y^2}\frac{\partial v}{\partial x}+2\,\frac{\partial\bar{U}}{\partial y}\frac{\partial^2 v}{\partial xy}+2\,\frac{\partial^2\bar{V}}{\partial y^2}\frac{\partial v}{\partial y}+2\,\frac{\partial\bar{V}}{\partial y}\frac{\partial^2 v}{\partial y^2}+2\,\frac{\partial^2\bar{W}}{\partial y^2}\frac{\partial v}{\partial z}+2\,\frac{\partial\bar{W}}{\partial y}\frac{\partial^2 v}{\partial yz}\\
&-\nabla^2\bar{U}\frac{\partial v}{\partial x}-2\frac{\partial\bar{U}}{\partial x}\frac{\partial^2 v}{\partial x^2}-2\frac{\partial\bar{U}}{\partial y}\frac{\partial^2 v}{\partial xy}-2\frac{\partial\bar{U}}{\partial z}\frac{\partial^2 v}{\partial xz}-\bar{U}\frac{\partial\nabla^2 v}{\partial x}\\
&-\nabla^2 v\frac{\partial\bar{V}}{\partial y}-2\frac{\partial v}{\partial x}\frac{\partial^2\bar{V}}{\partial xy}-2\frac{\partial v}{\partial y}\frac{\partial^2\bar{V}}{\partial y^2}-2\frac{\partial v}{\partial z}\frac{\partial^2\bar{V}}{\partial yz}-v\frac{\partial\nabla^2\bar{V}}{\partial y}\\
&-\nabla^2\bar{V}\frac{\partial v}{\partial y}-2\frac{\partial\bar{V}}{\partial x}\frac{\partial^2 v}{\partial xy}-2\frac{\partial\bar{V}}{\partial y}\frac{\partial^2 v}{\partial y^2}-2\frac{\partial\bar{V}}{\partial z}\frac{\partial^2 v}{\partial yz}-\bar{V}\frac{\partial\nabla^2 v}{\partial y}\\
&-\nabla^2\bar{W}\frac{\partial v}{\partial z}-2\frac{\partial\bar{W}}{\partial x}\frac{\partial^2 v}{\partial xz}-2\frac{\partial\bar{W}}{\partial y}\frac{\partial^2 v}{\partial yz}-2\frac{\partial\bar{W}}{\partial z}\frac{\partial^2 v}{\partial z^2}-\bar{W}\frac{\partial\nabla^2 v}{\partial z}\\
&+2\frac{\partial^2\bar{U}}{\partial yz}\frac{\partial w}{\partial x}+2\frac{\partial\bar{U}}{\partial z}\frac{\partial^2 w}{\partial xy}+2\frac{\partial^2\bar{V}}{\partial yz}\frac{\partial w}{\partial y}+2\frac{\partial\bar{V}}{\partial z}\frac{\partial^2 w}{\partial y^2}+2\frac{\partial^2\bar{W}}{\partial yz}\frac{\partial w}{\partial z}+2\frac{\partial\bar{W}}{\partial z}\frac{\partial^2 w}{\partial yz}\\
&-\nabla^2 w\frac{\partial\bar{V}}{\partial z}-2\frac{\partial w}{\partial x}\frac{\partial^2\bar{V}}{\partial xz}-2\frac{\partial w}{\partial y}\frac{\partial^2\bar{V}}{\partial yz}-2\frac{\partial w}{\partial z}\frac{\partial^2\bar{V}}{\partial z^2}-w\frac{\partial\nabla^2\bar{V}}{\partial z}-\nabla^2\left(u\frac{\partial v}{\partial x}\right)-\nabla^2\left(v\frac{\partial v}{\partial y}\right)-\nabla^2\left(w\frac{\partial v}{\partial z}\right),
\end{aligned}
\tag{F.6}
$$

it leads to the expression of the time-variation of the velocity v in function of the velocities u, v and w as [eq. 4.57]

$$
\begin{aligned}
\frac{\partial}{\partial t}\nabla^2 v \;=\; & \left[+2\,\frac{\partial^2\bar{U}}{\partial xy}\frac{\partial}{\partial x}+2\,\frac{\partial\bar{U}}{\partial x}\frac{\partial^2}{\partial xy}+2\,\frac{\partial\bar{V}}{\partial x}\frac{\partial^2}{\partial y^2}+2\,\frac{\partial^2\bar{W}}{\partial xy}\frac{\partial}{\partial z}+2\,\frac{\partial\bar{W}}{\partial x}\frac{\partial^2}{\partial yz}\right.\\
&\left.-\frac{\partial\bar{V}}{\partial x}\nabla^2-2\frac{\partial^2\bar{V}}{\partial x^2}\frac{\partial}{\partial x}-2\frac{\partial^2\bar{V}}{\partial xz}\frac{\partial}{\partial z}-\frac{\partial\nabla^2\bar{V}}{\partial x}\right]u\\
&+\left[\frac{1}{Re}\nabla^4+2\,\frac{\partial^2\bar{U}}{\partial y^2}\frac{\partial}{\partial x}+2\,\frac{\partial^2\bar{V}}{\partial y^2}\frac{\partial}{\partial y}+2\,\frac{\partial^2\bar{W}}{\partial y^2}\frac{\partial}{\partial z}\right.\\
&-\nabla^2\bar{U}\frac{\partial}{\partial x}-2\frac{\partial\bar{U}}{\partial x}\frac{\partial^2}{\partial x^2}-2\frac{\partial\bar{U}}{\partial z}\frac{\partial^2}{\partial xz}-\bar{U}\frac{\partial\nabla^2}{\partial x}\\
&-\frac{\partial\bar{V}}{\partial y}\nabla^2-2\frac{\partial^2\bar{V}}{\partial xy}\frac{\partial}{\partial x}-2\frac{\partial^2\bar{V}}{\partial y^2}\frac{\partial}{\partial y}-2\frac{\partial^2\bar{V}}{\partial yz}\frac{\partial}{\partial z}-\frac{\partial\nabla^2\bar{V}}{\partial y}\\
&-\nabla^2\bar{V}\frac{\partial}{\partial y}-2\frac{\partial\bar{V}}{\partial x}\frac{\partial^2}{\partial xy}-2\frac{\partial\bar{V}}{\partial z}\frac{\partial^2 v}{\partial yz}-\bar{V}\frac{\partial\nabla^2}{\partial y}\\
&\left.-\nabla^2\bar{W}\frac{\partial}{\partial z}-2\frac{\partial\bar{W}}{\partial x}\frac{\partial^2}{\partial xz}-2\frac{\partial\bar{W}}{\partial z}\frac{\partial^2}{\partial z^2}-\bar{W}\frac{\partial\nabla^2}{\partial z}\right]v\\
&+\left[2\frac{\partial^2\bar{U}}{\partial yz}\frac{\partial}{\partial x}+2\frac{\partial\bar{U}}{\partial z}\frac{\partial^2}{\partial xy}+2\frac{\partial\bar{V}}{\partial z}\frac{\partial^2}{\partial y^2}+2\frac{\partial^2\bar{W}}{\partial yz}\frac{\partial}{\partial z}+2\frac{\partial\bar{W}}{\partial z}\frac{\partial^2}{\partial yz}\right.\\
&\left.-\frac{\partial\bar{V}}{\partial z}\nabla^2-2\frac{\partial^2\bar{V}}{\partial xz}\frac{\partial}{\partial x}-2\frac{\partial^2\bar{V}}{\partial z^2}\frac{\partial}{\partial z}-\frac{\partial\nabla^2\bar{V}}{\partial z}\right]w.
\end{aligned}
\tag{F.7}
$$

Time-variation of the wall-normal vorticity η_y

To describe the complete 3D problem, the wall-normal vorticity $\eta(y)$ 4.43 is introduced and differentiated in time,

$$\frac{\partial \eta_y}{\partial t} = \frac{\partial}{\partial z}\frac{\partial u}{\partial t} - \frac{\partial}{\partial x}\frac{\partial w}{\partial t}. \tag{F.8}$$

The time-differentiation of stream-wise u and span-wise w components are eliminated with expressions 4.56a/F.4a and 4.56c/F.4c. Hereinafter are explicited the simplifications,

$$\begin{aligned}
\frac{\partial \eta_y}{\partial t} =& \frac{1}{Re}\nabla^2\eta_y \\
&- \frac{\partial u}{\partial z}\frac{\partial \bar{U}}{\partial x} - u\frac{\partial^2 \bar{U}}{\partial x z} - \frac{\partial \bar{U}}{\partial z}\frac{\partial u}{\partial x} - \bar{U}\frac{\partial^2 u}{\partial x z} - \frac{\partial u}{\partial z}\frac{\partial u}{\partial x} - u\frac{\partial^2 u}{\partial x z} \\
&- \frac{\partial v}{\partial z}\frac{\partial \bar{U}}{\partial y} - v\frac{\partial^2 \bar{U}}{\partial y z} - \frac{\partial \bar{V}}{\partial z}\frac{\partial u}{\partial y} - \bar{V}\frac{\partial^2 u}{\partial y z} - \frac{\partial v}{\partial z}\frac{\partial u}{\partial y} - v\frac{\partial^2 u}{\partial y z} \\
&- \frac{\partial w}{\partial z}\frac{\partial \bar{U}}{\partial z} - w\frac{\partial^2 \bar{U}}{\partial z^2} - \frac{\partial \bar{W}}{\partial z}\frac{\partial u}{\partial z} - \bar{W}\frac{\partial^2 u}{\partial z^2} - \frac{\partial w}{\partial z}\frac{\partial u}{\partial z} - w\frac{\partial^2 u}{\partial z^2} \\
&+ \frac{\partial u}{\partial x}\frac{\partial \bar{W}}{\partial x} + u\frac{\partial^2 \bar{W}}{\partial x^2} + \frac{\partial \bar{U}}{\partial x}\frac{\partial w}{\partial x} + \bar{U}\frac{\partial^2 w}{\partial x^2} + \frac{\partial u}{\partial x}\frac{\partial w}{\partial x} + u\frac{\partial^2 w}{\partial x^2} \\
&+ \frac{\partial v}{\partial x}\frac{\partial \bar{W}}{\partial y} + v\frac{\partial^2 \bar{W}}{\partial x y} + \frac{\partial \bar{V}}{\partial x}\frac{\partial w}{\partial y} + \bar{V}\frac{\partial^2 w}{\partial x y} + \frac{\partial v}{\partial x}\frac{\partial w}{\partial y} + v\frac{\partial^2 w}{\partial x y} \\
&+ \frac{\partial w}{\partial x}\frac{\partial \bar{W}}{\partial z} + w\frac{\partial^2 \bar{W}}{\partial x z} + \frac{\partial \bar{W}}{\partial x}\frac{\partial w}{\partial z} + \bar{W}\frac{\partial^2 w}{\partial x z} + \frac{\partial w}{\partial x}\frac{\partial w}{\partial z} + w\frac{\partial^2 w}{\partial x z},
\end{aligned} \tag{F.9}$$

which gives without the non-linear terms in cyan and simplifying the blue terms

$$\begin{aligned}
\frac{\partial \eta_y}{\partial t} =& \frac{1}{Re}\nabla^2\eta_y - \bar{U}\frac{\partial \eta_y}{\partial x} - \bar{V}\frac{\partial \eta_y}{\partial y} - \bar{W}\frac{\partial \eta_y}{\partial z} \\
&- \frac{\partial u}{\partial z}\frac{\partial \bar{U}}{\partial x} - u\frac{\partial^2 \bar{U}}{\partial x z} - \frac{\partial \bar{U}}{\partial z}\frac{\partial u}{\partial x} - \frac{\partial v}{\partial z}\frac{\partial \bar{U}}{\partial y} - v\frac{\partial^2 \bar{U}}{\partial y z} - \frac{\partial \bar{V}}{\partial z}\frac{\partial u}{\partial y} - \frac{\partial w}{\partial z}\frac{\partial \bar{U}}{\partial z} - w\frac{\partial^2 \bar{U}}{\partial z^2} - \frac{\partial \bar{W}}{\partial z}\frac{\partial u}{\partial z} \\
&+ \frac{\partial u}{\partial x}\frac{\partial \bar{W}}{\partial x} + u\frac{\partial^2 \bar{W}}{\partial x^2} + \frac{\partial \bar{U}}{\partial x}\frac{\partial w}{\partial x} + \frac{\partial v}{\partial x}\frac{\partial \bar{W}}{\partial y} + v\frac{\partial^2 \bar{W}}{\partial x y} + \frac{\partial \bar{V}}{\partial x}\frac{\partial w}{\partial y} + \frac{\partial w}{\partial x}\frac{\partial \bar{W}}{\partial z} + w\frac{\partial^2 \bar{W}}{\partial x z} + \frac{\partial \bar{W}}{\partial x}\frac{\partial w}{\partial z},
\end{aligned} \tag{F.10}$$

to finally the time-evolution of wall-normal vorticity η_y follows as [eq. 4.59]

$$\begin{aligned}
\frac{\partial \eta_y}{\partial t} =& \left[\frac{1}{Re}\nabla^2 - \bar{U}\frac{\partial}{\partial x} - \bar{V}\frac{\partial}{\partial y} - \bar{W}\frac{\partial}{\partial z} - \frac{\partial \bar{U}}{\partial x} - \frac{\partial \bar{W}}{\partial z}\right]\eta_y \\
&+ \left[- \frac{\partial^2 \bar{U}}{\partial x z} - \frac{\partial \bar{U}}{\partial z}\frac{\partial}{\partial x} - \frac{\partial \bar{V}}{\partial z}\frac{\partial}{\partial y} + \frac{\partial \bar{W}}{\partial x}\frac{\partial}{\partial x} + \frac{\partial^2 \bar{W}}{\partial x^2}\right]u \\
&+ \left[- \frac{\partial \bar{U}}{\partial y}\frac{\partial}{\partial z} - \frac{\partial^2 \bar{U}}{\partial y z} + \frac{\partial \bar{W}}{\partial y}\frac{\partial}{\partial x} + \frac{\partial^2 \bar{W}}{\partial x y}\right]v \\
&+ \left[- \frac{\partial \bar{U}}{\partial z}\frac{\partial}{\partial z} - \frac{\partial^2 \bar{U}}{\partial z^2} + \frac{\partial \bar{V}}{\partial x}\frac{\partial}{\partial y} + \frac{\partial \bar{W}}{\partial x}\frac{\partial}{\partial z} + \frac{\partial^2 \bar{W}}{\partial x z}\right]w.
\end{aligned} \tag{F.11}$$

Equations F.7 and F.11 form the velocity-vorticity formulation for the OSSE.

F.2 Streamwise and spanwise discretisation of the OSSE model

Streamwise and spanwise discretisation of the wall-normal vorticity η_y

Correlation of Fourier series applied to 4.59 leads to the expression of the wall-normal vorticity time-variation as a function of the different modes of η_y, u, v and w as

$$
\begin{aligned}
\frac{\partial \eta_y}{\partial t} = \Bigg[& \sum_{k_x=-\frac{N_x}{2}+1}^{N_x/2} \sum_{k_z=-\frac{N_z}{2}+1}^{N_z/2} \frac{1}{Re} \nabla^2 \left(\hat{\eta}_{\alpha,\beta}(y,t)\, \mathrm{e}^{\iota(\alpha x+\beta z)} \right) \\
& - \sum_{k'_x=-\frac{N'_x}{2}+1}^{N'_x/2} \sum_{k'_z=-\frac{N'_z}{2}+1}^{N'_z/2} \hat{U}_{\alpha',\beta'}(y,t)\, \mathrm{e}^{\iota(\alpha' x+\beta' z)} \sum_{k_x=-\frac{N_x}{2}+1}^{N_x/2} \sum_{k_z=-\frac{N_z}{2}+1}^{N_z/2} i\alpha \hat{\eta}_{\alpha,\beta}(y,t)\, \mathrm{e}^{\iota(\alpha x+\beta z)} \\
& - \sum_{k'_x=-\frac{N'_x}{2}+1}^{N'_x/2} \sum_{k'_z=-\frac{N'_z}{2}+1}^{N'_z/2} \hat{V}_{\alpha',\beta'}(y,t)\, \mathrm{e}^{\iota(\alpha' x+\beta' z)} \sum_{k_x=-\frac{N_x}{2}+1}^{N_x/2} \sum_{k_z=-\frac{N_z}{2}+1}^{N_z/2} \frac{\partial \hat{\eta}_{\alpha,\beta}(y,t)}{\partial y}\, \mathrm{e}^{\iota(\alpha x+\beta z)} \\
& - \sum_{k'_x=-\frac{N'_x}{2}+1}^{N'_x/2} \sum_{k'_z=-\frac{N'_z}{2}+1}^{N'_z/2} \hat{W}_{\alpha',\beta'}(y,t)\, \mathrm{e}^{\iota(\alpha' x+\beta' z)} \sum_{k_x=-\frac{N_x}{2}+1}^{N_x/2} \sum_{k_z=-\frac{N_z}{2}+1}^{N_z/2} i\beta \hat{\eta}_{\alpha,\beta}(y,t)\, \mathrm{e}^{\iota(\alpha x+\beta z)} \\
& - \sum_{k'_x=-\frac{N'_x}{2}+1}^{N'_x/2} \sum_{k'_z=-\frac{N'_z}{2}+1}^{N'_z/2} i\alpha' \hat{U}_{\alpha',\beta'}(y,t)\, \mathrm{e}^{\iota(\alpha' x+\beta' z)} \sum_{k_x=-\frac{N_x}{2}+1}^{N_x/2} \sum_{k_z=-\frac{N_z}{2}+1}^{N_z/2} \hat{\eta}_{\alpha,\beta}(y,t)\, \mathrm{e}^{\iota(\alpha x+\beta z)} \\
& - \sum_{k'_x=-\frac{N'_x}{2}+1}^{N'_x/2} \sum_{k'_z=-\frac{N'_z}{2}+1}^{N'_z/2} i\beta' \hat{W}_{\alpha',\beta'}(y,t)\, \mathrm{e}^{\iota(\alpha' x+\beta' z)} \sum_{k_x=-\frac{N_x}{2}+1}^{N_x/2} \sum_{k_z=-\frac{N_z}{2}+1}^{N_z/2} \hat{\eta}_{\alpha,\beta}(y,t)\, \mathrm{e}^{\iota(\alpha x+\beta z)} \Bigg] \\
+ \Bigg[& - \sum_{k'_x=-\frac{N'_x}{2}+1}^{N'_x/2} \sum_{k'_z=-\frac{N'_z}{2}+1}^{N'_z/2} (-1)\alpha'\beta' \hat{U}_{\alpha',\beta'}(y,t)\, \mathrm{e}^{\iota(\alpha' x+\beta' z)} \sum_{k_x=-\frac{N_x}{2}+1}^{N_x/2} \sum_{k_z=-\frac{N_z}{2}+1}^{N_z/2} \hat{u}_{\alpha,\beta}(y,t)\, \mathrm{e}^{\iota(\alpha x+\beta z)} \\
& - \sum_{k'_x=-\frac{N'_x}{2}+1}^{N'_x/2} \sum_{k'_z=-\frac{N'_z}{2}+1}^{N'_z/2} i\beta' \hat{U}_{\alpha',\beta'}(y,t)\, \mathrm{e}^{\iota(\alpha' x+\beta' z)} \sum_{k_x=-\frac{N_x}{2}+1}^{N_x/2} \sum_{k_z=-\frac{N_z}{2}+1}^{N_z/2} i\alpha \hat{u}_{\alpha,\beta}(y,t)\, \mathrm{e}^{\iota(\alpha x+\beta z)} \\
& - \sum_{k'_x=-\frac{N'_x}{2}+1}^{N'_x/2} \sum_{k'_z=-\frac{N'_z}{2}+1}^{N'_z/2} i\beta' \hat{V}_{\alpha',\beta'}(y,t)\, \mathrm{e}^{\iota(\alpha' x+\beta' z)} \sum_{k_x=-\frac{N_x}{2}+1}^{N_x/2} \sum_{k_z=-\frac{N_z}{2}+1}^{N_z/2} \frac{\partial \hat{u}_{\alpha,\beta}(y,t)}{\partial y}\, \mathrm{e}^{\iota(\alpha x+\beta z)} \\
& + \sum_{k'_x=-\frac{N'_x}{2}+1}^{N'_x/2} \sum_{k'_z=-\frac{N'_z}{2}+1}^{N'_z/2} i\alpha' \hat{W}_{\alpha',\beta'}(y,t)\, \mathrm{e}^{\iota(\alpha' x+\beta' z)} \sum_{k_x=-\frac{N_x}{2}+1}^{N_x/2} \sum_{k_z=-\frac{N_z}{2}+1}^{N_z/2} i\alpha \hat{u}_{\alpha,\beta}(y,t)\, \mathrm{e}^{\iota(\alpha x+\beta z)} \\
& + \sum_{k'_x=-\frac{N'_x}{2}+1}^{N'_x/2} \sum_{k'_z=-\frac{N'_z}{2}+1}^{N'_z/2} (-1)\alpha'^2 \hat{W}_{\alpha',\beta'}(y,t)\, \mathrm{e}^{\iota(\alpha' x+\beta' z)} \sum_{k_x=-\frac{N_x}{2}+1}^{N_x/2} \sum_{k_z=-\frac{N_z}{2}+1}^{N_z/2} \hat{u}_{\alpha,\beta}(y,t)\, \mathrm{e}^{\iota(\alpha x+\beta z)} \Bigg]
\end{aligned}
\tag{F.12}
$$

$$
\begin{aligned}
+\Bigg[&- \sum_{k'_x=-\frac{N'_x}{2}+1}^{N'_x/2} \sum_{k'_z=-\frac{N'_z}{2}+1}^{N'_z/2} \frac{\partial \hat{U}_{\alpha',\beta'}(y,t)}{\partial y} \, \mathrm{e}^{\iota(\alpha' x+\beta' z)} \sum_{k_x=-\frac{N_x}{2}+1}^{N_x/2} \sum_{k_z=-\frac{N_z}{2}+1}^{N_z/2} i\beta \hat{v}_{\alpha,\beta}(y,t) \, \mathrm{e}^{\iota(\alpha x+\beta z)} \\
&- \sum_{k'_x=-\frac{N'_x}{2}+1}^{N'_x/2} \sum_{k'_z=-\frac{N'_z}{2}+1}^{N'_z/2} i\beta' \frac{\partial \hat{U}_{\alpha',\beta'}(y,t)}{\partial y} \, \mathrm{e}^{\iota(\alpha' x+\beta' z)} \sum_{k_x=-\frac{N_x}{2}+1}^{N_x/2} \sum_{k_z=-\frac{N_z}{2}+1}^{N_z/2} \hat{v}_{\alpha,\beta}(y,t) \, \mathrm{e}^{\iota(\alpha x+\beta z)} \\
&+ \sum_{k'_x=-\frac{N'_x}{2}+1}^{N'_x/2} \sum_{k'_z=-\frac{N'_z}{2}+1}^{N'_z/2} \frac{\partial \hat{W}_{\alpha',\beta'}(y,t)}{\partial y} \, \mathrm{e}^{\iota(\alpha' x+\beta' z)} \sum_{k_x=-\frac{N_x}{2}+1}^{N_x/2} \sum_{k_z=-\frac{N_z}{2}+1}^{N_z/2} i\alpha \hat{v}_{\alpha,\beta}(y,t) \, \mathrm{e}^{\iota(\alpha x+\beta z)} \\
&+ \sum_{k'_x=-\frac{N'_x}{2}+1}^{N'_x/2} \sum_{k'_z=-\frac{N'_z}{2}+1}^{N'_z/2} i\alpha' \frac{\partial \hat{W}_{\alpha',\beta'}(y,t)}{\partial y} \, \mathrm{e}^{\iota(\alpha' x+\beta' z)} \sum_{k_x=-\frac{N_x}{2}+1}^{N_x/2} \sum_{k_z=-\frac{N_z}{2}+1}^{N_z/2} \hat{v}_{\alpha,\beta}(y,t) \, \mathrm{e}^{\iota(\alpha x+\beta z)} \Bigg] \\
+\Bigg[&- \sum_{k'_x=-\frac{N'_x}{2}+1}^{N'_x/2} \sum_{k'_z=-\frac{N'_z}{2}+1}^{N'_z/2} i\beta' \hat{U}_{\alpha',\beta'}(y,t) \, \mathrm{e}^{\iota(\alpha' x+\beta' z)} \sum_{k_x=-\frac{N_x}{2}+1}^{N_x/2} \sum_{k_z=-\frac{N_z}{2}+1}^{N_z/2} i\beta \hat{w}_{\alpha,\beta}(y,t) \, \mathrm{e}^{\iota(\alpha x+\beta z)} \\
&- \sum_{k'_x=-\frac{N'_x}{2}+1}^{N'_x/2} \sum_{k'_z=-\frac{N'_z}{2}+1}^{N'_z/2} (-1)\beta'^2 \hat{U}_{\alpha',\beta'}(y,t) \, \mathrm{e}^{\iota(\alpha' x+\beta' z)} \sum_{k_x=-\frac{N_x}{2}+1}^{N_x/2} \sum_{k_z=-\frac{N_z}{2}+1}^{N_z/2} \hat{w}_{\alpha,\beta}(y,t) \, \mathrm{e}^{\iota(\alpha x+\beta z)} \\
&+ \sum_{k'_x=-\frac{N'_x}{2}+1}^{N'_x/2} \sum_{k'_z=-\frac{N'_z}{2}+1}^{N'_z/2} i\alpha' \hat{V}_{\alpha',\beta'}(y,t) \, \mathrm{e}^{\iota(\alpha' x+\beta' z)} \sum_{k_x=-\frac{N_x}{2}+1}^{N_x/2} \sum_{k_z=-\frac{N_z}{2}+1}^{N_z/2} \frac{\partial \hat{w}_{\alpha,\beta}(y,t)}{\partial y} \, \mathrm{e}^{\iota(\alpha x+\beta z)} \\
&+ \sum_{k'_x=-\frac{N'_x}{2}+1}^{N'_x/2} \sum_{k'_z=-\frac{N'_z}{2}+1}^{N'_z/2} i\alpha' \hat{W}_{\alpha',\beta'}(y,t) \, \mathrm{e}^{\iota(\alpha' x+\beta' z)} \sum_{k_x=-\frac{N_x}{2}+1}^{N_x/2} \sum_{k_z=-\frac{N_z}{2}+1}^{N_z/2} i\beta \hat{w}_{\alpha,\beta}(y,t) \, \mathrm{e}^{\iota(\alpha x+\beta z)} \\
&+ \sum_{k'_x=-\frac{N'_x}{2}+1}^{N'_x/2} \sum_{k'_z=-\frac{N'_z}{2}+1}^{N'_z/2} (-1)\alpha'\beta' \hat{W}_{\alpha',\beta'}(y,t) \, \mathrm{e}^{\iota(\alpha' x+\beta' z)} \sum_{k_x=-\frac{N_x}{2}+1}^{N_x/2} \sum_{k_z=-\frac{N_z}{2}+1}^{N_z/2} \hat{w}_{\alpha,\beta}(y,t) \, \mathrm{e}^{\iota(\alpha x+\beta z)} \Bigg],
\end{aligned}
\tag{F.13}
$$

and after some rearranging [eq. 4.65]

$$
\begin{aligned}
\frac{\partial \eta_y}{\partial t} = & \sum_{k_x=-\frac{N_x}{2}+1}^{N_x/2} \sum_{k_z=-\frac{N_z}{2}+1}^{N_z/2} \frac{1}{Re} \nabla^2 \hat{\eta}_{\alpha,\beta}(y,t)\, \mathrm{e}^{\iota(\alpha x+\beta z)} \\
& + \sum_{k_x=-\frac{N_x}{2}+1}^{N_x/2} \sum_{k_z=-\frac{N_z}{2}+1}^{N_z/2} \sum_{k'_x=-\frac{N'_x}{2}+1}^{N'_x/2} \sum_{k'_z=-\frac{N'_z}{2}+1}^{N'_z/2} \mathrm{e}^{\iota(\alpha x+\beta z)} \\
& \quad \Bigg[- \Big(\iota(\alpha-\alpha')\hat{U}_{\alpha',\beta'}(y,t) + \hat{V}_{\alpha',\beta'}(y,t)\frac{\partial}{\partial y} + \iota(\beta-\beta')\hat{W}_{\alpha',\beta'}(y,t) \\
& \qquad + \iota\alpha'\hat{U}_{\alpha',\beta'}(y,t) + \iota\beta'\hat{W}_{\alpha',\beta'}(y,t) \Big) \hat{\eta}_{\alpha-\alpha',\beta-\beta'}(y,t) \\
& \quad + \Big(\alpha'\beta'\hat{U}_{\alpha',\beta'}(y,t) + \beta'(\alpha-\alpha')\hat{U}_{\alpha',\beta'}(y,t) - \iota\beta'\hat{V}_{\alpha',\beta'}(y,t)\frac{\partial}{\partial y} \\
& \qquad - \alpha'(\alpha-\alpha')\hat{W}_{\alpha',\beta'}(y,t) - \alpha'^2\hat{W}_{\alpha',\beta'}(y,t) \Big) \hat{u}_{\alpha-\alpha',\beta-\beta'}(y,t) \\
& \quad + \Big(- \iota(\beta-\beta')\frac{\partial \hat{U}_{\alpha',\beta'}(y,t)}{\partial y} - \iota\beta'\frac{\partial \hat{U}_{\alpha',\beta'}(y,t)}{\partial y} \\
& \qquad + \iota(\alpha-\alpha')\frac{\partial \hat{W}_{\alpha',\beta'}(y,t)}{\partial y} + \iota\alpha'\frac{\partial \hat{W}_{\alpha',\beta'}(y,t)}{\partial y} \Big) \hat{v}_{\alpha-\alpha',\beta-\beta'}(y,t) \\
& \quad + \Big(\beta'(\beta-\beta')\hat{U}_{\alpha',\beta'}(y,t) + \beta'^2\hat{U}_{\alpha',\beta'}(y,t) + \iota\alpha'\hat{V}_{\alpha',\beta'}(y,t)\frac{\partial}{\partial y} \\
& \qquad - \alpha'(\beta-\beta')\hat{W}_{\alpha',\beta'}(y,t) - \alpha'\beta'\hat{W}_{\alpha',\beta'}(y,t) \Big) \hat{w}_{\alpha-\alpha',\beta-\beta'}(y,t) \Bigg].
\end{aligned}
\tag{F.14}
$$

The Fourier basis $\{\mathrm{e}^{\iota\alpha x}\}$ and $\{\mathrm{e}^{\iota\beta z}\}$ are orthogonal. Consequently, each Fourier coefficient $\hat{\eta}_{\alpha,\beta}$ of the LHS of eq.4.65/F.14 can be expressed individually. Nonetheless, and on the contrary to the OSS derivation, due to the correlation of Fourier series on the RHS of eq.4.65/F.14, the coefficient $\hat{\eta}_{\alpha_i,\beta_j}$ is function of the entire set of coefficients $\hat{u}_{\alpha_k\neq\alpha_i,\beta_l\neq\beta_j}$, $\hat{v}_{\alpha_k\neq\alpha_i,\beta_l\neq\beta_j}$, $\hat{w}_{\alpha_k\neq\alpha_i,\beta_l\neq\beta_j}$ and $\hat{\eta}_{\alpha_k\neq\alpha_i,\beta_l\neq\beta_j}$. In other words, the derivation no longer diagonalizes with Fourier wavenumber.

For each wavenumber pair (α,β), the Fourier coefficients $\{\hat{u}_{\alpha,\beta}\}$ and $\{\hat{w}_{\alpha,\beta}\}$ of the steam- and span-wise velocity components are replaced by their respective expressions given in C.5 and C.4. The wavenumber pair $(\alpha=0,\beta=0)$ is a particular case, as $\hat{\eta}_{0,0}$ is not defined. Therefore, the Fourier coefficients $\{\hat{u}_{0,0}\}$ and $\{\hat{w}_{0,0}\}$ can not be retrieved with expressions C.5 and C.4. For this reason, the state will be composed of all the modes of the wall-normal velocity $\{\hat{v}_{\alpha,\beta}\}$, all the modes excepted the pair $(0,0)$ of the wall-normal vorticity $\{\hat{\eta}_{\alpha,\beta}\}$, and the Fourier coefficients $\hat{u}_{0,0}$ and $\hat{w}_{0,0}$.

By applying these remarks to eq. 4.65/F.14 and rearranging, the Fourier coefficients $\hat{\eta}_{\alpha,\beta}$ can be expressed as

$$
\begin{aligned}
\frac{\partial \hat{\eta}_{\alpha,\beta}}{\partial t} =& \frac{1}{Re}\nabla^2 \hat{\eta}_{\alpha,\beta}(y,t) \\
&+ \sum_{\substack{k'_x=-\frac{N'_x}{2}+1 \\ (k_x-k'_x,k_z-k'_z)\neq(0,0)}}^{N'_x/2} \sum_{k'_z=-\frac{N'_z}{2}+1}^{N'_z/2} \Bigg[-\hat{U}_{\alpha',\beta'}(y,t)\; i(\alpha-\alpha') - \hat{V}_{\alpha',\beta'}(y,t)\; \frac{\partial}{\partial y} \\
&\quad - \hat{W}_{\alpha',\beta'}(y,t)\; i(\beta-\beta') - i\alpha'\hat{U}_{\alpha',\beta'}(y,t)\; - i\beta'\hat{W}_{\alpha',\beta'}(y,t) \\
&\quad + \frac{1}{(\alpha-\alpha')^2+(\beta-\beta')^2}\Bigg[\\
&\qquad + i\beta'\hat{U}_{\alpha',\beta'}(y,t)\; (\alpha-\alpha')(\beta-\beta') + \beta'^2\hat{U}_{\alpha',\beta'}(y,t)\; i(\alpha-\alpha') \\
&\qquad - \alpha'\hat{V}_{\alpha',\beta'}(y,t)\; (\alpha-\alpha')\frac{\partial}{\partial y} - i\alpha'\hat{W}_{\alpha',\beta'}(y,t)\; (\alpha-\alpha')(\beta-\beta') \\
&\qquad - \alpha'\beta'\hat{W}_{\alpha',\beta'}(y,t)\; i(\alpha-\alpha') - \alpha'\beta'\hat{U}_{\alpha',\beta'}(y,t)\; i(\beta-\beta') \\
&\qquad - i\beta'\hat{U}_{\alpha',\beta'}(y,t)\; (\alpha-\alpha')(\beta-\beta') - \beta'\hat{V}_{\alpha',\beta'}(y,t)\; (\beta-\beta')\frac{\partial}{\partial y} \\
&\qquad + i\alpha'\hat{W}_{\alpha',\beta'}(y,t)\; (\alpha-\alpha')(\beta-\beta') + \alpha'^2\hat{W}_{\alpha',\beta'}(y,t)\; i(\beta-\beta')\Bigg]\Bigg] \eta_{\alpha-\alpha',\beta-\beta'}(y,t) \\
&+ \sum_{\substack{k'_x=-\frac{N'_x}{2}+1}}^{N'_x/2} \sum_{k'_z=-\frac{N'_z}{2}+1}^{N'_z/2} \Bigg[-\frac{\partial \hat{U}_{\alpha',\beta'}(y,t)}{\partial y}\; i(\beta-\beta') - i\beta'\frac{\partial \hat{U}_{\alpha',\beta'}(y,t)}{\partial y} \\
&\quad + \frac{\partial \hat{W}_{\alpha',\beta'}(y,t)}{\partial y}\; i(\alpha-\alpha') + i\alpha'\frac{\partial \hat{W}_{\alpha',\beta'}(y,t)}{\partial y}\Bigg] v_{\alpha-\alpha',\beta-\beta'}(y,t) \\
&+ \sum_{\substack{k'_x=-\frac{N'_x}{2}+1 \\ (k_x-k'_x,k_z-k'_z)\neq(0,0)}}^{N'_x/2} \sum_{k'_z=-\frac{N'_z}{2}+1}^{N'_z/2} \frac{1}{(\alpha-\alpha')^2+(\beta-\beta')^2}\Bigg[\\
&\quad + i\beta'\hat{U}_{\alpha',\beta'}(y,t)\; (\beta-\beta')^2\frac{\partial}{\partial y} + \beta'^2\hat{U}_{\alpha',\beta'}(y,t)\; i(\beta-\beta')\frac{\partial}{\partial y} \\
&\quad - \alpha'\hat{V}_{\alpha',\beta'}(y,t)\; (\beta-\beta')\frac{\partial^2}{\partial y^2} - i\alpha'\hat{W}_{\alpha',\beta'}(y,t)\; (\beta-\beta')^2\frac{\partial}{\partial y} \\
&\quad - \alpha'\beta'\hat{W}_{\alpha',\beta'}(y,t)\; i(\beta-\beta')\frac{\partial}{\partial y} + \alpha'\beta'\hat{U}_{\alpha',\beta'}(y,t)\; i(\alpha-\alpha')\frac{\partial}{\partial y} \\
&\quad + i\beta'\hat{U}_{\alpha',\beta'}(y,t)\; (\alpha-\alpha')^2\frac{\partial}{\partial y} + \beta'\hat{V}_{\alpha',\beta'}(y,t)\; (\alpha-\alpha')\frac{\partial^2}{\partial y^2} \\
&\quad - i\alpha'\hat{W}_{\alpha',\beta'}(y,t)\; (\alpha-\alpha')^2\frac{\partial}{\partial y} - \alpha'^2\hat{W}_{\alpha',\beta'}(y,t)\; i(\alpha-\alpha')\frac{\partial}{\partial y}\Bigg] v_{\alpha-\alpha',\beta-\beta'}(y,t) \\
&+ \left[\alpha\beta\bar{U}_{\alpha,\beta} - i\beta\bar{V}_{\alpha,\beta}\frac{\partial}{\partial y} - \alpha^2\bar{W}_{\alpha,\beta}\right] u_{0,0}(y,t) \\
&+ \left[\beta^2\bar{U}_{\alpha,\beta} + i\alpha\bar{V}_{\alpha,\beta}\frac{\partial}{\partial y} - \alpha\beta\bar{W}_{\alpha,\beta}\right] w_{0,0}(y,t),
\end{aligned}
\tag{F.15}
$$

which simplifies into

$$
\begin{aligned}
\frac{\partial \hat{\eta}_{\alpha,\beta}}{\partial t} =& \frac{1}{Re}\nabla^2 \hat{\eta}_{\alpha,\beta}(y,t) \\
&+ \sum_{\substack{k_x'=-\frac{N_x'}{2}+1 \\ (k_x-k_x',k_z-k_z')\neq(0,0)}}^{N_x'/2} \sum_{k_z'=-\frac{N_z'}{2}+1}^{N_z'/2} \Bigg[-i\alpha \hat{U}_{\alpha',\beta'}(y,t) - \hat{V}_{\alpha',\beta'}(y,t)\,\frac{\partial}{\partial y} - i\beta \hat{W}_{\alpha',\beta'}(y,t) \\
&\qquad + \frac{1}{(\alpha-\alpha')^2+(\beta-\beta')^2}\Bigg[-\big(\alpha'(\alpha-\alpha')+\beta'(\beta-\beta')\big)\hat{V}_{\alpha',\beta'}(y,t)\frac{\partial}{\partial y} \\
&\qquad\quad - i\big(\alpha'\beta-\beta'\alpha\big)\big(\beta'\hat{U}_{\alpha',\beta'}(y,t)-\alpha'\hat{W}_{\alpha',\beta'}(y,t)\big)\Bigg]\Bigg]\eta_{\alpha-\alpha',\beta-\beta'}(y,t) \\
&+ \sum_{k_x'=-\frac{N_x'}{2}+1}^{N_x'/2} \sum_{k_z'=-\frac{N_z'}{2}+1}^{N_z'/2} \Bigg[-i\beta\frac{\partial \hat{U}_{\alpha',\beta'}(y,t)}{\partial y} + i\alpha\frac{\partial \hat{W}_{\alpha',\beta'}(y,t)}{\partial y} \Bigg] v_{\alpha-\alpha',\beta-\beta'}(y,t) \\
&+ \sum_{\substack{k_x'=-\frac{N_x'}{2}+1 \\ (k_x-k_x',k_z-k_z')\neq(0,0)}}^{N_x'/2} \sum_{k_z'=-\frac{N_z'}{2}+1}^{N_z'/2} \frac{1}{(\alpha-\alpha')^2+(\beta-\beta')^2}\Bigg[-\big(\alpha'\beta-\beta'\alpha\big)\hat{V}_{\alpha',\beta'}(y,t)\,\frac{\partial}{\partial y} \\
&\qquad + i\big(\alpha(\alpha-\alpha')+\beta(\beta-\beta')\big)\big(\beta'\hat{U}_{\alpha',\beta'}(y,t)-\alpha'\hat{W}_{\alpha',\beta'}(y,t)\big)\Bigg]\frac{\partial}{\partial y} v_{\alpha-\alpha',\beta-\beta'}(y,t) \\
&+ \Bigg[\alpha\beta\bar{U}_{\alpha,\beta} - i\beta\bar{V}_{\alpha,\beta}\frac{\partial}{\partial y} - \alpha^2\bar{W}_{\alpha,\beta}\Bigg] u_{0,0}(y,t) \\
&+ \Bigg[\beta^2\bar{U}_{\alpha,\beta} + i\alpha\bar{V}_{\alpha,\beta}\frac{\partial}{\partial y} - \alpha\beta\bar{W}_{\alpha,\beta}\Bigg] w_{0,0}(y,t),
\end{aligned}
\tag{F.16}
$$

and leads to the final expression of the Fourier coefficients $\hat{\eta}_{\alpha,\beta}$ [eq. 4.66]

$$
\begin{aligned}
\frac{\partial \hat{\eta}_{\alpha,\beta}}{\partial t} =& \sum_{k_x'=-\frac{N_x'}{2}+1}^{N_x'/2} \sum_{k_z'=-\frac{N_z'}{2}+1}^{N_z'/2} F_{\substack{\alpha,\beta, \\ \alpha-\alpha',\beta-\beta'}}\, \hat{v}_{\alpha-\alpha',\beta-\beta'}(y,t) \\
&+ \sum_{\substack{k_x'=-\frac{N_x'}{2}+1 \\ (k_x-k_x',k_z-k_z')\neq(0,0)}}^{N_x'/2} \sum_{k_z'=-\frac{N_z'}{2}+1}^{N_z'/2} \frac{G_{\substack{\alpha,\beta, \\ \alpha-\alpha',\beta-\beta'}}}{(\alpha-\alpha')^2+(\beta-\beta')^2}\, \hat{v}_{\alpha-\alpha',\beta-\beta'}(y,t) \\
&+ \sum_{\substack{k_x'=-\frac{N_x'}{2}+1 \\ (k_x-k_x',k_z-k_z')\neq(0,0)}}^{N_x'/2} \sum_{k_z'=-\frac{N_z'}{2}+1}^{N_z'/2} \Bigg[H_{\substack{\alpha,\beta, \\ \alpha-\alpha',\beta-\beta'}} + \frac{J_{\substack{\alpha,\beta, \\ \alpha-\alpha',\beta-\beta'}}}{(\alpha-\alpha')^2+(\beta-\beta')^2}\Bigg] \hat{\eta}_{\alpha-\alpha',\beta-\beta'}(y,t) \\
&+ \frac{1}{Re}\nabla^2 \hat{\eta}_{\alpha,\beta}(y,t) + K_{\substack{\alpha,\beta, \\ 0,0}}\, \hat{u}_{0,0}(y,t) + L_{\substack{\alpha,\beta, \\ 0,0}}\, \hat{w}_{0,0}(y,t),
\end{aligned}
\tag{F.17}
$$

where the coefficients F, G, H, JK, L are given in the appendix D.1.

Streamwise and spanwise discretisation of the wall-normal velocity v

Equation 4.57/F.7 receives the same treatment in order to obtain an expression for all the Fourier coefficients $\hat{v}_{\alpha,\beta}$ as a function of all the modes of the wall-normal velocity $\{\hat{v}_{\alpha,\beta}\}$, all the modes excepted the pair $(0,0)$ of the wall-normal vorticity $\{\hat{\eta}_{\alpha,\beta}\}$, and the Fourier coefficients $\hat{u}_{0,0}$ and $\hat{w}_{0,0}$. For each wave-number pair, simplifications here coloured in cyan can be operated on equation 4.57/F.7,

$$
\begin{aligned}
\frac{\partial}{\partial t}\nabla^2 v \;=\; & \Bigg[+2\,\frac{\partial^2\bar{U}}{\partial xy}\frac{\partial}{\partial x} + 2\,\frac{\partial\bar{U}}{\partial x}\frac{\partial^2}{\partial xy} \\
& \quad +2\,\frac{\partial\bar{V}}{\partial x}\frac{\partial^2}{\partial y^2} + 2\,\frac{\partial^2\bar{W}}{\partial xy}\frac{\partial}{\partial z} + 2\,\frac{\partial\bar{W}}{\partial x}\frac{\partial^2}{\partial yz} \\
& \quad -\frac{\partial\bar{V}}{\partial x}\nabla^2 - 2\frac{\partial^2\bar{V}}{\partial x^2}\frac{\partial}{\partial x} - 2\frac{\partial^2\bar{V}}{\partial xz}\frac{\partial}{\partial z} - \frac{\partial\nabla^2\bar{V}}{\partial x}\Bigg]\, u \\
& + \Bigg[\frac{1}{Re}\nabla^4 \\
& \quad +2\,\frac{\partial^2\bar{U}}{\partial y^2}\frac{\partial}{\partial x} + 2\,\frac{\partial^2\bar{V}}{\partial y^2}\frac{\partial}{\partial y} + 2\,\frac{\partial^2\bar{W}}{\partial y^2}\frac{\partial}{\partial z} \\
& \quad -\nabla^2\bar{U}\frac{\partial}{\partial x} - 2\frac{\partial\bar{U}}{\partial x}\frac{\partial^2}{\partial x^2} - 2\frac{\partial\bar{U}}{\partial z}\frac{\partial^2}{\partial xz} - \bar{U}\frac{\partial\nabla^2}{\partial x} \\
& \quad -\frac{\partial\bar{V}}{\partial y}\nabla^2 - 2\frac{\partial^2\bar{V}}{\partial xy}\frac{\partial}{\partial x} - 2\frac{\partial^2\bar{V}}{\partial y^2}\frac{\partial}{\partial y} - 2\frac{\partial^2\bar{V}}{\partial yz}\frac{\partial}{\partial z} - \frac{\partial\nabla^2\bar{V}}{\partial y} \\
& \quad -\nabla^2\bar{V}\frac{\partial}{\partial y} - 2\frac{\partial\bar{V}}{\partial x}\frac{\partial^2}{\partial xy} - 2\frac{\partial\bar{V}}{\partial z}\frac{\partial^2 v}{\partial yz} - \bar{V}\frac{\partial\nabla^2}{\partial y} \\
& \quad -\nabla^2\bar{W}\frac{\partial}{\partial z} - 2\frac{\partial\bar{W}}{\partial x}\frac{\partial^2}{\partial xz} - 2\frac{\partial\bar{W}}{\partial z}\frac{\partial^2}{\partial z^2} - \bar{W}\frac{\partial\nabla^2}{\partial z}\Bigg]\, v \\
& + \Bigg[2\frac{\partial^2\bar{U}}{\partial yz}\frac{\partial}{\partial x} + 2\frac{\partial\bar{U}}{\partial z}\frac{\partial^2}{\partial xy} \\
& \quad +2\frac{\partial\bar{V}}{\partial z}\frac{\partial^2}{\partial y^2} + 2\frac{\partial^2\bar{W}}{\partial yz}\frac{\partial}{\partial z} + 2\frac{\partial\bar{W}}{\partial z}\frac{\partial^2}{\partial yz} \\
& \quad -\frac{\partial\bar{V}}{\partial z}\nabla^2 - 2\frac{\partial^2\bar{V}}{\partial xz}\frac{\partial}{\partial x} - 2\frac{\partial^2\bar{V}}{\partial z^2}\frac{\partial}{\partial z} - \frac{\partial\nabla^2\bar{V}}{\partial z}\Bigg]\, w \\
& - \Bigg[\nabla^2\left(u\frac{\partial v}{\partial x}\right) + \nabla^2\left(v\frac{\partial v}{\partial y}\right) + \nabla^2\left(w\frac{\partial v}{\partial z}\right)\Bigg].
\end{aligned}
\tag{F.18}
$$

For each wavenumber pair (α,β), the Fourier coefficients $\{\hat{u}_{\alpha,\beta}\}$ and $\{\hat{w}_{\alpha,\beta}\}$ of the steam- and span-wise velocity components are replaced by their respective expressions given in

C.5 and C.4. Neglecting the non-linear terms and replacing the terms, it leads to

$$
\begin{aligned}
\frac{\partial}{\partial t}\nabla^2 v \;=\; & +\frac{1}{Re}\nabla^4_{\alpha,\beta}\hat{v}_{\alpha,\beta}(y,t) \\
& +\left[i\alpha\bar{V}_{\alpha,\beta}\frac{\partial^2}{\partial y^2} - i\alpha\nabla^2_{\alpha,\beta}\bar{V}_{\alpha,\beta}\right]u_{0,0}(y,t) \\
& +\left[i\beta\bar{V}_{\alpha,\beta}\frac{\partial^2}{\partial y^2} - i\beta\nabla^2_{\alpha,\beta}\bar{V}_{\alpha,\beta}\right]w_{0,0}(y,t) \\
+ \sum_{k'_x=-\frac{N'_x}{2}+1}^{N'_x/2} \sum_{k'_z=-\frac{N'_z}{2}+1}^{N'_z/2} & \Bigg[+ 2i\frac{\partial^2\hat{U}_{\alpha',\beta'}(y,t)}{\partial y^2}\;(\alpha-\alpha') - i\nabla^2_{\alpha',\beta'}\hat{U}_{\alpha',\beta'}(y,t)\;(\alpha-\alpha') \\
& + 2i\alpha'\hat{U}_{\alpha',\beta'}(y,t)\;(\alpha-\alpha')^2 \\
& + 2i\beta'\hat{U}_{\alpha',\beta'}(y,t)\;(\alpha-\alpha')(\beta-\beta') \\
& - i\hat{U}_{\alpha',\beta'}(y,t)\;(\alpha-\alpha')\nabla^2_{\alpha-\alpha',\beta-\beta'} \\
& + 2\frac{\partial^2\hat{V}_{\alpha',\beta'}(y,t)}{\partial y^2}\;\frac{\partial}{\partial y} \\
& - \frac{\partial\hat{V}_{\alpha',\beta'}(y,t)}{\partial y}\;\nabla^2_{\alpha-\alpha',\beta-\beta'} \\
& + 2\alpha'\frac{\partial\hat{V}_{\alpha',\beta'}(y,t)}{\partial y}\;(\alpha-\alpha') \\
& - 2\frac{\partial^2\hat{V}_{\alpha',\beta'}(y,t)}{\partial y^2}\;\frac{\partial}{\partial y} \\
& + 2\beta'\frac{\partial\hat{V}_{\alpha',\beta'}(y,t)}{\partial y}\;(\beta-\beta') \\
& - \nabla^2_{\alpha',\beta'}\frac{\partial\hat{V}_{\alpha',\beta'}(y,t)}{\partial y} \\
& - \nabla^2_{\alpha',\beta'}\hat{V}_{\alpha',\beta'}(y,t)\;\frac{\partial}{\partial y} \\
& + 2\alpha'\hat{V}_{\alpha',\beta'}(y,t)\;(\alpha-\alpha')\frac{\partial}{\partial y} \\
& + 2\beta'\hat{V}_{\alpha',\beta'}(y,t)\;(\beta-\beta')\frac{\partial}{\partial y} \\
& - \hat{V}_{\alpha',\beta'}(y,t)\;\nabla^2_{\alpha-\alpha',\beta-\beta'}\frac{\partial}{\partial y} \\
& + 2i\frac{\partial^2\hat{W}_{\alpha',\beta'}(y,t)}{\partial y^2}\;(\beta-\beta') \\
& - i\nabla^2_{\alpha',\beta'}\hat{W}_{\alpha',\beta'}(y,t)\;(\beta-\beta') \\
& + 2i\alpha'\hat{W}_{\alpha',\beta'}(y,t)\;(\alpha-\alpha')(\beta-\beta') \\
& + 2i\beta'\hat{W}_{\alpha',\beta'}(y,t)\;(\beta-\beta')^2 \\
& - i\hat{W}_{\alpha',\beta'}(y,t)\;(\beta-\beta')\nabla^2_{\alpha-\alpha',\beta-\beta'} \\
& \Bigg]\hat{v}_{\alpha-\alpha',\beta-\beta'}(y,t)
\end{aligned}
$$

$$
\begin{aligned}
+ \sum_{\substack{k'_x=-\frac{N'_x}{2}+1 \\ (k_x-k'_x,k_z-k'_z)\neq(0,0)}}^{N'_x/2} \sum_{k'_z=-\frac{N'_z}{2}+1}^{N'_z/2} \frac{1}{(\alpha-\alpha')^2+(\beta-\beta')^2} \Big[& -2i\alpha' \frac{\partial \hat{U}_{\alpha',\beta'}(y,t)}{\partial y} \ (\alpha-\alpha')^2 \frac{\partial}{\partial y} \\
& -2i\alpha' \hat{U}_{\alpha',\beta'}(y,t) \ (\alpha-\alpha')^2 \frac{\partial^2}{\partial y^2} \\
& -2i\beta' \frac{\partial \hat{U}_{\alpha',\beta'}(y,t)}{\partial y} \ (\alpha-\alpha')(\beta-\beta') \frac{\partial}{\partial y} \\
& -2i\beta' \hat{U}_{\alpha',\beta'}(y,t) \ (\alpha-\alpha')(\beta-\beta') \frac{\partial^2}{\partial y^2} \\
& -2\alpha' \hat{V}_{\alpha',\beta'}(y,t) \ (\alpha-\alpha') \frac{\partial^3}{\partial y^3} \\
& +\alpha' \hat{V}_{\alpha',\beta'}(y,t) \ (\alpha-\alpha') \nabla^2_{\alpha-\alpha',\beta-\beta'} \frac{\partial}{\partial y} \\
& -2\alpha'^2 \hat{V}_{\alpha',\beta'}(y,t) \ (\alpha-\alpha')^2 \frac{\partial}{\partial y} \\
& -2\alpha'\beta' \hat{V}_{\alpha',\beta'}(y,t) \ (\alpha-\alpha')(\beta-\beta') \frac{\partial}{\partial y} \\
& +\alpha' \nabla^2_{\alpha',\beta'} \hat{V}_{\alpha',\beta'}(y,t) \ (\alpha-\alpha') \frac{\partial}{\partial y} \\
& +\beta' \hat{V}_{\alpha',\beta'}(y,t) \nabla^2_{\alpha-\alpha',\beta-\beta'} \ (\beta-\beta') \frac{\partial}{\partial y} \\
& -2\alpha'\beta' \hat{V}_{\alpha',\beta'}(y,t) \ (\alpha-\alpha')(\beta-\beta') \frac{\partial}{\partial y} \\
& -2\beta'^2 \hat{V}_{\alpha',\beta'}(y,t) \ (\beta-\beta')^2 \frac{\partial}{\partial y} \\
& +\beta' \nabla^2_{\alpha',\beta'} \hat{V}_{\alpha',\beta'}(y,t) \ (\beta-\beta') \frac{\partial}{\partial y} \\
& -2\beta' \hat{V}_{\alpha',\beta'}(y,t) \ (\beta-\beta') \frac{\partial^3}{\partial y^3} \\
& -2i\alpha' \frac{\partial \hat{W}_{\alpha',\beta'}(y,t)}{\partial y} \ (\alpha-\alpha')(\beta-\beta') \frac{\partial}{\partial y} \\
& -2i\alpha' \hat{W}_{\alpha',\beta'}(y,t) \ (\alpha-\alpha')(\beta-\beta') \frac{\partial^2}{\partial y^2} \\
& -2i\beta' \frac{\partial \hat{W}_{\alpha',\beta'}(y,t)}{\partial y} \ (\beta-\beta')^2 \frac{\partial}{\partial y} \\
& -2i\beta' \hat{W}_{\alpha',\beta'}(y,t) \ (\beta-\beta')^2 \frac{\partial^2}{\partial y^2} \Big] \hat{v}_{\alpha-\alpha',\beta-\beta'}(y,t)
\end{aligned}
$$

$$
\begin{aligned}
+ \sum_{\substack{k_x'=-\frac{N_x'}{2}+1 \\ (k_x-k_x',k_z-k_z')\neq(0,0)}}^{N_x'/2} \sum_{k_z'=-\frac{N_z'}{2}+1}^{N_z'/2} \frac{1}{(\alpha-\alpha')^2+(\beta-\beta')^2} \Big[& -2i\beta' \frac{\partial \hat{U}_{\alpha',\beta'}(y,t)}{\partial y} \ (\alpha-\alpha')^2 \\
& -2i\beta' \hat{U}_{\alpha',\beta'}(y,t) \ (\alpha-\alpha')^2 \frac{\partial}{\partial y} \\
& +2i\alpha' \frac{\partial \hat{U}_{\alpha',\beta'}(y,t)}{\partial y} \ (\alpha-\alpha')(\beta-\beta') \\
& +2i\alpha' \hat{U}_{\alpha',\beta'}(y,t) \ (\alpha-\alpha')(\beta-\beta') \frac{\partial}{\partial y} \\
& -2\beta' \hat{V}_{\alpha',\beta'}(y,t) \ (\alpha-\alpha') \frac{\partial^2}{\partial y^2} \\
& +\beta' \hat{V}_{\alpha',\beta'}(y,t) \ (\alpha-\alpha') \nabla^2_{\alpha-\alpha',\beta-\beta'} \\
& -2\alpha'\beta' \hat{V}_{\alpha',\beta'}(y,t) \ (\alpha-\alpha')^2 \\
& -2\beta'^2 \hat{V}_{\alpha',\beta'}(y,t) \ (\alpha-\alpha')(\beta-\beta') \\
& +\beta' \nabla^2_{\alpha',\beta'} \hat{V}_{\alpha',\beta'}(y,t) \ (\alpha-\alpha') \\
& +2\alpha' \hat{V}_{\alpha',\beta'}(y,t) \ (\beta-\beta') \frac{\partial^2}{\partial y^2} \\
& -\alpha' \hat{V}_{\alpha',\beta'}(y,t) \ (\beta-\beta') \nabla^2_{\alpha-\alpha',\beta-\beta'} \\
& +2\alpha'^2 \hat{V}_{\alpha',\beta'}(y,t) \ (\alpha-\alpha')(\beta-\beta') \\
& +2\alpha'\beta' \hat{V}_{\alpha',\beta'}(y,t) \ (\beta-\beta')^2 \\
& -\alpha' \nabla^2_{\alpha',\beta'} \hat{V}_{\alpha',\beta'}(y,t) \ (\beta-\beta') \\
& -2i\beta' \frac{\partial \hat{W}_{\alpha',\beta'}(y,t)}{\partial y} \ (\alpha-\alpha')(\beta-\beta') \\
& -2i\beta' \hat{W}_{\alpha',\beta'}(y,t) \ (\alpha-\alpha')(\beta-\beta') \frac{\partial}{\partial y} \\
& +2i\alpha' \frac{\partial \hat{W}_{\alpha',\beta'}(y,t)}{\partial y} \ (\beta-\beta')^2 \\
& +2i\alpha' \hat{W}_{\alpha',\beta'}(y,t) \ (\beta-\beta')^2 \frac{\partial}{\partial y} \\
\Big] & \hat{\eta}_{\alpha-\alpha',\beta-\beta'}(y,t)
\end{aligned}
$$

After rearranging, it leads to the expression [eq. 4.67]

$$\begin{aligned}\frac{\partial}{\partial t}\hat{\nabla}^2\hat{v}_{\alpha,\beta}(y,t) = \frac{1}{Re}\hat{\nabla}^4_{\alpha,\beta}\hat{v}_{\alpha,\beta}(y,t) &+ \sum_{k'_x=-\frac{N'_x}{2}+1}^{N'_x/2}\sum_{k'_z=-\frac{N'_z}{2}+1}^{N'_z/2} A_{\substack{\alpha,\beta,\\ \alpha-\alpha',\beta-\beta'}}\hat{v}_{\alpha-\alpha',\beta-\beta'}(y,t)\\ &+ \sum_{\substack{k'_x=-\frac{N'_x}{2}+1\\(k_x-k'_x,k_z-k'_z)\neq(0,0)}}^{N'_x/2}\sum_{k'_z=-\frac{N'_z}{2}+1}^{N'_z/2} \frac{B_{\substack{\alpha,\beta,\\ \alpha-\alpha',\beta-\beta'}}}{(\alpha-\alpha')^2+(\beta-\beta')^2}\hat{v}_{\alpha-\alpha',\beta-\beta'}(y,t)\\ &+ \sum_{\substack{k'_x=-\frac{N'_x}{2}+1\\(k_x-k'_x,k_z-k'_z)\neq(0,0)}}^{N'_x/2}\sum_{k'_z=-\frac{N'_z}{2}+1}^{N'_z/2} \frac{C_{\substack{\alpha,\beta,\\ \alpha-\alpha',\beta-\beta'}}}{(\alpha-\alpha')^2+(\beta-\beta')^2}\hat{\eta}_{\alpha-\alpha',\beta-\beta'}(y,t)\\ &+ D_{\substack{\alpha,\beta,\\0,0}}\hat{u}_{0,0}(y,t) + E_{\substack{\alpha,\beta,\\0,0}}\hat{w}_{0,0}(y,t),\end{aligned} \tag{F.20}$$

where the coefficients A, B, C, D, E are given in the appendix D.1.

Streamwise and spanwise discretisation of the streamwise velocity to determine $\hat{u}_{0,0}(y,t)$

The OSSE still requires the expression of $\hat{u}_{0,0}(y,t)$, which is obtained from equation 4.56a, considering only the pair $(\alpha=0,\beta=0)$

$$\begin{aligned}\frac{\partial\hat{u}_{\alpha=0,\beta=0}}{\partial t} &= \frac{1}{Re}\hat{\nabla}^2_{0,0}\hat{u}_{0,0} + \sum_{k'_x=-\frac{N'_x}{2}+1}^{N'_x/2}\sum_{k'_z=-\frac{N'_z}{2}+1}^{N'_z/2}\Big[-\iota\alpha'\hat{U}_{\alpha',\beta'}\hat{u}_{\alpha-\alpha',\beta-\beta'} - \iota(\alpha-\alpha')\hat{U}_{\alpha',\beta'}\hat{u}_{\alpha-\alpha',\beta-\beta'}\\ &\qquad - \frac{\partial\hat{U}_{\alpha',\beta'}}{\partial y}\hat{v}_{\alpha-\alpha',\beta-\beta'} - \hat{V}_{\alpha',\beta'}\frac{\partial\hat{u}_{\alpha-\alpha',\beta-\beta'}}{\partial y}\\ &\qquad - \iota\beta'\hat{U}_{\alpha',\beta'}\hat{w}_{\alpha-\alpha',\beta-\beta'} - \iota(\beta-\beta')\hat{W}_{\alpha',\beta'}\hat{u}_{\alpha-\alpha',\beta-\beta'}\Big],\\ &= \frac{1}{Re}\hat{\nabla}^2_{0,0}\hat{u}_{0,0} + \sum_{k'_x=-\frac{N'_x}{2}+1}^{N'_x/2}\sum_{k'_z=-\frac{N'_z}{2}+1}^{N'_z/2}\Big[-\frac{\partial\hat{U}_{\alpha',\beta'}}{\partial y}\hat{v}_{-\alpha',-\beta'} - \hat{V}_{\alpha',\beta'}\frac{\partial\hat{u}_{-\alpha',-\beta'}}{\partial y}\\ &\qquad - \iota\beta'\hat{U}_{\alpha',\beta'}\hat{w}_{-\alpha',-\beta'} + \iota\beta'\hat{W}_{\alpha',\beta'}\hat{u}_{-\alpha',-\beta'}\Big].\end{aligned} \tag{F.21}$$

Replacing $\hat{u}_{\alpha,\beta}$ and $\hat{w}_{\alpha,\beta}$ by their expressions C.5 and C.4 leads to

$$\begin{aligned}\frac{\partial \hat{u}_{0,0}}{\partial t} = &\left[\frac{1}{Re}\nabla_{0,0}^2 - \hat{V}_{0,0}\frac{\partial}{\partial y}\right]u_{0,0} \\ &+ \sum_{k'_x=-\frac{N'_x}{2}+1}^{N'_x/2}\sum_{k'_z=-\frac{N'_z}{2}+1}^{N'_z/2} -\frac{\partial \hat{U}_{\alpha',\beta'}}{\partial y} v_{-\alpha',-\beta'} \\ &+ \sum_{\substack{k'_x=-\frac{N'_x}{2}+1 \\ (k_x-k'_x,k_z-k'_z)\neq(0,0)}}^{N'_x/2}\sum_{k'_z=-\frac{N'_z}{2}+1}^{N'_z/2} \frac{1}{\alpha'^2+\beta'^2}\left[+i\alpha'\hat{V}_{\alpha',\beta'}\frac{\partial^2}{\partial y^2} - \beta'^2\hat{U}_{\alpha',\beta'}\frac{\partial}{\partial y} + \alpha'\beta'\hat{W}_{\alpha',\beta'}\frac{\partial}{\partial y}\right]v_{-\alpha',-\beta'} \\ &+ \sum_{\substack{k'_x=-\frac{N'_x}{2}+1 \\ (k_x-k'_x,k_z-k'_z)\neq(0,0)}}^{N'_x/2}\sum_{k'_z=-\frac{N'_z}{2}+1}^{N'_z/2} \frac{1}{\alpha'^2+\beta'^2}\left[-i\beta'\hat{V}_{\alpha',\beta'}\frac{\partial}{\partial y} - \alpha'\beta'\hat{U}_{\alpha',\beta'} - \beta'^2\hat{W}_{\alpha',\beta'}\right]\eta_{-\alpha',-\beta'}\end{aligned} \tag{F.22}$$

and finally the expression [eq. 4.69]

$$\begin{aligned}\frac{\partial \hat{u}_{0,0}}{\partial t} = &\left[\frac{1}{Re}\hat{\nabla}_{0,0}^2 - \hat{V}_{0,0}\frac{\partial}{\partial y}\right]\hat{u}_{0,0} + \sum_{k'_x=-\frac{N'_x}{2}+1}^{N'_x/2}\sum_{k'_z=-\frac{N'_z}{2}+1}^{N'_z/2} M_{\alpha',\beta'}\hat{v}_{-\alpha',-\beta'} \\ &+ \sum_{\substack{k'_x=-\frac{N'_x}{2}+1 \\ (k_x-k'_x,k_z-k'_z)\neq(0,0)}}^{N'_x/2}\sum_{k'_z=-\frac{N'_z}{2}+1}^{N'_z/2} \frac{N_{\alpha',\beta'}}{\alpha'^2+\beta'^2}\,\hat{v}_{-\alpha',-\beta'} + \sum_{\substack{k'_x=-\frac{N'_x}{2}+1 \\ (k_x-k'_x,k_z-k'_z)\neq(0,0)}}^{N'_x/2}\sum_{k'_z=-\frac{N'_z}{2}+1}^{N'_z/2} \frac{O_{\alpha',\beta'}}{\alpha'^2+\beta'^2}\,\hat{\eta}_{-\alpha',-\beta'},\end{aligned} \tag{F.23}$$

where the coefficients M, N, O are given in the appendix D.1.

Streamwise and spanwise discretisation of the spanwise velocity to determine $\hat{w}_{0,0}(y,t)$

Finally, the expression of $\hat{w}_{0,0}(y,t)$ is obtained from equation 4.56c, considering only the pair $(\alpha = 0, \beta = 0)$

$$\begin{aligned}
\frac{\partial w_{0,0}}{\partial t} = &\left[\frac{1}{Re}\hat{\nabla}^2_{0,0} - \hat{V}_{0,0}\frac{\partial}{\partial y}\right] w_{0,0} \\
&+ \sum_{k'_x=-\frac{N'_x}{2}+1}^{N'_x/2} \sum_{k'_z=-\frac{N'_z}{2}+1}^{N'_z/2} -\frac{\partial \hat{W}_{\alpha',\beta'}}{\partial y} v_{-\alpha',-\beta'} \\
&+ \sum_{\substack{k'_x=-\frac{N'_x}{2}+1 \\ (k_x-k'_x,k_z-k'_z)\neq(0,0)}}^{N'_x/2} \sum_{k'_z=-\frac{N'_z}{2}+1}^{N'_z/2} \frac{1}{\alpha'^2+\beta'^2}\left[-\alpha'^2\hat{W}_{\alpha',\beta'}\frac{\partial}{\partial y} + \alpha'\beta'\hat{U}_{\alpha',\beta'}\frac{\partial}{\partial y} + i\beta'\hat{V}_{\alpha',\beta'}\frac{\partial^2}{\partial y^2}\right] v_{-\alpha',-\beta'} \\
&+ \sum_{\substack{k'_x=-\frac{N'_x}{2}+1 \\ (k_x-k'_x,k_z-k'_z)\neq(0,0)}}^{N'_x/2} \sum_{k'_z=-\frac{N'_z}{2}+1}^{N'_z/2} \frac{1}{\alpha'^2+\beta'^2}\left[+\alpha'\beta'\hat{W}_{\alpha',\beta'} + \alpha'^2\hat{U}_{\alpha',\beta'} + i\alpha'\hat{V}_{\alpha',\beta'}\frac{\partial}{\partial y}\right] \eta_{-\alpha',-\beta'}
\end{aligned} \tag{F.24}$$

and rearranging it leads to [eq. 4.70]

$$\begin{aligned}
\frac{\partial \hat{w}_{0,0}}{\partial t} = &\left[\frac{1}{Re}\hat{\nabla}^2_{0,0} - \hat{V}_{0,0}\frac{\partial}{\partial y}\right]\hat{w}_{0,0} + \sum_{k'_x=-\frac{N'_x}{2}+1}^{N'_x/2} \sum_{k'_z=-\frac{N'_z}{2}+1}^{N'_z/2} P_{\alpha',\beta'}\hat{v}_{-\alpha',-\beta'} \\
&+ \sum_{\substack{k'_x=-\frac{N'_x}{2}+1 \\ (k_x-k'_x,k_z-k'_z)\neq(0,0)}}^{N'_x/2} \sum_{k'_z=-\frac{N'_z}{2}+1}^{N'_z/2} \frac{Q_{\alpha',\beta'}}{\alpha'^2+\beta'^2}\hat{v}_{-\alpha',-\beta'} + \sum_{\substack{k'_x=-\frac{N'_x}{2}+1 \\ (k_x-k'_x,k_z-k'_z)\neq(0,0)}}^{N'_x/2} \sum_{k'_z=-\frac{N'_z}{2}+1}^{N'_z/2} \frac{R_{\alpha',\beta'}}{\alpha'^2+\beta'^2}\hat{\eta}_{-\alpha',-\beta'},
\end{aligned} \tag{F.25}$$

where the coefficients P, Q, R are given in the appendix D.1.

Appendix G

OSSE actuated by wall-transpiration: Detailed derivation of the model

Actuated wall-normal velocity evolution $v_{\alpha,\beta}$

The lifted coefficients 5.18 are introduced into the OSSE system 4.73 and give [eq. 5.22]

$$
\begin{aligned}
&\frac{\partial}{\partial t}\mathring{\hat{\nabla}}^2\Big(\hat{v}^0_{\alpha,\beta}(y,t)+f^+(y)v^+_{\alpha,\beta}(t)+f^-(y)v^-_{\alpha,\beta}(t)\Big) = \\
&\quad\frac{1}{Re}\mathring{\hat{\nabla}}^4_{\alpha,\beta}\Big(\hat{v}^0_{\alpha,\beta}(y,t)+f^+(y)v^+_{\alpha,\beta}(t)+f^-(y)v^-_{\alpha,\beta}(t)\Big) \\
&\quad+\sum_{k'_x=-\frac{N'_x}{2}+1}^{N'_x/2}\sum_{k'_z=-\frac{N'_z}{2}+1}^{N'_z/2} A_{\substack{\alpha,\beta,\\ \alpha-\alpha',\beta-\beta'}}\Big(\hat{v}^0_{\substack{\alpha-\alpha'\\ \beta-\beta'}}(y,t)+f^+(y)\,v^+_{\substack{\alpha-\alpha'\\ \beta-\beta'}}(t)+f^-(y)\,v^-_{\substack{\alpha-\alpha'\\ \beta-\beta'}}(t)\Big) \\
&\quad+\sum_{\substack{k'_x=-\frac{N'_x}{2}+1\\ (k_x-k'_x,k_z-k'_z)\neq(0,0)}}^{N'_x/2}\sum_{k'_z=-\frac{N'_z}{2}+1}^{N'_z/2} B_{\substack{\alpha,\beta,\\ \alpha-\alpha',\beta-\beta'}}\Big(\hat{v}^0_{\substack{\alpha-\alpha'\\ \beta-\beta'}}(y,t)+f^+(y)\,v^+_{\substack{\alpha-\alpha'\\ \beta-\beta'}}(t)+f^-(y)\,v^-_{\substack{\alpha-\alpha'\\ \beta-\beta'}}(t)\Big) \\
&\quad+\sum_{\substack{k'_x=-\frac{N'_x}{2}+1\\ (k_x-k'_x,k_z-k'_z)\neq(0,0)}}^{N'_x/2}\sum_{k'_z=-\frac{N'_z}{2}+1}^{N'_z/2} C_{\substack{\alpha,\beta,\\ \alpha-\alpha',\beta-\beta'}}\Big(\hat{\eta}^0_{\substack{\alpha-\alpha'\\ \beta-\beta'}}(y,t)+g^+(y)\,\eta^+_{\substack{\alpha-\alpha'\\ \beta-\beta'}}(t)+g^-(y)\,\eta^-_{\substack{\alpha-\alpha'\\ \beta-\beta'}}(t)\Big) \\
&\quad+D_{\substack{\alpha,\beta,\\ 0,0}}\Big(\hat{u}^0_{0,0}(y,t)+f^+(y)\;u^+_{0,0}(t)+f^-(y)\;u^-_{0,0}(t)\Big) \\
&\quad+E_{\substack{\alpha,\beta,\\ 0,0}}\Big(\hat{w}^0_{0,0}(y,t)+f^+(y)\;w^+_{0,0}(t)+f^-(y)\;w^-_{0,0}(t)\Big).
\end{aligned}
\tag{G.1}
$$

Replacing the time-differentiation of $v^{\pm}_{\alpha,\beta}$ with equations 5.20, it follows

$$
\begin{aligned}
\frac{\partial}{\partial t}\mathring{\nabla}^2\,\hat{v}^0_{\alpha,\beta}(y,t) \;=\; & \frac{1}{Re}\mathring{\nabla}^4_{\alpha,\beta}\,\hat{v}^0_{\alpha,\beta}(y,t) \\
& + \Big[\frac{1}{\tau_{v_{\alpha,\beta}}}\nabla^2 f^+(y) + \frac{1}{Re}\nabla^4_{\alpha,\beta} f^+(y)\Big] v^+_{\alpha,\beta}(t) + \Big[\frac{1}{\tau_{v_{\alpha,\beta}}}\nabla^2 f^-(y) + \frac{1}{Re}\nabla^4_{\alpha,\beta} f^-(y)\Big] v^-_{\alpha,\beta}(t) \\
& - \frac{1}{\tau_{v_{\alpha,\beta}}}\nabla^2 f^+(y) q^+_{v_{\alpha,\beta}}(t) - \frac{1}{\tau_{v_{\alpha,\beta}}}\nabla^2 f^-(y) q^-_{v_{\alpha,\beta}}(t) \\
& + \sum_{k'_x=-\frac{N'_x}{2}+1}^{N'_x/2}\;\sum_{k'_z=-\frac{N'_z}{2}+1}^{N'_z/2} A_{\substack{\alpha,\beta,\\ \alpha-\alpha',\\ \beta-\beta'}} \Big(v^0_{\substack{\alpha-\alpha',\\ \beta-\beta'}}(y,t) + f^+(y)\; v^+_{\substack{\alpha-\alpha',\\ \beta-\beta'}}(t) + f^-(y)\; v^-_{\substack{\alpha-\alpha',\\ \beta-\beta'}}(t)\Big) \\
& + \sum_{\substack{k'_x=-\frac{N'_x}{2}+1\\ (k_x-k'_x,k_z-k'_z)\neq(0,0)}}^{N'_x/2}\;\sum_{k'_z=-\frac{N'_z}{2}+1}^{N'_z/2} B_{\substack{\alpha,\beta,\\ \alpha-\alpha',\\ \beta-\beta'}} \Big(v^0_{\substack{\alpha-\alpha',\\ \beta-\beta'}}(y,t) + f^+(y)\; v^+_{\substack{\alpha-\alpha',\\ \beta-\beta'}}(t) + f^-(y)\; v^-_{\substack{\alpha-\alpha',\\ \beta-\beta'}}(t)\Big) \\
& + \sum_{\substack{k'_x=-\frac{N'_x}{2}+1\\ (k_x-k'_x,k_z-k'_z)\neq(0,0)}}^{N'_x/2}\;\sum_{k'_z=-\frac{N'_z}{2}+1}^{N'_z/2} C_{\substack{\alpha,\beta,\\ \alpha-\alpha',\\ \beta-\beta'}} \Big(\eta^0_{\substack{\alpha-\alpha',\\ \beta-\beta'}}(y,t) + g^+(y)\; \eta^+_{\substack{\alpha-\alpha',\\ \beta-\beta'}}(t) + g^-(y)\; \eta^-_{\substack{\alpha-\alpha',\\ \beta-\beta'}}(t)\Big) \\
& + D_{\substack{\alpha,\beta,\\ 0,0}} \Big(\hat{u}^0_{0,0}(y,t) + f^+(y)\; u^+_{0,0}(t) + f^-(y)\; u^-_{0,0}(t)\Big) \\
& + E_{\substack{\alpha,\beta,\\ 0,0}} \Big(\hat{w}^0_{0,0}(y,t) + f^+(y)\; w^+_{0,0}(t) + f^-(y)\; w^-_{0,0}(t)\Big).
\end{aligned}
\tag{G.2}
$$

The only place where clamped boundary conditions are applied is ∇^4. Moreover, the operator $\mathring{\nabla}^2$ is simply ∇^2 without its first/last columns/rows. The fully-discretized system for all coefficients of the wall-normal velocity can be expressed, after considering the equality 5.8 applied on $\mathring{\nabla}$ and using Chebyshev series and differentiation matrices,

as

$$
\begin{aligned}
&\frac{\partial}{\partial t}\begin{bmatrix}1&0&0\\0&\mathring{\nabla}^2&0\\0&0&1\end{bmatrix}\begin{bmatrix}v^+_{\alpha,\beta}(t)\\ \hat{v}^0_{\alpha,\beta}(y,t)\\ v^-_{\alpha,\beta}(t)\end{bmatrix} = \\
&\quad\begin{bmatrix}-\frac{1}{\tau_{v_{\alpha,\beta}}} & 0 & 0\\ \left[\frac{1}{\tau_{v_{\alpha,\beta}}}\nabla^2 f^+(y)+\frac{1}{Re}\nabla^4_{\alpha,\beta}f^+(y)\right] & \frac{1}{Re}\mathring{\nabla}^4_{\alpha,\beta} & \left[\frac{1}{\tau_{v_{\alpha,\beta}}}\nabla^2 f^-(y)+\frac{1}{Re}\nabla^4_{\alpha,\beta}f^-(y)\right]\\ 0 & 0 & -\frac{1}{\tau_{v_{\alpha,\beta}}}\end{bmatrix}\begin{bmatrix}v^+_{\alpha,\beta}(t)\\ \hat{v}^0_{\alpha,\beta}(y,t)\\ v^-_{\alpha,\beta}(t)\end{bmatrix}\\
&\quad+\begin{bmatrix}\frac{1}{\tau_{v_{\alpha,\beta}}} & 0\\ -\frac{1}{\tau_{v_{\alpha,\beta}}}\nabla^2 f^+(y) & -\frac{1}{\tau_{v_{\alpha,\beta}}}\nabla^2 f^-(y)\\ 0 & \frac{1}{\tau_{v_{\alpha,\beta}}}\end{bmatrix}\begin{bmatrix}q^+_{v_{\alpha,\beta}}(t)\\ q^-_{v_{\alpha,\beta}}(t)\end{bmatrix}\\
&\quad+\sum_{k'_x=-\frac{N'_x}{2}+1}^{N'_x/2}\sum_{k'_z=-\frac{N'_z}{2}+1}^{N'_z/2} A_{\substack{\alpha,\beta,\\ \alpha-\alpha',\beta-\beta'}}\begin{bmatrix}0&0&0\\ f^+(y)&I&f^-(y)\\ 0&0&0\end{bmatrix}\begin{bmatrix}v^+_{\alpha-\alpha',\beta-\beta'}(t)\\ \hat{v}^0_{\alpha-\alpha',\beta-\beta'}(y,t)\\ v^-_{\alpha-\alpha',\beta-\beta'}(t)\end{bmatrix}\\
&\quad+\sum_{\substack{k'_x=-\frac{N'_x}{2}+1\\ (k_x-k'_x,k_z-k'_z)\neq(0,0)}}^{N'_x/2}\sum_{k'_z=-\frac{N'_z}{2}+1}^{N'_z/2} B_{\substack{\alpha,\beta,\\ \alpha-\alpha',\beta-\beta'}}\begin{bmatrix}0&0&0\\ f^+(y)&I&f^-(y)\\ 0&0&0\end{bmatrix}\begin{bmatrix}v^+_{\alpha-\alpha',\beta-\beta'}(t)\\ \hat{v}^0_{\alpha-\alpha',\beta-\beta'}(y,t)\\ v^-_{\alpha-\alpha',\beta-\beta'}(t)\end{bmatrix}\\
&\quad+\sum_{\substack{k'_x=-\frac{N'_x}{2}+1\\ (k_x-k'_x,k_z-k'_z)\neq(0,0)}}^{N'_x/2}\sum_{k'_z=-\frac{N'_z}{2}+1}^{N'_z/2} C_{\substack{\alpha,\beta,\\ \alpha-\alpha',\beta-\beta'}}\begin{bmatrix}0&0&0\\ g^+(y)&I&g^-(y)\\ 0&0&0\end{bmatrix}\begin{bmatrix}\eta^+_{\alpha-\alpha',\beta-\beta'}(t)\\ \hat{\eta}^0_{\alpha-\alpha',\beta-\beta'}(y,t)\\ \eta^-_{\alpha-\alpha',\beta-\beta'}(t)\end{bmatrix}\\
&\quad+D_{\substack{\alpha,\beta,\\ 0,0}}\begin{bmatrix}0&0&0\\ f^+(y)&I&f^-(y)\\ 0&0&0\end{bmatrix}\begin{bmatrix}u^+_{0,0}(t)\\ \hat{u}^0_{0,0}(y,t)\\ u^-_{0,0}(t)\end{bmatrix}+E_{\substack{\alpha,\beta,\\ 0,0}}\begin{bmatrix}0&0&0\\ f^+(y)&I&f^-(y)\\ 0&0&0\end{bmatrix}\begin{bmatrix}w^+_{0,0}(t)\\ \hat{w}^0_{0,0}(y,t)\\ w^-_{0,0}(t)\end{bmatrix}
\end{aligned}
\tag{G.3}
$$

which results with the matrices $\mathbb{E}_1, \mathbb{A}, \mathbb{B}, \mathbb{C}, \mathbb{D}, \mathbb{E}, \mathbb{B}_1$ given in the appendix E to [eq. 5.23]

$$
\begin{aligned}
&\frac{\partial}{\partial t}\begin{bmatrix}1&0&0\\0&\mathring{\nabla}^2&0\\0&0&1\end{bmatrix}\begin{bmatrix}v^+_{\alpha,\beta}(t)\\ \tilde{v}^0_{\alpha,\beta}(y,t)\\ v^-_{\alpha,\beta}(t)\end{bmatrix} = \mathbb{E}_1\begin{bmatrix}v^+_{\alpha,\beta}(t)\\ \tilde{v}^0_{\alpha,\beta}(y,t)\\ v^-_{\alpha,\beta}(t)\end{bmatrix}+\sum_{k'_x=-\frac{N'_x}{2}+1}^{N'_x/2}\sum_{k'_z=-\frac{N'_z}{2}+1}^{N'_z/2}\mathbb{A}\begin{bmatrix}v^+_{\alpha-\alpha',\beta-\beta'}(t)\\ \tilde{v}^0_{\alpha-\alpha',\beta-\beta'}(y,t)\\ v^-_{\alpha-\alpha',\beta-\beta'}(t)\end{bmatrix}\\
&\quad+\sum_{\substack{k'_x=-\frac{N'_x}{2}+1\\ (k_x-k'_x,k_z-k'_z)\neq(0,0)}}^{N'_x/2}\sum_{k'_z=-\frac{N'_z}{2}+1}^{N'_z/2}\mathbb{B}\begin{bmatrix}v^+_{\alpha-\alpha',\beta-\beta'}(t)\\ \tilde{v}^0_{\alpha-\alpha',\beta-\beta'}(y,t)\\ v^-_{\alpha-\alpha',\beta-\beta'}(t)\end{bmatrix}+\sum_{\substack{k'_x=-\frac{N'_x}{2}+1\\ (k_x-k'_x,k_z-k'_z)\neq(0,0)}}^{N'_x/2}\sum_{k'_z=-\frac{N'_z}{2}+1}^{N'_z/2}\mathbb{C}\begin{bmatrix}\eta^+_{\alpha-\alpha',\beta-\beta'}(t)\\ \tilde{\eta}^0_{\alpha-\alpha',\beta-\beta'}(y,t)\\ \eta^-_{\alpha-\alpha',\beta-\beta'}(t)\end{bmatrix}\\
&\quad+\mathbb{D}\begin{bmatrix}u^+_{0,0}(t)\\ \tilde{u}^0_{0,0}(y,t)\\ u^-_{0,0}(t)\end{bmatrix}+\mathbb{E}\begin{bmatrix}w^+_{0,0}(t)\\ \tilde{w}^0_{0,0}(y,t)\\ w^-_{0,0}(t)\end{bmatrix}+\mathbb{B}_1\begin{bmatrix}q^+_{v_{\alpha,\beta}}(t)\\ q^-_{v_{\alpha,\beta}}(t)\end{bmatrix}.
\end{aligned}
\tag{G.4}
$$

Actuated wall-normal vorticity evolution $\eta_{\alpha,\beta}$

The lifted coefficients 5.18 are introduced into the OSSE system 4.74 [eq. 5.24]

$$
\begin{aligned}
&\frac{\partial}{\partial t}\Big(\eta^0_{\alpha,\beta}(y,t) + g^+(y)\ \eta^+_{\alpha,\beta}(t) + g^-(y)\ \eta^-_{\alpha,\beta}(t)\Big) = \\
&\sum_{k'_x=-\frac{N'_x}{2}+1}^{N'_x/2}\ \sum_{k'_z=-\frac{N'_z}{2}+1}^{N'_z/2} F_{\substack{\alpha,\beta,\\ \alpha-\alpha',\beta-\beta'}}\ \Big(v^0_{\substack{\alpha-\alpha',\\ \beta-\beta'}}(y,t) + f^+(y)\ v^+_{\substack{\alpha-\alpha',\\ \beta-\beta'}}(t) + f^-(y)\ v^-_{\substack{\alpha-\alpha',\\ \beta-\beta'}}(t)\Big) \\
&+ \sum_{\substack{k'_x=-\frac{N'_x}{2}+1\\ (k_x-k'_x,k_z-k'_z)\neq(0,0)}}^{N'_x/2}\ \sum_{k'_z=-\frac{N'_z}{2}+\text{`}1}^{N'_z/2} G_{\substack{\alpha,\beta,\\ \alpha-\alpha',\beta-\beta'}}\ \Big(v^0_{\substack{\alpha-\alpha',\\ \beta-\beta'}}(y,t) + f^+(y)\ v^+_{\substack{\alpha-\alpha',\\ \beta-\beta'}}(t) + f^-(y)\ v^-_{\substack{\alpha-\alpha',\\ \beta-\beta'}}(t)\Big) \\
&+ \frac{1}{Re}\nabla^2\Big(\eta^0_{\alpha,\beta}(y,t) + g^+(y)\ \eta^+_{\alpha,\beta}(t) + g^-(y)\ \eta^-_{\alpha,\beta}(t)\Big) \\
&+ \sum_{\substack{k'_x=-\frac{N'_x}{2}+1\\ (k_x-k'_x,k_z-k'_z)\neq(0,0)}}^{N'_x/2}\ \sum_{k'_z=-\frac{N'_z}{2}+1}^{N'_z/2} \Big[H_{\substack{\alpha,\beta,\\ \alpha-\alpha',\beta-\beta'}} + J_{\substack{\alpha,\beta,\\ \alpha-\alpha',\beta-\beta'}}\Big]\Big(\eta^0_{\alpha,\beta}(y,t) + g^+(y)\ \eta^+_{\alpha,\beta}(t) + g^-(y)\ \eta^-_{\alpha,\beta}(t)\Big) \\
&+ K_{\substack{\alpha,\beta,\\ 0,0}}\ \Big(\hat{u}^0_{0,0}(y,t) + f^+(y)\ u^+_{0,0}(t) + f^-(y)\ u^-_{0,0}(t)\Big) \\
&+ L_{\substack{\alpha,\beta,\\ 0,0}}\ \Big(\hat{w}^0_{0,0}(y,t) + f^+(y)\ w^+_{0,0}(t) + f^-(y)\ w^-_{0,0}(t)\Big)
\end{aligned}
\tag{G.5}
$$

Replacing the time-differentiation of $\eta^{\pm}_{\alpha,\beta}$ with equations 5.20, it follows

$$
\begin{aligned}
&\frac{\partial}{\partial t}\eta^0_{\alpha,\beta}(y,t) = \sum_{k'_x=-\frac{N'_x}{2}+1}^{N'_x/2}\ \sum_{k'_z=-\frac{N'_z}{2}+1}^{N'_z/2} F_{\substack{\alpha,\beta,\\ \alpha-\alpha',\\ \beta-\beta'}}\ \Big(v^0_{\substack{\alpha-\alpha',\\ \beta-\beta'}}(y,t) + f^+(y)\ v^+_{\substack{\alpha-\alpha',\\ \beta-\beta'}}(t) + f^-(y)\ v^-_{\substack{\alpha-\alpha',\\ \beta-\beta'}}(t)\Big) \\
&+ \sum_{\substack{k'_x=-\frac{N'_x}{2}+1\\ (k_x-k'_x,k_z-k'_z)\neq(0,0)}}^{N'_x/2}\ \sum_{k'_z=-\frac{N'_z}{2}+1}^{N'_z/2} G_{\substack{\alpha,\beta,\\ \alpha-\alpha',\\ \beta-\beta'}}\ \Big(v^0_{\substack{\alpha-\alpha',\\ \beta-\beta'}}(y,t) + f^+(y)\ v^+_{\substack{\alpha-\alpha',\\ \beta-\beta'}}(t) + f^-(y)\ v^-_{\substack{\alpha-\alpha',\\ \beta-\beta'}}(t)\Big) \\
&+ \frac{1}{Re}\mathring{\nabla}^2\eta^0_{\alpha,\beta}(y,t) + \Big(\frac{1}{Re}\nabla^2 g^+(y)\ + \frac{1}{\tau_{\eta_{\alpha,\beta}}}g^+(y)\Big)\eta^+_{\alpha,\beta}(t) + \Big(\frac{1}{Re}\nabla^2 g^-(y)\ + \frac{1}{\tau_{\eta_{\alpha,\beta}}}g^-(y)\Big)\eta^-_{\alpha,\beta}(t) \\
&- \frac{1}{\tau_{\eta_{\alpha,\beta}}}g^+(y)q^+_{\eta_{\alpha,\beta}}(t) - \frac{1}{\tau_{\eta_{\alpha,\beta}}}g^-(y)q^-_{\eta_{\alpha,\beta}}(t) \\
&+ \sum_{\substack{k'_x=-\frac{N'_x}{2}+1\\ (k_x-k'_x,k_z-k'_z)\neq(0,0)}}^{N'_x/2}\ \sum_{k'_z=-\frac{N'_z}{2}+1}^{N'_z/2} \Big[H_{\substack{\alpha,\beta,\\ \alpha-\alpha',\\ \beta-\beta'}} + J_{\substack{\alpha,\beta,\\ \alpha-\alpha',\\ \beta-\beta'}}\Big]\Big(\eta^0_{\substack{\alpha-\alpha',\\ \beta-\beta'}}(y,t) + g^+(y)\ \eta^+_{\substack{\alpha-\alpha',\\ \beta-\beta'}}(t) + g^-(y)\ \eta^-_{\substack{\alpha-\alpha',\\ \beta-\beta'}}(t)\Big) \\
&+ K_{\substack{\alpha,\beta,\\ 0,0}}\ \Big(\hat{u}^0_{0,0}(y,t) + f^+(y)\ u^+_{0,0}(t) + f^-(y)\ u^-_{0,0}(t)\Big) \\
&+ L_{\substack{\alpha,\beta,\\ 0,0}}\ \Big(\hat{w}^0_{0,0}(y,t) + f^+(y)\ w^+_{0,0}(t) + f^-(y)\ w^-_{0,0}(t)\Big)
\end{aligned}
\tag{G.6}
$$

Similarly to the wall-normal velocity v, the fully-discretized system for all coefficients of the wall-normal velocity can be expressed, after considering the equality 5.8 applied on $\mathring{\nabla}$ and using Chebyshev series and differentiation matrices, as

$$
\begin{aligned}
\frac{\partial}{\partial t}\begin{bmatrix} \eta^+_{\alpha,\beta}(t) \\ \hat{\eta}^0_{\alpha,\beta}(y,t) \\ \eta^-_{\alpha,\beta}(t) \end{bmatrix} &= \begin{bmatrix} \frac{1}{\tau_{\eta_{\alpha,\beta}}} & 0 \\ -\frac{1}{\tau_{\eta_{\alpha,\beta}}} g^+(y) & -\frac{1}{\tau_{\eta_{\alpha,\beta}}} g^-(y) \\ 0 & \frac{1}{\tau_{\eta_{\alpha,\beta}}} \end{bmatrix} \begin{bmatrix} q^+_{\eta_{\alpha,\beta}}(t) \\ q^-_{\eta_{\alpha,\beta}}(t) \end{bmatrix} \\
&+ \sum_{k'_x=-\frac{N'_x}{2}+1}^{N'_x/2} \sum_{k'_z=-\frac{N'_z}{2}+1}^{N'_z/2} F_{\substack{\alpha,\beta,\\ \alpha-\alpha',\beta-\beta'}} \begin{bmatrix} 0 & 0 & 0 \\ f^+(y) & I & f^-(y) \\ 0 & 0 & 0 \end{bmatrix} \begin{bmatrix} v^+_{\alpha-\alpha',\beta-\beta'}(t) \\ \hat{v}^0_{\alpha-\alpha',\beta-\beta'}(y,t) \\ v^-_{\alpha-\alpha',\beta-\beta'}(t) \end{bmatrix} \\
&+ \sum_{\substack{k'_x=-\frac{N'_x}{2}+1 \\ (k_x-k'_x,k_z-k'_z)\neq(0,0)}}^{N'_x/2} \sum_{k'_z=-\frac{N'_z}{2}+1}^{N'_z/2} G_{\substack{\alpha,\beta,\\ \alpha-\alpha',\beta-\beta'}} \begin{bmatrix} 0 & 0 & 0 \\ f^+(y) & I & f^-(y) \\ 0 & 0 & 0 \end{bmatrix} \begin{bmatrix} v^+_{\alpha-\alpha',\beta-\beta'}(t) \\ \hat{v}^0_{\alpha-\alpha',\beta-\beta'}(y,t) \\ v^-_{\alpha-\alpha',\beta-\beta'}(t) \end{bmatrix} \\
&+ \begin{bmatrix} -\frac{1}{\tau_{\eta_{\alpha,\beta}}} & 0 & 0 \\ \left[\frac{1}{Re}\nabla^2 g^+(y) + \frac{1}{\tau_{\eta_{\alpha,\beta}}} g^+(y)\right] & \frac{1}{Re}\mathring{\nabla}^2 & \left[\frac{1}{Re}\nabla^2 g^-(y) + \frac{1}{\tau_{\eta_{\alpha,\beta}}} g^-(y)\right] \\ 0 & 0 & -\frac{1}{\tau_{\eta_{\alpha,\beta}}} \end{bmatrix} \begin{bmatrix} \eta^+_{\alpha,\beta}(t) \\ \hat{\eta}^0_{\alpha,\beta}(y,t) \\ \eta^-_{\alpha,\beta}(t) \end{bmatrix} \\
&+ \sum_{\substack{k'_x=-\frac{N'_x}{2}+1 \\ (k_x-k'_x,k_z-k'_z)\neq(0,0)}}^{N'_x/2} \sum_{k'_z=-\frac{N'_z}{2}+1}^{N'_z/2} \left[H_{\substack{\alpha,\beta,\\ \alpha-\alpha',\beta-\beta'}} + J_{\substack{\alpha,\beta,\\ \alpha-\alpha',\beta-\beta'}}\right] \begin{bmatrix} 0 & 0 & 0 \\ g^+(y) & I & g^-(y) \\ 0 & 0 & 0 \end{bmatrix} \begin{bmatrix} \eta^+_{\alpha-\alpha',\beta-\beta'}(t) \\ \hat{\eta}^0_{\alpha-\alpha',\beta-\beta'}(y,t) \\ \eta^-_{\alpha-\alpha',\beta-\beta'}(t) \end{bmatrix} \\
&+ K_{\substack{\alpha,\beta,\\ 0,0}} \begin{bmatrix} 0 & 0 & 0 \\ f^+(y) & I & f^-(y) \\ 0 & 0 & 0 \end{bmatrix} \begin{bmatrix} u^+_{0,0}(t) \\ \hat{u}^0_{0,0}(y,t) \\ u^-_{0,0}(t) \end{bmatrix} + L_{\substack{\alpha,\beta,\\ 0,0}} \begin{bmatrix} 0 & 0 & 0 \\ f^+(y) & I & f^-(y) \\ 0 & 0 & 0 \end{bmatrix} \begin{bmatrix} w^+_{0,0}(t) \\ \hat{w}^0_{0,0}(y,t) \\ w^-_{0,0}(t) \end{bmatrix},
\end{aligned}
\tag{G.7}
$$

which results with matrices $\mathbb{E}_2, \mathbb{F}, \mathbb{G}, \mathbb{H}, \mathbb{J}, \mathbb{K}, \mathbb{L}, \mathbb{B}_2$ given in the appendix E to [eq. 5.25]

$$
\begin{aligned}
\frac{\partial}{\partial t}\begin{bmatrix} \eta^+_{\alpha,\beta}(t) \\ \tilde{\eta}^0_{\alpha,\beta}(y,t) \\ \eta^-_{\alpha,\beta}(t) \end{bmatrix} &= \mathbb{E}_2 \begin{bmatrix} \eta^+_{\alpha,\beta}(t) \\ \tilde{\eta}^0_{\alpha,\beta}(y,t) \\ \eta^-_{\alpha,\beta}(t) \end{bmatrix} + \sum_{k'_x=-\frac{N'_x}{2}+1}^{N'_x/2} \sum_{k'_z=-\frac{N'_z}{2}+1}^{N'_z/2} \mathbb{F} \begin{bmatrix} v^+_{\alpha-\alpha',\beta-\beta'}(t) \\ \tilde{v}^0_{\alpha-\alpha',\beta-\beta'}(y,t) \\ v^-_{\alpha-\alpha',\beta-\beta'}(t) \end{bmatrix} \\
&+ \sum_{\substack{k'_x=-\frac{N'_x}{2}+1 \\ (k_x-k'_x,k_z-k'_z)\neq(0,0)}}^{N'_x/2} \sum_{k'_z=-\frac{N'_z}{2}+1}^{N'_z/2} \mathbb{G} \begin{bmatrix} v^+_{\alpha-\alpha',\beta-\beta'}(t) \\ \tilde{v}^0_{\alpha-\alpha',\beta-\beta'}(y,t) \\ v^-_{\alpha-\alpha',\beta-\beta'}(t) \end{bmatrix} + \sum_{\substack{k'_x=-\frac{N'_x}{2}+1 \\ (k_x-k'_x,k_z-k'_z)\neq(0,0)}}^{N'_x/2} \sum_{k'_z=-\frac{N'_z}{2}+1}^{N'_z/2} \left[\mathbb{H}+\mathbb{J}\right] \begin{bmatrix} \eta^+_{\substack{\alpha-\alpha',\\ \beta-\beta'}}(t) \\ \tilde{\eta}^0_{\substack{\alpha-\alpha',\\ \beta-\beta'}}(y,t) \\ \eta^-_{\substack{\alpha-\alpha',\\ \beta-\beta'}}(t) \end{bmatrix} \\
&+ \mathbb{K} \begin{bmatrix} u^+_{0,0}(t) \\ \tilde{u}^0_{0,0}(y,t) \\ u^-_{0,0}(t) \end{bmatrix} + \mathbb{L} \begin{bmatrix} w^+_{0,0}(t) \\ \tilde{w}^0_{0,0}(y,t) \\ w^-_{0,0}(t) \end{bmatrix} + \mathbb{B}_2 \begin{bmatrix} q^+_{\eta_{\alpha,\beta}}(t) \\ q^-_{\eta_{\alpha,\beta}}(t) \end{bmatrix}.
\end{aligned}
\tag{G.8}
$$

Actuated stream-wise velocity evolution $u_{0,0}$

The lifted coefficients 5.18 are introduced into the OSSE system 4.75 [eq. 5.26]

$$\begin{aligned}
\frac{\partial}{\partial t}\hat{u}^0_{0,0}(y,t) = &\left[\frac{1}{Re}\mathring{\nabla}^2_{0,0} - \bar{V}_{0,0}\frac{\mathring{\partial}}{\partial y}\right]\hat{u}^0_{0,0}(y,t) \\
&+ \left[\frac{1}{Re}\nabla^2_{0,0} - \bar{V}_{0,0}\frac{\partial}{\partial y}\right] f^+(y)\ u^+_{0,0}(t) + \frac{1}{\tau_{u_{0,0}}} f^+(y)\ u^+_{0,0}(t) \\
&+ \left[\frac{1}{Re}\nabla^2_{0,0} - \bar{V}_{0,0}\frac{\partial}{\partial y}\right] f^-(y)\ u^-_{0,0}(t)) + \frac{1}{\tau_{u_{0,0}}} f^-(y)\ u^-_{0,0}(t) \\
&- \frac{1}{\tau_{u_{0,0}}} f^+(y)\ q^+_{u_{0,0}}(t) - \frac{1}{\tau_{u_{0,0}}} f^-(y)\ q^-_{u_{0,0}}(t) \\
&+ \sum_{k'_x=-\frac{N'_x}{2}+1}^{N'_x/2} \sum_{k'_z=-\frac{N'_z}{2}+1}^{N'_z/2} M_{\alpha',\beta'}\left(v^0_{-\alpha',-\beta'}(y,t) + f^+(y)\ v^+_{-\alpha',-\beta'}(t) + f^-(y)\ v^-_{-\alpha',-\beta'}(t)\right) \\
&+ \sum_{\substack{k'_x=-\frac{N'_x}{2}+1 \\ (k_x-k'_x,k_z-k'_z)\neq(0,0)}}^{N'_x/2} \sum_{k'_z=-\frac{N'_z}{2}+1}^{N'_z/2} N_{\alpha',\beta'}\left(v^0_{-\alpha',-\beta'}(y,t) + f^+(y)\ v^+_{-\alpha',-\beta'}(t) + f^-(y)\ v^-_{-\alpha',-\beta'}(t)\right) \\
&+ \sum_{\substack{k'_x=-\frac{N'_x}{2}+1 \\ (k_x-k'_x,k_z-k'_z)\neq(0,0)}}^{N'_x/2} \sum_{k'_z=-\frac{N'_z}{2}+1}^{N'_z/2} O_{\alpha',\beta'}\left(\eta^0_{-\alpha',-\beta'}(y,t) + g^+(y)\ \eta^+_{-\alpha',-\beta'}(t) + g^-(y)\ \eta^-_{-\alpha',-\beta'}(t)\right)
\end{aligned} \tag{G.9}$$

Similarly to the wall-normal velocity v, after considering the equality 5.8 applied on $\mathring{\nabla}$, using Chebyshev series and differentiation matrices, and defining

$$\mathring{\mathcal{M}} = \left[\frac{1}{Re}\mathring{\nabla}^2_{0,0} - \bar{V}_{0,0}\frac{\mathring{\partial}}{\partial y}\right], \tag{G.10a}$$

$$\mathcal{M} = \left[\frac{1}{Re}\nabla^2_{0,0} - \bar{V}_{0,0}\frac{\partial}{\partial y}\right], \tag{G.10b}$$

the fully-discretized system for the fundamental mode of the stream-wise velocity can be expressed as

$$
\begin{aligned}
\frac{\partial}{\partial t}\begin{bmatrix} u^+_{0,0}(t) \\ \hat{u}^0_{0,0}(y,t) \\ u^-_{0,0}(t) \end{bmatrix} &= \begin{bmatrix} -\frac{1}{\tau_{u_{0,0}}} & 0 & 0 \\ \mathcal{M}f^+(y) + \frac{1}{\tau_{u_{0,0}}} f^+(y) & \mathring{\mathcal{M}} & \mathcal{M}f^-(y) + \frac{1}{\tau_{u_{0,0}}} f^-(y) \\ 0 & 0 & -\frac{1}{\tau_{u_{0,0}}} \end{bmatrix} \begin{bmatrix} u^+_{0,0}(t) \\ \hat{u}^0_{0,0}(y,t) \\ u^-_{0,0}(t) \end{bmatrix} \\
&+ \begin{bmatrix} \frac{1}{\tau_{u_{0,0}}} & 0 \\ -\frac{1}{\tau_{u_{0,0}}} f^+(y) & -\frac{1}{\tau_{u_{0,0}}} f^-(y) \\ 0 & \frac{1}{\tau_{u_{0,0}}} \end{bmatrix} \begin{bmatrix} q^+_{u_{0,0}}(t) \\ q^-_{u_{0,0}}(t) \end{bmatrix} \\
&+ \sum_{k'_x=-\frac{N'_x}{2}+1}^{N'_x/2} \sum_{k'_z=-\frac{N'_z}{2}+1}^{N'_z/2} \begin{bmatrix} 0 & 0 & 0 \\ M_{\alpha',\beta'} f^+(y) & M_{\alpha',\beta'} & M_{\alpha',\beta'} f^-(y) \\ 0 & 0 & 0 \end{bmatrix} \begin{bmatrix} v^+_{-\alpha',-\beta'}(t) \\ v^0_{-\alpha',-\beta'}(y,t) \\ v^-_{-\alpha',-\beta'}(t) \end{bmatrix} \\
&+ \sum_{\substack{k'_x=-\frac{N'_x}{2}+1 \\ (k_x-k'_x,k_z-k'_z)\neq(0,0)}}^{N'_x/2} \sum_{k'_z=-\frac{N'_z}{2}+1}^{N'_z/2} \begin{bmatrix} 0 & 0 & 0 \\ N_{\alpha',\beta'} f^+(y) & N_{\alpha',\beta'} & N_{\alpha',\beta'} f^-(y) \\ 0 & 0 & 0 \end{bmatrix} \begin{bmatrix} v^+_{-\alpha',-\beta'}(t) \\ v^0_{-\alpha',-\beta'}(y,t) \\ v^-_{-\alpha',-\beta'}(t) \end{bmatrix} \\
&+ \sum_{\substack{k'_x=-\frac{N'_x}{2}+1 \\ (k_x-k'_x,k_z-k'_z)\neq(0,0)}}^{N'_x/2} \sum_{k'_z=-\frac{N'_z}{2}+1}^{N'_z/2} \begin{bmatrix} 0 & 0 & 0 \\ O_{\alpha',\beta'} g^+(y) & O_{\alpha',\beta'} & O_{\alpha',\beta'} g^-(y) \\ 0 & 0 & 0 \end{bmatrix} \begin{bmatrix} \eta^+_{-\alpha',-\beta'}(t) \\ \eta^0_{-\alpha',-\beta'}(y,t) \\ \eta^-_{-\alpha',-\beta'}(t) \end{bmatrix}
\end{aligned}
\tag{G.11}
$$

which results with the matrices $\mathbb{E}_3, \mathbb{M}, \mathbb{N}, \mathbb{O}, \mathbb{B}_3$ given in the appendix E to [eq. 5.27]

$$
\begin{aligned}
\frac{\partial}{\partial t}\begin{bmatrix} u^+_{0,0}(t) \\ \tilde{u}^0_{0,0}(y,t) \\ u^-_{0,0}(t) \end{bmatrix} &= \mathbb{E}_3 \begin{bmatrix} u^+_{0,0}(t) \\ \tilde{u}^0_{0,0}(y,t) \\ u^-_{0,0}(t) \end{bmatrix} + \sum_{k'_x=-\frac{N'_x}{2}+1}^{N'_x/2} \sum_{k'_z=-\frac{N'_z}{2}+1}^{N'_z/2} \mathbb{M} \begin{bmatrix} v^+_{-\alpha',-\beta'}(t) \\ \tilde{v}^0_{-\alpha',-\beta'}(y,t) \\ v^-_{-\alpha',-\beta'}(t) \end{bmatrix} \\
&+ \sum_{\substack{k'_x=-\frac{N'_x}{2}+1 \\ (k_x-k'_x,k_z-k'_z)\neq(0,0)}}^{N'_x/2} \sum_{k'_z=-\frac{N'_z}{2}+1}^{N'_z/2} \mathbb{N} \begin{bmatrix} v^+_{-\alpha',-\beta'}(t) \\ \tilde{v}^0_{-\alpha',-\beta'}(y,t) \\ v^-_{-\alpha',-\beta'}(t) \end{bmatrix} + \sum_{\substack{k'_x=-\frac{N'_x}{2}+1 \\ (k_x-k'_x,k_z-k'_z)\neq(0,0)}}^{N'_x/2} \sum_{k'_z=-\frac{N'_z}{2}+1}^{N'_z/2} \mathbb{O} \begin{bmatrix} \eta^+_{-\alpha',-\beta'}(t) \\ \tilde{\eta}^0_{-\alpha',-\beta'}(y,t) \\ \eta^-_{-\alpha',-\beta'}(t) \end{bmatrix} \\
&+ \mathbb{B}_3 \begin{bmatrix} q^+_{u_{0,0}}(t) \\ q^-_{u_{0,0}}(t) \end{bmatrix},
\end{aligned}
\tag{G.12}
$$

Actuated spanwise velocity evolution $w_{0,0}$

The lifted coefficients 5.18 are introduced into the OSSE system 4.76 [eq. 5.28]

$$
\begin{aligned}
\frac{\partial}{\partial t}\hat{w}^0_{0,0}(y,t) = &\left[\frac{1}{Re}\mathring{\nabla}^2_{0,0} - \bar{V}_{0,0}\frac{\mathring{\partial}}{\partial y}\right]\hat{w}^0_{0,0}(y,t) \\
&+ \left[\frac{1}{Re}\nabla^2_{0,0} - \bar{V}_{0,0}\frac{\partial}{\partial y}\right] f^+(y)\ w^+_{0,0}(t) + \frac{1}{\tau_{w_{0,0}}} f^+(y)\ w^+_{0,0}(t) \\
&+ \left[\frac{1}{Re}\nabla^2_{0,0} - \bar{V}_{0,0}\frac{\partial}{\partial y}\right] f^-(y)\ w^-_{0,0}(t)) + \frac{1}{\tau_{w_{0,0}}} f^-(y)\ w^-_{0,0}(t) \\
&- \frac{1}{\tau_{w_{0,0}}} f^+(y)\ q^+_{w_{0,0}}(t) - \frac{1}{\tau_{w_{0,0}}} f^-(y)\ q^-_{w_{0,0}}(t) \\
&+ \sum_{k'_x=-\frac{N'_x}{2}+1}^{N'_x/2} \sum_{k'_z=-\frac{N'_z}{2}+1}^{N'_z/2} P_{\alpha',\beta'}\left(v^0_{-\alpha',-\beta'}(y,t) + f^+(y)\ v^+_{-\alpha',-\beta'}(t) + f^-(y)\ v^-_{-\alpha',-\beta'}(t)\right) \\
&+ \sum_{\substack{k'_x=-\frac{N'_x}{2}+1 \\ (k_x-k'_x,k_z-k'_z)\neq(0,0)}}^{N'_x/2} \sum_{k'_z=-\frac{N'_z}{2}+1}^{N'_z/2} Q_{\alpha',\beta'}\ \left(v^0_{-\alpha',-\beta'}(y,t) + f^+(y)\ v^+_{-\alpha',-\beta'}(t) + f^-(y)\ v^-_{-\alpha',-\beta'}(t)\right) \\
&+ \sum_{\substack{k'_x=-\frac{N'_x}{2}+1 \\ (k_x-k'_x,k_z-k'_z)\neq(0,0)}}^{N'_x/2} \sum_{k'_z=-\frac{N'_z}{2}+1}^{N'_z/2} R_{\alpha',\beta'}\ \left(\eta^0_{-\alpha',-\beta'}(y,t) + g^+(y)\ \eta^+_{-\alpha',-\beta'}(t) + g^-(y)\ \eta^-_{-\alpha',-\beta'}(t)\right)
\end{aligned}
\tag{G.13}
$$

Similarly to the wall-normal velocity v, after considering the equality 5.8 applied on $\mathring{\nabla}$, using Chebyshev series and differentiation matrices, and defining

$$
\mathring{\mathcal{M}} = \left[\frac{1}{Re}\mathring{\nabla}^2_{0,0} - \bar{V}_{0,0}\frac{\mathring{\partial}}{\partial y}\right], \tag{G.14a}
$$

$$
\mathcal{M} = \left[\frac{1}{Re}\nabla^2_{0,0} - \bar{V}_{0,0}\frac{\partial}{\partial y}\right], \tag{G.14b}
$$

the fully-discretized system for the fundamental mode of the stream-wise velocity can be expressed as

$$
\begin{aligned}
\frac{\partial}{\partial t}\begin{bmatrix} w^+_{0,0}(t) \\ \hat{w}^0_{0,0}(y,t) \\ w^-_{0,0}(t) \end{bmatrix} &= \begin{bmatrix} -\frac{1}{\tau_{w_{0,0}}} & 0 & 0 \\ \mathcal{M}f^+(y) + \frac{1}{\tau_{w_{0,0}}}f^+(y) & \mathring{\mathcal{M}} & \mathcal{M}f^-(y) + \frac{1}{\tau_{w_{0,0}}}f^-(y) \\ 0 & 0 & -\frac{1}{\tau_{w_{0,0}}} \end{bmatrix} \begin{bmatrix} w^+_{0,0}(t) \\ \hat{w}^0_{0,0}(y,t) \\ w^-_{0,0}(t) \end{bmatrix} \\
&+ \begin{bmatrix} \frac{1}{\tau_{w_{0,0}}} & 0 \\ -\frac{1}{\tau_{w_{0,0}}}f^+(y) & -\frac{1}{\tau_{w_{0,0}}}f^-(y) \\ 0 & \frac{1}{\tau_{w_{0,0}}} \end{bmatrix} \begin{bmatrix} q^+_{w_{0,0}}(t) \\ q^-_{w_{0,0}}(t) \end{bmatrix} \\
&+ \sum_{k'_x=-\frac{N'_x}{2}+1}^{N'_x/2} \sum_{k'_z=-\frac{N'_z}{2}+1}^{N'_z/2} \begin{bmatrix} 0 & 0 & 0 \\ P_{\alpha',\beta'}f^+(y) & P_{\alpha',\beta'} & P_{\alpha',\beta'}f^-(y) \\ 0 & 0 & 0 \end{bmatrix} \begin{bmatrix} v^+_{-\alpha',-\beta'}(t) \\ v^0_{-\alpha',-\beta'}(y,t) \\ v^-_{-\alpha',-\beta'}(t) \end{bmatrix} \\
&+ \sum_{\substack{k'_x=-\frac{N'_x}{2}+1 \\ (k_x-k'_x,k_z-k'_z)\neq(0,0)}}^{N'_x/2} \sum_{k'_z=-\frac{N'_z}{2}+1}^{N'_z/2} \begin{bmatrix} 0 & 0 & 0 \\ Q_{\alpha',\beta'}f^+(y) & Q_{\alpha',\beta'} & Q_{\alpha',\beta'}f^-(y) \\ 0 & 0 & 0 \end{bmatrix} \begin{bmatrix} v^+_{-\alpha',-\beta'}(t) \\ v^0_{-\alpha',-\beta'}(y,t) \\ v^-_{-\alpha',-\beta'}(t) \end{bmatrix} \\
&+ \sum_{\substack{k'_x=-\frac{N'_x}{2}+1 \\ (k_x-k'_x,k_z-k'_z)\neq(0,0)}}^{N'_x/2} \sum_{k'_z=-\frac{N'_z}{2}+1}^{N'_z/2} \begin{bmatrix} 0 & 0 & 0 \\ R_{\alpha',\beta'}g^+(y) & R_{\alpha',\beta'} & R_{\alpha',\beta'}g^-(y) \\ 0 & 0 & 0 \end{bmatrix} \begin{bmatrix} \eta^+_{-\alpha',-\beta'}(t) \\ \eta^0_{-\alpha',-\beta'}(y,t) \\ \eta^-_{-\alpha',-\beta'}(t) \end{bmatrix}
\end{aligned}
\tag{G.15}
$$

which results with the matrices $\mathbb{E}_4, \mathbb{P}, \mathbb{Q}, \mathbb{R}, \mathbb{B}_4$ given in the appendix E to [eq. 5.29]

$$
\begin{aligned}
\frac{\partial}{\partial t}\begin{bmatrix} w^+_{0,0}(t) \\ \tilde{w}^0_{0,0}(y,t) \\ w^-_{0,0}(t) \end{bmatrix} &= \mathbb{E}_4 \begin{bmatrix} w^+_{0,0}(t) \\ \tilde{w}^0_{0,0}(y,t) \\ w^-_{0,0}(t) \end{bmatrix} + \sum_{k'_x=-\frac{N'_x}{2}+1}^{N'_x/2} \sum_{k'_z=-\frac{N'_z}{2}+1}^{N'_z/2} \mathbb{P} \begin{bmatrix} v^+_{-\alpha',-\beta'}(t) \\ \tilde{v}^0_{-\alpha',-\beta'}(y,t) \\ v^-_{-\alpha',-\beta'}(t) \end{bmatrix} \\
&+ \sum_{\substack{k'_x=-\frac{N'_x}{2}+1 \\ (k_x-k'_x,k_z-k'_z)\neq(0,0)}}^{N'_x/2} \sum_{k'_z=-\frac{N'_z}{2}+1}^{N'_z/2} \mathbb{Q} \begin{bmatrix} v^+_{-\alpha',-\beta'}(t) \\ \tilde{v}^0_{-\alpha',-\beta'}(y,t) \\ v^-_{-\alpha',-\beta'}(t) \end{bmatrix} + \sum_{\substack{k'_x=-\frac{N'_x}{2}+1 \\ (k_x-k'_x,k_z-k'_z)\neq(0,0)}}^{N'_x/2} \sum_{k'_z=-\frac{N'_z}{2}+1}^{N'_z/2} \mathbb{R} \begin{bmatrix} \eta^+_{-\alpha',-\beta'}(t) \\ \tilde{\eta}^0_{-\alpha',-\beta'}(y,t) \\ \eta^-_{-\alpha',-\beta'}(t) \end{bmatrix} \\
&+ \mathbb{B}_4 \begin{bmatrix} q^+_{w_{0,0}}(t) \\ q^-_{w_{0,0}}(t) \end{bmatrix},
\end{aligned}
\tag{G.16}
$$

Appendix H

Linear Algebra

Let's consider the linear model

$$\frac{\partial x}{\partial t} = Ax, \qquad x(0) = x_0, \tag{H.1}$$

whose solution is of the form

$$x(t) = \exp(At)x_0. \tag{H.2}$$

The exponential of At is given by the power series

$$\exp(At) = \sum_{k=0}^{\infty} \frac{(At)^k}{k!} = I + At + \frac{(At)^2}{2!} + \frac{(At)^3}{3!} + ... \tag{H.3}$$

H.1 Eigenvalues decomposition of A

H.1.1 References

- ✓ `scipy.sparse.linalg.eigs`
- ✓ MATLAB (2013)
- ✓ Schmid and Henningson (2001, p139, "Estimates of growth")

H.1.2 Definition

First and foremost, the i-th eigenvalue of the matrix $\mathcal{A}$ is noted λ_i and associated with the i-th right-eigenvector v_i and the i-th left-eigenvector w_i. The right and left eigenvectors are already normalized by the `scipy.sparse.linalg.eigs` method, and do not require further transformation.

The ith eigenvalues and its associated right and left eigenvectors of a square matrix A of dimension n are the ith biggest scalar λ_i and the nonzero vectors v_i and w_i such that

$$Av_i = \lambda_i v_i, \tag{H.4a}$$
$$w_i^T A = \lambda_i w_i^T, \tag{H.4b}$$

The eigenvalues of a square matrix respects the proposition

$$\forall i, \quad (A - \lambda_i I)v_i = 0, \quad v_i \neq 0, \tag{H.5}$$

which implies that $A - \lambda_i I$ is singular,

$$\forall i, \quad det(A - \lambda_i I) = 0. \tag{H.6}$$

This determinant is called the "characteristic equation" or "characteristic polynomial" of A. Let's denote $V = \begin{bmatrix} v_1 & \dots & v_n \end{bmatrix}$ and $W = \begin{bmatrix} w_1 & \dots & w_n \end{bmatrix}^T$ the matrices of eigenvectors of A and $\Lambda = diag(\lambda_i)$ the associated diagonal matrix of eigenvalues, such that

$$AV = V\Lambda, \tag{H.7a}$$
$$WA = \Lambda W. \tag{H.7b}$$

Assuming that the eigenvectors are linearly independent (non-singularity of V and W), the "eigenvalue decomposition" of A can be written as

$$A = V\Lambda V^{-1}, \tag{H.8a}$$
$$A = W^{-1}\Lambda W. \tag{H.8b}$$

Thanks to this eigen-decomposition, the solution H.2 of the model H.1 simplifies into

$$\exp(At) = \exp(V\Lambda V^{-1}t), \tag{H.9}$$
$$= VV^{-1} + V\Lambda V^{-1}t + \frac{V\Lambda^2 V^{-1}t^2}{2!} + \frac{V\Lambda^3 V^{-1}t^3}{3!} + ..., \tag{H.10}$$
$$= V\left[I + \Lambda t + \frac{\Lambda^2 t^2}{2!} + \frac{\Lambda^3 t^3}{3!} + ...\right]V^{-1}, \tag{H.11}$$
$$= V\exp(\Lambda t)V^{-1}, \tag{H.12}$$

or by switching to the eigenvectors basis $z = V^{-1}x$,

$$z(t) = \exp(\Lambda t)z_0, \qquad z(0) = z_0 = V^{-1}x_0. \tag{H.13}$$

H.1.3 Eigenvalues sensitivity and accuracy

The sensitivity of the eigenvalues is estimated by the condition number of the matrix of eigenvectors (MATLAB, 2013, p.9). The condition number of the eigenvector matrix is an upper bound for the individual eigenvalue condition numbers (MATLAB, 2013, p.14). The `MATLAB eig` function or equivalent `Python` methhods are doing as well as can be expected on this problem with machine-precision. The inaccuracy of the computed eigenvalues is caused by their sensitivity.

H.1.4 Interpretation

Eigenvalues decomposition for **small** perturbations gives insights on the long-term time-evolution of the model and its stability, as the eigenvalue decomposition is related to matrix power A^k or exponential $exp(At)$ (Bau and Trefethen, 1997).

H.2 Singular values decomposition

H.2.1 References

- ✓ MATLAB (2013)
- ✓ Trefethen et al. (1993, lecture 4, lecture 5)
- ✓ Schmid and Henningson (2001, p112, p119)
- ✓ Green and Limebeer (1995, p28-33)

H.2.2 Definition

A singular value and pair of singular vectors of a square or rectangular matrix A are a non-negative scale σ and two nonzero u and v (MATLAB, 2013)

$$Av = \sigma u, \tag{H.14}$$

$$A^* u = \sigma v. \tag{H.15}$$

The term "singular value" relates to the distance between a matrix and the set of singular matrices. Written in matrix form, the defining equations for singular values and singular vectors are

$$AV = U\Sigma, \tag{H.16}$$

$$A^* U = V\Sigma^*, \tag{H.17}$$

where Σ is a diagonal matrix of singular values σ_i with $\sigma_1 \geq \sigma_2 \geq ... \geq \sigma_n$. Singular vectors can always be chosen to be perpendicular to each other, such that matrices U and V, whose columns are the normalized singular vectors, satisfy $U^*U = I$ and $V^*V = I$. In other words, U and V are orthogonal if they are real, and unitary if they are complex. Consequently, the singular value decompositon (SVD) of the matrix A can be written as

$$A = U\Sigma V^*, \tag{H.18}$$

with diagonal Σ and orthogonal or unitary U and V.

From Trefethen et al. (1993, lecture 4), the SVD is motivated by the following:

> The image of the unit sphere under any $m \times n$ matrix is a hyper-ellipse (an m-dimensional generalization of an ellipse) (Trefethen et al., 1993, p 29). It is clear that the image of the unit sphere in $\mathbb{R}^n$ under a map $A = U\Sigma V^*$ must be a hyper-ellipse in $\mathbb{R}^m$. The unitary map V^* preserves the sphere, the diagonal matrix Σ stretches the sphere into a hyper-ellipse aligned with the canonical basis, and the final unitary map U rotates or reflects the hyper-ellipse without changing its shape. Thus, if we can prove that every matrix has an SVD, we shall have proved that the image of the unit sphere under any linear map is a hyper-ellipse, as claimed at the outset of this lecture.

H.2.3 Singular values sensitivity and accuracy

Since U and V are orthogonal or unitary, they preserve norms. Consequently, perturbations of any size in any matrix cause perturbations of roughly the same size in its singular values. There is no need to define condition numbers for singular values because they would always be equal to one. Perturbations and accuracy are measured relative to the norm of the matrix or, equivalently, the largest singular value. The accuracy of the smallest singular values is measured relative to the largest one. If, as often the case, the singular values vary over several orders of magnitude, the smallest ones might not have full accuracy relative to the biggest ones. In particular, if the matrix is (nearly-)singular, then some of the σ_i must be (nearly-)zero. The computed values of these σ_i will usually be on the order of $\epsilon\|A\|_2$, where ϵ is the floating-point accuracy parameter (MATLAB, 2013, p.15).

H.2.4 Low rank approximation

From Bau and Trefethen (1997, p 35):

Theorem 5.7: A is the sum of r rank-one matrices,

$$A = \sum_{j=1}^{r} \sigma_j u_j v_j^*. \tag{H.19}$$

The formula H.19 represents a low-rank decomposition into rank-one matrices with a deeper property: the partial sum captures as much of the energy of A as possible for a given rank r. This statement hold with "energy" defined by either the 2-norm or the Frobenius norm. We can make it precise by formulating a problem of best approximation of a matrix A by matrices of lower rank r.

The geometric interpretation of the low-rank decomposition H.19 refers to the best approximation of a hyper-ellipsoid (the image-space of A of rank n) by lower-rank hyper-ellipsoid (the image-space of A_r of rank $r < n$) (Trefethen et al., 1993, p.36). For rank one, it is just the longest axis of the hyper-ellipsoid. For rank two, the second longest axis is added. Up to rank n where the entire hyper-ellipsoid, $A_r \approx A$, is captured.

H.2.5 Differences between Eigenvalues and Singular values

From MATLAB (2013):

> Eigenvalues plays an important role in situations where the matrix is a transformation from one vector space onto itself. Singular values play an important role where the matrix is a transformation from one vector space to a different vector space, possibly with a different dimension.
>
> (MATLAB, 2013, p.3) In abstract linear algebra terms, eigenvalues are relevant if a square, n-by-n matrix A is thought of as mapping n-dimensional space onto itself. We try to find a basis for the space so that the matrix becomes diagonal. This basis might be complex even if A is real. In fact, if the eigenvectors are not linearly independent, such a basis does not even exist. The SVD is relevant if a possibly rectangular m-by-n matrix A is thought of as a mapping n-space onto m-space. We try to find one change of basis in the domain and a usually different change of basis in the range so that the matrix becomes diagonal. Such bases always exist and are always real if A is real. In fact, the transforming matrices are orthogonal or unitary, so they preserve lengths and angles and do not magnify errors.
>
> (MATLAB, 2013, p.16) There are two difficulties with the eigenvalue decomposition. A theoretical difficulty is that the decomposition does not always exist. A numerical difficulty is that, even if the decomposition exists, it might not provide a basis for robust computation.

From Bau and Trefethen (1997, p.33):

> There are fundamental differences between the singular value decompositon and the eigenvalue decomposition.
>
> - One is that the SVD uses two different bases (the sets of left and right singular vectors), whereas the eigenvalue decomposition uses just one (the set of eigenvectors).
> - Another is that the SVD uses orthonormal bases, whereas the eigenvalue decomposition uses a basis that generally is not orthogonal.
> - A third is that not all matrices (even square ones) have an eigenvalue decomposition, but all matrices (even rectangular ones) have a singular value decomposition.
>
> In applications, eigenvalues tend to be relevant to problems involving the behavior of iterated forms of A, such as matrices powers A^k or exponential e^{tA} (i.e. the time evolution of the solution of the linear model associated with A), whereas singular vectors tend to be relevant to problems involving the behavior of A itself, or its inverse.

H.2.6 Relation between Eigenvalues and Singular values

From Bau and Trefethen (1997, p 34):

> Theorem 5.4: The nonzero singular values of A are the square roots of the nonzero eigenvalues of A^*A or AA^*. (These matrices have the same nonzero eigenvalues.)

H.3 Cholesky decomposition

Hermitian positive-definite matrices can be decomposed into triangular factors twice as quickly as general matrices. The standard algorithm for this, the Cholesky factorization, is a variant of Gaussian elimination that operates on both the left and the right of the matrix at once, preserving and exploiting symmetry (Bau and Trefethen, 1997, lecture 23). The Cholesky factorization has the form,

$$A = R^*R, \qquad r_{jj} > 0, \tag{H.20}$$

where R is upper-triangular. Every hermitian positive-definite matrix $A \in \mathbb{C}^{m\times m}$ has a unique Cholesky factorization (Bau and Trefethen, 1997, p.174).

H.3.1 Normality and transient energy growth

Literature review

From Reddy and Henningson (1993):

> In recent work it has been shown that there can be substantial transient growth in the energy of small perturbations to plane Poiseuille and Couette flows if the Reynolds number is below the critical value predicted by linear stability analysis. This growth, which may be as large as $\mathcal{O}(1000)$, occurs in the absence of nonlinear effects and can be explained by the non-normality of the governing linear operator —that is, the non-orthogonality of the associated eigenfunctions. [...] These results emphasize the fact that subcritical transition can occur for Poiseuille and Couette flows because the governing linear operator is non-normal.

From Waleffe (1995):

> A critique is presented of recent works promoting the concept of non-normal operators and transient growth as the key to understanding transition to turbulence in shear flows. The focus is in particular on a simple model [Baggett et al., Phys. Fluids 7 (1995)] illustrating that view. It is argued that the question of transition is really a question of existence and basin of attraction of nonlinear self-sustaining solutions that have little contact with the non-normal linear problem. An alternative nonlinear point of view [Hamilton et al., J. Fluid Mech. 287 (1995)] that seeks to isolate a self-sustaining nonlinear process, and the critical Reynolds number below which it ceases to exist, is discussed and illustrated by a simple model. Connections with the Navier-Stokes equations and observations are highlighted throughout.

From Kerswell (2005):

> Mathematically, this "transient growth" is caused by the apparently generic non-normality of the linear operator governing the temporal evolution of infinitesimal disturbances in shear flows. This non-normality means that the eigenfunctions of the linear operator are not orthogonal (under the energy norm) with the consequence that certain initial flow conditions are poorly spanned. This ill-conditioning means that the eigenfunction expansion for some certain initial conditions requires unusually large coefficients due to a subset of eigenfunctions significantly cancelling. When each eigenfunction decays exponentially over time (otherwise the flowwould be linearly unstable) they do so with different rates so that the initial cancellation melts

> away. This uncovers the large coefficients in the expansion which has the effect of producing a period of algebraic growth. A simple example from the appendix of Schmid and Henningson (1994) illustrates the point nicely (see also Eckhardt and Pandit (2003)).

From Kim and Bewley (2007):

> A flow perturbation initialized as, for example, the second eigenmode minus the third eigenmode in Figure 2a is characterized by a very low initial energy due to destructive interference; however, as one eigenmode decays more quickly in time than the other, this destructive interference is reduced with time, and thus the overall energy of the perturbation actually increases quite substantially before it eventually decreases due to the stability of both modes (Butler & Farrell 1993, Reddy and Henningson (1993)). This effect is referred to as transient energy growth in the fluids literature and peaking in the controls literature. Transient energy growth is a direct result of eigenvector non-orthogonality/non-normality, and is accompanied by very large input/output transfer function norms in such systems when the system is considered from the input/output perspective (see Bewley (2001) and Lim & Kim 2004).

From Kim and Bewley (2007), relative to normality and results presented in section 5.4:

> A system is stabilizable if all unstable eigenmodes of the system maybe made stable by control feedback; that is if all unstable eigenmodes of the system are controllable. In practice, stabilizability is all one really needs. Typically, accurate discretizations of PDE systems are uncontrollable (i.e., not all of the eigenmodes of the system are controllable), as some of the highly damped modes (which, in the closed-loop system, ultimately have very little effect) nearly always have negligible support at the actuators. Lack of controllability in itself is thus not a matter of much practical concern. However, typical fluids systems usually exhibit a gradual loss of linear stabilizability as the Reynolds number is increased, as discussed in detail for the complex Ginzburg Landau model of spatially developing flows in Lauga and Bewley (2003) This gradual loss of stabilizability is related to an increase in non-normality of the eigenvectors of the closed-loop system (and the associated increased transfer function norms) as the Reynolds number is increased, and may be quantified by a metric based on adjoint eigenvector analysis, which extends readily to three-dimensional computational fluid dynamics codes via the implicitly restarted Arnoldi method (Sorenson 1992). When linear stabilizability is lost, stabilization of the system is virtually impossible by any

means. Thus, the quantification of the stabilizability of a given system of interest is a matter of significant practical relevance. Similar arguments can be made about detectability vs observability in the estimation problem.

Mathematical measure

We estimate the maximal energy growth $\dot{\mathcal{E}}_T$ for a linear system of the form H.1, through the calculation of the leading eigenvalues of the operator $A + A^*$, and for the closed loop system $(A + B_2K) + (A + B_2K)^*$. This measure derives from the decomposition from Jorge Vidal-Ribas master-thesis (p.28), starting from the expressoin of the kinetic energy density eq.5.31,

$$\begin{aligned}\dot{\mathcal{E}}_T &= \frac{1}{2}\frac{\partial}{\partial t}\mathcal{E}_T \\ &= \frac{1}{2}\frac{\partial}{\partial t}\boldsymbol{x}^* Q_x \boldsymbol{x} \\ &= \frac{1}{2}(\dot{\boldsymbol{x}}^* Q_x \boldsymbol{x} + \boldsymbol{x}^* Q_x \dot{\boldsymbol{x}}) \\ &= \frac{1}{2}(\boldsymbol{x}^* A^* Q_x \boldsymbol{x} + \boldsymbol{x}^* Q_x A \boldsymbol{x}) \\ &= \frac{1}{2}\boldsymbol{x}^*(A^* Q_x + Q_x A)\boldsymbol{x},\end{aligned} \tag{H.21}$$

where $Q_x = C_1^* C_1$ from 5.37, and similarly,

$$\dot{\mathcal{E}}_T = \frac{1}{2}\boldsymbol{x}^*((A + B_2K)^* Q_x + Q_x(A + B_2K))\boldsymbol{x}, \tag{H.22}$$

for the closed-loop system considering $\dot{\boldsymbol{x}} = (A + B_2K)\boldsymbol{x}$.

The direction of maximal growth is the solution of

$$\max_{\|x\|=1} \dot{E}_T = \frac{1}{2}\boldsymbol{x}^*(A^* Q_x + Q_x A)\boldsymbol{x} \tag{H.23}$$

which can be solved by applying the Lagrangian multipliers method for the cost function

$$J = \frac{1}{2}\boldsymbol{x}^*(A^* Q_x + Q_x A)\boldsymbol{x} - \lambda(\boldsymbol{x}^*\boldsymbol{x} - 1) \tag{H.24}$$

The extrema of the cost J appears when $\boldsymbol{x}$ is the normalized leading eigenvector of $A^* + A$ and λ its leading eigenvalue. Therefore, the calculation of the leading eigenvalues of $\frac{1}{2}(A^* Q_x + Q_x A)$ gives an indication of the possible transient energy growth of the system. We can thus determine if there is a initial drop or increase in the energy, source of a transient growth, which might break our linear controller.

Appendix I

Supplement on the validation of the OSSE model

This appendix gathers figures of the simulations run for the validation process of the OSSE model described in section 5.5.2, with the non-laminar Nagata (1990) lower-branch as baseflow and a sinusoidal forcing

$$q^{+}_{v_{\alpha,\beta}} = q^{-}_{v_{\alpha,\beta}} = 0.0005 \ \sin(\frac{2\pi t}{10}). \tag{I.1}$$

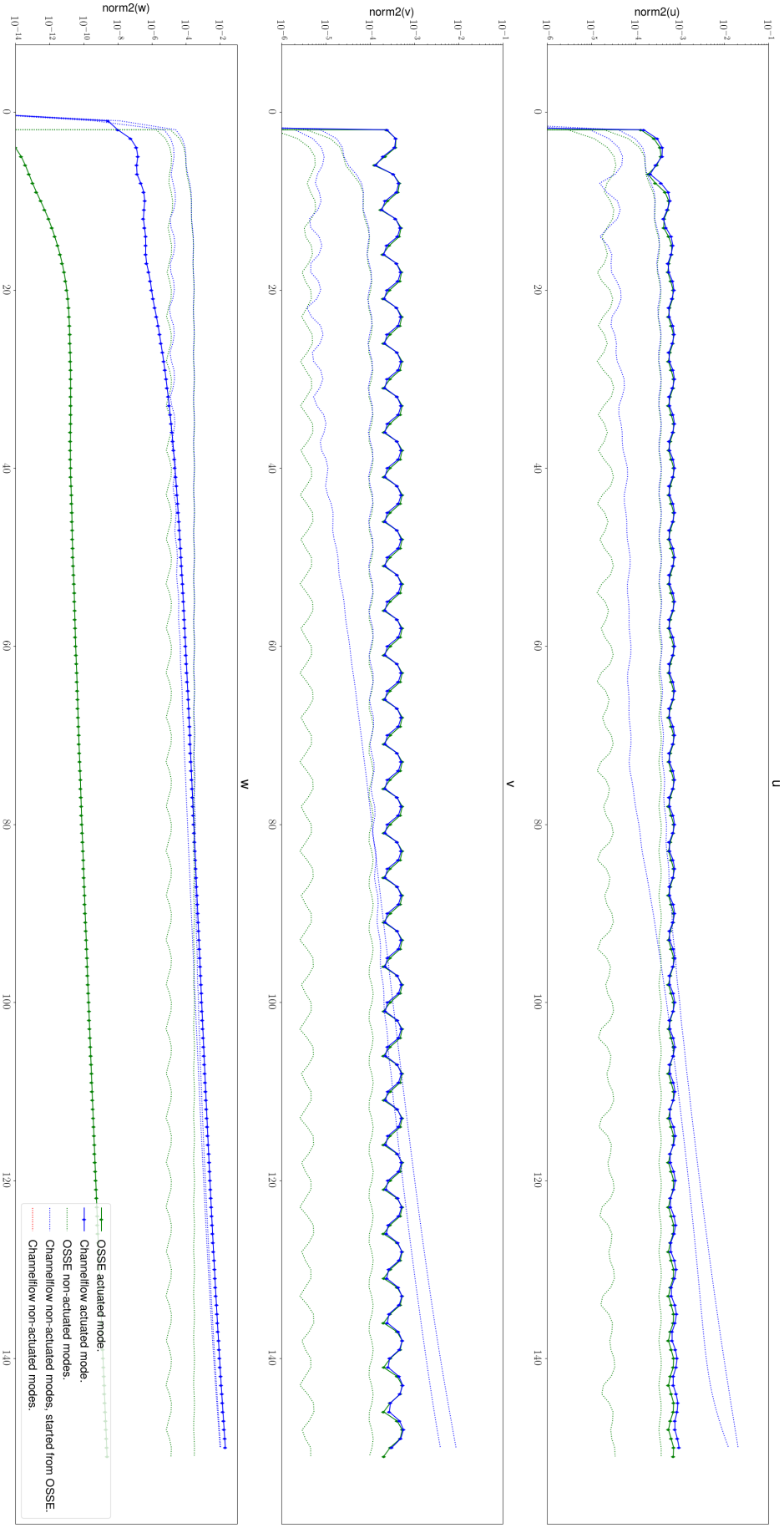

FIGURE I.1: Non-linear validation: Time-evolution of the norm of the three velocity components of the Fourier mode $(1,0)$ actuated under the sinusoidal boundary constraints 5.63 (diamond-thick line) and of the other non-actuated modes $(0,1)$ and $(1,1)$ (dotted lines) for two different simulations: OSSE model (green), Channelflow (blue). (times $t = [0, 150]$, EQ1 baseflow, resolution $21 \times 65 \times 21$ for Channelflow and $21 \times 35 \times 21$ for the OSSE model, $Re = 400$, $\tau = 0.05$).

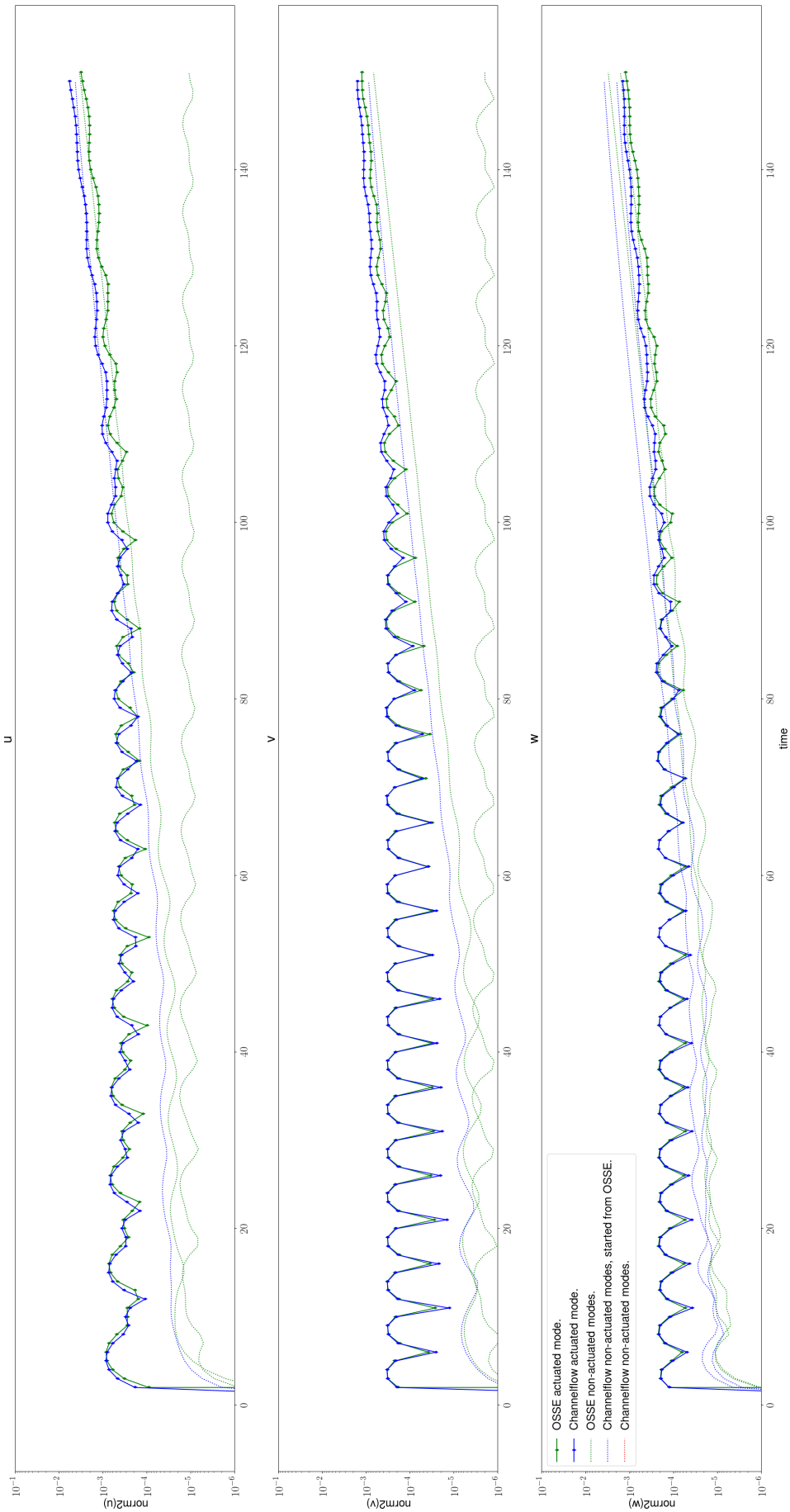

FIGURE I.2: Non-linear validation: Time-evolution of the norm of the three velocity components of the Fourier mode $(0, 1)$ actuated under the sinusoidal boundary constraints 5.63 (diamond-thick line) and of the other non-actuated modes $(1, 0)$ and $(1, 1)$ (dotted lines) for two different simulations: OSSE model (green), Channelflow (blue). (times $t = [0, 150]$, EQ1 baseflow, resolution $21 \times 65 \times 21$ for Channelflow and $21 \times 35 \times 21$ for the OSSE model, $Re = 400$, $\tau = 0.05$).

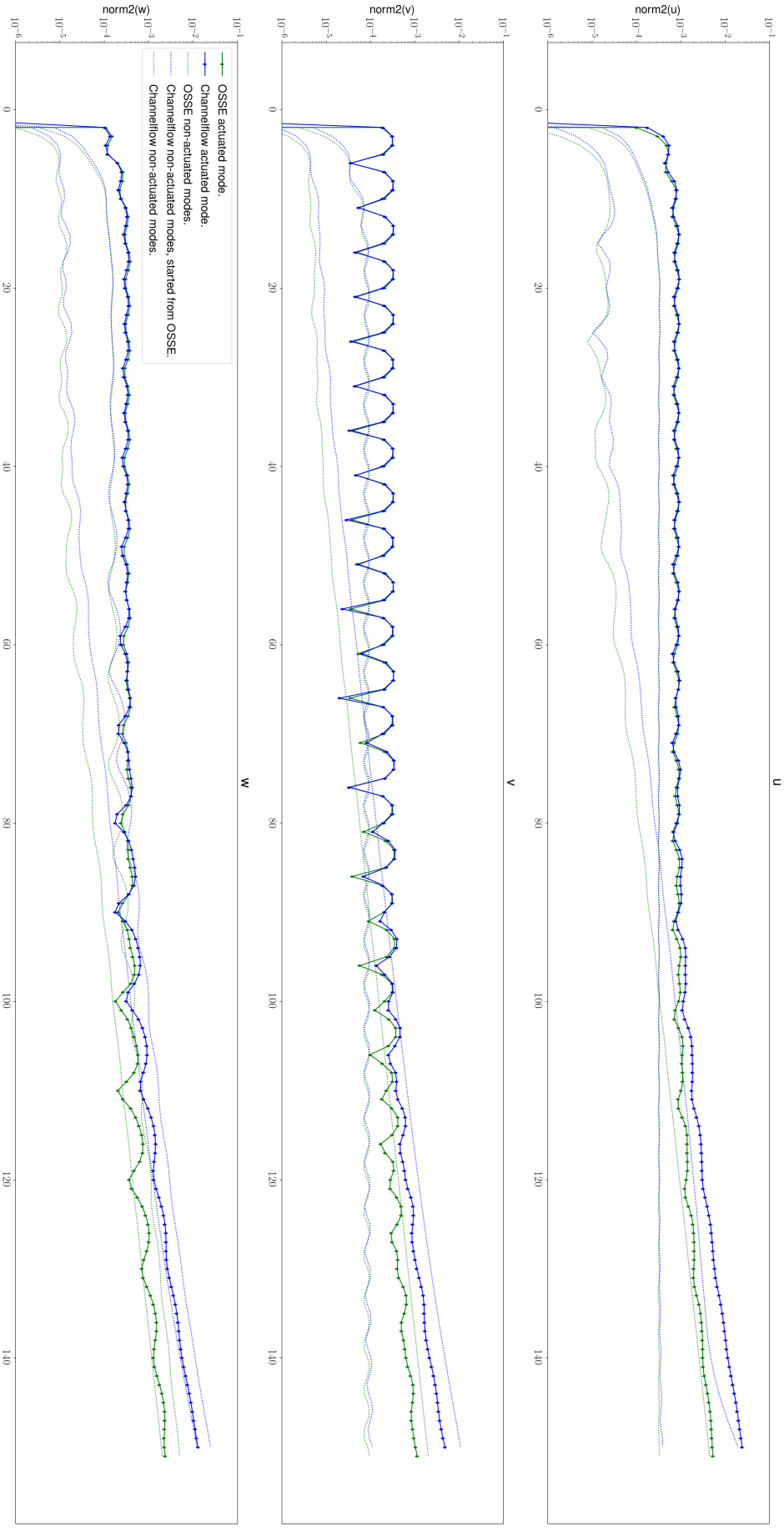

FIGURE I.3: Non-linear validation: Time-evolution of the norm of the three velocity components of the Fourier mode $(1,1)$ actuated under the sinusoidal boundary constraints 5.63 (diamond-thick line) and of the other non-actuated modes $(0,1)$ and $(1,0)$ (dotted lines) for two different simulations: OSSE model (green), Channelflow (blue). (times $t = [0, 150]$, EQ1 baseflow, resolution $21 \times 65 \times 21$ for Channelflow and $21 \times 35 \times 21$ for the OSSE model, $Re = 400$, $\tau = 0.05$).

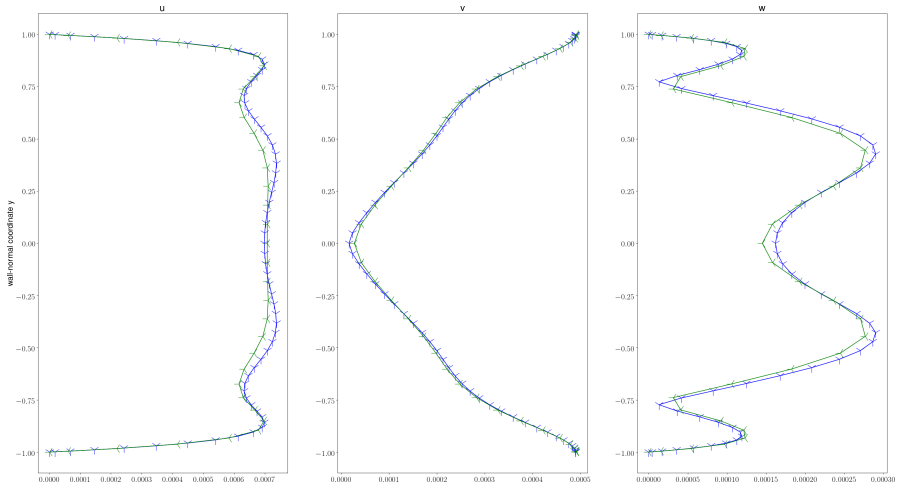

A) $t = 40$

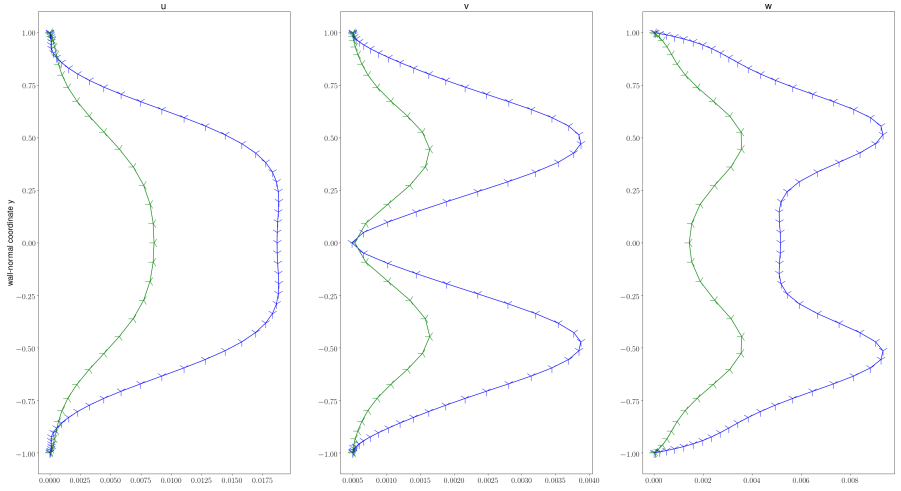

B) $t = 100$

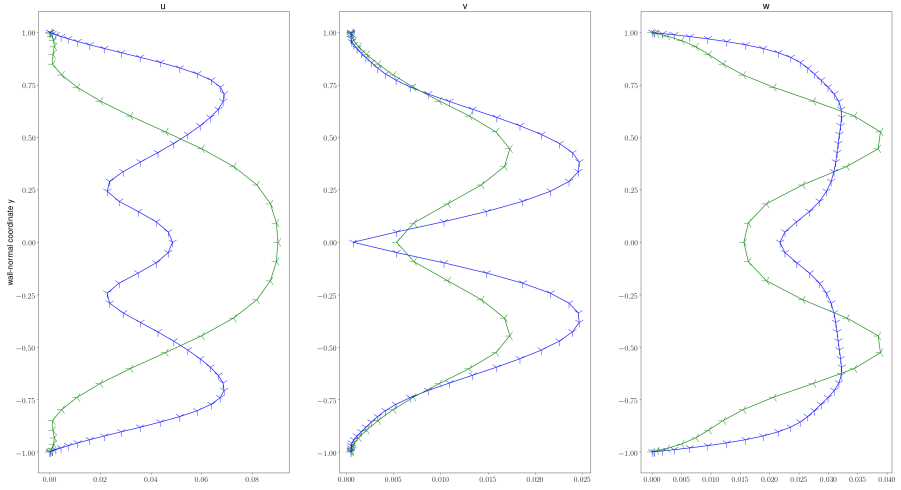

C) $t = 150$

FIGURE I.4: Non-linear validation: Velocity components profiles (absolute value) of Fourier mode $(1, 1)$ actuated under the boundary constraints 5.54, for two different simulations: OSSE model (green $\prec$) and Channelflow 1.4.2 (blue $\succ$) (times $t = 40, 100, 150$, EQ1 baseflow, resolution $21 \times 65 \times 21$ for Channelflow and $21 \times 35 \times 21$ for the OSSE model, $Re = 400$, $\tau = 0.05$).

Glossary

Adiabatic Process An adiabatic process occurs without transfer of heat or mass of substances between a thermodynamic system and its surroundings. In an adiabatic process, energy is transferred to the surroundings only as work. The adiabatic process provides a rigorous conceptual basis for the theory used to expound the first law of thermodynamics, and as such it is a key concept in thermodynamics. (Bailyn, 1994, p.21) 13

Bounded A mathematical object (such as a set or function) is said to bounded if it possesses a bound, i.e., a value which all members of the set, functions, etc., are less than. (Weisstein, Eric W., 1999) 43

Causal In control theory, a causal system (also known as a physical or nonanticipative system) is a system where the output depends on past and current inputs but not future inputs. (Wikipedia contributors, 2011c) 32, 39, 42

Control, Closed-loop Feedback control systems are often referred to as closed-loop control systems. In practice, the terms feedback control and closed-loop control are used interchangeably. In a closed-loop control system the actuating error signal, which is the difference between the input signal and the feedback signal (which may be the output signal itself or a function of the output signal and its derivatives and/or integrals), is fed to the controller so as to reduce the error and bring the output of the system to a desired value. The term closed-loop control always implies the use of feedback control action in order to reduce system error (Ogata, 2009). 3, 44

Control, Feedback A system that maintains a prescribed relationship between the output and the reference input by comparing them and using the difference as a means of control is called a feedback control system (Ogata, 2009). 3, 27, 29, 42, 43, 89

Description, Eularian For continuum deformation, the Eulerian specification of the flow field is a way of looking at fluid motion that focuses on specific locations in the space through which the fluid flows as time passes. (calltech.edu, 2000) 12

Description, Lagrangian For continuum deformation, the Lagrangian specification of the field is a way of looking at fluid motion where the observer follows an individual fluid parcel as it moves through space and time. Derivatives are noted as $\frac{D}{Dt}$. (calltech.edu, 2000) 13

Deterministic Contrary of stochastic. 15

Equation, Algebraic In mathematics, an equation or polynomial equation of the form $P = 0$ where P is a polynomial with coefficients in some field, often the field of the rational numbers. (Wikipedia contributors, 2011a) 6, 34, 35, 40, 272

Equation, Differential In mathematics, an equation that relates some function with its derivatives. (Wikipedia contributors, 2011e) 3, 34, 35, 37, 40, 48, 272

Equation, Ordinary Differential (ODE) In mathematics, an Ordinary-differential equation (ODE) is a differential equation containing one or more functions of one independent variable and the derivatives of those functions. The term ordinary is used in contrast with the term partial differential equation which may be with respect to more than one independent variable. (Zill, 2017) xxiv, 48, 272

Equation, Partial Differential (PDE) In mathematics, a differential equation that contains unknown multivariable functions and their partial derivatives. (Wikipedia contributors, 2011e) 48, 53, 108, 148, 272

Equation, Partial Differential Algebraic (PDAE) In mathematics, an incomplete system of partial-differential equations that is closed with a set of algebraic equation. (Wikipedia contributors, 2011k) xxiv, 12, 46

Expectation, Expected value In probability theory, the expected value of a random variable, intuitively, is the long-run average value of repetitions of the experiment it represents. For example, the expected value in rolling a six-sided die is 3.5, because the average of all the numbers that come up in an extremely large number of rolls is close to 3.5. Less roughly, the law of large numbers states that the arithmetic mean of the values almost surely converges to the expected value as the number of repetitions approaches infinity. The expected value is also known as the expectation, mathematical expectation, EV, average, mean value, mean, or first moment. (Wikipedia contributors, 2011f) xxviii, 31

Fluid, Incompressible Theoretical fluid where the density of the fluid is everywhere equal and constant, thus does not change with pressure. 10, 13, 14

Fluid, Inviscid Fluid with viscosity equal to zero. The Reynolds number of inviscid flow approaches infinity as the viscosity approaches zero. When viscous forces are neglected, such as the case of inviscid flow, the Navier-Stokes equation can be simplified to a form known as the Euler equation. (Bird et al., 2007) 13

Fluid, Newtonian In continuum mechanics, a Newtonian fluid is a fluid in which the viscous stresses arising from its flow, at every point, are linearly proportional to the local strain rate — the rate of change of its deformation over time. That is equivalent to saying those forces are proportional to the rates of change of the fluid's velocity vector as one moves away from the point in question in various directions. (Wikipedia contributors, 2011j) 13, 14

Function, Gaussian In mathematics, a Gaussian function, often simply referred to as a Gaussian, is a function of the form:

$$f : x \mapsto f(x) = a \exp^{-\frac{(x-b)^2}{2c^2}} \tag{I.2}$$

for arbitrary real constants a, b and non zero c. It is named after the mathematician Carl Friedrich Gauss. The graph of a Gaussian is a characteristic symmetric "bell curve" shape. The parameter a is the height of the curve's peak, b is the position of the center of the peak and c (the standard deviation, sometimes called the Gaussian RMS width) controls the width of the "bell". (Wikipedia contributors, 2011g) 29, 44

Function, Homogeneous In mathematics, a homogeneous function is one with multiplicative scaling behaviour: if all its arguments are multiplied by a factor, then its value is multiplied by some power of this factor. (Wikipedia contributors, 2011h) 90

Funtion, Smoothness In mathematical analysis, the smoothness of a function is a property measured by the number of derivatives it has that are continuous. A smooth function is a function that has derivatives of all orders everywhere in its domain. (Bailyn, 1994, p.21) 12

Matrix, Hermitian For a complex matrix $A \in \mathbb{R}^{m \times m}$, the analogous property to symmetric real matrices is that A is hermitian. A hermitian matrix has entries below the diagonal that are complex conjugates of those above the diagonal: $a_{ij} = a^*_{ji}$, hence $A = A^*$. Note that this means that the diagonal entries of a hermitian matrix must be real. A hermitian matrix A satisfies $x^*Ay = y^*Ax$ for all x, y in $\mathbb{R}^m$. (Bau and Trefethen, 1997, p.172). 260, 261, 273

Matrix, Negative Definite Negative definite and negative semi-definite matrices are the analog of positive-definite matrices. 42, 43

Matrix, Positive Definite In linear algebra, a symmetric real matrix $M \in \mathbb{R}^{n \times n}$ is said to be positive definite if the scalar $z^T M z$ is strictly positive for every non-zero column vector $z \in \mathbb{R}^n$. M is positive definite if and only if all of its eigenvalues are positive. A complex hermitian matrix $M \in \mathbb{R}^{n \times n}$ is said to be positive definite if the scalar zMz is strictly positive for every non-zero column vector $z \in \mathbb{C}^n$.

The matrix is Positive semi-definite when $z^T Mz$ or zMz is positive or zero. M is positive semi-definite if and only if all of its eigenvalues are non-negative. Negative definite and negative semi-definite matrices are defined analogously. A matrix that is not positive semi-definite and not negative semi-definite is called indefinite. M is indefinite if and only if it has both positive and negative eigenvalues. 89, 260, 261, 273

Matrix, Symmetric A real matrix $A \in \mathbb{R}^{m \times m}$ is symmetric if it has the same entries below the diagonal as above: $a_{ij} = a_{ji}$ for all i, j, hence $A = A^T$. Such a matrix satisfies $x^T Ay = y^T Ax$ for all vectors x and y in $\mathbb{R}^m$ (Bau and Trefethen, 1997, p.172). 273

Memorylessness In probability and statistics, memorylessness is a property of certain probability distributions. It usually refers to the cases when the distribution of a "waiting time" until a certain event, does not depend on how much time has elapsed already. (Wikipedia contributors, 2011i) 42, 43

Noise, Uncorrelated Uncorrelated white noise means that no two points in the noise's time domain are associated with each other. It is impossible to predict any noise value at any other time $t \neq t_1$ from the noise level at given time t_1. The correlation coefficient is 0. 29, 44

Noise, White In signal processing, white noise is a random signal having equal intensity at different frequencies, giving it a constant power spectral density. (Carter and Mancini, 2017) 29, 31, 44

Normality see appendix section H.3.1. 43

Singular Value see appendix H.2. xxiv, 31, 103, 258, 260

Stochastic Stochastic is synonymous with "random". The word is of Greek origin and means "pertaining to chance" (Parzen, E. Stochastic Processes. Oakland CA: Holden Day, p. 7, 1962). It is used to indicate that a particular subject is seen from point of view of randomness. Stochastic is often used as counterpart of the word "deterministic", which means that random phenomena are not involved. Therefore, stochastic models are based on random trials, while deterministic models always produce the same output for a given starting condition. (Origlio, Vincenzo, 1999) 15, 43, 272

System, Controllability A system is stated as "controllable" if it is feasible to find a finite-energy controller sequence such that any final state can be reached from any initial state in finite time. 108

System, Stabilizibility A system is stated as "stabilizable" when all uncontrollable state variables can be made to have stable dynamics. Stabilizibility is a weaker

notion than controllability. Thus, even though some of the state variables cannot be controlled, all the state variables will still remain bounded during the system's behavior. 34, 108

Viscosity Material property which relates the viscous stresses in a material to the rate of change of a deformation. Viscosity can be seen as measure of the resistance of a material to deformation at a given rate. xxvi, 11

Bibliography

Ahmed, M. A. (2018). *Low-dimensional exact coherent states in plane Couette flow*. PhD thesis, University of Southampton.

Ahmed, M. A. and Sharma, A. (2017). New equilibrium solution branches of plane Couette flow discovered using a project-then-search method. *arXiv:1706.05312*.

Alla, A. and Simoncini, V. (2017). Order reduction approaches for the algebraic Riccati equation and the LQR problem.

Amitay, M. and Glezer, A. (2006). Aerodynamic Flow Control Using Synthetic Jet Actuators. pages 45–73.

Antoulas, A. C. (2006). A survey of model reduction methods for large-scale systems. *American Mathematical Society*, 280:1–28.

Arrowsmith, D. K. and Place, C. M. (1992). *Dynamical systems: differential equations, maps, and chaotic behaviour*. Chapman and Hall, London, United-Kingdom.

Artuso, R., Aurell, E., and Cvitanovic, P. (1990a). Recycling of strange sets: I. Cycle expansions. *Nonlinearity*, 3(2):325–359.

Artuso, R., Aurell, E., and Cvitanovic, P. (1990b). Recycling of strange sets: II. Applications. *Nonlinearity*, 3(2):361–386.

Bailyn, M. (1994). *A Survey of Thermodynamics*. Amer Inst of Physics.

Bamieh, B., Paganini, F., and Dahleh, M. A. (2002). Distributed Control of Spatially Invariant Systems. *IEEE Transactions on Automatic Control*, 47(7):1091–1107.

Bannier, A., Garnier, E., and Sagaut, P. (2016). Riblets Induced Drag Reduction on a Spatially Developing Turbulent Boundary Layer. pages 213–224.

Bänsch, E., Benner, P., Saak, J., and Weichelt, H. K. (2015). Riccati-based Boundary Feedback Stabilization of Incompressible Navier-Stokes Flows. *SIAM Journal on Scientific Computing*, 37(2):A832–A858.

Bau, D. and Trefethen, L. N. (1997). *Numerical linear algebra*.

Bearman, P. and Morel, T. (1983). Effect of free stream turbulence on the flow around bluff bodies. *Progress in Aerospace Sciences*, 20(2-3):97–123.

Belardinelli, E. and Cavalcanti, S. (1991). A new nonlinear two-dimensional model of blood motion in tapered and elastic vessels. *Computers in Biology and Medicine*, 21(1-2):1–13.

Benner, P. (2004). Solving Large-Scale Control Problems. *IEEE Control Systems*, 24(1):44–59.

Benner, P., Li, J.-R., Penzl, T., Benner, P., Li, J.-R., and Penzl, T. (2008). Numerical solution of large-scale Lyapunov equations, Riccati equations, and linear-quadratic optimal control problems. Technical report.

Benner, P. and Saak, J. (2013). Numerical solution of large and sparse continuous time algebraic matrix Riccati and Lyapunov equations: A state of the art survey. *GAMM Mitteilungen*.

Berkooz, G., Holmes, P., and Lumley, J. L. (1993). The proper orthogonal decomposition in the analysis of turbulent flows. *Annual Review of Fluid Mechanics*, 25(1971):539–575.

Bewley, T., Luchini, P., and Pralits, J. (2016). Methods for solution of large optimal control problems that bypass open-loop model reduction. *Meccanica*, 51(12):2997–3014.

Bewley, T. R. (2001). Flow control: New challenges for a new Renaissance. *Progress in Aerospace Sciences*, 37(1):21–58.

Bewley, T. R. and Liu, S. (1998). Optimal and robust control and estimation of linear paths to transition. *Journal of Fluid Mechanics*, 365:305–349.

Bewley, T. R., Moin, P., and Temam, R. (2001). DNS-based predictive control of turbulence: An optimal benchmark for feedback algorithms. *Journal of Fluid Mechanics*, 447:179–225.

Bird, R. B., Stewart, W. E., and Lightfoot, E. N. (2007). *Transport phenomena*. New York : Wiley.

Boldyrev, S., Nordlund, Å., and Padoan, P. (2002). Supersonic Turbulence and Structure of Interstellar Molecular Clouds. *Physical Review Letters*, 89(3):031102.

Borggaard, J. and Burns, J. (2002). A Continuous Control Design Method. In *3rd Theoretical Fluid Mechanics Meeting*, Reston, Virigina. American Institute of Aeronautics and Astronautics.

Bucci, M. A., Semeraro, O., Allauzen, A., Wisniewski, G., Cordier, L., and Mathelin, L. (2019). Control of chaotic systems by deep reinforcement learning. *Proceedings of the Royal Society A: Mathematical, Physical and Engineering Sciences*, 475(2231):20190351.

Busse, F. H. and Clever, R. M. (1992). Three-dimensional convection in an inclined layer heated from below. *Journal of Engineering Mathematics*, 26(1):1–19.

Camphouse, R. C. and Myatt, J. (2004). Feedback Control for a Two-Dimensional Burgers' Equation System Model. In *2nd AIAA Flow Control Conference*, Reston, Virigina. American Institute of Aeronautics and Astronautics.

Canuto, C., Hussaini, M., Quarteroni, A., and Zang, T. (2006). *Spectral Methods: Evolution to Complex Geometries and Applications to Fluid Dynamics*. Scientific Computation. Springer Berlin Heidelberg, Berlin, Heidelberg.

Canuto, C., Hussaini, M. Y., Quarteroni, A., and Zang, T. A. (1988). *Spectral Methods in Fluid Dynamics*. Springer Berlin Heidelberg, Berlin, Heidelberg.

Carter, B. and Mancini, R. (2017). *Op Amps for Everyone*. Elsevier Ltd, 5th edition.

Chan, S. M. (1984). Modal controllability and observability of power-system models. *International Journal of Electrical Power and Energy Systems*, 6(2):83–88.

Chandler, G. J. and Kerswell, R. R. (2013). Invariant recurrent solutions embedded in a turbulent two-dimensional Kolmogorov flow. *Journal of Fluid Mechanics*, 722:554–595.

Clever, R. and Busse, F. H. (1997). Tertiary and quaternary solutions for plane Couette flow. *Journal of Fluid Mechanics*, (344):137–153.

Collis, S. S., Joslin, R. D., Seifert, A., and Theofilis, V. (2004). Issues in active flow control: theory, control, simulation, and experiment. *Progress in Aerospace Sciences*, 40(4-5):237–289.

Cooley, J. W. and Tukey, J. W. (1965). An algorithm for the machine calculation of complex Fourier series. *Mathematical Computation*, 19:297–301.

Cortelezzi, L. and Speyer, J. L. (1998). Robust reduced-order controller of laminar boundary layer transitions. *Physical Review E*, 58(2):1906–1910.

Cossu, C. and Brandt, L. (2004). On Tollmien-Schlichting-like waves in streaky boundary layers. *European Journal of Mechanics, B/Fluids*, 23(6):815–833.

Cvitanović, P. (1988). Invariant measurement of strange sets in terms of cycles. *Physical Review Letters*, 61(24):2729–2732.

Cvitanović, P., Atuso, R., Mainieri, R., Tanner, G., and Vattay, G. (2013). Chaos : Classical and Quantum I : Deterministic Chaos. page 995.

Dimotakis, P. E. (2005). TURBULENT MIXING. *Annual Review of Fluid Mechanics*, 37(1):329–356.

Doyle, J. C. (1978). Guaranteed margins for LQG regulators. *IEEE Transactions on automatic Control*, 23(4):756–757.

Drazin, P. G. and Reid, W. H. (2004). *Hydrodynamic Stability*. Cambridge University Press, Cambridge.

Druskin, V. and Simoncini, V. (2011). Adaptive rational Krylov subspaces for large-scale dynamical systems. *Systems and Control Letters*.

Duguet, Y., Pringle, C. C. T., and Kerswell, R. R. (2008). Relative periodic orbits in transitional pipe flow. *Physics of Fluids*, 20(11):114102.

Faisst, H. and Eckhardt, B. (2003). Traveling Waves in Pipe Flow. *Physical Review Letters*, 91(22):224502.

Farano, M., Cherubini, S., Robinet, J. C., De Palma, P., and Schneider, T. M. (2019). How hairpin structures emerge from exact solutions of shear flows. *Journal of Fluid Mechanics*, 858:1–12.

Farazmand, M. (2016). An adjoint-based approach for finding invariant solutions of Navier-Stokes equations. *Journal of Fluid Mechanics*, 795:278–312.

Gad-el Hak, M. (2000). *Flow control: passive, active, and reactive flow management*. Cambridge University Press.

Gatti, D., Cimarelli, A., Hasegawa, Y., Frohnapfel, B., and Quadrio, M. (2018). Global energy fluxes in turbulent channels with flow control. *Journal of Fluid Mechanics*, 857:345–373.

Gatti, D. and Quadrio, M. (2016). Reynolds-number dependence of turbulent skin-friction drag reduction induced by spanwise forcing. *Journal of Fluid Mechanics*, 802:553–582.

Gautier, N., Aider, J.-L., Duriez, T., Noack, B. R., Segond, M., and Abel, M. (2015). Closed-loop separation control using machine learning. *Journal of Fluid Mechanics*, 770:442–457.

Generalis, S. C. and Itano, T. (2010). Characterization of the hairpin vortex solution in plane Couette flow. *Physical Review E - Statistical, Nonlinear, and Soft Matter Physics*, 82(6):1–7.

Gibson, J. (2014). Channelflow: a spectral Navier-Stokes simulator in C++. *University of New Hampshire*, (July):1–41.

Gibson, J. F., Halcrow, J., and Cvitanovic, P. (2008). Visualizing the geometry of state space in plane Couette flow. *Journal Of Fluid Mechanics*, 611:107–130.

Gibson, J. F., Halcrow, J., and Cvitanović, P. (2009). Equilibrium and traveling-wave solutions of plane Couette flow. *Journal of Fluid Mechanics*, 638(1997):243–266.

Gibson, J. F., Reetz, F., Azimi, S., Ferraro, A., Kreilos, T., Schrobsdorff, H., Farano, M., Yesil, A. F., Schutz, S. S., Culpo, M., and Schneider, T. M. (2019). Channelflow 2.0 in preparation, see https://www.channelflow.ch.

Gomes, S. N., Papageorgiou, D. T., and Pavliotis, G. A. (2015). Stabilising nontrivial solutions of the generalised Kuramoto-Sivashinsky equation using feedback and optimal control. 1(March 2016):1–42.

Gottlieb, D. and Orszag, S. A. (1977). *Numerical Analysis of Spectral Methods*. Society for Industrial and Applied Mathematics.

Green, M. and Limebeer, D. J. (1995). *Linear robust control*, volume 31. Mineola, N.Y. : Dover Publications, Inc.

Green, M. A., Rowley, C. W., and Haller, G. (2007). Detection of Lagrangian coherent structures in three-dimensional turbulence. *Journal of Fluid Mechanics*, 572:111–120.

Grimble, M. J. and Kucera, V. (1996). *Polynomial Methods for Control Systems Design*. Springer London, London.

Gunzburger, M. D. (2002). *Perspectives in Flow Control and Optimization*. Society for Industrial and Applied Mathematics.

Halcrow, J. J. (2008). *Charting the state space of plane Couette flow: Equilibria, relative equilibria, and heteroclinic connections*. PhD thesis.

Hall, P. and Smith, F. T. (1991). On strongly nonlinear vortex/wave interactions in boundary-layer transition. *Journal of Fluid Mechanics*, 227(1991):641.

Hamilton, J. M., Kim, J., and Waleffe, F. (1995). Regeneration mechanisms of near-wall turbulence structures. *Journal of Fluid Mechanics*, 287(1995):317–348.

Hanjalić, K., Casciola, C. M., and Mastorakos, E. (2019). Advances in Turbulence, Heat and Mass Transfer Preface. *Flow, Turbulence and Combustion*, 103(4):845–846.

Hasegawa, Y., Quadrio, M., and Frohnapfel, B. (2014). Numerical simulation of turbulent duct flows with constant power input. *Journal of Fluid Mechanics*, 750:191–209.

Heins, P. H. (2015). *Modelling , Simulation and Control of Turbulent Flows Peter Hywel Heins*. PhD thesis, University of Sheffield.

Heins, P. H., Jones, B. L., and Sharma, A. S. (2014). Passivity-Based Feedback Control of a Channel Flow For Drag Reduction. (July):0–5.

Heins, P. H., Jones, B. L., and Sharma, A. S. (2016). Passivity-based output-feedback control of turbulent channel flow. *Automatica*, 69:348–355.

Henderson, A. (2004). The ParaView Guide: A Parallel Visualization Application. *The ParaView Guide*, page 340.

Heyouni, M. and Jbilou, K. (2008). An extended block Arnoldi algorithm for large-scale solutions of the continuous-time algebraic Riccati equation. *Electronic Transactions on Numerical Analysis*.

Hoepffner, J., Chevalier, M., Bewley, T. R., and Henningson, D. S. (2005). State estimation in wall-bounded flow systems. Part I. Perturbed laminar flows. *Journal of Fluid Mechanics*, 534:263–294.

Hogberg, M., Bewley, T. R., and Henningson, D. S. (2003). Linear feedback control and estimation of transition in plane channel flow. *Journal of Fluid Mechanics*, 481:S0022112003003823.

Högberg, M., Bewley, T. R., and Henningson, D. S. (2003). Relaminarization of Reτ=100 turbulence using gain scheduling and linear state-feedback control. *Physics of Fluids*, 15(11):3572–3575.

Holmes, P., Lumley, J., Berkooz, G., and Rowley, C. (2012). *Turbulence , Coherent Structures , Dynamical Systems and Symmetry*. Cambridge University Press, cambridge edition.

Hopf, E. (1948). A mathematical example displaying features of turbulence. *Communications on Pure and Applied Mathematics*, 1(4):303–322.

Huang, W. and Sloan, D. M. (1994). The Pseudospectral Method for Solving Differential Eigenvalue Problems. *Journal of Computational Physics*, 111(2):399–409.

Hunter, J. D. (2007). Matplotlib: A 2D Graphics Environment. *Computing in Science & Engineering*, 9(3):90–95.

IPCC (2014). Climate Change 2014: Synthesis Report. Contribution of Working Groups I, II and III to the Fifth Assessment Report of the Intergovernmental Panel on Climate Change [Core Writing Team, R.K. Pachauri and L.A. Meyer (eds.)]. Technical report, IPCC, Geneva, Switzerland.

IPCC (2018). Global Warming of 1.5C. An IPCC Special Report on the impacts of global warming of 1.5C above pre-industrial levels and related global greenhouse gas emission pathways. Technical report, World Meteorological Organization, Geneva, Switzerland.

Itano, T. and Generalis, S. C. (2009). Hairpin vortex solution in planar Couette flow: A tapestry of knotted vortices. *Physical Review Letters*, 102(11):1–4.

Itano, T. and Toh, S. (2001). The Dynamics of Bursting Process in Wall Turbulence. *Journal of the Physical Society of Japan*, 70(3):703–716.

Jaimoukha, I. M. and Kasenally, E. M. (1994).] and the Generalised Minimum Residual method (GMRES) [Saad and Schultz. Technical Report 1.

Jaimoukha, I. M. and Kasenally, E. M. (1995). Oblique projection methods for large scale model reduction. *SIAM J. Matrix Anal. Appl.*, 16(2):602–627.

Jbilou, K. (2003). Block Krylov subspace methods for large algebraic Riccati equations. *Numerical Algorithms*.

Jbilou, K. (2006). An Arnoldi based algorithm for large algebraic Riccati equations. *Applied Mathematics Letters*.

Jiménez, J. and Kawahara, G. (2013). Dynamics of Wall-Bounded Turbulence. *Ten Chapters in Turbulence*, pages 221–268.

Jiménez, J., Kawahara, G., Simens, M. P., Nagata, M., and Shiba, M. (2005). Characterization of near-wall turbulence in terms of equilibrium and "bursting" solutions. *Physics of Fluids*, 17(1):1–16.

Jones, B. L., Heins, P. H., Kerrigan, E. C., Morrison, J. F., and Sharma, A. S. (2015). Modelling for Robust Feedback Control of Fluid Flows. (Bushnell):1–35.

Joshi, S. S., Speyer, J. L., and Kim, J. (1997). A systems theory approach to the feedback stabilization of infinitesimal and finite-amplitude disturbances in plane Poiseuille flow. *Journal of Fluid Mechanics*, 332(1997):157–184.

Joslin, R. D. and Miller, D. N. (2009). *Fundamentals and Applications of Modern Flow Control*. American Institute of Aeronautics & Astronautics.

Jung, W. J., Mangiavacchi, N., and Akhavan, R. (1992). Suppression of turbulence in wallbounded flows by highfrequency spanwise oscillations. *Physics of Fluids A: Fluid Dynamics*, 4(8):1605–1607.

Kailath, T. (1973). Some new algorithms for recursive estimation in constant linear systems. *IEEE Transactions on Information Theory*, 19(6):750–760.

Kawahara, G. and Kida, S. (2001). Periodic motion embedded in plane Couette turbulence: regeneration cycle and burst. *Journal of Fluid Mechanics*, 449:291.

Kawahara, G., Uhlmann, M., and van Veen, L. (2012). The Significance of Simple Invariant Solutions in Turbulent Flows. *Annual Review of Fluid Mechanics*, 44(1):203–225.

Kawasaki, M. and Sasa, S.-i. (2005). Statistics of unstable periodic orbits of a chaotic dynamical system with a large number of degrees of freedom. *Physical Review E*, 72(3):37202.

Keefe, L. R., Moin, P., and Kim, J. (1992). The dimension of attractors underlying periodic turbulent Poiseuille flow. *Journal of Fluid Mechanics*, 242(January):1–29.

Kenney, C. and Leipnik, R. (1985). Numerical integration of the differential matrix Riccati equation. *IEEE Transactions on Automatic Control*, 30(10):962–970.

Kerswell, R. R. (2005). Recent progress in understanding the transition to turbulence in a pipe. *Nonlinearity*, 18:R17–R44.

Kim, J. and Bewley, T. R. (2007). A linear systems approach to flow control. *Annual Review of Fluid Mechanics*, 39:383–417.

Kim, J. and Lim, J. (2000). A linear process in wall-bounded turbulent shear flows. *Physics of Fluids*, 12(8):1885–1888.

Kim, J., Moin, P., and Moser, R. (1987). Turbulence statistics in fully developed channel flow at low Reynolds number. *Journal of Fluid Mechanics*, 177(-1):133.

Kline, S. J., Reynolds, W. C., Schraub, F. a., and Runstadler, P. W. (1967). The structure of turbulent boundary layers. *Journal of Fluid Mechanics*, 30(04):741.

Lainiotis, D. (1976). Generalized Chandrasekhar algorithms: Time-varying models. *IEEE Transactions on Automatic Control*, 21(5):728–732.

Lauga, E. and Bewley, T. R. (2003). The decay of stabilizability with Reynolds number in a linear model of spatially developing flows. *Proceedings of the Royal Society A: Mathematical, Physical and Engineering Sciences*, 459(2036):2077–2095.

Lee, K. H., Cortelezzi, L., Kim, J., and Speyer, J. (2001). Application of reduced-order controller to turbulent flows for drag reduction. *Physics of Fluids*, 13(5):1321–1330.

Lewis, S. L. and Maslin, M. A. (2015). Defining the Anthropocene. *Nature*, 519(7542):171–180.

Liepmann, H. W. (1952). Aspects of the turbulence problem. *ZAMP Zeitschrift für angewandte Mathematik und Physik*, 3(5):321–342.

Liepmann, H. W. and Nosenchuck, D. M. (1982). Active control of laminar-turbulent transition. *Journal of Fluid Mechanics*, 118(-1):201.

Lighthill, M. J. (1956). The Structure of Turbulent Shear Flow , by A. A. T OWNSEND . Cambridge University Press, 1956. 315 pp. 40 s . or $7.50. *Journal of Fluid Mechanics*, 1(5):554–560.

Liu, J. (1988). Contributions to the Understanding of Large-Scale Coherent Structures in Developing Free Turbulent Shear Flows. pages 183–309.

Luchini, P. and Bottaro, A. (2014). Adjoint Equations in Stability Analysis. *Annual Review of Fluid Mechanics*, 46(1):493–517.

Luo, L. and Schuster, E. (2009). Mixing enhancement in 2D magnetohydrodynamic channel flow by extremum seeking boundary control. In *2009 American Control Conference*, pages 1530–1535. IEEE.

Mårtensson, K. (2012). *Gradient Methods for Large-Scale and Distributed Linear Quadratic Control*. PhD thesis, Lund University.

Martinelli, F., Quadrio, M., McKernan, J., and Whidborne, J. F. (2011). Linear feedback control of transient energy growth and control performance limitations in subcritical plane Poiseuille flow. *Physics of Fluids*, 23(1).

Massei, S., Mazza, M., and Robol, L. (2019). Fast solvers for two-dimensional fractional diffusion equations using rank structured matrices. 2014:2016–2018.

Massei, S., Palitta, D., and Robol, L. (2018). Solving Rank-Structured Sylvester and Lyapunov Equations. *SIAM Journal on Matrix Analysis and Applications*, 39(4):1564–1590.

MATLAB (2013). *Eigenvalues and Singular Values (MATLAB tutorial)*.

McKeon, B. J. and Sharma, A. S. (2010). A critical-layer framework for turbulent pipe flow. *Journal of Fluid Mechanics*, 658(2010):336–382.

McKernan, J. (2006). *Control of plane poiseuille flow: a theoretical and computational investigation*. PhD thesis.

McKernan, J., Papadakis, G., and Whidborne, J. F. (2006). A linear state-space representation of plane Poiseuille flow for control design: a tutorial. *International Journal of Modelling, Identification and Control*, 1(4):272.

Meseguer, A. and Mellibovsky, F. (2007). On a solenoidal Fourier{\textendash}Chebyshev spectral method for stability analysis of the Hagen{\textendash}Poiseuille flow. *Appl. Numer. Math.*, 57(8):920–938.

Moore, B. (1981). Principal component analysis in linear systems: Controllability, observability, and model reduction. *IEEE Transactions on Automatic Control*, 26(1):17–32.

Nagata, M. (1990). Three-dimensional finite-amplitude solutions in plane Couette flow: bifurcation from infinity. *Journal of Fluid Mechanics*, 217:519–527.

Nagata, M. (1997). Three-dimensional traveling-wave solutions in plane Couette flow. *Physical Review E*, 55(2):2023–2025.

Newton, I. (1687). Philosophiae Naturalis Principia Mathematica. *Pan*, page 510.

Nouar, C., Bottaro, A., and Brancher, J. P. (2007). Delaying transition to turbulence in channel flow: revisiting the stability of shear-thinning fluids. *Journal of Fluid Mechanics*, 592:177–194.

Ogata, K. (2009). *Modern Control Engineering (fith edition)*. Prentice h edition.

Oreskes, N. (2004). The Scientific Consensus on Climate Change. *Science*, 306(5702):1686–1686.

Orr, W. M. (1907a). The stability or instability of the steady motions of a liquid. Part I. *Proceedings of the Royal Irish Academy*, A 27:9–68.

Orr, W. M. (1907b). The stability or instability of the steady motions of a liquid. Part II. *Proceedings of the Royal Irish Academy*, A 27:69–138.

Palitta, D. (2019). The projected Newton-Kleinman method for the algebraic Riccati equation. pages 1–25.

Peyret, R. (2002). *Spectral Methods for Incompressible Viscous Flow*, volume 148 of *Applied Mathematical Sciences*. Springer New York, New York, NY.

Powers, R. (1983). An application of Chandrasekhar-type algorithms for optimal control of delay-differential systems. *Proc. 15th IEEE Southeastern Symp. Syst. Theory*.

Pralits, J., Bewley, T., and Luchini, P. (2008). Feedback stabilization of the wake behind a steady cylinder. In *7th ERCOFTAC SIG33 - Flubio workshop on open issues in transition and flow control*.

Pralits, J. O. and Luchini, P. (2010). Riccati-less optimal control of bluff-body wakes. In *P. Schlatter and D.S. Henningson (eds.), Seventh IUTAM Symposium on Laminar-Turbulent Transition, IUTAM Bookseries 18*, number November 2010, pages 325–330.

Press, W. H., Flannery, B. P., Teukolsky, S. A., and Vetterling, W. T. (2007). *Numerical Recipes: The Art of Scientific Computing (third edition)*.

Pringle, C. C. T. and Kerswell, R. R. (2007). Asymmetric, Helical, and Mirror-Symmetric Traveling Waves in Pipe Flow. *Physical Review Letters*, 99(7):074502.

Reddy, S. C. and Henningson, D. S. (1993). Energy growth in viscous channel flows. *Journal of Fluid Mechanics*, 252(April 2006):209.

Reetz, F., Kreilos, T., and Schneider, T. M. (2019). Exact invariant solution reveals the origin of self-organized oblique turbulent-laminar stripes. *Nature Communications*, 10(1):2277.

Reguera, Bonilla, and Rubi (2000). *Coherent Structures in Complex Systems*. spain barcelona.

Ricco, P., Ottonelli, C., Hasegawa, Y., and Quadrio, M. (2012). Changes in turbulent dissipation in a channel flow with oscillating walls. *Journal of Fluid Mechanics*, 700(February):77–104.

Robinson, S. K. (1991). Coherent Motions in the Turbulence Boundary Layer. *Annual Reviews of Fluid Mechanics*, 23:601–639.

Romanov, V. A. (1973). Stability of plane-parallel Couette flow. *Functional Analysis and Its Applications*, 7(2):137–146.

Rosenzweig, C., Karoly, D., Vicarelli, M., Neofotis, P., Wu, Q., Casassa, G., Menzel, A., Root, T. L., Estrella, N., Seguin, B., Tryjanowski, P., Liu, C., Rawlins, S., and Imeson, A. (2008). Attributing physical and biological impacts to anthropogenic climate change. *Nature*, 453(7193):353–357.

Rowley, C. W. (2005). Model Reduction for Fluids, Using Balanced Proper Orthogonal Decomposition. *International Journal of Bifurcation & Chaos*, 15(3):997–1013.

Rowley, C. W., Mezić, I., Bagheri, S., Schlatter, P., and Henningson, D. S. (2009). Spectral analysis of nonlinear flows. *Journal of Fluid Mechanics*, 641(Rowley 2005):115.

Ruhe, A. (1984). Rational Krylov sequence methods for eigenvalue computation. *Linear Algebra and its Applications*, 58:391–405.

Saad, Y. (1990). Numerical Solution of Large Lyapunov Equations. (1).

Saiki, Y. and Yamada, M. (2008). Time averaged properties along unstable periodic orbits and chaotic orbits in two map systems. *Nonlinear Processes in Geophysics*, 15(4):675–680.

Schlichting, D. H. and Gersten, K. (1979). Boundary-layer theory. *European Journal of Mechanics - B/Fluids*, 20:817.

Schmid, P. J. (2010). Dynamic mode decomposition of numerical and experimental data. *Journal of Fluid Mechanics*, 656(November):5–28.

Schmid, P. J. and Henningson, D. S. (2001). *Stability and Transition in Shear Flows*.

Schmiegel, A. (1999). *Transition to turbulence in linearly stable shear flows*. PhD thesis, Philipps-Universitat Marburg.

Schuster, E., Luo, L., and Krstić, M. (2008). MHD channel flow control in 2D: Mixing enhancement by boundary feedback. *Automatica*, 44(10):2498–2507.

Semeraro, O. and Pralits, J. O. (2017). Full-order optimal compensators for flow control: the multi-input case. *eprint arXiv:1701.08403*.

Semeraro, O., Pralits, J. O., Rowley, C. W., and Henningson, D. S. (2013). Riccati-less approach for optimal control and estimation: an application to two-dimensional boundary layers. *Journal of Fluid Mechanics*, 731:394–417.

Sharma, A. S., Mezić, I., and McKeon, B. J. (2016). On the correspondence between Koopman mode decomposition, resolvent mode decomposition, and invariant solutions of the Navier-Stokes equations.

Sharma, A. S., Morrison, J. F., McKeon, B. J., Limebeer, D. J. N., Koberg, W. H., and Sherwin, S. J. (2011). Relaminarisation of Re(tau) = 100 channel flow with globally stabilising linear feedback control. *Physics of Fluids*, 23(12).

Shewchuk, J. R. (1994). An Introduction to the Conjugate Gradient Method Without the Agonizing Pain.

Simoncini, V. (2007). A New Iterative Method for Solving Large-Scale Lyapunov Matrix Equations. *SIAM Journal on Scientific Computing*, 29(3):1268–1288.

Simoncini, V. (2016). Analysis of the Rational Krylov Subspace Projection Method for Large-Scale Algebraic Riccati Equations. *SIAM Journal on Matrix Analysis and Applications*.

Simoncini, V., Szyld, D. B., and Monsalve, M. (2014). On two numerical methods for the solution of large-scale algebraic Riccati equations. *IMA Journal of Numerical Analysis*.

Smits, A. J. and Delo, C. (2001). Self-Sustaining Mechanisms of Wall Turbulence. In Panton, R., editor, *Reguera D., Rubí J.M., Bonilla L.L. (eds) Coherent Structures in Complex Systems. Lecture Notes in Physics, vol 567. Springer, Berlin, Heidelberg*, volume 37, pages 17–38.

Sommerfeld, A. (1908). Ein Beitrag zur hydrodynamische Erklärung der turbulenten Flüssigkeitsbewegungen. *Proceedings of the 4th International Congress of Mathematicians*, III. Rome:116–124.

Strogatz, S. H. (2018). *Nonlinear Dynamics and Chaos*. CRC Press.

Szoke, M. and Azarpeyvand, M. (2017). Active Flow Control Methods for the Reduction of Trailing Edge Noise. In *23rd AIAA/CEAS Aeroacoustics Conference*, Reston, Virginia. American Institute of Aeronautics and Astronautics.

Tillmark, N. and Alfredsson, P. H. (1992). Experiments on transition in plane Couette flow. *Journal of Fluid Mechanics*, 235(-1):89.

Trefethen, L. N., Trefethen, A. E., Reddy, S. C., and Driscoll, T. A. (1993). Hydrodynamic stability without eigenvalues. *Science*, 261(5121):578–584.

Tu, J. H., Rowley, C. W., Luchtenburg, D. M., Brunton, S. L., and Kutz, J. N. (2014). On dynamic mode decomposition: Theory and applications. *Journal of Computational Dynamics*, 1(2):391–421.

Viswanath, D. (2007). Recurrent motions within plane Couette turbulence. *Journal of Fluid Mechanics*, 580:339–358.

Waleffe, F. (1995). Transition in shear flows. Nonlinear normality versus non-normal linearity. *Physics of Fluids*, 7:3060.

Waleffe, F. (1997). On a self-sustaining process in shear flows. *Physics of Fluids*, 9(June 1996):883.

Waleffe, F. (1998). Three-Dimensional Coherent States in Plane Shear Flows. *Physical Review Letters*, 81(19):4140–4143.

Waleffe, F. (2001). Exact coherent structures in channel flow. *Journal of Fluid Mechanics*, 435(June 2001):93–102.

Waleffe, F. (2003). Homotopy of exact coherent structures in plane shear flows. *Physics of Fluids*, 15(6):1517–1534.

Wang, J. and Feng, L. (2018). *Flow Control Techniques and Applications*. Cambridge University Press.

Wedin, H. and Kerswell, R. R. (2004). Exact coherent structures in pipe flow: travelling wave solutions. *Journal of Fluid Mechanics*, 508:333–371.

Weideman, J. a. C. and Reddy, S. C. (2000). A MATLAB differentiation matrix suite. *ACM Transactions on Mathematical Software*, 26(4):465–519.

Wygnanski, I., Sokolov, M., and Friedman, D. (1975). On transition in a pipe. Part 2. The equilibrium puff. *Journal of Fluid Mechanics*, 69(2):283–304.

Wygnanski, I. J. and Champagne, F. H. (1973). On transition in a pipe. Part 1. The origin of puffs and slugs and the flow in a turbulent slug. *Journal of Fluid Mechanics*, 59(2):281–335.

Zill, D. G. (2017). *A First Course in Differential Equations with Modeling Applications*. Cengage Learning, 11th edition.

Online sources

[web1] calltech.edu (2000). An internet book on fluid dynamics — lagrangian and eulerian time derivatives. http://www.brennen.caltech.edu/fluidbook/basicfluiddynamics/descriptions/accelerations.pdf. [Online; accessed 30-December-2019].

[web2] Foundation, P. S. (2015). Python: A dynamic, open source programming language. https://www.python.org/. [Online; accessed 1-January-2020].

[web3] ISO (2011). *ISO/IEC 14882:2011 Information technology — Programming languages — C++*. Third edition.

[web4] Jones, E., Oliphant, T., Peterson, P., et al. (2001). SciPy: Open source scientific tools for Python. [Online; accessed 1-January-2020].

[web5] Oliphant, T. (2006). NumPy: A guide to NumPy. USA: Trelgol Publishing. [Online; accessed 1-January-2020].

[web6] Origlio, Vincenzo (1999). Stochastic — MathWorld, a wolfram web resource, created by eric w. weisstein. http://mathworld.wolfram.com/Stochastic.html. [Online; accessed 30-December-2019].

[web7] Weisstein, Eric W. (1999). Bounded — MathWorld, a wolfram web resource. http://mathworld.wolfram.com/Bounded.html. [Online; accessed 30-December-2019].

[web8] Wikipedia contributors (2011a). Algebraic equation — Wikipedia, the free encyclopedia. https://en.wikipedia.org/wiki/Algebraic_equation. [Online; accessed 30-December-2019].

[web9] Wikipedia contributors (2011b). Cauchy momentum equation — Wikipedia, the free encyclopedia. https://en.wikipedia.org/wiki/Cauchy_momentum_equation. [Online; accessed 30-December-2019].

[web10] Wikipedia contributors (2011c). Causal system — Wikipedia, the free encyclopedia. https://en.wikipedia.org/wiki/Causal_system. [Online; accessed 30-December-2019].

[web11] Wikipedia contributors (2011d). Derivation of the navier-stokes equations — Wikipedia, the free encyclopedia. https://en.wikipedia.org/wiki/Derivation_of_the_Navier%E2%80%93Stokes_equations. [Online; accessed 30-December-2019].

[web12] Wikipedia contributors (2011e). Differential equation — Wikipedia, the free encyclopedia. https://en.wikipedia.org/wiki/Differential_equation. [Online; accessed 30-December-2019].

[web13] Wikipedia contributors (2011f). Expected value — Wikipedia, the free encyclopedia. https://en.wikipedia.org/wiki/Expected_value. [Online; accessed 30-December-2019].

[web14] Wikipedia contributors (2011g). Gaussian function — Wikipedia, the free encyclopedia. https://en.wikipedia.org/wiki/Gaussian_function. [Online; accessed 30-December-2019].

[web15] Wikipedia contributors (2011h). Homogeneous function — Wikipedia, the free encyclopedia. https://en.wikipedia.org/wiki/Homogeneous_function. [Online; accessed 30-December-2019].

[web16] Wikipedia contributors (2011i). Memorylessness — Wikipedia, the free encyclopedia. https://en.wikipedia.org/wiki/Memorylessness. [Online; accessed 30-December-2019].

[web17] Wikipedia contributors (2011j). Newtonian fluid — Wikipedia, the free encyclopedia. https://en.wikipedia.org/wiki/Newtonian_fluid. [Online; accessed 30-December-2019].

[web18] Wikipedia contributors (2011k). Partial differential algebraic equation — Wikipedia, the free encyclopedia. https://en.wikipedia.org/wiki/Partial_differential_algebraic_equation. [Online; accessed 30-December-2019].

[web19] Wikipedia contributors (2011l). Wikipedia, the free encyclopedia. https://en.wikipedia.org. [Online; accessed 30-December-2019].